

Heteropolyacids accelerated multi-component synthesis of *N*-phenylquinazolin-4-amines by using silica-supported Preyssler nanoparticles in green solvent

A. Gharib^{1,2,*}, N. Noroozi Pesyan³, M. Jahangir¹, M. Roshani¹, J. (Hans) W. Scheeren⁴, L. Bakhtiari², S. Mohadeszadeh², Sh. Lagzian², S. Ahmadi²

¹Department of Chemistry, Islamic Azad University, Mashhad, IRAN

²Agricultural Researches and Services Center, Mashhad, IRAN

³Department of Chemistry, Faculty of Science, Urmia University, 57159, Urmia, IRAN

⁴Cluster for Molecular Chemistry, Department of Organic Chemistry, Radboud University Nijmegen, The Netherlands

Received: April 17, 2012; revised: January 22, 2013

N-phenylquinazolin-4-amines derivatives were obtained in high yields with excellent purity from the reaction of 2-aminobenzamide, orthoesters, and substituted anilines in the presence of Silica-Supported Preyssler Nanoparticles and various heteropolyacids (HPAs).

Keywords: Silica-Supported Preyssler Nanoparticles (SPNP), *N*-phenylquinazolin-4-amines; Recyclable catalysts; Heteropolyacids; Multi-component; Green.

INTRODUCTION

In recent years, multicomponent reactions (MCRs) have become important tools in modern preparative synthetic chemistry because these reactions increase the efficiency by combining several operational steps without any isolation of intermediates or change of the conditions [1] and MCRs have recently emerged as valuable tools in the preparation of structurally diverse chemical libraries of drug-like heterocyclic compounds [2]. They showed various applications in organic, medicinal chemistry [3] and in drug discovery as well as 'green chemistry' [4]. On the other hand heteropolyacid (HPA) has been successfully employed as a heterogeneous catalyst in organic synthesis [5]. They are noncorrosive and are environmentally benign, as they can be reused and recycled [6]. Owing to all these characteristic features of multicomponent reaction and heteropolyacid, heterogeneous systems show great potential since the use of toxic solvent is drastically reduced, the chemo selectivity and atom-efficiency are often improved, the product isolation is simplified, and the volume of waste is significantly reduced. Over the last decade, due to the unique properties of nanoparticles along with their novel properties and potential applications in different fields [7] the synthesis and characterization of catalysts with lower dimension has become an

active topic of research. Moreover, due to quantum size effects, nanometresized particles may exhibit unique properties for a wide range of applications [8]. Along this line, polyoxometalates (POMs) are attracting much attention as building blocks for functional composite materials because of their interesting nanosized structures [9]. In recent years, considerable effort has been devoted to the design and controlled fabrication of nanostructured POMs for using in green reactions. This interest has resulted in the development of numerous protocols for the synthesis of nanostructured materials over a range of sizes. Therefore the field of nano POMs and their applications continue to attract significant attention, so the number of publications and patents continue to grow, and new researchers are entering the field. However, in spite of extensive investigations on synthesis and characterization of Keggin-type nanocatalysts [10], the synthesis of sodium 30-tungstophosphate nanocatalysts has been largely overlooked. The catalyst consists of an anion with a formula of $[\text{NaP}_5\text{W}_{30}\text{O}_{110}]^{14-}$ which has an unusual five-fold symmetry achieved by fusion of five $\{\text{PW}_6\text{O}_{22}\}$ groups. The central sodium ion lies not on the equator of the anion but in a plane roughly defined by oxygen atoms of the phosphate groups. The presence of the sodium cation reduces the overall anion symmetry from D_{5h} to C_{5v} [11].

Natural and synthetic compounds possessing the quinazoline structural motif display a wide range of biological activities. Recently, quinazolin-4(3*H*)-

* To whom all correspondence should be sent:
E-mail: aligharib5@yahoo.com

ones were prepared via cyclocondensation of 2-aminobenzamides with orthoesters catalyzed by H_2SO_4/SiO_2 under anhydrous and microwave conditions [12]. In other work, quinazolin-4(3*H*)-one and quinazolin-2,4-dione derivatives were obtained under microwave irradiation [13]. There has been renewed interest in *N*-phenylquinazolin-4-amines connected with reports on the very high activity of 6,7-dimethoxy-4-(3-bromophenylamino)quinazoline (PD 153035) as a tyrosine kinase inhibitor [14]. Analogues of PD 153035 with more complex structures [15] as well as simple derivatives of 4-phenylaminoquinazoline without, for example, methoxy groups [16], also show interesting biological activity. Despite their biological activities, no recent progress on their syntheses has been made. *N*-phenylquinazolin-4-amines can be obtained via reactions of 4-halo- or 4-mercaptoquinazolines with aromatic amines [17]; however, the yields of these reactions do not usually [18] exceed 50%. *N*-phenylquinazolin-4-amines have also been produced by reactions of 4(3*H*)-quinazolone with aromatic amine hydrochlorides in the presence of phosphorus pentoxide and dimethylcyclohexylamine [19]. 4-Phenylaminoquinazoline was obtained by desulfurization of 4-phenylaminoquinazol-2-thione using Raney nickel W7 [20]. In addition to the reactions mentioned above, *N*-phenylquinazolin-4-amines have been obtained by the reaction of 2-aminobenzonitrile and various anilines in the presence of $AlCl_3$, and by subsequent condensation of the products with formic acid [21]. The drawback of this method is that the synthesis of 2-amino-*N*-aryl-benzamides is limited by the substituents on the anilines. Since the pathogenesis of allergic diseases is associated with elevated levels of immunoglobulin E (IgE), Berger et al, developed a high throughput reporter gene assay in a human B-cell line to screen for low molecular weight IgE inhibitory compounds. Monitoring the IL-4 driven IgE-germline promoter activity (IgE-GLP) [22]. Quinoline, isoquinoline, quinoxaline, and quinazoline derivatives were synthesized using microwave-assisted synthesis and their CB1/CB2 receptor activities were determined using the [^{35}S]GTP γ S binding assay. Most of the prepared quinoline, isoquinoline, and quinoxalanyl phenyl amines showed low-potency partial CB2 receptor agonists activity [23]. An efficient "one-step" synthesis of cyclic amidines and guanidines has been developed. Treatment of cyclic amides and ureas with benzotriazol-1-yloxytris (dimethylamino) phosphonium hexafluorophosphate (BOP), base, and nitrogen nucleophiles leads to the

formation of the corresponding cyclic amidines and guanidines, typically in good to excellent yields. This method has also been used to prepare heteroaryl ethers and thioethers using phenol and thiophenol nucleophiles. [24]. A new multi-component synthesis of 4-arylaminoquinazolines from the reaction of 2-aminobenzamide, orthoesters and substituted anilines in presence of catalytic amounts of sodium 30-tungstophosphate, so-called Preyssler heteropolyacid, is reported [25]. Also, some 4-*N*-(3'- or 4'-substituted-phenyl)amino-6,7-dimethoxyquinazolines and the corresponding unsubstituted compounds were synthesized from 2-amino-4,5-dimethoxybenzoic acid and the appropriate substituted anilines [26].

EXPERIMENTAL

Chemicals and Apparatus

All the chemicals were obtained from Merck Company and used as received. The melting points were obtained using an Electrothermal IA 9100 digital melting point apparatus. The IR spectra were recorded on a Bruker (4000–400 cm^{-1}) spectrometer. 1H NMR spectra were recorded on a 400 MHz spectrometer using TMS as internal standard (in most spectra trimethylsilane (TMS) is used to reference the signal to a zero (0.00) and all other signals are relative to this standard).

Catalyst Preparation

Heteropolyacid Preyssler was prepared according to the procedure reported before [29-31]. Supported heteropolyacid catalysts were prepared by impregnating a support in the form of powder (nano SiO_2) with an aqueous solution of the heteropolyacid with different concentrations. Samples were dried at 120-140°C, and the catalysts were calcined at 220°C in a furnace prior to use. $H_{14}[NaP_5W_{30}O_{110}]/SiO_2$ nanoparticles, $H_4[PMo_{11}VO_{40}]$, $H_5[PMo_{10}V_2O_{40}]$, $H_6[PMo_9V_3O_{40}]$, $H_{14}[NaP_5W_{30}O_{110}]/SiO_2(40\%)$, $H_3[PMo_{12}O_{40}]/SiO_2(40\%)$, $H_4[PMo_{11}VO_{40}]/SiO_2(40\%)$, and $H_3[PW_{12}O_{40}]/SiO_2(40\%)$ and $H_3[PMo_{12}O_{40}]$ were prepared according to reports in the literature [29, 30]. Melting points were measured using Barnstead Electro thermal. Yields are based on GC/mass analysis using an Agilent 6890 GC system Hp-5 capillary 30 m \times 530 μm \times 1.5 μm nominal.

General Procedure

Synthesis of *N*-phenylquinazolin-4-amine derivatives from the reaction of 2-aminobenzamide, orthoester (trimethoxymethane) with substituted aniline:

A mixture of 2-aminobenzamide (10 mmol), orthoester (10 mmol), and substituted aniline (15 mmol) and heteropolyacid (0.03 mmol) was refluxed in proper solvent (10 mL). The progress of the reaction was monitored by TLC and GC. After completion of the reaction, the catalyst was filtered off. The pure products were obtained by column chromatography. All products were identified by comparison of their physical and spectroscopic data with those reported for authentic samples [21, 24].

Selected spectral data

N-phenylquinazolin-4-amine (**3a**): mp: 220 °C, ¹H-NMR (400 MHz, DMSO-*d*₆, δ/ppm): 9.15 (s, 1H, NH), 8.67 (s, 1H, CH=N), 7.44 (m, 5H), 7.76 (m, 4H); ¹³C-NMR (400 MHz, DMSO-*d*₆, δ/ppm): 169.6 (C-1), 156.4 (C-2), 149.9 (C-3), 140.8 (C-4), 132.2 (C-5), 129.5 (C-6), 128.6 (C-7), 127.8 (C-8), 126.5 (C-9), 122.5 (C-10), 117.9, 116.7. IR (KBr, cm⁻¹): 3325, 1604; Anal. Calc. for C₁₄H₁₁N₃: C, 76.00; H, 5.02; N, 18.99%. Found: C, 75.93; H, 4.98; N, 18.96%. HRMS (EI) Calcd. for C₁₄H₁₁N₃ [M]⁺, 221.1005, Found 221.1008;

N-*p*-tolylquinazolin-4-amine (**3e**): Mp: 192 °C, ¹H-NMR (400 MHz, DMSO-*d*₆, δ/ppm): 9.15 (s, 1H, NH), 8.65 (s, 1H, CH=N), 7.22 (m, 4H), 7.80 (m, 4H), 2.31 (s, 3H, CH₃); ¹³C-NMR (400 MHz, DMSO-*d*₆, δ/ppm): 169.6 (C-1), 156.4 (C-2), 149.7 (C-3), 137.9 (C-4), 132.3 (C-5), 131.5 (C-6), 132.1 (C-7), 129.8 (C-8), 128.8 (C-9), 127.5 (C-10), 127.8 (C-10), 126.6 (C-11), 120.5 (C-11), 116.6 (C-12). IR (KBr, cm⁻¹): 3327, 1602; MS: m/z 235 [M⁺]. HRMS (EI) Calcd. for C₁₅H₁₃N₃ [M]⁺, 235.1002, Found 235.1004; Anal. Calc. for C₁₅H₁₃N₃: C, 76.57; H, 5.57; N, 17.86%. Found: C, 76.53; H, 5.51; N, 17.85%.

N-(4-nitrophenyl)quinazolin-4-amine (**3g**): Mp: 212 °C, ¹H-NMR (400 MHz, DMSO-*d*₆, δ/ppm): 9.20 (s, 1H, NH), 8.45 (s, 1H, CH=N), 8.11 (t, 1H, CH), 7.78 (m, 4H), 7.55 (m, 4H); ¹³C-NMR (400 MHz, DMSO-*d*₆, δ/ppm): 169.7 (C-1), 156.2 (C-2), 149.8 (C-3), 147 (C-4), 137.9 (C-5), 132.1 (C-6), 131.5 (C-7), 128.8 (C-8), 127.7 (C-9), 126.5 (C-10), 124.6 (C-11), 119.1 (C-12), 116.3 (C-12). IR

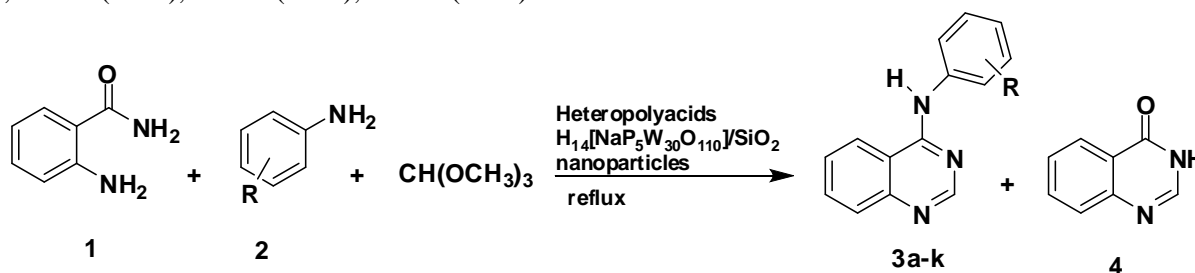
(KBr, cm⁻¹): 3320, 1552, 1350; MS: m/z 266 [M⁺]. HRMS (EI) Calcd. for C₁₄H₁₀N₄O₂ [M]⁺, 266.1001, Found 266.1003; Anal. Calc. for C₁₄H₁₀N₄O₂: C, 63.17; H, 3.79; N, 21.05%. Found: C, 63.43; H, 3.84; N, 21.23%.

N-(2-nitrophenyl)quinazolin-4-amine (**3h**): Mp: 219 °C, ¹H-NMR (400 MHz, DMSO-*d*₆, δ/ppm): 9.40 (s, 1H, C-NH), 8.46 (s, 1H, CH=N), 8.20 (t, 1H, CH), 7.80 (m, 4H), 7.57 (m, 4H); ¹³C-NMR (400 MHz, DMSO-*d*₆, δ/ppm): 169.7 (C-1), 156.2 (C-2), 149.8 (C-3), 147 (C-4), 137.9 (C-5), 132.2 (C-6), 128.7 (C-7), 127.9 (C-8), 126.5 (C-9), 125.6 (C-10), 119.5 (C-11), 116.1 (C-12), 110.4 (C-12). IR (KBr, cm⁻¹): 3322, 1585, 1364; MS: m/z 266 [M⁺]. HRMS (EI) Calcd. for C₁₄H₁₀N₄O₂ [M]⁺, 266.1001, Found 266.1003; Anal. Calc. for C₁₄H₁₀N₄O₂: C, 63.17; H, 3.79; N, 21.05%. Found: C, 63.43; H, 3.84; N, 21.23%.

N-(2-methoxyphenyl)quinazolin-4-amine (**3i**): Mp: 208 °C, ¹H-NMR (400 MHz, DMSO-*d*₆, δ/ppm): 9.40 (s, 1H, NH), 8.48 (s, 1H, CH=N), 8.12 (t, 1H, CH), 7.82 (m, 4H), 7.57 (m, 4H); ¹³C-NMR (400 MHz, DMSO-*d*₆, δ/ppm): 169.8 (C-1), 156.1 (C-2), 149.9 (C-3), 147.2 (C-4), 137.9 (C-4), 132.7 (C-5), 132.1 (C-6), 128.8 (C-7), 127.6 (C-8), 126.6 (C-9), 122.6 (C-10), 121.7 (C-11), 116.3 (C-12). IR (KBr, cm⁻¹): 3329, 1288; MS: m/z 251 [M⁺]. HRMS (EI) Calcd. for C₁₅H₁₃N₃O [M]⁺, 266.1001, Found 266.1003; Anal. Calc. for C₁₅H₁₃N₃O: C, 71.70; H, 5.21; N, 16.72%. Found: C, 71.65; H, 5.15; N, 16.79%.

RESULTS AND DISCUSSION

Herein we wish to report a simple method for the synthesis of *N*-phenylquinazolin-4-amine derivatives from reaction of 2-aminobenzamide, orthoesters, and various substituted anilines using silica-supported Preyssler nanoparticles, H₁₄[NaP₅W₃₀O₁₁₀]/SiO₂ and three different Keggin types of HPAs including, H₅[PMo₁₀V₂O₄₀], H₄[PMo₁₁VO₄₀] and H₃[PMo₁₂O₄₀] as the catalysts (Scheme 1).



Scheme 1. Synthesis of *N*-phenylquinazolin-4-amine derivatives using Preyssler nanoparticles, H₁₄[NaP₅W₃₀O₁₁₀]/SiO₂

In connection with our program of using heteropolyacid in organic reactions [27], we wish to report the result of a study on the use of silica-supported Preyssler nanoparticles, $H_{14}[NaP_5W_{30}O_{110}]/SiO_2$ and three Keggin types of HPAs including $H_4[PMo_{11}VO_{40}]$, $H_5[PMo_{10}V_2O_{40}]$ and $H_3[PMo_{12}O_{40}]$ in the synthesis *N*-phenylquinazolin-4-amine derivatives and the effects of reaction parameters such as the type, amount of HPA and solvent on the yield of reaction. The results of synthesis of *N*-phenylquinazolin-4-amines from reaction of 2-aminobenzamide, orthoesters, and various anilines using $H_{14}[NaP_5W_{30}O_{110}]/SiO_2$ nanoparticles are summarized in Table 1. In all the reactions, 3-quinazolin-4-one, 4, was obtained as a byproduct in low yield (Scheme 1). To investigate the effect of silica-supported Preyssler nanoparticles, we carried out comparative experiments with some silica-gel-supported heteropolyacids, and the comparative results are summarized in Table 2.

Comparison of silica-supported Preyssler nanoparticles, $H_{14}[NaP_5W_{30}O_{110}]/SiO_2$, $H_3[PMo_{12}O_{40}]$, $H_5[PMo_{10}V_2O_{40}]$, $H_4[PMo_{11}VO_{40}]$, $H_6[PMo_9V_3O_{40}]$, $H_3[PW_{12}O_{40}]$, $H_{14}[NaP_5W_{30}O_{110}]/SiO_2(40\%)$, $H_3[PMo_{12}O_{40}]/SiO_2(40\%)$, $H_4[PMo_{11}VO_{40}]/SiO_2(40\%)$, and $H_3[PW_{12}O_{40}]/SiO_2(40\%)$ shows that silica-supported Preyssler nanoparticles led to greater yields.

Silica nanostructures were obtained through a sol-gel method. All of the conditions are shown in the experimental section. The BET surface area, pore volume, and average pore size of nanosized SiO_2 were obtained as $287\text{ m}^2/\text{g}$, $0.28\text{ cm}^3/\text{g}$, and 0.25 nm , respectively. After the impregnation of HPA (with 30% being the best loading), the BET surface area, pore volume, and average pore size were obtained as $201\text{ m}^2/\text{g}$, $0.10\text{ cm}^3/\text{g}$, and 0.21 nm , respectively. The BET surface area and pore volume decreased, indicating that the pores of nanosized silica are being filled and the supported HPA blocked some pores of the support. The obtained nano structures were characterized by TEM as shown in Fig. 1. This figure shows 40 nm spheres. The XRD pattern of nano- SiO_2 with sharp peaks in the 2θ range from 7° to 36° confirmed the crystalline nature of SiO_2 . In addition, lack of an XRD peak centered at 2θ angle 22° (typical for amorphous SiO_2) confirmed the crystallinity. The patterns of the spherical products confirm the SiO_2 structure.

The synthesis of *N*-phenylquinazolin-4-amine derivatives show that reaction of 2-

aminobenzamide, orthoesters, and various anilines using heteropolyacids under refluxing conditions leads to better yields and anilines with electron-donating groups gave slightly better yields than anilines with electron-withdrawing groups. The synthesis of *N*-phenylquinazolin-4-amine derivatives from the reaction of 2-aminobenzamide, orthoesters, and various anilines using silica-supported Preyssler nanoparticles, $H_{14}[NaP_5W_{30}O_{110}]/SiO_2$ as catalyst was selected as a model reaction. The results are summarized in Tables 1 and 2. As shown in this table the sever condition is required for synthesis of *N*-phenylquinazolin-4-amine derivatives from the reaction of 2-aminobenzamide, orthoesters, and various anilines.

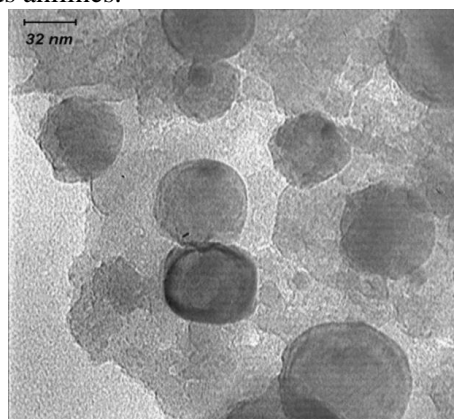
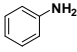
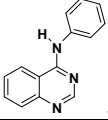
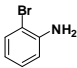
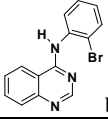
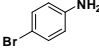
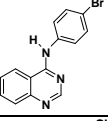
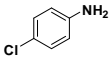
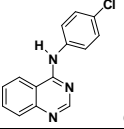
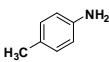
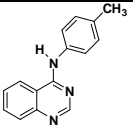
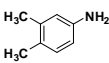
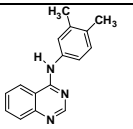
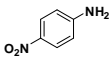
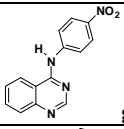
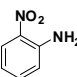
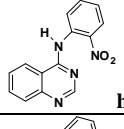
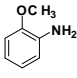
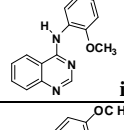
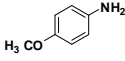
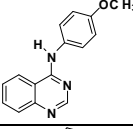
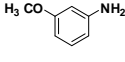
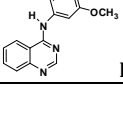


Fig. 1. TEM image of the synthesized nano- SiO_2 .

The efficiency of silica-supported Preyssler nanoparticles, $H_{14}[NaP_5W_{30}O_{110}]/SiO_2$, $H_3[PMo_{12}O_{40}]$, $H_4[PMo_{11}VO_{40}]$, $H_5[PMo_{10}V_2O_{40}]$, $H_6[PMo_9V_3O_{40}]$, $H_3[PW_{12}O_{40}]$, $H_3[PMo_{12}O_{40}]/SiO_2(50\%)$, $H_4[PMo_{11}VO_{40}]/SiO_2(50\%)$, and $H_3[PW_{12}O_{40}]/SiO_2(50\%)$ were also studied. Among silica-supported Preyssler nanoparticles, $H_{14}[NaP_5W_{30}O_{110}]/SiO_2$ and the Keggin heteropolyacids, $H_3[PMo_{12}O_{40}]$ and Keggin-type vanadium-substituted heteropolymolybdates: silica-supported Preyssler nanoparticles, $H_{14}[NaP_5W_{30}O_{110}]/SiO_2$, $H_4[PMo_{11}VO_{40}]$ and $H_5[PMo_{10}V_2O_{40}]$, the last one gave the best results in the reactions. The Keggin anions have an assembly of 12 corner-shared octahedral MoO_6 from trimetallic groups $[Mo_3O_{13}]$ around a heteroatom tetrahedron PO_4 . The introduction of vanadium (V) into the Keggin framework of $[PMo_{12}O_{40}]^{3-}$ is beneficial for catalysis reactions. Usually positional isomers are possible and coexist when two or more vanadium atoms are incorporated into the Keggin structure. Studies on these isomers in catalytic reactions indicate that

Table 1. Synthesis of various *N*-phenylquinazolin-4-amine derivatives in the presence of silica-supported Preyssler nanoparticles, H₁₄[NaP₅W₃₀O₁₁₀]/SiO₂ and under reflux conditions in water (as green solvent) for 1.5 hours.

Entry	Aniline	Product (3)	^a Yield (%)	Mp (°C)	
				Found	Reported(lit. 13)
1		 a	93.5	219-220	220-221
2		 b	85	130-131	131-132
3		 c	88.5	190-191	189-190
4		 d	90.5	193-194	194-195
5		 e	93	192-194	191-193
6		 f	96.5	196-197	196.5-198
7		 g	87.5	185-187	-
8		 h	85.5	181-183	-
9		 i	97.5	177-178	-
10		 j	98	174-175	165 [28]
11		 k	91.5	171-173	170-172 [22]

^aYields isolated.

different isomers cause different reactivities to show. With respect to the catalytic performances for these catalysts and the overall effects of all isomers, for synthesizing them, we cannot control the reaction conditions for the synthesis of positional vanadium-substituted isomers separately, revealing the relationship between the structures of H_{3+x}PMo_{12-x}V_xO₄₀ ($x = 1, 2, 3$) and hence study of

their catalytic activity is difficult. The abundance of different isomers may also play an important role in catalytic performance. In addition, different positional Mo atom(s) substituted by the V atom(s) in [PMo₁₂O₄₀]³⁻ may create different vanadium chemical environments, thus causing these catalysts to exhibit varying catalytic performances. The introduction of vanadium (V) into the Keggin

framework is beneficial for redox catalysis, shifting its reactivity from acid-dominated to redox-dominated. In addition the amount of introduced vanadium (V) has a dramatic effect on the yields. One of the difficulties encountered in interpreting data obtained from reactions of vanado-molybdophosphate anions is that in solution, a mixture of heteropoly anions are usually present. In addition positional isomers of the polyvanadium anions are also apparent. Another complication inherent in the study of multielectron oxidations by polyvanadium-containing anions is the capacity of these oxidants to be reduced by one or more electrons (reduction of each V(V) ion to V(IV)). However it is difficult to clarify the different activities between these catalysts in this reaction. We believe there is a complex relationship between the activity and structure of polyanion. Transition metal cations have an important effect on the catalytic properties of these compounds when they substitute molybdenum cations in the Keggin units.

Table 2. Comparative study of various heteropolyacids catalysts for the preparation of *N*-phenylquinazolin-4-amine (**3a**) under reflux conditions.

Entry	Catalyst	Time (h)	^a Yield (%)
1	H ₁₄ [NaP ₅ W ₃₀ O ₁₁₀]/SiO ₂ Nanoparticles	1.5	93.5
2	H ₁₄ [NaP ₅ W ₃₀ O ₁₁₀]/SiO ₂ (40%)	1.5	90.5
3	H ₅ [PMo ₁₂ O ₄₀]	3	81
4	H ₄ [PMo ₁₁ VO ₄₀]	3	84
5	H ₅ [PMo ₁₀ V ₂ O ₄₀]	3	85.5
6	H ₆ [PMo ₉ V ₃ O ₄₀]	2	89
7	H ₃ [PW ₁₂ O ₄₀]	3	82.5
8	H ₃ [PMo ₁₂ O ₄₀]/SiO ₂ (40%)	3	80
9	H ₄ [PMo ₁₁ VO ₄₀]/SiO ₂ (40%),	3	82.5
10	H ₃ [PW ₁₂ O ₄₀]/SiO ₂ (40%)	3	81

^aYields isolated.

The case of vanadium, which can occupy both anionic and cationic positions, is more complex. It is suggested that the interactions of the polarized polyanion with substrate and the number of vanadium atoms are important factors in catalytic activity in our reaction.

Selection of the solvent type

Due to the increase in environmental consciousness in chemical research and industry, the challenge for a sustainable environment calls for clean procedures that avoid the use of harmful organic solvents. One of the most important principles of the green chemistry is the elimination of hazardous solvents in chemical synthesis and avoids using toxic solvent and the generation of waste.

The use of water, the most abundant chemical on earth, as a solvent has been neglected for many

Table 3. Effect of varying the solvent on the yield of *N*-phenylquinazolin-4-amine (**3a**)

Entry	Solvent	Product (3)	Time (h)	^a Yield (%)
1	Water		1.5	93.5
2	C ₂ H ₅ OH		2	90.5
3	CH ₃ CN		2	87.5
4	CH ₃ OH		2.5	88.5
5	CHCl ₃		2.5	88
6	THF		2.5	84
7	DMF		2.5	73.5

^aYields isolated. ^bYields were analyzed by GC. In the presence of silica-supported Preyssler nanoparticles, H₁₄[NaP₅W₃₀O₁₁₀]/SiO₂ and water as green solvent.

years by organic chemists since water has been traditionally considered to have destructive effects on many reagents and synthetic reactions, unless water is used as a reagent or in workup procedures. To investigate the effect of solvent in these reactions, the reactions were done in different solvents. The results are reported in Tables 2 and 3.

The results show that the efficiency of solvents vary as water>ethanol>methanol>chloroform>acetonitril>THF >>DMF.

Reusability of Catalyst

At the end of the reaction, the catalyst could be recovered by a simple filtration. The recycled catalyst could be washed with dichloromethane and subjected to a second run of the reaction process. In Table 4 the comparison of efficiency of silica-supported Preyssler nanoparticles, H₁₄[NaP₅W₃₀O₁₁₀]/SiO₂ in the synthesis of *N*-phenylquinazolin-4-amine derivatives from reaction of 2-aminobenzamide, orthoester, and substituted aniline after five times is reported. The results indicated that the catalysts were not soluble in the

solvent, and the yields of reactions using silica-supported Preyssler nanoparticles, $H_{14}[NaP_5W_{30}O_{110}]/SiO_2$ catalyst over three runs indicated only a slight loss of activity (Table 4).

Table 4. Reuse of the catalyst for synthesis of *N*-phenylquinazolin-4-amine (**3a**) using silica-supported Preyssler nanoparticles heteropolyacid catalyst, $H_{14}[NaP_5W_{30}O_{110}]/SiO_2$ at reflux conditions in 1.5 h and water as green solvent

Run	^a Yield (%)
1	93
2	92
3	92
4	90.5
5	90

^a Yields refer to isolated product.

CONCLUSION

In conclusion, we have presented use of Silica-supported Preyssler nanoparticles as a catalyst for efficient synthesis of *N*-phenylquinazolin-4-amine derivatives and the yields are excellent. For all the presented reactions, the water solvent was used which is relatively environmentally benign and supporting to Green Chemistry. The advantages of the reported method are the use of cheap, mild, and easily available catalyst, easy work-up, and better yields. The catalyst can be reused after a simple work-up, a gradual decline of its activity being observed. High yields, shorter reaction times, simplicity of operation and easy work-up are some of the advantages of this protocol.

Acknowledgements: The authors are thankful from Agricultural Researches & Services Centre, Mashhad, Feyzabad, Iran and Mashhad Islamic Azad University and Chemistry Department, University of Oslo, Norway and National Research Council Canada for support of this work.

REFERENCES

- J. Zhu, H. Bienayme, H. *Multicomponent Reactions*; Wiley-VCH: Weinheim: 2005.
- I. Ugi, A. Dömling, B. Werner, *J. Heterocycl. Chem.*, **37**, 647 (2000).
- S.L. Dax, J.J. McNally, M.A. Youngman, *Curr. Med. Chem.*, **6**, 255 (1999).
- A. Domling, I. Ugi, *Angew. Chem. Int. Ed.*, **39**, 3168 (2000).
- T. Okuhara, N. Mizuno, M. Misono, *Adv. Catal.*, **41**, 113 (1996).
- M.A. Schwegler, H. Van Bekkum, N. Munck, *Appl. Catal.*, **74**, 191 (1991).
- C.R. Gorla, N.W. Emanetoglu, S. Liang, W. E. Mago, Y. Lu, M. Wraback, H. Shen, *J. App. Phys.*, **85**, 2595 (1999).

- J. Zhang, R.M.J. Dickson, *Phys. Rev. Lett.*, **93**, 077402 (2004).
- B. Ding, J. Gong, J. Kim, S. Shiratori, *Nanotechnology*, **16**, 785 (2005).
- D.P. Sawant, A. Vinu, N.E. Jacob, F. Lefebvre, S. B. Halligudi, *J. Catalysis.*, **235**, 2, 341 (2005).
- A. Müller, F. Peters, M.T. Pope, D. Gatteschi, *Chem. Rev.*, **98**, 239 (1998).
- N. Montazeri, K. Rad-Moghadam, *Phosphorus, Sulfur, Silicon.*, **179**, 2533 (2004).
- M.M. Heravi, S. Sadjadi, N. Mokhtari Haj, H. A. Oskooie, R. Hekmat Shoar, F. F. Bamoharram, *Tetrahedron Lett.*, **50**, 943 (2009).
- D.W. Fry, A.J. Kraker, A. McMichael, L.A. Ambroso, J.M. Nelson, W.R. Leopold, R.W. Connors, A. Bridges, *J. Science*, **265**, 1093 (1994).
- G.W. Rewcastle, B.D. Palmer, A.J. Bridges, H.D. Showalten, L. Sun, J. Nelson,
- A. McMichael, A.J. Kraker, D.W. Fry, W.A. Denny, *J. Med. Chem.*, **39**, 918 (1996).
- W.A. Denny, G.W. Rewcastle, A.J. Bridges, D.W. Fry, A. Kraker, *J. Clin. Exp. Pharmacol. Physiol.*, **23**, 424 (1996).
- N.J. Leonard, D.Y. Curtin, *J. Org. Chem.*, **11**, 346 (1946).
- W.L.F. Armarego, *Heterocyclic Compounds, Fused Pyrimidines, Part I, Quinazolines*; Interscience Publishers: New York, 1967.
- N.S. Gifts, J. Moiler, E.B. Pedersen, *Chem. Scripta.*, **26**, 617 (1986).
- E.C. Taylor, R.V. Ravindranathan, *J. Org. Chem.*, **27**, 2622 (1962).
- W. Szczepankiewicz, J. Suwinski, *Tetrahedron Lett.*, **369**, 1785 (1998).
- M. Berger, B. Albrecht, A. Berces, P. Etmayer, W. Neruda, M. Woisetschlager, *J Med Chem.*, **44**, 3031 (2001).
- R. Saari, J.-C.. Törmä, T. Nevalainen, *Bioorg. Med. Chem.*, **19**, 939 (2011).
- Z.K. Wan, S. Wacharasindhu, C.G. Levins, M. Lin, K. Tabei, T. S. Mansour, *J. Org. Chem.*, **72**, 10194 (2007).
- F.F. Bamoharram, M.M. Heravi, M. Roshani, M. Monabati, *Asian J. Chem.*, **23**, 511 (2011).
- S.A. Rocco, J.E. Barbarini, R. Rittner, *Synthesis.*, **3**, 429 (2004).
- M.H. Alizadeh, H. Razavi, F.F. Bamoharram, M.K. Hassanzadeh, R. Khoshnavazi, F. Mohammadi Zonoz, *Kinet. Catal.*, **44**, 524 (2003).
- A. Foucourt, C. Dubouilh-Benard, E. Chosson, C. Corbière, C. Buquet, M. Iannelli, B. Leblond, F. Marsais, T. Besson, *Tetrahedron* **66**, 4495 (2010).
- F.F. Bamoharram, M.M. Heravi, M. Roshani, A. Gharib, M. Jahangir, *J. Mol. Catal.*, 252, 90 (2006).
- M.M. Heravi, S. Sadjadi, S. Sadjadi, H.A. Oskooie, R. Hekmat Shoar, F.F. Bamoharram, *S. Afr. J. Chem.*, **62**, 1 (2009).
- D.J. Connolly, D. Cusack, T.P. O'Sullivan, P.J. Guiry, *Tetrahedron.*, **61**, 10153 (2005).

УСКОРЕНА МНОГО-КОМПОНЕНТНА СИНТЕЗА НА *N*-ФЕНИЛХИНАЗОЛИН-4-АМИНИ
ИЗПОЛЗВАЙКИ PREYSSLER'ОВИ НАНОЧАСТИЦИ ВЪРХУ НОСИТЕЛ ОТ СИЛИЦИЕВ
ДИОКСИД И ХЕТЕРОПОЛИКИСЕЛИНИ В "ЗЕЛЕН" РАЗТВОРИТЕЛ

А. Гариб^{1,2,*}, Н. Н. Песян³, М. Джахангир¹, М. Рошани¹, Й. (Ханс) В. Схеерен⁴, Л. Бахтиари², С.
Мохадезаде², Ш. Лагзян², С. Ахмади²

¹Департамент по химия, Ислямски университет „Азад“, Маишад, Иран

²Земеделски център за изследвания и услуги, Маишад, Иран

³Департамент по химия, Научен факултет, Университет Урмия, 57159, Урмия, Иран

⁴Клъстер за молекулярна химия, Департамент по органична химия, Университет Радбуд, Наймехен, Холандия

Постъпила на 17 април 2012 г.; коригирана на 22 януари, 2013 г.

(Резюме)

Получени са производни на *N*-фенилхиназолин-4-амините с високи добиви и отлична чистота чрез реакции на 2-аминобензамид, орто-естери и субституирани анилини в присъствие на Preyssler'ови наночастици върху носител от силициев диксид и различни хетерополикиселини (HPAs).

Preyssler heteropolyacid supported on nano-SiO₂, H₁₄[NaP₅W₃₀O₁₁₀]/SiO₂: a green and reusable catalyst in the synthesis of polysubstituted quinolines

A. Gharib^{1, 2*}, B. R. Hashemipour Khorasani², M. Jahangir¹, M. Roshani¹, L. Bakhtiari², S. Mohadeszadeh², S. Ahmadi²

¹Department of Chemistry, Islamic Azad University, Mashhad, IRAN

²Agricultural Researches and Services Center, Mashhad, IRAN

Received: May 28, 2012; revised: February 5, 2013

Synthesis of polysubstituted quinolines in the presence of silica-supported Preyssler nanoparticles (SPNP), H₁₄[NaP₅W₃₀O₁₁₀]/SiO₂, Preyssler H₁₄[NaP₅W₃₀O₁₁₀] and Keggin heteropolyacids, H₃PW₁₂O₄₀, H₇[PMo₈V₄O₄₀], H₆[PMo₉V₃O₄₀], H₅[PMo₁₀V₂O₄₀], H₄[PMo₁₁VO₄₀], H₃[PMo₁₂O₄₀] as catalyst under aqueous conditions is described. The best conditions were observed using Preyssler and silica-supported Preyssler nanoparticles as catalysts. The catalyst is recyclable and reusable.

Keywords: Nano-SiO₂-supported; Preyssler; Heteropolyacids; Polysubstituted quinoline; Quinolines; Catalyst

INTRODUCTION

The synthesis of quinoline derivatives has been considered of great interest to organic chemists owing to its wide range of biological and pharmaceutical properties such as anti-malarial, anti-inflammatory, anti-asthmatic, anti-bacterial, anti-hypertensive and tyrosine kinase inhibiting agents [1]. In addition, quinolines are valuable synthones used for the preparation of nano- and meso-structures with enhanced electronic and photonic properties [2]. Consequently, various methods were developed for the synthesis of quinoline derivatives. The Friedländer annulation has been catalyzed by both acids and bases. Under base catalyzed conditions 2-aminobenzophenone fails to react with simple ketones such as cyclohexanone or α -ketoesters [3]. Brønsted acids like hydrochloric acid, sulphuric acid, *p*-toluene sulphonic acid, phosphoric acids are widely used as catalysts for this conversion [4]. However, many of these classical methods require high temperatures, longer reaction times, drastic conditions, and low yields. Therefore, new catalytic systems are continuously explored. As a result, recently Lewis acids such as Ag₃PW₁₂O₄₀, Y(OTf)₃, FeCl₃ or Mg(ClO₄)₂, NaAuCl₄ · 2H₂O, SnCl₂ or ZnCl₂, Bi(OTf)₃, NaF, SnCl₂·2H₂O, CeCl₃·7H₂O, ZnCl₂, and I₂ have been used in presence of organic solvent for the synthesis of quinolines [5]. Also, microwave irradiations have been used for the synthesis of these compounds [6]. Quinolines are very important compounds because of their wide occurrence in natural products [7] and their

interesting biological activities such as antimalarial, anti-inflammatory agents, antiasthmatic, antibacterial, antihypertensive, and tyrosine kinase inhibiting agents [8]. In addition, quinolines have been used for the preparation of nanostructures and polymers that combine enhanced electronic, optoelectronic or non-linear optical properties with excellent mechanical properties [9]. As a result of their importance as substructures in a broad range of natural and designed products, significant effort continues to be directed toward the development of new quinoline-based structures and new methods for their construction [10]. Synthesis of the corresponding heterocyclic compounds could be of interest from the viewpoint of chemical reactivity and biological activity. Heteropolyacids are widely used in variety of acid catalyzed reactions [11]. Heteropolyacids as solid acid catalysts are green with respect to corrosiveness, safety, quantity of waste and separability and it is well known that the use of heteropolyacid catalysts for organic synthesis reactions can give a lot of benefits. One of the unique features that make solid heteropoly acids economically and environmentally attractive is their stability and bronsted acidity.

The catalytic function of heteropolyacids (HPAs) and related polyoxometalate compounds has attracted much attention, particularly in the last two decades [12]. Polyoxometalates (POMs) are a class of molecularly defined organic metal-oxide clusters; they possess intriguing structures and diverse properties [12]. These compounds exhibit high activity in acid-base type catalytic reactions, hence they are used in many catalytic areas as

* To whom all correspondence should be sent:
E-mail: aligharib5@yahoo.com

homogeneous and heterogeneous catalysts. Numerous attempts to modify the catalytic performance of heteropolyacids, such as supporting them on mobile composition of matter (MCM), silica gel and others have been reported [13]. The application of Preyssler catalysts is highly limited and only a few examples of catalytic activity have been reported [14]. The important advantages of this heteropolyacid are: strong Brønsted acidity with 14 acidic protons, high thermal stability, high hydrolytic stability (pH 0–12), reusability, safety, quantity of waste, ease of separation, corrosiveness, high oxidation potential, and application as a green reagent along with an exclusive structure. All these characteristics have attracted much attention in the recent literature [15,16]. Over the last decade, due to the unique properties of nanoparticles along with their novel properties and potential applications in different fields [17], the synthesis and characterization of catalysts with lower dimension has become an active topic of research. As the particle size decreases, the relative number of surface atoms increases, and thus activity increases. Moreover, due to quantum size effects, nanometre-sized particles may exhibit unique properties for a wide range of applications [18]. In spite of extensive investigations on Keggin-type nanocatalysts [19,20], the synthesis of Preyssler-type nanocatalysts has been largely overlooked. Recently we have explored the application of a Preyssler catalyst in various organic reactions.

EXPERIMENTAL

Instrument and chemical materials

All Chemicals were of analytical grade and purchased from Aldrich and Fluka companies. ¹H NMR spectra were recorded on a FT NMR Bruker 400 MHz spectrometer at 298 K. Melting points were recorded on an Electrothermal type 9100 melting point apparatus and were uncorrected. Chemical shifts were reported in ppm (δ -scale) relative to internal standard TMS (0.00 ppm) and using CDCl₃ as solvent a reference. IR spectra were obtained with a Buck 500 scientific spectrometer (KBr pellets). The products were identified by comparison of their mp., IR and NMR spectra with those of authentic samples. Elemental analyses were performed on Perkin Elmer 2400, series II microanalyzer.

Synthesis of SiO₂ Nanoparticles

The materials used in this work include tetraethyl orthosilicate (TEOS) (Merck, 98%) as the SiO₂ precursor. Besides the main precursor, nitric

acid (65%) and double distilled water were used for peptization and solvent, respectively. The sol–gel precursor solution was obtained by mixing tetraethyl orthosilicate (TEOS) and ethanol with specific molar ratios of ethanol to TEOS. The mixture was stirred using magnetic stirring.

Catalyst Preparation

Preyssler catalyst, H₁₄[NaP₅W₃₀O₁₁₀] was prepared by passage of a solution of the potassium salt (30 mL) in water (30 mL) through a column (50 cm × 1 cm) of Dowex 50w×8 in the H⁺ form. The eluent was evaporated to dryness under vacuum [21,22].

Catalyst Synthesis Procedure

To a solution of the surfactant, sodium bis(2-ethylhexyl) sulphosuccinate, in cyclohexane (0.2 mol L⁻¹), a solution of Preyssler acid in a specified amount of water was added. The molar ratio of water to surfactant was selected to be 3, 5 and 7. Tetraethoxysilane (TEOS) was then added to the micro-emulsion phase. After mixing for various times (8, 12, 18, 25 and 30 h) at room temperature, dispersed Preyssler acid/SiO₂ nanostructures were centrifuged and the particles were rinsed with acetone (4 times) and dried in a vacuum oven. The optimum ratio of water to surfactant was 3:1 and the optimum time was 30 h. The catalysts of H₄[PMo₁₁VO₄₀], H₅[PMo₁₀V₂O₄₀], H₆[PMo₉V₃O₄₀], H₇[PMo₈V₄O₄₀] and Wells-Dawson, H₆[P₂W₁₈O₆₂] were prepared in according to the literature [23–33]. H₆[P₂W₁₈O₆₂], H₇[PMo₈V₄O₄₀], H₆[PMo₉V₃O₄₀], H₅[PMo₁₀V₂O₄₀], H₄[PMo₁₁VO₄₀] and H₃[PMo₁₂O₄₀] were prepared according to the literatures [30–34]. The integrity of the synthesized heteropolyacids has been proven by comparing of spectral data with those reported in literatur [35–38].

General experimental procedure

Preparation of 1-(2-methyl-4-phenylquinolin-3-yl)ethanone and ethyl 2-methyl-4-phenylquinoline-3-carboxylate derivatives:

A mixture of 2-aminoaryl ketone (1.0 mmol), α -methylene ketone (1 mmol) and heteropolyacid as catalyst (0.05 mmol) and water (1.0 mL) was stirred at room temperature for the specified time (Table 2). The progress of the reaction was monitored by TLC. At the end of the reaction, the catalyst was filtered, washed with dichloromethane, dried at 130 °C for 1 h, and re-used in another reaction. The recycled catalyst was used for five reactions without observation of an appreciable loss in its catalytic activities.

Selected spectra data:

Methyl 2,4-dimethyl quinoline-3-carboxylate (4b): IR (neat, cm⁻¹): 1731, 1612; ¹H-NMR (400 MHz, CDCl₃, δ/ppm): 8.05 (d, *J* = 8.4 Hz, 1H), 7.95 (d, *J* = 8.4 Hz, 1H), 7.66 (t, *J* = 7.5 Hz, 1H), 7.47 (t, *J* = 7.5 Hz, 1H), 3.61 (s, 3H), 2.70 (s, 3H), 2.65 (s, 3H); ¹³C-NMR (400 MHz, CDCl₃, δ/ppm): 168.6, 154.5, 147.0, 141.2, 129.7, 128.9, 127.7, 126.3, 125.8, 123.7, 52.6, 23.9, 15.7; Anal. Calcd for C₁₃H₁₃NO₂: C, 72.54; H, 6.09; N, 6.51. Found: C, 72.40; H, 6.15; N, 6.58. HRMS (EI) Calcd. for C₁₃H₁₃NO₂ [M]⁺, 215.1003, Found 215.1005;

Methyl 4-(2-chlorophenyl)-2-methylquinoline-3-carboxylate (4c): IR (KBr, cm⁻¹): 1725, 1612; ¹H-NMR (400 MHz, CDCl₃, δ/ppm): 7.96 (m, 8H), 3.63 (s, 3H), 2.75 (s, 3H); ¹³C-NMR (400 MHz, CDCl₃, δ/ppm): 168.6, 154.4, 146.9, 141.5, 133.3, 130.2, 129.8, 129.5, 128.8, 128.5, 128.1, 127.7, 127.1, 126.5, 126.1, 125.3, 52.6, 23.9; Anal. Calcd for C₁₈H₁₄ClNO₂: C, 69.35; H, 4.53; N, 4.49. Found: C, 69.26; H, 4.61; N, 4.59. HRMS (EI) Calcd. for C₁₈H₁₄ClNO₂ [M]⁺, 311.1003, Found 311.1007;

Methyl 6-chloro-2,4-dimethylquinoline-3-carboxylate (4d): IR (KBr, cm⁻¹): 1726, 1615; ¹H-NMR (400 MHz, CDCl₃, δ/ppm): 8.12 (d, *J* = 8.4 Hz, 1H), 7.75 (s, 1H), 7.60 (d, *J* = 8.4 Hz, 1H), 3.62 (s, 3H), 2.75 (s, 3H), 2.65 (s, 3H); ¹³C-NMR (400 MHz, CDCl₃, δ/ppm): 168.5, 154.4, 146.2, 135.5, 132.6, 130.3, 129.4, 128.5, 127.7, 124.9, 52.8, 24.4, 16.6; Anal. Calcd for C₁₃H₁₂ClNO₂: C, 62.53; H, 4.84; N, 5.61. Found: C, 62.47; H, 4.92; N, 5.52. HRMS (EI) Calcd. for C₁₃H₁₂ClNO₂ [M]⁺, 249.1003, Found 249.1008;

Methyl 6-chloro-2-methyl-4-phenylquinoline-3-carboxylate (4e): IR (KBr, cm⁻¹): 1735, 1587; ¹H-NMR (400 MHz, CDCl₃, δ/ppm): 8.04 (d, *J* = 8.0 Hz, 1H), 7.60 (dd, *J* = 8.0 Hz, 1H), 7.50 (m, 4H), 7.34 (m, 2H), 3.57 (s, 3H), 2.76 (s, 3H); ¹³C-NMR (400 MHz, CDCl₃, δ/ppm): 168.2, 154.9, 148.2, 145.5, 135.0, 132.1, 131.0, 130.4, 129.4, 128.9, 128.4, 127.5, 125.7, 125.3, 52.5, 24.8; Anal. Calcd for C₁₈H₁₄ClNO₂: C, 69.35; H, 4.53; N, 4.49. Found: C, 69.29; H, 4.48; N, 4.41. HRMS (EI) Calcd. for C₁₈H₁₄ClNO₂ [M]⁺, 311.1002, Found 311.1004;

Methyl 6-chloro-4-(2-chlorophenyl)-2-methylquinoline-3-carboxylate (4f): IR (KBr, cm⁻¹): 1733, 1606; ¹H-NMR (400 MHz, CDCl₃, δ/ppm): 8.06 (d, *J* = 9.2 Hz, 1H), 7.49 (m, 6H), 3.56 (s, 3H), 2.78 (s, 3H); ¹³C-NMR (400 MHz, CDCl₃, δ/ppm): 168.1, 154.7, 139.5, 135.5, 134.6, 133.4, 132.4, 130.5, 129.8, 129.1, 128.7, 128.3, 128.0, 127.5, 126.5, 125.7, 52.5, 23.9; Anal. Calcd for C₁₈H₁₃Cl₂NO₂: C,

62.45; H, 3.78; N, 4.05. Found: C, 62.38; H, 3.67; N, 4.10. HRMS (EI) Calcd. for C₁₈H₁₃Cl₂NO₂ [M]⁺, 345.0005, Found 345.1008;

Methyl 6-nitro-2,4-dimethylquinoline-3-carboxylate (4g): IR (KBr, cm⁻¹): 1736, 1615; ¹H-NMR (400 MHz, CDCl₃, δ/ppm): 8.45 (d, *J* = 8.4 Hz, 1H), 7.80 (s, 1H), 7.66 (d, *J* = 8.4 Hz, 1H), 3.65 (s, 3H), 2.76 (s, 3H), 2.65 (s, 3H); ¹³C-NMR (400 MHz, CDCl₃, δ/ppm): 168.4, 154.5, 148.4, 135.5, 132.7, 130.5, 129.6, 128.6, 127.5, 125.3, 52.7, 24.3, 16.8; Anal. Calcd for C₁₃H₁₂N₂O₄: C, 60.00; H, 4.65; N, 10.76. Found: C, 59.91; H, 4.46; N, 10.66. HRMS (EI) Calcd. for C₁₃H₁₂N₂O₄ [M]⁺, 260.1006, Found 260.1008;

Methyl 2-methyl-6-nitro-4-phenylquinoline-3-carboxylate (4h): IR (KBr, cm⁻¹): 1731, 1620, 1525; ¹H-NMR (400 MHz, CDCl₃, δ/ppm): 7.95 (m, 8H), 3.65 (s, 3H), 2.72 (s, 3H); ¹³C-NMR (400 MHz, CDCl₃, δ/ppm): 168.4, 155.2, 148.5, 145.7, 135.5, 132.5, 131.0, 130.6, 129.4, 128.9, 128.6, 127.8, 125.5, 124.7, 52.6, 24.9; Anal. Calcd for C₁₈H₁₄N₂O₄: C, 67.08; H, 4.38; N, 8.69. Found: C, 66.97; H, 4.67; N, 8.60. HRMS (EI) Calcd. for C₁₈H₁₄N₂O₄ [M]⁺, 322.1002, Found 322.1006;

Methyl 4-benzyl-2-methylquinoline-3-carboxylate (4i): IR (KBr, cm⁻¹): 1725, 1567; ¹H-NMR (400 MHz, CDCl₃, δ/ppm): 8.05 (d, *J* = 8.4 Hz, 1H), 7.95 (d, *J* = 8.4 Hz, 1H), 7.60 (t, *J* = 7.5 Hz, 1H), 7.47 (t, *J* = 7.5 Hz, 1H), 7.30 (m, 5H), 3.97 (s, 2H), 3.54 (s, 3H), 2.60 (s, 3H); ¹³C-NMR (400 MHz, CDCl₃, δ/ppm): 168.2, 154.6, 147.4, 141.5, 131.2, 129.7, 128.8, 128.5, 128.2, 127.9, 127.7, 126.6, 126.2, 124.3, 51.9, 37.7, 23.6; Anal. Calcd for C₁₉H₁₇NO₂: C, 78.33; H, 5.88; N, 4.81. Found: C, 78.24; H, 5.82; N, 4.97. HRMS (EI) Calcd. for C₁₉H₁₇NO₂ [M]⁺, 291.1002, Found 291.1006;

Methyl 4-benzyl-6-chloro-2-methylquinoline-3-carboxylate (4j): IR (KBr, cm⁻¹): 1725, 1580; ¹H-NMR (400 MHz, CDCl₃, δ/ppm): 8.06 (d, *J* = 8.4 Hz, 1H), 7.73 (s, 1H), 7.60 (d, *J* = 8.4 Hz, 1H), 7.32 (m, 2H), 7.20 (m, 3H), 3.96 (s, 2H), 3.62 (s, 3H), 2.65 (s, 3H); ¹³C-NMR (400 MHz, CDCl₃, δ/ppm): 168.6, 154.2, 146.5, 135.8, 132.5, 131.6, 130.4, 129.4, 128.9, 128.4, 128.2, 127.9, 127.6, 125.6, 52.4, 37.8, 24.4; Anal. Calcd for C₁₉H₁₆ClNO₂: C, 70.05; H, 4.95; N, 4.30. Found: C, 69.86; H, 4.87; N, 4.38. HRMS (EI) Calcd. for C₁₉H₁₆ClNO₂ [M]⁺, 325.1002, Found 325.1007;

Methyl 4-benzyl-2-methyl-6-nitroquinoline-3-carboxylate (4k): IR (KBr, cm⁻¹): 1733, 1619; ¹H-NMR (400 MHz, CDCl₃, δ/ppm): 8.44 (d, *J* = 8.4 Hz, 1H), 7.85 (s, 1H), 7.70 (d, *J* = 8.4 Hz, 1H), 7.36 (m, 5H), 4.01 (s, 2H), 3.64 (s, 3H), 2.65 (s, 3H); ¹³C-NMR (400 MHz, CDCl₃, δ/ppm): 168.6, 154.5,

148.6, 135.1, 133.1, 131.4, 130.7, 129.5, 129.2, 128.6, 128.2, 127.9, 127.8, 126.1, 52.7, 37.9, 24.8; Anal. Calcd for C₁₉H₁₆N₂O₄: C, 67.85; H, 4.80; N, 8.33. Found: C, 67.72; H, 4.73; N, 8.40.

HRMS (EI) Calcd. for C₁₉H₁₆N₂O₄ [M]⁺, 336.1002, Found 336.1004;

1-(2-methyl-4-phenylquinolin-3-yl)ethanone

(**3q**): IR (KBr, cm⁻¹): 3027, 2963, 1708, 1615, 1573, 1480, 705; ¹H-NMR (400 MHz, CDCl₃, δ/ppm): 1.80 (s, 3H), 2.02 (s, 3H), 7.12 (m, 2H), 7.23 (t, *J* = 8.4 Hz, 1H), 7.26 (m, 3H), 7.30 (d, *J* = 8.6 Hz, 1H), 7.35 (t, *J* = 8.4 Hz, 1H), 7.94 (d, *J* = 8.6 Hz, 1H); ¹³C-NMR (400 MHz, CDCl₃, δ/ppm): 23.2, 29.1, 31.4, 124.5, 125.4, 126.0, 128.1, 128.4, 129.6, 134.8, 147.0, 153.1, 205.5; Anal. Calcd for C₁₈H₁₅NO: C, 82.73; H, 5.78; N, 5.36. Found: C, 82.71; H, 5.80; N, 5.33. HRMS (EI) Calcd. for C₁₈H₁₅NO [M]⁺, 261.1004, Found 261.1009;

1-(6-chloro-2-methyl-4-phenylquinolin-3-yl)ethanone (**4l**):

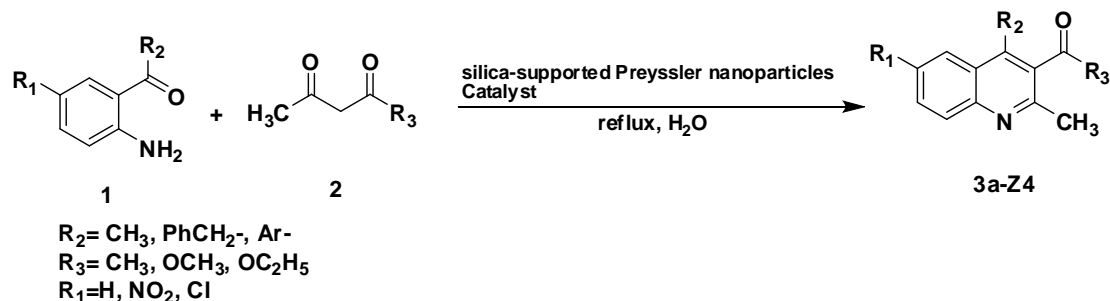
IR (KBr, cm⁻¹): 3030, 2962, 1702, 1606, 1569, 1485, 909, 695; ¹H-NMR (400 MHz, CDCl₃, δ/ppm): 1.91 (s, 3H), 2.62 (s, 3H), 7.32 (m, 2H), 7.56 (m, 5H), 7.92 (d, *J* = 8.7 Hz, 1H); ¹³C-NMR (400 MHz, CDCl₃, δ/ppm): 23.5, 31.7, 124.6, 125.7, 128.6, 129.2, 129.8, 130.7, 132.4, 134.5, 135.6, 142.8, 145.8, 153.8, 204.7; Anal. Calcd for C₁₈H₁₄ClNO: C, 73.09; H, 4.77; N, 4.73. Found: C,

73.05; H, 4.74; N, 4.77. HRMS (EI) Calcd. for C₁₈H₁₄ClNO [M]⁺, 295.1000, Found 295.1006;

RESULTS AND DISCUSSION

Herein we wish to report the catalytic ability of this catalyst in the synthesis of Polysubstituted Quinolines by the reaction of a variety of α-methyleneketones and or 2-aminoaryl ketones and dimedones under mild reaction conditions with the use of heteropolyacids (HPAs) as a catalyst in the synthesis of quinolines with excellent yields. The effects of various parameters such as solvent, catalyst type, temperature (under reflux and room temperature) and times of the reactions were studied.

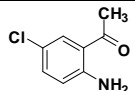
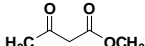
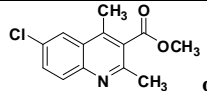
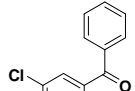
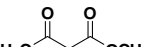
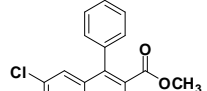
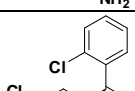
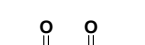
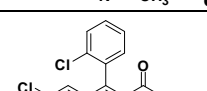
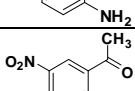
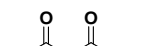
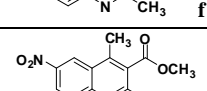
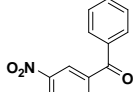
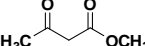
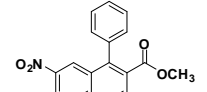
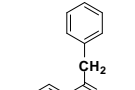
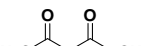
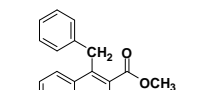
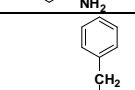
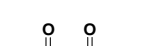
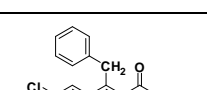
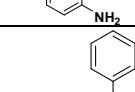

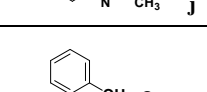
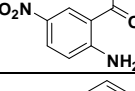
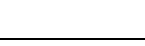
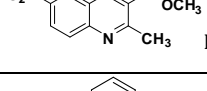
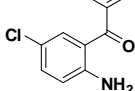
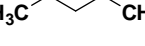
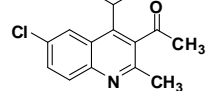
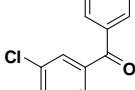
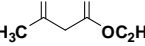
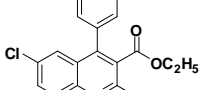
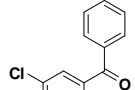
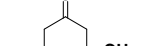
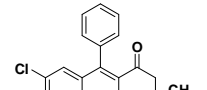
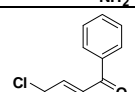
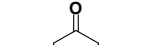
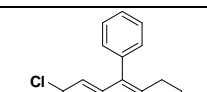
Using the best conditions reported in Table 1, we then continued to study the reaction by using variety of 2-aminoaryl and α-methylene ketones respectively. The results were summarized in Table 1 indicating that both cyclic and acyclic ketones underwent smooth reaction with 2-aminoaryl ketones to give high yields of products. The present protocol is highly effective for substituted 2-aminoaryl ketones such as 2-aminobenzophenone and 2-amino-5-chlorobenzophenone. In general, the yields of the quinoline derivatives were high. It is noteworthy to mention that the method is clean and free from side reactions which normally observed under basic conditions.

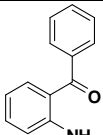
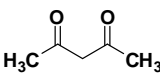
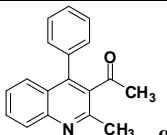
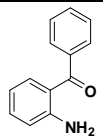
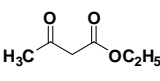
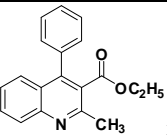
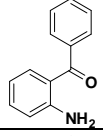
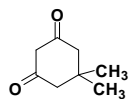
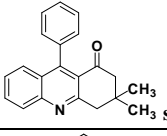
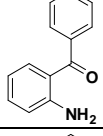
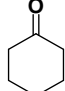
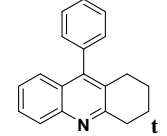
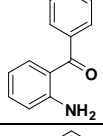
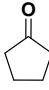
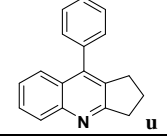
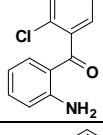
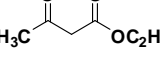
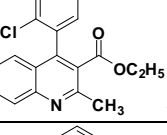
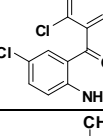
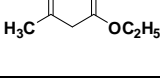
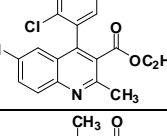
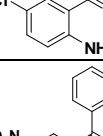
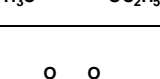
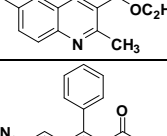
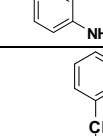
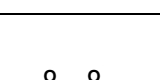
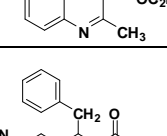
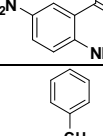
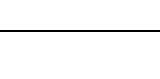
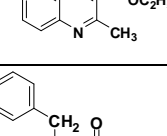
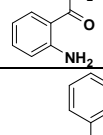
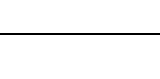
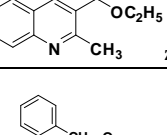
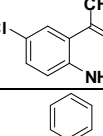
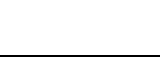
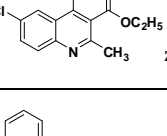
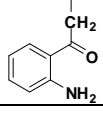
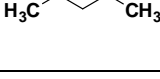
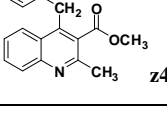


Scheme 1. The reaction of 2-aminobenzophenone (**1**), and ethyl acetoacetate (**2**) under solvent-free condition at reflux conditions in the presence of silica-supported Preyssler nanoparticles catalyst, H₁₄[NaP₅W₃₀O₁₁₀]/SiO₂

Table 1. Synthesis of quinolines in the presence of silica-supported Preyssler nanoparticles, H₁₄[NaP₅W₃₀O₁₁₀]/SiO₂ under reflux and solvent-free conditions in 2 hours (**3a-Z4**). (^aIsolated yield)

Entry	Substrate (1)	Substrate (2)	Product	^a Yield (%)	Mp(°C)	
					Found	Reported
1				93	112	-
2				97	oil	Oil, (lit .39)
3				95	123-126	-

4				93.5	65-67	-
5				92	132-133	134-136, (lit.40)
6				91.5	134-137	-
7				94.5	79-81	-
8				93.5	160-162	-
9				92	103-105	-
10				93	118-120	-
11				94	165-166	-
12				94	152-153	150-151, (lit.39)
13				95.5	125-127	-
14				95	206-207	208-209
15				92	164-166	164-165
16				85	106-108	106-107

17				94	110-112	111-112
18				96	102-103	100-101
19				97.5	192-194	190-192
20				92	153-154	156-157
21				90.5	130-131	130-132
22				94	128-131	-
23				95	139-141	-
24				93	137-138	-
25				89	122-124	-
26				92	127-128	-
27				94.5	117-119	-
28				94	120-121	-
29				93	114-116	-

Effect of the catalyst

As could be seen in Table 3, the best result was obtained in the presence of silica-supported Preyssler nanoparticles heteropolyacid, H₁₄[NaP₅W₃₀O₁₁₀]/SiO₂ under reflux and room temperatures and any further increase in the reaction time did not have any effect on the yield. Furthermore, we also tested the catalytic activity of different catalysts such as HClO₄, *p*-toluenesulfonic acid (TsOH), H₂SO₄, silica sulfuric acid (SSA), and ZnCl₂, and obtained only moderate yields at reflux and room temperatures conditions. One of the most interesting points in this work is the difference of the catalytic activity between simple mineral acids (HClO₄ and H₂SO₄, Table 3, entries 10, 11), silica-supported Preyssler nanoparticles, H₁₄[NaP₅W₃₀O₁₁₀]/SiO₂, Preyssler heteropolyacid, H₁₄[NaP₅W₃₀O₁₁₀] and other keggin heteropolyacids catalysts at reflux and room temperatures conditions (Table 3). Encouraged by this result, we turned our attention to various substituted substrates. The procedure gave the products in high yields and avoids problems associated with solvents and liquid acids use (cost, handling, safety, pollution, corrosiveness, separation, and recovery) (Tables 1 and 3). In a control experiment, it was observed that in the absence of the catalyst, the reaction did not proceed even at higher temperatures. Lowering the reaction temperature was detrimental to the efficiency of this procedure. Usually positional isomers are possible and coexist when two or more vanadium atoms are incorporated into the Keggin structure (for example 5 and 13 isomers for x=2 and 3, respectively) [39]. Studies on these isomers in catalytic reactions indicate that different isomers cause to show different reactivities [40]. Because the metal substitution may modify the energy and composition of the LUMO and redox properties, for mentioned heteropolyacids with different charges, the energy and composition of the LUMOs have significant effects on the catalytic activity [41]. Substitution of vanadium ions into the molybdenum framework stabilize the LUMOs because these orbitals derive, in part from vanadium d-orbitals which have been assumed to be more stable than those of molybdenum and tungsten [41]. The abundance of different isomers may also play an important role in catalytic performance. In addition, different positional Mo atom(s) substituted by the V atom(s) in [PMo₁₂O₄₀]³⁻ may create different vanadium chemical environments, thus causing these catalysts to exhibit varying catalytic performances. By variation of the addenda atoms,

the electrochemical character of them can be widely changed. The addenda atoms can be ordered by decreasing oxidizing ability in the following way: V(V) > Mo(VI) > W(VI) [33].

In order to confirm the utility of HPAs, as effective catalysts, this reaction was repeated in the absence of the HPAs.

Effect of the solvent

The effect of solvent on the model reaction was studied by carrying out the reaction in a solvent-free system and in a variety of solvents including chloroform, dichloromethane, and acetonitrile at different temperatures. As shown in (Table 2) the best results in terms of yield and time have been achieved in solvent-free systems. The synthesis of quinoline derivatives at reflux temperature was carried out using various common solvents such as acetic acid, ethanol, methanol, THF and acetonitrile. The results are shown in Table 2. With using all of the catalysts the highest yield of products was obtained under solvent-free condition.

Table 2. Synthesis of methyl 2,4-dimethylquinoline-3-carboxylate (**3b**) and ethyl 2-methyl-4-phenylquinoline-3-carboxylate (**3r**) in the presence of silica-supported Preyssler nanoparticles heteropolyacid catalyst and different solvents under reflux conditions.

Entry	Solvent	Temperature (°C)	Time (h)	Yield (%)	
				3b	3r
1	Free	Reflux	2	98.5	97.5
2	Water	Reflux	2.5	92	90.5
3	C ₂ H ₅ OH	Reflux	2.5	88	83
4	CHCl ₃	Reflux	3.5	77.5	74.5
5	CCl ₄	Reflux	4.5	73	70
6	THF	Reflux	5	70	66.5
7	CH ₃ CN	Reflux	4	90	88
8	CH ₂ Cl ₂	Reflux	4.5	76	73.5
9	CH ₃ COOH	Reflux	3	86.5	82

^aIsolated yield.

In addition, the time required for completion of the reaction was found to be less under solvent-free condition. In our studies, we investigated the activity of silica-supported Preyssler nanoparticles H₁₄[NaP₅W₃₀O₁₁₀]/SiO₂, Preyssler and various Keggin-type heteropolyacids. Representative results in (Table 2) are shown. The results indicate that the nature of the catalyst plays an important role on their catalytic activities. The highest yield of products has been achieved in the presence of silica-supported Preyssler nanoparticles H₁₄[NaP₅W₃₀O₁₁₀]/SiO₂ as catalyst, and H₂SO₄ gave the lowest yields. Due to the complicated nature of the reaction, obtaining the variety of products, it seemed rather difficult to make an exact assessment of the catalyst role. The Keggin anion has an assembly of 12 cornershared octahedral MoO₆ from trimetallic groups [Mo₃O₁₃] around a heteroatom

Table 3. Effect of silica-supported Preyssler nanoparticles, Preyssler and various Keggin-type heteropolyacids on the yields of Polysubstituted Quinolines (**3b** and **3r**) under reflux and room temperatures and in solvent-free conditions

Entry	Catalyst	Time (h)		^a Yield (%) at Room Temperature		^a Yield (%) at reflux	
		Reflux	Room	3b	3r	3b	3r
1	Silica-supported Preyssler nanoparticles, H ₁₄ [NaP ₅ W ₃₀ O ₁₁₀]/SiO ₂	2	14	51.5	59.5	98.5	97.5
2	H ₁₄ [NaP ₅ W ₃₀ O ₁₁₀]	2	16	45.5	46	97	96
	H ₇ [PMo ₈ V ₄ O ₄₀]	3	16	42.5	44.5	92.5	94
2	H ₆ [PMo ₉ V ₃ O ₄₀]	3	16	39	43.5	90.5	92.5
3	H ₅ [P Mo ₁₀ V ₂ O ₄₀]	3	16	41	43	88.5	90.5
4	H ₄ [PMo ₁₁ V ₁ O ₄₀]	3	16	40.5	42	86	88
5	H ₃ [PW ₁₂ O ₄₀]	3	16	37.5	39	83.5	84
6	H ₄ [SiW ₁₂ O ₄₀]	4	18	34	32.5	80	81.5
7	H ₃ [PMo ₁₂ O ₄₀]	4	18	29	32	77	79
8	H ₄ [SiMo ₁₂ O ₄₀]	4	18	31.5	30.5	75	76
9	H ₆ [P ₂ W ₁₈ O ₆₂]	4	18	40	41	91	93
10	HClO ₄	6	21	19.5	20	41	43
11	H ₂ SO ₄	6	21	10.5	10	35	36.5
12	T ₃ OH	6	21	31	30	53.5	52
13	SSA	6	19	28.5	31	64	63
14	ZnCl ₂	6	21	12	11	37	37.5
15	Free	10	24	-	-	-	-

tetrahedron PO₄. The introduction of vanadium (V) into the Keggin framework of [PMo₁₂O₄₀]³⁻ is beneficial for catalysis reactions [42].

Effect of the catalyst type

To study the effect of catalyst type, the synthesis of Polysubstituted Quinolines was selected as a model reaction and the efficiency using Preyssler and four Keggin-type heteropolyacids (H₁₄[NaP₅W₃₀O₁₁₀], H₇[PMo₈V₄O₄₀], H₆[PMo₉V₃O₄₀], H₅[PMo₁₀V₂O₄₀], H₄[PMo₁₁VO₄₀], H₆[P₂W₁₈O₆₂] and H₃[PMo₁₂O₄₀]) was studied. The results are reported in Table. 3 with the order of efficiency as follows: silica-supported Preyssler nanoparticles, H₁₄[NaP₅W₃₀O₁₁₀]/SiO₂ > H₁₄[NaP₅W₃₀O₁₁₀] > H₇[PMo₈V₄O₄₀] > H₆[P₂W₁₈O₆₂] > H₆[PMo₉V₃O₄₀] > H₅[PMo₁₀V₂O₄₀] > H₄[PMo₁₁VO₄₀] > H₃[PMo₁₂O₄₀].

Reusability of the catalyst

In order to know whether the catalysts would succumb to poisoning and lose of catalytic activity during the reaction, we investigate the reusability of the catalyst. For this purpose, we first carried out the reaction in the presence of the catalyst. After completion of the reaction, the catalyst was removed and washed with diethyl ether, dried at 80 °C for 1 h, and subjected to a second run of the reaction process with the same substrate. The results of the first experiment and subsequent experiments were almost consistent in yields. We

have found that silica-supported Preyssler nanoparticles catalyst can be reused several times without any appreciable loss of activity. The several time recoveries had only slightly decreased the catalytic activity, pointing to the stability and retention capability of this useful polyanion. In Table 4 the comparison of efficiency of the catalyst after five times reuse is reported.

Table 4. Reuse of the silica-supported Preyssler nanoparticles, H₁₄[NaP₅W₃₀O₁₁₀]/SiO₂ for the synthesis of **3r** (ethyl 2-methyl-4-phenylquinoline-3-carboxylate) in solvent-free under reflux conditions.

Entry	Run	Time (h)	^a Yield (%)
1	1	2	97
2	2	2	97
3	3	2	95.5
4	4	2	95
5	5	2	94

^aIsolated Yields.

CONCLUSIONS

In conclusion, we have developed a simple, convenient and efficient protocol for the synthesis of wide range of quinolines under solvent-free conditions is reported. The high yields of products, easy work up procedure, and use of a very small amount of heteropolyacid make it the preferred procedure for the preparation of different kind of quinolines. In our studies, we investigated the activity of various Keggin-type heteropolyacids. The highest yield of products has been achieved in

the presence of silica-supported Preyssler nanoparticles, H₁₄[NaP₅W₃₀O₁₁₀]/SiO₂ and H₇[PMo₈V₄O₄₀] as catalyst, and H₂SO₄ gave the lowest yields.

Acknowledgements: The authors are thankful from Agricultural Researches & Services Center, Mashhad, Feyzabad, Iran and Mashhad Islamic Azad University and Chemistry Department, University of Oslo, Norway and National Research Council Canada for support of this work and with special thanks from Professor. Dr. J. (Hans) W. Scheeren from Organic Chemistry Department, Radboud University Nijmegen, The Netherlands.

REFERENCES:

1. R. D. Larsen, E. G. Corley, A. O. Kind, D. Carrol, P. Devis, T. R. Verhoeven, R. Zamboni, *J. Org. Chem.*, **61**, 3398 (1996).
2. A. K. Aggrawal, S. A. Jenekhe, *Macromolecules.*, **24**, 6806 (1991).
3. Fehnel, E. A. *J. Org. Chem.*, **31**, 2899 (1966).
4. L. Streckowski, A. Czamy, H. Lee, *J. Fluorine Chem.*, **104**, 281 (2000).
5. S. K. De, R. A. Gibbs, *Tetrahedron Lett.*, **46**, 1647 (2005).
6. Song, S. J.; Cho, S. J.; Park, D. K.; Kwon, T. W.; Jenekhe, S. A. *Tetrahedron Lett.*, **44**, 255 (2003).
7. J. P. Michael, *Nat. Prod. Rep.*, **14**, 605 (1997).
8. M. P. Maguire, K. R. Sheets, K. Mcvety, A. P. Spada, A. Zilberstein, *J. Med. Chem.*, **37**, 2129 (1994).
9. S. A. Jenekhe, L. Lu, M. M. M. Alam, *Macromolecules.*, **34**, 7315 (2001).
10. V. V. Kouznetsov, L. Y. V. Mendez, C. M. M. Gomez, *Curr. Org. Chem.*, **9**, 141 (2005).
11. M. M. Heravi and S. Sadjadi, *J Iran Chem Soc.*, **6**, 1 (2009).
12. M. M. Heravi, S. Sajadi, H.A. Oskooie, R. H. Shoar and F. F. Bamoharram, *Catal. Commun.*, **9**, 470 (2008).
13. Y. Izumi, K. Urabe and M. Onaka, *Zeolite Clay and Heteropolyacid in Organic Reactions*, vol. 99, Kodansha, Tokyo, Japan, 1992.
14. H. Firouzabadi and A. A. Jafari, *J. Iranian Chem. Soc.*, **2**, 85 (2005).
15. M. K. Harrup and C. L. Hill, *Inorg. Chem.*, **33**, 5448 (1994).
16. F. F. Bamoharram, M. M. Heravi, M. Roshani, M. Jahangir and A. Gharib, *Appl. Catal.*, **302**, 42 (2006).
17. M. M. Heravi, R. Motamedi, N. Seifi and F. F. Bamoharram, *J. Mol. Catal.*, **249**, 1 (2006).
18. C. R. Gorla, N. W. Emanetoglu, S. Liang, W. E. Mago, Y. Lu, M. Wraback and H. Shen, *J. Appl. Phys.*, **85**, 2595 (1999).
19. J. Zhang and R. M. J. Dickson, *Phys. Rev. Lett.*, **93**, 077402 (2004).
20. D. P. Sawant, A. Vinu, N. E. Jacob, F. Lefebvre and S. B. Halligudi, *J. Catal.*, **235**, 341 (2005).
21. R. Hekmatshoar, S. Sajadi, M. M. Heravi, F. F. Bamoharram, *Molecules.*, **12**, 2223 (2007).
22. M. H. Alizadeh, S. P. Harmalker, Y. Jeannin, J. Martin-Frere, M. T. Pope, *J. Am. Chem. Soc.*, **107**, 2662 (1985).
23. I. V. Kozhevnikov, *Chem. Rev.*, **98**, 171 (1998).
24. F. F. Bamoharram, *J. Mol. Catal. A: Chemical.*, **271**, 126 (2007).
25. F. F. Bamoharram, M. M. Heravi, M. Roshani, A. Gharib, M. Jahangir, *J. Mol. Catal. A: Chemical.*, **252**, 90 (2006).
26. F. F. Bamoharram, M. M. Heravi, M. Roshani, N. Tavakoli, *J. Mol. Catal. A: Chemical.*, **252**, 219 (2006).
27. G. A. Tsigdinos, C. Hallada, *J. Inorg. Chem.*, **7**, 437 (1968).
28. Y. Mahha, A. Atlamsani, J. C. Blais, M. Tessier, J. M. Brégeault, L. Salles, *J. Mol. Catal. A: Chem.*, **234**, 63 (2005).
29. Y. Ding, Q. Gao, G. Li, H. P. Zhang, J. M. Wang, L. Yan, J. S. Suo, *J. Mol. Catal. A: Chem.*, **218**, 161 (2004).
30. a) M. Misono, *Stud. Surf. Sci. Catal.*, 1993, **75**, 69–101. b) M. Misono, *Catal. Rev. Sci. Eng.*, **29**, 269 (1987).
31. M. Misono, N. Nojiri, *Appl. Catal.*, **64**, 1 (1990).
32. T. Okuhara, N. Mizuno, M. Misono, *Adv. Catal.*, **41**, 113 (1996).
33. I. V. Kozhevnikov, *Appl. Catal. A: Gen.*, **256**, 3 (2003).
34. I. V. Kozhevnikov, K. I. Matveev, *Appl. Catal.*, **5**, 135 (1983).
35. M. H. Alizadeh, S. P. Harmalker, Y. Jeanenin, J. Martin-Frere and M. T. Pope, *J Am Chem Soc.*, **107**, 2662 (1985).
36. G. A. Tsigdinos and C. J. Hallada, *Inorg Chem.*, **7**, 437 (1968).
37. Pope M T, *Heteropoly and Isopoly Oxometalates*, Springer, Berlin, 1983.
38. G. T. Baronetti, L. Briand, U. Sedran and H. Thomas, *Appl Catal A: Gen.*, **172**, 265 (1998).
39. M. T. Pope, T. F. Scully, *Inorg. Chem.*, **14**(4), 953 (1975).
40. A. M. Khenkin, A. Rosenberger, R. Neumann, *J. Catal.*, **182**, 82 (1999).
41. X. Lopez, C. Bo, J. M. Poblet, *J. Am. Chem. Soc.*, **124**, 12574 (2002).
42. M. T. Pope, *Heteropoly and Isopoly Oxometalates*, Springer, Berlin, 1983.

PREYSSLER'ОВИ ХЕТЕРОПОЛИКИСЕЛИНИ $H_{14}[NaP_5W_{30}O_{110}]$, НАНЕСЕНИ ВЪРХУ
НАНОЧАСТИЦИ ОТ СИЛИЦИЕВ ДИОКСИД: ЗЕЛЕН И РЕЦИКЛИРУЕМ КАТАЛИЗАТОР
ЗА СИНТЕЗАТА НА ПОЛИ-ЗАМЕСТЕНИ ХИНОЛИНИ

А. Гариб^{1,2*}, Б.Р.Х. Хоразани², М. Джахангир¹, М. Рошани¹, Л. Бахтиари², С. Мохадесзаде², С.
Ahmadi²

¹Департамент по химия, Ислямски университет "Азад", Маишад, Иран

²Земеделски център за изследвания и услуги, Маишад, Иран

Постъпила на 28 май 2012 г.; коригирана на 5 февруари, 2013 г.

(Резюме)

Описани са синтезите на поли-заместени хинолини в присъствие на катализатори от наночастици, нанесени върху подложка от силициев диоксид (**SPNP**): $H_{14}[NaP_5W_{30}O_{110}]/SiO_2$, Preyssler'ови $H_{14}[NaP_5W_{30}O_{110}]$ и Keggin'ови хетерополикиселини, $H_3PW_{12}O_{40}$, $H_7[PMo_8V_4O_{40}]$, $H_6[PMo_9V_3O_{40}]$, $H_5[PMo_{10}V_2O_{40}]$, $H_4[PMo_{11}VO_{40}]$, $H_3[PMo_{12}O_{40}]$ във водна среда. Най-добри условия са наблюдавани при използването на Preyssler'ови хетерополикиселини като катализатор. Катализаторите са рециклируеми и годни за многократна употреба.

Preliminary study on *in vivo* toxicity of monensin, salinomycin and their metal complexes

V. N. Atanasov^{a,b}, S. S. Stoykova^a, Y. A. Goranova^a, A. N. Nedzhib^a, L. P. Tancheva^c,
Ju. M. Ivanova^d, I. N. Pantcheva^{a,*}

^a Laboratory of Biocoordination and Bioanalytical Chemistry, Department of Analytical Chemistry, Faculty of Chemistry and Pharmacy, Sofia University "St. Kl. Ohridski", 1, J. Bourchier Blvd., 1164 Sofia, Bulgaria

^b Emergency Toxicology Clinic, Military Medical Academy, 3, St. G. Sofiiski St., 1606 Sofia, Bulgaria

^c Institute of Neurobiology, Bulgarian Academy of Sciences, Acad. G. Bonchev St., blok 23, 1113 Sofia, Bulgaria

^d Department of Chemistry, Biochemistry, Physiology and Pathophysiology, Medical Faculty, Sofia University "St. Kl. Ohridski", 1, Kozyak St., 1407 Sofia, Bulgaria

Received October 8, 2012; Accepted January 7, 2013

The acute toxicity of the polyether ionophores monensin, salinomycin and their metal complexes with Na(I), Mg(II), Ca(II), Mn(II), Co(II), Zn(II) was evaluated in mice. The experimental data revealed that Ca(II) and Mg(II) complexes of salinomycin display the highest toxicity among the compounds tested, with LD₅₀ values of 20.5 mg/kg b.w. (13 μmol/kg b.w.) and 25.8 mg/kg b.w. (17 μmol/kg b.w.), respectively. The preliminary evaluation of biochemical indices of survived animals showed that no significant changes occur within a three-day treatment with ionophorous antibiotics and their complexes.

Keywords: polyether ionophores, metal complexes, acute toxicity, biochemical indices

INTRODUCTION

Polyether ionophores are natural compounds produced by *Streptomyces spp.* and are applied in veterinary medicine as coccidiostats, antimicrobial agents and growth promoters [1]. Although known as monovalent ionophores for their affinity to bind alkali cations, these compounds also form various divalent metal derivatives depending both on the antibiotic form (acidic or sodium) and on the nature of the metal(II) ion [2-9].

Generally, the metal complexes of monensin and salinomycin possess more pronounced biological activity than non-coordinated ionophores as the antibacterial (*B. subtilis*, *B. mycoides*, *M. luteus*) and the anticancer studies (human squamous cell carcinoma, glioblastoma multiforme, cancers of lung, breast, liver and uterine cervix, chronic myeloid leukemia) revealed [9-12]. At the same time there are limited data on the toxicity of the polyether ionophorous antibiotics and especially of their metal-containing compounds in animal models [13, 14]. The aim of the present research is to evaluate both the acute toxicity of metal complexes of monensin and salinomycin in mice and their effect on some clinical parameters of survived animals.

EXPERIMENTAL

The protocol was approved by the Institutional Animal Care and Use Committee of the Institute of Neurobiology, Bulgarian Academy of Sciences (IN-BAS) according to the Guidelines for Animal Experimentation.

Test compounds

Sodium forms of monensin and salinomycin were kindly provided by Biovet Ltd. Peshtera, Bulgaria. Acidic forms of antibiotics and their metal(II) complexes were prepared as previously described [2,3,5,6,9].

Animals and house conditions

Male ICR mice (18-25 g) were used in the experiments, housed in plastic cages with stainless steel top in the animal care facility of IN-BAS, where room temperature, humidity and ventilation were controlled according to international standards. The animals had access to food and water *ad libitum* and were maintained at 24 ± 2 °C with a 12 h light/dark cycle.

Experimental design

The compounds tested were administered *per os* (gavage) on an empty stomach (12 h without food before testing) as aqueous suspensions. The acute

* To whom all correspondence should be sent:
E-mail: ipancheva@chem.uni-sofia.bg

toxicity (LD₅₀, mg/kg b.w., μmol/kg b.w.) was measured by the Prozorovsky's method [15].

The animals survived after acute toxicity test with the selected substances were subjected to additional two-day treatment with the corresponding dose of the compounds (total 72 h treatment). After that the animals were sacrificed under anesthesia (chloralhydrate, 50 mg/kg, *i.p.*). Blood samples were collected by cardiac puncture.

Clinical observations

The observation period was one or three days post administration for acute toxicity assay and 72 h treatment, respectively. Clinical signs of toxidromes (tremors, excitability, salivation, etc.) and mortality were observed while dosing, during the first two hours after administration and on the 12th / 24th h after the treatment.

Biochemical analyses

Biochemical examinations were performed using blood collected in plain tubes. Blood samples were centrifuged (3 000 rpm / 5 min) and the serum was collected for assays. The following parameters were measured on a Mindray clinical chemistry analyzer (China) using Sentinel (Italy) diagnostic kits: albumin (ALB), total protein (TP), aspartate aminotransferase (AST), alanin aminotransferase (ALT), alkaline phosphatase (ALP), lactatdehydrogenase (LDH), creatinine (CR), urea (URE).

Statistical analysis

The reference biochemical values of control animals were calculated by the parametric method [16]. The values of biochemical parameters do not usually follow the normal distribution and for that reason the reference limits are calculated using 2.5 and 97.5 percentile ranges.

RESULTS

The majority of acute toxicity tests performed aims to determine only the minimum lethal or maximum non-lethal dose. At the same time these tests can provide preliminary but useful information on the toxic nature of compounds for which no toxicological information is available. Such data base can be used to deal with cases of accidental ingestion of a large amount of the corresponding compound; to determine possible target organs and/or special tests that should be conducted in repeated-dose toxicity tests; and to select doses for short-term and sub-chronic toxicity tests when no other toxicology information is existing [17].

Monensin and salinomycin are well known and widely applied antibiotics in veterinary medicine. These compounds form metal(II) complexes of various compositions and structures depending on the antibiotic form used in the synthetic procedure (acidic or sodium) and on the nature of the metal(II) ion [2-9]. To the best of our knowledge there are no literature data regarding any toxicology information about metal(II) complexes of polyether ionophores. The following compounds were used in the present study:

- sodium monensin (MonNa), [Mn(MonNa)₂Cl₂], [Co(MonNa)₂Cl₂],
- monensic acid (MonH), [Co(Mon)₂(H₂O)₂], [Zn(Mon)₂(H₂O)₂],
- sodium salinomycin (SalNa), [Mg(Sal)₂(H₂O)₂], [Ca(Sal)₂(H₂O)₂], [Co(Sal)₂(H₂O)₂] and [Zn(Sal)₂(H₂O)₂].

The complexes of sodium monensin with Mn(II) and Co(II) have distorted tetrahedral geometry, while the rest of the divalent metal compounds are isostructural with an octahedral environment of the metal(II) ion.

Table 1. LD₅₀ of monensin, salinomycin and some of their metal complexes (ICR mice, *per os*, 24 h treatment)

Compound	LD ₅₀ (confidence interval)	
	mg / kg b.w.	μmol / kg b.w.
MonNa *	> 100	> 144
[Mn(MonNa) ₂ Cl ₂] *	> 79.4	> 52
[Co(MonNa) ₂ Cl ₂] *	> 31.6	> 21
MonH	87.0 (63-120)	130 (94-179)
[Co(Mon) ₂ (H ₂ O) ₂] *	> 31.6	> 22
[Zn(Mon) ₂ (H ₂ O) ₂]	34.2 (23-51)	24 (16-35)
SalNa	21.6 (15-32)	28 (19-41)
[Mg(Sal) ₂ (H ₂ O) ₂]	25.8 (21-32)	17 (13-21)
[Ca(Sal) ₂ (H ₂ O) ₂]	20.5 (17-25)	13 (11-16)
[Co(Sal) ₂ (H ₂ O) ₂]	44.7 (38-60)	27 (23-37)
[Zn(Sal) ₂ (H ₂ O) ₂]	108.0 (73-160)	67 (46-100)

“ * ” - to be precisely determined

Table 2. Representative biochemical indices of survivals (ICR mice, *per os*, 72 h treatment)

Compound	Dose, mg/kg b.w.	ALB, g/L	TP, g/L	AST, U/L	ALT, U/L	ALP, U/L	LDH, U/L	CR, $\mu\text{mol/L}$	URE, mmol/L
[Mg(Sal) ₂ (H ₂ O) ₂]	20.0	36.6	-	640	91	362	1435	43.4	-
	25.0	29.4	-	173	68	203	1888	-	-
	31.6	33.0	-	385	83	330	905	62.2	-
	50.1	28.1	-	510	93	391	1750	-	-
[Ca(Sal) ₂ (H ₂ O) ₂]	10.0	35.8	-	178	58	228	796	-	-
	12.6	34.3	60.0	240	95	216	-	66.5	12.7
	15.8	34.8	64.5	173	73	316	-	60.5	11.5
	20.0	43.7	-	175	95	219	954	37.2	-
	25.0	40.3	55.6	280	108	317	1571	40.4	10.2
	31.6	37.9	51.1	705	305	412	-	44.1	-
	39.8	34.6	63.4	255	70	129	-	55.3	13.9
	50.1	50.3	-	385	170	324	1255	43.1	-
Controls		23-34	50-74	95-474	32-105	150-326	695-2634	27-59	5-17

“ - “ – not determined

The data on the acute toxicity of the compounds tested are presented in Table 1. As it can be seen, the most toxic compounds are [Ca(Sal)₂(H₂O)₂] and [Mg(Sal)₂(H₂O)₂], whereby MonH is the least toxic among all substances studied with precisely determined LD₅₀ values. It should be mentioned that Zn(II) analogues of monensin and salinomycin differ significantly in their toxicity, as compared to the starting antibiotics. Thus monensinic acid is five times less toxic than [Zn(Mon)₂(H₂O)₂], while sodium salinomycin possesses two-fold increased acute toxicity if juxtaposed with [Zn(Sal)₂(H₂O)₂].

The clinical signs of the treated animals depend both on the type and concentration of compounds studied. The death of animals treated with MonH and MonNa is not accompanied by any behavior changes and other symptoms, while the treatment with [Zn(Mon)₂(H₂O)₂] leads to adynamia, bradypnea, loss of postural reflex, clonic seizures. The treatment with low doses of SalNa during the first 2-3 hours is accompanied by increased physical activity, while at high doses decreased physical activity and tachypnea were observed. Later ataxia, loss of postural reflex and aggressive behavior in survived animal groups were noticed. The compounds [Co(Sal)₂(H₂O)₂] and [Zn(Sal)₂(H₂O)₂] do not provoke significant changes in the animal status at the beginning – the animals are agitated with increased physical activity. After several hours, considerable alterations are noted – mice become oppressed, drowsy and lose postural reflex. In the group treated with [Mg(Sal)₂(H₂O)₂] and [Ca(Sal)₂(H₂O)₂] tremor, disorientation and ataxia are observed. All

clinical signs of toxicity are indicative for central nerve system (CNS) toxic effect of high doses of antibiotics administered (acute toxicity).

Salinomycin complexes with ions of Mg(II) and Ca(II) showed highest toxicity, and for that reason we studied their effect on animals by additional biochemical assays using survivals. For this purpose a three-day treatment was applied with the same dose of the given compound used during acute toxicity experiments. Representative data on the parameters tested (ALB, TP, AST, ALT, ALP, LDH, CR, URE) upon treatment with salinomycin complexes are summarized in Table 2.

From the clinical chemistry results obtained it can be concluded that 72 h treatment (once per day) with salinomycin metal(II) complexes does not significantly influence most of the paraclinic laboratory parameters of the treated animals and the differences with the control group are not significant. The normal serum creatinine and urea values are indicative that there is no acute kidneys damage displaying renal insufficiency. Increased ALB in the group treated with [Ca(Sal)₂(H₂O)₂] can result from dehydration of the animals (referred to behavior changes of intoxicated animal) followed by subsequent hemoconcentration. The increased AST values measured for some animals suggest possible myocardial damage when salinomycin complexes were applied because the toxicity mechanism of the tested compounds is related to ion-channel disturbances in the myocardium. However, more detailed studies on the myocardium toxicity related to high doses of these compounds must be performed combined with histological

studies. The liver function seems to be intact for the period of testing without serious disturbances.

From the biochemical analyses performed it can be concluded that a three-day treatment with Mg(II) and Ca(II) complexes of salinomycin does not affect liver and kidneys functions. Possible myocardium dysfunction is suggested, but to have more deep insights into the mechanism of toxicity resulting from application of antibiotics complexes, a prolonged treatment (chronic/sub-chronic toxicity studies) should be performed.

CONCLUSION

The LD₅₀ values of monensin, salinomycin and their metal complexes were determined on ICR mice. The data showed that the least toxic compound among the substances studied is monensinic acid, whereby the Ca(II) and Mg(II) complexes of salinomycin are the most toxic ones. The 72 h treatment of animals does not significantly change most of the biochemical parameters. From the clinical signs of toxicity observed and based on the preliminary biochemical data obtained it can be suggested that the lethal outcome is associated with CNS toxicity and breath insufficiency.

Acknowledgement: The authors are grateful to Sofia University Fund for Science Research for the financial support of this work (grant 068/2009, project leader Ju. Ivanova).

REFERENCES

1. The role of enteric antibiotics in livestock production, Avcare Ltd., Canberra, 2003, and references therein
2. P. Dorkov, I. N. Pantcheva, W. S. Sheldrick, H. Mayer-Figge, R. Petrova, M. Mitewa, *J. Inorg. Biochem.* **102**, 26 (2008).
3. I. N. Pantcheva, M. Io. Mitewa, W. S. Sheldrick, I. M. Oppel, R. Zhorova, P. Dorkov, *Curr. Drug Discov. Techn.* **5**, 154 (2008).
4. I. N. Pantcheva, P. Dorkov, V. N. Atanasov, M. Mitewa, B. L. Shivachev, R. P. Nikolova, H. Mayer-Figge, W. S. Sheldrick, *J. Inorg. Biochem.* **103**, 1419 (2009).
5. I. N. Pantcheva, R. Zhorova, M. Mitewa, S. Simova, H. Mayer-Figge, W. S. Sheldrick, *BioMetals* **23**, 59 (2010).
6. I. N. Pantcheva, J. Ivanova, R. Zhorova, M. Mitewa, S. Simova, H. Mayer-Figge, W. S. Sheldrick, *Inorg Chim Acta* **363**, 1879 (2010).
7. J. Ivanova, I. N. Pantcheva, M. Mitewa, S. Simova, H. Mayer-Figge, W. S. Sheldrick, *Centr. Eur. J. Chem.* **8**, 852 (2010).
8. J. Ivanova, I. N. Pantcheva, M. Mitewa, S. Simova, M. Tanabe, K. Osakada, *Chem. Centr. J.* **5**, 52 (2011).
9. J. Ivanova, I. N. Pantcheva, R. Zhorova, G. Momekov, S. Simova, R. Stoyanova, E. Zhecheva, S. Ivanova, M. Mitewa, *J. Chem. Chem. Eng. David Publ.* **6**, 551 (2012).
10. M. Mitewa, I. Pantcheva, R. Alexandrova, in: Recent Researches in Modern Medicine, O. Braissant, H. Wakamatsu, I. Kuo-Kang, K. Allegaert, Y. Lenbury, A. Wachholtz (eds), WSEAS Press, Cambridge, 2011, pp. 439.
11. R. I. Alexandrova, T. Zhivkova, I. N. Pantcheva, M. Io. Mitewa, *Intern. J. Biol. Biomed. Eng.* **5**, 93 (2011).
12. R. I. Alexandrova, T. Zhivkova, M. Alexandrov, G. Miloshev, M. Georgieva, I. N. Pantcheva, M. Io. Mitewa, *Cent. Eur. J. Chem.* **10**, 1464 (2011).
13. C. J. Dutton, B. J. Banks, C. B. Cooper, *Nat. Prod. Rep.*, **12**, 165 (1995).
14. J. W. Westley, Polyether Antibiotics: Naturally Occurring Acid Ionophores, vol. 1: Biology, Marcel Dekker Inc., 1982.
15. V. B. Prozorovsky, M. P. Prozorovskaya, B. M. Demchenko, *Pharmacol. Toxicol.* **4**, 497 (1978).
16. M. Penev, P. Dokova-Peneva, Laboratory Chematology, ARTIK-2001, Sofia, 2007.
17. S. C. Gad, C. P. Chengelis, Acute toxicity testing perspectives and horizons, The Telford Press, Caldwell, NJ, 1988.

**IN VIVO ТОКСИЧНОСТ НА МОНЕНЗИН, САЛИНОМИЦИН
И ТЕХНИ МЕТАЛНИ КОМПЛЕКСИ (ПРЕДВАРИТЕЛНО ИЗСЛЕДВАНЕ)**

В. Н. Атанасов^{a,b}, С. С. Стойкова^a, Я. А. Горанова^a, А. Н. Неджиб^a, Л. П. Танчева^c,
Ю. М. Иванова^d, И. Н. Панчева^{a,*}

^a Лаборатория по биокоординационна и биоаналитична химия, катедра „Аналитична химия“, Факултет по химия и фармация, Софийски университет “Св. Климент Охридски”, София

^b Клиника по спешна токсикология, Военно-медицинска академия, София

^c Институт по невробиология, Българска академия на науките, София

^d Катедра по химия, биохимия, физиология и патофизиология, Медицински факултет, Софийски университет “Св. Климент Охридски”, София

Постъпила на 8 октомври, 2012 г.; приета на 7 януари, 2013 г.

Изследвана е острата токсичност на полиетерните йонофори монензин, салиномицин и комплексите им с Na(I), Mg(II), Ca(II), Mn(II), Co(II), Zn(II) върху мишки, порода ICR. Установено е, че от тестваните съединения Ca(II) и Mg(II) комплекси на салиномицин са най-токсични със стойности за LD₅₀ 20.5 mg/kg b.w. (13 μmol/kg b.w.) и 25.8 mg/kg b.w. (17 μmol/kg b.w.), съответно. Предварителната оценка показва, че триденното третиране с полиетерни йонофорни антибиотици и техните комплекси не води до съществени промени в биохимичните показатели на преживелите животни.

Syntheses, structural and biological studies of Mn(II), Cu(II), Zn(II), Fe(III) and MoO₂(VI) complexes of a tridentate OOS donor thiazolidin-4-one

D. Kumar¹, A. Kumar^{2*}, D. Dass³

¹Department of Chemistry, National Institute of Technology, Kurukshetra 136119, Haryana, India

²Department of Chemistry, Haryana College of Technology & Management, Kaithal, 136027, Haryana, India

³Department of Chemistry, Shri Krishan Institute of Engineering & Technology, Kurukshetra 136118, Haryana, India

Received: January 7, 2013; revised: January 4, 2014

A new thiazolidinone, N-(2-hydroxymethylphenyl)-C-(3'-carboxy-2'-hydroxyphenyl)thiazolidin-4-one, LH₃ (**I**) has been synthesized by the cyclization of a dry benzene solution of the Schiff base, N-(2-hydroxymethylphenyl)-3'-carboxy-2'-hydroxybenzylideneimine with mercaptoacetic acid. A methanolic solution of **I** reacts with Mn(II), Cu(II), Zn(II), Fe(III) and MoO₂(VI) ions and forms the coordination compounds, [Mn(LH)(MeOH)₃], [M'(LH)(MeOH)] [here M' = Cu (II), Zn(II), MoO₂(VI)] and [FeCl(LH)(MeOH)₂]. All the coordination compounds are monomeric in nature. The coordination compounds have been characterized on the basis of elemental analyses, molar conductance, molecular weight, spectral (IR, NMR, reflectance, ESR) studies and magnetic susceptibility measurements. **I** behaves as a dibasic tridentate OOS donor ligand in these compounds. The compounds are non-electrolytes ($\Lambda_M = 6.1-13.5 \text{ mho cm}^2 \text{ mol}^{-1}$) in DMF. A square-planar structure for [Cu(LH)(MeOH)], a tetrahedral structure for [Zn(LH)(MeOH)] and an octahedral structure for the remaining compounds are suggested. The compounds were screened for antimicrobial activity.

Keywords: thiazolidin-4-one, monomeric, gram positive, magnetic susceptibility, strong field and covalent character

INTRODUCTION

Thiazolidin-4-ones are a traditionally known class of biologically active compounds. They have played an important role in medicinal chemistry. Moreover they have been studied extensively because of their ready accessibility, diverse chemical reactivity and broad spectrum of biological activity [1]. In recent years, a large number of innovative drugs containing the thiazolidinone moiety have been developed, including hypoglycemic thiazolidinediones (pioglitazone and its analogs), dual COX-2/5-LOX inhibitors (darbufelon), new generation diuretics (etozolin) etc [2].

Metal complexes play an important role in plant and animal life due to their physico-chemical and biological properties. Organosulphur compounds, in the form of their metal complexes, exhibit a wide range of biological properties. Heavy metals in traces are essential for all forms of life. Heavy metals like Cu, Fe, Mo and occasionally Mn assist oxidation-reduction equilibria while those like Zn and Mn are concerned with hydrolytic processes [3]. However, coordination metal complexes are gaining increasing importance in the design of respiratory, slow release and long acting drugs.

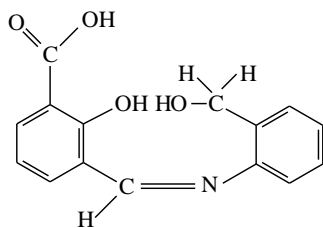
Metal ions are therefore known to accelerate drug actions. The efficacies of some therapeutic agents are known to increase upon co-ordination [4]. Some metal complexes are known to exhibit remarkable antitumour, antifungal, antiviral and special biological activities [3].

Thiazolidin-4-ones, a saturated form of thiazole with carbonyl group on fourth carbon, possess almost all type of biological activities like antitubercular [5], antibacterial [6], anticonvulsant [7], antifungal [8], amoebicidal [9], antioxidant [10], pesticidal [11], antiviral [12] and antitumour [13].

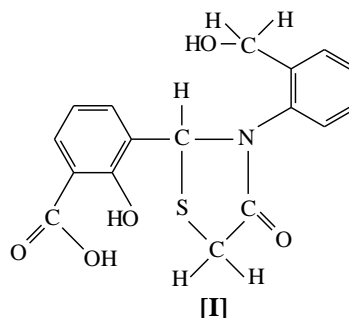
Due to this, the investigation of chemistry and biology of these compounds continue to appeal the synthetic and medicinal organic chemists. A perusal of the literature reveals that much has been reported on the syntheses and characterization [14] of a variety of thiazolidin-4-ones, relatively little is known about their coordination compounds [15, 16].

Keeping this in mind, it was worth while to synthesize and characterize a new thizaolidinone, N-(2-hydroxymethylphenyl)-C-(3'-carboxy-2'-hydroxyphenyl)thiazolidin-4-one, LH₃ (**I**) and its coordination compounds with Mn(II), Cu(II), Zn(II), Fe(III) and MoO₂(VI) ions.

* To whom all correspondence should be sent:
E-mail: amit_vashistha2004@yahoo.co.in



[Schiff base]



[I]

EXPERIMENTAL

Materials

o-Aminobenzylalcohol [Aldrich]; manganese(II) acetate tetrahydrate, iron(III) chloride (anhydrous) [Sarabhai]; copper(II) acetate monohydrate, zinc(II) acetate dihydrate [SD's Fine]; ammonium molybdate(VI) tetrahydrate, methanol, ethanol, mercaptoacetic acid, dry benzene, sodium bicarbonate [Ranbaxy] were used as supplied for the syntheses. 3-formylsalicylic acid and bis(acetylacetonato)dioxo-molybdenum(VI) were synthesized by following the reported procedures [17].

Analyses and physical measurements

The organic skeleton of the respective coordination compounds was decomposed by the slow heating of ~ 0.1 g of the latter, with conc. HNO₃. The residue was dissolved in minimum amount of conc. HCl and the corresponding metal ions were estimated as follows: The Mn(II) and Zn(II) contents of the respective coordination compounds were estimated by complexometric titration method against standardized EDTA solution using eriochrome black-T and xylenol orange as the indicators respectively. The Cu(II) contents was estimated iodometrically against a standard solution of sodium thiosulphate to the starch end point. The Fe(III) ions were reduced to Fe(II) ions with aqueous SnCl₂ and then estimated against standard K₂Cr₂O₇ solution using N-phenylanthranilic acid as an indicator. The molybdenum contents was estimated gravimetrically after decomposing the given MoO₂(VI) compound with a few drops of conc. HNO₃ and conc. H₂SO₄ and then igniting the residue in an electric Bunsen at 500 °C. MoO₃ obtained was dissolved in 6*N* NaOH and then molybdenum was estimated as bis(8-hydroxyquinolino)dioxo-molybdenum(VI). The C, H and N contents of LH₃ and its coordination compounds were determined by CHN Eager analyzer model-300. The S and Cl contents were

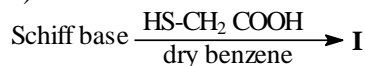
estimated gravimetrically as BaSO₄ and AgCl respectively. The molecular weight measurements were carried out by the Rast method using diphenyl as the solvent [18]. The molar conductances (Λ_M) of the coordination compounds were measured in DMF with the help of a Toshniwal conductivity bridge (CL01-02A) and a dip type cell calibrated with KCl solutions. The ESR spectrum of [Cu(LH)(MeOH)] was recorded at liquid nitrogen temperature in polycrystalline solids on a Varian V4502-12 X-band ESR spectrophotometer with 100 KHz modulation using diphenylpicrylhydrazide as a *g*-marker and monitoring the frequency with frequency meter. The IR spectra were recorded in KBr pellets (4000-400 cm⁻¹) on a Beckman-20 spectrophotometer. The reflectance spectra were recorded on a Beckmann DU spectrophotometer attached with a reflectance arrangement. The magnetic susceptibility measurements were carried out at room temperature, using Hg[Co(NCS)₄] as the standard [19]. The diamagnetic corrections were computed using Pascal's constants. The magnetic susceptibilities were corrected for temperature independent paramagnetism term (TIP) [19] using value of 60 × 10⁻⁶ cgs units for Cu(II), zero for Mn(II) and Fe(III) ions.

Synthesis of *N*-(2-hydroxymethylphenyl)-3'-carboxy-2'-hydroxybenzylideneimine (Schiff base). A MeOH solution (30 mL) of *o*-aminobenzylalcohol (1.23 g, 10 mmol) was added to a MeOH solution (30 mL) of 3-formylsalicylic acid (1.66 g, 10 mmol) and the mixture was then refluxed for 1 h. The precipitates formed were suction filtered, washed with MeOH and dried *in vacuo* at room temperature over silica gel for 24 h. Yield = 58%. The elemental analyses of the compound gave the satisfactory results.

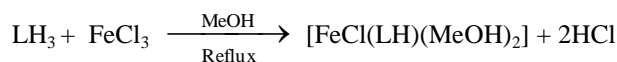
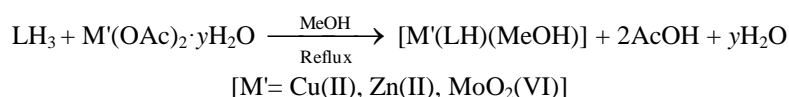
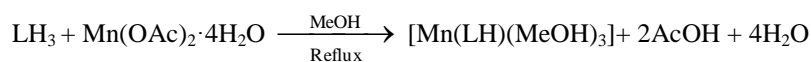
Synthesis of *N*-(2-hydroxymethylphenyl)-C-(3'-carboxy-2'-hydroxyphenyl)thiazolidin-4-one, LH₃ (I). A dry benzene solution of the Schiff base (2.71 g, 10 mmol) and mercaptoacetic acid (0.92 g, 10 mmol) were refluxed for 12 h on a water bath. The mixture was cooled to room temperature and then was washed with 10% sodium bicarbonate solution.

The benzene layer was separated using a separating funnel. The partial evaporation of the benzene layer gave a solid product, which was filtered, washed with and recrystallized from petroleum ether. The compounds were dried as mentioned above. Yield = 14%. *Anal.*: (I, C₁₇H₁₅NO₅S) (obsd: C, 58.91%; H, 4.37%; N, 4.12%; S, 9.11%. calc.: C, 59.13%; H, 4.35%; N, 4.06%; S, 9.28%); IR bands (KBr): 2860 cm⁻¹ [ν (O–H)(intramolecular H-bonding)], 1710 cm⁻¹ [ν (C=O) (thiazolidinone ring)], 1675 cm⁻¹ [ν (C=O)(carboxylic)], 1570 cm⁻¹ [ν (C–N)(thiazolidinone ring)], 1520 cm⁻¹ [ν (C–O)(phenolic)], 1225 cm⁻¹ [ν (C–O)(alcoholic)], and 830 cm⁻¹ [ν (C–S)(thiazolidinone ring)].

Syntheses of coordination compounds of I. A MeOH solution (30-50 mL) of the appropriate metal salt (10 mmol) was added to a MeOH solution (50 mL) of I (3.45 g, 10 mmol) and the



Scheme 1: Preparative scheme of LH₃ (I)



Scheme 2: Preparative scheme of coordination compounds of LH₃ (I)

The coordination compounds are air-stable at room temperature. They are insoluble in H₂O, partially soluble in MeOH, EtOH and completely soluble in DMSO and DMF. Their molar conductance measurements ($\Lambda_M = 6.1$ -13.5 mho cm² mol⁻¹) in DMF indicate their non-electrolytic

mixture was then refluxed for 3-4 h. The solid products formed were suction filtered, washed with and recrystallized from MeOH and were then dried as mentioned above. Yield = 50–75%.

RESULTS AND DISCUSSION

A dry benzene solution of the Schiff base reacts with mercaptoacetic acid and forms N-(2-hydroxymethylphenyl)-C-(3'-carboxy-2'-hydroxyphenyl)thiazolidin-4-one, LH₃ (I). The reaction of I with appropriate metal salt in 1:1 molar ratio in MeOH produces the coordination compounds, [Mn(LH)(MeOH)₃], [M'(LH)(MeOH)] [where M' = Cu(II), Zn(II), MoO₂(VI)] and [FeCl(LH)(MeOH)₂]. The formations of I from the Schiff base and the coordination compounds of I take place according to the Schemes 1 and 2.

nature. The analytical data of I and its coordination compounds are presented in Table 1.

Infrared spectral studies

The infrared spectra of the Schiff base, I and the coordination compounds of the latter were recorded in KBr and the prominent peaks (in cm⁻¹) are shown in Table 2

Table 1. Analytical, molar conductance (Λ_M) and molecular weight data of I and its coordination compounds.

Compound	Mol. formula	Λ_M (mho cm ² Mol ⁻¹)	Mol. Wt Obsd (calcd)	obsd(calcd)%				
				M	C	H	N	S
LH ₃ (I)	C ₁₇ H ₁₅ NO ₅ S	–	345 ^a (345.0)	–	58.91 (59.13)	4.37 (4.35)	4.12 (4.06)	9.11 (9.28)
[Mn(LH)(MeOH) ₃]	MnC ₂₀ H ₂₅ NO ₈ S	6.1	467.1 ^b (493.9)	11.23 (11.12)	48.37 (48.59)	5.13 (5.06)	2.74 (2.83)	6.37 (6.48)
[Cu(LH)(MeOH)]	CuC ₁₈ H ₁₇ NO ₆ S	9.6	417.6 438.5 ^b	14.22 (14.48)	49.37 (49.26)	3.84 (3.88)	3.08 (3.19)	7.46 (7.30)
[Zn(LH)(MeOH)]	ZnC ₁₈ H ₁₇ NO ₆ S	8.2	462.1 ^b (440.4)	14.70 (14.85)	48.90 (49.05)	3.94 (3.86)	3.00 (3.18)	7.15 (7.27)
FeCl(LH)(MeOH) ₂	FeC ₁₉ H ₂₁ NO ₇ SCl	13.5	461.5 ^b (498.5)	11.37 (11.23)	45.43 (45.74)	4.14 (4.21)	2.84 (2.81)	6.37 (6.42)
[MoO ₂ (LH)(MeOH)]	MoC ₁₈ H ₁₇ NO ₈ S	7.1	487.6 ^b (502.9)	19.36 (19.07)	42.71 (42.95)	3.47 (3.38)	2.83 (2.78)	6.22 (6.36)

Abbreviations: ^aMass spectral data, ^bRast method data

Table 2. IR, reflectance spectral data (cm⁻¹) and magnetic moments of the coordination compounds of I

Compound	$\nu_{as}(\text{COO})$	$\nu_s(\text{COO})$	$\nu(\text{C-O})$ (phenolic)	$\nu(\text{C-S})$	$\nu(\text{C-O})$ (MeOH)	ν_{max}	Mag. moment (B. M.)
LH ₃ (I)	–	–	1520	830	–	–	Diamagnetic
[Mn(LH)(MeOH) ₃]	1562	1350	1525	815	978	17460, 22380, 25280	5.84
[Cu(LH)(MeOH)]	1560	1335	1530	800	974	17240	1.89
[Zn(LH)(MeOH)]	1567	1352	1527	805	964	–	Diamagnetic
[FeCl(LH)(MeOH) ₂]	1572	1352	1528	812	980	12500, 15900, 24300	5.85
[MoO ₂ (LH)(MeOH)]	1577	1365	1525	795	969	–	Diamagnetic

The Schiff base exhibits the $\nu(\text{C=N})$ (azomethine) stretch at 1640 cm⁻¹. This band disappears in **I** and a new band appears at 1570 cm⁻¹ due to the $\nu(\text{C-N})$ (thiazolidinone ring) stretch [20] indicating the conversion of the Schiff base into **I**. The formation of **I** is further supported by the appearance of a new band at 830 cm⁻¹ due to the $\nu(\text{C-S})$ (thiazolidinone ring) stretch [21]. A negative shift of 15-35 cm⁻¹ of the $\nu(\text{C-S})$ (thiazolidinone ring) stretch in the coordination compounds indicates the involvement of the S atom of the thiazolidinone moiety towards coordination [22]. **I** shows the $\nu(\text{C=O})$ (thiazolidinone ring) stretch [23] at 1710 cm⁻¹. This band remains unchanged in the coordination compounds indicating the non-involvement of O atom towards the coordination. The $\nu(\text{C-O})$ (alcoholic) stretch [24] of **I** occurs at 1225 cm⁻¹ which remain unchanged in the complexes. **I** exhibits a strong band at 2860 cm⁻¹ due to the intramolecular H-bonded OH group of phenolic and/or carboxylic acid moieties [25]. This band disappears in the coordination compounds indicating the breakdown of H-bonding and subsequent deprotonation of the OH group followed by the involvement of phenolic and carboxylic acid O atoms towards coordination. The presence of a broad band at ~ 3400 cm⁻¹ due to $\nu(\text{O-H})$ (MeOH) and the decrease of $\nu(\text{C-O})$ (MeOH) stretch from 1034 cm⁻¹ to lower energy by 54-70 cm⁻¹ in the coordination compounds of **I** indicate the involvement of the O atom of MeOH towards coordination [26]. The appearance of two new bands between 1560-1577 cm⁻¹, $\nu_{as}(\text{COO})$ and 1335-1365 cm⁻¹, $\nu_s(\text{COO})$ stretches indicate the presence of the coordinated carboxylate group in the coordination compounds. The energy difference ($\Delta\nu = 212-225$ cm⁻¹) between these stretches is > 210 cm⁻¹ which indicates the monodentate nature of the carboxylate moiety [27]. The $\nu(\text{C-O})\phi$ stretch [26] of **I** occurs at 1520 cm⁻¹. This band shifts to higher energy by 5-10 cm⁻¹ in the coordination compounds indicating the involvement of phenolic O

atom of 3-formylsalicylic acid moiety towards coordination. The absence of a band between 820-860 cm⁻¹ in [FeCl(LH)(MeOH)₂] precludes the presence of the (Fe-O-Fe) bridged structure [28]. [MoO₂(LH)(MeOH)] exhibits the $\nu_s(\text{O=Mo=O})$ and $\nu_{as}(\text{O=Mo=O})$ stretches at 945 and 908 cm⁻¹ respectively [29]. These bands occur in the usual ranges: $\nu_s(\text{O=Mo=O})$ stretch, 892-964 cm⁻¹ and $\nu_{as}(\text{O=Mo=O})$ stretch, 842-928 cm⁻¹, reported for the majority of MoO₂(VI) compounds. The presence of two bands due to the $\nu(\text{O=Mo=O})$ stretch is indicative of a *cis*-MoO₂ configuration as the compound with *trans*-MoO₂ structure shows only $\nu_{as}(\text{O=Mo=O})$ stretch since the $\nu_s(\text{O=Mo=O})$ stretch is IR inactive [30]. The absence of a band at ~775 cm⁻¹ in the MoO₂(VI) compound indicates the absence of an oligomeric chain with $\cdots\text{Mo}\cdots\text{Mo}\cdots\text{Mo}\cdots$ interaction [31]. The new non-ligand bands in the present coordination compounds in the low frequency region are assigned to the $\nu(\text{M-O})$ (550-570 cm⁻¹) and the $\nu(\text{M-S})$ (345-375 cm⁻¹) and these bands [32] are in the expected order of increasing energy: $\nu(\text{M-S}) < \nu(\text{M-O})$.

NMR Spectral Studies

The NMR spectra of **I** and [Zn(LH)(MeOH)] were recorded in DMSO-*d*₆. The chemical shifts (δ) are expressed in ppm downfield from TMS. The prominent resonance signals of these compounds were compared with the reported peaks [33]. **I** exhibits a singlet at δ 17.5 ppm due to the carboxylic proton, a sharp singlet at δ 13.60 ppm due to phenolic proton, a singlet at δ 2.35 ppm due to alcoholic proton, multiplets due to methylene protons at δ 4.70-4.79 ppm, multiplets between δ 7.34-7.50 ppm due to the aromatic protons. The occurrence of the resonance signal at the same frequency (δ 2.35 ppm) due to alcoholic proton (CH₂OH) indicates the non-involvement of the alcoholic group towards coordination. The absence of the signal at δ 17.5 ppm due to the COOH proton in [Zn(LH)(MeOH)] indicates the

deprotonation of the COOH group, followed by the involvement of its O atom in coordination. The absence of the resonance signal at δ 13.60 ppm due to the phenolic proton in [Zn(LH)(MeOH)] indicates the deprotonation of the phenolic OH group followed by its involvement in coordination [34]. The appearance of resonance signals at 2.81-2.85 ppm due to alcoholic proton and at 3.0-3.1 ppm due to methyl protons in the coordination compound supports the presence of MeOH in it.

Reflectance spectral studies

[Mn(LH)(MeOH)₃] exhibits three bands at 17460, 22380 and 25280 cm⁻¹ due to ⁶A_{1g} → ⁴T_{1g}(G), ⁶A_{1g} → ⁴T_{2g}(G) and ⁶A_{1g} → ⁴A_{1g}(G) transitions, respectively in an octahedral environment [35]. The presence of an asymmetric broad band at 17240 cm⁻¹ due to the ²B_{1g} → ²A_{1g}, ²B_{2g} and ²E_g transitions in [Cu(LH)(MeOH)] suggests a square-planar arrangement of I around Cu(II) ion [36]. The absence of a band in the range 8000-10000 cm⁻¹ precludes the presence of a tetrahedral structure. [FeCl(LH)(MeOH)₂] exhibits three bands at 12500, 15900 and 24300 cm⁻¹ due to ⁶A_{1g} → ⁴T_{1g}(G), ⁶A_{1g} → ⁴T_{2g}(G) and ⁶A_{1g} → ⁴A_{1g}(G) transitions, respectively in an octahedral environment [37].

Magnetic measurements

The room temperature magnetic moments of the coordination compounds of I are presented in Table 2. The magnetic moments of [Mn(LH)(MeOH)₃], [Cu(LH)(MeOH)] and [FeCl(LH)(MeOH)₂] are 5.84, 1.89 and 5.85 B.M. respectively. These values are indicative of the magnetically dilute high-spin octahedral coordination compounds of Mn(II) and Fe(III) ions [38]. The coordination compounds of other ions are diamagnetic.

ESR Studies

[Cu(LH)(MeOH)] exhibits two g values ($g_{\parallel} = 2.25$, $g_{\perp} = 2.09$) and this indicates the presence of tetragonal type symmetry about the Cu(II) ions [39]. The spin Hamiltonian parameters are: $A_{\parallel} = 1.683 \times 10^{-2}$ cm⁻¹, $A_{\perp} = 4.49 \times 10^{-3}$ cm⁻¹, $G = 2.73$, $\alpha_{Cu}^2 = 0.79$, $(\alpha')^2 = 0.27$, $\kappa = 0.58$ and $P_d = 1.58 \times 10^{-2}$ cm⁻¹. The data indicate that $g_{\parallel} > g_{\perp}$ and $A_{\parallel} > A_{\perp}$ which are indicative of the presence of the unpaired electron in the $d_{x^2-y^2}$ orbital [19]. For ionic environments, g_{\parallel} is normally ≥ 2.3 and is < 2.3 for covalent environments. The g_{\parallel} value (2.25) indicates that the metal-ligand bonding in the compound is covalent. For tetragonal Cu(II) compounds, if G is less than 4.0, the ligand forming

the Cu(II) compound is regarded as a strong field ligand. G value (2.73) indicates the strong field nature of the ligand. The in-plane covalence parameter (α_{Cu}^2) has been calculated using the relation: $\alpha_{Cu}^2 = (g_{\parallel} - 2.002) + 3/7 (g_{\perp} - 2.002) - (A_{\parallel}/0.036) + 0.04$, where α is related to the overlap integral (S) according to the relation [40]: $\alpha^2 - 2\alpha\alpha'S + (\alpha')^2 = 1$. The values of α_{Cu}^2 (0.79) and α'^2 (0.35) indicate its covalent nature. The smaller the value of α_{Cu}^2 , the more covalent is the bonding; $\alpha_{Cu}^2 = 1$ indicates completely ionic bonding, while $\alpha_{Cu}^2 = 0.5$ indicates completely covalent bonding. The larger the value of α'^2 , the more covalent is the bonding; $\alpha'^2 = 0$ suggests a complete ionic bonding [19]. The symbol κP_d represents the Fermi contact contribution (A) to the coupling, where P_d is the dipolar contribution. The value of P_d and κ have been calculated using the relation [39]: $P_d = -(A_{\parallel} - A_{\perp})/0.78$ and $\kappa = -0.48 - (A_{\parallel}/P_d)$. The positive value of κ suggests that A_{\parallel} should be greater than A_{\perp} and it has also been observed by us. The lower value of P_d in comparison to that of the free ion value (3.5×10^{-2} cm⁻¹) indicates the presence of covalent character between the metal-ligand bonding. The absence of any band ~ 1500 G due to the $\Delta M_s = 2$ transition precludes the presence of M-M interaction.

Antimicrobial Activity

The antimicrobial activity of the ligand and the complexes were tested against two selected bacterias which include *E.Coli* (Gram Negative) and *S. aureus* (Gram positive) by using disc-diffusion method. Stock solution was prepared by dissolving compounds in DMSO. Under aseptic conditions, plain sterilised discs were soaked in solution of compounds for overnight. Test culture was spread over the plates containing Mueller Hinton Agar (MHA) by using sterile swab. Inoculated plates were dried for 30 minutes and discs were placed on these inoculated plates. The plates were left for 30 minutes at room temperature to allow diffusion. The plates were then incubated at 37 °C for 24-48 hours. After incubation diameter of zone of inhibition was noted on each disc.

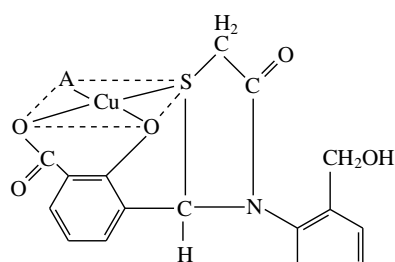
As we consider all results obtained from antibacterial tests we can say that the entire compounds tested are active towards both gram positive and gram negative bacteria. The metal complexes are more active than the parental ligand.

Table 3. Antimicrobial activity of Ligand (I) and its Coordination compounds (zone of Inhibition in mm)

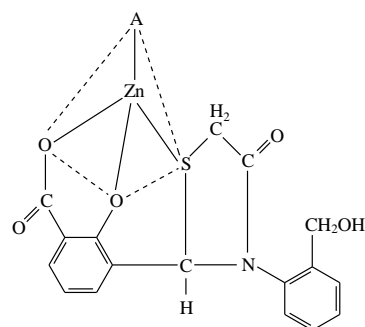
Compound	<i>E. coli</i> (Gram negative)	<i>S. aureus</i> (Gram positive)
LH ₃ (I)	4	6
[Mn(LH)(MeOH) ₃]	8	9
[Cu(LH)(MeOH)]	6	12
[Zn(LH)(MeOH)]	10	10
[FeCl(LH)(MeOH) ₂]	8	11
[MoO ₂ (LH)(MeOH)]	12	14

CONCLUSIONS

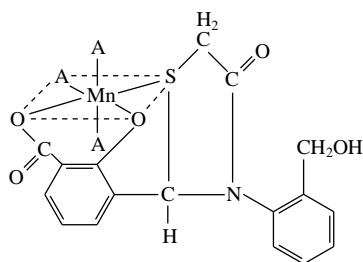
Thus, on the basis of analytical data, valence requirements, molecular weight, spectral and the magnetic studies, it is proposed that **I** behaves as a dibasic tridentate OOS donor ligand in the square-planar coordination compound, [Cu(LH)(MeOH)] (**II**), in the tetrahedral compound, [Zn(LH)(MeOH)] (**III**) and in the octahedral compounds, [Mn(LH)(MeOH)₃] (**IV**), [FeCl(LH)(MeOH)₂] (**V**) and [MoO₂(LH)(MeOH)] (**VI**).



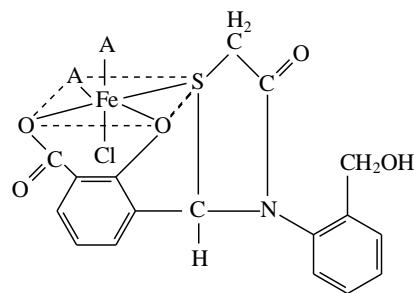
[II, A = MeOH]



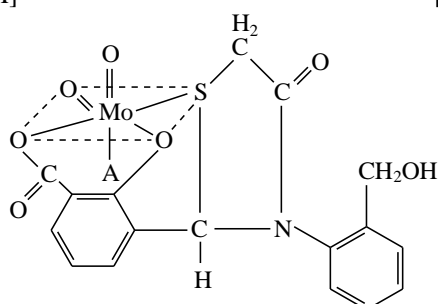
[III, A = MeOH]



[IV, A = MeOH]



[V, A = MeOH]



[VI, A = MeOH]

REFERENCES

1. M. Pulici, F. Quartieri, *Tetrahedron Lett.* **46**, 2387 (2005).
2. R.B. Lesyk, B.S. Zimenkovsky, *Curr. Org. Chem.* **8**, 1547 (2004).
3. A.O. Ajibola, *Essential of Medicinal Chemistry*. 2nd edition. Sharson Jersey, pp. 28-446 (1990).
4. J.A. Obaleye, J.B. Nde-aga, E.A. Balogun, *Afr. J. Sci.* **1**, 10 (1997).
5. K. Babaoglu, M.A. Page, V.C. Jones, M.R. McNeil, C. Dong, J.H. Naismith, R.E. Lee, *Bioorg. Med. Chem. Lett.* **13**, 3227 (2003).
6. B.P. Choudhari, V.V. Mulwad, *Indian J. Chem.*, **44B**, 1074 (2005).
7. A. Gursoy, N. Terzioglu, *Turk J Chem*, **29**, 247 (2005).
8. J. Tao, L.H. Cua, C.H. Wang, *J. Chin. Chim. Soc.*, **53**, 117 (2006).
9. K.A. Thaker, B.R. Parekh, N.C. Desai, *J. Indian Chem. Soc.*, **64**, 491 (1987).

10. T. Kato, T. Ozaki, K. Tamura, Y. Suzuki, M. Akima, N.J. Ohi, *Med. Chem.*, **42**, 3134 (1999).
11. T. Singh, S. Sharma, V.K. Srivastava, A. Kumar, *Indian J. Chem.*, **45B**, 1557 (2006).
12. R.K. Rawal, Y.S. Prabhakar, S.B. Katti, E. De Clercq, *Bioorg. Med. Chem.* **13**, 6771 (2005).
13. F. Delmas, A. Avellaneda, C. Di Giorgio, M. Robin, E. De Clercq, P. Timon-David, J. P. Galy, *Eur. J. Med. Chem.*, **39**, 685 (2004).
14. S. Gaikwad, V. Suryawanshi, Y. Vijapure, V. Shinde. *J. Chemical and Pharma. Research*, **4**, 1851 (2012).
15. A.M. Rehab Al-Hasani, M.M. Sinan Al-byatti, M.S. Sarab Al Azawi, *Engg. and Tech. Journal*, **29**, 3067 (2011).
16. D. Kumar, A. Kumar, J. Sharma, *Journal of Chemistry*, **2013**, Article ID, 870325, (2012).
17. A. Syamal, D. Kumar, A.K. Singh, P.K. Gupta, Jaipal, L.K. Sharma, *Indian J. Chem.*, **41 A**, 1385 (2002).
18. F.G. Mann, B.C. Saunders, *Practical Organic Chemistry*, London: Longmans, p. 435 (1961).
19. R.L. Dutta and A. Syamal, *Elements of Magnetochemistry*, 2nd Edn., New Delhi: Affiliated East West Press Pvt. Ltd. (1993).
20. D. Kumar, A. Kumar, *E-J.Chem.*, **9**, 2532 (2012).
21. M.J.M. Campbell, R.J. Grazeskiowiak, *J. Chem. Soc.(A)*, 396 (1967).
22. R.K. Patel, *Asian J. Chem.*, **13**, 89 (2001).
23. P.V. Patel, K.R. Desai, *Orient. J. Chem.*, **18**, 311 (2002).
24. A. Syamal, O.P. Singhal, *Trans. Met. Chem.*, **4**, 179 (1979).
25. A. Syamal, D. Kumar, *Synth. React. Inorg. Met.-org. Chem.*, **14**, 325 (1984).
26. A. Syamal, D. Kumar, *Indian J. Chem.*, **24A**, 62 (1985).
27. J.R. Anacona, C. Toledo, *Trans. Met. Chem.*, **26**, 228 (2001).
28. D.J. Howkin, W.P. Griffith, *J. Chem. Soc. A*, 472 (1966).
29. D. Kumar, A. Syamal, L.K. Sharma, *J. Coord. Chem.*, **61**, 1788 (2008).
30. A. Syamal, M.R. Maurya, *Trans. Met. Chem.*, **11**, 235 (1986).
31. A. Syamal, M.M. Singh, D. Kumar, *React. Funct. Polym.*, **39**, 27 (1999).
32. M.R. Charasia, *J. Inorg. Nucl. Chem.*, **37**, 1547 (1975).
33. J. K. Nag, S. Pal, C. Sinha, *Trans. Met. Chem.*, **30**, 523 (2005).
34. D. Kumar, A. Syamal, A.Gupta, M. Rani, P.K. Gupta, *J. Indian Chem. Soc.*, **87**, 1185 (2010).
35. A.B.P. Lever, *Inorganic Electronic Spectroscopy*, 2nd Edn., Amsterdam: Elsevier, 1984 and references therein.
36. S.G. Shirodkar, P.S. Mane, T.K. Chondhekar, *Indian J. Chem.*, **40A**, 1114 (2001).
37. D. Kumar, A. Syamal, A.K. Singh, *Indian J. Chem.*, **42A**, 280 (2003).
38. F.A. Cotton, G. Wilkinson, C.A. Murillo and M. Bochmann, *Advanced Inorganic Chemistry*, 6th Edn., (New York: John Wiley) (1999).
39. R.S. Drago, *Physical Methods in Chemistry*, 2nd Edn., W. B. Saunders Co., Philadelphia, 1976.
40. D. Kivelson, R. Neiman, *J. Chem. Phys.*, **35**, 149 (1961).

СИНТЕЗИ, СТРУКТУРНИ И БИОЛОГИЧНИ ИЗСЛЕДВАНИЯ НА КОМПЛЕКСИ НА Mn(II), Cu(II), Zn(II), Fe (III) И MoO₂(VI) С ДОНОР ОТ ТРИДЕНТАТ-4-ОН

Д. Кумар¹, А. Кумар^{2*}, Д. Дас³

¹Департамент по химия, Национален технологичен институт, Курукиетра 136119, Харияна, Индия

²Департамент по химия, Колеж по технология и управление в Харияна, Кайтал 136027, Индия

³Департамент по химия, Институт по инженерство и технология „Шри КришнанКурукиетра 136118, Харияна, Индия

Постъпила на 7 януари 2013 г., коригирана на 4 януари 2014 г.

(Резюме)

Синтезиран е нов тиазолидинон N-(2-хидроксиетилфенил)-C-(3'-карбокси-2'-хидроксиетилфенил)тиазолидин-4-он, LH₃ (I) чрез циклизирането на Шифова база (N-(2-хидроксиетилфенил)-3'-карбокси-2'-хидроксибензилиденимин) с меркапто-оцетна киселина. Метанолов разтвор на I реагира с иони Mn(II), Cu(II), Zn(II), Fe(III) и MoO₂(VI) и образува координационни съединения, [Mn(LH)(MeOH)₃], [M'(LH)(MeOH)] [тук M' = Cu (II), Zn(II), MoO₂(VI)] и [FeCl(LH)(MeOH)₂]. Всички координационни съединения са мономери. Те са охарактеризирани на базата на елементни анализи, моларна проводимост, молекулна маса, спектрални изследвания (IR, NMR, отражателни спектри, ESR) и магнитния susceptibilitet. I се отнася като дву-основен тридентатен OOS донорен лиганд в тези съединения. Съединенията са не-електролити ($\Lambda_m = 6.1-13.5 \text{ mho cm}^2 \text{ mol}^{-1}$) в DMF. Предложени са квадратно-планарна структура за [Cu(LH)(MeOH)], тетраедрична структура за [Zn(LH)(MeOH)] и октаедрична за останалите съединения. Те са изследвани за антимикуробна активност.

Synthesis, characterization and biological evaluation of some novel Benzimidazole derivatives

A. Ahmadi

Department of Chemistry, Faculty of Science, Islamic Azad University, Karaj Branch, Karaj, Iran

Received February 18, 2013; revised June 17, 2013

The benzimidazole nucleus has a significant importance in medicinal chemistry and many benzimidazole-containing compounds exhibit important biological activities. In the present study, synthesis, spectral studies and biological evaluation of nine novel benzimidazole derivatives were investigated. The structures of the synthesized compounds were characterized by IR, $^1\text{H-NMR}$, $^{13}\text{C-NMR}$, Mass spectroscopy and CHN elemental analyzer and the target new synthesized compounds (**1c-9c**) screened for antibacterial activity against various strains of *Escherichia coli* and *Staphylococcus aureus* and antifungal activity against *Candida albicans*.

Keywords: Benzimidazole, Antibacterial activity, Antifungal activity, Gram-positive bacteria, Gram-negative bacteria.

INTRODUCTION

Infectious microbial diseases remain pressing problems worldwide, because resistance to a number of antibiotics agents among variety of clinically significant species of microorganisms has become an important global health problem. One way to battle with this challenge is the conscious usage of the currently marketed antibiotics and the other is the development of novel drugs. They are natural and synthetic heterocyclic compounds and classified by medicinal chemists as the privileged sub-structures for drug design. In light of the affinity, they display towards a variety of enzymes and protein receptors [1] i.e., as selective neuropeptide YY1 receptor antagonists [2–5], 5-lipoxygenase inhibitors for use as novel anti-allergic agents [6], factor Xa (FXa) inhibitors [7], poly (ADP-ribose) polymerase (PARP) inhibitors [8] and as human cytomegalovirus (HCMV) inhibitors [9]. A wide variety of Benzimidazole derivatives are known for their chemotherapeutic importance and antimicrobial [10-15], antifungal [16-18], anti-inflammatory [19] and antioxidant [20-24] activities in this context. Because of their wide range of pharmacological activities and industrial and synthetic applications, several methods have been reported in the literature for their synthesis and biological evaluations. Traditionally, the synthesis of benzimidazoles involves the condensation of *o*-phenylenediamine with aldehydes and carboxylic acids or their derivatives.

These methods include cyclo-condensation reaction of *o*-phenylenediamines with carboxylic acids or derivatives [25-29]. In view of these valid observations and as a continuation of our work, prompted us to synthesize new 2-substituted benzimidazole derivatives (**1b-9b** and **1c-9c**) (Figure 1) and the structures of the synthesized compounds were characterized by analysis techniques and the target synthesized compounds (**1c-9c**) were screened for their antibacterial activity against various strains of *Escherichia coli* and *Staphylococcus aureus* and antifungal activities against *Candida albicans*.

EXPERIMENTAL

Material and Equipment

All chemicals and solvents were obtained from E-Merck and Sigma-Aldrich and used without further purification. All melting points are uncorrected and taken with an Electrothermal melting point apparatus (Electrothermal Eng. Ltd, Essex, UK). IR spectra were determined in KBr on a Shimadzu Dr-8031 instrument. The ^1H and $^{13}\text{C-NMR}$ spectrums of the synthesized compounds were measured in DMSO- d_6 or CDCl_3 solution and TMS as the internal standard using a Varian Mercury 400, 400MHz instrument. All Chemical shifts were reported as δ (ppm) values. The Mass Spectra were recorded on a LCQ ion trap mass spectrometer (Thermo Fisher. San Jose.CA, USA), equipped with an EI source. Elemental analyses were carried out using a Perkin-Elmer, CHN elemental analyzer.

* To whom all correspondence should be sent:
E-mail: ahmadikiau@yahoo.com

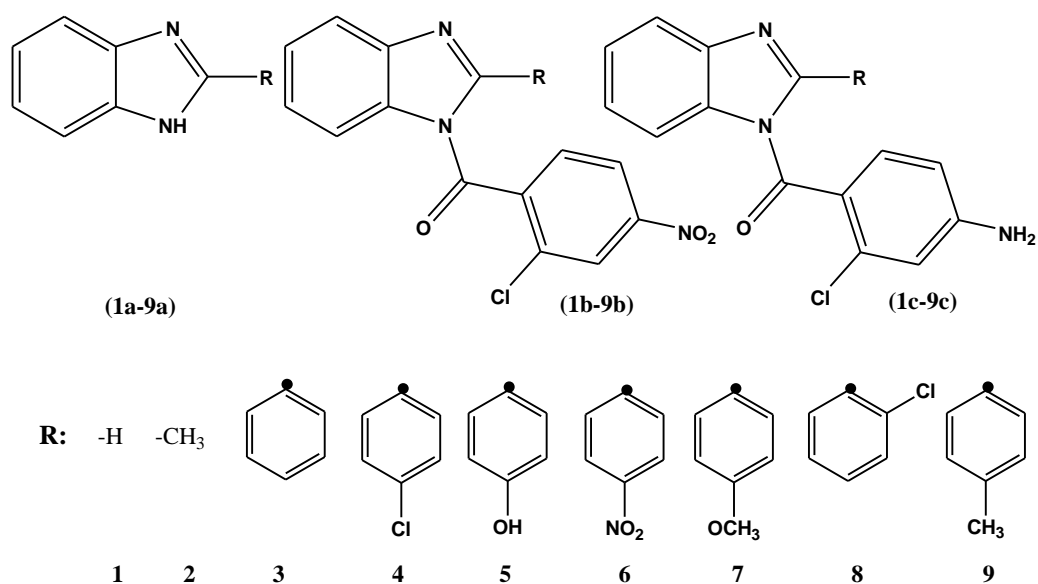


Figure 1. Structural formulae for intermediates (1a-9a) and final synthesized compounds (1b-9b, and 1c-9c).

Synthesis of Compounds

These compounds (**1a-9a**) were prepared based on a known methods with some modification [30,31].

1*H*-benzimidazole (**1a**):

o-phenylenediamine (5.4 g, 0.25 mole) and formic acid 90% (3.2 g, 0.34 mole) were heated on water bath for 2 h at 100 °C. The mixture was slowly cooled, basified with aqueous sodium hydroxide and the solid compound was obtained, filtered and re-crystallized from boiling water (Scheme 1).

(**1a**: White powder, m.p. 169-171 °C, 92.8% yield).

2-Methyl-1*H*-benzimidazole (**2a**):

o-phenylenediamine dihydrochloride (5.43 g, 0.03 mole) in 20 ml of water and (5.4 g, 0.09) of acetic acid were heated under reflux for 45 min. The mixture was slowly cooled, basified with ammonia solution and the solid compound filtered and re-crystallized from ethanol (Scheme 1).

(**2a**: Light beige to brown powder, m.p. 175–177 °C, 91.8% yield)

General procedure for the preparation of the compounds (**3a-9a**):

o-phenylenediamine (0.055 mol), appropriate benzoic acid (0.05 mol) and HCl (4N, 25 ml) were refluxed for 2 h. The reaction mixture was cooled, poured into crushed ice and the product was re-crystallized in boiled water (Scheme 1).

2-Phenyl-1*H*-benzimidazole (**3a**):

(**3a**: White to beige-grey powder, m.p. 293–296 °C, 89.1% yield)

IR (KBr, cm^{-1}): 3345, 3060, 2925, 1671, 1444, 1276, 922, 744, 696; ^1H NMR (CDCl_3 , δ/ppm): 7.22 (m, 2H), 7.48 (m, 5H), 7.58 (s, 1 H), 8.04 (dd,

2H); ^{13}C -NMR (CDCl_3 , δ/ppm): 111.6 (benzimidazole, CH=), 122.1 (benzimidazole, CH=), 135.4 (benzimidazole, C), 149.3 (N-C=N), 134.3 (phenyl, C), 126.8, 129.4 (phenyl, CH=); Anal. Calcd. for $\text{C}_{13}\text{H}_{10}\text{N}_2$: C, 80.33; H, 5.15; N, 14.42 %. Found: C, 80.12; H, 5.08; N, 14.22%; MS, m/z : 195 $[\text{M}+\text{H}]^+$.

2-(4-Chlorophenyl)-1*H*-benzimidazole (**4a**):

(**4a**: White powder, m.p. 301–303 °C, 90.7% yield)

IR (KBr, cm^{-1}): 3369, 2918, 1604, 1515, 1341, 855, 745, 710; ^1H NMR (DMSO-d_6 , δ/ppm): 12.70 (br s, 1H), 8.08 (d, 2H), 7.59 (m, 1H), 7.26–7.20 (m, 3H), 7.18–7.04 (m, 2H); ^{13}C -NMR (CDCl_3 , δ/ppm): 111.5 (benzimidazole, CH=), 119.1 (benzimidazole, CH=), 136.7 (benzimidazole, C), 142.1 (N-C=N), 132.4 (phenyl, C), 130.9 (phenyl, Cl), 128.8, 129.8 (phenyl, CH=); Anal. Calcd. for $\text{C}_{13}\text{H}_9\text{ClN}_2$: C, 68.21; H, 3.93; N, 12.24 %. Found: C, 68.12; H, 3.89; N, 12.18%; MS, m/z : 229 $[\text{M}+\text{H}]^+$.

2-(4-Hydroxyphenyl)-1*H*-benzimidazole (**5a**):

(**5a**: White powder, m.p. 240-242 °C, 91.1% yield)

IR (KBr, cm^{-1}): 3420, 2921, 1610, 1447, 1280, 838, 746; ^1H NMR (DMSO-d_6 , δ/ppm): 8.16–8.22 (m, 2H), 7.21–7.73 (m, 6H), 4.60 (d, 1H); ^{13}C -NMR (CDCl_3 , δ/ppm): 111.6 (benzimidazole, CH=), 120.2 (benzimidazole, CH=), 137.8 (benzimidazole, C), 144.1 (N-C=N), 151.9 (phenyl, OH), 128.4 (phenyl, C), 127.8, 117.8 (phenyl, CH=); Anal. Calcd. for $\text{C}_{13}\text{H}_{10}\text{ON}_2$: C, 74.28; H, 4.76; N, 13.33 %. Found: C, 74.01; H, 4.65; N, 13.18%; MS, m/z : 211 $[\text{M}+\text{H}]^+$.

2-(4-Nitrophenyl)-1*H*-benzimidazole (**6a**):

(**6a**: Cream powder, m.p. 312-314 °C, 88.4% yield)

IR (KBr, cm^{-1}): 3369, 3058, 1604, 1515, 1341, 855, 745; ^1H NMR (DMSO- d_6 , δ/ppm): 8.00–8.08 (m, 2H), 7.20–7.60 (m, 6H); ^{13}C -NMR (CDCl_3 , δ/ppm): 112.2 (benzimidazole, CH=), 119.2 (benzimidazole, CH=), 138.6 (benzimidazole, C), 143.5 (N-C=N), 150.1 (phenyl, NO_2), 144.4 (phenyl, C), 125.8, 128.6 (phenyl, CH=); Anal. Calcd. for $\text{C}_{13}\text{H}_9\text{O}_2\text{N}_3$: C, 65.27; H, 3.76; N, 17.57 %. Found: C, 65.14; H, 3.69; N, 17.43%; MS, m/z : 240 $[\text{M}+\text{H}]^+$.

2-(4-Methoxyphenyl)-1H-benzimidazole (7a):

(7a): White powder, m.p. 225–226 °C, 85.9% yield)

IR (KBr, cm^{-1}): 3675, 3346, 1650, 1548, 1420, 1182, 812, 742; ^1H NMR (DMSO- d_6 , δ/ppm): 8.00–8.08 (m, 2H), 7.20–7.60 (m, 6H), 3.52 (m, 3H); ^{13}C -NMR (CDCl_3 , δ/ppm): 56.7 (CH_3), 111.7 (benzimidazole, CH=), 118.9 (benzimidazole, CH=), 136.9 (benzimidazole, C), 142.3 (N-C=N), 161.1 (phenyl, OMe), 129.3 (phenyl, C), 113.8, 127.9 (phenyl, CH=); Anal. Calcd. for $\text{C}_{14}\text{H}_{12}\text{ON}_2$: C, 75.02; H, 5.36; N, 12.51 %. Found: C, 74.91; H, 5.30; N, 12.43%; MS, m/z 224 $[\text{M}]^+$.

2-(2-Chlorophenyl)-1H-benzimidazole (8a):

(8a): White powder, m.p. 232–234 °C, 86.3% yield)

IR (KBr, cm^{-1}): 3372, 2922, 1599, 1521, 1348, 850, 739, 712; ^1H NMR (DMSO- d_6 , δ/ppm): 8.00–8.08 (m, 2H), 7.20–7.60 (m, 6H); ^{13}C -NMR (CDCl_3 , δ/ppm): 112.3 (benzimidazole, CH=), 121.1 (benzimidazole, CH=), 135.9 (benzimidazole, C), 140.9 (N-C=N), 139.4 (phenyl, C), 134.6 (phenyl, Cl), 127.8, 128.8, 130.1 (phenyl, CH=); Anal. Calcd. for $\text{C}_{13}\text{H}_9\text{ClN}_2$: C, 68.21; H, 3.93; N, 12.24 %. Found: C, 68.14; H, 3.87; N, 12.15%; MS, m/z : 228 $[\text{M}]^+$.

2-p-Tolyl-1H-benzimidazole (9a):

(9a): White to beige-grey powder, m.p. 268–270 °C, 84.9% yield)

IR (KBr, cm^{-1}): 3392, 2919, 1616, 1515, 1384, 1274, 821, 747; ^1H NMR (CDCl_3 , δ/ppm): 8.00–8.08 (m, 2H), 7.20–7.60 (m, 6H), 2.60 (m, 3H); ^{13}C -NMR (CDCl_3 , δ/ppm): 21.3 (CH_3), 112.4 (benzimidazole, CH=), 119.9 (benzimidazole, CH=), 138.3 (benzimidazole, C), 145.1 (N-C=N), 138.9 (phenyl, Me), 134.7 (phenyl, C), 128.8, 130.1 (phenyl, CH=); Anal. Calcd. for $\text{C}_{14}\text{H}_{12}\text{N}_2$: C, 80.77; H, 5.77; N, 13.46 %. Found: C, 80.65; H, 5.59; N, 13.37%; MS, m/z : 209 $[\text{M}+\text{H}]^+$.

General procedure for the preparation of the compounds (1b-9b):

A solution of 2-Chloro-4-nitrobenzoyl chloride (2.2 g, 0.01 mol) in acetone (2.5 ml) was drop wise

added to the solution (25 ml) of benzimidazoles (**1a-9a**) (0.01 mol) in NaOH (1g). The mixture was stirred and heated under reflux for 2 h. After completion, the reaction was slowly cooled, water added and the solid compound obtained, filtered, dried and re-crystallized from THF (Scheme 1) [30].

Benzimidazole-1-yl-(2-chloro-4-nitrophenyl)-methanone (1b):

(1b): Yellowish powder, m.p. 137–142 °C, 86.3% yield)

IR (KBr, cm^{-1}): 3068, 2973, 1731, 1571, 1501, 1285, 684; ^1H -NMR (CDCl_3 , δ/ppm): 7.40–7.75 (m, 4H, benzimidazole), 8.01(s, 1H), 7.95–8.21 (m, 3H, Ar-H); ^{13}C -NMR (CDCl_3 , δ/ppm): 112.9–135.2 (benzimidazole, C), 120.6–151.9 (Phenyl, C), 145.1 (N-C=N), 187.6 (C=O). Anal. Calcd. for $\text{C}_{14}\text{H}_8\text{ClN}_3\text{O}_3$: C, 55.74; H, 2.67; N, 13.93 %. Found: C, 55.68; H, 2.60; N, 13.85 %. MS, m/z : 301 $[\text{M}]^+$.

(2-Chloro-4-nitrophenyl)-(2-methyl-benzimidazole-1-yl)-methanone (2b):

(2b): Pale cream powder, m.p. 145–147 °C, 88.9% yield)

IR (KBr, cm^{-1}): 3059, 2963, 1745, 1580, 1483, 1270, 825, 684; ^1H -NMR (CDCl_3 , δ/ppm): 2.52 (s, 3H), 7.38–7.80 (m, 4H, benzimidazole), 7.95–8.21 (m, 3H, Ar-H); ^{13}C -NMR (CDCl_3 , δ/ppm): 17.9 (CH_3), 116.1–136.2 (benzimidazole, C), 121.6–154.3 (Phenyl, C), 144.3 (N-C=N), 191.1 (C=O). Anal. Calcd. for $\text{C}_{15}\text{H}_{10}\text{ClN}_3\text{O}_3$: C, 57.06; H, 3.19; N, 13.31 %. Found: C, 57.01; H, 3.05; N, 13.22 %. MS, m/z : 315 $[\text{M}]^+$.

(2-Chloro-4-nitrophenyl)-(2-phenyl-benzimidazole-1-yl)-methanone (3b):

(3b): Cream powder, m.p. 155–157 °C, 90.7% yield)

IR (KBr, cm^{-1}): 3033, 2955, 1756, 1570, 1496, 1263, 840, 675; ^1H -NMR (CDCl_3 , δ/ppm): 7.30–7.75 (m, 4H, benzimidazole), 7.45–8.52 (m, 8H, Ar-H); ^{13}C -NMR (CDCl_3 , δ/ppm): 113.1–135.7 (benzimidazole, C), 124.5–133.4 (Phenyl, C), 146.7 (N-C=N), 190.8 (C=O). Anal. Calcd. for $\text{C}_{20}\text{H}_{12}\text{ClN}_3\text{O}_3$: C, 63.59; H, 3.20; N, 11.12 %. Found: C, 63.51; H, 3.16; N, 11.02 %. MS, m/z : 377 $[\text{M}]^+$.

(2-Chloro-4-nitrophenyl)-[2-(4-chlorophenyl)-benzimidazole-1-yl]-methanone (4b):

(4b): Yellow powder, m.p. 160–162 °C, 93.1% yield)

IR (KBr, cm^{-1}): 3044, 2966, 1766, 1578, 1501, 1272, 851, 669; ^1H -NMR (CDCl_3 , δ/ppm): 7.32–7.80 (m, 4H, benzimidazole), 7.51–8.48 (m, 7H, Ar-H); ^{13}C -NMR (CDCl_3 , δ/ppm): 112.4–136.9

(benzimidazole, C), 130.5-157.4 (Phenyl, C), 142.5 (N-C=N), 191.3 (C=O). Anal. Calcd. for $C_{20}H_{11}Cl_2N_3O_3$: C, 58.27; H, 2.69; N, 10.19 %. Found: C, 58.19; H, 2.60; N, 10.10 %. MS, m/z : 411[M]⁺.

(2-Chloro-4-nitrophenyl)-[2-(4-hydroxyphenyl)-benzimidazole-1-yl]-methanone (5b):

(5b): White-grey powder, m.p. 175-178 °C, 88.1% yield)

IR (KBr, cm^{-1}): 3430, 3015, 2940, 1750, 1540, 1478, 1233, 902, 701; ¹H-NMR (CDCl₃, δ/ppm): 5.44 (s, 1H, OH), 7.30-7.75 (m, 4H, benzimidazole), 7.44-8.56 (m, 7H, Ar-H); ¹³C-NMR (CDCl₃, δ/ppm): 111.9-137.3 (benzimidazole, C), 130.5-148.4 (Phenyl, C), 160.3 (Phenyl, C-OH), 147.5 (N-C=N), 195.3 (C=O). Anal. Calcd. for $C_{20}H_{12}ClN_3O_4$: C, 61.01; H, 3.08; N, 10.67 %. Found: C, 60.92; H, 3.01; N, 10.58 %. MS, m/z : 393[M]⁺.

(2-Chloro-4-nitrophenyl)-[2-(4-nitrophenyl)-benzimidazole-1-yl]-methanone (6b):

(6b): White-grey powder, m.p. 175-178 °C, 88.1% yield)

IR (KBr, cm^{-1}): 3022, 2970, 1801, 1555, 1465, 1238, 889, 707; ¹H-NMR (CDCl₃, δ/ppm): 7.25-7.75 (m, 4H, benzimidazole), 7.90-8.45 (m, 7H, Ar-H); ¹³C-NMR (CDCl₃, δ/ppm): 112.8-138.8 (benzimidazole, C), 129.8-143.4 (Phenyl, C), 154.3 (Phenyl, C-NO₂), 145.5 (N-C=N), 194.4 (C=O). Anal. Calcd. for $C_{20}H_{11}ClN_4O_5$: C, 56.82; H, 2.62; N, 13.25 %. Found: C, 56.75; H, 2.53; N, 13.11 %. MS, m/z : 422[M]⁺.

(2-Chloro-4-nitrophenyl)-[2-(4-methoxyphenyl)-benzimidazole-1-yl]-methanone (7b):

(7b): White-cream powder, m.p. 163-167 °C, 90.8% yield)

IR (KBr, cm^{-1}): 3053, 2975, 1781, 1563, 1488, 1247, 1115, 877, 705; ¹H-NMR (CDCl₃, δ/ppm): 3.69 (s, 3H, CH₃), 7.33-7.75 (m, 4H, benzimidazole), 7.01-8.22 (m, 7H, Ar-H); ¹³C-NMR (CDCl₃, δ/ppm): 59.6 (CH₃) 115.8-137.6 (benzimidazole, C), 114.8-140.4 (Phenyl, C), 167.3 (Phenyl, O-CH₃), 144.1 (N-C=N), 192.2 (C=O). Anal. Calcd. for $C_{21}H_{14}ClN_3O_4$: C, 61.85; H, 3.46; N, 10.30 %. Found: C, 61.79; H, 3.40; N, 10.22 %. MS, m/z : 407[M]⁺.

(2-Chloro-4-nitrophenyl)-[2-(2-chlorophenyl)-benzimidazole-1-yl]-methanone (8b):

(8b): Pale yellow powder, m.p. 160-162 °C, 93.1% yield)

IR (KBr, cm^{-1}): 3044, 2966, 1766, 1578, 1501, 1272, 851, 669; ¹H-NMR (CDCl₃, δ/ppm): 7.28-

7.85 (m, 4H, benzimidazole), 7.19-8.40 (m, 7H, Ar-H); ¹³C-NMR (CDCl₃, δ/ppm): 113.8-137.9 (benzimidazole, C), 131.5-149.4 (Phenyl, C), 146.3 (N-C=N), 190.9 (C=O). Anal. Calcd. for $C_{20}H_{11}Cl_2N_3O_3$: C, 58.27; H, 2.69; N, 10.19 %. Found: C, 58.22; H, 2.63; N, 10.12 %. MS, m/z : 413[M+2H]⁺.

(2-Chloro-4-nitrophenyl)-(2-p-tolyl)-benzimidazole-1-yl)-methanone (9b):

(9b): White powder, m.p. 170-172 °C, 88.3% yield)

IR (KBr, cm^{-1}): 3044, 2983, 1786, 1575, 1492, 1265, 1133, 881, 693; ¹H-NMR (CDCl₃, δ/ppm): 2.83 (s, 3H, CH₃), 7.25-7.80 (m, 4H, benzimidazole), 7.10-8.30 (m, 7H, Ar-H); ¹³C-NMR (CDCl₃, δ/ppm): 30.6 (CH₃) 114.4-135.8 (benzimidazole, C), 118.7-142.5 (Phenyl, C), 142.1 (N-C=N), 193.1 (C=O). Anal. Calcd. for $C_{21}H_{14}ClN_3O_3$: C, 64.37; H, 3.60; N, 9.05 %. Found: C, 64.28; H, 3.52; N, 8.95 %. MS, m/z : 391[M]⁺.

General procedure for the preparation of the compounds (1c-9c):

Reduction of 2-substituted-1H-benzoyl imidazol-1-yl (2-Chloro-4-nitrophenyl) methanone

Synthesized products (1b-9b) (0.1 mol), tin powder (30 g, 0.25 mol) and conc. HCl solution (15 ml) were refluxed for 1 h. The reaction mixture was then cooled; added water and ammonia solution, heated on water bath for 30 min, filtered and wash with hot water for obtaining the liquid compound, acidified with glacial acetic acid, evaporated, filtered and dried (Scheme 1) [30].

(4-Amino-2-chloro-phenyl)-(benzimidazol-1-yl)-methanone (1c):

(1c): Pale brown powder, m.p. 270-272 °C, 79.3% yield)

IR (KBr, cm^{-1}): 3304, 3298, 2956, 2983, 1645, 1601, 1482, 1275, 890, 705; ¹H-NMR (DMSO-d₆, δ/ppm): 4.40 (br s, 2H, NH₂), 7.05-7.60 (m, 4H, benzimidazole), 6.69-7.68 (m, 3H, Ar-H), 8.01 (s, 1H); ¹³C-NMR (CDCl₃, δ/ppm): 115.4-131.98 (benzimidazole, C), 123.7-140.8 (Phenyl, C), 143.8 (N-C=N), 166.3 (Phenyl, C-NH₂), 189.1 (C=O). Anal. Calcd. for $C_{14}H_{10}ClN_3O$: C, 61.89; H, 3.71; N, 15.47 %. Found: C, 61.78; H, 3.66; N, 15.39 %. MS, m/z : 271[M]⁺.

(4-Amino-2-chloro-phenyl)-(2-methyl-benzimidazol-1-yl)-methanone (2c):

(2c): Brown powder, m.p. 282-285 °C, 76.8% yield)

IR (KBr, cm^{-1}): 3245, 3198, 2920, 2893, 1678, 1586, 1469, 1315, 907, 659; ¹H-NMR (DMSO-d₆, δ/ppm): 2.11 (s, 3H, CH₃), 5.20 (br s, 2H, NH₂), 7.12-7.65 (m, 4H, benzimidazole), 6.45-7.68 (m,

3H, Ar-H); ^{13}C -NMR (CDCl_3 , δ/ppm): 12.8 (CH_3), 116.4-132.8 (benzimidazole, C), 126.7-142.8 (Phenyl, C), 146.2 (N-C=N), 159.8 (Phenyl, C-NH₂), 190.8 (C=O). Anal. Calcd. for $\text{C}_{15}\text{H}_{12}\text{ClN}_3\text{O}$: C, 63.05; H, 4.23; N, 14.71 %. Found: C, 62.92; H, 4.06; N, 14.62 %. MS, m/z : 285[M]⁺.

(4-Amino-2-chloro-phenyl)-(2-phenyl-benzimidazol-1-yl)-methanone (3c):

(3c: Pale brown powder, m.p. 298-301 °C, 75.6% yield)

IR (KBr, cm^{-1}): 3225, 3075, 3171, 2938, 2893, 1671, 1595, 1455, 1323, 875, 708; ^1H -NMR (DMSO-d_6 , δ/ppm): 5.10 (br s, 2H, NH₂), 7.18-7.85 (m, 4H, benzimidazole), 6.95-7.55 (m, 8H, Ar-H); ^{13}C -NMR (CDCl_3 , δ/ppm): 111.9-129.5 (benzimidazole, C), 122.7-146.8 (Phenyl, C), 142.2 (N-C=N), 156.5 (Phenyl, C-NH₂), 188.1 (C=O). Anal. Calcd. for $\text{C}_{20}\text{H}_{14}\text{ClN}_3\text{O}$: C, 69.07; H, 4.06; N, 12.08 %. Found: C, 68.92; H, 3.98; N, 11.95 %. MS, m/z : 347[M]⁺.

(4-Amino-2-chloro-phenyl)-[2-(4-chloro-phenyl)-benzimidazol-1-yl]-methanone (4c):

(4c: Pale yellow powder, m.p. 288-291 °C, 74.7% yield)

IR (KBr, cm^{-1}): 3346, 3267, 3028, 2946, 2812, 1680, 1611, 1501, 1312, 885, 720; ^1H -NMR (DMSO-d_6 , δ/ppm): 4.90 (br s, 2H, NH₂), 7.22-7.75 (m, 4H, benzimidazole), 6.85-7.75 (m, 7H, Ar-H); ^{13}C -NMR (CDCl_3 , δ/ppm): 113.1-128.6 (benzimidazole, C), 125.7-139.8 (Phenyl, C), 145.2 (N-C=N), 160.5 (Phenyl, C-NH₂), 189.4 (C=O). Anal. Calcd. for $\text{C}_{20}\text{H}_{13}\text{Cl}_2\text{N}_3\text{O}$: C, 62.84; H, 3.43; N, 10.99 %. Found: C, 62.78; H, 3.38; N, 10.91 %. MS, m/z : 383[M+2]⁺.

(4-Amino-2-chloro-phenyl)-[2-(4-hydroxy-phenyl)-benzimidazol-1-yl]-methanone (5c):

(5c: Pale orange powder, m.p. 302-304 °C, 71.9% yield)

IR (KBr, cm^{-1}): 3448, 3367, 3128, 2956, 2832, 1690, 1641, 1511, 1332, 890, 672; ^1H -NMR (DMSO-d_6 , δ/ppm): 4.95 (br s, 2H, NH₂), 7.12-7.65 (m, 4H, benzimidazole), 6.65-7.85 (m, 7H, Ar-H) 11.95 (br s, 1H, OH); ^{13}C -NMR (CDCl_3 , δ/ppm): 114.1-129.8 (benzimidazole, C), 128.7-142.8 (Phenyl, C), 141.9 (N-C=N), 161.1 (Phenyl, C-NH₂), 164.2 (Phenyl, C-OH) 181.4 (C=O). Anal. Calcd. for $\text{C}_{20}\text{H}_{14}\text{ClN}_3\text{O}_2$: C, 66.03; H, 3.88; N, 11.55 %. Found: C, 65.95; H, 3.82; N, 11.49 %. MS, m/z : 363[M]⁺.

(4-Amino-2-chloro-phenyl)-[2-(4-nitro-phenyl)-benzimidazol-1-yl]-methanone (6c):

(6c: Orange powder, m.p. 300-302 °C, 72.5% yield)

IR (KBr, cm^{-1}): 3342, 3136, 2948, 2844, 1685, 1652, 1493, 1312, 897, 721; ^1H -NMR (DMSO-d_6 , δ/ppm): 4.60 (br s, 2H, NH₂), 7.13-7.80 (m, 4H, benzimidazole), 6.51-8.35 (m, 7H, Ar-H); ^{13}C -NMR (CDCl_3 , δ/ppm): 115.3-134.6 (benzimidazole, C), 126.3-143.5 (Phenyl, C), 143.6 (N-C=N), 164.3 (Phenyl, C-NH₂), 178.4 (C=O). Anal. Calcd. for $\text{C}_{20}\text{H}_{13}\text{ClN}_4\text{O}_3$: C, 61.16; H, 3.34; N, 14.26 %. Found: C, 61.10; H, 3.28; N, 14.19 %. MS, m/z : 392[M]⁺.

(4-Amino-2-chloro-phenyl)-[2-(4-methoxy-phenyl)-benzimidazol-1-yl]-methanone (7c):

(7c: Cream powder, m.p. 283-286 °C, 75.8% yield)

IR (KBr, cm^{-1}): 3203, 2948, 1745, 1602, 1542, 1321, 1175, 802, 715; ^1H -NMR (CDCl_3 , δ/ppm): 2.29 (s, 3H, CH₃), 5.34 (br s, 2H, NH₂), 7.18-7.65 (m, 4H, benzimidazole), 6.53-7.42 (m, 7H, Ar-H); ^{13}C -NMR (CDCl_3 , δ/ppm): 54.7 (CH₃) 116.8-138.1 (benzimidazole, C), 122.8-148.4 (Phenyl, C), 147.1 (N-C=N), 169.5 (Phenyl, O-CH₃), 179.2 (C=O). Anal. Calcd. for $\text{C}_{21}\text{H}_{16}\text{ClN}_3\text{O}_2$: C, 66.76; H, 4.27; N, 11.12 %. Found: C, 66.69; H, 4.20; N, 11.02 %. MS, m/z : 377[M]⁺.

(4-Amino-2-chloro-phenyl)-[2-(2-chloro-phenyl)-benzimidazol-1-yl]-methanone (8c):

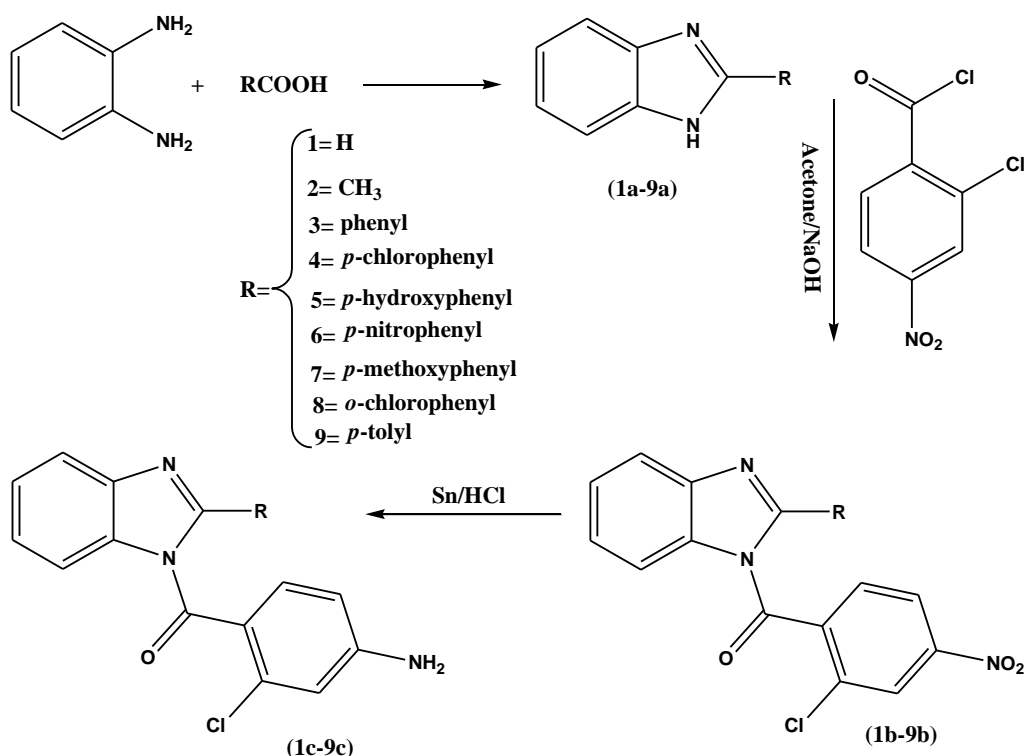
(8c: Yellow powder, m.p. 275-278 °C, 73.4% yield)

IR (KBr, cm^{-1}): 3332, 3222, 2931, 2825, 1692, 1601, 1495, 1344, 875, 707; ^1H -NMR (DMSO-d_6 , δ/ppm): 4.93 (br s, 2H, NH₂), 7.23-7.78 (m, 4H, benzimidazole), 6.88-7.83 (m, 7H, Ar-H); ^{13}C -NMR (CDCl_3 , δ/ppm): 113.5-128.2 (benzimidazole, C), 125.1-139.3 (Phenyl, C), 144.8 (N-C=N), 162.5 (Phenyl, C-NH₂), 180.1 (C=O). Anal. Calcd. for $\text{C}_{20}\text{H}_{13}\text{Cl}_2\text{N}_3\text{O}$: C, 62.84; H, 3.43; N, 10.99 %. Found: C, 62.76; H, 3.36; N, 10.90 %. MS, m/z : 383[M+2]⁺.

(4-Amino-2-chloro-phenyl)-(2-p-tolyl-benzimidazol-1-yl)-methanone (9c):

(9c: White-grey powder, m.p. 268-272 °C, 74.8% yield)

IR (KBr, cm^{-1}): 3033, 2975, 1778, 1582, 1465, 1287, 1167, 892, 722; ^1H -NMR (CDCl_3 , δ/ppm): 2.78 (s, 3H, CH₃), 5.22 (br s, 2H, NH₂), 7.20-7.85 (m, 4H, benzimidazole), 7.14-8.20 (m, 7H, Ar-H); ^{13}C -NMR (CDCl_3 , δ/ppm): 32.1 (CH₃), 115.8-136.5 (benzimidazole, C), 120.1-145.5 (Phenyl, C), 144.1 (N-C=N), 189.8 (C=O). Anal. Calcd. for $\text{C}_{21}\text{H}_{16}\text{ClN}_3\text{O}$: C, 69.71; H, 4.46; N, 11.61 %. Found: C, 69.66; H, 4.39; N, 11.55 %. MS, m/z : 361[M]⁺.



Scheme 1. Schematic synthesis of intermediates (1a-9a) and new compounds (1b-9b and 1c-9c).

In Vitro Biological Evaluation Test

The antibacterial and antifungal screening of newly synthesized compounds (**1c-9c**) were tested by filter paper disc method. The antibacterial activity of test compounds were evaluated against Gram-positive bacteria, *Staphylococcus aureus* and Gram-negative bacteria, *Escherichia coli*. Antifungal activity was screened against fungal strain, *Candida albicans*. The antimicrobial activity was performed at concentrations 50 & 100 µg/ml. Mueller hinton agar (MHA) & Potato dextrose agar (PDA) were employed as culture medium and DMSO was used as solvent control for antimicrobial activity. Ciprofloxacin and Amphotericin B were used as standard for antibacterial and antifungal activities respectively. The potato dextrose agar (PDA) media dissolved in distilled water then was sterilized by autoclaving at 121°C for 20 min at the appropriate pressure. The media removed and cooled at 40-45 °C. Whatman filter paper-1 discs (6 mm) were sterilized by dry heat were saturated with test solution and placed on (PDA) media in Petri dishes in triplicate. The Petri dishes were covered and set aside for an hour, and then incubated at 37 °C for 48 hrs. After incubation, the zones of inhibition around the disc were observed. Results were interpreted in terms of diameter (mm) of zone of inhibition. The zones of inhibition were measured and the average of three readings was calculated [32-34].

RESULTS AND DISCUSSIONS

Chemistry

In continuation of our interest to investigate of new pharmaceutical potential compounds, the syntheses of biologically active 2-substituted benzimidazole derivatives were carried out in this study. To materialize the proposed project, initially, some intermediates were synthesized (**1a-9a**) in good yields by coupling of *o*-phenylenediamine dihydrochloride with some carboxylic acids such as formic, acetic, benzoic, 4-chloro-benzoic, 4-hydroxy-benzoic, 4-nitro-benzoic, 4-methoxy-benzoic, 2-chloro-benzoic and 4-methyl-benzoic respectively based on a known method with some modification for increasing yields. Benzoylation of the 2-substituted benzimidazoles were applied in presence of 2-Chloro-4-nitrobenzoyl chloride yield 2-substituted-1*H*-benzoyl imidazol-1-yl (2-Chloro-4-nitrophenyl) methanones (**1b-9b**). Reductions of these compounds by tin powder produce the final products (**1c-9c**). TLC was used for monitoring the progress of the reaction and the structures of new compounds were assessed by interpretation of obtained spectra (IR, ¹H-NMR, ¹³C-NMR, Mass Spectra and CHN analysis).

Biological Evaluation

For evaluation of the biological activities, the synthesized compounds (**1c-9c**) were screened for their *in vitro* antibacterial activity against

Table 1. Zone of inhibition (mm±S.D) of test sample and Standard Drug (Ciprofloxacin and Amphotericin B) against *S. Aureus*, *E. coli* and *C. albicans*

Test samples	Diameter of zone of inhibition in mm [mean ± SD (n=3)]					
	<i>S. Aureus</i>		<i>E. coli</i>		<i>C. albicans</i>	
	50 µg/ml	100 µg/ml	50 µg/ml	100 µg/ml	50 µg/ml	100 µg/ml
1c	9.52±0.42	12.281±0.42	8.42±0.50	11.60±0.32	N/A	N/A
2c	9.90±1.30	12.80±0.30	8.15±0.50	11.22±0.60	N/A	N/A
3c	9.70±0.75	12.95±0.20	8.10±0.64	11.25±0.15	N/A	N/A
4c	9.75±0.44	12.96±0.40	8.40±0.25	11.86±0.36	N/A	N/A
5c	9.58±0.71	12.64±1.30	8.86±1.11	11.10±0.46	N/A	N/A
6c	9.32±0.36	12.88±0.32	8.88±0.78	11.66±0.35	N/A	N/A
7c	9.85±0.66	13.10±0.68	8.76±0.38	11.20±0.45	N/A	N/A
8c	9.45±0.60	13.25±0.20	8.26±0.30	11.20±0.25	N/A	N/A
9c	9.35±0.60	13.15±0.20	8.46±0.40	11.30±0.40	N/A	N/A
Ciprofloxacin	14.36±0.36	19.24±0.35	11.36±0.44	16.45±0.28	-	-
Amphotericin B	-	-	-	-	9.35±0.24	14.56±0.45

"N/A" = Not Active, "-" = Not Applicable

Staphylococcus aureus and *Escherichia coli* and antifungal activity against *Candida albicans* by measuring the zone of inhibition in mm in comparison with those of the standard drugs Ciprofloxacin and Amphotericin B. The preliminary screening results for the compounds (**1c-9c**) established that the newly synthesized compounds have not shown antifungal activity against *Candida albicans*. But the antibacterial activity data reveals that the compounds (**1c-9c**) exhibited good antibacterial activity against various strains of bacteria as compared to standard Ciprofloxacin. The results are tabulated in Table 1.

CONCLUSION

A series of some novel 2-Substituted benzimidazole derivatives were synthesized and evaluated for their potential antimicrobial and antifungal activities. Based on results, it can be concluded that all the target synthesized compounds (**1c-9c**) showed good to moderate antimicrobial activities. The results indicated that new antimicrobial compounds could be prepared by changing of different substrates on various benzimidazole derivatives. Although further pharmacological activities of these new compounds could be evaluated in future studies.

ACKNOWLEDGEMENTS: The author gratefully acknowledges beneficial support of Islamic Azad University Karaj Branch for this research project.

REFERENCES

1. R. Varala, R. Enugala, *Chem. Pharm. Bull.*, **55**, 1254 (2007).
2. H. Zarrinmayeh, A. M. Nunes, P. L. Ornstein, D. A. Zimmerman, S. L. Gackenheimer, F. Bruns, P. A. Hipskind, T. C. Britton, B. E. Cantrell, D. R. Gehlert, *J. Med. Chem.*, **41**, 2709 (1998).
3. G. L. Gravatt, B. C. Baguley, W. R. Wilson, W. A. Denny, *J. Med. Chem.*, **37**, 4338 (1994).
4. B. Jayashankara, K. M. L. Rai, *ARKIVOC*, **11**, 75 (2008).
5. K. C. Ravindra, H. M. Vagdevi, V. P. Vaidya, *ARKIVOC*, **11**, 1 (2008).
6. H. Nakano, T. Inoue, N. Kawasaki, H. Miyataka, H. Matsumoto, T. Taguchi, N. Inagaki, H. Nagai, T. Satoh, *Bioorg. Med. Chem.*, **8**, 373 (2000).
7. Z. S. Zhao, D.O. Arnaiz, B. Griedel, S. Sakata, J. L. Dallas, M. Whitlow, L. Trinh, J. Post, A. Liang, M. M. Morrissey, K. J. Shaw, *Bioorg. Med. Chem. Lett.*, **10**, 963 (2000).
8. A. W. White, R. Almassy, A. H. Calvert, N. J. Curtin, R. J. Griffin, Z. Hostomsky, K. Maegley, D. R. Newell, S. Srinivasan, B. T. Golding, *J. Med. Chem.*, **43**, 4084 (2000).
9. Z. Zhu, B. Lippa, J. C. Drach, L. B. Townsend, *J. Med. Chem.*, **43**, 2430 (2000).
10. S. Utku, M. Gokce, B. Ozelik, E. Bercin, *Turk J. Pharm. Sci.*, **5**, 107 (2008).
11. H. Nakano, T. Inoue, N. Kawasaki, H. Miyataka, H. Matsumoto, T. Taguchi, N. Inagaki, H. Nagai, T. Satoh, *Chem. Pharm. Bull.*, **47**, 1573 (1999).
12. V. J. Habernickel, *Drugs made in Germany*, **35**, 97 (1992).
13. I. Islam, E.B. Skibo, R.T. Dorr, D.S. Alberts, *J. Med. Chem.*, **34**, 2954 (1991).
14. L.L. Kruse, D.L. Ladd, R.B. Harrsch, F.L. McCabe, S.M. Mong, L. Faucette, *J. Med. Chem.*, **32**, 409 (1989).
15. T. Fukuda, Y. Morimoto, R. Iemura, T. Kawashima, G. Tsukamoto, K. Ito, *Arzneim. Forsch./Drug Res.*, **34**, 801 (1984).
16. G. Ayhan-Kilcigil, C. Kus, T. Çoban, B. Can-Eke, *J. Enz. Inhib. Med. Chem.*, **19**, 129 (2004).
17. C. Kus, G. Ayhan-Kilcigil, B. Can-Eke, M. Iscan, *Arch. Pharm. Res.*, **27**, 156 (2004).

18. B. Can-Eke, M.O. Puskullu, E. Buyukbingol, M. Iscan, *Chemico-Biological Interactions.*, **113**, 65 (1998).
19. H. Göker, G.A. Kilcigil, M. Tuncbilek, C. Kus, R. Ertan, E. Kendi, S. Özbey, M. Fort, C. Garcia, A.J. Farré, *Heterocycles.*, **51**, 2561 (1999).
20. H. Göker, C. Kus, D.W. Boykin, S. Yildiz, N. Altanlar, *Biorg. Med. Chem.*, **10**, 2589 (2002).
21. N.S. Habib, S. Abdel-Hamid, M. El-Hawash, *Farmaco*, **44**, 1225 (1989).
22. R.A. Coburn, M.T. Clark, R.T. Evans, R.J. Genco, *J. Med. Chem.*, **30**, 205 (1987).
23. F.S.G. Soliman, S.M. Rida, E.A.M. Badawey, T. Kappe, *Arch. Pharm.*, **317**, 951 (1984).
24. A.E. Abdel-Rahman, A.M. Mahmoud, G.M. El-Naggar, H.A. El-Sherief, *Pharmazie*, **38**, 589 (1983).
25. R.W. Middleton, D.G. Wibberley, *J. Heterocycl. Chem.*, **17**, 1757 (1980).
26. T. Hisano, M. Ichikawa, K. Tsumoto, M. Tasaki, *Chem. Pharm. Bull.*, **30**, 2996 (1982).
27. T.A. Fairley, R.R. Tidwell, I. Donkor, N.A. Naiman, K.A. Ohemeng, R.J. Lombardy, J. A. Bentley, M. Cory, *J. Med. Chem.*, **36**, 1746 (1993).
28. A. Czarny, W. D. Wilson, D. W. Boykin, *J. Heterocycl. Chem.*, **33**, 1393 (1996).
29. M.R. Grimmett, Otago University Academic Press: New Zealand, (1997).
30. B.S. Furniss and A.J. Hannaford, P.W.G. Smith, A.R. Tatchell, Vogel textbook of practical organic chemistry, Longman-ELBS., **5**, 1162 (2007).
31. Sh. Ming-Gui, C. Chun, *Journal of Fluorine Chemistry*, **128**, 232 (2007).
32. E.I. Alcamo, Fundamentals of microbiology, Jones and Bartlett Publishers, 11-115 (1994).
33. Pharmacopoeia of India, Govt. Of India, Ministry of Health and Family Welfare, New Delhi, Vol II, , A-111 (1996).
34. S.K. Srivastava, S. Verma, S.D. Srivastava. *J. Chem. Pharm. Res.*, **2**, 270 (2010).

СИНТЕЗА, ХАРАКТЕРИСТИКИ И БИОЛОГИЧНА ОЦЕНКА НА НЯКОИ НОВИ ПРОИЗВОДНИ НА БЕНЗИМИДАЗОЛА

А. Ахмади

Департамент по химия, Научен факултет, Ислямски университет "Азад", Клон в Карадж, Иран

Постъпила на 18 февруари; коригирана на 17 юни, 2013

(Резюме)

Бензимидазолото ядро има важно значение в медицинската химия, а много съединения, съдържащи бензимидазолово ядро проявяват важни биологично активни свойства. В настоящата работа се изследва синтезата, спектралните свойства и се оценява биологичната активност на девет нови производни на бензимидазола. Структурите на синтезираните съединения са охарактеризирани чрез ИЧ-спектроскопия, $^1\text{H-NMR}$, $^{13}\text{C-NMR}$, мас-спектроскопия и CHN – елементен анализ. Целевите нови съединения (**1c-9c**) са скринирани за антибактериална активност срещу щамове на *Escherichia coli* и *Staphylococcus aureus*, антигъбичната активност срещу *Candida albicans*.

Synthesis of dimethyl carbonate from urea and methanol catalyzed by iron-chloride ionic liquid

Sh. Feng¹, T. Sun¹, B. Lu², Q. Cai²

¹ College of Science, Heilongjiang Bayi Agricultural University

² Key Laboratory for Photonic and Electronic Bandgap Materials, Ministry of Education, School of Chemistry and Chemical Engineering, Harbin Normal University, 1 Shida Road Limin development Zone, Harbin 150025, P. R. China

Received February 25, 2013; revised July 5, 2013

The direct synthesis of dimethyl carbonate (DMC) from methanol and urea using iron-chloride ionic liquid as catalyst was investigated with a batch operation. The results showed that the ionic liquid $\text{Et}_3\text{NHCl-FeCl}_3$ is an effective catalyst; the raised yield (about 27%) and high selectivity (ca.100%) of DMC at 180°C were achieved without any specially designed equipment. The effect of the reaction conditions, such as reaction temperature, the molar ratio of urea to methanol, the amount and composition of catalysts, on the reaction was also discussed. The suggested reaction mechanism was proposed, which is very different from the reported ones in literatures.

Keywords: dimethyl carbonate; urea; methanol; ionic liquids; carbonylation

INTRODUCTION

Dimethyl carbonate (DMC) has been attracting much attention as an important chemical feedstock. It can be effectively used as an environmentally benign substitute for highly toxic phosgene and dimethyl sulfate in carbonylation and methylation [1], as monomer for several types of polymers and an intermediate in the synthesis of pharmaceutical and agricultural chemicals. Furthermore, DMC has been considered as an option for meeting the oxygenate specifications for transportation fuels [2]. The conventionally synthesis method of DMC is the oxidative carbonylation of methanol by carbon monoxide and transesterification of ethylene (or propylene) carbonate with methanol [3, 4]. It is expensive in using CO, epoxide as raw materials and accompanied by a potential explosion and poison hazard. Recently, utilization of carbon dioxide, a readily available, inexpensive and environmentally acceptable starting material, as raw material of DMC synthesis has widely been investigated [5-7]. But, the direct synthesis of DMC from methanol and carbon dioxide is still far from satisfactory due to the difficulty in activation of carbon dioxide, deactivation of the catalysts and the thermodynamic limitation. As an indirect method of utilizing CO_2 for DMC

synthesis, the synthesis of DMC from urea and methanol has been developed recently due to some advantages, such as abundant resource and low cost of urea and methanol, ternary azeotrope of methanol-water-DMC not to be formed because of no water produced and easiness of the product separation. Thus, this new route is considered to have alluring foreground in industry application. Although many research works on the new route have been reported yet [8-10], there are also several shortcomings, such as low conversion of the reactant or selectivity to DMC, higher reaction temperature and specially designed equipment to be used *etc.*

Recently, our group has disclosed the homogeneous and heterogeneous synthesis of DMC from urea and methanol catalyzed by zinc-chloride ionic liquid [11] and over $\text{Fe}_2\text{O}_3/\text{HMCM-49}$ [12]. As our continuous research work, here we wish report the direct synthesis of DMC from urea and methanol catalyzed by the ionic liquid $\text{Et}_3\text{NHCl-FeCl}_3$. The raised yield and high selectivity to DMC were achieved. The effect of various reaction conditions, such as reaction temperature, time and amount of the catalyst was also discussed in this paper.

EXPERIMENTAL SECTION

The catalyst $\text{Et}_3\text{NHCl-FeCl}_3$ was synthesized according to literature method [11, 13]. All

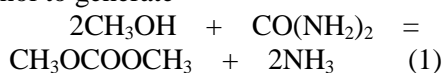
* To whom all correspondence should be sent:
E-mail: caiqinghai@yahoo.com

experiments were carried out in a stainless steel reactor with inner volume of 500 mL fixed with a mechanical stirrer and an electric heater. In a typical procedure, 67 mL (1.83 mol) of anhydrate methanol, 1 g (0.017 mol) of urea and 6.5 mmol of catalyst were added to the reactor. After being purged three times with N₂ gas, the reactor was heated to 180°C with stirring and the reaction was carried out for 6 h. At the end of the reaction, the reaction mixture was distilled to separate the catalyst from the mixture. The distillate was cooled, sampled and analyzed by GC and GC-MS. The yield was calculated on the basis of urea.

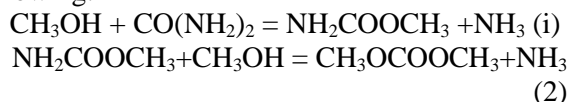
RESULTS AND DISCUSSION

Ionic liquid, Et₃NHCl-FeCl₃, exhibited a good catalytic activity for synthesis of DMC from methanol and urea (Fig. 1). The yield of DMC increased with amount of catalyst, it reached maximum 26.8% with 6.5 mmol of Et₃NHCl-FeCl₃ used. Then it declined as the amount of the catalyst was continuously increased. The fall of the yield was ascribed to the reduction of the selectivity to DMC since excess catalyst can also catalyze further conversion of the products into some by-products such as N-methyl urea, N-methyl methyl carbamate etc, which were detected by GC-MS in the reaction mixture.

According to the report [14], the synthesis reaction (1) from methanol and urea includes two steps: at first, urea reacts with one molecule of methanol to generate



carbamate (i); and then the carbamate continuously reacts with another one molecule of methanol to produce DMC (ii), as shown in following:



It was found that methyl carbamate (MC) was easily prepared from urea and methanol even in the absence of catalyst. It means the step (i) is a fast one and the second step (ii) is rate-determining step. In the case that the amount of the catalyst dose not exceeds 6.5 mmol, MC has been not detected in the samples, implying that the rate of the step (ii) was so fast that the intermediate rapidly reacted with urea once it was generated. In other words, the catalyst catalyzing the step (ii) is very effective and the selectivity is very high, nearly 100%.

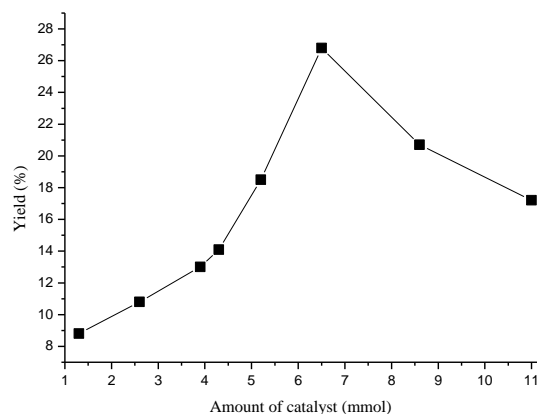


Fig. 1. Effect of catalyst amount on the reaction Conditions: T=180°C; CH₃OH/Urea ratio = 107.6/1; t = 6 h; FeCl₃/Et₃NHCl = 2:1.

The effect of the reaction time on the yield of DMC was investigated (the data not list here). It is known from the data that the yield reached to about 27% at the reaction time of 6 h. With the time continuously prolonged, the yield basically kept on constant. This finding suggested that the equilibrium state of the reaction was almost achieved under this condition. In addition, we can also calculate the ratio of initial urea concentration C₀ to its surplus concentration C in the reacting mixture from the data, then the ratio was taken logarithm, and the plot of ln(C₀/C) vs t (reaction time) is drawn in Fig. 2. It is evident that the relation curve is almost straight line, which indicated that the synthesis reaction is one order reaction for urea concentration in this system. Rate constant obtained from the figure is k_{Fe} = 0.0584 h⁻¹. As compared with zinc-chloride ionic liquid system (k_{Zn} = 0.0412 h⁻¹), Et₃NHCl-FeCl₃ system possesses higher reaction rate.

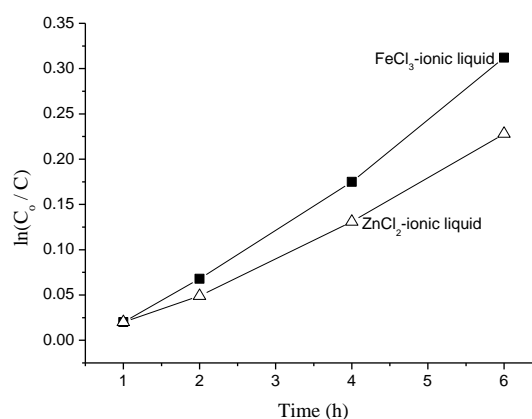


Fig. 2. Plot of ln(C₀/C) vs time. The lines fit the kinetic equation of first-order reaction.

As the raise of temperature, the yield increased rapidly to about 27% at 180 °C, and then fell to very low at 200 °C (Fig. 3). The changing rule of the yield is maybe attributed to the thermodynamic character of the reaction and reactant urea at higher temperatures. It

was reported that the heat of the synthesis reaction is $\Delta H^\ominus = 47.11$ KJ/mol [15], which shows that it is an endothermic reaction. Thus, in view of the thermodynamics, the increase of the reaction temperature is of a great advantage to the generation of DMC. On the other hand, from a view point of kinetics, raise of the reaction temperature can accelerate the reaction and shorten the time approaching to the equilibrium. Therefore, the yield increased with the temperature rising in the range from 130°C to 180 °C. On the other hand, it was recorded that the melting point of urea is 133-135 °C and it begins to decompose into HNCO and NH₃ [16] when the temperature increased more than its melting point. The increase of the temperature can promote the decomposition leading to

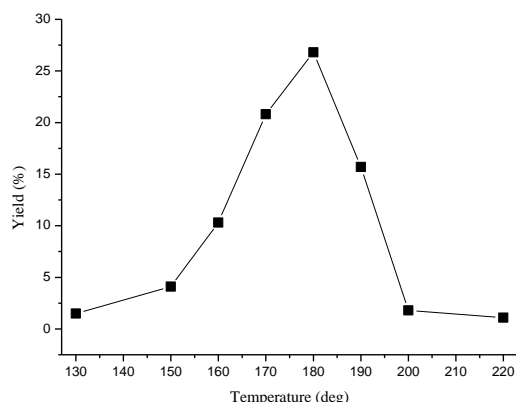


Fig. 3. Effect of reaction temperature on the reaction. Conditions: catalyst 6.5 mmol; CH₃OH/urea ratio = 107.6/1; t = 6 h; FeCl₃/Et₃NHCl = 2:1.

the increase of the HNCO concentration. The excess active particles HNCO caused some side reactions happened, resulting in the fall of the selectivity and the reduction of the yield.

Molar ratio of FeCl₃ to Et₃NHCl in the ionic liquid can greatly affect the synthesis reaction; the results were shown in Fig. 4. It is evident that a maximum of DMC yield was achieved when the ratio was 2:1; and when only the salt FeCl₃ was used as catalyst, the yield of DMC was merely 10.9%. This result implied that the ionic liquid formed by FeCl₃ and Et₃NHCl is very important for catalyzing DMC synthesis reaction. The better performance of the ionic liquid is most likely due to its enhancement to polarity and electrostatic field of the reaction medium, which may stabilize the charged intermediate [17]. In addition, the catalytic activity of metal-chloride ionic liquids is ascribed to their stronger acidity, which can absorb the released NH₃ to shift the reaction equilibrium to the direction producing DMC [11,

12]. Contrarily, too strong acidity of the ionic liquid is disadvantageous to the reaction according to our previous reports, which may cause strong

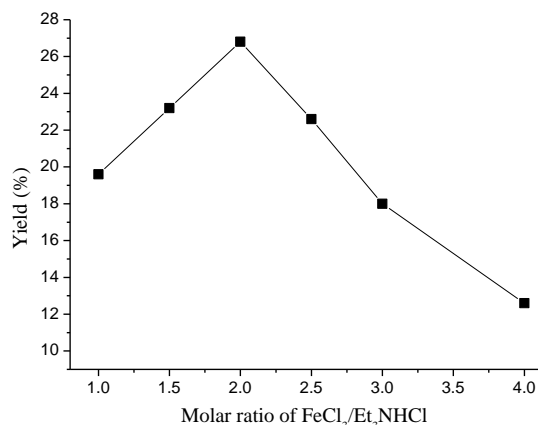
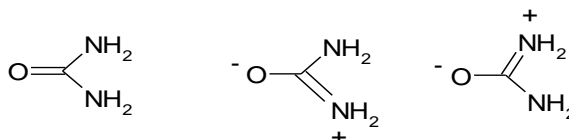


Fig. 4 Effect of molar ratio of FeCl₃ or ZnCl₂ to Et₃NHCl on the reaction. Conditions: catalyst 6.5 mmol; CH₃OH/urea ratio = 107.6/1; t = 6 h; T=180°C.

interaction with NH₂ in urea molecule to restrain its further reaction. Therefore, the catalyst with medium acidity could effectively activate urea and methanol and interact with release NH₃ gas produced in the reaction to promote shift of the reaction equilibrium to the direction producing DMC.

Suggested reaction mechanism

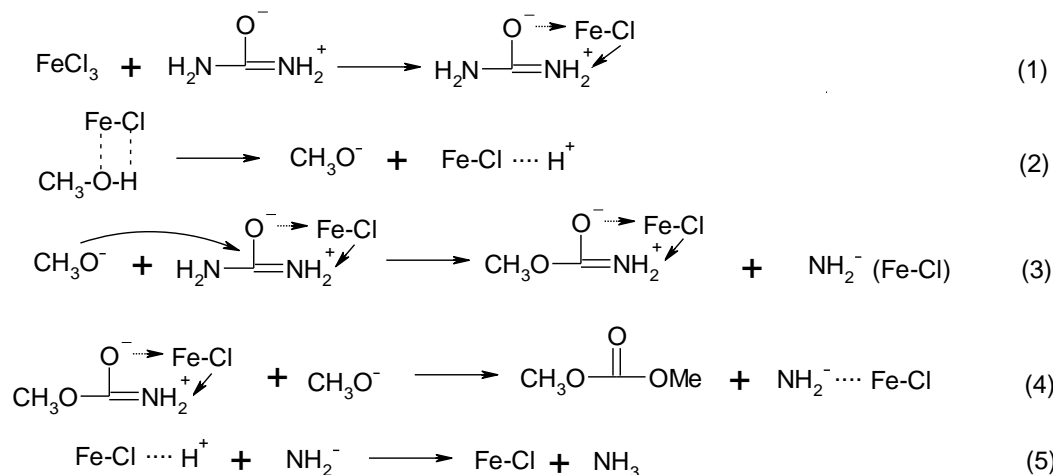
It was reported that the molecular structure of urea involves resonance between the three structures (following molecular structure of urea), the observed values of the interatomic distance indicating 30% double bond character for the carbon-to-nitrogen bonds leaving 40% for carbon-to-oxygen bond [18].



The molecular structure of urea

Therefore, the complexes were easily formed by urea molecules coordinating with metal ions through the oxygen as well as the nitrogen atoms. For example, six urea molecules coordinate with iron chloride to generate a complex, Fe[OC(NH₂)₂]₆Cl₃. The complex was formed by urea molecules coordinating with iron (III) ion through the oxygen atom [19]. On the basis of the above facts, the reaction mechanism of DMC synthesis from urea and methanol involved mutual activation of methanol and urea by the catalyst was proposed, as shown in Scheme 1.

This network involves the activation of urea and methanol by means of interaction of them with



Scheme 1. Suggested reaction mechanism.

catalysts to form two activated intermediates, complex of urea coordinated with (1) and methoxide anion CH_3O^- (2). Then, methoxide anion CH_3O^- attacks the carbon charged positively in the molecule of activated urea to generate methyl carbamate(3), which is also in the form of complex coordinated to FeCl_3 . The produced NH_2^- was stabilized by the ionic liquid $\text{Et}_3\text{NHCl}-\text{FeCl}_3$ due to its higher polarity and the stronger electrostatic interaction between the cations and anions, which is very advantageous to the step shifting to the right hand side. Finally, the activated methyl carbamate reacts with another CH_3O^- to produce the target product DMC (4), and the step (5) realize the catalytic cycle. As seen from the mechanism, it was the existence of the three activated particles, such as methoxide anion, complexes of urea and methyl carbamate coordinated with the transition metals Fe (III) in the catalyst, which results in high efficiency of the synthesis reaction via greatly accelerating the step (3) and (4). This is also the reason that no byproduct, methyl carbamate, was detected in the samples.

CONCLUSIONS

When the synthesis reaction of DMC was carried out in a batch operation and without any specially designed equipment, the ionic liquid $\text{Et}_3\text{NHCl}-\text{FeCl}_3$ is an effective catalyst for the direct synthesis of dimethyl carbonate (DMC) from methanol and urea by one step reaction; the raised yield (27%) and high selectivity (100%) to DMC under temperature of 180°C were achieved. Besides, the results were basically explained by the thermodynamics and kinetics of the reaction. The reaction mechanism that is different from that reported was proposed

ACKNOWLEDGEMENTS: We make a great acknowledgement for the financial support of this work by Foundation of the Natural Science Foundation, Educational Department and Harbin Science and Technology Bureau of Heilongjiang Province, China (Nos. B201119, 12511143 and 2013RFXXJ009).

REFERENCES

1. T. Pietro, S. Maurizio, *Acc. Chem. Res.*, **35**, 706 (2002).
2. A. P. Michael, L. M. Christopher, *Energy & Fuels*, **11**, 2 (1997).
3. A. Behr, *Angew Chem. Int. Ed. Engl.*, **27**, 661 (1988)
4. T. Matsuzaki, A. Nakamura, A., *Catal. Surv. Jpn.*, **1**, 77 (1997).
5. T. Zhao, Y. Han, Y. Sun, *Fuel. Proc. Tech.*, **62**, 187 (2000).
6. S. Fang, K. Fujimoto, *Appl. Catal. A: General*, **142**, L1 (1996)
7. S. Fujita, M. Bhalchandra, Y. Ikushima, M. Arai, *Green Chem.*, **3**, 87 (2000).
8. M. Wang, N. Zhao, W. Wei, Y. Sun, *Ind. Eng. Chem. Res.* **44**, 7596 (2005).
9. J. Sun, B. Yang, X. Wang, D. Wang, H. Lin, *J. Mol. Catal. A: Chem.* **239**, 82 (2005)
10. B. Yang, D. Wang, H. Lin, J. Sun, X. Wang, *Catal. Commun.* **7**, 472 (2006).
11. H. Wang, B Lu, X. Wang, J. Zhang, Q. Cai, *Fuel. Proc. Tech.*, **90**, 1198 (2009).
12. C. Zhang, B .Lu, X. Wang, J. Zhao, Q. Cai, *Catal. Sci. Technol.*, **2**, 305 (2012).
13. P. Bonhôte, A. Dias, N. Papageorgiou, K. Kalyanasundaram, M. Grätzel, *Inorg. Chem.*, **35**, 1168 (1996).

14. X. Q. Zhao, Y. J. Wang, Q. B. Shen, H. J. Yang, J. Y. Zhang, *Shi You Xue Bao-Shi You Jia Gong* (Acta Petrolei Sinica-Petroleum Processing Section), **5**, 47 (2002).
15. X. Q. Zhao, C. C. Wu, H. J. Yang, Y. J. Wang, J. Y. Zhang, Shi You Xue Bao, *Hua Xue Fan Ying Gong Cheng Yu Gong Yi* (Chemical Reaction Engineering and Technology, in Chinese), **3**, 200 (2002).
16. H. Wang, M. Wang, W. Zhao, W. Wei, Y. Sun, *Reac. Kinet. Mech. Catal.*, **99**, 381 (2010).
17. Q. Cai, J. Li, F. Bao, Y. Shan, *Appl. Catal. A: General*, **279**, 139 (2005).
18. P. Vaughan, J. Donohue, *Acta Cryst.*, **5**, 530 (1952).
19. W. D. Kumler, G. M. Fohlen, *J. Am. Chem. Soc.*, **64**, 1944 (1942).

СИНТЕЗА НА ДИМЕТИЛ-КАРБОНАТ ОТ КАРБАМИД И МЕТАНОЛ, КАТАЛИЗИРАНА ОТ ЙОННА ТЕЧНОСТ И ЖЕЛЕЗЕН ТРИХЛОРИД)

Ш. Фенг¹, Т. Сун¹, Б. Лу², К. Цай²

¹ Колеж за наука, Хейлонгджан, Земеделски университет Байи, Китай

² Целева лаборатория за фотонни и електронни материали, Министерство на образованието, Училища по химия и химично инженерство, Университет в Харбин, Харбин 150025, Китай

Постъпила на 25 февруари; коригирана на 5 юли, 2013

(Резюме)

Изследвана е синтезата на диметил-карбонат (DMC) от карбамид и метанол при периодични условия при използването на железен три хлорид като катализатор и йонна течност. Резултатите показват че йонната течност Et₃NHCl-FeCl₃ е ефективен катализатор с повишен добив (около 27%), като се постига висока селективност (близо до 100%) спрямо DMC at 180°C в проста апаратура. Обсъдени са ефекта на условията на реакцията (температура, моларното отношение на карбамида към метанола, количеството и състава на катализатора). Предложен е нов механизъм на реакцията, различен от известните досега.

Characterization and electrokinetic properties of montmorillonite

B. A. Fil^{1,2*}, C. Özmetin², M. Korkmaz²

¹Atatürk University, Department of Environmental Engineering, 25240 Erzurum, Turkey

²Balıkesir University, Department of Environmental Engineering, 10145 Çağış-Balıkesir, Turkey

Received: March 6, 2013; revised: August 29, 2013

The determination of surface properties of montmorillonite clay is an important criterion for establishment of its adsorption ability against anionic and cationic species from wastewaters. In this study, electrokinetic surface properties of montmorillonite were investigated using the microelectrophoresis technique. The zeta-potential (ζ) analysis of the montmorillonite was done by streaming potential measurements as a function of salt concentration and equilibrium pH of solution. It was found that the zeta potential of the clay particles was negative for monovalent cations (KCl, LiCl, NaCl) added to solution phase. Divalent cations (CaCl_2 , $\text{Ca}(\text{NO}_3)_2$, $\text{Pb}(\text{NO}_3)_2$) could provide a neutral charge at just maximum concentrations. In addition, montmorillonite had a negative charge even at pH 2 and only trivalent cations ($\text{Fe}(\text{NO}_3)_3$, FeCl_3) provided positive surface charge at just maximum concentration. The characterization of the montmorillonite was performed by using XRD, XRF, FTIR, SEM imaging, and N_2 -BET analyses. The determined porous structure and strong negative surface charge of the montmorillonite showed that this clay would be used effectively in removal of cationic species from waters.

Keywords: Montmorillonite; XRD; Electrokinetic; Zero charge point; SEM; FTIR

INTRODUCTION

Clay is a soil particle smaller than 2 μm . Clays have a high specific surface area which mainly influences the soil colloidal properties as well as the stability of soil structure. Besides, clays have a high stability in both wet and dry conditions. Colloid is a particle which may be a molecular aggregate with a diameter changing from 0.1 to 0.001 μm . Clay and soil organic matter are often called as soil colloids because they have particle sizes that are within, or approach to the colloidal dimensions. Clay minerals which are hydrous aluminum silicates have a large interlayer space that can retain significant amounts of water. Clays are encompassed of large surface area that allow swelling and shrinking [1, 2].

Montmorillonite is a very soft phyllosilicate mineral that typically forms in microscopic crystals. Montmorillonite, a member of the smectite family, is 2:1 layered clay and it has 2 tetrahedral sheets sandwiching a central octahedral sheet. The montmorillonite particles are plate-shaped with an average diameter of approximately 1 micrometer. The particle thickness is extremely small (~1 nm).

It is the main constituent of the volcanic ash weathering product, bentonite. The water content of montmorillonite is variable and it increases greatly in volume when it absorbs water. Chemically it is hydrated sodium calcium aluminum magnesium silicate hydroxide $(\text{Na,Ca})_{0.33}(\text{Al,Mg})_2(\text{Si}_4\text{O}_{10})(\text{OH})\cdot n\text{H}_2\text{O}$. Potassium, iron, and other cations commonly substitute with structural cations of the montmorillonite and the exact ratios of cations vary based on the clay deposit [3-5].

Montmorillonite is used in the oil drilling industry as a component of drilling mud to make the mud slurry viscous which helps in keeping the drill bit cool and in removal of drilled solids. Montmorillonite is also used as a soil additive in dry soils to hold soil water content at maximum ratio. Montmorillonite is preferred in construction of earth dams to prevent the leakage of fluids. It is also used as a component of foundry sand and as a desiccant to remove moisture from air and gases. Montmorillonite clays have been extensively utilized in catalytic processes for over 60 years. Other acid based catalysts also utilize acid treated montmorillonite clays [6].

* To whom all correspondence should be sent:
E-mail: baybarsalifil2@gmail.com

The clay samples shows different surface charge density and cation content based on its mined deposit. Therefore, the characterization and surface properties of the montmorillonite samples belonging to different regions should be determined as separately. Also, the purity of the montmorillonite samples changes from a deposit to another. For these reason, in this work, we investigated the effect of the mono- and multivalent salts including NaCl, KCl, LiCl, CaCl₂, Ca(NO₃)₂, Pb(NO₃)₂, Fe(NO₃)₃, and FeCl₃ on the electrokinetic behavior of montmorillonit. The effects of clay concentration, initial pH, and electrolyte type on the zeta potential were also investigated. In addition, the structure and properties of the montmorillonite were examined by XRD, XRF, SEM, FT-IR and N₂-BET analyses.

MATERIAL AND METHODS

Characterization of Montmorillonite

The montmorillonite sample was obtained from Süd-Chemie Clay Processing Plants located in Balikesir in Turkey. Before being used in the experiments, the montmorillonite sample was treated as follows: the bulk solution containing 10 g L⁻¹ montmorillonite was mechanically stirred for 24 h, and the bulk solution delayed for about two minutes and then the supernatant suspension was filtered through a what-man filter paper ($\Phi = 12.5$ cm (diameter of filter paper)). The clay sample was dried at 110 °C for 24 h, and then sieved by 45-90-mesh sieve. The sample of montmorillonite was characterized by using X-ray diffraction (XRD), X-ray fluorescence (XRF), infrared (FT-IR), scanning electron microscopic (SEM) and BET N₂ adsorption technique.

Zeta Potential

The zeta potential of samples were measured using a Zeta Meter 3.0 (Zeta Meter Inc.) equipped with a microprocessor unit. The unit automatically calculates the electrophoresis mobility of the particles and converts it to the zeta potential using the Smoluchowski equation. This equation is the most elementary expression of zeta potential and gives a direct relation between zeta potential and electrophoresis mobility of particles;

$$\zeta = \frac{4\pi V_t}{D_t} EM \quad (1)$$

Where, EM is electrophoresis mobility at actual temperature, V_t is viscosity of the suspending liquid, D_t is dielectric constant, π is constant and ζ is zeta potential. A 0.15 g montmorillonite amount

was conditioned in 100 ml distilled water for 3 h. Each data point is an average of approximately 10 measurements. All zeta potential measurements were carry out at natural pH of the suspension except those in which the effect of pH was investigated. The pH of the suspension was adjusted using diluted HCl and NaOH. The electrolyte concentrations of the solutions were adjusted using 1 M electrolyte solutions containing different salts. Electrolyte concentrations of the solutions were adjusted with an automatic pipette.

RESULTS AND DISCUSSION

Characterization of Montmorillonite Clay

XRD, XRF, N₂-BET, SEM and FT-IR analysis. The XRD pattern of the montmorillonite is shown in Figure 1 and the crystallographic parameters are evaluated by measuring the (001) and (080) peaks. The peaks marked as montmorillonite are indicative of 2:1 swelling clay and confirm the characteristics of the montmorillonite type clay. The other peaks are impurities corresponding to quartz. Montmorillonite exhibits a diffraction peak of the (001) plane at $2\theta = 19.733$, which corresponds to its basal spacing of 4.99 Å. The (080) reflection at $2\theta = 68.823$ indicates that montmorillonite has a dioctahedral structure [7, 8].

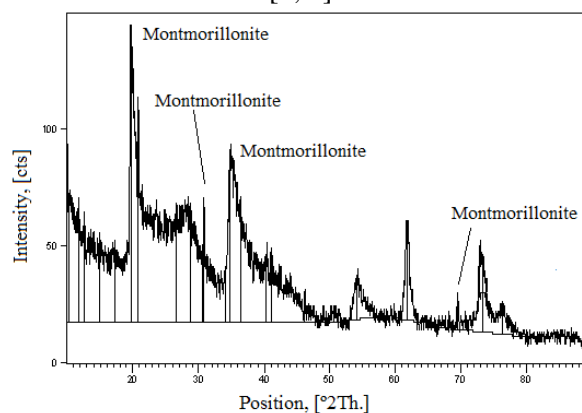


Fig. 1. XRD pattern of montmorillonite clay.

X-ray fluorescence (XRF) method has been used to identify the major minerals and chemical compounds present in the clays. The specific surfaces area of montmorillonite (measured by N₂-BET) was 95.36 m² g⁻¹. The chemical compositions and some index properties of the montmorillonite sample were given in Table 1.

SEM image of the montmorillonite is given in Figure 2. The surface morphology of montmorillonite demonstrates a layered surface with some large flakes, which is the typical structure for montmorillonite. When this image was analyzed, it could be observed that surface of the

Table 1. Chemical composition of montmorillonite (a) and physicochemical properties of montmorillonite (b).

	Component	Weight (%)
(a)	SiO ₂	49.40
	Al ₂ O ₃	19.70
	MgO	0.27
	CaO	1.50
	Fe ₂ O ₃	0.30
	Na ₂ O	1.50
	H ₂ O	25.67
	Parameters	Value
(b)	Color	White
	Density (g cm ⁻³)	2.3 – 3
	Transparency	Semi-transparent and opaque
	Brightness	Matt
	Surface Area (m ² g ⁻¹)	95.36
	Reflective index	1 – 2

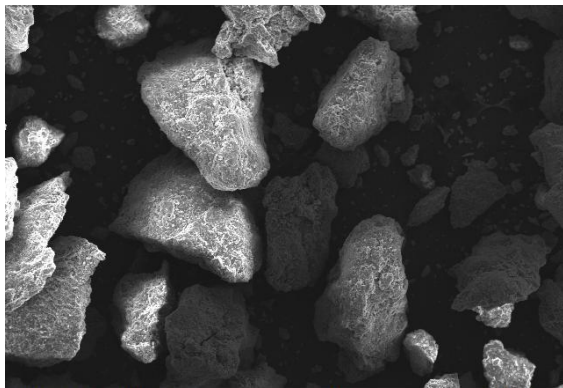


Fig. 2. SEM picture of montmorillonite particles.

clay didn't have homogenous dispersion. In addition, clay structure has pores which randomly distributed with different sizes. Surface images of montmorillonite clay sample used in this study are similar to the literature [9, 10].

In the FT-IR spectrum (Fig. 3) of montmorillonite the broad band centered near 3495 cm⁻¹ is due to the –OH stretching mode of the interlayer water. The overlaid absorption peak in the region of 1654 cm⁻¹ is assigned to the –OH bending mode of adsorbed water. The characteristic peak at 1127 cm⁻¹ is due to the Si–O–Si stretching and out of plane Si–O–Si stretching mode for montmorillonite. The band at 1048 cm⁻¹ is assigned to the Si–O–Si stretching (inplane) vibration for layered silicates. The band in the region of 873 cm⁻¹ is due to the Si–O–Al stretching mode for montmorillonite. The FT-IR peaks at 531 cm⁻¹ and 472 cm⁻¹ are assigned to the Si–O–Al and Si–O–Si bending vibration, respectively [11, 12].

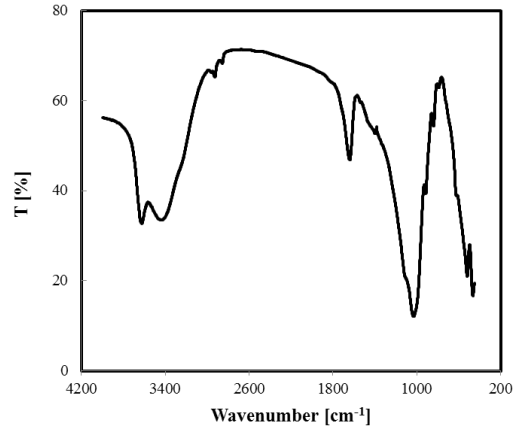


Fig. 3. FT-IR spectra of montmorillonite.

Measurement of Zeta Potential and pH profiles of montmorillonite

The pH profiles of montmorillonite in a 1.5 wt % suspension as a function of time is presented in Fig. 4 at natural, acidic and basic pHs. When montmorillonite was added to distilled water of pH 5.45, the suspension pH raised to 8.15 in 45 min and to 7.7 after 75 min and then remained almost constant upon reaching to the equilibrium pH of 7.7. The reason for the rapid rise in the suspension pH in the first 45 min can be ascribed to the rapid adsorption of H⁺ ions in water both onto the negatively charged montmorillonite surface and as potential determining ions (pdi) in the electrical double layer (EDL) in order to provide electroneutrality. In addition, the H⁺ ions in solution exchanged with some of the cations in the montmorillonite lattice leading to the consumption of H⁺ ions in suspension. When the initial pH was adjusted to 4.00, after montmorillonite addition, the suspension pH raised to 6.20 in 30 min, and then increased till it reached equilibrium around pH 7.24.

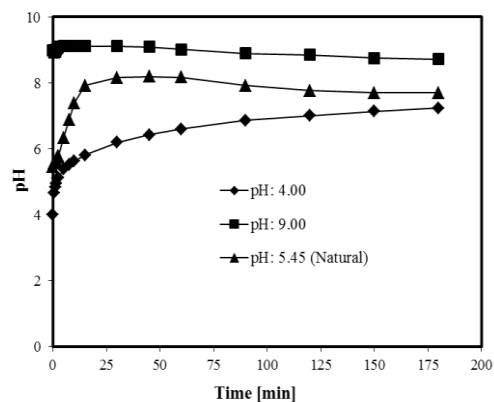


Fig. 4. The pH variation of montmorillonite suspension at different pHs.

The reasons for the rapid rise in pH are the same as above. When the initial pH was adjusted to 9.00, after montmorillonite addition, the suspension pH decreased to 8.89 in 90 min, and reached its equilibrium at pH 8.72 in about 180 min. The decrease of the suspension pH can be attributed to the adsorption of OH⁻ ions onto the positive sites on the montmorillonite surface. Thus, montmorillonite suspensions exhibited a buffer pH around pH 8 [13, 14].

Effect of solid concentration

The solid concentration in solution is a major parameter governing the surface charge generation. To determine the effect of solid-to-solution ratio on the zeta potential, different montmorillonite dispersions were prepared at concentrations between 0.01–0.50 g/100 mL in distilled water and their zeta potentials were measured (Fig. 5). It was observed that there is no significant effect of the solid concentration on the zeta potential of montmorillonite suspensions. Thus, subsequent experiments were carried out at 0.15 g/100 mL solid-to-solution ratio [15].

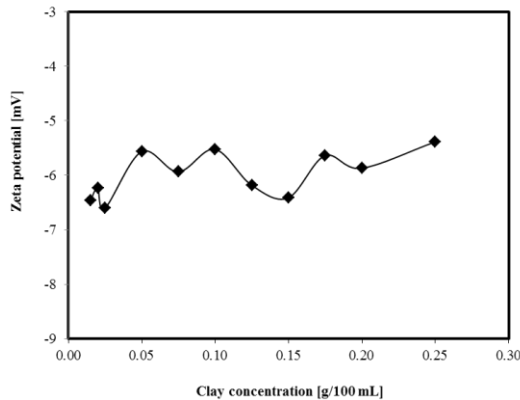
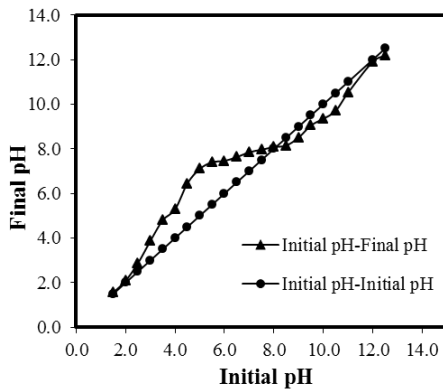


Fig. 5. Zeta potential of montmorillonite as a function of solid concentration.



Zero point charged of montmorillonite

The zeta potential of montmorillonite particles was plotted as a function of the dispersion pH (Figure 6). Zeta potential has low negative value for pH values less than pH 8.04 and it is essentially pH independent at pH range of 2 and 8.04. But, zeta potential has more negative value for pH values higher than pH: 8.04. In this figure, two different types of charge on the montmorillonite particle surface are apparent. The decrease in zeta potential at pH>8.04 was mainly due to the adsorption of OH⁻ on the positive edges of the clay particles, which acquire negative charge. At the lowest pH values, the zeta potential analysis indicated lower negative values owing to the H⁺ adsorption on the negative charged sites on the particle surface [17]. The montmorillonite particles dissolved at pH values lower than 2 and this resulted in more negative surface charge.

Effect of metal salts on the zeta potential of montmorillonite

The results obtained at natural pH of the medium with monovalent electrolytes such as NaCl, KCl and LiCl and were shown in Figure 7. The increasing concentrations of monovalent cations (NaCl, KCl and LiCl) converted the negative surface charge to less negative value. This result can be explained in the following manner: the monovalent ions added to the solution are known as indifferent electrolytes except their ion exchange tendency [18]; they cannot adsorb specifically onto montmorillonite, and are not capable of causing a charge reversal. Fig. 7 showed the zeta potential of montmorillonite in the presence of various divalent electrolytes such as. CaCl₂, Ca(NO₃)₂ and Pb(NO₃)₂.

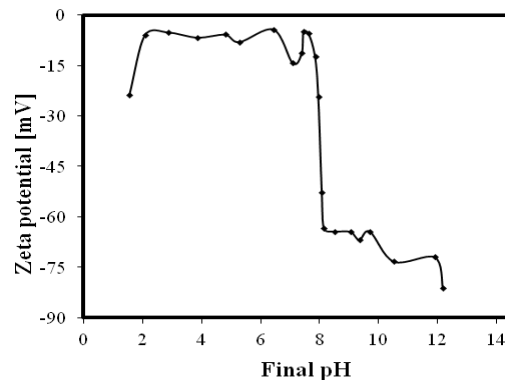


Figure 6. Zeta potential of montmorillonite as a function of pH

As the concentration of divalent electrolytes ions increase in the solution, the zeta potential of montmorillonite decreases (becomes less negative). CaCl_2 , $\text{Ca}(\text{NO}_3)_2$ and $\text{Pb}(\text{NO}_3)_2$ electrolytes species were selected as divalent ions because natural water normally contains an appreciable quantity of them. It was found that montmorillonite were negatively charged each of the three electrolyte concentrations less than 1×10^{-2} M. In each of the three types of salt, at 1×10^{-1} M concentration montmorillonite surface of the electrolyte concentration is almost zero charged [15]. Fig. 7 has shown the effect of trivalent electrolyte ions such as FeCl_3 and $\text{Fe}(\text{NO}_3)_3$ on the zeta potential of montmorillonite sample. Addition of FeCl_3 and $\text{Fe}(\text{NO}_3)_3$ reduces the zeta potential of montmorillonite suspensions steadily starting from 1×10^{-5} to 1×10^{-1} M. Zeta potentials of montmorillonite samples were positive in the presence of FeCl_3 and $\text{Fe}(\text{NO}_3)_3$ at concentration of more than 1×10^{-3} M and 1×10^{-2} M, respectively [14]

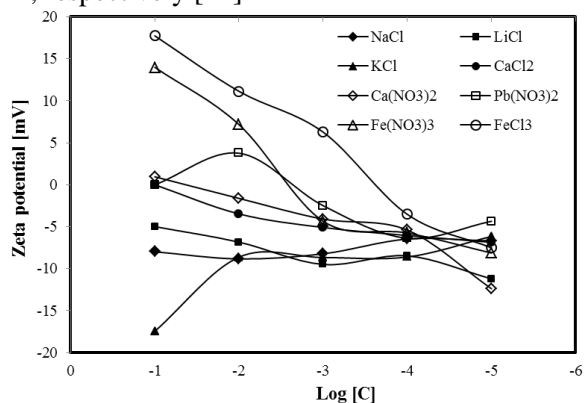


Figure 7. The variation of zeta potential of montmorillonite samples with monovalent, divalent and trivalent electrolytes at various concentrations.

CONCLUSIONS

The main results of the present study can be given as follows:

- The characterization of the montmorillonite was performed by using XRD, XRF, FTIR, SEM imaging, and N_2 -BET analysis
- Montmorillonite suspensions exhibit a buffer pH around pH 8.
- It was observed that there is no significant effect of the solid concentration on the zeta potential of montmorillonite suspensions.
- Natural montmorillonite particles didn't have point of zero charge even at pH 2.
- In presence of monovalent electrolytes (NaCl, KCl and LiCl), the surface is, at first, more negatively charged, and then the negative charge decreases as the concentration of electrolyte

increases. While the divalent cations such as Ca^{2+} and Pb^{2+} provided neutral charge at 1×10^{-1} M concentration, iron ions caused the charge reversal from the negative to positive at 1×10^{-1} M concentration.

- The results of characterization and electrokinetic experiments showed that montmorillonite clay would be used effectively in removal of cationic species from waters. The strong negative surface charge and porous structure of montmorillonite will enable to adsorb more organic and inorganic cations to its interior.

ACKNOWLEDGEMENTS: The authors thank the Balikesir University Research Center of Applied Science (BURCAS).

REFERENCES

1. B. Gu, H. E. Doner, *Clay Miner.*, **38**, 493 (1990).
2. P. Stathi, I. T. Papadas, A. Enotiadis, R. Y. N. Gengler, D. Gournis, P. Rudolf, Y. Deligiannakis, *Langmuir*, **25**, 6825 (2009).
3. B.A. Fil, Master Thesis, Institute of Science, Department of Environmental Engineering, Balikesir University, Balikesir, 2007.
4. W.-T. Tsai, H.-C. Hsu, T.-Y. Su, K.-Y. Lin, C.-M. Lin, T.-H. Dai, *J. Hazard. Mater.*, **147**, 1056 (2007).
5. M. Rafatullah, O. Sulaiman, R. Hashim, A. Ahmad, *J. Hazard. Mater.*, **177**, 70 (2010).
6. L. Lloyd, "Handbook of Industrial Catalysts," ed New York: Springer, 2011, pp. 181.
7. J. Hu, X. Tan, X. Ren, X. Wang, *Dalton Trans.*, **41**, 10803 (2012).
8. W.P. Gates, P. Komadel, J. Madejová, J. Bujdák, J. W. Stucki, R.J. Kirkpatrick, *Appl. Clay Sci.*, **16**, 257 (2000).
9. R.E. Grim, *Clay Mineralogy*. New York: McGraw-Hill, Inc., 1968.
10. G. Karthikeyan, A. Pius, G. Alagumuthu, *Indian J. Chem. Technol.*, **12**, 263 (2005).
11. S. Akyüz, T. Akyüz, A. E. Yakar, *J. Mol. Struct.*, **565/566**, 487 (2001).
12. H.A. Patel, R.S. Somani, H.C. Bajaj, R.V. Jasra, *Appl. Clay Sci.*, **35**, 194 (2007).
13. M. Alkan, Ö. Demirbaş, M. Dogan, *Micropor. Mesopor. Mater.*, **84**, 192 (2005).
14. M. Alkan, O. Demirbas, M. Dogan, *J. Colloid Interface Sci.*, **281**, 240 (2005).
15. O. Duman, S. Tunç, *Sep. Sci. Technol.*, **43**, 3755 (2008).
16. D.-S. Kim, *Environ. Eng. Res.*, **8**, 222 (2003).
17. M.M. Barbooti, K.S. Al-Bassam, B.H. Qasim, *Iraqi J. Sci.*, **53**, 479 (2012).
18. M. Alkan, Ö. Demirbaş, M. Doğan, *Micropor. Mesopor. Mater.*, **83**, 51 (2005).

ОХАРАКТЕРИЗИРАНЕ И ЕЛЕКТРОКИНЕТИЧНИ СВОЙСТВА НА МОНТМОРИЛОНИТ

Б. А. Фил^{1,2}, Дж. Йозметин², М. Коркмаз²

¹ *Департамент по екологично инженерство, Университет Ататюрк, 25240 Ерзурум, Турция*

² *Департамент по екологично инженерство, Университет Бахкесир, 10145 Чаис-Бахкесир, Турция*

Постъпила на 6 март; коригирана на 29 август, 2013

(Резюме)

Определянето на повърхностните свойства на монтморилонитови глинени е важен критерий за адсорбционните му способности спрямо аниони и катиони, съдържащи се в отпадъчни води. В настоящата работа са изследвани електро-кинетичните му повърхостни свойства използвайки микроелектрофореза. Анализът на ζ -потенциала е извършен чрез измервания на електро-кинетичния потенциал като функция на концентрацията на соли и равновесното рН на разтворите. Намерено е, че ζ -потенциалът на частиците е отрицателен за едновалентни катиони (KCl, LiCl, NaCl), добавени към разтвора. Двувалентните катиони (CaCl₂, Ca(NO₃)₂, Pb(NO₃)₂) могат да доведат до неутрален заряд при максимални концентрации. В допълнение, монтморилонитът има отрицателен заряд дори при рН 2 и сам тривалентни катиони (Fe(NO₃)₃, FeCl₃) осигуряват положителен заряд на повърхността при високи концентрации. Охарактеризирането на монтморилонит е извършено чрез XRD, XRF, FTIR, SEM образи и N₂-BET-анализи. Определената поръозна структура и силният отрицателен повърхостен заряд показват, че тази глина може да се използва успешно за отстраняването на катиони от водите.

Synthesis of some novel and water-soluble 2,4,6-substituted 3,5-dihydroxymethylpyridines

D. Shahabi¹, M.A. Amrollahi¹, A. Mobinikhaledi*²

¹Department of Chemistry, Faculty of Science, Yazd University, 89195-741, Iran

²Department of Chemistry, Faculty of Science, Arak University, Arak, Iran

Received: March 19, 2013; revised: September 11, 2013

The reduction of 2,4,6-substituted pyridine-3,5-dicarboxylate derivatives to give novel and water-soluble corresponding 2,4,6-substituted 3,5-dihydroxymethylpyridines was achieved in good yields using lithium aluminum hydride at 0-30°C in dry THF.

Keywords: Pyridine derivatives, Esters, Lithium aluminum hydride, Reduction

INTRODUCTION

The pyridine ring has found as a most prevalent heterocyclic ring in biological active compounds, drugs and medicinal chemistry[1-14]. In pragmatical industry, the pyridine ring forms the nucleus of over 7000 existing drugs.^[7,8] Keeping in view the above-mentioned applications of this important ring, the synthesis of some pyridine derivatives which can be probe in biological media is a topic of current interest. Reduction of ester groups of organic materials with LiAlH₄, which is a known procedure,^[14-18] increases their water solubility. In view of this report and also as a continuation of our work on the synthesis of pyridine derivatives,^[19] the present work aimed at designing and synthesizing of some water-soluble pyridine derivatives, which could function in an organic solvent-free solution and thereby could function in biological systems.

EXPERIMENTAL

All chemicals were purchased from Merck company. Hantzsch 1,4-dihydropyridines were prepared using the appropriate aldehyde, ammonium carbonate and ethyl acetoacetate.¹⁹ Diethyl 2,6-dimethyl-4-arylpyridine-3,5-dicarboxylates were prepared from corresponded 1,4-dihydropyridines by oxidation with H₂O₂-AcOH/NaI. Column chromatography was carried out on flash silica gel (230-400 mesh, Merck) using

the indicated eluent. The spectroscopic data of synthesized compound were assigned by IR and NMR spectroscopy. IR spectra were recorded on Bruker spectrometer FT-IR. NMR spectra were obtained using 9.4 T vertical bore spectrometer (1H 400 MHz; 13C 100 MHz) or 11.7 T vertical bore spectrometer (1H 500 MHz; 13C 125 MHz; 19F 470 MHz). 1H and 13C chemical shifts are referenced to TMS as an internal standard, 19F to a dilute solution of trifluoroacetic acid (TFA) in capillary column as an external reference. Chemical shifts are given as δ ppm values and J values are given in hertz (Hz). The elemental analysis was carried out in Microanalytical Lab, Department of Chemistry, Tarbiyat Moallem University, Tehran, Iran.

3,5-Dihydroxymethyl-4-(phenyl)-2,6-dimethylpyridine (5a).

To a magnetically stirred slurry of LiAlH₄ (2.2 mmol, 0.083 g) in anhydrous THF (5.0 mL), a solution of diethyl 2,6-dimethyl-4-phenylpyridine-3,5-dicarboxylate (1 mmol, 0.33 g) in anhydrous THF (5.0 mL) was added drop-wise at 0 °C for 5 min. The reaction mixture was further stirred magnetically for 2.5 h at 30 °C. Excess LiAlH₄ was quenched by adding saturated aqueous sodium sulfate solution and the reaction mixture was filtered. The solid cake was washed with THF and the filtrate concentrated under reduced pressure. The latter was extracted with chloroform (2×25 mL) and water (12.5 mL) and dried (Na₂SO₄), organic layer was concentrated under reduced pressure to give a crud mass, which was

* To whom all correspondence should be sent:
E-mail: akbar_mobini@yahoo.com

chromatographed over SiO₂ column using chloroform/ethyl acetate (30:70) as eluent to give 3,5-dihydroxymethyl-2,6-dimethyl-4-phenylpyridine as a pale yellow oil, Yield 87%. FT-IR: ν_{max} (neat): 3322 (OH-stretching); ¹H NMR (500 MHz, CDCl₃): δ 2.70 (s, 6H, 2×CH₃), 3.54 (s, 2H, 2×OH), 4.38 (s, 4H, 2×CH₂), 7.22-7.48 (m, 5Harom) ppm; ¹³C NMR (100 MHz, CDCl₃): δ 19.9, 58.7, 127.6, 128.6, 129.5, 137.6, 150.3, 156.7 ppm. Anal. Calcd. for C₁₅H₁₇NO₂: C, 74.03; H, 7.04. Found: C, 73.85; H, 7.34.

3,5-Dihydroxymethyl-4-(2-fluorophenyl)-2,6-dimethylpyridine (5b)

Reduction of diethyl 2,6-dimethyl-4-(2-fluorophenyl)-pyridine-3,5-dicarboxylate (1 mmol, 0.34 g) with LiAlH₄ (2.2 mmol, 0.083 g) and work-up as described above gave 3,5-dihydroxymethyl-4-(2-fluorophenyl)-2,6-dimethylpyridine as pale yellow oil, Yield 83%. FT-IR: ν_{max} (neat): 3161 (OH-stretching); ¹H NMR (500 MHz, CDCl₃): δ 2.71 (s, 6H, 2×CH₃), 3.70 (s, 2H, 2×OH), 4.32-4.45 (m, 4H, 2×CH₂), 7.22-7.27 (m, 3Harom), 7.44-7.45 (m, 1Harom) ppm; ¹³C NMR (100 MHz, CDCl₃): δ 22.5, 58.6, 115.3 (2JC-F= 21.0 Hz), 124.0 (4JC-F= 2.6 Hz), 124.9 (J= 20 Hz), 130.1 (3JC-F= 3.6 Hz), 130.2 (3JC-F= 7.9 Hz), 132.0, 143.7, 156.5, 159.5 (1JC-F= 246 Hz) ppm; ¹⁹F NMR (470 MHz, D₂O): δ -114.69 ppm. Anal. Calcd. for C₁₅H₁₆FNO₂: C, 68.93; H, 6.17. Found: C, 69.22; H, 6.24.

3,5-Dihydroxymethyl-4-(3-fluorophenyl)-2,6-dimethylpyridine (5c)

Reduction of diethyl 2,6-dimethyl-4-(3-fluorophenyl)-pyridine-3,5-dicarboxylate (1 mmol, 0.34 g) with LiAlH₄ (2.2 mmol, 0.083 g) and work-up as described above gave 3,5-dihydroxymethyl-4-(3-fluorophenyl)-2,6-dimethylpyridine as pale yellow oil, Yield 84%. FT-IR: ν_{max} (neat): 3350 (OH-stretching); ¹H NMR (400 MHz, CDCl₃): δ 2.70 (s, 6H, 2×CH₃), 3.61 (s, 2H, 2×OH), 4.38 (s, 4H, 2×CH₂), 7.00-7.43 (m, 4Harom) ppm; ¹³C NMR (125 MHz, CDCl₃): δ 22.7, 59.2, 115.6 (2JC-F= 20.8 Hz), 116.5 (2JC-F= 22.2 Hz), 125.0 (4JC-F= 2.9 Hz), 128.3, 130.2 (3JC-F= 8.4 Hz), 139.0 (3JC-F= 7.9 Hz), 147.3, 154.1, 162.7 (1JC-F= 246 Hz) ppm; ¹⁹F NMR (470 MHz, D₂O): δ -113.95 ppm. Anal. Calcd. for C₁₅H₁₆FNO₂: C, 68.93; H, 6.17. Found: C, 68.95; H, 6.02.

3,5-Dihydroxymethyl-4-(4-fluorophenyl)-2,6-dimethylpyridine (5d)

Reduction of diethyl 2,6-dimethyl-4-(4-fluorophenyl)-pyridine-3,5-dicarboxylate (1 mmol, 0.34 g) with LiAlH₄ (2.2 mmol, 0.083 g) and work-up as described above gave 3,5-dihydroxymethyl-4-(4-fluorophenyl)-2,6-dimethylpyridine as pale

yellow oil, Yield 83%. FT-IR: ν_{max} (neat): 3382 (OH-stretching); ¹H NMR (500 MHz, CDCl₃): δ 2.65 (s, 6H, 2×CH₃), 2.19 (s, 2H, 2×OH), 4.29 (s, 4H, 2×CH₂), 7.09 (t, J= 8.7 Hz, 2Harom), 7.22-7.25 (m, 2Harom) ppm; ¹³C NMR (100 MHz, CDCl₃): δ 22.2, 58.5, 115.1 (2JC-F= 22.0 Hz), 128.4, 130.5 (3JC-F= 8.0 Hz), 132.4 (4JC-F= 2.9 Hz), 147.3, 159.3, 162.6 (1JC-F= 248 Hz) ppm; ¹⁹F NMR (470 MHz, D₂O): δ -115.0 ppm. Anal. Calcd. for C₁₅H₁₆FNO₂: C, 68.93; H, 6.17. Found: C, 69.18; H, 5.97.

3,5-Dihydroxymethyl-4-(4-trifluoromethylphenyl)-2,6-dimethylpyridine (5e)

Reduction of diethyl 2,6-dimethyl-4-(4-trifluoromethylphenyl)-pyridine-3,5-dicarboxylate (1 mmol, 0.40 g) with LiAlH₄ (2.2 mmol, 0.083 g) and work-up as described above gave 3,5-dihydroxymethyl-4-(4-trifluoromethylphenyl)-2,6-dimethylpyridine as a pale yellow oil, Yield 78%. FT-IR: ν_{max} (neat): 3420 (OH-stretching); ¹H NMR (400 MHz, DMSO): δ 2.54 (s, 6H, 2×CH₃), 4.78 (s, 2H, 2×OH), 4.06 (s, 4H, 2×CH₂), 7.46-7.48 (m, 2Harom), 7.79-7.81 (m, 2Harom) ppm; ¹³C NMR (100 MHz, CDCl₃): δ 20.0, 58.5, 124.6, 128.8, 129.2, 129.4, 130.0, 141.8, 149.0, 156.7 ppm; ¹⁹F NMR (470 MHz, D₂O): δ -109.77 ppm. Anal. Calcd. for C₁₆H₁₆F₃NO₂: C, 61.71; H, 5.17. Found: C, 61.55; H, 5.25.

3,5-Dihydroxymethyl-4-(2-pyridyl)-2,6-dimethylpyridine (5f)

Reduction of diethyl 2,6-dimethyl-4-(2-pyridyl)-pyridine-3,5-dicarboxylate (1 mmol, 0.33 g) with LiAlH₄ (2.2 mmol, 0.083 g) and work-up as described above gave 3,5-dihydroxymethyl-4-(2-pyridyl)-2,6-dimethylpyridine as a pale yellow oil, Yield 81%. FT-IR: ν_{max} (neat): 3329 (OH-stretching); ¹H NMR (400 MHz, CDCl₃): δ 2.68 (s, 6H, 2×CH₃), 3.68 (s, 2H, 2×OH), 4.30 (s, 4H, 2×CH₂), 7.40-7.43 (m, 2Harom), 7.55-7.57 (m, 1Harom), 7.84-7.86 (m, 1Harom) ppm; ¹³C NMR (100 MHz, CDCl₃): δ 19.7, 59.3, 123.3, 124.0, 125.4, 136.8, 148.8, 149.0, 156.2, 157.2 ppm. Anal. Calcd. for C₁₄H₁₆N₂O₂: C, 68.81; H, 6.60. Found: C, 68.70; H, 6.77.

3,5-Dihydroxymethyl-4-(3-pyridyl)-2,6-dimethylpyridine (5g)

Reduction of diethyl 2,6-dimethyl-4-(3-pyridyl)-pyridine-3,5-dicarboxylate (1 mmol, 0.33 g) with LiAlH₄ (2.2 mmol, 0.083 g) and work-up as described above gave 3,5-dihydroxymethyl-4-(3-pyridyl)-2,6-dimethylpyridine as a pale yellow oil, Yield 82%. FT-IR: ν_{max} (neat): 3300 (OH-stretching); ¹H NMR (500 MHz, CDCl₃): δ 2.70 (s, 6H, 2×CH₃), 3.58 (s, 2H, 2×OH), 4.32 (s, 4H, 2×CH₂), 7.34-8.54 (m, 4Harom) ppm; ¹³C NMR

(125 MHz, CDCl₃): δ 19.8, 58.2, 125.4, 133.1, 133.8, 145.9, 147.2, 159.3 ppm. Anal. Calcd. for C₁₄H₁₆N₂O₂: C, 68.81; H, 6.60. Found: C, 68.84; H, 6.79.

3,5-Dihydroxymethyl-4-(4-pyridyl)-2,6-dimethylpyridine (5h)

Reduction of diethyl 2,6-dimethyl-4-(4-pyridyl)-pyridine-3,5-dicarboxylate (1 mmol, 0.33 g) with LiAlH₄ (2.2 mmol, 0.083 g) and work-up as described above gave 3,5-dihydroxymethyl-4-(4-pyridyl)-2,6-dimethylpyridine as a pale yellow oil, Yield 80%. FT-IR: ν_{\max} (neat): 3323 (OH-stretching); ¹H NMR (500 MHz, CDCl₃): δ 2.62 (s, 6H, 2×CH₃), 3.60 (s, 2H, 2×OH), 4.36 (s, 4H, 2×CH₂), 7.20-7.26 (m, 2Harom), 8.61-8.64 (m, 2Harom) ppm; ¹³C NMR (125 MHz, CDCl₃): δ 20.0, 67.6, 124.5, 125.9, 144.2, 147.7, 148.8, 156.8 ppm. Anal. Calcd. for C₁₄H₁₆N₂O₂: C, 68.81; H, 6.60. Found: C, 68.53; H, 6.82.

3,5-Dihydroxymethyl-4-(3-hydroxyphenyl)-2,6-dimethylpyridine (5i)

Reduction of diethyl 2,6-dimethyl-4-(3-hydroxyphenyl)-pyridine-3,5-dicarboxylate (1 mmol, 0.34 g) with LiAlH₄ (2.2 mmol, 0.083 g) and work-up as described above gave 3,5-dihydroxymethyl-4-(3-hydroxyphenyl)-2,6-dimethylpyridine as a pale yellow oil, Yield 80%. FT-IR: ν_{\max} (neat): 3441 (OH-stretching); ¹H NMR (500 MHz, CDCl₃): δ 2.68 (s, 6H, 2×CH₃), 3.54 (s, 2H, 2×OH), 4.32 (s, 4H, 2×CH₂), 6.28-7.32 (m, 4Harom) ppm; ¹³C NMR (100 MHz, CDCl₃): δ 19.2, 58.3, 115.3, 116.1, 120.1, 124.3, 133.4, 142.0, 150.1, 156.9, 160.4 ppm. Anal. Calcd. for C₁₅H₁₇N₂O₃: C, 69.46; H, 6.60. Found: C, 69.63; H, 6.48.

3,5-Dihydroxymethyl-4-(4-hydroxyphenyl)-2,6-dimethylpyridine (5j)

Reduction of diethyl 2,6-dimethyl-4-(4-hydroxyphenyl)-pyridine-3,5-dicarboxylate (1 mmol, 0.34 g) with LiAlH₄ (2.2 mmol, 0.083 g) and work-up as described above gave 3,5-dihydroxymethyl-4-(4-hydroxyphenyl)-2,6-dime-

thylpyridine as a pale yellow oil, Yield 82%. FT-IR: ν_{\max} (neat): 3268 (OH-stretching); ¹H NMR (500 MHz, CDCl₃): δ 2.63 (s, 6H, 2×CH₃), 3.58 (s, 2H, 2×OH), 4.20 (s, 4H, 2×CH₂), 7.24-7.56 (m, 4Harom) ppm; ¹³C NMR (125 MHz, CDCl₃): δ 19.8, 58.0, 115.1, 125.4, 131.4, 132.2, 150.5, 156.3, 164.1 ppm. Anal. Calcd. for C₁₅H₁₇N₂O₃: C, 69.46; H, 6.60. Found: C, 69.79; H, 6.72.

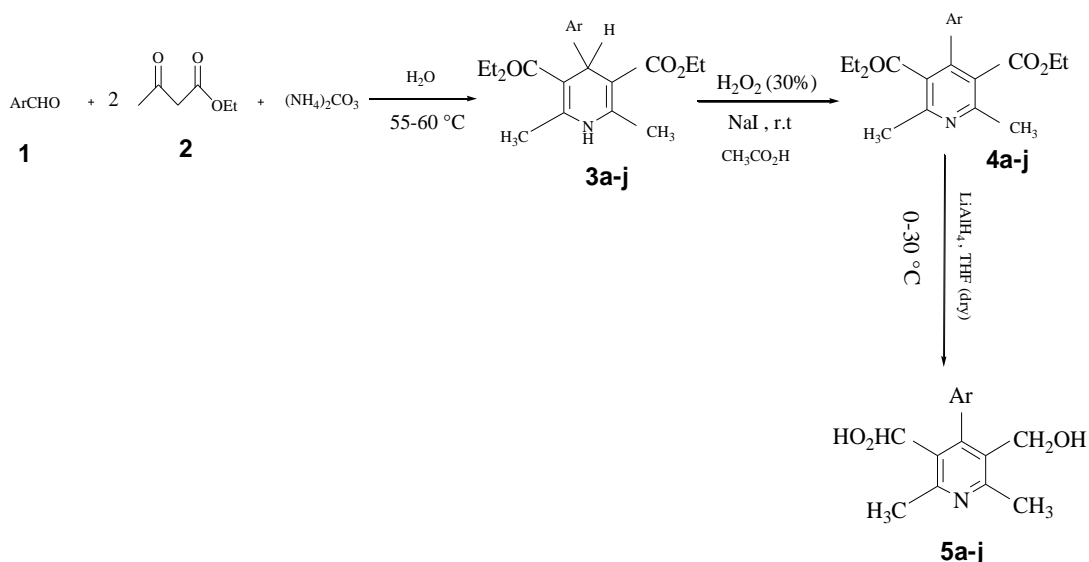
RESULTS AND DISCUSSION

Initially, the condensation of an aromatic aldehyded 1, ethyl acetoacetate 2, and ammonium carbonate resulted in Hantzsch 1,4-dihydropyridines (1,4-DHPs) 3.[19] 1,4-Dihydropyridines 3 was then converted to corresponding pyridine derivatives 4a-j using H₂O₂-AcOH/NaI oxidation system[20] as shown in Scheme 1. These synthesized compounds containing one phenyl and two ester groups are not water-soluble. The reduction of two ester groups on the pyridine ring was tested by using molar ratios of diethyl 2,6-dimethyl-4-phenylpyridine-3,5-dicarboxylate/LiAlH₄ of 1:2, 1:2.2 and 1:3 equiv, respectively, in anhydrous THF to give 5a-j. It was found that the second ratio is sufficient to carry out the reduction successfully so as to afford the desired product namely 3,5-dihydroxymethyl-2,6-dimethyl-4-phenylpyridine in 87% yield (Table 1, 5a). A reduction in the amount of LiAlH₄ from 2.2 to 1.1 equiv showed one ester group is unreacted. An increase in the amount of LiAlH₄ from 2.2 to 3 equiv showed no substantial improvement in the yield. The conversion proceeded smoothly within 2.3-2.5 h at 0-30 °C. Under this optimized cost-effective reaction condition, the scope of the reduction of ester groups on the pyridine ring of the diethyl 2,6-dimethyl-4-arylpyridine-3,5-dicarboxylate was explored to prepare the corresponding 3,5-dihydroxymethyl-4-aryl-2,6-dimethylpyridine 5a-j. In all cases, the yield of reaction was 78-87% (Table 1) without further reduction products.

Table 1. Reduction of 4a-j with LiAlH₄ in anhydrous THF at 0-30 °C to give 5a-j.

Compound 5	Ar	Time (h)	Yield ^a (%)
a	Ph	2.5	87
b	2-F-ph	2.5	83
c	3-F-ph	2.5	84
d	3-F-ph	2.5	83
e	4-CF ₃ -ph	2.4	78
f	2-pyridil	2.3	81
g	3-pyridil	2.3	82
h	4-pyridil	2.4	80
i	3-OH-ph	2.5	80
j	4-OH-ph	2.5	82

^aYields refer to isolated pure products.



Scheme 1. Synthetic pathway of 3,5-Dihydroxymethyl-4-aryl-2,6-dimethylpyridines 5a-j

3,5-Dihydroxymethyl-4-aryl-2,6-dimethylpyridines were easily characterized using elemental analysis, physical and spectral data. They were pale yellow oily liquid and water-soluble compounds.

The IR spectra showed an absorption band at 3100-3500 cm^{-1} belongs to the stretch vibrations of the two hydroxymethyl groups on the pyridine ring of 5a-j and a further hydroxy group on the phenyl ring. The ^1H NMR spectra of the products showed a singlet at 2.54-2.71 ppm region due to the resonance of CH_3 protons at C-2 and C-6 positions and another singlet at 4.06-4.38 ppm as a resonance of the methylene protons of the two hydroxymethyl groups. This singlet is indicative of the presence of the hydroxymethyl group on the pyridine ring, which is in support of the expected reaction. The ^1H NMR spectrum of 3,5-dihydroxymethyl-4-(2-fluorophenyl)-2,6-dimethylpyridine (Table 1, 5b) showed a multiple signal at 4.32-4.45 ppm, typical of the coupling of fluorine atom with hydroxymethyl group on the pyridine ring.

CONCLUSION

3,5-Dihydroxymethyl-4-aryl-2,6-dimethylpyridines could be synthesized in good yields by reduction of 1 equiv of diethyl 2,6-dimethyl-4-arylpyridine-3,5-dicarboxylate with 2.2 equiv of LiAlH_4 in anhydrous THF at 0-30 °C. The advantage of such molecules is their water solubility which, could function effectively in biological systems.

ACKNOWLEDGMENTS: We thank the Research Council of Yazd University for providing the partial support of this work.

REFERENCES

- H. Bischoff, R. Angerbauer, J. Bender, E. Bischoff, A. Faggiotto, D. Petzinna, J. Pfitzner, M.C. Porter, D. Schmidt, G. Thomas. *Atherosclerosis*, **135**, 119 (1997).
- (a) A. Mobinikhaledi, N. Foroughifar, S. M. Shariatzade, M. Fallah, *Heterocycl Commun*, **12**, 427 (2006); (b) G.D. Henry, *Tetrahedron*, **60**, 6043 (2004); (c) J.P. Michael, *Nat. Prod. Rep.*, **22**, 627 (2005).
- N. Farhanullah, A. Agarwal, V.J. Goel. *J. Org. Chem.*, **68**, 2983 (2003).
- (a) U. Eisner, J. Kuthan, *Chem. Rev.*, **72**, 1 (1972); (b) D.M. Stout, A.I. Meyers. *Chem. Rev.*, **82**, 223 (1982).
- (a) R.J. Kill, D.A. Widdowson. *Bioorganic Chemistry*; E.E. van Tamelen (Ed.), Academic: New York, **4**, 239 (1978); (b) R.H. Bocker, F.P. Guengerich., *J. Med. Chem.* **29**, 1596 (1986).
- J.A. Joule, G. Smith, K. Mills. *Heterocyclic Chemistry*; third Ed.; Chapman and Hall: London. p. 72 (1995).
- H.J. Roth, A. Kleemann. *Pharmaceutical Chemistry, Drug Synthesis*. Eds; Prentice Hall Europe, London, Vol 1, p. 407 (1998).
- MDDR: MDL Drug Data Registry, by MDL InformationSystems, Inc; San Leandro: California, USA.
- A.H. Li, S. Moro, N. Forsyth, N. Melman, X.D. Ji, K.A. Jacobsen, *J. Med. Chem.*, **42**, 706 (1999).
- B. Vacher, B. Bonnaud, F. Funes, N. Jubault, W. Koek, M.B. Assie, C. Cosi, M. Kleven, *J. Med. Chem.*, **42**, 1648 (1999).

11. W. B. Choi, I.N. Houppis, H.R. O. Churchill, A. Molina, J.E. Lynch, R.P. Volante, P.J. Reider, A.O.A. King, *Tetrahedron Lett.*, **36**, 4571 (1995).
12. Y. Abe, H. Kayakiri, S. Satoh, T. Inoue, Y. Sawada, N. Inamura, M. Asano, I. Aramori, C. Hatori, H. Sawai, T. Oku, H. Tanaka. *J. Med. Chem.* **41**, 4062 (1998).
13. Z.S. Song, M. Zhao, R. Desmond, P. Devine, D. M. Tschaen, R. Tillyer, L. Frey, R. Heid, F. Xu, B. Foster, J. Li, R. Reamer, R. Volante, E. J. Grabowski, U. H. Dolling, P.J. Reider, *J. Org. Chem.*, **64**, 9658 (1999).
14. B. Khadikar, S. Borkat, *Synth. Commun.*, **28**, 207 (1998).
15. D. Katiyar, V.K. Tiwari, N. Tewari, S.S. Verma, S. Sinha, A. Gaikwad, A. Srivastava, V. Chaturvedi, R. Srivastava, B.S. Srivastava, R.P. Tripathi, *Eur. J. Med. Chem.*, **40**, 351 (2005).
16. R.P. Tripathi, V.K. Tiwari, N. Tewari, D. Katiyar, N. Saxena, S. Sinha, A. Gaikwad, A. Srivastava, V. Chaturvedi, Y.K. Manju, R. Srivastava, B.S. Srivastava, *Bioorg. Med. Chem.*, **13**, 5668 (2005).
17. H. X. Jin, H. H. Liu, Q. Zhang, Y. Wu. *J. Org. Chem.*, **70**, 4240 (2005).
18. H.C. Hsu, D.R. Hou, *Tetrahedron Lett.*, **50**, 7169 (2009).
19. M.A. Amrollahi Biyouki, R.A.J. Smith, J.J. Bedford, J.P. Leader, *Synth. Commun.*, **28**, 3817 (1998).
20. F. Tamaddon, Z. Razmi, A.A. Jafari, *Tetrahedron Lett.*, **51**, 1187 (2010).

СИНТЕЗА НА НЯКОИ НОВИ ВОДО-РАЗТВОРИМИ 2,4,6-ЗАМЕСТЕНИ 3,5-ДИГИДРОМЕТИЛ-ПИРИДИНИ

Д. Шахаби¹, М.А. Амролахи¹, А. Мобинихаледи*²

¹Катедра по химия, Научен факултет, Университет в Язд, 89195-741, Иран

²Катедра по химия, Научен факултет, Университет в Арак, Арек, Иран

Постъпила на 6 март; коригирана на 29 август, 2013

(Резюме)

Постигната е редукция на 2,4,6-заместени производни на пиридин -3,5-дикарбоксилкатализа получаването на нови и водно-разтворими 2,4,6,-заместени 3,5-дихидроксиметилпиридини с добър добив при използването на литиево-алуминиев хидрид при 0-30°C в сух тетраhydroфуран.

The antioxidant, hemolytic and cholinesterase inhibition properties of *Galium verum* L. and *Tragopogon pratensis* subsp. *pratensis*

V. D. Mitic^{1*}, V. P. Stankov-Jovanovic¹, M. D. Ilic¹, P. J. Vasiljevic², A. Lj. Zabar²,
G. S. Stojanovic¹

¹Department of Chemistry, University of Nis, Faculty of Science and Mathematics, Nis, Serbia

²Department of Biology and Ecology, University of Nis, Faculty of Science and Mathematics, Nis, Serbia

Received: March 28, 2013; revised: August 12, 2013

The antioxidant properties of *Galium verum* L. (Lady's Bedstraw) and *Tragopogon pratensis* subsp. *pratensis* (Goat's beard) methanol extracts, from localities in Serbia were evaluated, through determination of total phenolics and flavonoids content, as well as DPPH[•] (1,1-diphenyl-2-picrylhydrazyl) radical scavenging, ABTS^{•+} (2,2-azinobis-(3-ethylbenzthiazoline-6-sulfonic acid) radical cation decolorization and ferricyanide methods. Methanol extracts of *G. verum* showed stronger free radical scavenging activity (IC₅₀ values of 26.98 µg/mL for DPPH[•] decolorization assays and 125.14 mg Trolox/ g dry extract for ABTS^{•+} radical cation decolorization assays) and total reducing power (70.31 µg/mL) than methanol extracts of *T. pratensis* (SC₅₀ values of 59.25 µg/mL for DPPH[•] decolorization assays and 6.31 mg Trolox/ g dry extract for ABTS^{•+} radical cation decolorization assays and 15.66 µg/mL of extract for total reducing power). Observed could be connected with a much higher content of phenolic and flavonoid constituents in *G. verum* extracts. Applying modified Ellman's method, *G. verum* methanol extracts showed slight activation of humane serum cholinesterase (16.28 ± 0.09 %), while methanol extract of *T. pratensis* was proven as a weak inhibitor of the enzyme (4.65 ± 0.08 %). Also, methanol extracts of *G. verum* and *T. pratensis* were tested *in vitro* using standard Drabkin's method to evaluate whether these extracts have hemolytic activity. Extracts of *T. pratensis* showed very strong hemolytic activity (after the first hour of incubation 50% of hemolysis induced concentration of 501.97 ± 32.65 µg/mL, the second hour 499.98 ± 38.45 µg/mL, 498.656 ± 39.85 µg/mL of the third and fourth 421.33 ± 34.98 µg/mL) while *G. verum* extracts had weak hemolytic activity.

Keywords: antioxidant activity, hemolytic activity, cholinesterase inhibition, *Galium verum* L., *Tragopogon pratensis* subsp. *pratensis*

INTRODUCTION

Serbian flora represents an abundant resource for scientific investigation. Above all, the genus *Galium* (Rubiaceae) is represented by 37 species [1, 2]. *Galium verum* L. (Lady's Bedstraw) is widely distributed a perennial herbaceous plant with golden yellow flowers that are 2-3 mm in diameter and grouped in many-flowered panicles [3]. The aerial parts of *G. verum* were used as a diuretic, sedative or spasmolytic, as well as for rheumatic diseases in the traditional medicine [4]. Upper herbaceous parts of *G. verum* have beneficial effects on nervousness, phobias, cardiovascular diseases and liver disorders [5]. This herb has been shown to contain speruloside, monotropein, scandoside and geniposidic acid [4, 6, 7, 8], as well as small amounts of tannins, saponins, essential oils, waxes, pigments and vitamin C [8].

The genus *Tragopogon* L. comprises approximately 100 species with a number of widely introduced species [9]. The genus comprises annual, biennial or mostly perennial herbs,

Tragopogon pratensis subsp. *pratensis* (Goat's beard) is a annual/perennial plant, growing to 0.6 m. *T. pratensis* is considered to be a useful remedy for the liver and gallbladder. It appears to have a detoxifying effect and may stimulate the appetite and digestion. Its high inulin content makes this herb a useful food for diabetics. The root is astringent, depurative, diuretic, expectorant, nutritive and stomachic. Experimental studies of methanol extracts of *T. pratensis* have shown that phenolic compounds have antiproliferative and tumor arresting effects [10].

Polyphenols are the major plant compounds that are characterized by antioxidant activity. This antioxidant activity of polyphenols is believed to be mainly due to their redox properties [11], in adsorbing and neutralizing free radicals, quenching singlet and triplet oxygen, or decomposing peroxides. Flavonoids are the most common and widely distributed group of plant phenolics compounds, occurring in almost all plants. Flavonoids may have an additive effect to the endogenous scavenging compounds and can prevent injury caused by free radicals in various ways. One way is the direct scavenging of free radicals.

* To whom all correspondence should be sent:
E-mail: violetamitic@yahoo.com

Flavonoids are oxidized by radicals, resulting in a more stable, less-reactive radical.

For evaluations of antiradical activity of the herbs extracts the most spread DPPH[•] and ABTS^{•+} methods were used. Both radicals show similar bi-phase kinetic reactions with many antioxidants. Both of them are characterized by excellent reproducibility under certain assay conditions, but they also show significant differences in their response to antioxidants. The DPPH free radical (DPPH[•]) does not require any special preparation, while the ABTS radical cation (ABTS^{•+}) must be generated by enzymes or chemical reactions [12]. Another important difference is that ABTS can be dissolved in aqueous and organic media, in which the antioxidant activity can be measured, due to the hydrophilic and lipophilic nature of the compounds in samples. In contrast, DPPH can only be dissolved in organic media, especially in ethanol, this being an important limitation when interpreting the role of hydrophilic antioxidants [13].

Radical cation ABTS^{•+} interacts with the extract or standard Trolox that suppressed the absorbance of the ABTS^{•+}. Trolox [6-hydroxy-2,5,7,8-tetramethylchroman-2-carboxylic acid], a water soluble vitamin E analog, serves as a positive control inhibiting the formation of the radical cation in a dose dependent manner. Results are expressed as trolox equivalents that cause the same reduction in absorbance as an appropriate concentration of the sample.

Reducing power is considered to be a strong indicator of the antioxidant activity and was determined using a modified iron (III) to iron (II) reduction assay. Reducing agents, react with potassium ferricyanide to form potassium ferrocyanide, which then reacts with ferric chloride to form ferric ferrous complex that has an absorption maximum at 700 nm. Compounds with reducing power are electron donors and can reduce the oxidized intermediates of lipid peroxidation processes, so they can act as primary and secondary antioxidants. The reducing ability is generally associated with the presence of reductants which exert antioxidant action through breaking the free radical chain by donating a hydrogen atom or preventing peroxide formation [14].

Acetylcholinesterase (AChE) plays the key role in the hydrolysis of acetylcholine at the cholinergic synapses, ending the transmission of nerve impulses. Inhibition of the acetylcholinesterase is considered as a promising strategy in confronting neurological disorders such as Alzheimer's disease, senile dementia, ataxia and myasthenia gravis. As potent source of AChE inhibitors is are numerous

plant natural products. Studies carried out earlier, in order to find new molecules or a group of molecules that can be used in the therapy without the toxicity of the synthesized chemical compounds, included in the beginning screening of plant's extracts [15,16].

Taking into account the above mentioned characteristics of *G. verum* and *T. pratensis* we thought that it could be of relevance for their medical use to examine the antioxidant capacity, hemolytic activity and activity against cholinesterase.

Methanolic herbs extracts were characterized by total polyphenol and flavonoides content. Free radical scavenging capacity was evaluated by measuring the scavenging capacity of extracts on DPPH and ABTS^{•+} radicals scavenging methods, and reducing power assay Fe(III) to Fe(II). Anti-cholinesterase action of selected extracts was tested applying modified Ellman's method [17]. Hemolytic assay was done by using standard Drabkin's method to determine the percentage of hemolysis in the RBC suspension [18].

MATERIALS AND METHODS

Chemicals and reagents

Folin-Ciocalteu reagent, 2,2-diphenyl-1-picrylhydrazyl (DPPH), ferrous chloride, gallic acid, 2,2'-azino-bis-(3-ethylbenzothiazoline-6-sulfonic acid (ABTS), 6-hydroxy-2,5,7,8-tetramethylchroman-2-carboxylic acid (Trolox), butyrylthiocholine iodide (purity > 99%), DTNB, neostygmine bromide were purchased from Sigma Co. St. Louis, Missouri, USA.

All other chemicals and reagents used (K₃[Fe(CN)₆], NaH₂PO₄-Na₂HPO₄, CCl₃COOH, ascorbic acid, butylhydroxytoluene (BHT), AlCl₃ rutin, CH₃COONa, Na₂CO₃, potassium persulfate, Methanol, were purchased from Merck, Darmstadt, Germany. All the chemicals and reagents were of analytical grade.

Apparatus

All spectrophotometric measurements of antioxidative potential of selected plant extracts and were performed on a spectrophotometer Perkin Elmer lambda 15.

All spectrophotometric measurements of inhibition of humane serum cholinesterase were performed on a Konelab 20 analyzer (Thermofisher Scientific) with flow thermostatted cells, length 7 mm (at wave length 405 nm). The advantage of the Konelab 20 analyzer, besides a significant reduction in reagent consumption (200 μL), was the possibility of performing up to 20 analyses per hour.

Plant material

Plant samples of the selected species *Galium verum* L. and *Tragopogon pratensis* subsp *pratensis* were collected from Seličevica (43° 13' 58" N 21° 55' 51" E) and Lalinac (43° 20' 19" N 21° 47' 04" E) in June 2010, identified by dr Bojan Zlatkovic, Department of Biology, and voucher specimens were deposited at the same department, Faculty of Science and Mathematics, Nis, Serbia.

Samples were dried under shade for seven days. Dried samples were ground into a uniform powder using a blender and stored in polyethylene bags at room temperature.

Preparation of extracts - ultrasonic extraction

Grounded air-dried plant material (10 g) was extracted with 100 mL 80 % methanol in the presence of low-frequency ultrasound. Sonication was performed 2 x 30 minutes using an ultrasonic cleaning bath (Sonic, Niš, Serbia; internal dimensions: 30, 15, 20 cm; total nominal power: 350 W; and frequency: 40 kHz). The temperature was maintained at 25 °C. At the end of the extraction process, the combined MeOH extracts were evaporated under vacuum to give crude MeOH extracts that were subject to subsequent analysis.

Determination of total phenolic content

The total phenolic concentration was determined spectrophotometrically according to the Folin-Ciocalteu colorimetric method [19] with slight modifications. Methanol extract solution (0.1 mL), 1 mL of Folin-Ciocalteu reagent, were mixed into a 20 mL calibrated flask. After 1 min, 4 mL of sodium carbonate (20 %, v/v) was added and the volume was made to 20 mL with distilled water; finally, the mixture was allowed to stand at room temperature in dark for 30 min and the absorbance of the solution at 750 nm was measured with a Perkin-Elmer Lambda 15 UV-VIS spectrophotometer. If the sample absorbance exceeded, the sample was appropriately diluted to give reading less than total phenolics were quantified by calibration curve obtained from measuring the absorbance of the known concentrations of gallic acid standard solutions (15-350 µg/mL in 80 % methanol). Since ascorbic acid also contributes to the formation of the blue molybdenum-tungsten complex, it is important to correct for the absorbance originating from it. An ascorbic acid calibration curve was therefore prepared. The total phenol compounds reported in this paper have all been corrected for ascorbic acid.

Data were expressed as mg of gallic acid equivalents (GAE)/g of extract [20].

Determination of total flavonoid content

The amount of total flavonoids was determined with aluminium chloride (AlCl₃) colorimetric assay according to a known method [13]. Briefly, 0.5 mL of each extract was made up to a final volume of 1 mL with reaction medium (MeO/H₂O/CH₃COOH=14:5:1). Prepared solution was mixed with AlCl₃ reagent (4 mL, 133 mg of AlCl₃·6H₂O and 400 mg of CH₃COONa dissolved in 100 mL H₂O). After 5 min, the absorbance level was measured versus prepared reagent blank (containing the same chemicals, except for the sample) at 430 nm (Perkin-Elmer Lambda 15 UV-VIS spectrophotometer). Total flavonoid content was calculated on the basis of the calibration curve of rutin and expressed by mg rutin/g dry extract. [19].

Antioxidant assay

The free radical-scavenging activity was determined by different in-vitro methods such as the DPPH• free radical scavenging assay, the ABTS•+ radical cation decolorization assay and reducing power methods. All the assays were carried out in triplicate and average value was considered.

DPPH• radical scavenging activity

DPPH• scavenging activity of the plant extract was carried out according to the method [13]. Briefly, 10 µL of each extract was mixed with 90 µmol/L DPPH• in methanol (1.0 mL) and made up with methanol to a final volume of 4.0 mL. The mixtures were shaken vigorously and incubated in dark for 60 min at room temperature. Absorbance of the resulting solution was measured at 517 nm (Perkin-Elmer Lambda 15 UV-VIS spectrophotometer). All reactions were carried out with BHA (Butylated Hydroxy Anisole) as a positive control. The DPPH• scavenging activity was expressed by radical scavenging capacity using the following equation:

$$\text{DPPH}\cdot \text{RSC} (\%) = 100 (A_0 - A_1 / A_0)$$

where A₀ was the absorbance of the control reaction (full reaction, without the tested extract or BHT) and A₁ was the absorbance in the presence of the sample. DPPH• stock solution was stored at 4 °C until it was used. The SC₅₀ value, which represented the concentrations of the extracts in the reaction mixture that caused 50 % inhibition, was determined by the linear regression analysis from the obtained. Decreased absorbance of the reaction

mixture indicates stronger DPPH• radical-scavenging activity.

ABTS•+ radical cation decolorization assay

Antioxidant capacity was measured based on the scavenging of ABTS•+ radical cation method. Concentration of ABTS solution was 7mM and it mixed with 2.45 mM potassium persulfate and incubated for 12-16 h in dark to generate ABTS•+ radical cation. The ABTS•+ solution was diluted with ethanol, to give an absorbance of 0.700 ± 0.050 at 734 nm. All samples were diluted appropriately to give absorbance values 20-80 % of that of the blank. Then fifty microlitres of diluted sample were mixed with 1.9 mL of diluted ABTS•+ solution.

The mixture was allowed to stand for 6 min at room temperature and the absorbance was immediately recorded at 734 nm. Trolox solution (final concentration 0-15 μM) was used as a reference standard. The results were expressed as mg Trolox/ g dry extract [21].

Reducing power assay Fe(III) to Fe(II)

Each prepared extract (10 μL) was mixed with $\text{K}_3[\text{Fe}(\text{CN})_6]$ (1 mL, 1 %) and $\text{NaH}_2\text{PO}_4\text{-Na}_2\text{HPO}_4$ buffer (1 mL, 0.2 mol/L, pH 6.6). These mixtures were incubated at 50 $^\circ\text{C}$ for 30 min, then trichloroacetic acid (1 mL, 10 %) was added and mixtures were centrifuged at 3000 rpm for 10 min. Finally, the supernatant fractions (1 mL) were mixed with distilled water (1 mL) and FeCl_3 (0.2 mL, 0.1 %). The absorbances of resulting solutions were measured at 700 nm. For each sample three replicates were carried out. Reducing power assay Fe(III) to Fe(II) was calculated by the following equation:

$$\text{AEAC} = C_A(\text{A}_S / \text{A}_A)$$

where C_A - final concentration of ascorbic acid in $\mu\text{g/mL}$, A_S - absorbance of the sample, A_A - absorbance of ascorbic acid [19]. Reducing power was expressed as Ascorbate Equivalent Antioxidant Capacity, AEAC, (μg of ascorbic acid/mL of extract). Increased absorbance of the reaction mixture indicates stronger reducing power.

CHOLINESTERASE INHIBITION PROPERTIES

Cholinesterase source for the assay

A total of 10 healthy volunteers (18-65 years old from both sexes), from the Pirot General Hospital, donated blood with written consent. According to the questionnaire, none of them had serious medical disorders, nor are or have been drug, cigarette, or

alcohol abusers. At least a month before the blood donation, none of them had been taking any medication. From all participants, a 5 mL blood sample was collected in a Vacutainer tube, centrifuged at 3000 rpm for 10 min and the serum supernatant was collected and used as the source of the enzyme for the assay and for the spiked sample preparations.

PROCEDURE

Serum cholinesterase catalyzes the hydrolysis of butyrylthiocholine to thiocholine, which reacts with chromogen DTNB. The reaction rate is determined from the rate of 5-thio-2-nitro benzoic acid formation, measured at 405 nm, in six cycles of 28 sec. Analysed solutions (10 μL) were mixed with 10 μL of the pooled serum (diluted with the phosphate buffer in ratio 1:9, v/v), and the phosphate buffer solution (160 μL). These were preincubated for 10 minutes (at 310 K) when a DTNB solution (10 μL) was added. After being allowed to stand 60 sec, finally the substrate solution (BuTC, 10 μL) was added.

RBC HEMOLYSIS ASSAY

Erythrocyte preparation

For the study healthy male Wistar rats 16 weeks of age were used. Animals were kept in group cages with 12 h light and 12 h dark cycle. Body weight was in the range of 200-250 g and food and water were supplied ad libitum. Experiment was done with the approval of ethic committee of Faculty of Medicine, University of Niš. Blood was obtained by cardiac puncture and collected in heparinized tubes. Whole blood was centrifuged at 2200 rpm for 10 minutes at 4 $^\circ\text{C}$. The buffy coat and plasma were removed from the tube and the equal amount of PBS (pH 7.4) was added to the packed erythrocytes at the bottom. The procedure was repeated three times to obtain washed erythrocytes. At the end erythrocytes were diluted with PBS to obtain 4 % suspension. Erythrocytes suspension was used the same day for the experiment.

Sample preparation and hemolytic assay

Plant extracts of both species were dissolved in PBS (pH 7.4) and the final concentrations were made up to give 750 $\mu\text{g/mL}$, 500 $\mu\text{g/mL}$, 250 $\mu\text{g/mL}$ and 100 $\mu\text{g/mL}$.

Hemolytic assay was done as previously described with some modifications [18]. Briefly, 200 μL of different concentrations of both plant extracts were added to 200 μL of erythrocytes suspension in a microtube. The positive control consisted of 200 μL of distilled water and 200 μL of

erythrocytes suspension. The negative control consisted of 200 μ L of phosphate-buffered saline (PBS, pH 7.4) and 200 μ L of erythrocytes suspension. The mixtures were incubated at room temperature and the percentage of hemolysis was determined after first, second, third and fourth hour of incubation. Drabkin's method was used to measure the absorbance of hemoglobin and to calculate the percentage of hemolysis, as previously described [22].

In the end of incubation period, samples were centrifuged at 2000 rpm for 10 minutes at 40C. Supernatant volume of 200 μ L was added to 3 mL of Drabkin's reagent. Mixture was shaken vigorously and the absorbance was measured at 540 nm (Shimadzu UV-1650PC). Hemolysis percentage was calculated by the equation:

$$\% \text{ hemolysis} = \frac{(\text{Ab of sample} - \text{Ab of negative control}) / \text{Ab of positive control}}{\text{Ab of positive control}} \times 100.$$

Statistical evaluation of data

The evaluation of the obtained analytical data was performed by statistical means. All analyses were run in triplicate. The elimination of outliers was done by Grubb's test, for each method the arithmetic mean and the standard deviation were calculated by Statistica 7 program. Significant

differences ($p \leq 0.05$) between the means were determined using Student's t- test.

RESULTS AND DISCUSSION

The results of investigation of antioxidant capacity, activity toward cholinesterase and hemolytic activity are given in Tables 1 and 2, and Fig. 1 and 2.

From the results it can be seen that:

- The *G. verum* methanol extract has much higher antioxidant capacity compared to *T. pratensis* methanol extract. Total flavonoid content was fivefold higher, total phenol content two times higher, and reducing power toward Fe^{3+} approximately four and half times higher. In DPPH• assay the lower IC₅₀ (extract concentration required for 50% inhibition of the DPPH radical absorbance), means a better radical scavenging ability [23]. *G. verum* extract has 2.2 time lower IC₅₀ than *T. pratensis* extract, and 1.5 times lower than commercial antioxidant BHT, which means that its antioxidant capacity was 2.2 and 1.5 higher than capacity of *T. pratensis* and BHT, respectively.

- Almost twenty times higher concentration of Trolox equivalent (125.14 mg Trolox/ g dry extract) was found in *G. verum* extracts than in *T. pratensis* extracts (6.31 mg Trolox/ g dry extract).

Table 1. *In vitro* antioxidant activity, total phenols content, total flavonoids content and inhibition of humane serum cholinesterase of *T. pratensis* subsp. *pratensis* and *G. verum* L. methanol extracts

	<i>T. pratensis</i>	<i>G. verum</i>
Total flavonoids content (mg RE/g dry extract)	4.48 \pm 0.38	9.05 \pm 0.94
Total phenols content (mg GAE/g dry extract)	21.97 \pm 1.08	118.13 \pm 9.64
Reducing power assay $\text{Fe}(\text{III})$ to $\text{Fe}(\text{II})$ (μ g of ascorbic acid/mL of extract)	15.66 \pm 0.67	70.31 \pm 2.95
DPPH• decolorization assays, IC ₅₀ (μ g/mL of extract)	59.25 \pm 2.12	26.97 \pm 1.21
ABTS•+ radical cation decolorization assays (mg Trolox/ g dry extract)	6.31 \pm 0.66	125.14 \pm 9.98
Inhibition of humane serum cholinesterase (%) *	-4.65 \pm 0.08	+16.28 \pm 0.09

Results are average \pm SD for three independent observations

* Methanol extract of *T. pratensis* and *G. Verum* in concentration of 994.0 μ g/mL GAE - gallic acid equivalents

RE - rutin equivalents

Table 2. Hemolytic activity (shown as percentage) of methanol extracts *T. pratensis* subsp. *pratensis* and *G. verum* L. after first, second, third and fourth hour of incubation

Conc. (μ g/ml)	1h			2h			3h			4h		
	<i>T.praten</i> <i>sis</i>	<i>G.veru</i> <i>m</i>	<i>p-value</i>	<i>T.prate</i> <i>nsis</i>	<i>G.ver</i> <i>um</i>	<i>p-value</i>	<i>T.</i> <i>pratens</i> <i>is</i>	<i>G.ver</i> <i>um</i>	<i>p-value</i>	<i>T.</i> <i>praten</i> <i>sis</i>	<i>G.ver</i> <i>um</i>	<i>p-value</i>
100	1.389 \pm 0.45	0.967 \pm 0.30	0.124	2.043 \pm 0.66	1.042 \pm 0.65	0.067	1.699 \pm 0.08	0.445 \pm 0.25	0.000*	3.127 \pm 0.19	0.445 \pm 0.26	0.000*
250	2.908 \pm 0.27	0.989 \pm 0.22	0.000*	11.291 \pm 0.85	0.416 \pm 0.11	0.000*	19.443 \pm 2.21	0.224 \pm 0.19	0.000*	27.063 \pm 2.42	0.277 \pm 0.09	0.000*
500	26.259 \pm 2.40	1.200 \pm 0.30	0.000*	51.716 \pm 1.52	1.599 \pm 0.13	0.000*	56.547 \pm 3.16	0.396 \pm 0.27	0.000*	57.182 \pm 3.22	0.717 \pm 0.24	0.000*
750	89.063 \pm 13.60	1.981 \pm 0.20	0.000*	85.701 \pm 6.12	2.126 \pm 0.19	0.000*	85.651 \pm 9.84	1.123 \pm 0.22	0.000*	85.244 \pm 3.22	1.275 \pm 0.21	0.000*

Results are average \pm SD for three independent observations

* $p \leq 0.05$ is significantly different by comparing methanol extracts *T. pratensis* subsp. *pratensis* and *G. verum* L.

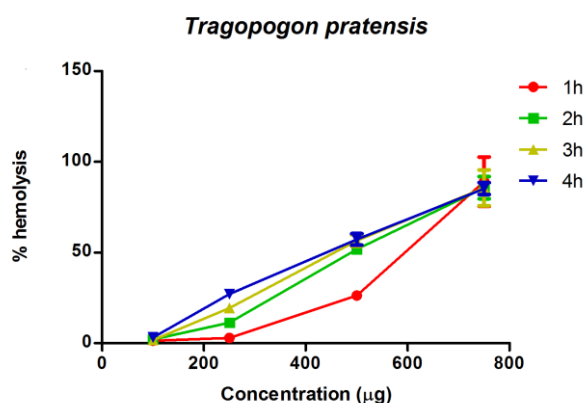


Fig. 1. Percentage of hemolysis MeOH extracts *T. pratensis* subsp. *pratensis* after first, second, third and fourth hour of incubation.

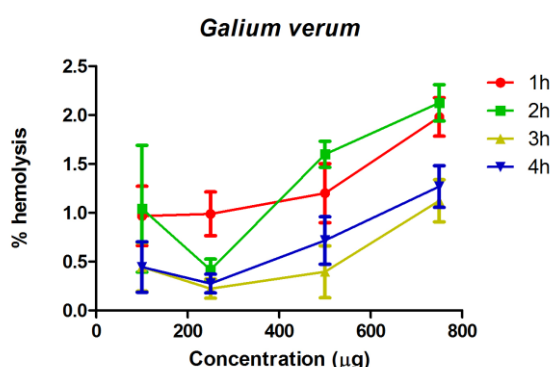


Fig. 2. Percentage of hemolysis MeOH extracts *G. verum* L. after first, second, third and fourth hour of incubation.

- Methanol extract of *T. pratensis* in concentration of 994.0 µg/mL showed only 4.65 ± 0.08 % inhibition of human serum cholinesterase, while *G. verum* in the same concentration, showed slight activation of the enzyme (+16.28 ± 0.09 %) in comparison to neostigmine bromide 30 µg/mL solution, applied as reference standard, that showed inhibition of -35.26 ± 0.12 %. Also, extract of *T. pratensis* could be considered as very weak inhibitor of human serum cholinesterase, but *G. verum* didn't exhibit inhibition capacity at all. On the contrary, it acted as an activator of cholinesterase and in that way could be treated as potentially harmful, concerning Alzheimer disease treatment. Though in our experiments pooled human serum was used as source of cholinesterase, obtained data are trustworthy in estimating potentials of the studied plants as a source of neurological valuable compounds.

- Methanol extract of *T. pratensis* shows hemolytic activity for each test exposure period (Table 2 and Fig. 1) with the highest percentage of 89% while the highest percentage for *G. verum* extract was 2.126%.

For *T. pratensis* extract hemolytic activity depends on the concentration and length of exposure proportionally. For *G. verum* extract (Table 2 and Fig. 2) applies the same, except for the concentration of 250 µg/mL. After the first hour of incubation 50% of hemolysis induced concentration of 501.97 ± 32.65 µg/mL, the second hour 499.98 ± 38.45 µg/mL, 498.656 ± 39.85 µg/mL of the third and fourth 421.33 ± 34.98 µg/mL.

Observed results can be explained by the chemical composition of the extracts. The phytochemical screening of *G. verum* extracts and *T. pratensis* extracts has shown the presence of saponins (tragopogonosides) in *T. pratensis* extracts [24].

Saponins are natural surfactants. Increasing the hemolytic activity of methanol extracts of *T. pratensis* in a dose-dependent manner may be explained by Fick's law, diffusion flux from a membrane is proportional to concentration difference of both sides. So the increase in the concentration of saponins in contact with the cell membrane leads to its diffusion in the membrane itself, which leads to membrane rupture and hemolysis of erythrocytes [25].

-As far as we know there are no data concerning the antioxidant, hemolytic and cholinesterase inhibition properties of *Tragopogon pratensis* subsp. *pratensis* methanol extracts as well as for *G. verum* hemolytic and cholinesterase activities.

Water and methanol extracts of *G. verum* in the range 50-500 mg/L have been the subject of research of Ahmet M. et al [26]. Methanol extract of *G. verum* has higher antioxidant activity than its water extract. The values of published data can not be compared with our results, because of the different experimental protocols and expression of results.

Our results are comparable with the results published by Lakić et al. [5]. The level of *G. verum* phenolics (2.44–4.65 mg and 4.57–5.16 mg GAE/g dry extract) was less than we found (118.13 mg GAE/g dry extract). Also, our IC50 value for *G. verum* extracts (26.98 µg/mL), was higher than previously published (3.1-8.04 mg/L).

CONCLUSIONS

The results of exhibited antioxidant activities are a good reference for performing its in vivo tests, and qualify it as a promising natural source of antioxidants. On the other hand *T. pratensis* subsp. *pratensis* methanol extract might be a good

hemolytic agent. *T. pratensis* could be considered as very weak inhibitor of human serum cholinesterase, but *G. verum* didn't exhibit inhibition capacity at all. On the contrary, it acted as an activator of cholinesterase.

ACKNOWLEDGEMENTS: Financial support of the Ministry of Education, Science and Technological Development of Serbia (Project No. 172047) is gratefully acknowledged.

REFERENCES

1. M. Gajić, in: Flora of Serbia, M. Josifović (eds.), Vol. V, Serbian Academy of Sciences and Arts, Belgrade, 1973.
2. V. Nikolić, A. Sigunov, N. Diklić, in: Flora of Serbia, M. Sarić (eds.), Vol. X, Serbian Academy of Sciences and Arts, Belgrade, 1986.
3. M. Josifović, Serbian Flora V, Serbian Academy of Arts and Science, Belgrade, 1973, (in Serbian).
4. K. Bojthe-Horvath, F. Hetenyi, A. Kocsis, L. Szabo, M. Varga-Balazs, Jr. Mathe, P. Tetenyi, *Phytochemistry*, **21**, 2917 (1980).
5. N. Lakić, N. Mimica-Dukić, J. Isak, B. Božin, *Cent. Eur. J. Biol.*, **5**, 331 (2010).
6. K. Bojthe-Horvath, A. Kocsis, L. Parkany, K. Simon, *Tetrahedron Lett.*, **23**, 965 (1982).
7. M.B. Arnao, *Trends Food Sci. Tech.*, **11**, 419 (2000).
8. A. Wojdylo, J. Oszmianski, R. Czemerys, *Food Chem.*, **105**, 940 (2007).
9. A. Kumaran, R.J. Karunakaran, *Food Chem.*, **97**, 109 (2006).
10. P.K. Mukherjee, V. Kumar, M. Mal, P.J. Houghton, *Phytomedicine*, **14**, 28910 (2007)
11. K. Ingkaninan, P. Temkitthawon, K. Chuenchon, T. Yuyaem, W. Thongnoi, *J. Ethnopharmacol.*, **89**, 261 (2003).
12. V. Stankov-Jovanović, S. Nikolic-Mandić, Lj. Mandić, V. Mitić, *J. Clin. Lab. Anal.*, **21**, 124 (2007).
13. G. D. Noudeh, F. Sharififar, M. Khatib, E. Behravan, M.A. Afzadi, *Afr. J. Biotechnol.*, **9**, 110 (2010).
14. G. Stojanović, I. Stojanović, V. Stankov-Jovanović, V. Mitić, D. Kostić, *Cent. Eur. J. Biol.*, **5**, 808 (2010).
15. N. Mimica-Dukic, N. Simin, J. Cvejic, E. Jovin, D. Orcic, B. Bozin, *Molecules*, **13**, 1455 (2008).
16. H.B. Li, K.W. Cheng, C.C. Wong, K.W. Fan, F. Chen, Y. Jiang, *Food Chem.*, **102**, 771 (2007).
17. L.A. Gould, A.B. Lansley, M.B. Brown, B. Forbes, G.P. Martin, *J. Pharm. Pharmacol.*, **52**, 1203 (2000).
18. E.N. Frankel, *J. Sci. Food Agr.*, **54**, 495 (1991).
19. T. Miyase, H. Kohsaka, A. Ueno, *Phytochemistry*, **31**, 2087 (1992).
20. H. Kleszczynska, D. Bonarska, J. Luczynski, S. Witek, J. Sarapuk *J. Fluoresc.* **15**, 137 (2005).
21. A. Mavi, Z. Terzi, U. Ozgen, A. Yildirim, M. Coskun, *Biol. Pharm. Bull.* **27**, 702 (2004)

АНТИОКСИДАНТНИ И ХЕМОЛИТИЧНИ СВОЙСТВА И ИНХИБИРАНЕ НА ХОЛИНЕСТЕРАЗА ЧРЕЗ *Galium verum* L. И *Tragopogon pratensis* subsp. *pratensis*

В. Д. Митич^{1*}, В. П. Станков-Йованович¹, М. Д. Илич¹, П. Й. Васильевич², А. Л. Забар²,
Г. С. Стоянович¹

¹Департамент по химия, Факултет за наука и математика, Университет в Ниш, Сърбия

²Департамент по биология и екология, Факултет за наука и математика, Университет в Ниш, Сърбия

Постъпила на 6 март; коригирана на 29 август, 2013

(Резюме)

Определени са антиоксидантните свойства на метанолови екстракти от *Galium verum* L. (енъвче) и *Tragopogon pratensis* subsp. *pratensis* (полска козя брада), брани от различни места в Сърбия. Определяно е общото съдържание на феноли и флавоноиди, както и DPPH^{*} (1,1-дифенил-2-пикрилхидразил)-радикал-отстраняваща активност, ABTS⁺⁺ (2,2-азинобис-(3-етилбензтиазолин-6-сулфонова киселина) радикал-катионово обезцветяване и по ферицианиден метод. Метаноловите екстракти от *G. verum* показват по-силна активност за отстраняване на свободни радикали (IC₅₀-стойности при 26.98 µg/mL за обезцветяване на DPPH^{*} и 125.14 mg Trolox/g сух екстракт за ABTS⁺⁺-радикал-катионово обезцветяване) и обща редукиционна способност (70.31 µg/mL), отколкото метаноловите екстракти от *T. pratensis* (SC₅₀-стойности при 59.25 µg/mL for DPPH^{*} - обезцветяване и 6.31 mg Trolox/g сух екстракт за ABTS⁺⁺-радикал-катионово обезцветяване и 15.66 µg/mL за обща редукиционна способност). Наблюдаваните резултати може да се обяснят с много по-високото съдържание на феноли и флавоноиди в екстрактите от *G. verum*. С помощта на модифицирания метод на Ellman's method се показва, че метаноловите екстракти от *G. Verum* показват слаба активност на човешката серумна холинестераза (16.28 ± 0.09 %), докато екстрактите от *T. pratensis* имат слабо инхибиращо действие спрямо същия ензим (4.65 ± 0.08 %). Също така, метаноловите екстракти от *G. verum* и *T. pratensis* са изпитани *in vitro* с помощта на стандартния метод на Drabkin's за да се оцени тяхната хемолитична активност. Екстрактите от *T. pratensis* показват много силна хемолитична активност (след първия час на инкубиране 50% или 501.97 ± 32.65 µg/mL, след втория час - 499.98 ± 38.45 µg/mL, 498.656 ± 39.85 µg/mL след третия и 421.33 ± 34.98 µg/mL след четвъртия), докато екстрактите от *G. verum* имат слаба хемолитична активност.

Activated carbon from cotton waste as an adsorbent in the purification process of azo-dyes

N. Djordjevic¹, D. Djordjevic^{1*}, M. Miljkovic², S. Urosevic³

¹University of Nis, Faculty of Technology, Leskovac, Serbia

²University of Nis, Faculty of Mathematics and Natural Sciences, Nis, Serbia

³University of Belgrade, Technical Faculty, Bor, Serbia

Received: April 1, 2013; revised: July 2, 2013

The treatment of azo dyes from the aqueous solution by adsorption process on activated carbon prepared from waste cotton fibers from weaving plants was investigated in this study. They are waste airborne fibers that arise as a by-product in the process of weaving. Waste cotton material is used for the production of activated carbon, which is then used for the reduction of textile azo dyes coloration in the solution. Qualitative and quantitative characterization of activated carbon shows that carbon is predominant in its chemical composition with the presence of several other elements. Based on the results, it can be said that the activated carbon produced from waste cotton fibers has potential as an adsorbent for the removal of azo dyes from aqueous solutions. Prolonged contact time means a greater amount of dye on the adsorbent, i.e. the dye concentration in the solution decreases with the duration of the adsorption. The percentage of removed dye decreases with the increase of initial dye concentration in the solution, but the actual amount of adsorbed dye increases with the increase of dye concentration.

Keywords: activated carbon, waste cotton fibers, azo-dye, adsorption.

INTRODUCTION

One of the main methods for removing pollutants from wastewater is the use of porous solid adsorbents. Porous materials properties that make them useful for the treatment of water are high porosity and surface area, as well as the physical and chemical nature of the internal adsorption surfaces. Large amounts of waste water polluted with dyes are discharged from the textile industry, leather and laundries. Pollutants include dyes, suspended solids, alkali, heavy metals and organic matters.

There are several studies on the adsorption of dye on different materials. These include the absorption of basic dyes on carbon, peat, wood and pith. Some studies indicate that the absorption rate is determined based on the adsorption equilibrium (unfavorable, linear, favorable or completely irreversible) and control mechanism (external diffusion, internal pore diffusion, inner solid-phase diffusion or longitudinal diffusion) [1-5].

Activated carbons are the most commonly used adsorbents in separation and purification processes. Lately, the efforts of scientists to find alternative adsorbent to replace the costly activated carbon

have been intensified. Some of the potential low-cost adsorbents for the removal of metals and organic substances are industrial waste materials. The purpose of activation is to obtain effective low-cost adsorbent. Activation can be carried out by chemical and physical methods. In chemical activation, the basic material is impregnated by various chemical substances, and then carbonized. Physical activation involves carbonization of carbonaceous feedstock, followed by gas processing of the obtained carbonizate, or direct activation of the initial material by activating agents (such as CO₂, water vapor, N₂, H₂, O₂ ...) [4-9].

Azo dyes are aromatic nitrogen compounds that dissolve in water due to existing sulfuric groups or other hydrophilic groups - carboxyl and hydroxyl. They are usually used for dyeing cellulose materials (cotton, viscose...) in the presence of electrolytes and wetting agents. Starting from the chemical frame of azo dyes, there are the carriers of free electrolyte pair groups that behave as electron donors, and carriers of hydrogen atom group - electron acceptor [10-14].

This paper deals with the adsorption process of azo dyes from aqueous solution on activated carbon produced from waste cotton fiber from the weaving plants. These airborne waste fibers are formed as a by-product in the weaving process using cotton yarns on looms. The aim is to use the waste cotton material, make it into activated carbon and use it

* To whom all correspondence should be sent:
E-mail: drag_64@yahoo.com

for coloration reduction, i.e. removal of textile azo dyes by adsorption on activated carbon.

EXPERIMENTAL

Materials

Activated carbon obtained by chemical and physical modification of waste cotton fibers from the weaving plants was used as an adsorbent. After the collection of waste fibers, they were washed in warm distilled water (40°C), dried and subjected to the treatment by concentrated sulfuric acid (1 g of waste fiber: 5 g H₂SO₄) for 24 h at room temperature. The samples were then heated at 180°C for 1 hour, followed by rinsing with distilled water and neutralization to pH=7 (with sodium bicarbonate). After drying, the obtained residue (activated carbon) was milled and then sieved to a particle size of 0.5 mm. Thus, prepared activated carbon was used in the experiment.

The dye used is a triazo class dye with 4 sulfo groups and one amino functional group. It is a dye that belongs to the group of azo dyes, CI Direct Blue 71, soluble in water, 10 g·dm⁻³ (60°C), 20 g·dm⁻³ (97°C) and exists in the anionic form, soluble in ethanol and insoluble in other organic solvents, Fig. 1.

Adsorption process

Adsorption test was performed in Erlenmeyer flasks in which the adsorbent (activated carbon) was suspended in azo dyes solution (adsorbate). Erlenmeyer flasks were placed on the shaker with 120 rpm·min⁻¹ at a temperature of 20°C and shaken for a given time. The amount of activated carbon was 3 g, while the solution in a constant volume of 100 cm³, contained dye concentrations of 10, 30, 50, 70 and 100 mg·dm⁻³. Processing time, with continuous stirring, was 10, 20, 30, 50 and 60 min. Experiments were conducted at neutral pH of the dye solutions, since there are no major variations in the wide range of pH.

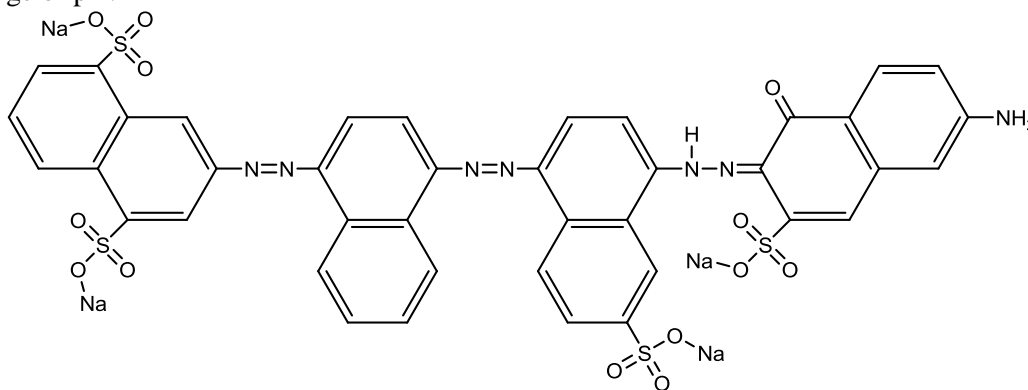


Fig. 1. Structure of the studied azo-dye.

The dye concentrations mentioned were taken for the simple reason that they mostly correspond to the amount of dye remaining in the waste solution after dyeing cotton textiles. It was found that the adsorption equilibrium time of dye adsorption on activated carbon was achieved in 60 min, and an extension of time of treatment did not significantly change the adsorption. Upon completion of the adsorption, dye solutions and activated carbon were passed through a filter paper.

Methods

Determination of the absorption of the solution was performed on a UV-VIS spectrophotometer (Cary 100 Conc UV-VIS, Varian) at 595 nm (maximum wavelength of the spectrum of the dye solution used).

SEM measurements were carried out on a JEOL JSM - 6610LV device using a secondary electron detector. In addition, as the SEM is equipped with Energy-dispersive spectroscopy (EDS) X-rays detector, characteristic X-rays of major elements (> 10 wt.%) were measured. EDS system enabled rapid assessment of the elemental composition of the sample - the adsorbent.

Analyses of specific surface area and pore distribution of the synthesized activated carbons were carried out by nitrogen adsorption at -196oC on a Sorptomatic 1990 analyzer (Thermo Fisher Scientific Inc.). Before measurements, the samples were degassed for 12 h at 110oC. Determination of the specific surface area of samples was performed by Brunauer-Emmett-Teller (BET) method, the mesopore volume and surface area were determined by Barret-Joyner-Halenda (BJH) method, and the micropore volume was obtained by using the Dubinin-Radushkevich equation [7-9].

The degree of dye removal (dye exhaustion) was calculated based on the dye concentration

before and after treatment [7, 9]:

$$R = \frac{C_0 - C_t}{C_0} \cdot 100 \quad (1)$$

where C_0 and C_t are the initial and final concentrations of dye solutions, respectively.

The amount of dye adsorbed (adsorbate) per unit mass of activated carbon (adsorbent), q_t (mg·g⁻¹), was determined as follows [7, 9]:

$$q_t = \frac{(C_0 - C_t) \cdot V}{M} \quad (2)$$

where: M , g - mass of adsorbent, V , dm³ - volume of solution from which adsorption is carried out.

RESULTS AND DISCUSSION

The activated carbon used is relatively fine bulk material with heterogeneous porous particles of diverse shapes and forms. Within larger particles, there are conspicuous cracks, cavities and channels that form the basis of the microporosity of materials. Otherwise, the inherent high porosity of activated carbons is provided by the presence of particles of irregular shape, a high degree of amorphization and a number of gaps in the structure. Micrograph in Figure 2 gives the appearance with $\times 750$ magnification. In addition to differences in shape, pores vary according to their availability for adsorbate molecules, which is associated with the fact that they can be closed, open at one end or both ends, they can be isolated or joined [4-7]. Taking into account the classification of pores according to their size, meso- and macropores can be said to be dominant in the sample used.

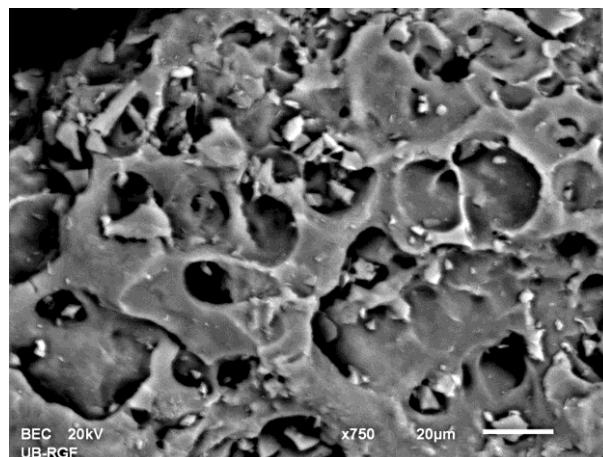


Fig. 2. Micrograph of the adsorbent used (activated carbon).

EDS system allows rapid assessment of the elemental composition of the sample. Sample analysis is non-destructive and quantitative analysis can be obtained by a spatial resolution of the order of magnitude of 1 μm . Table 1 shows the quantitative composition of active carbon, i.e., the percentage of one element in relation to the sum of all detected elements. All elements (e.g., C, O, Na, Al, Si, S, and Ca) detected in this analysis constitute 100 % and the individual percentages of each element means that 100 g of all detected elements contain that exact quantity in grams of each element.

Textural properties of activated carbon are given in Table 2. The results show different parameters, which by their numeric values characterize the specific surface area, pore volume, pore diameter, etc.

Table 1. Quantitative composition of the adsorbent used according to EDS spectrum analysis

Spectrum	C	O	Na	Al	Si	S	Ca	Total
Weight %	57.69	36.13	4.16	0.05	0.10	1.84	0.03	100.00
Mean	57.69	36.13	4.16	0.05	0.10	1.84	0.03	100.00
Std. deviation	0.00	0.00	0.00	0.00	0.00	0.00	0.00	
Max.	57.69	36.13	4.16	0.05	0.10	1.84	0.03	
Min.	57.69	36.13	4.16	0.05	0.10	1.84	0.03	

Table 2. Activated carbon textural characteristics obtained by analyzing the adsorption and desorption of N₂.

S_{BET} (m ² ·g ⁻¹)	$V_{0.98}$ (cm ³ ·g ⁻¹)	V_{mic} (cm ³ ·g ⁻¹)	S_{mic} (m ² ·g ⁻¹)	V_p (cm ³ ·g ⁻¹)	D_{max} (nm)	D_{av} (nm)
2.14	0.0051	0.00085	2.40	0.0041	8.7	2.3

S_{BET} - specific area according to BET method;

$V_{0.98}$ - total pore volume at a relative pressure p/p_0 - 0.98 to Gurvich method;

V_{mic} and S_{mic} - micropore volume and specific surface area - by Dubinin and Raduskevich method

V_p , D_{max} , D_{av} - micropore volume, maximum porediameter and average pore diameter from the distribution according to Dollimore and Heal method for mesopore

The adsorption-desorption isotherm (Figure 3) represents a change in the amount of adsorbed gas (V_{ads}), on the solid material as a function of the equilibrium pressure (p/p_0), at constant temperature. Pore volume according to Gurvich for p/p_0 of 0.98 was $0.0051 \text{ cm}^3 \cdot \text{g}^{-1}$. The shape of adsorption-desorption isotherm depends on the porous structure of the solid material. According to IUPAC classification, there are six types of adsorption isotherms, which enable determination of the textural properties (specific surface area, pore volume, pore volume distribution by diameter).

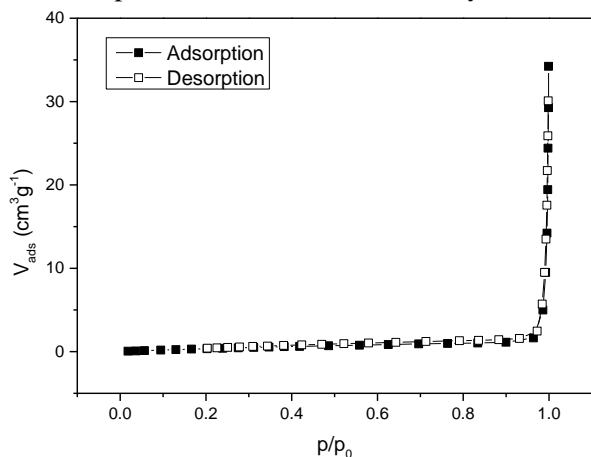


Fig. 3. Adsorption-desorption isotherms of activated carbon.

The curves shown in Figure 3 correspond to type III isotherms according to the IUPAC classification. The absence of a sharp decline in the area of low relative pressure indicates the absence of micropores. Isotherm has a reversible form throughout the range of the relative pressure. In type III the convexity to the x-axis extends along the entire isotherm. Isotherm convexity means that the particles that have been adsorbed tend to improve the adsorption of other particles from the depth of the phase. It is concluded that the interaction between the adsorbate particles is of primary importance here. Weak interactions at the beginning of adsorption (at low relative pressure) results in less pronounced adsorption. As the pressure increases, and new particles are adsorbed, the attraction between the adsorbate particles is increasingly favouring the adsorption, so the isotherm becomes convex.

The effect of contact time on the removal of azo dyes by the adsorbent is shown in Figure 4. The dye was quickly adsorbed in the first twenty minutes, and then the adsorption rate decreased gradually and reached equilibrium in about 60 minutes. At the beginning, the adsorption rate was high because the dye ions were adsorbed by the outer surface of

activated carbon. When the adsorption of the exterior surface reached saturation, dye ions were adsorbed by the interior surface of particles. This phenomenon has a relatively long contact time. It is believed that adsorption of matter on activated carbon also depends on the pore structure and chemical properties of the carbon surface as the adsorbate. From the point of view of the free energy of adsorption, the compounds are first adsorbed in the pores of similar size as the adsorbate due to the larger number of points of contact between the molecule and the adsorbent.

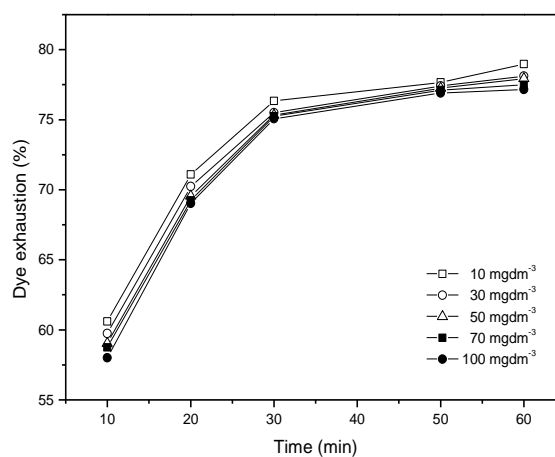


Fig. 4. The effect of adsorption time on the amount of exhausted azo-dyes .

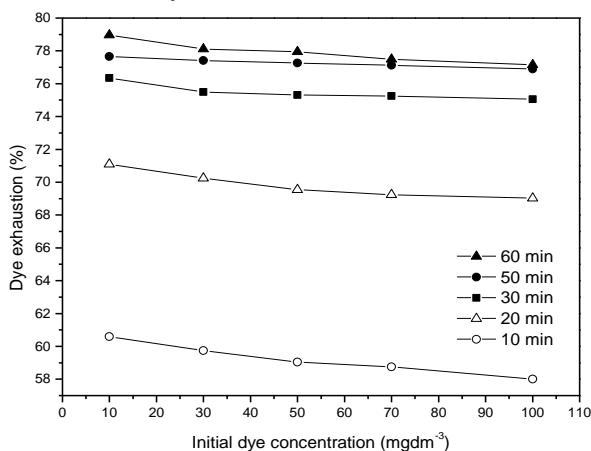


Fig. 5. The effect of the initial dye concentrations in the solution on the amount of azo dye removed.

Figure 5 shows the dependence of the degree of dye exhaustion on the initial dye concentrations for different times of adsorption. At lower dye concentrations, a slightly higher degree of dye removal is achieved. In reality, however, larger quantities of dye are adsorbed on activated carbon at largest initial concentration of azo dyes as will be explained further.

The results of the changed adsorbed amount of adsorbates on the adsorbent during time, for different starting dye concentrations, are showed on

diagrams on the figure 6. The continuity of changes in the period of time is present, i.e. longer time brings larger amount of adsorbed dye per adsorbent mass, i.e. there is the highest adsorption at the highest applied dye concentrations.

The continuous increase of the amount of exhausted dyes compared to the mass of adsorbent is also evident. At a given initial dye concentrations, a major change of the adsorbed dye occurs in the first 10 minutes of dyeing process, while in the later stage of adsorption these changes are minor.

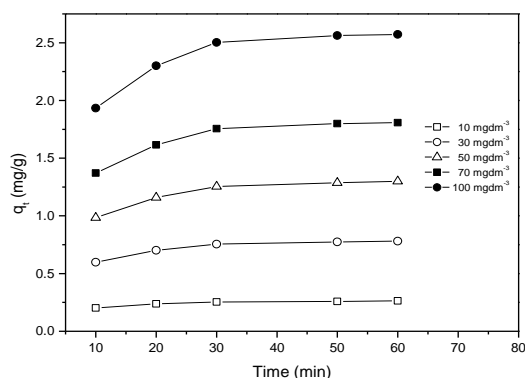


Fig. 6. Adsorbed amount of dye during time.

CONCLUSION

The thermochemical conversion of waste cotton fibers in powdered activated carbon was made with sulfuric acid as the activating agent. Activated carbon was investigated in terms of physical and chemical properties. A survey was done of azo dye adsorption onto activated carbon. In the elemental composition of the produced activated carbon dominated carbon, which was expected and in line with the theoretical data for activated carbon, which lead to conclusion that this material could be considered as a suitable carbon precursor for effective subjection to conversion into activated carbon.

Removal of azo dyes using activated carbon was investigated under various conditions. It was found that the adsorption depends on contact time and the initial dye concentration.

Based on the experimental results the following conclusions can be drawn:

- Activated carbon derived from waste cotton fibers can be an effective adsorbent for the removal of azo dyes from aqueous solutions with a logical tendency of application in industrial environments.
- Prolonged contact time means a greater amount of dye on the activated carbon, i.e. the dye concentration in the solution decreases with the duration of the adsorption.
- The percentage of the removed dye decreases with increasing the initial dye concentration in the solution, but the actual amount of the adsorbed dye increases with the increase of dye concentration.

The results obtained in this work indicate the possibility a practical application of removal of water coloration in the textile industry thus providing support of environmental protection both from economic and practical standpoint.

REFERENCES

1. B.H. Hameed, R.R. Krishni, S.A. Sata, J. Hazard. Mater. 162, 305 (2009).
2. P. Sharma, H. Kaur, M. Sharma, V. Sahore, Environ. Monit. Assess. 183, 151 (2011).
3. Y. Safa, H.N. Bhatti, Chem. Eng. J. 167, 35 (2011).
4. P.K. Malik, J. Hazard. Mater. B113, 81 (2004).
5. S. Wang, Z.H. Zhu, Dyes. Pigments. 75, 306 (2007).
6. H. Denga, G. Li, H. Yanga, J. Tanga, J. Tanga, Chem. Eng. J. 163, 373 (2010).
7. P.K. Malik, Dyes. Pigments. 56, 239 (2003).
8. B.S. Girgis, M.F. Ishak, Mater. Lett. 39, 107 (1999).
9. M. Ozdemira, T. Bolgaza, C. Sakab, O. Sahinc, J. Anal. Appl. Pyrol. 92, 171 (2011).
10. K. Sawada, M. Ueda, Dyes. Pigments. 58, 37 (2003).
11. M. Chairat, S. Rattanaphani, J. B. Bremner, V. Rattanaphani, Dyes. Pigments. 64, 231 (2005).
12. S.M. Burkinshaw, A. Gotsopoulos, Dyes. Pigments. 42, 179 (1999).
13. F. Carrillo, M.J. Lis, J. Valdeperas, Dyes. Pigments. 53, 129 (2002).
14. N.K. Amin, J. Hazard. Mater. 165, 52 (2009).

АКТИВЕН ВЪГЛЕН ОТ ПАМУЧНИ ОТПАДЪЦИ КАТО АДСОРБЕНТ ПРИ ПРЕЧИСТВЕАНИЕТО ОТ АЗО-БАГРИЛА

Н. Джорджевич¹, Д. Джорджевич^{1*}, М. Милькович², С Урошевич³

¹*Факултет по технология, Университет в Ниш, Лесковац, Сърбия*

²*Факултет по математика и естествени науки, Университет в Ниш, Ниш, Сърбия*

³*Технически факултет, Университет в Белград, Бор, Сърбия*

Постъпила на 1 април; коригирана на 2 юли, 2013

(Резюме)

В настоящата работа е изследвано пречистването на азо-багрила от водни разтвори чрез адсорбция върху активен въглен, приготвен от отпадъчни памучни влакна. С получения активен въглен се намалява оцветяването на отпадъчните води от предачни предприятия. Количествените и качествените характеристики на активния въглен показват, че въглеродът преобладава в присъствие на няколко други елемента. На базата на получените резултати може да се заключи, че произведеният активен въглен има потенциала да адсорбира азо-багрила от водни разтвори. Продължителният контакт на активния въглен с водния разтвор води до по-висока степен на отстраняване на багрилата. Процентната част на отстранените багрила намалява с нарастването на началната концентрация на багрилото, но общото количество на адсорбираното багрило нараства с нарастване на началната му концентрация.

Electroless deposition of composite Co-P-diamond layers and their polishing properties

D. Stoychev^{1*}, E. Dobreva², N. Razkazov², M. Stoycheva³, N. Koteva²

¹ Institute of Physical Chemistry "Acad. R.Kaischew", Bulgarian Academy of Sciences, Sofia 1113, Bulgaria

² Technical University, Bulgaria

³ Institute of Electrochemistry and Energy Systems "Acad. E. Budewsky", Bulgarian Academy of Sciences, Sofia 1113, Bulgaria

Received April 15, 2013; revised August 8, 2013

The options for electroless deposition of Co-P-diamond composite layers on substrate of polyethylene terephthalate have been studied using alkaline chloride electrolytes and NaH_2PO_2 as reducing agent. The effects of the concentration (1-25 g/L) and the particle size (0,03 – 100 μm) of the dispersed phase (diamond powder), added to the working electrolyte have been studied, with the view to determine the amounts of diamond particles co-deposited in the cobalt matrix, as well as the mass and the average thickness of the composite layers being formed. Thereupon the ranges of sizes and concentrations of the diamond particles in the electrolyte have been defined, at which the quantities of the particles included in the cobalt matrix are satisfactory in regard to the formed composite layers, applicable to the production of flexible PETF/Co-P-D polishing discs. Preliminary testing of the polishing effect of the PETF/Co-P-D discs has been carried out under laboratory conditions (the discs contain diamond particles of sizes: 63-75; 38-45; 20-28; 14-20; 7-10; 3-7 and 0.03-0,5 μm) on limestone samples and on two kinds of marble samples. The obtained results for the values of the coefficients R_c and R_a are completely in accordance with the requirements for finishing surface polishing treatment of similar materials.

Keywords: Electroless deposition, composite Co-P-Diamond layers, Polishing properties

INTRODUCTION

The chemically deposited cobalt coatings are used in the technique mainly in view of their hardness, resistance to abrasion and magnetic properties. By chemical cobalt coating it is possible to obtain composite layers/materials possessing great hardness, on the basis of co-deposition and incorporation into the solid cobalt matrix of some very hard nano- or micro-particles such as ceramic materials, carbon nanotubes, diamond, SiC, boron nitrides and others.

One of the important advantages of the chemical method for deposition of metal coatings is the option to cover dielectrics with metal coatings. In this case the operation "activation" is determining a series of properties of the deposited composite coating on their surface. It exerts considerable influence on the quality and on the properties of the system coating-matrix, as it determines the nature and the character of the distribution of the active sites, on which the process of reduction of the metal ions is taking place, and thereupon it influences

also the co-deposition of the solid dispersoid.

It is known that the alkaline electrolytes are the most suitable for the electroless deposition of cobalt coatings. The occurring of the process in acidic medium is unfavorable due to the low rate of deposition [1, 2].

The authors [3] compare the chemical (electroless) deposition of composite coatings on the basis of nickel or cobalt matrix and SiC particles. They established substantial differences in the process of deposition of the two metals-matrixes, although they have similar physical and chemical properties. Maleic acid is added to the electrolytes for depositing metal coatings in its function as a stabilizer. Its optimal concentration depends on the nature of the deposited metal. It has been ascertained that the inclusion of SiC in the coating is of greater quantity in the case of cobalt matrix compared to the nickel one. The observation of the morphology of the composite coatings Ni-P/SiC and Co-P/SiC also shows that the nickel coating is compact and it is shaped in regular sphere grains, while the cobalt coating is characterized by higher smoothness, needle-like

* To whom all correspondence should be sent:
E-mail: stoychev@ipc.bas.bg

structure and in some cases by formation of pitting defects.

The presence of SiC in the solution reduces the rate of deposition of the metal matrix. This effect is most probably due to the fact that the solid-non-metal particles exert no catalytic effect on the oxidation of NaH_2PO_2 . They are adsorbed on the substrate, upon which the coating is being deposited and this hinders the contact between the metallic surface and the electrolyte thus reducing the quantity of the deposited metal. The investigations show that OH^- groups are being adsorbed on the surface of SiC. In this connection it is supposed that the negative charge of the particles adsorbed on the substrate repels the anion of the reducing agent and therefore the rate of deposition is decreased.

The authors [4] consider the properties of the chemically deposited composite coating of Co-P/PTFE having a thickness of 5-10 μm , which is deposited on the steel surface. The reasons for choosing cobalt as a metal matrix of the composite coating are its good functional properties and strong adhesion to the surface of steel articles. The composite coating contains 9% PTFE, 5.1 % P and 85.9% cobalt. The properties and the structure of the coating have been studied by X-ray diffraction analysis, scanning electron microscopy and electron spectroscopy for chemical analysis. The results show that it has a good adhesion to the substrate, hexagonal crystalline structure and great hardness. The investigations, carried out so far, have established a definite orientation of the particles of PTFE. The fluorine atoms are dominating on the surface of the coating, while the phosphorus and the cobalt are included uniformly in the form of elemental phosphorus and Co^{3+} . The Co-P/PTFE composite layers possess good tribological properties. Their hardness is increasing upon heating them.

Chemically deposited nano-composites on the basis of nickel and cobalt (Ni-P/diamond; Ni-W-P/SiC; Ni-W-B/SiC; Co-B/diamond; Co-P/diamond; Ni-P/diamond; Ni-P/SiC), which could be used as alternative to hard chromium coatings, have been reported in [5]. It is known that toxic chemicals are being used during the electrodeposition of chromium coatings – the salts of the six-valence chromium Cr^{6+} . Aiming at protection of the environment and improving the working conditions there is an ongoing search of alternatives to chromium coatings. Ref. [5] provides evidence that such alternatives could be the nano-composite cobalt coatings, characterized by improved properties with respect to hardness,

losses due to abrasion and corrosion stability. This search has ascertained that in analogy to coating nickel chemically, the deposition of cobalt coating, the properties of the composite coating appear to be function of the content of P or B, which depend on the concentration of reducing agent; the conditions of treatment at high temperature; the nature and the concentration of the dispersed phase and others. In the case of chemical coatings for example the incorporation of nanosized diamond particles improves their hardness, which in its turn promotes the stability of the performance of the so prepared abrasive material. Co-P coatings (4 to 6 wt.%), which have 500 nm size of the included diamond particles has identical or even better properties compared to the hard chromium coating. Therefore very often the composite coatings, containing nanoparticles of great hardness, are better than the conventional coatings deposited chemically or electrochemically.

Ref. [6] analyzes the influence of particles of diamond, B_4C , BN, WC on the properties of electrochemically deposited cobalt coatings, containing phosphorus. It has been reported that Co-P (2-5%) shows identical or even better properties than the hard chromium coating, and the stability of Co-P/ B_4C (22%) to abrasion wearing away is greater.

Studies on the corrosion stability of electrochemically deposited cobalt coatings (nano-Co and nano-Co-P with a thickness of about 50 μm), carried out in the course of 1000 hours in a salty fog and compared to the hard chromium coating (~ 100 μm) prove that both kinds of cobalt coating are more durable. The content of P in the coating improves also its corrosion stability. According to these authors there are no published data on the corrosion resistance of composite cobalt coatings, which do not contain any phosphorus.

Other composite systems, containing nano- or micro-particles, have also been studied with the view to replace the chromium coatings [7]. Electrochemically prepared nano-crystalline cobalt with or without co-deposited WC has also been studied, as well as chemically deposited nickel (Ni-P) with diamond particles of various size (150, 1000, 2000 and 150÷1000 nm), Ni-P, Ni-Co-P, Co-P and Ni-B with or without incorporated diamond particles. Their adhesion, thickness, hardness and abrasion resistance have been studied. The results show that all the chemically deposited coatings (Ni-P, Co-P, Ni-Co-P having included diamond particles) possess the needed adhesion, hardness and tribological properties and they can eliminate

the necessity of using chromium coatings in the technique.

Based on the current literature survey a conclusion was drawn that the chemically deposited Co-P composite coatings (with included very hard particles) are characterized by better properties both in the aspect of improving the adhesion, as well as with respect to the hardness, resistance to abrasion and their corrosion protective ability in comparison to the electrochemically or chemically deposited composite coatings based on the Co-B matrix. There are, however, quite a few data on chemically deposited composite coatings on non-metal substrate (and in particular flexible ones), which could illustrate directly the inter-connection between the nature and the quantity of the co-deposited dispersoids on one hand, and their tribological properties on the other hand.

In this aspect the aim of the present study was to establish the options of chemical (electroless) deposition of Co-P matrix on flexible substrate of polyethylene terephthalate (PETF), with some diamond particles included in the matrix. The realization of such a system (PETF/Co-P-Diamond) represents special interest for the production technology for polishing and finishing flexible disks for surface treatment of different mineral and metal materials (rocky materials, non-ferrous metals, alloys and others).

EXPERIMENTAL SECTION

All the studies have been carried out using samples of dimensions 9 x 2 cm, cut out of gauffer (wafer-type) sheet of polyethylene terephthalate (non-woven textile of thickness 1,5 mm), placed horizontally in the working cell of volume 1 L. These were treated following the technological scheme:

Preliminary treatment

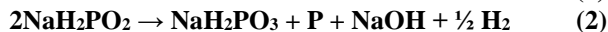
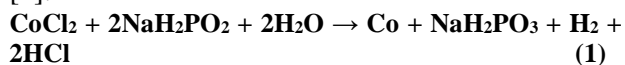
- etching (15 min) in solution of 250 g/L NaOH at 60°C;
- treatment (5 min) in 3M HCl solution at room temperature;
- activation (5 min) in colloid solution of PdCl₂ (0.4 g/L) at room temperature;
- acceleration (5 min) in solution of NaOH (40 g/L) at room temperature.

The chemical coating of cobalt was done in an electrolyte with a composition, optimized (concerning: concentrations of CoCl₂, NaH₂PO₂, pH and co-deposited P, evaluating hydrogen and thickness of the cobalt coating, respectively) previously by us [8], which contains:

CoCl ₂ .6H ₂ O	30 g/L
NaH ₂ PO ₂ .H ₂ O	20 g/L

Sodium citrate	100 g/L
NH ₄ Cl	50 g/L

at pH 9 and temperature of the solution 90°C, in accordance with the following reaction mechanism [1]:



The options to deposit composite Co-P-diamond coatings were studied, whereupon different concentrations (1 - 25 g/L) of synthetically prepared diamond particles (diamond powder) were added to the basic electrolyte for coating cobalt chemically and their sizes varied: 0,03-0,5 μm, 3-5 μm, 7-10 μm, 14-20 μm, 20-28 μm and 60-70 μm. To improve the degree of wetting of the diamond particles they were subjected to preliminary treatment in a solution of sodium laurylsulfonate (0.1 g/L) for 15 min at room temperature. The composite coatings were prepared under continuous or interrupted (2 min of stirring/10 min of rest) stirring of the solution with magnetic stirrer (speed of 400 rpm).

The morphology and the structure of the composite coating, as well as the distribution of the included particles, were studied by means of scanning electron microscopy (electron microscope model YSM C390 - Japan), while their mass and the conditional thickness were determined gravimetrically. The content of co-deposited phosphorus was determined by X-ray fluorescent analysis.

The polishing effect and the tribological behavior of the composite layers, deposited on model disks of PETF (with diameter of 70 mm and thickness of 2 mm), was tested on the home-made apparatus specially designed by us. It enabled realizing the experiments at various velocities of rotation of the studied disk (100 up to 3000 rpm) and at pressure upon the tested samples (limestone, two kinds of marble and granite) 0.2-2 kg/cm². The changes in the surface roughness (average deviation, R_a and attitude roughnesses, R_z) were determined by means of profile-recorder-profile gauge Perthen.

EXPERIMENTAL RESULTS AND DISCUSSION

3.1. Influence of the size and the concentration of the diamond particles in the working solution on the thickness and quantity of co-deposited diamond particles in the chemically deposited composite layers.

Table 1. Dependence of the thickness of the chemically deposited composite Co-P-D coatings on PETF substrate on the concentration (1 to 25 g/L) of the diamond particles, dispersed in the working solution, with particle size 0.03 – 0.5 μm . Deposition time interval 30 min.

Diamond particle size, μm	Concentration of dispersed diamond, g/L	Thickness of the deposited composite coating, μm	Weight of the deposited composite coating, g
0,03 - 0,5	1,0	0,61	0,0097
0,03 - 0,5	3,0	0,68	0,0108
0,03 - 0,5	5,0	0,74	0,0117
0,03 - 0,5	7,0	0,93	0,0150
0,03 - 0,5	10,0	1,60	0,0257
0,03 - 0,5	15,0	1,78	0,0285
0,03 - 0,5	25,0	3,77	0,0597

During the first cycle of the investigations carried out the effect of the diamond particle size was studied as well as their concentration in the solution for chemical cobalt deposition on the mass, respectively on the thickness of the deposited composite coating of Co-P(5%)-Diamond denoted as (Co-P-D). The obtained results are represented in Tables 1-3.

Table 1 comprises the results, obtained in the course of the formation process of the composite coating from solutions containing 1 to 25 g/L diamond powder, which is characterized by particle size 0.03 – 0.5 μm . It is seen from the table that with the increase in the concentration of the particles in the electrolyte the mass is growing up, respectively the thickness, of the deposited composite layer. A similar effect has also been observed by other investigators in the chemical deposition of nickel composites coatings, including polycrystalline diamond particles in them [9]. The explanation put forward in this case is connected with the presence of catalytically active sites, catalyzing the oxidation reaction of H_2PO_2^- , determined by the specific morphological peculiarities of the diamond particles and/or by residual transition metals used (and included) in its synthesis [10,11].

SEM observations of the same samples confirm this supposition. It is seen from the represented micrographs that the reduction of the cobalt ions is accomplished both on the growing cobalt matrix as well as on the diamond particles. This leads to a substantial increase in the number of the diamond particles co-deposited in the cobalt matrix (Fig.1b-e) and as a result of their coalescence there is a substantial growth in the thickness of the composite layer with the increase in the concentration of the particles in the electrolyte. While in the case of diamond particles concentration in the working solution 1 g/L, the number of the particles in the Co matrix co-deposited upon the fibers (Fig.1a) is very

low (Fig.1b), at the other concentrations (Fig.1c – 3 g/L, Fig. 1d – 7 g/L and Fig.1e – 10 g/l) it is growing up considerably, following a proportional dependence.

Thereupon an increase in the number of grains is observed, respectively in the roughness of the composite Co-P-D coating. This result is in accordance with the above made supposition about the role of the specific morphological peculiarities of the diamond particles and/or the presence of catalytically active transition metals included in them during the synthesis. In support of such a hypothesis comes the registering of increased frequency of appearance of spheroid agglomerates of diamond particles with the increase in particles concentration in the electrolyte (Fig.1d, 1e), being formed as a consequence of the chemical deposition of Co on the diamond particles. Their “self-cobalting” process, occurring in parallel to the process of formation of the cobalt matrix on the PETF substrate, is leading (as a consequence of superficial forces of interaction) to formation of such agglomerates and their growing up. Obviously, their addition to the cobalt matrix is accomplished via “bridges” of metallic cobalt (Fig.1d, 1e). The further increase in the concentration of the diamond powder in the working solution does not change substantially the number of the particles co-deposited in the Co matrix, but it is only increasing the amount of spheroid agglomerates grown on the surface of the composite coating. For this reason it can be accepted that the optimal working concentration for this size of the diamond particles lies within the interval 3-5 g/L.

It should be pointed out as an important feature of the process of formation of the composite Co-P-D coatings on gauffer (wafer) type of substrate of PETF the considerable differences in the numbers of co-deposited diamond particles on the fibers and

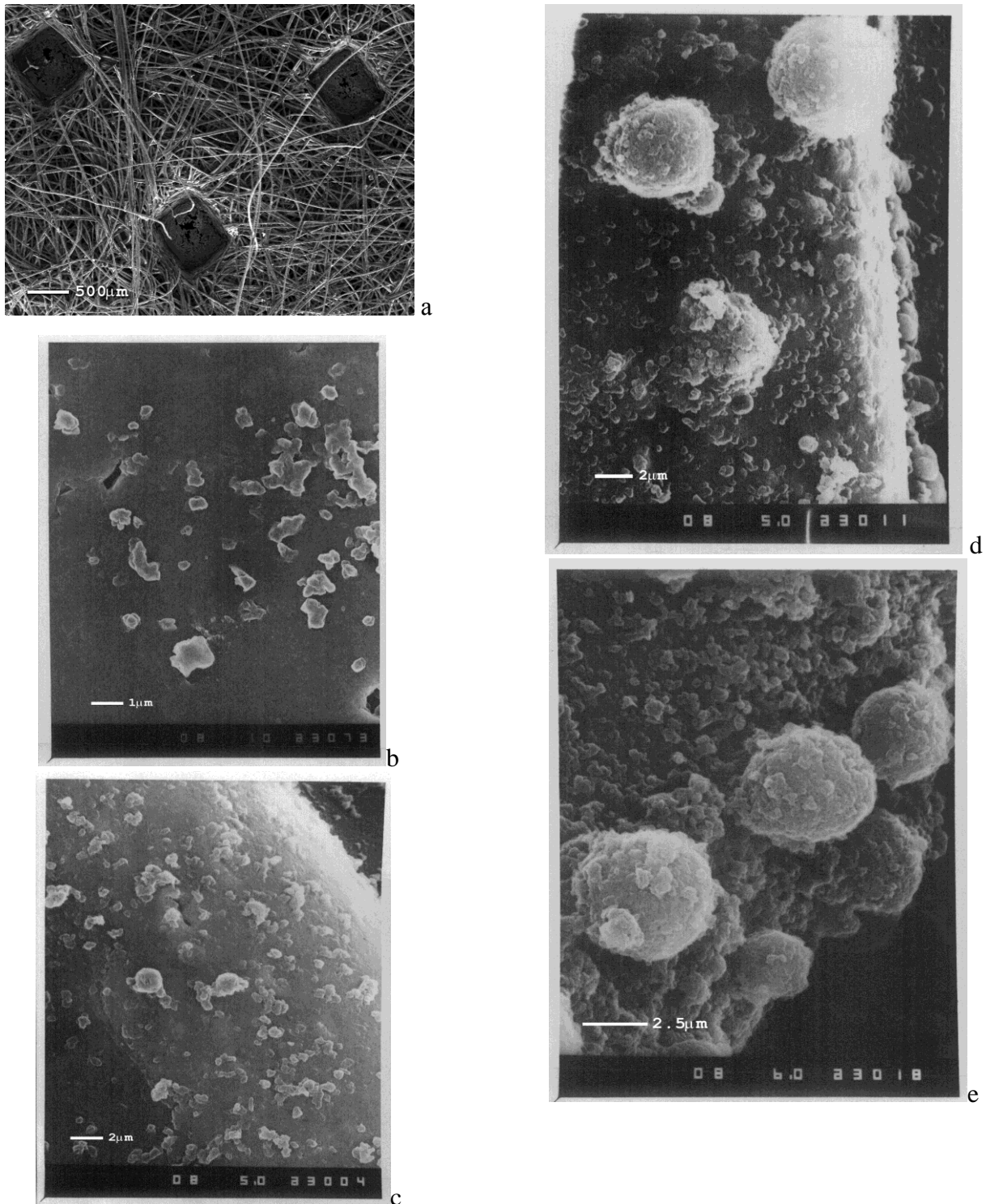


Fig.1. SEM micrographs of the PETF substrate surface (a), after electroless deposition of cobalt-diamond composite coating on the fibrous of the substrate in electrolytes containing different concentrations (b- 1 g/L; c - 3 g/L; d - 7 g/L; e - 10 g/L) of diamond particles with sizes 0,03-0,5 μm on the bottom rhomboid zones (Fig. 1a) of the substrate. As a consequence of sedimentation and convection effects, the number of the particles on the bottom of the pressed sections for all the studied sizes and concentrations of the studied particles was considerably greater (and sufficient from technological point of view) than the number of co-deposited on fibrous zones of the substrate. For this reason in Fig. 1, as well as in the next figures, the illustrative photographs of the concave sections are not given here.

Part of the results from analogous investigations, carried out with diamond particles of sizes 3 -7 μm and 7 - 10 μm , are shown in Table 2 and in Fig. 2.

It is seen from the table that in this case upon increasing the concentration of the diamond particles in the working electrolyte, the thickness of the deposited composite coating is growing up. Thereupon the conditional thickness of the coatings is higher than that, obtained in the case of the composite coatings, in which particles of sizes 0,03 – 0,5 μm are included (Table1). At the same time aiming at obtaining a desired number of particles, included in cobalt matrix, the particles on the fibers sections, it is necessary to increase the concentration of the diamond powder in the working electrolyte in the interval 5 – 10 g/L (Fig. 2b and 2d). When the size of the particles is 7 – 10 μm , the effect of decreasing the number of co-deposited diamond particles with the growth in their size is better expressed (Fig 2c, 2d). It is obviously connected both with the higher rate of sedimentation of the larger dispersed particles, as well as with the fact that having such size of the particles at several times smaller thickness of the layer of the cobalt matrix, their direct addition and incorporation inside the cobalt matrix becomes already impossible. It becomes quite clear from Fig. 2d that these large particles are sticking out above the formed Co matrix and their connection with it is accomplished by means of co-bonding of the cobalt coating being formed simultaneously on the PETF substrate and on the diamond particles. In this connection it can be also noted that in the case of particle sizes 3 -7 μm the number of spheroid agglomerates being formed is still substantial (Fig. 2b), while at sizes 7 – 10 μm their number is abruptly decreased – the cobalt matrix comprises practically only separate diamond particles (Fig. 2d). At the next increase in the diamond particle size (20-28 μm ; 38-45 μm ; 63-75 μm ; 80-100 μm), added in the form of diamond powder to the working electrolyte, the number of the co-deposited

particles continues to drop down. At sizes above 80 μm the deposited composite coating are already unable to answer the requirements for number of included particles, necessary for the production of composite layers, which are applicable to the manufacturing of polishing and finishing instruments/disks. For this range of sizes, the diamond particles are included in the cobalt matrix mainly in the pressed sections of the PETF (Fig. 3a), as well as in the zones, in which the fibers of PETF are overlapped and/or form sections advantageous for attachment to the growing cobalt matrix (Fig. 3b). In this case also the inclusion of the diamond particles is accomplished by means of binding bridges (Fig.3c), which are leading to the effect of “co-bonding” (Fig. 3d) as a consequence of the simultaneous deposition of the metallic cobalt both on the PETF and on the diamond particles.

The comparative Table 3 lists the averaged values of the thickness and the mass of the cobalt composite coatings (prepared under the same conditions – concentration of the particles in the solution – 5 g/L and time interval of deposition – 30 min), depending on the size of the diamond particles added to the working solution, respectively incorporated into the cobalt matrix.

It is seen from the above given results that upon increasing of the particle size from 0.03 to 10 μm both the average thickness of the composite Co-P-D coatings and the mass of the incorporated composite are growing up. Within a range of particle sizes 14 to 28 μm it is observed that the thickness (respectively the mass) of the deposited composite layers is decreasing. This is connected with the significantly lower number of particles of the separate particles, the average weight of the coating is diminishing.

Table 2. Dependence of the thickness of the chemically deposited composite Co-P-D coatings on PETF substrate on the concentration (1 - 5 g/L) of the diamond particles dispersed in the working solution at particle sizes 3 – 7 μm and 7 – 10 μm . Time interval of deposition 30 min.

Size of the diamond particles, μm	Concentration of the diamond particles, g/L	Thickness of the composite coating, μm
3-7	1	1,07
3-7	3	2,10
3-7	5	2,00
7-10	1	0,70
7-10	3	2,90
7-10	5	3,10

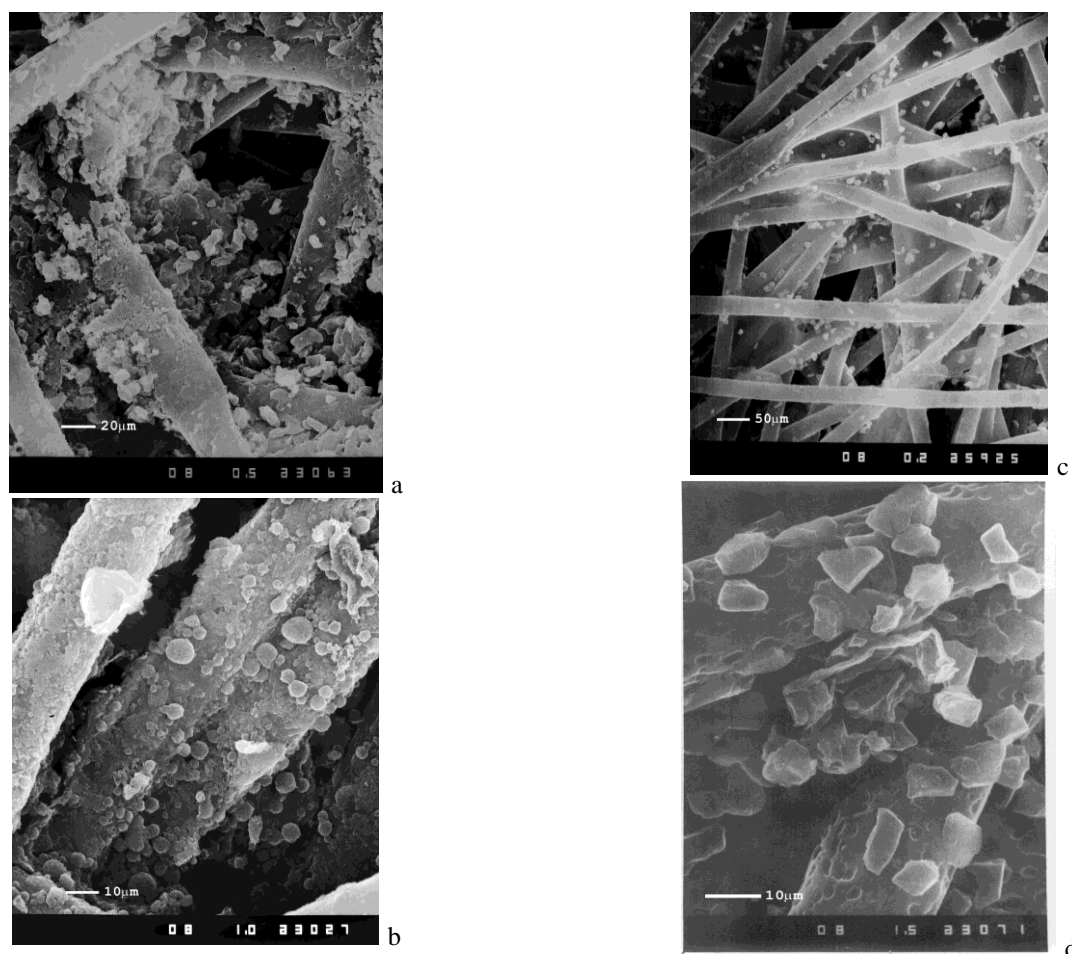


Fig.2. SEM micrographs of the cobalt-diamond composite coating on the fibrous of the substrate in electrolytes containing different concentrations - a- 1 g/L and b – 5 g/L - of diamond particles with sizes 3-7 μm , and - c- 1 g/L and d – 10 g/L - of diamond particles with sizes 7-10 μm .

included in a unit of volume of the composite coating (as a result of the increased rate of sedimentation of the particles but also as a result of considerable misbalance of the ratio “thickness of the incorporating metal matrix/size of the co-deposited particles”) and in spite of the larger mass.

In the case of sizes of the co-deposited diamond particles within the interval 38-75 μm , the mass of the considerably greater diamond particles is obviously compensating the smaller number of included particles, as a consequence of which the

measured average thickness and mass of the composite coatings is again increased. At particle size above 80 μm , however, the number of the co-deposited diamond particles is decreased even more drastically, and therefore the thickness (respectively the mass) of the deposited Co-P-D coating become much lower. The composite layers, obtained at such sizes of the diamond particles, are practically inapplicable for the production of polishing PETF disks.

Table 3. Average value of the thickness and of the mass of cobalt composite coatings depending on the size of the diamond grains used as dispersed phase.

Size of the diamond particles, μm	Thickness of the coating, μm	Mass of the coating, g
0,05- 0,5	0,74	0,0117
3 - 7	2,0	0,0317
7 - 10	3,1	0,0490
14 - 20	2,4	0,0379
20 - 28	2,50	0,0395
38 - 45	3,35	0,0540
63 - 75	5,49	0,0857
80 -100	1,0	0,0158

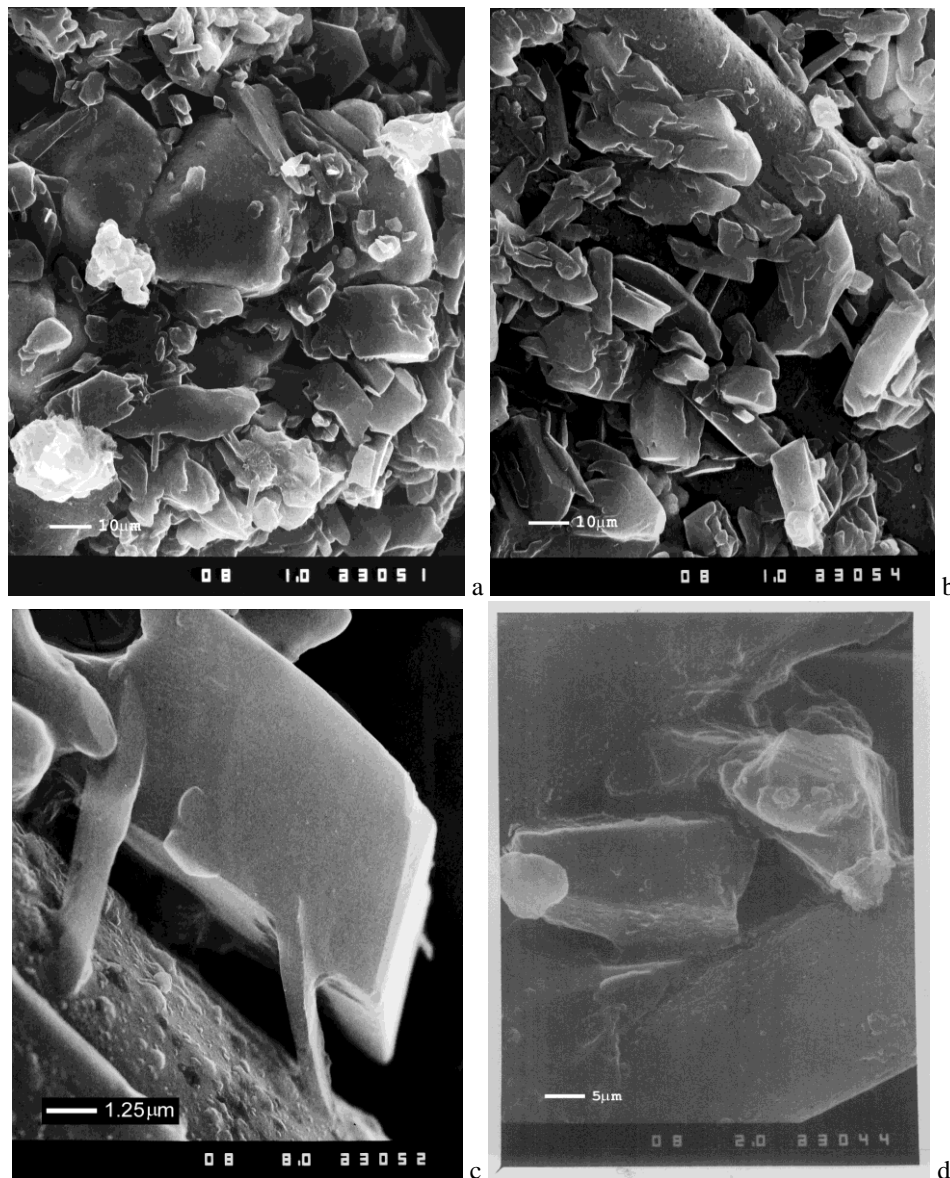


Fig.3. SEM micrographs of the cobalt-diamond composite coating at the bottom of the rhomboidal press-hole (a) and at the fibrous (b-d) of the PETF substrate obtained in electrolyte containing 10 g/L diamond particles with sizes 20-28 μm .

3.2 Characterization of the polishing effect of the composite layers, containing diamond particles of various sizes.

In this cycle of experimental runs the influence of the size of the co-deposited inside the cobalt matrix diamond particles was studied with respect to the polishing effect of the deposited on the flexible PETF substrate composite Co-P-D coating during the processing of different rocky materials – limestone and two kinds of marble. The studies were carried out at various loading/pressure and rate of rotation of the polishing PETF/Co-P-D disc. We estimated the polishing effect based on the changes in the surface roughness (R_a and R_z) of the

studied samples. The obtained results are represented in Table 4.

The samples for the testing were cut out in the form of cylindrical cores of diameter 20 mm and length of 20-30 mm from rocky materials, the deposits of which are located in Mezdra quarry – west part of Balkan mountains (for the limestone); in Ilinden stone-pit – south part of Pirin mountain (for “Ilinden” marble) and in Chernomorets stone-pit – nord-east part of Strandzha mountain (for “Strandzha” marble). Each one of the samples, after its being cut out of the rock, was subjected consecutively to preliminary (rough) polishing with commercially available discs Bulcat-100, IDT-800 and IDT-1800, with the aim to achieve a certain

degree of roughness, requiring thereafter finer polishing and finishing using the PETF discs, developed by us. This treatment was carried out in the following order of using the discs: PETF/Co-P-D_{63-70µm} → PETF/Co-P-D_{40-28µm} → PETF/Co-P-D_{28-20µm} → PETF/Co-P-D_{3-5µm} → PETF/Co-P-D_{0,05-0,5µm}. The obtained results have been summarized in Table 4.

The data in Table 4 show that after the preliminary rough polishing of the samples of limestone they were characterized by a coefficient of roughness $R_z=12$ and $R_a - 1,94$. In the next cycles I-IV of processing with the discs, which contain diamond particles of size 63-70 µm, the achieved coefficients were $R_z=7,44-4,95$ µm and $R_a - 1,70-0,61$ µm; upon using the discs, which contain diamond particles of size 40-28 µm; respectively - $R_z = 4,35-3,58$ µm and $R_a = 0,58-0,47$; $R_z = 3,54-3,50$ µm and $R_a = 0,45-0,37$ µm with the discs, containing diamond particles of size 28-20 µm; $R_z = 3,40-3,26$ µm and $R_a = 0,44-0,34$ µm with the disks containing diamond particles of size 3-5 µm; $R_z = 3,10-3,00$ µm and $R_a = 0,32-0,31$ µm with discs, containing diamond particles of size 0.05 – 0.5 µm.

Table 4. Measured values of R_a and R_z on the consecutively treated with polishing discs (PETF/Co-P-D_{70-0,05µm}) samples (Limestone "Mezdra", Marble "Ilinden" and Marble "Strandzha" of dimensions Φ -20 mm and L-25 mm), obtained at pressure on the polishing disc 0.35 kN/cm² and rate of rotation of the disc 1000 rpm. Number of cycles of polishing for each disc – 4. Duration of one cycle – 2 min.

Size of the diamond particles [µm], included in PETF/Co-P-D polishing disc; No of the cycle	Limestone "Mezdra"		Marble "Ilinden"		Marble "Strandzha"	
	R_z , µm (value before polishing 12,00)	R_a , µm (value before polishing 1,94)	R_z , µm (value before polishing 10,82)	R_a , µm (value before polishing 1,84)	R_z , µm (value before polishing 11,54)	R_a , µm (value before polishing 2,10)
63/70						
I	7,44	1,70	6,98	1,03	7,19	1,35
II	7,02	1,51	5,86	0,73	6,01	0,92
III	5,70	0,74	5,08	0,72	4,92	0,71
IV	4,95	0,61	4,23	0,64	4,68	0,69
40/28						
I	4,35	0,58	3,91	0,81	4,43	0,53
II	3,92	0,55	3,74	0,51	4,10	0,43
III	3,66	0,47	3,62	0,50	3,66	0,38
IV	3,58	0,47	3,56	0,45	3,48	0,37
28/20						
I	3,54	0,45	3,74	0,51	3,62	0,37
II	3,50	0,46	3,34	0,50	3,48	0,37
III	3,50	0,35	3,11	0,43	3,42	0,36
IV	3,50	0,37	2,98	0,42	3,23	0,35
3/5						
I	3,40	0,44	3,10	0,39	3,43	0,37
II	3,36	0,44	2,82	0,33	3,29	0,35
III	3,36	0,36	2,80	0,34	3,10	0,31
IV	3,26	0,34	2,54	0,35	2,96	0,31
0,05/0,5						
I	3,10	0,32	2,88	0,40	3,10	0,30
II	3,00	0,33	2,80	0,35	2,84	0,29
III	3,00	0,31	2,50	0,34	2,74	0,29
IV	3,00	0,31	2,32	0,35	2,65	0,29

The surface treatment with the same discs, in analogous order and the same duration, of the marble samples "Ilinden", for which after their preliminary rough polishing the following coefficients of roughness were achieved $R_z=10,82$ and $R_a - 1,84$, leading later to their values of $R_z = 6,98$ µm and $R_a = 1,03$ µm up to $R_z = 2,32$ µm and $R_a = 0,35$ µm. In the case of marble "Strandzha" samples, for which after their preliminary rough polishing the following coefficients of roughness were achieved $R_z=11,54$ µm and $R_a - 2,10$ µm, this treatment enables achieving values of R_z and R_a respectively 7,19 µm and 1,35 µm until the final values were obtained 2,65 µm and 0,29 µm (Table 4).

The final values of the coefficients R_z and R_a for the three kinds of materials, represented in Table 4, were compared with the values, measured for them on samples, taken after analogous treatment in the case of serial production/treatment with polishing discs, which are commercially available products, imported from foreign companies. The results from this comparison are illustrated in Table 5.

Table 5. Measured final values of R_a and R_z on samples of “Limestone”, Marble “Ilinden” and Marble “Strandzha”, treated consecutively using the polishing discs, made by us (PETF/Co-P-D_{70-0,05μm}) and on samples of the same materials, taken after analogous treatment using commercially available serially production discs.

Type of the treated material	R_z , μm, obtained using the discs made by us	R_a , μm, obtained using our discs	R_z , μm, obtained using commercial discs	R_a , μm, obtained using commercial discs
Limestone	3,00	0,31	5,90	0,97
Marble “Ilinden”	2,32	0,35	1,32	0,19
Marble “Strandzha”	2,65	0,29	2,76	0,37

It is seen from the results represented in Table 5 that the polishing effect when using the discs, prepared by chemical deposition under laboratory conditions, is comparable to the effect, obtained with the imported discs, generally accepted for industrial practice. It is even slightly better in the case of limestone and marble “Strandzha”, while in the case of samples of “Ilinden” marble there is insignificant advantage in favor of the imported discs.

In the next cycle of studies the weight losses of the composite layers will be evaluated also on non-treated mineral materials samples and on this basis their tribological behavior will be characterized, respectively the “productivity” of the polishing discs PETF/Co-P-D. There follows, on the basis of the obtained results, to carry out on a larger scale some semi-industrial testing experiments, aiming at the optimization of the procedure of chemical deposition of Co-P-D composite layers, respectively to achieve the polishing effect on larger scale.

CONCLUSIONS

It follows from the above presented results that upon increasing the concentration of the diamond micro-particles in the working electrolyte, used for the chemical deposition of Co-P-D composite layers on a flexible support of polyethylene terephthalate, quantitative and qualitative changes are being observed in their structure and layer thickness. Thereupon it has been ascertained that the process of chemical deposition of cobalt is occurring simultaneously both on the PETF substrate, as well as on the diamond particles. As a result of this the incorporation of the particles is accomplished through joining of the fronts of the growing layers of cobalt on the surface of both phases – PETF and diamond. This mechanism of incorporation of the diamond particles determines their regular distribution/inclusion in the cobalt matrix up to sizes of 3-5 μm, which are juxtaposable with the thickness of the cobalt coating/matrix, being formed upon the PETF substrate. Upon increasing the size of the diamond particles, the number of the particles included in the

cobalt matrix becomes lower as a result of their lower resistance to sedimentation (i.e. smaller number in the volume of the working electrolyte) and the longer time intervals needed for their binding (i.e. co-binding) via the growing cobalt layers on both phases. In this aspect with the aim to co-deposit the desired number of diamond particles in the composite layer, it becomes necessary to increase their concentration in the electrolyte when their size is increased – from 3 - 5 g/L for particles with a size up to 5 μm, further at 5 – 15 g/L for particles of size 7-10 μm. The positive effect achieved upon increasing their concentration, however, is valid only up to size 63-70 μm. At larger sizes of the diamond particles, their deposition number in the cobalt matrix does not satisfy the requirements for the formation of a composite layer, applicable in the production of polishing discs.

The preliminary testing of the polishing effect of discs PETF/Co-P-D, prepared under laboratory conditions upon limestone samples and two kinds of marble showed that values were reached for the coefficients R_z and R_a , which completely answer the requirements of the industrial practice for finishing surface treatment of such materials.

Acknowledgement: This work is supported by the Bulgarian National Science Fund under Project ID 02/102/07.2009 (Contract DID 02/28.12.2009).

REFERENCES

1. K.M. Gorbunova, A.A. Nikiforova, G.A. Sadakov, V.P. Moiseev, M.I. Ivanov, Physico-chemical basis of the chemical deposition of cobalt coatings (in Russian), Nauka Publ.H., Moscow (1974).
2. M. Shalkauskas, A. Vashkjalis, Chemical metallization of plastics (in Russian), Khimia Publ.H., Leningrad (1985).
3. E. Rudnik, K. Kokoszka, J. Lapsa, *Surface & Coating Technol.*, **202**, 2584 (2008).
4. J. Tang, S. Zhou, Y. Xie, *Plating & Metal Finishing*, **84**, 241 (1998).
5. E.W. Brooman, *J. Appl. Surface Finishing*, **1**, 38 (2006).
6. E.W. Brooman, *Galvanotechnology*, **104**, 58 (2006).
7. M.L. Klingenberg, E.W. Brooman, *Plating & Metal Finishing*, 92, 42 (2005).

8. D. Stoychev, N. Koteva, M. Stoycheva, E. Velkova, D. Dobrev, *Materiale Plastice*, **49**, 20 (2012).
9. N. Feldstein, T. Lancsek, J. Electrochem. Soc., **131**, 3026 (1984).
10. M. Seal, *Industrial Diamond Review*, p.104, March (1968).
11. R. Komanduri, *Proceeding, Diamond Partner in Productivity*, p.174 (1974)].

БЕЗЕЛЕКТРОЛИЗНО ОТЛАГАНЕ НА КОМПОЗИТНИ СЛОЕВЕ ОТ КОБАЛТ, ФОРСФОР И ДИАМАНТИ И ТЕХНИТЕ ПОЛИРАЩИ СВОЙСТВА

Д. Стойчев^{1*}, Е. Добрева², Н. Разказов², М. Стойчева³, Н. Котева²

¹ *Институт по физикохимия "Акад. Р. Каишев", Българска академия на науките, София 1113*

² *Технически университет, София*

³ *Институт по електрохимия и енергийни системи "Акад. Ев. Будевски", Българска академия на науките, София 1113*

Постъпила на 15 април; коригирана на 8 август, 2013

(Резюме)

Изследвани са възможностите за безелектролизно отлагане на композитни слоеве от кобалт, фосфор и диаманти върху носител от полиетилен терефталат (PETF). Използвани са електролити от алкални хлориди и NaH_2PO_2 като редутор. Изследвани са ефектите на концентрацията (1-25 g/L) и размера на частиците (0,03 – 100 μm) на дисперсната фаза (диамантов прах), добавени към работния електролит, с оглед определянето на количеството диамантени частици, сътаени с кобалтовата матрица, както и средната дебелина на формираните композитни слоеве. В резултат на това са определени размерите и концентрациите на диамантените частици, при които се формират композитни слоеве за Co-P-D-покрития при гъвкави полиращи дискове върху PETF.

Предварителните изпитания за полиращия ефект на PETF/Co-P-D-дисковете са извършени в лабораторни условия (при диамантени частици с размери: 63-75; 38-45; 20-28; 14-20; 7-10; 3-7 и 0.03-0,5 μm) върху образци от варовик и върху два вида мраморни образци. Получените резултати за коефициентите R_z и R_a са изцяло в съгласие с изискванията за повърхностно полиране на тези материали.

Optimal design and planning of biodiesel supply chain considering crop rotation model

Part 1. Mathematical model formulation of the problem

B. Ivanov^{1*}, B. Dimitrova¹, D. Dobrudzhaliev²

¹*Institute of Chemical Engineering-BAS, Acad. G. Bonchev Str., Bl. 103, Sofia 1113-Bulgaria*

E-mail: bivanov@bas.bg, systmeng@bas.bg

²*Prof. Dr. Assen Zlatarov University, Bourgas 8000-Bulgaria*

Received June 3, 2013; revised January 3, 2014

This paper addresses the optimal design and location facility of biodiesel supply chains (BSC) under economic and environmental criteria. The economical aspect scale is assessed by the total annualized cost. The environmental objective is evaluated by the total GHG (Green House Gases) emissions for a whole life cycle. A mathematical model that can be used to design the supply chain (SC) and manage the logistics of a biodiesel is proposed. The model determines the number, size and location of biorefineries needed to produce biodiesel using the available biomass. Mixed-integer linear programming model is proposed that takes into account infrastructure compatibility, demand distribution, as well as the size and location of biorefineries needed to produce biodiesel using the available biomass and carbon tax. An important feature of the model proposed is the account requirement of crop rotation important from agronomic perspective. In second part of this study Bulgaria is examined as the testing ground of the model.

KEYWORDS: Biodiesel supply chains, Energy crops, Production cost, Carbon tax, Crop rotation, MILP

INTRODUCTION

Aimed at mitigating emissions, diversifying the energy supply and reducing dependence on imported fossil fuels, the European Union (EU) has set ambitious targets for a transition to renewable energy. The integrated energy and climate change policy adopted in 2008 defines general targets of 20% greenhouse gas reduction, 20% reduced energy use through increased energy efficiency and a 20% share of renewable energy by 2020 [8].

Among the available alternative energy sources that would help to respond to such challenges, biomass crops have many advantages over conventional energy and over some other renewable energy sources (e.g. wind, photovoltaic, etc.). In particular, this is due to reduced dependence on short-term weather changes, promotion of regional economic structures and provision of alternative sources of employment in rural areas.

Because biomass can replace fossil fuels in the transport sector increased production and use of bioenergy is promoted as a key to faster the

targets. In order to explicitly stimulate a shift to renewables in transportation, the European Commission has, in addition to the overall 20% renewable energy target, set a mandatory target of 10% renewable energy in transport by 2020 [8], with a transitional target of 5.75% for 2010 [4].

A number of policy instruments that directly or indirectly affect the production and use of biofuels are today in place in the EU. Targeted biofuel policies such as exemption from or reduction of transport fuel taxes, quotas and blend obligations effect directly the competitiveness and market shares of biofuels.

This paper presents development and use of a optimisation model suitable for extensive analysis of biofuel production scenarios aimed at determination and investigation of advantageous locations for biodiesel production. The main focus is on assessing how different parameters affect biodiesel production regarding costs, plant locations, production volumes and the possibility of reducing global fossil emissions. Key parameters to be studied are economic policy instruments affecting biodiesel production, such as targeted biofuel support and the cost for emitting, energy prices, feedstock costs and availability, and capital

* To whom all correspondence should be sent:
E-mail: : bivanov@bas.bg.

costs. The above mentioned 5.75% share of biofuels for meeting the 2010 target is used as a starting point, with the analysis focusing on boundary conditions that affect the possibility of meeting this goal.

The paper is focused on the creation of conditions for stable operation of BSC by providing a stable supply of feedstock. According to recent research in agricultural activities [21,17,12,18] crop rotation is the basis for sustainable yields. The model proposed includes conditions for crop rotation as realistic ones.

LITERATURE REVIEW

The papers most relevant to the problem addressed in this work are on the optimal design and operations of the process (SC). A general review of this area is presented by *Shah (2005)* [5] and *Papageorgiou (2009)* [9]. Some recent work specifically focused on BSCs is reviewed below.

Zamboni et al. (2009) [10] presented a MILP model for the strategic design of biofuel supply networks. The model takes into account the issues affecting a general BSC simultaneously, such as agricultural practice, biomass supplier allocation, production site locations and capacity assignment, logistics distribution, and transport system optimisation.

Eksioglu et al. (2009) [11] proposed a MILP model for the design and operations of a biomass to biorefinery SC. The model determines the optimal number, size, and location of biorefineries and feedstock collection as well as the amount of biomass to be processed and shipped and biomass inventory levels through a multi period formulation.

Recently, *Kim et al. (2011)* [13] proposed a MILP model for the optimal design of biorefinery supply chains. The model aims to maximize the overall profit and takes into account different types of biomass, conversion technologies, and several feedstock and plant locations.

Another recent contribution in this area is the work by *Aksoy et al. (2011)* [14]. The authors investigated four biorefinery technologies for feedstock allocation, optimal facility location, economic feasibility, and their economic impacts in Alabama, through a MILP based facility location model that minimizes the total transportation cost and takes into account county-level information.

Akgul et al. (2011) [15] presented recently a MILP model based on the one proposed by *Zaboni et al. (2009)* [10] for the optimal design of a bioethanol SC with the objective of minimizing the total SC cost. Their model aims to optimize the locations and scales of the bioethanol production

plants, biomass and bioethanol flows between regions, and the number of transport units required for the transfer of these products between regions as well as for local delivery. The model also determines the optimal bioethanol production and biomass cultivation rates.

You and Wang (2011) [16] recently addressed the life cycle optimisation of biomass-to-liquids SC under the economic and environmental criteria. Their work shows that distributed biomass processing followed by centralized upgrading of intermediates may lead to economically viable and environmentally sustainable biofuels supply chains.

Akgul, O., et al. (2012) [18] presents a multi-objective, static modeling framework for the optimisation of hybrid first/second generation biofuel supply chains. Using the proposed modelling framework, different aspects are analysed including the potential GHG savings, the impact of carbon tax on the economic and environmental performance of a BSC, the trade-off between the economic and environmental objectives and the maximum bioethanol throughput that can be achieved at different cap levels on the total SC cost. The trade-off between the conflicting objectives is analysed by solving the proposed multi-objective model using the ϵ -constraint method.

Bioenergy represent a sustainable solution for energy generation. To achieve these goals, one must create the conditions for sustainable yields of energy crops. According to research conducted in recent years [17,18] this can be achieved by rotation of crops. Further studies [12,21] in this direction indicate that crop rotation has a beneficial impact on reducing greenhouse gases generated in the cultivation of energy crops.

Crop rotation has been long recognized as a system that can reduce soil erosion, improve soil structure, enhance permeability, increase the soil microbial activity, enhance soil water storage capacity, and increase soil organic matter [1,2]. Moreover, crop rotation can reduce the use of external inputs through internal nutrient recycling, maintenance of the long-term productivity of the land, avoidance of accumulation of pests associated with monoculture, and consequently increase crop yields [2]. The aforementioned beneficial effects on soil physical, chemical and biological properties can further be improved by combining crop rotations with cover crops and reduced or no tillage practices

An additional novelty of our work is that the proposed model takes into account most of the major characteristics of the BSC and is integrated

with LCA. From the literature available in this area it can be concluded that the models of BSC biofuels used account for the basic characteristics but no works go into details to account for the rational use of the available land. The models do not include also agronomic conditions for long-term cultivation of crops for biofuel production such as the ones the needed for different bio cultures.

AIM

The main objective this study is to propose an optimisation model that could predict determine location and size of biodiesel production plants, given the locations of feedstock and energy demand. The model comes to minimise the costs of the complete BSC of the studied system, including biomass harvest, biomass transportation, and conversion to biodiesel, transportation and delivery of biodiesel. Economic performances can be evaluated in terms of Net Present Value (NPV). Environmental impact based on GHG emissions reduction, calculated through LCA, is important in order to ensure proper or wise criteria approach to sustainability and to allow distinguishing the differences between various feedstock as. Fossil emissions must be also considered, by including costs for emissions, such as tax or tradable emission permits. Sustainability of the work of BSC can be ensured through sustainable supply of bio-resources, that in turn is guaranteed by annual rotation areas for different bio cultures.

PROBLEM STATEMENT

The problem addressed in this work can be stated formally, as follows. A set of biofuel crops that can be converted to biodiesel. These include agricultural e.g. sunflower, energy crops and a.s.o. A planning horizon of one year government regulations including manufacturing, construction and carbon tax is considered. A BSC network superstructure, including a set of harvesting sites and a set of demand zones, as well as the potential locations of a number of collection facilities and bio refineries is descanted. Feed stocks can be shipped to the bio refineries directly.

Unit cost and emission data for biofuel crops production and harvesting are also given. For each potential collection facility, we the fixed and variable cost of facility construction are given. For each potential biorefinery given the cost of production for different levels and capacity.

For each demand zone, the biofuel demand is given, and the environmental burden associated with biofuel distribution in local region is known.

For each transportation link, the transportation capacity (in both volume and weight), available transportation modes, unit transportation cost of each mode, transportation distance, and emissions of each transportation type are known.

General formulation of the problem

Finally, the overall problem can be summarized as:

Given are:

- ◆ potential locations of biofuel demand centers and their biofuel demand,
- ◆ demand for liquid fuels (diesel) for each of the demand centers for fuel,
- ◆ the minimum required ratio between classical proportions fuels and biofuels for blending,
- ◆ biomass feedstock types and their geographical availability,
- ◆ unit biomass cultivation cost for each feedstock type,
- ◆ unit production cost of biodiesel based on the technology and feedstock type,
- ◆ transport logistics characteristics (cost, modes),
- ◆ capital investment cost for the biodiesel production facilities,
- ◆ specific GHG emission factors of the biodiesel life cycle stages,
- ◆ carbon tax,
- ◆ government incentives for biodiesel production and use.

MATHEMATICAL FORMULATION OF THE PROBLEM

Given the scenario, the role of the optimization model is to identify what combination of options is most efficient to supply the facility. A very important efficiency measure is to minimize the facility supply cost taken as a present value.

The problem for optimal location of biodiesel (B100) production plants and efficient use of the available land is formulated as a mixed integer linear programming (MILP) model with the notations, given in **Tables 1-3**.

As noted in item 3, the assessment work of BSC production and distribution of biodiesel (B100) will be carried out based on two criteria, namely, economically and environmentally. The optimal solution would be a compromise between these two criteria.

Table 1. Input Sets used in the model

Sets	Description of Sets/Indices
I	Set of biomass types indexed by i ;
L	Set of transport modes for biomass indexed by l ;
B	Set of transport modes for biodiesel is a subset of L ($B \subset L$) indexed by b ;
S	Set of life cycle stages of a BSC indexed by s ;
P	Set of plant size intervals indexed by p ;
G	Set of regions of the territorial division indexed by g
F	Set of candidate regions for biodiesel plants established, which is a subset of G indexed by f ;
C	Set of biodiesel customer zones, which is a subset of G ($C \subset G$) indexed by c .

Table 2 Input variables for the problem

Symbol	Description
$EFBC_{ig}$	Emission factor for cultivation of biomass type i in region g , $kg CO_2 - eq / ton biomass$
$EFBP_i$	Emission factor for biodiesel(B100) production from biomass type $i \in I$, $kg CO_2 - eq / ton biofuel$
$EFTRA_{il}$	Emission factor for transport of biomass per unit of type $i \in I$ with transport type l , $kg CO_2 - eq / ton km$
$EFTRB_b$	Emission factor for transport of biodiesel(B100) with transport type $b \in B$, $kg CO_2 - eq / ton km$
$EFTM_l$	Transportation emission factor of for mode $l \in L$, $kg CO_2 - eq / ton km$
$GHGB$	GHG emission from BSC, $kg CO_2 - eq / ton$
ADD_{gfl}	Actual delivery distance between regions producing biomass and regions producing biodiesel(B100) via model l , km
ADF_{fcb}	Actual delivery distance between regions producing biodiesel(B100) and demand regions $c \in C$ via model $b \in B$, km
γ_i	Biomass to biodiesel(B100) conversion factor for biomass type $i \in I$ to biodiesel(B100) $(ton biodiesel) / (ton biomass)$, Dimensionless
C_{CO_2}	Carbon tax per unit of carbon emitted from the operation of the BSC, $\$/kg CO_2 - eq$
YO_c	Years demands of petroleum diesel in the customer zones, $ton / year$
ENO	Energy equivalent unit of petroleum diesel , GJ / ton
ENB	Energy equivalent unit of biodiesel(B100), GJ / ton
PO	Price of petroleum diesel, $\$/ton$
PB	Price of biodiesel(B100) produced from biomass, $\$/ton$
$Cost_p$	Capital cost of plant size $p \in P$ for biodiesel(B100) production, $\$$
$PB_p^{MIN/MAX}$	Minimum/Maximum annual capacity of the plant of size $p \in P$ for biodiesel(B100) production, $ton / year$
ZB_c^{MAX}	The annual demand for biodiesel(B100) in the customer zones, $ton / year$
QI_{ig}^{MAX}	Maximum flow rate of biomass $i \in I$ from region $g \in G$, ton / d
QB_f^{MAX}	Maximum flow rate of biodiesel(B100) from region $f \in F$, ton / d
$PBI_{ig}^{MIN/MAX}$	Minimum/Maximum biomass of type $i \in I$ which can be produced in the region $g \in G$ per year, $ton / year$

α_g	Operating period for the region $g \in G$ in a year, $d / year$
αf_f	Operating period for biodiesel(B100) production plants in region $f \in F$ in a year, $d / year$
αc_c	Operating period for the region $c \in C$ in a year, $d / year$
INS_f	The government incentive includes construction incentive and volumetric, $\$/ton$
ECB	Emissions emitted during the combustion of CO_2 unit biodiesel(B100), $kg CO_2 - eq / ton biofuel$
ECG	Emissions emitted during the combustion of CO_2 unit petroleum diesel, $kg CO_2 - eq / ton biofuel$
CCF	Capital charge factor, $year^{-1}$
UCC_{ig}	Unit biomass cultivation cost of biomass type i in region g , $\$/ton$
UPC_{ipf}	Unit biodiesel production cost from biomass type i at a biorefinery of scale p installed in region $f \in F$, $\$/ton$
UTC_{igfl}	Unit transport cost of biomass $i \in I$ via mode $l \in L$ between region $g \in G$ and biorefinery $f \in F$, $\$/ton$
UTB_{fcb}	Unit transport cost of biodiesel(B100) via mode $b \in B$ between biorefinery $f \in F$ and demand regions $c \in C$, $\$/ton$
A_g^S	Set-aside area available in region $g \in G$, ha
A_g^{Food}	Set-aside area available in region for food $g \in G$, ha
$TEIF^{MAX}$	Maximum permissible values for the total environmental impact of biodiesel(B100) network of SC and fossil fuel in the regions, $kg CO_2 - eq / d$
TDC^{MAX}	Maximum total cost of a biodiesel(B100) SC network, $\$$
β_{ig}	The yield per hectare of type $i \in I$ biomass in the region $g \in G$, ton / ha
QB_i^{Food}	The total amount of bio-resources of type $i \in I$, which must be provided for all regions $g \in G$ for food security, ton
QT_{il}^{MIN}	Optimal capacity of transport $l \in L$ used for transportation of biomass $i \in I$, ton
QTB_b^{MIN}	Optimal capacity of transport $b \in B$ used for transportation of biodiesel(B100), ton
K_c^{mix}	Proportion of biodiesel(B100) and petroleum-diesel subject of mixing for each of the customer zones. The ratio of biodiesel(B100) and petroleum diesel is more energy equivalent between the two fuels. $K_c^{mix} = \frac{ENB \sum_{c \in C} QEB_c}{ENO \sum_{c \in C} YO_c}$, Dimensionless
M_f^{const}	Factor to the change of the base price, depending on the region $f \in F$ where the plant is installed $M_f^{const} \geq 1$, Dimensionless

Table 3. Decision variables for the problem

Positive Continuous Variables	
PBB_{ig}	Production rate of biomass $i \in I$ in region $g \in G$, ton / d
QI_{igfl}	Flow rate of biomass $i \in I$ via mode $l \in L$ from region $g \in G$ to $f \in F$, ton / d
QB_{ipfcb}	Flow rate of biodiesel produced from biomass $i \in I$ via mode $b \in B$ from region $f \in F$ to $c \in C$ at a plant of scale p located in region $f \in F$, ton / d

QEO_c	Quantity of petroleum diesel to be supplied to meet the energy needs of the region $c \in C$, ton/ year
QEB_c	Quantity of biodiesel(B100) produced from biomass to be supplied to meet the energy needs of the region $c \in C$, ton/ year
A_{ig}	Land occupied by first generation crop i in region g , ha
A_{ig}^F	Land by crops $i \in I$ needed for food security of the population in the region $g \in G$, ha
Binary variables	
X_{igfl}	0-1 binary variable, equal to 1 if a biomass type $i \in I$ is transported from region $g \in G$ to $f \in F$ using transport $l \in L$ and 0 otherwise
Y_{fcb}	0-1 binary variable, equal to 1 if a biodiesel is transported from region $f \in F$ to $c \in C$ using transport $b \in B$ and 0 otherwise
Z_{pf}	0-1 binary variable, equal to 1 if a plant size $p \in P$ is installed in $f \in F$ and 0 otherwise

Basic relationships

Total environmental impact at work on BSC. The environmental impact of the BSC is measured in terms of total GHG emissions ($kgCO_2 - eq$) stemming from SC activities and the total emissions are converted to carbon credits by multiplying them with the carbon price (per $kgCO_2 - eq$) in the market.

The three main greenhouse gases emitted from the SC are methane (CH_4), nitrous oxide (N_2O) and carbon dioxide (CO_2). The values of these parameters for life cycle inventory are obtained. Life Cycle Inventory after grouping the GHGs (i.e., CO_2 , CH_4 and N_2O) into a single indicator in terms of carbon dioxide equivalent emissions ($CO_2 - eq/ year$) by using their respective global warming potentials (GWPs) based on the recommendation of Intergovernmental Panel on Climate Change (IPCC, 2007) [6] for the 100 year time horizon is, as follows: 1 for CO_2 , 25 for CH_4 , and 298 for N_2O .

The environmental objective is to minimize the total annual GHG emission (te) resulting from the operations of the biodiesel supply chains. The formulation of this objective is based on the field-to wheel life cycle analysis that takes into account the following life cycle stages of biomass-based liquid transportation fuels:

- ◆ biomass cultivation, growth, and acquisition,
- ◆ biomass transportation from source locations to processing facilities,

- ◆ emissions from biodiesel production,
- ◆ transportation of biodiesel(B100) facilities to the demand zones,
- ◆ emissions from biodiesel(B100) usage in vehicle operations.

Ecological assessment criteria will represent the total environmental impact at work on BSC through the resulting greenhouse gas emissions. These emissions are equal to the sum of the impact that each of the stages of the life cycle has on the environment and are expressed by the dependence:

$$TEI = EL_{BC} + EL_{BP} + EL_{TR} + EB_{CAR} \quad (1)$$

where

TEI Total environmental impact at work on BSC ($kg CO_2 - eq d^{-1}$);

EL_{BC}
 EL_{BP}
 EL_{TR} } Environmental impact of life cycle stages ($kg CO_2 - eq d^{-1}$);

EB_{CAR} Emissions from biodiesel usage in vehicle operations ($kg CO_2 - eq d^{-1}$);

The environmental impact is evaluated at every stage $s \in S$ of the life cycle as:

- A. Growing biomass (including drying, storage);
- B. Production of biodiesel(B100);
- C. Transportation resources (biomass and biodiesel(B100)).

Greenhouse gases to grow biomass is:

$$EL_{BC} = \sum_{i \in I} \sum_{g \in G} \left(EFBC_{ig} \frac{\beta_{ig} A_{ig}}{\alpha_g} \right) \quad (2)$$

where, EL_{BC} denotes the total environmental impact of biomass cultivation, which in general represents the production rate of resource $i \in I$ in region $g \in G$, refers in this equation to the cultivation rate of biomass $i \in I$ in that region.

Total emissions from biodiesel(B100) production is determined by the equation:

$$EL_{BP} = \sum_{g \in G} \sum_{i \in I} \sum_{f \in F} \sum_{l \in L} (EFBP_{ifl} \gamma_i QI_{igfl}) \quad (3)$$

where EL_{BP} is total environmental impact of biodiesel(B100) production through given technology ($kg CO_2 - eq d^{-1}$).

The environmental impact of transportation is calculated by:

$$EL_{TR} = \sum_{i \in I} \sum_{g \in G} \sum_{f \in F} \sum_{l \in L} (EFTRA_{it} ADD_{gfl} QI_{igfl}) + \sum_{i \in I} \sum_{p \in P} \sum_{f \in F} \sum_{c \in C} \sum_{b \in B} (EFTRB_b ADF_{fcb} QB_{ipfcb}) \quad (4)$$

where EL_{TR} is environmental impact of transportation of resources ($kg CO_2 - eq d^{-1}$);

Emissions from biodiesel (B100) usage in vehicle operations:

$$EB_{CAR} = \sum_{i \in I} \sum_{p \in P} \sum_{f \in F} \sum_{c \in C} \sum_{b \in B} (ECB QB_{ipfcb}) \quad (5)$$

where EB_{CAR} is emissions from biodiesel(B100) usage in vehicle operations ($kg CO_2 - eq d^{-1}$).

Total environmental impact of the used fuels (biodiesel(B100) and diesel) to provide the energy balance of the region. Environmental goal is to reduce the annual equivalent of greenhouse gases, resulting from the operations of SC of biodiesel(B100) and diesel to meet the energy needs of the regions.

Annual equivalent of greenhouse gases of the used fuels is determined by the equation:

$$TEIF = TEI + EG_{CAR} \quad (6)$$

where

TEIF Total environmental impact of the used fuels (biodiesel (B100) and petroleum diesel) to provide the energy balance of the region ($kg CO_2 - eq d^{-1}$);

TEI Environmental impact at work on BSC ($kg CO_2 - eq d^{-1}$);

EG_{CAR} Emissions from petroleum diesel usage in vehicle operations ($kg CO_2 - eq d^{-1}$);

Emissions from petroleum diesel usage in vehicle to supplement the energy balance:

$$EG_{CAR} = \sum_{c \in C} \left(\frac{ECG QEO_c}{\alpha_c} \right) \quad (7)$$

Total cost of a BSC network. The annual operational cost includes the biomass feedstock acquisition cost, the local distribution cost of final fuel product, the production costs of final products, and the transportation costs of biomass, and final products. In the production cost, we consider both the fixed annual operating cost, which is given as a percentage of the corresponding total capital investment, and the net variable cost, which is proportional to the processing amount. In the transportation cost, both distance-fixed cost and distance-variable cost are considered. The economic criterion will be the cost of living expenses to include total investment cost of biodiesel(B100) production facilities and operation of the BSC for the operating period. This price is expressed through the dependence:

$$TDC = TIC + TPC + TTC + TTAXB - TL \quad (8)$$

where

TDC Total cost of a BSC network for year ($\$ year^{-1}$);

TIC Investment costs of production capacity of biodiesel(B100) relative to the operational period of redemption and up time of the plant per year ($\$ year^{-1}$);

TPC Production cost ($\$ year^{-1}$);

TTC Transportation cost ($\$ year^{-1}$);

TTAXB A carbon tax levied according to the total amount of CO_2 generated in the work of the whole BSC for year ($\$ year^{-1}$);

B. Ivanov et al: Optimal design and planning of biodiesel supply chain..... production and use ($\$ year^{-1}$).

a/ Total investment costs model:

The components **TIC** of (8) shall be determined under the following relationships:

$$TIC = CCF \sum_{f \in F} \sum_{p \in P} (Cost_{pf}^F Z_{pf}) \quad (9)$$

The refinery capital cost consists of fixed and variable capital cost. The fixed capital cost varies by the refinery locations. The variable capital cost

of biomass-to-biodiesel(B100) plants, is mainly influenced by the plant size, since the technology is considered mature.

Variable capital cost are scaled using the general relationship [20].

$$\frac{Cost_p}{Cost_{base}} = \left(\frac{Size_p}{Size_{base}} \right)^R,$$

where $Cost_p$ is variable capital cost and $Size_p$ represents the investment cost and plant capacity respectively for the new plant, $Cost_{base}$ indicates the known investment cost for a certain plant capacity $Size_{base}$, and R is the scaling factor usually between 0.6 and 0.8.

Capital cost of biorefinery for each region is determined by the equation:

$$Cost_{pf}^F = M_f^{cost} Cost_p, \forall p, f,$$

where M_f^{cost} is a correction factor in the price of bio-refineries in the region $f \in F$ according to its installed $M_f^{cost} \geq 1$.

b/ Total production cost model

$$TPC = \sum_{i \in I} \sum_{g \in G} (UCC_{ig} A_{ig} \beta_{ig}) + \sum_{i \in I} \sum_{p \in P} \sum_{f \in F} \left(\alpha_f UPC_{pf} \sum_{c \in C} \sum_{b \in B} QB_{ipfcb} \right), \quad (10)$$

c/ Total transportation cost model

$$TTC = \sum_{g \in G} \sum_{l \in L} \sum_{i \in I} \sum_{f \in F} (\alpha_g UTC_{igfl} QI_{igfl}) + TI \quad (11)$$

where,

$$\left. \begin{aligned} UTC_{igfl} &= IA_{il} + (IB_{il} ADD_{gfl}) \\ UTB_{fcb} &= OA_b + (OB_b ADF_{fcb}) \\ TI &= \sum_{i \in I} \sum_{p \in P} \sum_{f \in F} \sum_{b \in B} \sum_{c \in C} (\alpha_f UTB_{fcb} QB_{ipfcb}) \end{aligned} \right\},$$

IA_{il} and IB_{il} are fixed and variable cost for transportation biomass type $i \in I$ and (OA_b, OB_b) are fixed and variable cost for transportation biodiesel (B100).

The biomass transportation cost UTC_{igfl} is described by Börjesson and Gustavsson, 1996 [3]. They are composed of a fixed cost (IA_{il}, OA_b) and a variable cost (IB_{il}, OB_b) . Fixed costs include loading and unloading costs. They do not depend on the distance of transport. Variable costs include fuel cost, driver cost, maintenance cost etc. They are dependent on the distance of transport.

d/ Government incentives for biodiesel (B100) production cost model

Government incentives for biodiesel(B100) production and use is determined by the equation:

$$TL = \sum_{f \in F} \left(INS_f \sum_{g \in G} \left(\sum_{i \in I} (\gamma_i A_{ig} \beta_{ig}) \right) \right) \quad (12)$$

e/ A carbon tax levied cost model

A carbon tax levied is determined by the equation:

$$TTAXB = \left(\begin{matrix} YEL_{BC} + YEL_{BP} + \\ YEL_{TR} + FEB_{CAR} \end{matrix} \right) C_{CO_2} \quad (13)$$

where, YEL_{BC} is the total GHG emissions for biomass cultivation, YEL_{TR} is the environmental impact of transportation of resources within the network and YEL_{BP} is the environmental impact of biodiesel (B100) production a year working in the BSC and determined by the following equations:

$$YEL_{BC} = \sum_{i \in I} \sum_{g \in G} (EFBC_{ig} A_{ig} \beta_{ig}),$$

$$YEL_{BP} = \sum_{g \in G} \sum_{i \in I} \sum_{f \in F} \sum_{l \in L} (\alpha_g \gamma_i EFBP_{il} QI_{igfl}),$$

$$YEL_{TR} = \sum_{i \in I} \sum_{g \in G} \sum_{f \in F} \sum_{l \in L} (\alpha_g EFTRA_{il} ADD_{gfl} QI_{igfl}) +$$

$$\sum_{i \in I} \sum_{p \in P} \sum_{f \in F} \sum_{c \in C} \sum_{b \in B} (\alpha_f EFTRB_b ADF_{fcb} QB_{ipfcb})$$

$$FEB_{CAR} = \sum_{c \in C} (ECBQEB_c),$$

$$QEB_c = \sum_{i \in I} \sum_{p \in P} \sum_{f \in F} \sum_{b \in B} (\alpha_f QB_{ipfcb}).$$

Total cost of fuel used by the regions. The annual cost of providing the energy balance in the region includes the cost of diesel and the production and transportation cost in the stores for blending biodiesel (B100). In manufacturing costs, we consider both fixed annual operating costs, which is given as a percentage by the total amount of investment capital and net variable cost that is proportional to the amount of processing. In transport costs, distance fixed price and distance variable costs are considered. The economic criterion will be the total cost of year's base, including investment costs for biodiesel (B100) production and use of the BSC for the lifetime and cost of the used classic fuel supplement on the energy balance of the region. This price is given by the equation:

$$TBG = TDC + TG \quad (14)$$

where

TBG Total cost of fuel used (conventional and biofuels(B100)) to ensure region's energy balance (\$ year⁻¹);

TDC Total cost of a BSC network for year (\$ year⁻¹);

TG Total cost of petroleum diesel used from the regions (\$ year⁻¹);

The component **TG** of (14) shall be determined under the following relationships:

$$TG = PO \sum_{c \in C} QEO_c \quad (15)$$

5.6. Restrictions

Plants capacity limited by upper and lower bounds constrains. Plants capacity is limited by upper and lower bounds, as indicated by Eqs. (16), where the minimal production level in each region is obtained affecting the capacity installed.

$$PB_p^{MIN} Z_{pf} \leq \alpha_f \sum_{i \in I} \sum_{c \in C} \sum_{b \in B} QB_{ipfcb} \leq \quad (16)$$

$$PB_p^{MAX} Z_{pf}, \quad \forall p, f$$

Balance of biodiesel(B100) to be produced from biomass available in the regions.

$$\left. \begin{aligned} \sum_{c \in C} QEB_c &\leq \sum_{i \in I} \sum_{g \in G} (\gamma_i PB_{ig}^{MAX}) \\ \sum_{c \in C} QEB_c &\leq \sum_{i \in I} \sum_{g \in G} (\gamma_i \beta_{ig} A_g^S) \end{aligned} \right\}, \quad (17)$$

$$\begin{aligned} \sum_{i \in I} \sum_{g \in G} \sum_{l \in L} (\gamma_i \alpha_g QI_{igfl}) &= \\ \sum_{i \in I} \sum_{p \in P} \sum_{b \in B} \sum_{c \in C} (\alpha_f QB_{ipfcb}), \quad \forall f, \end{aligned} \quad (18)$$

Logical constraints.

A/ *Restriction guarantees that a given region g installed power plant with p for biodiesel(B100) production*

Constraint (19) determined that only one size of the plant can be installed in a given region:

$$\sum_{p \in P} Z_{pf} \leq 1, \quad \forall f \quad (19)$$

B/ *Limitation of assurance is provided that the biomass plant installed in a region g ∈ G of at least one different region g ∈ G*

$$\sum_{g \in G} \sum_{l \in L} X_{igfl} \geq \sum_{p \in P} Z_{pf}, \quad \forall i, f \quad (20)$$

C/ *Limit guarantee that each region g will provide only one plant of biomass type i ∈ I*

$$\sum_{f \in F} \sum_{l \in L} X_{igfl} \leq 1, \quad \forall i, g \quad (21)$$

D/ *Limitation of assurance is provided that at least one region g ∈ G produces biomass that is connected in a plant located in a region f ∈ F*

$$\sum_{c \in C} \sum_{b \in B} Y_{fcb} \geq \sum_{p \in P} Z_{pf}, \quad \forall f \quad (22)$$

$$\sum_{b \in B} Y_{fcb} \leq 1, \quad \forall f, c \quad (23)$$

$$\sum_{c \in C} \sum_{b \in B} Y_{fcb} \geq \sum_{g \in G} \sum_{l \in L} X_{igfl}, \quad \forall i, f \quad (24)$$

Transport links.

A/ *The quantity transported between different regions is limited by upper and lower bounds, as indicate by Eq. (25)*

$$\frac{PBI_{ig}^{MIN}}{\alpha_g} \leq \quad (25)$$

$$\sum_{f \in F, f \neq g} \sum_{l \in L} QI_{igfl} \leq \frac{(A_g^S - A_g^{Food}) \beta_{ig}}{2\alpha_g}, \quad \forall i, g$$

B/ *Restrictions on transportation of biomass are*

$$\begin{aligned} \sum_{l \in L} QI_{igfl} &\leq \\ 0.5(A_g^S - A_g^{Food}) \beta_{ig} \sum_{l \in L} X_{igfl}, \quad \forall i, g, f \end{aligned} \quad (26)$$

C/ *Limitation that ensures the admissibility of flow rate for biomass and biofuel*

Productivity of biomass in the region restriction

$$QI_{ig}^{MAX} X_{igfl} \geq QI_{igfl} \geq \quad (27)$$

$$QT_{il}^{MIN} X_{igfl}, \quad \forall i, g, f, l$$

Flow rate of biomass restricting

$$QB_f^{MAX} Y_{fcb} \geq \sum_{i \in I} \sum_{p \in P} QB_{ipfcl} \geq \quad (28)$$

$$QTB_b^{MIN} Y_{fcb}, \quad \forall f, c, b$$

Supply chain design constraints. These constraints are material balances among the different nodes in the SC. The following are constraints between different SC nodes:

A/ *Productivity of biomass in the region restriction*

$$PBB_{ig} \leq \frac{(A_g^S - A_g^{Food}) \beta_{ig}}{2}, \quad \forall i, g \quad (29)$$

Restriction for total environmental impact of all regions.

$$TEIF \leq TEIF^{MAX} \quad (30)$$

where $TEIF^{MAX}$ is maximum permissible values for the total environmental impact of biodiesel(B100) network of SC and fossil fuel in the regions ($kg CO_2 - eq d^{-1}$)

Mass balances between biodiesel(B100) plants and biomass regions. The connections between biodiesel (B100) plants and biomass regions are determined by the equation:

$$\sum_{l \in L} \sum_{g \in G} \sum_{i \in I} (\gamma_i QI_{igfl}) \leq \sum_{p \in P} (PB_p^{MAX} Z_{pf}), \forall f \quad (31)$$

Mass balances between biodiesel(B100) plants and biofuel customer zones.

$$\sum_{i \in I} \sum_{p \in P} \sum_{b \in B} \sum_{f \in F} (\alpha_f Q B_{ipfcb}) \leq ZB_c^{MAX}, \forall c \quad (32)$$

Land constraints.

A/ The constraints explained in this section mainly aim to avoid the negative impacts on food production to avoid competition with other sectors for biomass use and to maintain the sustainable use of land.

$$\sum_{g \in G} (\beta_{ig} A_{ig}) \geq \sum_{g \in G} (\alpha_g PBB_{ig}), \forall i \quad (33)$$

The land used for raw materials cultivation and for food security must not exceed the available land for each region:

$$\sum_{i \in I} (A_{ig} + A_{ig}^F) \leq (A_g^S - A_g^{Food}), \forall g, \quad (34)$$

B/ Limitation guaranteeing crop rotation

The crop rotation allows to ensure control of pests, improve soil fertility, maintenance of the long-term productivity of the land, and consequently increase the yields and profitability of the rotation. Other criteria to take in consideration when planning crop rotation with energy crops are the environmental and economic conditions in a given region. Moreover, the combination of crop rotation and fallowing is a common practice that is gaining momentum again due to environmental benefits and promoted reduction in the dependence on external inputs.

Crop rotation can be applied if the quantity of energy crops in a given year can be produced in the next one but in other areas of the region. This can be achieved if land A_{ig} and A_{ig}^F such that inequalities are implemented.

$$(A_{ig} + A_{ig}^F) 2.0 \leq (A_g^S - A_g^{Food}), \forall i, g \quad (35)$$

Energy restriction.

A/ Limitation ensuring that the overall energy balance in the region is provided

Limitation of enforceability of the energy balance:

$$EGD + EB \geq EO. \quad (36)$$

Energy equivalent diesel, which is necessary to meet the energy needs of the all customer zones where no use biodiesel(B100) is determined by the equation:

$$EO = ENO \sum_{c \in C} YO_c, \quad (36a)$$

where EO is annual requirement of energy (petroleum diesel) of all regions ($GJ year^{-1}$).

The energy equivalent of petroleum diesel that must be added, in order to balance the energy required for all customer zones is determined by the equation:

$$EGD = ENO \sum_{c \in C} QEO_c, \quad (36b)$$

where EGD is annual energy added to petroleum diesel fuel to balance the required energy for all regions ($GJ year^{-1}$).

The Energy equivalent of biodiesel (B100) received per year of work BSC is determined according to the dependence:

$$EB = ENB \sum_{c \in C} QEB_c, \quad (36c)$$

where EB is annual energy received from the extracted biofuel (biodiesel(B100)) of BSC for all customer zone ($GJ year^{-1}$).

B/ Limitation ensuring that the overall energy balance in each customer zones is provided

Limitation of enforceability of the energy balance for each region:

$$ENO QEO_c + ENB QEB_c \geq ENO YO_c, \forall c \quad (37)$$

C/ Limitation ensuring that each region will be provided in the desired proportions fuels

$$ENB \sum_{i \in I} \sum_{p \in P} \sum_{f \in F} \sum_{b \in B} (\alpha_f Q B_{ipfcb}) \geq \quad (38)$$

$$K_c^{mix} ENO QEO_c, \forall c$$

Total cost of a BSC network restriction

$$TDC^{MAX} \geq TDC \quad (39)$$

where TDC^{MAX} is maximum total cost of a BSC network (\$).

Optimisation problem formulation

The problem for the optimal design of a BSC is formulated as a mixed integer linear programming (MILP) model for different target functions as follows:

Minimizing GHG emissions. As discussed in section 4.5.2 environmental objective is to minimize the total annual CO_2 -equivalent greenhouse gas emissions resulting from the operations of the BSC and petroleum diesel used to provide the energy balance of the regions. The formulation of this objective is based on total GHG emissions in the SC and other fuels are estimated based on life cycle assessment (LCA) approach, where emissions are added every life stage.

The task of determining the optimal location of facilities in the regions and their parameters is formulated as follows:

$$\left\{ \begin{array}{l} \text{Find : } X[\text{Decision variables}]^T \\ \text{MINIMIZE } \{TEIF(X)\} \rightarrow (Eq.6) \\ \text{s.t. : } \{Eq.16 - Eq.39\} \end{array} \right\} \quad (40)$$

Minimizing annualized total cost. The economic objective is to minimize the annualized total cost, including the total annualized capital cost, the annual operation cost, the annual governmental incentive, and the cost for emitting CO_2 . The task of determining the optimal location of facilities in the regions and their parameters is formulated as (41)

The problem 5.7.1 and 5.7.2 is an ordinary Mixed Integer Linear Program (MILP) and can thus be solved using standard MILP techniques. The model was developed in the commercial software GAMS [7] using the solver CPLEX. The model will choose the less costly pathways from one set of biomass supply points to a specific plant and further to a set of biodiesel(B100) demand points. The final result of the optimisation problem would then be a set of plants together with their corresponding biomass and biodiesel(B100) demand points.

$$\left\{ \begin{array}{l} \text{Find : } X[\text{Decision variables}]^T \\ \text{MINIMIZE } \{TDC(X)\} \rightarrow (Eq.8) \\ \text{s.t. : } \{Eq.16 - Eq.39\} \end{array} \right\} \quad (41)$$

CONCLUSIONS

This study considers the optimal location of biodiesel (B100) production plants and the operation of the BSC. MILP approach for the design and planning of BSC under economic and environmental criteria is developed. The significance of the problem has been expressed by the extensive investigation of the biofuels sector that has been taking place during the recent years

for particular fatal replacement of the highly polluting conventional fuels. An optimisation model was developed that enables decision making for the infrastructure of biofuel conversion processing including processing locations, volumes, supply networks, and logistics of transportation from regions of biomass to bio-refineries and from bio-refineries to markets. The development of a flexible optimisation model may solve a wide spectrum of biofuel problems since this area is very rapidly changing (not only in economic but also in other dimensions, such as strategic decisions concerning the development and progress in the field, i.e. land dedicated to biofuels). All these can very easily be accommodated in the optimisation model, resulting in significant benefits from the optimisation approach. One of the valuable features of the approach is the capability to identify and solve a wide range of different scale and level problems, such as facility location, raw materials selection, conversion facilities location and design and operational characteristics. Furthermore, the model itself could be easily extended to accommodate strategic planning issues, such as investing or not on new production facilities, their siting, and the introduction of environmental and other externalities in the calculation of the total cost. The model that has been developed includes technical constraints as well as constraints originating from the limits in various problem parameters. The optimisation criteria of the model will in any case express the goals of the stakeholder and may include maximum economic efficiency, best environmental behavior, minimum land occupation, minimum total cost, etc. Another characteristic of the proposed approach is that the model is rather simple and can easily be solved with the available solvers, without needing to develop new codes or optimisation methods. This characteristic is important in the potential future exploitation of the approach and the development of a Decision Support System. However, the main critical point in the implementation of this approach is the difficulty to identify reliable quantitative information of the various problem parameters. Therefore, significant progress in other fields or research in order to provide reliable quantitative information and data (such as the agricultural materials properties, the conversion process efficiency, various costs, land availability etc.) are critical factors in the performance and the contribution of the present work.

A final conclusion is that in order to reach the EU targets particularly in Bulgaria a more improved interdisciplinary and improved cross-

sectoral in the energy system will be needed. Correspondingly the model developed and used within this study, may constitute a key component for this kind of studies. Consequently, it is which makes it highly relevant for policy makers.

REFERENCES

1. D.G. Bullock, *Crit Rev Plant Sci.* **11**, 309 (1992).
2. D.L. Karlen, G.E. Varvel, D.G. Bullock, R.M. Cruse, *Adv. Agron.* **53**, 1 (1994).
3. P. Börjesson, L. Gustavsson, *Energy*, **21**, 747 (1996).
4. <http://europa.eu.int>
5. N. Shah, *Computers & Chem.Eng.*, **29**, 1225 (2005).
6. www.ipcc.ch/publications_and_data
7. B.A. McCarl, A. Meeraus, P. Eijk, M. Bussieck, S. Dirkse, P. Steacy, McCarl Expanded GAMS user Guide, 2008.
8. *Dir 2009/28/EC*. Directive 2009/28/EC of the European Parliament and of the Council of 23 April 2009 *Directives 2001/77/EC and 2003/30/EC*.
9. L.G. Papageorgiou, *Computers & Chem.Eng.*, **32**, 1931 (2009).
10. A. Zamboni, N. Shah, F. Bezzo, *Energy & Fuels*, **23**, 5121 (2009).
11. S.D. Eksioğlu, A. Acharya, L.E. Leightley, S. Arora, *Computers & Ind. Eng.*, **57**, 1342 (2009).
12. A. Iriarte, J. Rieradevall, X. Gabarrell, *J. of Cleaner Prodcn*, **18**, 336 (2010).
13. J. Kim, M.J. Realf, J.H. Lee, C. Whittaker, L. Furtner, *Biomass & Bioenergy*, **35**, 853 (2011).
14. B. Aksoy, H. Cullinan, D. Webster, K. Gue, S. Sukumaran, M. Eden, N.S. Jrd, *Environ. Prog. Sustain. Energy*, **30**, 720 (2011).
15. O. Akgul, A. Zamboni, F. Bezzo, N. Shah, L.G. Papageorgiou, *Ind. Eng. Chem. Res.*, **50**, 4927 (2011).
16. You F, Wang B., *Ind. Eng. Chem. Res.*, **50**, 10102 (2011).
17. M.M. Moreno, C. Lacasta, R. Meco, C. Moreno, *Soil & Tillage Research*, **114**, 18 (2011).
18. W. Zegada-Lizarazu, A. Monti, *Biomass and Bioenergy*, **35**, 12, (2011).
19. O. Akgul, N. Shah, L.G. Papageorgiou, *Computers & Chem. Eng.*, **42**, 101 (2012).
20. E. Wetterlund, S. Leduc, E. Dotzauer, G. Kindermann, *Energy*, **41**, 462 (2012).
21. P.B. Parajuli, P. Jayakodya, G.F. Sassenrathb, Y. Ouyangc, J.W. Potea, *Agric. Water Management*, **119**, 32 (2013).

ОПТИМАЛНО ПРОЕКТИРАНЕ И ПЛАНИРАНЕ НА РЕСУРСНО ОСИГУРИТЕЛНАТА ВЕРИГА ЗА ПРОИЗВОДСТВО И ДОСТАВКИ НА БИОДИЗЕЛ С ОТЧИТАНЕ НА СЕИТБООБРАЩЕНИЕТО. ЧАСТ 1. ФОРМУЛИРОВКА НА МАТЕМАТИЧНИЯ МОДЕЛ

Б.Иванов^{1*}, Б.Димитрова¹, Д.Добруджалиев²

¹⁾ *Институт по инженерна химия, Българска академия на науките, 1113 София*

²⁾ *Университет "Проф. Асен Златаров", 8000 Бургас*

Постъпила на 3 юни, 2013 г.; коригирана на януари, 2014 г.

(Резюме)

Тази статия е насочена към решаване на проблема за оптимално проектиране на ресурсно осигурителни вериги за производство и разпространение на биодизел. Използвани са два критерия за оценка на оптималността на веригата (икономически и екологичен). Икономическият критерий оценява общите годишни разходите, докато екологичният критерий оценява общите емисии на парникови газове в атмосферата за целия жизнен цикъл на продукта. Предложен е математически модел, който може да се използва за проектиране на веригата за доставки (SC) и управление на логистиката на биодизел. Моделът определя броя, размера и местоположението на биорафинериите необходими за производството на биодизел като се използва наличната биомаса. Моделът се формулира в термините на смесеното линейно програмиране. Важна особеност на този модел е че отчита влиянието на ротацията на биокултурите.

Optimal design and planning of biodiesel supply chain considering crop rotation model. Part 2. Location of biodiesel production plants on the Bulgarian scale

B. Ivanov^{1*}, B. Dimitrova¹, D. Dobrudzhaliev²

¹*Institute of Chemical Engineering-BAS, Acad. G. Bonchev Str., Bl. 103, Sofia 1113-Bulgaria
E-mail: bivanov@bas.bg, systmeng@bas.bg*

²*Prof. Dr. Assen Zlatarov University Bourgas, Prof. Yakimov Str. 1, Bourgas 8000-Bulgaria
E-mail: dragodob@yahoo.com*

Received June 3, 2013; revised January 3, 2014

The mixed integer linear programming (MILP) model for optimal design and planning of Bulgarian biodiesel supply chain proposed in Part 1 is applied in this paper. The given feed stocks are sunflower and rapeseed. The country has been divided into twenty seven regions corresponding to its provinces, each one including existing crops, oil and biodiesel plants and potential ones associated to binary variables. The mathematical model has been implemented in GAMS providing a complete decision tool that can be applied to other regions or countries by adjusting the system-specific data.

Key words: Biodiesel Supply Chain, Crop rotation, Optimum design, Bulgarian scale

INTRODUCTION

Biodiesel production is been explored throughout the world to ensure economical and environmental profits in replacing increasing percentages of fossil-based diesel by biodiesel. In order to produce its own biodiesel, each country needs analyzing the economical and environmental feasibility of the complete production chain beginning from the availability of raw materials, their transformation in intermediate and final products and the storing and distribution of these one to internal and external markets. The result is a large network combining several stages with different options in each stage extending from alternative biomass crops to the location of product storage and conversion facilities, modes of transportation and flows of biomass and products between regions.

The EU Strategy for Biofuels (2006), the Biomass Action Plan (2005), and the adoption of the Biofuels Directive (2003/30/EC) by the EU Commission all sent a clear signal that the EU wishes to establish and support the bioenergy industry (Commission of the European Communities, 2003). Furthermore, biofuels have been required to account for at least 2% of the total

transportation fuels used in EU member states since 2005. That minimum level increases to 5.75% in 2010 and 10 percent by 2020.

Supply chain (SC) analysis and optimization have been extensively reported in the literature applied to different process industries. However, biofuel production is mainly focused on individual aspects of supply chain, as plantation or transportation and there are only a few papers that address the entire biofuel supply chain analysis and optimization. A mathematical model to solve the problem of designing and managing the BSC for biodiesel, based on the method of MILP of crop rotation was proposed in the first part of this work.. The aim of this study work is to apply the mathematical model for the case of biodiesel production at the real conditions in Bulgaria.

CASE STUDY: POTENTIAL BIODIESEL (B100) PRODUCTION IN BULGARIA

The model described in part 1 has been applied to a case study of biodiesel (B100) production in the Bulgaria. Two major types of biomass resources in this case, namely, sunflower and rapeseed for production of first generation biodiesel (B100) is used.

A demand scenario has been investigated based on Bulgarian domestic target for 2010 (5.75% by energy content) [16].

* To whom all correspondence should be sent:
E-mail: bivanov@bas.bg

Model input data

Territorial division of Bulgaria and data on energy consumption of petroleum diesel for transport. According to the Geodesy, Cartography and Cadastre Agency at the Ministry of Regional Development and Public Works, the 'Territorial balance of the Republic of Bulgaria as of 31.12.2000'. Bulgaria's total area is 111001.9 square kilometers out of which 63764.8 square kilometers is agricultural land. From this land, arable land and utilized agricultural area for 2011 is 3,162,526 hectares (STATISTICAL YEARBOOK 2011 [17]). The main energy crops for biodiesel (B100) that are suitable for growing in Bulgaria are sunflower and rapeseed. These crops are now grown mainly for ensuring food security. Areas that are employed for this purpose for 2011 are 734,314 ha for sunflower and 209,347 ha for industrial oleaginous crops including rapeseed. The agricultural land of Bulgaria is almost 0.7 ha per inhabitant, compared to 0.4 ha at the average of EU-25 [1]. Hence, producing the feedstock required internally becomes easier. In general, feedstock availability is directly related to land availability. Therefore, land availability is an important and critical factor affecting the feedstock amount.

Territorial division of Bulgaria. Bulgaria comprises 27 regions. In this case study, each region in Bulgaria is considered to be a feedstock production region, a potential location of a biorefinery facility and also a demand zone. In other words, the biofuel supply chain network consists of 27 areas for feedstock production, 27 potential biorefinery locations and 27 demand zones. In the case study, we assumed a 10-year service life of biorefineries and the fixed cost parameter for building refineries is amortized into annual cost to be consistent with other cost components.

For the purposes of this study, data on population, cultivated area, as well as the free cultivated area, which in principle can be used for the production of energy crops for biodiesel(B100) production are taken from STATISTICAL YEARBOOK-2011 [17]. The consumption of petroleum diesel fuel for transportation in the country is known and for the year 2011 it amounted to 1,711,000 tons. For the purposes of this study, the consumption of petroleum diesel fuel for each region is assumed to be approximately proportional to its size.

Data on energy consumption of petroleum diesel for transport by regions. **Table 1** presents the data on cultivated area distribution corresponding to

each region, population size and fixed consumption of petroleum diesel fuel for transport.

Petroleum Diesel.* The values for the used amount of petroleum diesel corresponding to for each region is assumed to be proportional to their population in the total set for Bulgaria in 2011, according to [17].

Feedstock supply chain components for biodiesel(B100) production in Bulgaria. Biodiesel (B100) is produced from vegetable oils that are derived from seeds or pulp of a range of oil-bearing crops. Such oil crops for Bulgarian climate are rapeseed and sunflower. Oil from sunflower was the first type used for biodiesel (B100) production. Today, in Bulgaria, sunflower is still the main feedstock for biodiesel (B100) production. It is grown throughout Bulgaria and sunflower seed crops are grown mainly in the warmer areas. Bulgaria has great potential and traditions for rapeseed and sunflower cultivation. Therefore the main energy crops that will be discussed in this study are, as follows: rapeseed and sunflower for biodiesel (B100) production.

Emission factor for cultivation of feedstock and yields. Greenhouse gas emissions in the agronomy phase for cultivation of sunflower and rapeseed lifecycle phases include soil preparation, seeding, tillage, fertilization, and finally harvest.

For different regions in Bulgaria aggregate Green House Gases (GHG) emissions for the entire life cycle of growing energy crops vary greatly depending on terrain, weather conditions, the technology of growing crops and imported fertilizer to increase yields. **Table 2** gives GHG emissions in the agronomy phase to rapeseed and sunflower for different regions of Bulgaria.

Data for the production cost of energy crops (sunflower and rapeseed) in Bulgaria. Unit biomass cultivation cost includes all costs associated with the cultivation of biomass, and a final selling price in the region (not including shipping costs for delivery to biorefineries). Cultivation cost is variable and is a function of the Regions, the technology of cultivation of the species on earth and bio cultures

The specific annual yield of each raw material per hectare of cultivated area differs significantly from one region to the other, depending on various parameters, such as climate, soil, etc. **Table 3** show the specific annual yield of each raw material (Sunflower and Rapeseed) for biodiesel(B100) production, respectively, as well as the available land in each region in Bulgaria

Table 1. The distribution of set-aside land per regions in Bulgaria

No	Name of regions Units	Population [17]	Current cultivated	Land reserved	Petroleum
			area [4]	for food [4]	Diesel*
			<i>ha</i>		<i>ton/ year</i>
1	Region-1 ⇒ Vidin	99481	90 853	45426	23230
2	Region-2 ⇒ Montana	145984	130 243	65121	34089
3	Region-3 ⇒ Vratsa	184662	175 528	87764	43120
4	Region-4 ⇒ Sofia	1542231	68 201	34100	360130
5	Region-5 ⇒ Pernik	131987	33 980	16990	30820
6	Region-6 ⇒ Kyustendil	134990	18 537	9268	31521
7	Region-7 ⇒ Blagoevgrad	322025	20 512	10256	75196
8	Region-8 ⇒ Pazardjik	273803	57 675	28837	63936
9	Region-9 ⇒ Lovech	139609	66 834	33417	32600
10	Region-10 ⇒ Pleven	266865	289 355	144677	62316
11	Region-11 ⇒ V.Tarnovo	256279	168 194	84097	59844
12	Region-12 ⇒ Gabrovo	121389	21 507	10753	28345
13	Region-13 ⇒ Plovdiv	680884	179 416	89708	158995
14	Region-14 ⇒ Smolyan	120456	5 095	2547	28128
15	Region-15 ⇒ Kardjali	152009	12 751	6375	35496
16	Region-16 ⇒ Haskovo	243955	116 657	58328	56966
17	Region-17 ⇒ St.Zagora	331135	173 465	86732	77324
18	Region-18 ⇒ Yambol	130056	149 686	74843	30369
19	Region-19 ⇒ Sliven	196712	85 021	42510	45934
20	Region-20 ⇒ Targovishte	119865	98 038	49019	27990
21	Region-21 ⇒ Rouse	233767	170 072	85036	54587
22	Region-22 ⇒ Razgrad	123600	140 215	70107	28862
23	Region-23 ⇒ Shumen	179668	140 824	70412	41954
24	Region-24 ⇒ Silistra	118433	146 411	73205	27655
25	Region-25 ⇒ Dobrich	188088	329 809	164904	43920
26	Region-26 ⇒ Varna	474344	160 786	80393	110765
27	Region-27 ⇒ Bourgas	414947	177 572	88786	96895
	Total	7327224	3162526	1613611	1711000

Table 2. Greenhouse gas emissions in the agronomy phase and potential yields from rapeseed and sunflower in the regions in Bulgaria

No	Regions [5] Units	GHG emissions in the agronomy phase		The yield cultivation in regions	
		<i>kg CO₂ – eq ton⁻¹ biomass</i>		<i>ton/ ha</i>	
		Sunflower	Rapeseed	Sunflower	Rapeseed
1	Region-1 ⇒ Vidin	1425	1120	2.8	2.2
2	Region-2 ⇒ Montana	1150	890	2.2	2.6
3	Region-3 ⇒ Vratsa	875	660	1.8	2.0
4	Region-4 ⇒ Sofia	1700	1350	1.5	1.8
5	Region-5 ⇒ Pernik	1425	1120	1.8	2.2
6	Region-6 ⇒ Kyustendil	1700	1350	1.5	1.8
7	Region-7 ⇒ Blagoevgrad	1700	1350	1.5	1.8
8	Region-8 ⇒ Pazardjik	1700	1350	2.2	3.2
9	Region-9 ⇒ Lovech	1425	1120	1.8	3.2
10	Region-10 ⇒ Pleven	600	430	2.8	3.5
11	Region-11 ⇒ V.Tarnovo	875	660	2.4	3.0
12	Region-12 ⇒ Gabrovo	1425	1120	1.8	2.2
13	Region-13 ⇒ Plovdiv	1425	1120	1.8	2.2
14	Region-14 ⇒ Smolyan	1700	1350	1.5	1.8

15	Region-15 ⇒ Kardjali	1700	1350	1.5	1.8
16	Region-16 ⇒ Haskovo	1425	1120	1.8	2.2
17	Region-17 ⇒ St.Zagora	875	660	2.8	3.0
18	Region-18 ⇒ Yambol	1150	890	2.6	2.6
19	Region-19 ⇒ Sliven	1150	890	2.4	2.6
20	Region-20 ⇒ Targovishte	1150	890	2.2	2.6
21	Region-21 ⇒ Rouse	600	430	3.3	3.5
22	Region-22 ⇒ Razgrad	875	660	2.8	3.0
23	Region-23 ⇒ Shumen	875	660	2.8	3.0
24	Region-24 ⇒ Silistra	875	660	2.8	3.0
25	Region-25 ⇒ Dobrich	600	430	3.4	3.5
26	Region-26 ⇒ Varna	875	660	2.8	3.0
27	Region-27 ⇒ Bourgas	1425	1120	2.8	2.8

Table 3. Unit biomass cultivation cost and maximum amount of biomass that can be produced in the regions of Bulgaria

No	Regions	Cultivation costs per unit biomass [7,10]		Maximum biomass production	
		\$ ton ⁻¹ biomass		ton year ⁻¹	
		Energy crops	Sunflower	Rapeseed	Sunflower
1	Region-1 ⇒ Vidin	213	236	47698	40884
2	Region-2 ⇒ Montana	198	233	68378	58609
3	Region-3 ⇒ Vratsa	195	230	92152	78987
4	Region-4 ⇒ Sofia	227	239	35806	30690
5	Region-5 ⇒ Pernik	213	236	17839	15291
6	Region-6 ⇒ Kyustendil	227	239	9732	8342
7	Region-7 ⇒ Blagoevgrad	227	239	10768	9230
8	Region-8 ⇒ Pazardjik	227	239	30279	25954
9	Region-9 ⇒ Lovech	213	236	35087	30075
10	Region-10 ⇒ Pleven	192	227	151911	130210
11	Region-11 ⇒ V.Tarnovo	195	230	88301	75687
12	Region-12 ⇒ Gabrovo	213	233	11291	9678
13	Region-13 ⇒ Plovdiv	213	236	94193	80737
14	Region-14 ⇒ Smolyan	227	239	2675	2293
15	Region-15 ⇒ Kardjali	227	239	6694	5738
16	Region-16 ⇒ Haskovo	213	236	61245	52496
17	Region-17 ⇒ St.Zagora	195	230	91069	78059
18	Region-18 ⇒ Yambol	198	233	78585	67358
19	Region-19 ⇒ Sliven	198	233	44636	38259
20	Region-20 ⇒ Targovishte	198	233	51469	44117
21	Region-21 ⇒ Rouse	192	227	89287	76532
22	Region-22 ⇒ Razgrad	195	230	73613	63097
23	Region-23 ⇒ Shumen	195	230	73932	63370
24	Region-24 ⇒ Silistra	195	230	76866	65885
25	Region-25 ⇒ Dobrich	192	227	173150	148414
26	Region-26 ⇒ Varna	195	230	84412	72353
27	Region-27 ⇒ Bourgas	213	236	93225	79907

Data for the biodiesel production cost Unit biodiesel production cost from Sunflower and Rapeseed for biorafinery of all scale p for each 27 regions is 214\$ /ton biodiesel

Required feedstock (rapeseed and sunflower) to ensure food security in Bulgaria

Table 4. Value of biological resources to ensure food security in Bulgaria

Type of Energy crops	Total bio-resources amount for food security	Cultivated area used for food security
Units	ton/year	ha
1 Sunflower	1321765	734314
2 Rapeseed	376824	209347

Table 4 presents data taken from the STATISTICAL YEARBOOK-2011 [17]. It describes cultivated area in 2011 for production of sunflower and rapeseed to ensure food security of Bulgaria. In this work, we assume the data as basis that ensures food security to all regions of Bulgaria.

Potential sites for locations of biorefineries in Bulgaria. Suitable potential biorefinery locations throughout the state have been chosen based on a set of criteria considering the accessibility to water and transportation infrastructures and zoning requirements. In total, all 27 regions were selected as candidate refinery locations and they are dispersed across the Bulgarian territory.

The technology of biodiesel (B100) production used in this study. It is based on the use of technology for producing biodiesel (B100) by esterification of vegetable oils. It is assumed that pure vegetable oil is obtained from rapeseed oil or sunflower by mechanical pressing or solvent extraction.

Production route is as follows: Oilseeds are crushed to produce oil, which after filtering is mixed with ethanol or methanol at about 50°C. The resultant esterification reaction produces fatty acid methyl esters (FAME), which are the basis for biodiesel (B100), and the co-product glycerine which can be used in soap manufacture. Approximately 100 kg of glycerine is produced per tone of biodiesel(B100). Another co-product is the residue "cake" from the crushing of the oilseeds, which is rich in protein and is used for animal feed.

This technology for extracting oil from oilseeds has remained the same for the last 10-15 years and is not likely to change significantly. Similarly, biodiesel(B100) production from the oil is a relatively simple process and so there is little potential for efficiency improvement. There is, however, ongoing research into the better utilisation of co-products.

Biomass to biodiesel(B100) conversion factor. Conversion efficiency of rapeseed and sunflower biodiesel(B100) ranges from 389l/ton to 454l/ton[15]. We use a conversion efficiency of

421l/ton(371kg/ton) for sunflower and 344l/ton(303kg/ton) for rapeseed, which is the average of the lowest and highest conversion efficiency found in literature.

Biorefinery costs and capacity. The refinery capital cost (as shown in Part 1) consists of fixed and variable capital cost. The fixed capital cost varies according to refinery locations while the variable capital cost of biomass-to-biodiesel plants, is mainly influenced by the plant size, since the technology is considered mature.

Variable capital cost is scaled using the general relationship [20]

$$\frac{Cost_p}{Cost_{base}} = \left(\frac{Size_p}{Size_{base}} \right)^R$$

where $Cost_p$ is variable capital cost and $Size_p$ represent the investment cost and plant capacity for the new plant, respectively

$Cost_{base} = 3.5 M\$$ for $Size_{base} = 8500 ton/year$ and then adopted base price is 412 \$/ton according to [15].

Capital cost of biorefinery for each region is determined by the equation:

$$Cost_{pf}^F = M_f^{cost} Cost_p, \quad \forall p \in P, \forall f \in F,$$

where $M_f^{cost} = 1$; in our case it is assumed that all 27 regions $f \in F$.

The refinery capacity at all candidate locations can be up to $PB_p^{MAX} = 100000 ton/year$. They are broken down into discrete order shown in Table 5.

Biodiesel(B100) production costs. Production costs per unit of biodiesel (B100) in a biorefinery installed in the region in case the Keys to Manufacturing Operating expenses such as: Chemicals and catalysts, gas, electricity, makeup water, wastewater treatment and disposal, administrative and operating costs and direct labor and Benefits. As discussed in [7], the average costs are 125 \$/ton for each region of biodiesel (B100), not including the costs of raw materials. In the case study, we assumed a 10 year service life of biorefineries, and the fixed cost parameter for building refineries is amortized into annual cost to be consistent with other cost components.

Data for biodiesel(B100) and petroleum diesel. The data necessary for the purposes of this study were taken from the literature [12,13,14] and the parameters of biodiesel and petroleum diesel are given in Table 6.

Table 5. Total specific investment cost of biodiesel(B100) production plants as a function of their size

Size of the biodiesel(B100) plant [9,10]	Variable capital cost of the biodiesel (B100) plant $Cost_p$	MIN capacity of the biodiesel (B100) plant PB_p^{MIN}	MAX capacity of the biodiesel (B100) plant PB_p^{MAX}	Average capital costs per unit of the biodiesel (B100)
Units	M\$	ton/ year		\$/ton
Size-1	3.5000	1000	8500	411.76
Size-2	4.3018	6000	11000	391.07
Size-3	6.3790	8000	18000	354.39
Size-4	8.0297	10000	24000	334.57
Size-5	10.8589	14000	35000	310.25
Size-6	14.4447	25000	50000	288.89
Size-7	18.4731	30000	68000	271.66
Size-8	19.7660	38000	74000	267.11
Size-9	22.0835	44000	85000	259.81
Size-10	25.1497	55000	100000	251.50

Table 6. Emission coefficient of fuel and energy equivalent

Type of fuel	Emission coefficient	Energy equivalent	Energy equivalent	Density (average)	Price of biofuel
Source	[13]		[12]		[14]
Unit	kgCO ₂ – eq/ton	GJ/ton	MWh/ton	ton/m ³	\$/ton
Petroleum Diesel	3623	42.80	11.880	0.840	1192.70
Biodiesel(B100)	1204	37.80	7.720	0.880	-

Biodiesel (B100) and petroleum diesel proportion, subject of mixing. In order to set national indicative targets for the consumption of biofuels in any country, the European Council's Directive 2003/30/EC (8-9 March 2007) has set out and adopted new targets for increasing the share of biofuels. In the above documents are targets for biofuels: indicative target of 5.75% for 2010; binding target for the share of biofuels of 10% for all states-states in the total consumption of petrol and petroleum diesel for transport in the EU by 2020 to be achieved in a cost effective manner. Production of biodiesel (B100) is used as a component in mixtures of petroleum diesel oil produced in a specific proportion [11]. Bulgaria in 2011 is to use biodiesel–petroleum diesel blend ratio of 6% biofuel (B100) and 94% petroleum diesel.

Data for cost transportation for biomass and biodiesel (B100). In order to estimate the costs of transportation of the feedstock and fuels in the entire supply chain system, a GIS-based

transportation network was introduced. This network contains local, rural, urban roads and major highways. The shortest distances between feedstock fields, refineries, and demand cities were calculated based on this network. Since only in-state production and delivery are considered, we assume that all transportations are performed by tractor, truck and rail for transporting biomass (Sunflower and Rapeseed) and for biodiesel (B100) transportation by truck and rail. Transportation costs include three components: loading/unloading cost, time dependent travel cost, and distance dependent travel cost. Time dependent cost includes labor and capital cost of trucks, while distance dependent cost includes fuel, insurance, maintenance, and permitting cost.

The biomass transportation cost is described by Leduc [6], and detailed in Table 7 and Table 8., for transportation by tractor, truck and train for biomass (sunflower and rapeseed) and biodiesel (B100).

Table 7. Unit transportation cost for each mode of transportation and type of the biomass

Energy crops	Fixed cost IA_{il}			Variable cost IB_{il}		
Unit	$\$ton^{-1}km^{-1}$					
Type of transport	Tractor	Truck	Train	Tractor	Truck	Train
Sunflower	2.486	9.28	19.63	0.14	0.209	0.029
Rapeseed	2.486	9.28	19.63	0.14	0.209	0.029

Table 8. Unit costs for each transportation mode and biodiesel (B100), rcf. [6].

		Fixed cost OA_b		Variable cost OB_b	
Unit		$\$ton^{-1}km^{-1}$			
Type of transport		Truck	Train	Truck	Train
1	Biodiesel(B100)	24.11	7.86	0.436	0.173

Data for emission factors for transportation biomass and biodiesel(B100). The simplest approach for estimating emissions from road and rail transport is based on the amounts of each fuel consumed. The approach for CO₂ is indicated in **Table 9**. This is based directly on the carbon content of the fuel. The default average emission factors used in this guideline are based on the average emission factors recommended in [2,3,8]. Data for Actual delivery distance between regions in Bulgaria.

A/ Actual delivery distance between regions.

Distances in kilometers between settlements in Bulgaria for the purposes of this study were taken from the National Transport Agency for each type of transport (tractor, truck, rail).

B/ Average local delivery distance. While the distance between a region with them will be the average distance of the feedstock being transported to the factory (assuming it is installed in a certain place of the region). To calculate the transportation distance required, the coordinates of each biomass site, namely the potential biorefinery location was identified. The data used in this paper is given at the level of a county, therefore the coordinates of the center point of a county are used to calculate the geographical distances between locations. In general, the average distance can be determined according to the relationship:

$$d_{gg} = \frac{\sum_{m \in M_g} (S_{gm} d_m^{Plant})}{\sum_{m \in M_g} S_{gm}} \quad (1)$$

where d_{gg} is the average distance that is expected for transport of the feedstock produced in region $g \in G$, $g = g'$ to the factory installed in place *Plant* (Figure 1) installed in the specified location of this region, S_{gm} is the area of sub-region $m \in M_g$, and d_m^{Plant} indicates the distance between landmark center sub region $m \in M_g$ and places in which it is permissible to install biorefinery.

Table 9. Emission factor of transportation for mode *l*

Type of transport [2,3,8]	Emission factor of transportation biomass	Emission factor of transportation biofuel
Unit	$kg CO_2-eq.km^{-1}ton^{-1}$	
1 Tractor	0.591	-
2 Truck	0.228	0.228
3 Van < 3.5 t	1.118	1.118
4 Truck, 16 t	0.304	0.304
5 Truck, 32 t	0.153	0.153
6 Train, freight	0.038	0.038

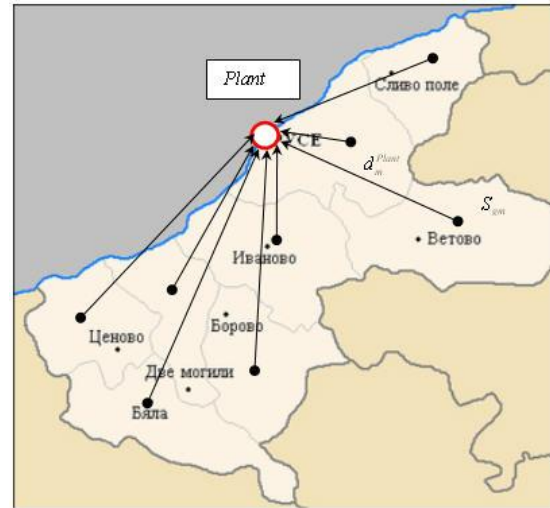


Fig. 1. Scheme to determine the average distance for the transport of feedstock in a region where the biorefinery is located in the same region

Table 10 presents the average distance for each of the 27 regions of Bulgaria. It is used in the method described above.

Computational results and analysis

In this section, we present the results from the case study described, identifying the optimal system design, the system costs, and feedstock supply strategies.

The mathematical model proposed in the first part of this work is used to solve the case study at the conditions at present in Bulgaria. The Software code is carried out by using GAMS intended for solving specific problems with real data.

Table 10. Average distance for each region determined by (1).

	Type of transport	Tractor	Truck	Rail
	Name of regions	<i>km</i>		
1.	Region-1 to Region-1	25	25	25
2.	Region-2 to Region-2	27	27	27
3.	Region-3 to Region-3	27	27	27
4.	Region-4 to Region-4	46	46	46
5.	Region-5 to Region-5	17	17	17
6.	Region-6 to Region-6	36	36	36
7.	Region-7 to Region-7	44	44	44
8.	Region-8 to Region-8	25	25	25
9.	Region-9 to Region-9	38	38	38
10.	Region-10 to Region-10	35	35	35
11.	Region-11 to Region-11	36	36	36
12.	Region-12 to Region-12	13	13	13
13.	Region-13 to Region-13	33	33	33
14.	Region-14 to Region-14	39	39	39
15.	Region-15 to Region-15	26	26	26
16.	Region-16 to Region-16	40	40	40
17.	Region-17 to Region-17	33	33	33
18.	Region-18 to Region-18	21	21	21
19.	Region-19 to Region-19	27	27	27
20.	Region-20 to Region-20	18	18	18
21.	Region-21 to Region-21	25	25	25
22.	Region-22 to Region-22	22	22	22
23.	Region-23 to Region-23	31	31	31
24.	Region-24 to Region-24	24	24	24
25.	Region-25 to Region-25	32	32	32
26.	Region-26 to Region-26	27	27	27
27.	Region-27 to Region-27	44	44	44

Table 11. Flow rate biomass from grow region to biodiesel (B100) plants

No	Name of regions	Criterion 1		Criterion 2	
		(a)-Min. GHG emission		(b)-Min. Cost BSC	
	Type of transport	TRACTOR	RAIL	TRACTOR	TRACTOR
	Type of energy crops	Sunflower	Rapeseed	Sunflower	Rapeseed
	Unit	<i>ton/day</i>			
1.	Region-10 to Region-9	1.00	405.76	257.94	1.00
2.	Region-10 to Region-10	1.00	517.42	590.43	1.00
3.	Region-21 to Region-21	1.00	77.98	0.00	0.00
4.	Region-25 to Region-26	1.00	384.55	193.25	1.00
5.	Region-25 to Region-25	0.00	0.00	90.83	1.00

Table 12. Distribution of greenhouse gases stages of the life cycle.

No.	Unit	Criterion 1		Criterion 2	
		(a)-min. GHG emission		(b)-min. cost BSC	
		<i>kg CO₂-eq/day</i>	%	<i>kg CO₂-eq/day</i>	%
1.	GHG emission to grow	598253.76	31.48	681193.39	33.58
2.	GHG emission for biodiesel prod.	809051.27	42.57	824122.93	40.63
3.	GHG emission of transportation	2914.98	0.15	32901.26	1.62
4.	GHG emission from biodiesel usage	490033.59	25.78	490033.59	24.16
5.	Total GHG emission for BSC	1900253.61	100	2028251.18	100

Biomass supply. The optimal biomass flows are given in **Table 11.** *Distribution of greenhouse gases stages of the life cycle of biodiesel (B100).* Table 12 shows the distribution of greenhouse gas life cycle

stages of biodiesel (B100) relative to day work BSC

Solutions obtained in the case of optimal synthesis conforming to criterion (a) minimum total

GHG emission in the work of BSC and minimum annualized total cost of BSC showed that GHG emission is only 6.31% lower in case (a) than in case (b), while the price of biodiesel (B100) is 37.63% higher in case (a) than in case (b). This is due to the increased capital and operational costs (a). Furthermore, the reduction of GHG emission at the expense of optimization of transport emissions in (a) and use as canola feedstock at (a) instead of sunflower seeds in (b).

The cost structure for biodiesel (B100) in the supply chain. The total system cost consists of four components: feedstock procurement cost, refinery capital cost, production cost, and transportation cost. The refinery capital cost contains fixed and variable capital costs. The transport cost includes both the delivery cost of feedstock to refineries and fuel distribution cost from refineries to cities.

Table 12 shows the breakdown of cost for one-year work BSC throughout the planning period, send the optimal solution for the design of the

supply chain for both evaluation criteria (economic and environmental).

The solutions obtained in the case of an optimal synthesis at criterion (a) Minimum Total GHG emission and Minimum Annualized Total Cost of BSC showed that emissions of greenhouse gases are only 6.31% lower in case (a) than case (b), while the price of biodiesel(B100) extracted is 37.63% higher in case (a) than in case (b). This is due to the increased capital costs of case (a) than of case (b). Furthermore, case greenhouse gas emissions are at the reduced expense of optimization of transport emissions in case (a) and use as feedstock rapeseed instead of sunflower seeds in case (b). The rapeseed shows less emissions and growing production in refineries compared sunflower, used in case (b). In genera, the cost of biodiesel produced is less competitive (i.e. in the range of \$0.76-\$1.05 per kg) over the year. Accounting for the largest portion in the total cost (between 67% and 70%) total biomass cost of in the range a BSC is identified as the major cost drive in the system.

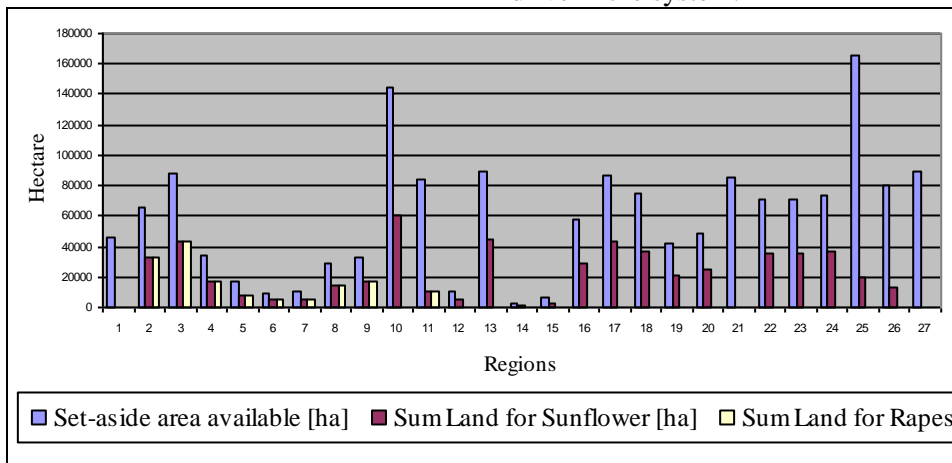


Fig. 2. Distribution of agricultural land by way of use for each of the regions in case (b)-Minimum Annualized Total Cost

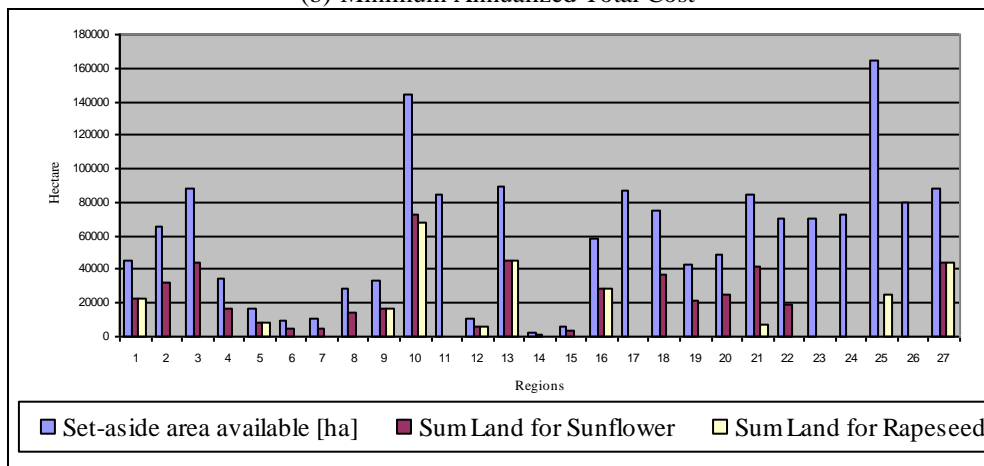


Fig. 3. Distribution of agricultural land by way of use for each of the regions in case (a)-Minimum Total GHG emission.

Table 13. Biodiesel (B100) cost structures in case (a)-Minimum Total GHG emission and (b) Minimum Annualized Total Cost.

No	Unit	Criterion 1 (a)-Min. GHG emission		Criterion 2 (b)-Min. Cost BSC	
		\$/ year	%	\$/ year	%
1.	Total inv. cost a BSC per year	6681600.00	6.00	4365600.00	5.40
2.	Total production cost of a BSC	13167282.72	11.83	13167282.72	16.29
3.	Total biomass cost of a BSC	78830839.68	70.88	54584871.32	67.55
4.	Total transport cost of a BSC	9713152.54	8.73	5066114.10	6.27
5.	Carbon tax levied per year	11876585.08	10.67	12676569.85	15.69
6.	Government incentives per year	9059090.51	8.14	9059090.51	11.21
7.	Total cost BSC	111210369.50	100	80801347.49	100
8.	Price of biodiesel(B100)	1055.745 \$/ ton		767.065 \$/ ton	

Distribution of land.

Table 14. Distribution of arable land for different purposes and in the regions in case (b) -Minimum Annualized Total Cost

No	Regions Type of energy crops Unit	Land for biodiesel (B100)		Land for food security		FREE Land	All Land
		Sunflower	Rapeseed	Sunflower	Rapeseed		
		<i>ha</i>					
1	Region-1 ⇒ Vidin	0	0	22713	0	22713	45426
2	Region-2 ⇒ Montana	0	0	32561	0	32561	65121
3	Region-3 ⇒ Vratsa	0	0	43882	0	43882	87764
4	Region-4 ⇒ Sofia	0	0	17050	0	17050	34100
5	Region-5 ⇒ Pernik	0	0	8495	0	8495	16990
6	Region-6 ⇒ Kyustendil	0	0	4634	0	4634	9268
7	Region-7 ⇒ Blagoevgrad	0	0	5128	0	5128	10256
8	Region-8 ⇒ Pazardjik	0	0	14419	0	14419	28837
9	Region-9 ⇒ Lovech	0	0	16708	11572	5136	33417
10	Region-10 ⇒ Pleven	52356	142	19982	72196	0	144677
11	Region-11 ⇒ V.Tarnovo	0	0	8491	0	75605	84097
12	Region-12 ⇒ Gabrovo	0	0	5377	0	5377	10753
13	Region-13 ⇒ Plovdiv	0	0	44854	44854	0	89708
14	Region-14 ⇒ Smolyan	0	0	1274	0	1274	2547
15	Region-15 ⇒ Kardjali	0	0	3188	0	3188	6375
16	Region-16 ⇒ Haskovo	0	0	29164	0	29164	58328
17	Region-7 ⇒ St.Zagora	0	0	0	0	86733	86732
18	Region-18 ⇒ Yambol	0	0	37421	0	37421	74843
19	Region-19 ⇒ Sliven	0	0	21255	0	21255	42510
2	Region 20 ⇒ Targovishte	0	0	24509	0	24509	49019
21	Region-21 ⇒ Rouse	0	0	42518	0	42518	85036
22	Region-22 ⇒ Razgrad	0	0	35054	0	35054	70107
23	Region-23 ⇒ Shtumen	0	0	0	0	70412	70412
24	Region-24 ⇒ Silistra	0	0	0	0	73206	73205
25	Region-25 ⇒ Dobrich	28591	71	0	0	136241	164904
26	Region-26 ⇒ Varna	0	0	40196	0	40196	80393
27	Region-27 ⇒ Bourgas	0	0	44393	0	44393	88786

Table 15. Distribution of arable land for different purposes

No	Unit	Criterion 1 (a)-Min. GHG emission		Criterion 2 (b)-Min. Cost BSC	
		<i>ha</i>			
1.	BIOFUELS Land	99264		81175	
2.	RESERVATION Land	1613611		1613611	
3.	FOOD Land	668093		657463	
4.	FREE Land	846267		874986	

Biodiesel (B100) production plant locations.

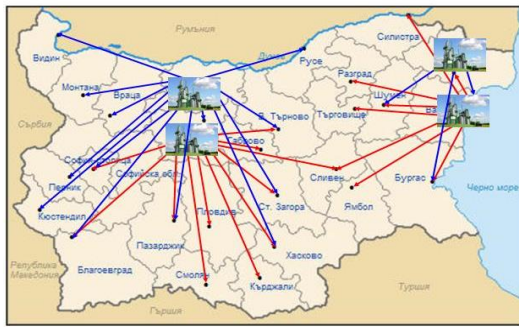


Fig. 4. Optimal BG biodiesel(B100) supply chain configuration in case (b)–Minimum Annualized Total Cost for BSC.

Table 16. Optimal biorefinery locations, Min/Max capacity and annual production of biodiesel (B100) for different criteria.

No	Biodiesel production plant locations	MIN Capacity of Plants	MAX Capacity of Plants	Annual Biodiesel produced in factories
		Units <i>ton/year</i>		
Minimum Total GHG emission				
1.	Region-9	30000	68000	30829
2.	Region-10	30000	68000	39286
3.	Region-21	1000	8500	6000
4.	Region-26	25000	50000	29222
Minimum Annualized Total Cost				
1.	Region-9	10000	24000	24000
2.	Region-10	30000	68000	54838
3.	Region-25	1000	8500	8500
4.	Region-26	8000	18000	18000



Fig. 5. Optimal BG biodiesel(B100) supply chain configuration in case (a)–Minimum GHG emission for BSC.

Table 16 presents the results of the optimization for optimal locations of biorefineries (their minimum and maximum capacity) and the annual quantities of biodiesel to be produced, in order to meet the needs of all regions.

Biodiesel (B100) distribution. The main mode preferred for biodiesel (B100) transportation from biodiesel (B100) plants to customer zones is rail with its lower unit cost and higher capacity compared to road transport.

Table 17. Flow rate of biodiesel from biodiesel plants to costumer zones in case: (a)–Min. Total GHG emission and (b)–Min. Annualized Total Cost.

Name of regions	Transportation biodiesel from rail	
	Unit	<i>ton/day</i>
Variant of criterion	Case (a)-	Case (b)
Region-9 to Region-4	0	5.00
Region-9 to Region-7	13.52	0
Region-9 to Region-8	15.75	8.31
Region-9 to Region-11	5.00	5.00
Region-9 to Region-12	6.98	6.98
Region-9 to Region-13	39.15	39.15
Region-9 to Region-14	6.93	6.93
Region-9 to Region-15	8.74	8.74
Region-9 to Region-16	8.21	5.00
Region-9 to Region-17	19.04	5.00
Region-9 to Region-19	0	5.89
Region-10 to Region-1	5.72	5.72
Region-10 to Region-2	8.39	8.39
Region-10 to Region-3	10.62	10.62
Region-10 to Region-4	88.69	83.69
Region-10 to Region-5	7.59	7.59
Region-10 to Region-6	7.76	7.76
Region-10 to Region-7	5.00	18.52
Region-10 to Region-8	0	7.44
Region-10 to Region-9	8.03	8.03
Region-10 to Region-10	15.35	15.35
Region-10 to Region-11	0	9.74
Region-10 to Region-16	0	9.03
Region-10 to Region-17	0	14.04
Region-10 to Region-21	0	13.44
Region-21 to Region-11	9.74	0
Region-21 to Region-16	5.82	0
Region-21 to Region-21	8.44	0
Region-25 to Region-23	0	5.00
Region-25 to Region-25	0	5.82
Region-25 to Region-26	0	18.18
Region-25 to Region-27	0	5.00
Region-26 to Region-18	7.48	7.48
Region-26 to Region-19	11.31	5.42
Region-26 to Region-20	6.89	6.89
Region-26 to Region-21	5.00	7.11
Region-26 to Region-22	7.11	5.33
Region-26 to Region-23	10.33	6.81
Region-26 to Region-24	6.81	0
Region-26 to Region-25	10.82	5.00
Region-26 to Region-26	27.28	9.09
Region-26 to Region-27	23.86	18.86

Table 17 is a daily flow of biodiesel (B100) from biodiesel (B100) plants to costumer zones as optimal form of rail transport.

Table 18. Summary of computational results in case: (a)-Minimum Total GHG emission and (b)-Minimum Cost BSC

		Units	Criterion 1 (a)-Min. GHG emission	Criterion 2 (b)-Min. Cost BSC
Min. Total GHG emission	(a)	$kg CO_2 - eq d^{-1}$	25347651.82	25475649.38
Min. Cost BSC	(b)	$\$/ year$	111210369.50	80801347.49
Min. GHG emissions BSC		$kg CO_2 - eq d^{-1}$	1900253.61	2028251.18
GHG emission for diesel		$kg CO_2 - eq y^{-1}$	23447398.21	23447398.21
GHG emission to grow biomass		$kg CO_2 - eq d^{-1}$	598253.76	681193.39
GHG emission for production:		$kg CO_2 - eq d^{-1}$	809051.27	824122.93
GHG emission from transport:		$kg CO_2 - eq d^{-1}$	2914.98	32901.26
GHG emission from biofuel:		$kg CO_2 - eq d^{-1}$	490033.59	490033.59
Total cost biodiesel(B100) plants		$\$$	55680000.00	36380000.00
Total operating expenses for year		$\$/ year$	45043178.40	37336187.02
Investment. cost a BSC per year:		$\$/ year$	6681600.00	4365600.00
Total biomass&prod. cost of a BSC:		$\$/ year$	91998122.40	67752154.04
Total production cost of a BSC:		$\$/ year$	13167282.72	13167282.72
Total biomass cost of a BSC:		$\$/ year$	78830839.68	54584871.32
Transport cost of a BSC:		$\$/ year$	9713152.54	5066114.10
Carbon tax levied:		$\$/ year$	11876585.08	12676569.85
Government incentives:		$\$/ year$	-9059090.51	-9059090.51
Total Land all regions:		ha	3227237.00	3227237.00
Total BIOFUELS Land:		ha	99264.74	81175.40
Total RESERVATION Land:		ha	1613611.00	1613611.00
Total FOOD Land:		ha	668093.45	657463.95
Total FREE Land:		ha	846267.81	874986.65
Sunflower Land for biodiesel		ha	285.71	80889.69
Rapeseed Land for biodiesel(B100)		ha	98979.03	285.71
Sunflower Land for foods		ha	514930.25	504300.75
Rapeseed Land for foods		ha	153163.20	153163.20
FOOD&BIOFUEL(Sunflower)		ha	515215.96	585190.44
FOOD&BIOFUEL(Rapeseed)		ha	252142.23	153448.91
Diesel to meet the energy		$ton/ year$	1710987.00	1710987.00
Biodiesel(B100) in regions		$ton/ year$	105338.26	105338.26
Petroleum diesel in regions		$ton/ year$	1617954.61	1617954.61
GHG emission by biodiesel(B100)		$\frac{kg CO_2 - eq}{ton biodiesel}$	4509.80	4811.90
GHG emission by petroleum diesel		$\frac{kg CO_2 - eq}{ton diesel}$	3623.00	3623.00
Price of biodiesel(B100)		$\$/ ton$	1055.745	767.065

The model proposed was solved in GAMS 22.8 using CPLEX 11.1 solver on an Intel Core 2 Duo P8600 2.4 GHz with 4 GB RAM on a 32-bit platform. The mixed integer linear model is composed of 13510 constraints and 12123 variables (out of which 6102 are binary variables that

represent the investment decisions and management). The solution was obtained in less than 539s using the simplex and barrier algorithms available in the CPLEX solver.

DISCUSSION AND CONCLUSIONS

The biofuel industry is anticipated to rapidly expand in the decades to come, and the impacts of the industry growth on agricultural industry and regional economy need to be investigated. In recent years the “food versus energy” competition has been heatedly debated. This paper studies the interactions of biofuel supply chain design with agricultural land use and local food market equilibrium. We focus on economic behavior of the stakeholders in the biofuel supply chain, and incorporate them into the supply chain design model.

In this paper, a systems optimisation framework has been introduced for the optimal design of a Bulgaria first generation biodiesel(B100) supply chain. The model proposed has been applied to a case study of biodiesel(B100) production in Bulgaria. Different instances have been investigated for years 2012 (5.75% by energy content) based on the domestic biofuel targets. For 2012, first generation technologies have been studied. The use of set-aside land for these two special energy crops has also been taken into account.

This paper presents the issues related to designing and managing the biomass-to-biorefinery supply chain. A mathematical model is proposed that can be used to design and manage this supply chain. Bulgaria is used, as a case study to show how this model can be used to identify potential location for biorefineries, and give insights about the factors that impact the delivery cost of biodiesel(B100).

The data used to validate the model and perform the computational analyses presented above is collected from a number of sources such as research articles and the statistical yearbook of Bulgaria. Due to data availability, only two major sources of biomass feedstock sunflower and rapeseed relevant to Bulgaria are considered.

A similar model could be used to design the supply chain of a biorefinery provided other biomass feedstock is being used.

Based on the inputs and outputs of the optimal synthesis in criterion for minimizing total annual costs (see **Table 18**), one could say that about 19.9% of the price for the supply of biodiesel(B100) are due to investment costs, approximately 20.5% are due operating costs, 35% are due to raw material costs for collection, approximately 35% are due to carbon tax collected approximately 14.47% are due to transportation costs and about -25% are due to government

incentives for the production and use of biodiesel(B100). It is then understandable why our computational results indicate that changes due to raw material costs affect greatly the biodiesel delivery cost.

Improvements in the technology of biomass feedstock conversion to biodiesel(B100) have high impact on the cost of biodiesel(B100). This is due to the fact that less biomass will be required to produce the same amount of biodiesel(B100). As a result, less biomass will need to be harvested and transported. This in turn will decrease the cost of producing a ton of biodiesel(B100). The cost of biodiesel(B100) is also affected by factors such as the project life and Government incentives for biodiesel(B100) production and use.

Future research may be carried out in several directions. This study assumes that the production of biodiesel(B100) feedstock uses only sunflower and rapeseed. Future studies may consider other energy source such as waste oils from food or livestock. This paper suggests that the factories are specialized to produce only biodiesel(B100), but in fact arrivals intermediate is used for food purposes. Further studies should consider such combined plants. This paper suggests the use of local raw materials. Inclusion in the model and the possibilities of imported raw materials would enrich the study and may lead to another configuration of supply chain. To maximize net social benefits, the impact of biofuel supply chain design on food and fuel consumer surpluses could be considered as an objective of biofuel supply design problem. How to consider all these factors in the model will be a challenging topic that is worth exploring in future research. Finally, we have only considered one time investment of building biofuel refineries and static land use decision. A more realistic multi-year biofuel refinery location problem with dynamic land use choice may be worthy of investigation in the future. In the following developments approaches should be developed that account changing requirements demand for biofuels over time, leading to phased infrastructure development.

The experimental results indicate that the running time of CPLEX for these problems is relatively small. The minimum running time is 167 CPUs and the maximum 539 CPUs. Increasing the problem size (which would be the case when one uses this model to design and manage larger supply chains considering larger number of biomass feedstock options and larger number of biomass supply sources, etc.) may result in longer running times for CPLEX or failure of CPLEX to read the problem created. Therefore, future work include

design of various solution approaches that would provide good quality solutions to these problems in a reasonable amount of time.

REFERENCES

1. E.M. Kondili, J.K. Kaldellis, *Renewable and Sustainable Energy Reviews* **11**, 2137 (2007).
2. G. Edwards-Jonesa et al., *Trends in Food Science & Technology*, **19**, 265 (2008).
3. A. Zamboni, F. Bezzo, N. Shah, *Energy & Fuels*, **23**, 5134 (2009).
4. <http://www.mzh.government.bg>
5. A. Iriarte, J. Rieradevall, X. Gabarrell, *J. Cleaner Production*, **18**, 336 (2010).
6. S. Leduc, PhD Thesis, Department of Applied Physics and Mechanical Engineering, Luleå University of Technology, Luleå, Sweden
7. http://www.biofuels.apec.org/pdfs/ewg_2010_biofuel-production-cost.pdf
8. European Commission, Well-to-wheels analysis of future automotive fuels and powertrains in the European context. (2006) (online).
9. S. Giarola, A. Zamboni, F. Bezzo, *Computers & Chem. Eng.*, **35**, 1782 (2011).
10. O. Akgul, N. Shah, L.G. Papageorgion, *Computers & Chem. Eng.*, **42**, 101 (2012).
11. B.R. Moser, *Fuel*, **99**, 254 (2012).
12. http://www.evworld.com/library/energy_numbers.pdf
13. <http://www.iea.org/stats/unit.asp>
14. <http://ekipbg.com/2012/05/25/gpricesbg/>
15. <http://igitur-archive.library.uu.nl/chem/2007-0320-200551/NWS-E-2005-141.pdf>
16. <http://eurlex.europa.eu>
17. <http://www.nsi.bg>

ОПТИМАЛНО ПРОЕКТИРАНЕ И ПЛАНИРАНЕ НА РЕСУРСНО ОСИГУРИТЕЛНАТА ВЕРИГА ЗА ПРОИЗВОДСТВО И ДОСТАВКИ НА БИОДИЗЕЛ С ОТЧИТАНЕ НА СЕИТЪОБРАЩЕНИЕТО. ЧАСТ 2. ОПРЕДЕЛЯНЕ НА МЕСТОПОЛОЖЕНИЕТО НА БИОРАФИНИЕРИТЕ ЗА ТЕРИТОРИЯТА НА БЪЛГАРИЯ

Б.Иванов^{1*}, Б.Димитрова¹, Д.Добруджалиев²

¹⁾ *Институт по инженерна химия, Българска академия на науките, 1113 София*

²⁾ *Университет "Проф. Асен Златаров", 8000 Бургас*

Постъпила на 3 юни, 2013 г.; коригирана на януари, 2014 г.

(Резюме)

В тази част на работата се демонстрира използването на предложени в част 1 математичен модел за проектиране на ресурсно осигурителни вериги за производство и разпространение на биодизел за територията на България. Биосуровините за производство на биодизел са слънчоглед и рапица. Територията на България е разделена на 27 области, съответстващи на съществуващото териториално деление. Решението на проблема за оптимално разполагане на биорафинериите е извършено с използване на пакета GAMS и математичния модел, предложен в част 1.

MHD flow of a dusty fluid between two infinite parallel plates with temperature dependent physical properties under exponentially decaying pressure gradient

H.A. Attia^{1*}, A.L. Aboul-Hassan², M.A.M. Abdeen², A.El-Din Abdin³

¹ Department of Engineering Mathematics and Physics, Faculty of Engineering, El-Fayoum University, El-Fayoum-63514, Egypt

² Department of Engineering Mathematics and Physics, Faculty of Engineering, Cairo University, Giza 12211, Egypt

³ National Water Research Center, Ministry of Water Resources and Irrigation, Egypt

Received May 29, 2013; revised July 4, 2014

In this study, the unsteady magnetohydrodynamic (MHD) flow and heat transfer of a dusty electrically conducting fluid between two infinite horizontal plates with temperature dependent physical properties are investigated. The fluid is acted upon by an exponentially decaying pressure gradient in the axial direction and an external uniform magnetic field perpendicular to the plates. The governing coupled momentum and energy equations are solved numerically by using the method of finite differences. The effects of the variable physical properties and the applied magnetic field on the velocity and temperature fields for both the fluid and dust particles are studied.

Key words: Two-phase flow, heat transfer, parallel plates, variable properties, numerical solution.

INTRODUCTION

The flow and the heat transfer of dusty fluids in a channel have been studied by many authors [1-7]. The study of this type of flow gets its importance from its wide range of applications especially in the fields of fluidization, combustion, use of dust in gas cooling systems, centrifugal separation of matter from fluid, petroleum industry, purification of crude oil, electrostatic precipitation, polymer technology, and fluid droplets sprays. The flow of a dusty conducting fluid through a channel in the presence of a transverse magnetic field has a variety of applications in MHD generators, pumps, accelerators, and flowmeters. In these devices, the solid particles in form of ash or soot are suspended in the conducting fluid as a result of the corrosion and wear activities and/or the combustion processes in MHD generators and plasma MHD accelerators. The consequent effect of the presence of solid particles on the performance of such devices has led to studies of particulate suspensions in conducting fluids in the presence of externally applied magnetic field [8-13].

Most of the above mentioned studies are based on constant physical properties. More accurate prediction for the flow and heat transfer can be achieved by taking into account the variation of

these properties with temperature [14]. Klemp et al. [15] studied the effect of temperature dependent viscosity on the entrance flow in a channel in the hydrodynamic case. Attia and Kotb [16] studied the steady MHD fully developed flow and heat transfer between two parallel plates with temperature dependent viscosity. Later Attia [17] extended the problem to the transient state.

In the present work, the transient flow and heat transfer of an electrically conducting, viscous, incompressible dusty fluid with temperature-dependent viscosity and thermal conductivity are studied. The fluid is flowing between two electrically insulating infinite plates maintained at two constant but different temperatures. The fluid is acted upon by an exponentially decaying pressure gradient and an external uniform magnetic field perpendicular to the plates. The magnetic Reynolds number is assumed very small so that the induced magnetic field is neglected. It is assumed that the flow is laminar and the dust particles occupy a constant finite volume fraction. This configuration is a good approximation of some practical situations such as heat exchangers, flow meters, and pipes that connect system components. This problem is chosen due to its occurrence in many industrial engineering applications [18].

In general, there are two basic approaches for modeling two-phase fluid-particle flows. They are based on the Eulerian and the Lagrangian descriptions known from fluid mechanics. The

* To whom all correspondence should be sent:
E-mail: ah1113@yahoo.com

former treats both the fluid and the particle phases as interacting continua [19-21], while the latter treats only the fluid phase as a continuum with the particle phase being governed by the kinetic theory [22]. The present work employs the continuum approach and employs the dusty-fluid equations discussed by Marble [19].

The flow and temperature distributions of both the fluid and dust particles are governed by a coupled set of the momentum and energy equations. The Joule and viscous dissipations are taken into consideration in the energy equation. The governing coupled nonlinear partial differential equations are solved numerically by using finite differences. The effects of the external uniform magnetic field and of the variable viscosity and thermal conductivity on the time development of the velocity and temperature distributions for both the fluid and dust particles are discussed.

DESCRIPTION OF THE PROBLEM

In this paper, the dusty fluid is assumed to be flowing between two infinite horizontal electrically non-conducting stationary plates located at the $y=\pm h$ planes and kept at two constant temperatures T_1 for the lower plate and T_2 for the upper plate with $T_2>T_1$ so natural convection is eliminated. The dust particles are assumed to be spherical in shape and uniformly distributed throughout the fluid. The motion of the fluid is produced by an exponential decaying pressure gradient $dP/dx = -Ge^{-\alpha x}$ in the x -direction, where G and α are constants. This is an example of a time-dependent pressure gradient. Other forms of time-dependent pressure gradients may be considered in future work. A uniform magnetic field B_0 is applied in the positive y -direction. Geometry of the problem is illustrated in Figure 1.

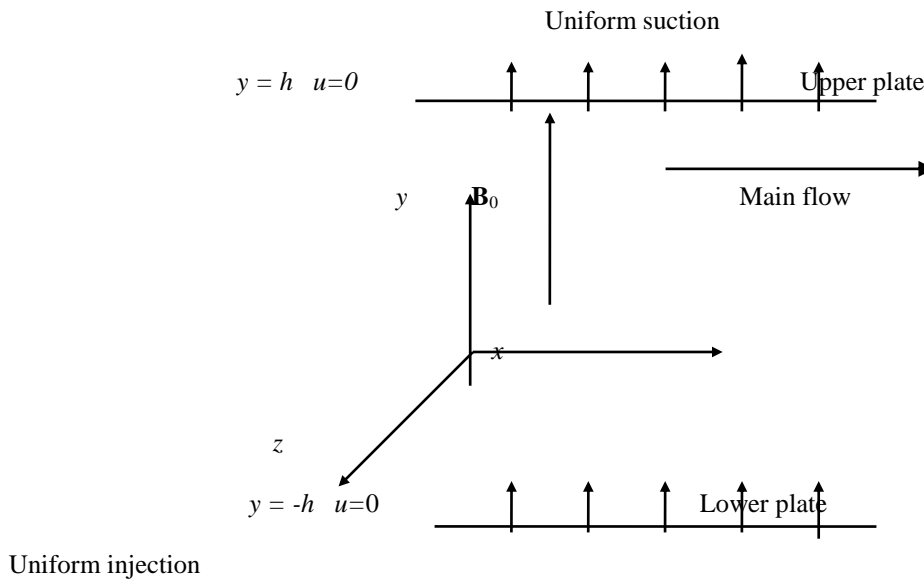


Fig. .1 The geometry of the problem

The fluid motion starts from rest at $t=0$, and the no-slip condition at the plates implies that the fluid and dust particles velocities vanish at $y=\pm h$. The initial temperatures of the fluid and of dust particles are assumed equal to T_1 . The viscosity and the thermal conductivity of the fluid are taken to be temperature dependent. The viscosity is taken to vary exponentially with temperature whereas a linear dependence on temperature of the thermal conductivity is assumed. Since the plates are infinite in the x and z -directions, the physical variables are invariant in these directions and the problem is essentially one-dimensional with velocities $u(y,t)$ and $u_p(y,t)$ along the x -axis for fluid and particle phase respectively.

To formulate the governing equations for this investigation, the balance laws of mass and linear momentum are considered along with information about interfacial and external body forces and stress tensors for both phases. The balance laws of mass (for the fluid and particulate phases, respectively) may be written as

$$\partial_t \phi - \vec{\nabla} \cdot ((1 - \phi)\vec{V}) = 0, \quad (1a)$$

$$\partial_t \phi + \vec{\nabla} \cdot (\phi \vec{V}_p) = 0, \quad (1b)$$

where t is time, ϕ is the particulate volume fraction, \vec{V} is the fluid-phase velocity vector, and \vec{V}_p is the particulate-phase velocity vector. The

fluid is assumed incompressible and the densities for both phases are assumed constant.

The balance laws of linear momentum (for the fluid and particulate phases, respectively) may be written as

$$\rho(1-\phi)(\partial_t \vec{V} + \vec{V} \cdot \nabla \vec{V}) = \nabla \cdot \vec{\varepsilon} - \vec{f} + \vec{b}, \quad (2a)$$

$$\rho_p \phi (\partial_t \vec{V}_p + \vec{V}_p \cdot \nabla \vec{V}_p) = \vec{f} + \vec{b}_p \quad (2b)$$

where ρ is the fluid-phase density, $\vec{\varepsilon}$ is the fluid-phase stress tensor, \vec{f} is the interphase force per unit volume associated with the relative motion between the fluid and particle phases, \vec{b} is the fluid-phase body force per unit volume, and \vec{b}_p is the particle-phase body force per unit volume.

Along with Eqs. (1) and (2), the following constitutive equations are used

$$\vec{\varepsilon} = (1-\phi)(-P\vec{I} + \mu(\nabla \vec{V} + (\nabla \vec{V})^T)), \quad (3a)$$

$$\vec{f} = N\rho_p \phi (\vec{V} - \vec{V}_p), \quad (3b)$$

$$\vec{b} = \sigma(\vec{V} \wedge \vec{B}_o) \wedge \vec{B}_o, \quad (3c)$$

$$\vec{b}_p = \vec{0}, \quad (3d)$$

where P is the fluid pressure, \vec{I} is the unit tensor, μ is the fluid dynamic viscosity, μ_p is the particle-phase dynamic viscosity, N is the momentum transfer coefficient [24], which for spherical dust particles = $\frac{6\pi\mu r}{m}$, r is the average radius of dust particles, m is the average mass of dust particles, $\rho_p = \frac{4\pi r^3}{3m}$ is the material density of dust particles, σ is the electric conductivity of the fluid and a transposed T denotes the transpose of a second-rank tensor. In the present work it is assumed that the suspension is dilute and thus no particle-particle interaction exists [19]. In Eq. (3c) it is assumed that the magnetic Reynolds number $Re_m = \sigma\mu L_o U_o$, which is the ratio of the induced magnetic field to the applied external magnetic field, is very small and hence the induced magnetic field is neglected [23] and B_o is the only magnetic field in the problem. The quantities $\mu L_o U_o$ are respectively the magnetic permeability of the fluid, the characteristic length, which in this case = h , and

the characteristic velocity of the fluid. It should be pointed out that in the present work the hydrodynamic interactions between the phases are limited to the drag force. This assumption is feasible when the particle Reynolds number is assumed to be small. Other interactions such as the virtual mass force [25], the shear force associated with the turbulent motion of dust particles [26], and the spin-lift force [27] are assumed to be negligible compared to the drag force [28]. To recapitulate, it is assumed that the flow is laminar, the fluid is incompressible, dust particles occupy a constant finite volume fraction, induced magnetic field is negligible, the virtual mass force, shear force, and spin lift force on dust particles are negligible.

Substituting Eqs. (3) into Eqs. (1) and (2) yields, after some arrangements

$$\rho \frac{\partial u}{\partial t} = Ge^{-\alpha y} + \frac{\partial}{\partial y} \left(\mu \frac{\partial u}{\partial y} \right) - \sigma B_o^2 u - \kappa N(u - u_p), \quad (4)$$

$$\frac{\partial u_p}{\partial t} = N(u - u_p), \quad (5)$$

where $\kappa = \rho_p \phi / (1 - \phi)$. The first three terms in the right-hand side of Eq. (4) are respectively the pressure gradient, viscous forces, and Lorentz force terms. The last term represents the force due to the relative motion between fluid and dust particles. The initial and boundary conditions on the velocity fields are respectively given by

$$t = 0 : u = u_p = 0. \quad (6a)$$

For $t > 0$, the no-slip condition at the plates implies that

$$y = -h : u = u_p = 0, \quad (6b)$$

$$y = h : u = 0, u_p = 0. \quad (6c)$$

Heat transfer takes place from the upper hot plate to the lower cold plate by conduction through the fluid, and there is heat generation due to both the Joule and viscous dissipations. Dust particles gain heat from the fluid by conduction through their surface. To describe the temperature distributions for both the fluid and dust particles, two energy equations are required, which are [29, 30]

$$\rho c \frac{\partial T}{\partial t} = \frac{\partial}{\partial y} \left(k \frac{\partial T}{\partial y} \right) + \mu \left(\frac{\partial u}{\partial y} \right)^2 + \sigma B_o^2 u^2 + \frac{\rho_p C_s}{\gamma_T} (T_p - T), \quad (7)$$

$$\frac{\partial T_p}{\partial t} = -\frac{1}{\gamma_T}(T_p - T), \tag{8}$$

where T is the temperature of the fluid, T_p is the temperature of the particles, c is the specific heat capacity of the fluid at constant volume, C_s is the specific heat capacity of the particles, k is the thermal conductivity of the fluid, γ_T is the temperature relaxation time = $3Pr\gamma_p C_s / 2c$, γ_p is the velocity relaxation time = $2\rho_{pr}^2/9\mu$, Pr is the Prandtl number = $\mu_o c / k_o$, μ_o and k_o are, respectively, the viscosity and thermal conductivity of the fluid at T_1 . The last three terms in the right-hand side of Eq. (7) represent, respectively, the viscous dissipation, the Joule dissipation, and the heat conduction between the fluid and dust particles. The initial and boundary conditions of the temperature fields are

$$t \leq 0 : T = T_p = T_1, \tag{9a}$$

$$t > 0, y = -h : T = T_p = T_1, \tag{9b}$$

$$t > 0, y = h : T = T_p = T_2. \tag{9c}$$

The viscosity of the fluid is assumed to depend on temperature and is defined as, $\mu = \mu_o f_1(T)$. For practical reasons relevant to most fluids [15, 30, 31], the viscosity is assumed to vary exponentially with temperature. The function $f_1(T)$ takes the form [13,14], $f_1(T) = e^{-a(T-T_1)}$. The parameter a is positive values for liquids such as water, benzene or crude oil. In some gases like air, helium or methane a is negative, that is the viscosity increases with temperature [9, 24, 30].

The thermal conductivity of the fluid is assumed to vary with temperature as $k = k_o f_2(T)$. We assume linear dependence of the thermal conductivity on temperature, that is, $f_2(T) = 1 + b(T - T_1)$, where the parameter b may be positive for some fluids such as air or water vapor or negative for others fluids such as liquid water or benzene [30, 31].

The problem is given more generality if the equations are written in the non-dimensional form. To do this, define the following non-dimensional quantities,

$$(\hat{x}, \hat{y}) = \left(\frac{x}{h}, \frac{y}{h}\right),$$

$$\hat{t} = \frac{t\mu_o}{\rho h^2},$$

$$(\hat{u}, \hat{u}_p) = \left(\frac{u\rho h}{\mu_o}, \frac{u_p\rho h}{\mu_o}\right),$$

$$\hat{T} = \frac{T - T_1}{T_2 - T_1}, \hat{T}_p = \frac{T_p - T_1}{T_2 - T_1},$$

$$\hat{G} = \frac{Gh^3\rho}{\mu_o^2},$$

$\hat{a} = a(T_2 - T_1)$ is the viscosity parameter,

$\hat{b} = b(T_2 - T_1)$ is the thermal conductivity parameter,

$$\hat{f}_1(\hat{T}) = e^{-\hat{a}\hat{T}},$$

$$\hat{f}_2(\hat{T}) = 1 + \hat{b}\hat{T},$$

$Ha^2 = \sigma B_o^2 h^2 / \mu_o$, Ha is the Hartmann number,

$R = \kappa N h^2 / \mu_o$ is the particle concentration parameter,

$G_1 = \mu_o / N\rho h^2$ is the particle mass parameter,

$Pr = \mu_o c / k_o$ is the Prandtl number,

$Ec = \mu_o^2 / \rho^2 h^2 c_p (T_2 - T_1)$ is the Eckert number.

$L_o = \rho h^2 / \mu_o \gamma_T$ is the temperature relaxation time parameter.

In terms of the above non-dimensional variables and parameters Eqs. (4)-(9) take the form (hats are dropped for convenience)

$$\frac{\partial u}{\partial t} = Ge^{-\hat{a}t} + f_1(T) \frac{\partial^2 u}{\partial y^2} + \frac{\partial f_1(T)}{\partial y} \frac{\partial u}{\partial y} - Ha^2 u - R(u - u_p) \tag{10}$$

$$\frac{\partial u_p}{\partial t} = \frac{1}{G_1}(u - u_p) \tag{11}$$

$$t \leq 0 : u = u_p = 0. \tag{12a}$$

$$t > 0, y = -1 : u = u_p = 0, \tag{12b}$$

$$t > 0, y = 1 : u = 1, u_p = 0, \tag{12c}$$

$$\frac{\partial T}{\partial t} = \frac{1}{Pr} f_2(T) \frac{\partial^2 T}{\partial y^2} + \frac{1}{Pr} \frac{\partial f_2(T)}{\partial y} \frac{\partial T}{\partial y} + Ec f_1(T) \left(\frac{\partial u}{\partial y} \right)^2 + Ec Ha^2 u^2 + \frac{2R}{3Pr} (T_p - T), \quad (13)$$

$$\frac{\partial T_p}{\partial t} = -L_o (T_p - T), \quad (14)$$

$$t \leq 0 : T = T_p = 0, \quad (15a)$$

$$t > 0, y = -1 : T = T_p = 0, \quad (15b)$$

$$t > 0, y = 1 : T = T_p = 1, \quad (15c)$$

Equations (10), (11), (13), and (14) represent a system of coupled, nonlinear partial differential equations which may be solved numerically under the initial and boundary conditions (12) and (15) using the finite difference approximations. The Crank-Nicolson implicit method is used [32]. Finite difference equations relating the variables are obtained by writing the equations at the mid point of the computational cell and then replacing the different terms by their second order central difference approximations in the y-direction. The diffusion term is replaced with the average of the central differences at two successive time levels. The nonlinear terms are first linearized and then an iterative scheme is used at every time step to solve the linearized system of difference equations. The solution at a certain time step is chosen as an initial guess for next time step and the iterations are continued till convergence, within a prescribed accuracy. Finally, the resulting block tri-diagonal system is solved using the generalized Thomas-algorithm [32]. We define the variables $A = \partial u / \partial y$ and $H = \partial \theta / \partial y$ to reduce the second order differential Eqs. (10) and (13) to first order differential equations, and an iterative scheme is used at every time step to solve the linearized system of difference equations. In the numerical solution some parameters are not varied and given the following fixed values: $R=0.5$, $G_1=0.8$, $G=5$, $\alpha=1$, $Pr=1$, $Ec=0.2$, and $L_o=0.7$. Step sizes $\Delta t=0.001$ and $\Delta y=0.01$ for time and space, respectively are chosen. Smaller step sizes do not show any significant change in the results. The iterative scheme continues until the fractional difference between two successive iterations becomes less than a specified small value. Convergence of the scheme is assumed when all of the unknowns u , A , T and H for the last two approximations differ from unity by less than 10^{-6} for all values of y in $-1 < y < 1$ at every time step.

The required accuracy is usually reached after about 7 iterations. It should be mentioned that the results obtained herein reduce to those reported by Singh [8] and Aboul-Hassan et al. [12] for the case of fluid with constant properties. These comparisons lend confidence in the accuracy and correctness of the solutions presented.

A linearization technique is first applied to replace the nonlinear terms at a linear stage, with the corrections incorporated in subsequent iterative steps until convergence is reached. Then the Crank-Nicolson implicit method is used at two successive time levels [26]. An iterative scheme is used to solve the linearized system of difference equations. The solution at a certain time step is chosen as an initial guess for next time step and the iterations are continued till convergence, within a prescribed accuracy. Finally, the resulting block tri-diagonal system is solved using the generalized Thomas-algorithm [26]. Finite difference equations relating the variables are obtained by writing the equations at the mid point of the computational cell and then replacing the different terms by their second order central difference approximations in the y-direction. The diffusion terms are replaced by the average of the central differences at two successive time-levels. The computational domain is divided into meshes each of dimension Δt and Δy in time and space, respectively. We define the variables $A = \partial u / \partial y$, $B = \partial w / \partial y$ and $H = \partial \theta / \partial y$ to reduce the second order differential Eqs. (9), (10) and (12) to first order differential equations, and an iterative scheme is used at every time step to solve the linearized system of difference equations. All calculations are carried out for the non-dimensional variables and parameters given by, $G=5$, $Pr=1$, and $Ec=0.2$ where G is related to the externally applied pressure gradient and where the chosen given values for Pr and Ec are suitable for steam or water vapor. Grid-independence studies show that the computational domain $0 < t < \infty$ and $-1 < y < 1$ is divided into intervals with step sizes $\Delta t=0.0001$ and $\Delta y=0.005$ for time and space respectively. Smaller step sizes do not show any significant change in the results. Convergence of the scheme is assumed when all of the unknowns u , w , A , B , θ and H for the last two approximations differ from unity by less than 10^{-6} for all values of y in $-1 < y < 1$ at every time step. Less than 7 approximations are required to satisfy this convergence criteria for all ranges of the parameters studied here.

RESULTS AND DISCUSSIONS

Figures 2a, 2b, 3a, and 3b show the effect of the viscosity parameter a on the time development of the velocities u and u_p , and the temperatures T and T_p , respectively, at the center of the channel ($y=0$) for $Ha = 0$ and $b = 0$. Figures 1a and 1b indicate that increasing a increases u and u_p and increases the time required to approach the steady state. This is a result of decreasing the viscous forces. The effect of the parameter a on the steady state time is more pronounced for positive values of a than for

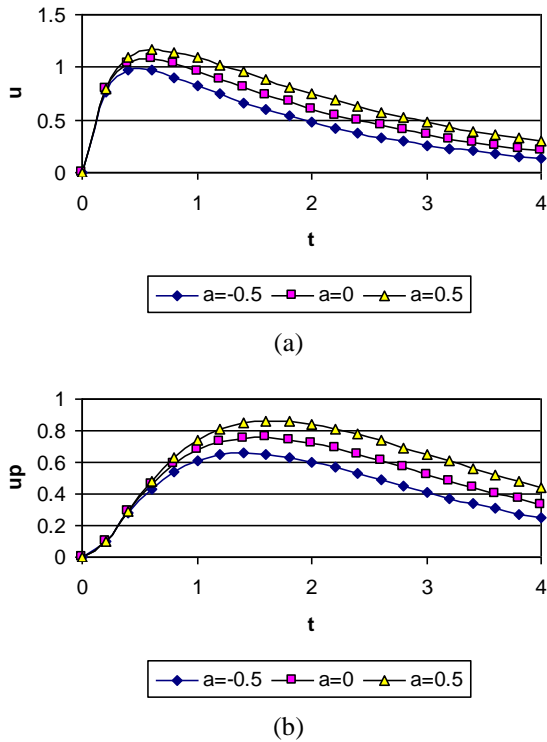


Fig. 2. Effect of the viscosity parameter a on the time variation of: (a) the fluid velocity u at the center of the channel ($y=0$); (b) the particle phase velocity u_p at the center of the channel ($y=0$). ($Ha=0$)

Figures 4a, 4b, 5a, and 5b present the effect of the viscosity parameter a on the time development of u , u_p , T and T_p , respectively, at the centre of the channel ($y=0$) for $Ha=1$ and $b=0$. The introduction of the uniform magnetic field adds one resistive term to the momentum equation and the Joule dissipation term to the energy equation. As shown in Figures 4a, and 4b the magnetic field results in

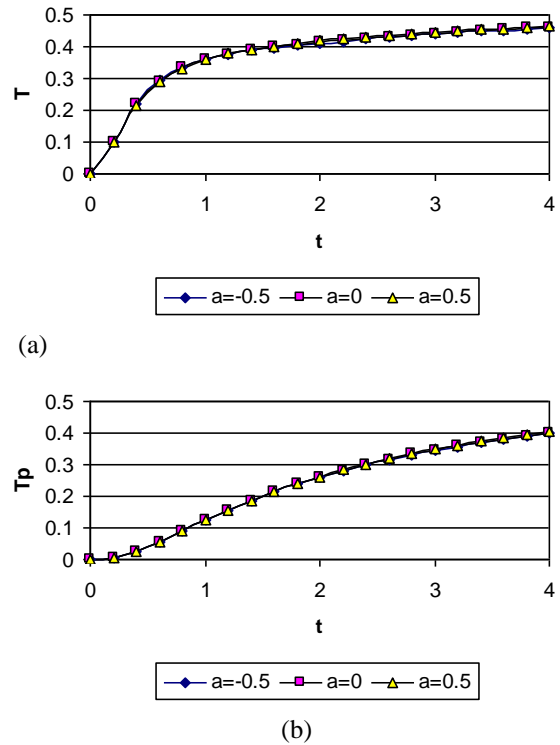
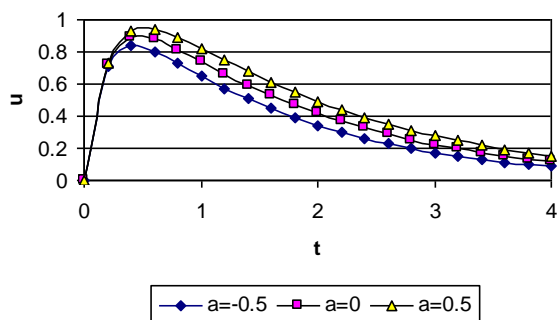
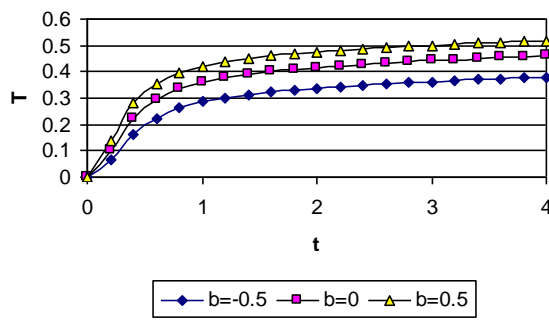


Fig. 3. Effect of the viscosity parameter a on the time variation of: (a) the fluid temperature T at the center of the channel ($y=0$); (b) the particle phase temperature T_p at the center of the channel ($y=0$). ($Ha=0$).

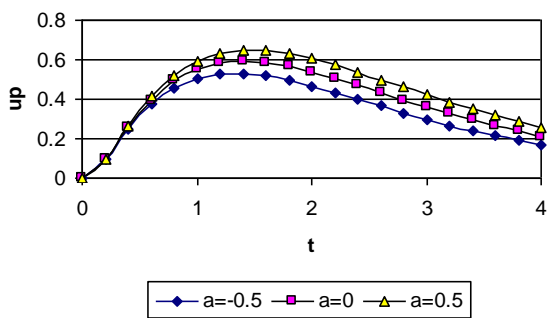
a reduction in the velocities u and u_p and their steady state times for all values of a due to its damping effect. Figures 5a, and 5b confirm that the parameter a has a negligible effect on temperature and the viscous dissipation is negligible. Comparing with Figures 3 and 5, it is observed that the temperature are slightly higher in the presence of the magnetic field ($Ha = 1$). This means that the Joule dissipation is small but now negligible. Notice that u reaches the steady state faster than u_p which is expected because the fluid velocity is the source for the dust particles velocity. Figures 3a and 3b show that the viscosity parameter a has a negligible effect on temperature. This means that the viscous dissipation is negligible. Of course there is no Joule dissipation when $Ha = 0$. The time at which T_p reaches the steady state is longer than that for T since T_p always follows T .



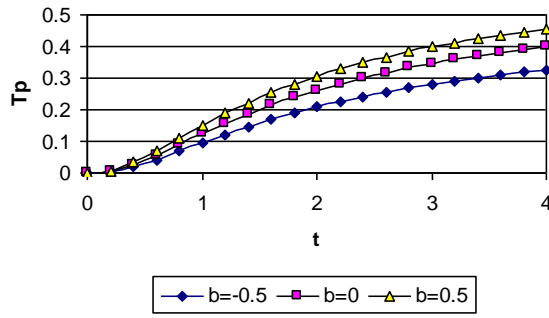
(a)



(a)



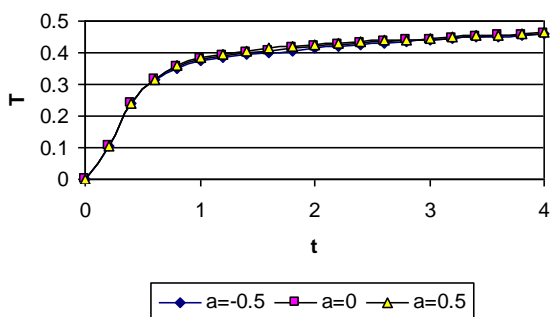
(b)



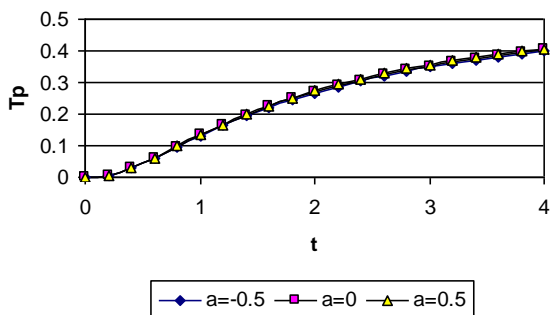
(b)

Fig. 4. Effect of the viscosity parameter a on the time variation of: (a) the fluid velocity u at the center of the channel ($y=0$); (b) the particle phase velocity u_p at the center of the channel ($y=0$). ($Ha=1$).

Fig. 6. Effect of the thermal conductivity parameter b on the time variation of: (a) the fluid temperature T at the center of the channel ($y=0$); (b) the particle phase temperature T_p at the center of the channel ($y=0$). ($Ha=0$)



(a)

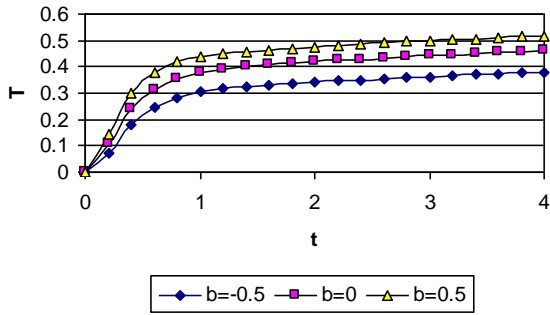


(b)

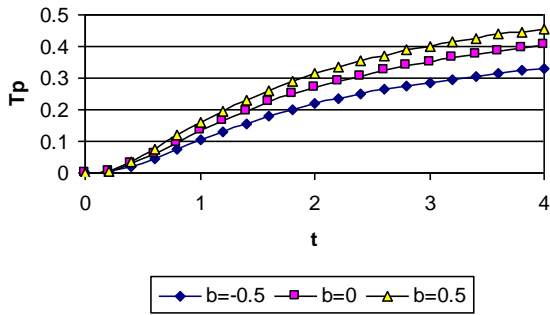
Fig. 5. Effect of the viscosity parameter a on the time variation of: (a) the fluid temperature T at the center of the channel ($y=0$); (b) the particle phase temperature T_p at the center of the channel ($y=0$). ($Ha=1$)

Figures 6a, and 6b show the effect of the thermal conductivity parameter b on the time development of the temperatures T and T_p , respectively, at the center of the channel ($y=0$) for $Ha=0$ and $a=0$. The figures show that increasing b increases T and T_p as a result of increasing the thermal conductivity. In Figure 6a it is interesting that the steady state value of the fluid temperature at the center of the channel exceeds 0.5 for positive values of b although the Joule and viscous dissipations are absent. The reason is that the thermal conductivity in the upper half of the channel is more than in the lower half if b is positive.

Figures 7a, and 7b present the effect of the thermal conductivity parameter b on the time development of the temperatures T and T_p , respectively, at the center of the channel ($y=0$) for $Ha=1$ and $a=0$. The introduction of the magnetic field increases both T and T_p for all values of b due to the increase in the dissipation.



(a)



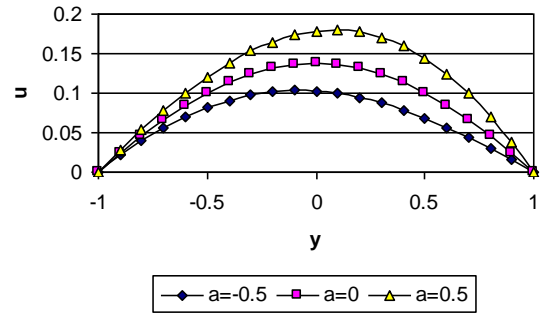
(b)

Fig. 7. Effect of the thermal conductivity parameter b on the time variation of: (a) the fluid temperature T at the center of the channel ($y=0$); (b) the particle phase temperature T_p at the center of the channel ($y=0$). ($Ha=1$)

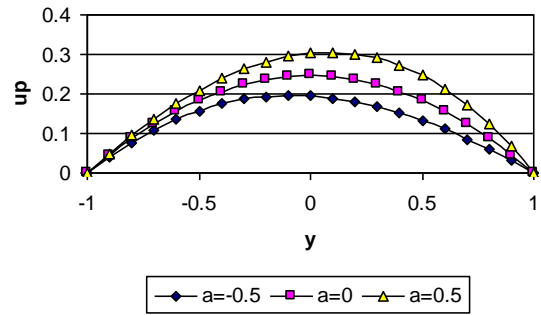
Figures 8a, 8b, 9a, and 9b present the effect of the viscosity parameter a on the profiles of the velocities u and u_p , and the temperatures T and T_p for $Ha=1$ and $b=0$ at $t=6$.

Increasing a increases the velocity and displaces the peak of the velocity profile towards the upper plate where the viscosity is less. This effect is akin to the displacement of the peak of the velocity distribution where there is suction at one plate and injection at the other plate. Positive values of a correspond to a suction velocity from the cold plate to the hot plate, while negative values of a correspond to a suction velocity from the hot plate to the cold plate. Figures 9a, and 9b show that increasing a increases the temperatures T and T_p for all values of y . It is clear from Figures 8, and 9 that the effect of the parameter a on the velocities is more pronounced than on the temperatures.

Figures 10a, and 10b present the effect of the thermal conductivity parameter b on the temperature profiles at $t=0$, for $Ha=1$ and $a=0$. The figures indicate that increasing b increases T and T_p for all values of y . This because increasing b means that the thermal conductivity near the hot plate gets more than near the cold plat.

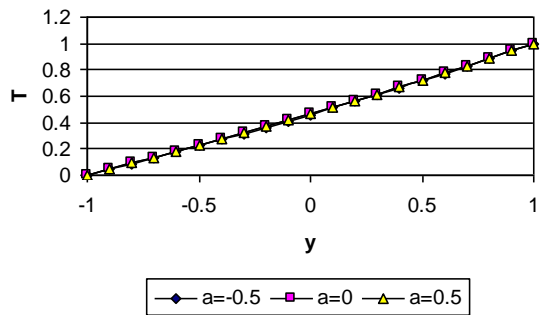


(a)

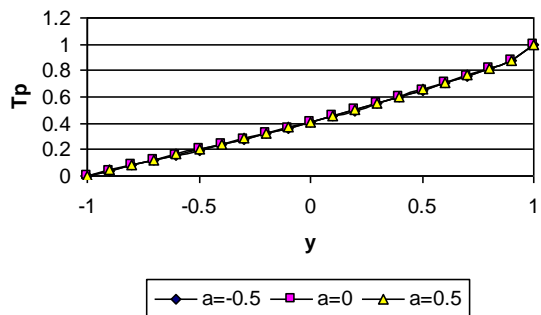


(b)

Fig. 8. Effect of the viscosity parameter a on the profile of: (a) the fluid velocity u at $t=6$; (b) the particle phase velocity u_p at $t=6$. ($Ha=1$)

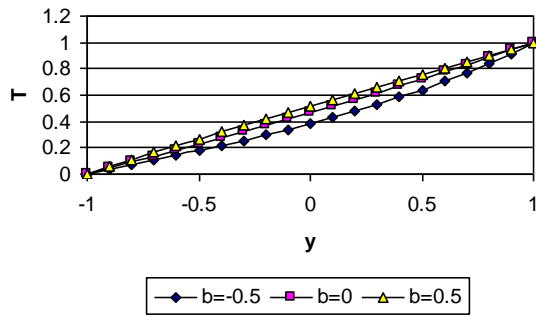


(a)

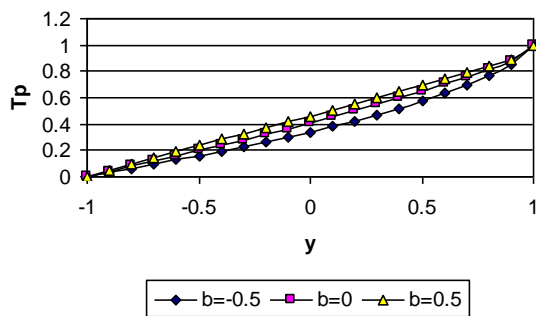


(b)

Fig. 9. Effect of the viscosity parameter a on the profile of: (a) the fluid temperature T at $t=6$; (b) the particle phase temperature T_p at $t=6$. ($Ha=1$)



(a)



(b)

Fig. 10. Effect of the thermal conductivity parameter b on the profile of: (a) the fluid temperature T at $t = 6$; (b) the particle phase temperature T_p at $t = 6$. ($Ha=1$).

Table 1. Variation of u at $y=0$ for various values of a and b at $t=6$ ($Ha=1$)

u	$a=-0.5$	$a=-0.1$	$a=0.0$	$a=0.1$	$a=0.5$
$b=-0.5$	0.0882	0.0862	0.0857	0.0854	0.0842
$b=-0.1$	0.1096	0.1091	0.1089	0.1089	0.1086
$b=0.0$	0.1154	0.1154	0.1154	0.1154	0.1154
$b=0.1$	0.1214	0.1219	0.1220	0.1221	0.1225
$b=0.5$	0.1473	0.1502	0.1508	0.1513	0.1532

Table 2. Variation of u_p at $y=0$ for various values of a and b at $t=6$ ($Ha=1$)

u_p	$a=-0.5$	$a=-0.1$	$a=0.0$	$a=0.1$	$a=0.5$
$b=-0.5$	0.1716	0.1683	0.1676	0.1669	0.1651
$b=-0.1$	0.2029	0.2022	0.2020	0.2019	0.2014
$b=0.0$	0.2112	0.2112	0.2112	0.2112	0.2112
$b=0.1$	0.2197	0.2204	0.2206	0.2207	0.2212
$b=0.5$	0.2549	0.2588	0.2597	0.2604	0.2629

Table 3. Variation of T at $y=0$ for various values of a and b at $t=6$ ($Ha=1$)

T	$a=-0.5$	$a=-0.1$	$a=0.0$	$a=0.1$	$a=0.5$
$b=-0.5$	0.3782	0.4440	0.4587	0.4723	0.5149
$b=-0.1$	0.3799	0.4455	0.4601	0.4736	0.5159
$b=0.0$	0.3803	0.4459	0.4605	0.4739	0.5163
$b=0.1$	0.3807	0.4463	0.4609	0.4743	0.5166
$b=0.5$	0.3829	0.4482	0.4627	0.4761	0.5181

Table 4. Variation of T_p at $y=0$ for various values of a and b at $t=6$ ($Ha=1$).

T_p	$a=-0.5$	$a=-0.1$	$a=0.0$	$a=0.1$	$a=0.5$
$b=-0.5$	0.3271	0.3962	0.3998	0.4125	0.4536
$b=-0.1$	0.3296	0.3886	0.4021	0.4148	0.4557
$b=0.0$	0.3303	0.3892	0.4028	0.4154	0.4563
$b=0.1$	0.3309	0.3899	0.4034	0.4160	0.4568
$b=0.5$	0.3340	0.3929	0.4063	0.4188	0.4593

Tables 1-4 present the variation of u , u_p , T , and T_p , respectively, at the center of the channel ($y=0$) at $t=6$ for various values of a and b and for $Ha=1$. It is clear that increasing a increases the temperatures for both the fluid and dust particle for all values of b . However, its effect on the velocities depends on the value of b . For negative b , increasing a decreases u and u_p but for positive b , increasing a increases them. Increasing the parameter b increases the velocities u and u_p and the temperatures T and T_p for all values of a .

CONCLUSIONS

In this paper the transient MHD flow and heat transfer of a dusty and electrically conducting fluid are studied in the presence of an external uniform magnetic field taking into consideration the variations of the viscosity and thermal conductivity of the fluid with temperature. The variation of the viscosity of the fluid with temperature has an apparent effect on the velocity of both the fluid and dust particles. The peak of the velocity distribution displaces from the center of the channel towards regions of less viscosity. Changing the viscosity has a negligible effect on temperatures and it is inferred that the viscous dissipation is negligible. Variation of the thermal conductivity of the fluid with temperature has a pronounced effect on temperature distributions. Temperatures shift towards the temperature of the plate near which the thermal conductivity is higher. Increasing the magnetic field decreases the velocity for both phases at all positions and times. It also produces a small increase in temperature and it is inferred that the Joule dissipation is small but not negligible.

REFERENCES

1. P.G. Saffman, *J. Fluid Mech.*, **13**, 120 (1962).
2. R.K.Gupta, S.C. Gupta, *J. Appl. Mathem.&Physics*, **27**, 119 (1976).
3. V.R. Prasad, N.C.P. Ramacharyulu, *Def. Sci. J.*, **30**, 125 (1979).
4. L.A. Dixit, *Ind. J. Theor. Physics*, **28**, 129 (1980).
5. A.K. Ghosh, D.K. Mitra, *Rev. Roum. Phys.*, **29**, 631 (1984).

6. H.A. Attia, M.A.M. Abdeen, *J. Theor. Appl. Mech.*, **51**, 53 (2013).
7. H.A. Attia, M.A.M. Abdeen, A. El-Din Abdin, *J. Eng. Physics & Thermophysics*, **86**, 677 (2013).
8. K.K. Singh, *Ind. J. Pure & Appl. Mathem.* **8**, 1124 (1976).
9. P. Mitra, P. Bhattacharyya, *Acta Mechanica*, **39**, 171 (1981).
10. K. Borkakotia, A. Bharali, *Quart. Appl. Mathem.*, 461 (1983).
11. A.A. Megahed, A.L. Aboul-Hassan, H. Sharaf El-Din, Proc. Fifth Miami international Symposium on Multi-Phase Transport and Particulate Phenomena, Miami, Florida, USA, vol. 3, pp. 111, 1988.
12. A.L. Aboul-Hassan, H. Sharaf El-Din, A.A. Megahed, Proc. First International Conference of Engineering Mathematics and Physics, Cairo, pp. 723-734, 1991.
13. H.A. Attia, K.M. Ewis, I.H. Abd Elmaksoud, M.A. M. Abdeen, *J. Physical Chem. A*, **86**, 141 (2012).
14. H. Herwig, G. Wicken, *Waerme und Stoffuebertragung*, **20**, 47 (1986).
15. K. Klemp, H. Herwig, M. Selmann, Proc. Third International Congress of Fluid Mechanics, Cairo, Egypt, vol. 3, pp. 1257-1266, 1990.
16. H.A. Attia, N.A. Kotb., *Acta Mechanica*, **117**, 215 (1996).
17. H.A. Attia, *Mech. Res. Commun.*, **26**, 115 (1999).
18. K.R. Rajagopal, Tao, L., *World Scientific*, 1995.
19. F.E. Marble, *Ann. Rev. Fluid Mech.*, **2**, 397 (1970).
20. S.L. Soo, *Multiphase fluid dynamics*, Science Press, New York, 1990.
21. M. Ishii, *Thermo-fluid dynamics Theory of Two-Phase flow*, Eyrolles, Paris, 1975.
22. A. Berlemont, *Int. J. Multiphase Flow*, **16**, 19 (1990).
23. G.W. Sutton, A. Sherman, *Engineering Magneto-hydrodynamics*, McGraw-Hill, 1965.
24. A.J. Chamkha, *Int. J. Engng. Sci.*, **33**, 437 (1995).
25. N. Zuber, *Chem. Eng. Sci.*, **19**, 897 (1964).
26. P.G. Saffman, *J. Fluid Mech.*, **22**, 385 (1965).
27. S.I. Rubinow, J.B. Keller, *J. Fluid Mech.*, **11**, 447 (1961).
28. N. Apazidis, *Int. J. Multiphase Flow*, **11**, 675 (1985).
29. A.J. Chamkha, *Appl. Math. Modelling*, **21**, 287 (1997).
30. H. Schlichting, *Boundary layer theory*, McGraw-Hill, 1968.
31. M.F. White, *Viscous fluid flow*, McGraw-Hill, 1991.
32. W.F. Ames, *Numerical solutions of partial differential equations*, Second Edition, Academic Press, New York, 1977.

МАГНИТОХИДРОДИНАМИЧНО ТЕЧЕНИЕ НА ЗАПРАШЕН ФЛУИД МЕЖДУ ДВЕ БЕЗКРАЙНИ УСПОРЕДНИ ПЛОСКОСТИ С ТЕМПЕРАТУРНО ЗАВИСИМИ ФИЗИЧНИ СВОЙСТВА ПРИ ЕКСПОНЕНЦИАЛНО ЗАТИХВАЩ ГРАДИЕНТ НА НАЛЯГАНЕТО

Х.А. Атия^{1*}, А.Л. Абул-Хасан², М.А.М. Абдиин², А. Ел-Дин Абдин³

¹ Департамент по инженерство, математика и физика, Факултет по инженерство, Университет в Ел-Фаюм, Ел-Фаюм 63514, Египет

² Департамент по инженерство, математика и физика, Факултет по инженерство, Университет в Кайро, Гиза 12211, Египет

³ Национален център по водни изследвания, Министерство на водните проблеми и напояването, Египет

Постъпила на 29 май, 2013 г.; коригирана на 4 юли, 2013 г.

(Резюме)

В тази работа е изследвано нестационарното магнитохидродинамично течение (МНД) и топлообмена в запрашен електропроводящ флуид между две безкрайни успоредни плоскости при температурно зависими физични свойства. Флуидът се намира под действието експоненциално затихващ градиент на налягането по оста на течението и при хомогенно външно магнитно поле перпендикулярно на плоскостите. Спрегнатите уравнения на движението и на топлопроводността са решени числено по метода на крайните разлики. Изследван е и ефекта на променливите физични параметри и на приложеното магнитно поле върху скоростта на течението и температурното поле за флуида и за праховите частици.

Physico-chemical properties of *Trichilia emetica* seeds oil and its comparison with some selected oilseed oils

B. Adinew

Department of chemistry, Mizan-Tepi University, Tepi campus, Ethiopia, East Africa.

Received April 4, 2013; Revised August 9, 2013

The physico-chemical properties of *trichilia emetica* seeds have been studied for their domestic and commercial applications. The color of the oil was yellow and it was solid at room temperature. The seeds have been found to have good oil yield of 65.81% which is comparable to the oil yield of some selected commercial seed oils such as cottonseed, safflower, soybean and olive oil. Iodine value (60.15mgI₂/100g), peroxide value (0.56mgO₂/g), saponification value (180.09mgKOH/g), acid value (8.13mgKOH/g), kinematic viscosity (49.85mm²/s), refractive index (1.47) and unsaponifiable matter (1.79) of the oil were determined by A.O.A.C. High saponification value guarantees the use of the oils in cosmetics and soap making industry. The acid value of the *trichilia emetica* seeds is higher than the maximum permissible acid level of 4mgKOH/g fat or oil required for edible virgin fats and oils and therefore it is necessary to purify the oil to make suitable for consumption. However the oil recorded low iodine values suggesting *trichilia emetica* seeds oil is highly saturated and may not be susceptible to rancidity. This study shows that, *trichilia emetica* seeds oil is a good source of edible oil for the local community after purification.

Keywords: *Trichilia emetica* seeds oil, physico-chemical properties,

drained, rich soils and high ground water [1].

INTRODUCTION

Woodland mahogany (*Trichilia emetica*) is a large, much branched evergreen reaching 8-25m high with a dense rounded crown. This species is in great demand in rural areas of Africa because it provides edible oil, medicine, timber, fuel wood and is used in agro forestry systems. Bark grey-brown or red-brown with fine, shallow striations and smallish scales. Branches erect or partly spreading, producing a pyramid-shaped crown when young, oval to rounded and dense when mature with a diameter sometimes exceeding 15m. Leaves up to 50cm long, unevenly compound with 3-5 pairs of leaflets plus a terminal one, dark green and glossy above, covered with short brownish hairs below, margins entire, veins prominent on lower surface. The flowers form pear-shaped red-brown fruit capsules which dry and split into three segments revealing a bunch of vivid red seeds. In other words; fruit rounded, furry, red-brown capsules to 3cm across, split into 3 or 4 parts to reveal 3-6 shiny black seeds 14-18 mm in length, each with a fleshy scarlet or orange-red aril almost covering the seed. A clear neck to 1cm long connects the capsule to the fruit stalk. The trees are commonly found in Uganda, Ethiopia, Kenya and Tanzania, south to Mozambique. It prefers well-

Fats and oils are an important food source for man, and are supplying essential fatty acids such as linoleic and arachidonic acids. Fats and oils are also used for producing drug dispersants in therapeutics [2]. Oils from seeds are both edible and non-edible depending on the type. These oils are often available as raw materials for chemical and industrial applications. Because of the high demand and economic importance of these oil seeds to the chemical industry, attention have therefore been focused on underutilized *Trichilia emetica* seeds for possible development and use.

The objective of this study was therefore to extract oil from *Trichilia emetica* seeds, assess the physical and chemical characteristics and suggest possible uses for the oil as a prelude to an investigation into the scientific basis for its use for edible purposes. Comparisons between *Trichilia emetica* seeds oil and other oils from other plant sources are also made.

EXPERIMENTAL

Collection of seeds and identification

Trichilia emetica seeds were purchased from local market Tepi, South-west of Ethiopia. The plant was identified and authenticated by Ethiopian institute of agricultural research Tepi national spice research center, Tepi, Ethiopia. Seeds were obtained by removing/ breaking/ external cover manually (Fig. 1 & 2). These seeds samples were

* To whom all correspondence should be sent:
E-mail: buzeadinew@gmail.com

cleaned with water to remove the impurities and stored in chemistry laboratory for further analysis.



Fig. 1. *Trichilia emetica* seed before removing the husk (Directly collected from local market)



Fig. 2. *Trichilia emetica* seed after removed the external cover, cleaned with water & dried

Extraction of seed oil

A known weight of the seeds was grounded into powder using an electrical coffee mill grinder machine (Nima, Japan) to increase surface area for oil extraction processes. Thereafter oil was extracted from this *Trichilia emetica* seeds powder with n-hexane using a soxhlet extractor. The solvent (hexane) and oil are separated using distillation at a temperature of slightly higher than the boiling temperature of hexane, which is recovered again for further extraction with fresh hexane (Fig.3). The oil was stored in the chemistry laboratory room for physico- chemical properties analysis.

Determination of the Physicochemical Properties of the Oil

Standard methods were used to determine the physical and chemical properties of the oil, which includes the kinematic viscosity, peroxide value, iodine value, acid value, insoluble impurity, saponification value, un saponification value, refractive index and moisture content [13]. All tests were performed in triplicate and average experimental results evaluated.

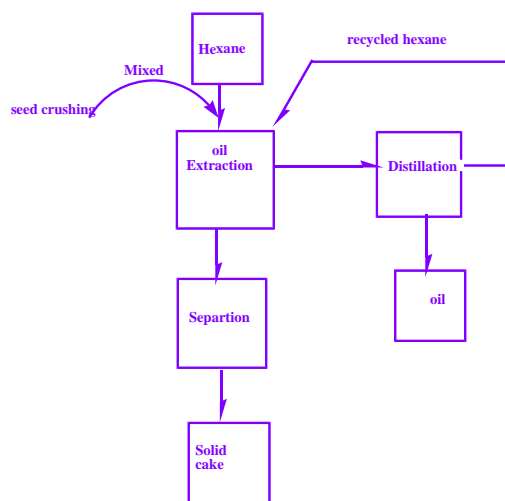


Figure 3 Oil extraction flow chart using hexane solvent

RESULTS AND DISCUSSION

Table 1 present the physicochemical properties of *Trichilia emetica* seeds oil. The oil extracted from *Trichilia emetica* seeds has yellow color; solid at room temperature and agreeable odor. The oil content of *Trichilia emetica* seed in the present study was found to be (65.81%) which exceed that of some common edible oils such as cottonseed (22-24%), safflower (30-35%), soybean (18- 22%), rapeseed (40-48%), and olive (12- 50%) and unconventional oilseeds such as canarium *schwenfurthii* fruits (36.1%) and *Balanites aegyptiaca* almonds (48.3%) [4]. Therefore, the *Trichilia emetica* seed can be considered as a potential source of vegetable oil for domestic and industrial purposes. Moisture content is another important quality characteristic for oils and fats. It is desirable to keep the moisture content low as it will increase the shelf life by preventing oxidation and rancidity processes. The moisture content of the oil is very low (4.81) compared with soybean seed oil (8.1), cotton seed oil (9.9), mustard seed oil (8.5) and linseed oil (6.5) and results shows that can be stored for a long time. *Trichilia emetica* seed oil has low iodine value (60.15) as compared with some conventional edible oils such as mustard seed oil (108), sunflower seed oil (128), linseed oil (174) and almond seed oil (96). But the IV of the present study was higher than some conventional edible oil like soybean seed oil (1.08), coconut oil (8.4), and cashew seed oil 41.3 [5]. The iodine value obtained is less than <100 suggesting the absence of unsaturated fatty acids and this places the oil in the non-drying groups.

Table 1. Physicochemical characteristics of the *Trichilia emetica* seed oil

Parameter	Value
Kinematic viscosity (mm ² /s)	49.854
Moisture & Volatile Matter (%)	4.81
Insoluble Impurity (%)	0.14
Peroxide Value	0.56
Acid Value (mgKOH/g)	8.13
Iodine Value (mgKOH/g)	60.15
Saponification Value (mgKOH/g)	180.09
Unsaponifiable Matter	1.79
Refractive Index	1.47
State at room temperature	Solid
Color	Yellow

The saponification value (180.09) obtained for *Trichilia emetica* seed oil is slightly lower than those of the common oils such as soybean (189-195), Peanut (187 - 196) and cotton seed oil (189-198) [6]. But the SV of *Trichilia emetica* seed oil is higher than Mustard Seed Oil (174), *Persea gratesima* seed oil (106), *Telferia occidentalis* seed oil (158). The relatively high saponification value recorded for *Trichilia emetica* the seed oils is indicative that they have potential for use in the industry. The peroxide values (PV) of the present studied oil is low (0.56) compared to the maximum acceptable value 10meq KOH/g set by the Codex Alimentarius Commission for groundnut seed. The low values of PV are indicative of low levels of oxidative rancidity of the oils and also suggest strong presence or high levels of antioxidant. The oil is thus stable and would not easily go rancid. Refractive index is used by most processors to measure the change in unsaturation as the fat or oil is hydrogenated.

The refractive index of oils depends on their molecular weight, fatty acid chain length, degree of unsaturation, and degree of conjugation [7]. The *Trichilia emetica* seed oil showed a refractive index of 1.47, which was similar to Linseed Oil (1.4736), Sunflower Seed Oil (1.4672) and Soybean Seed Oil (1.4658) seed oils. Pure oils have marked ranges of refractive index and density; thus, the degree of variation of typical oil from its true values may indicate its relative purity.

Acid value is an important index of physicochemical property of oil which is used to indicate the quality, age, edibility and suitability of oil for use in industries such as paint. The higher acid value of the *Trichilia emetica* seed oil when compared with that of soybean oil suggests that the *Trichilia emetica* seed oil is more susceptible to lipase action. This value (8.13KOH mg/g) for the *Trichilia emetica* seed oil is higher than the 0.6 mg/g proposed for edible vegetable oil [8]. The

higher acid value of *Trichilia emetica* seed oil is due to the presence of free fatty acid in the oil. The seed oil requires refining to minimize their acidity before to envisage eventual food use.

The unsaponifiable matter obtained in this study was 1.47% however higher than those of other oils such as *cannarium schweinfuhil* Engl (1.3%), sesame (1.2%), white melon (1.1%), corn oil (0.92%), palm kernel oil (0.22%), coco kernel oil (0.09%), rubber seed oil (0.7%) and castor seed oil (0.5%) [9].

CONCLUSIONS

The seed of *trichilia emetica* contains high level of oil, with a value of 65.81% (w/w). The value compares well with oil content of seed oils such as cottonseed, safflower, soybean and olive oil. The physico-chemical properties of *trichilia emetica* seeds oil viz., iodine value, peroxide value, saponification value, acid value, kinematic viscosity, refractive index, unsaponifiable matter have been studied for their domestic and commercial applications. The color of the oil was yellow and it was solid at room temperature. High saponification value (180.09mgKOH/Kg) guarantees for a variety of industrial applications such as cosmetics and soap making. The acid value of the *trichilia emetica* seeds is higher than the maximum permissible acid level of 4 mg KOH/g fat or oil required for edible virgin fats and oils and therefore it is necessary to purify the oil to make suitable for consumption. However the oil recorded low iodine values suggesting *trichilia emetica* seeds oil is highly saturated and may not be susceptible to rancidity. This study shows that, *trichilia emetica* seeds oil is a good source of edible oil for the local community after purification.

REFERENCES

1. E. Palmer, N. Pitman, *Trees of Southern Africa*. Capetown. A.A. Balkemen, 1972, p.235
2. M.D. Rauken, R.C. Kill, *Fats and Fatty Foods*. In Rauken, M.D. and Kill, R. C (Eds.). *Food Industry Manual*, London: Longmans, 1993, p. 288-327.
3. AOAC. *Official Methods of Analysis of the Association of Official Analytical Chemists 15th ed*, Association of Official Analytical Chemists Washington DC, 1990.
4. J.M. Nzikou, M. Mvoula-Tsieri, E. Matouba, J.M. Ouamba, C. Kapseu, M. Parmentier, S. Desobry., *Afr. J. Biotechn.*, **5**, 2469 (2006).
5. T.F. Akinhanmi, V.N. Atasie, P.O. Akintokun, *J. Agric. Food Environ.*, **2**, 1 (2008).
6. Codex Alimentarius Commission. *Graisses huiles vegetables*, Division 11, version abregée FAO/WHO Codex Stan 20 -1981, 23 (1993).

7. A.B. Roger, R.A. Rebecca, A. Georges, I.O. Mathias, *Eur. J. Sci. Res.*, **391**, 514 (2010).

8. E.U. Usoro, E. Suyamsothy, G. A. Sani, Manual of chemical methods of food analysis. Bencox International Ltd. Lagos, Nigeria. 1982.

9. J. E. Asuquo, PhD Thesis, University of Port Harcourt. Nigeria, 2008.

ФИЗИКО-ХИМИЧНИ СВОЙСТВА НА МАСЛОДАЙНИ СЕМЕНА ОТ *TRICHILIA* ЕМЕТИСА И СРАВНЯВАНЕ С НЯКОИ ИЗБРАНИ РАСТИТЕЛНИ МАСЛА

Б. Адиню

Катедра по химия, Университет Мизан-Тепи, Тепи, Етиопия

Постъпила на 4 април, 2013 г.; коригирана на 9 август, 2013 г.

(Резюме)

Физико-химичните свойства на семена от *trichilia emetica* са изследвани за техните битови и търговски приложения. Маслото е с жълт цвят и е твърдо вещество при стайна температура. Семената имат добър добив на масло от 65,81%, който е сравним с добива на масло на някои избрани търговски растителни масла като памучно, шафран, соя и зехтин. Стойността по йод ($60.15 \text{mgI}_2/100\text{g}$), стойността по пероксид ($0.56 \text{mgO}_2/\text{g}$), стойност на осапуняване (180.09mgKOH/g), киселинната стойност (8.13mgKOH/g), кинематичен вискозитет ($49.85 \text{mm}^2/\text{s}$), индекса на пречупване (1.47) и неосапуняемата материя (1.79) на маслото бяха определени по АОАС. Високата стойност на осапуняване гарантира използването на маслата в козметиката и сапунената индустрията. Киселинната стойност на еметиса семена *trichilia* е по-висока от максимално допустимата стойност от 4mgKOH/g мазнини или масло, необходимо за ядливи прясно пресовани мазнини и масла и поради това е необходимо маслото да се пречисти за да се направи подходящо за консумация. Въпреки това регистрираните ниски стойности по йод, предполагат, че е силно наситено и не може да бъде податливо на гранясване. Това проучване показва, че маслото от семена на *trichilia emetica* е добър източник на хранителни масла за местната общност след пречистване.

Biodiesel production from *Trichilia emetica* seeds using in-situ transesterification

B. Adinew

Department of chemistry, Mizan-Tepi University, Tepi campus, Ethiopia, East Africa.

Received April 8, 2013; Revised August 9, 2013

The main purpose of this research work was production of biodiesel from trichilia emetic seeds by in-situ transesterification. The process was studied at reaction temperature 80°C and reaction time 100min. The physico-chemical parameters of the biodiesel were checked by ASTM D 6751 standards. In this study, copper strip corrosion, kinematic viscosity, cloud point, ash content have 1a, 5.44mm²/s, 18°C and 0.062% respectively. These values satisfy the quality criteria of biodiesel set by ASTM D6751. However, the flash point and the acid values of biodiesel don't meet the quality criteria set by ASTM D6751, due to the presence of unreacted (residual) alcohol and residual mineral acids from the production process respectively. In other words, 60% the physico-chemical properties of the biodiesel satisfies the quality criteria set by ASTM D6751 and pretreatment of the seeds is necessary to increases the quality of biodiesel.

Keywords: Biodiesel, in-situ transesterification, trichilia emetica seeds, physico-chemical parameters

INTRODUCTION

Biodiesel obtained from vegetable oil can be used as conventional diesel in diesel engines, because its properties are very close to petroleum diesel. For example, biodiesel has the proper viscosity; high flash point; high cetane number and no engine modification are required when using biodiesel [1]. Several biodiesel production methods have been developed, among which in-situ transesterification in the preference of alkali catalyst gives high level of conversion of triglycerides to their corresponding methyl ester in short reaction time. The process of in-situ transesterification is affected by the reaction condition: molar ratio of alcohol to oil; type of alcohol; type and amount of catalysts; reaction temperature and pressure; reaction time and contents of free fatty acids; particle size and water in oils or fats [2]. In-situ transesterification is the direct transesterification of ground oil bearing materials instead of purified oils with alcohol and catalyst, to produce alkyl fatty acid esters. The efficiency or yield of in-situ transesterification is defined as the percentage of biodiesel-rich phase over oil content in raw material which is determined by hexane soxhlet extraction.

Biodiesel has a higher cetane number than petroleum diesel fuel, no aromatics, and contains 10-11 % oxygen by weight. These characteristics of biodiesel reduce the emissions of carbon monoxide, hydrocarbons, and particulate matter in the exhaust

gas compared with diesel fuel. However, NO_x emissions of biodiesel increase, because of combustion and some fuel characteristics' [3]. Biodiesel has been mainly produced from edible vegetables oils all over the world. More than 95% of global biodiesel production is made from edible vegetable oils. The largest biodiesel producers were the European Union, the United States, Brazil, Indonesia, with a combined use of edible oil for biodiesel production of about 8.6 million tons in 2007 compared to global edible oil production of 132 million tons [4]. Rapeseed and sunflower oils are used in EU, palm oil predominates in biodiesel production in tropical countries, and soybean oil is the major feedstock in the United States [5].

The preparation of biodiesel from various vegetable oils based on alkaline transesterification of triglycerides with polyhydric alcohol has been studied for several decades, and a major amount of industrial production has been achieved with this method [6]. However, the transformation of jatropha seed in oil industry requires extra steps during the extraction and refining processes. As the cost of the vegetable oil production contributes to approximately 70% of the biodiesel production cost [7], there is a need for the development of a new biodiesel production process that is simple, compact, efficient, low-cost, and that consumes less energy. On the other hand, the preparation of biodiesel based on in situ transesterification has been successfully carried out from various oilseeds [8]. In situ transesterification is a biodiesel production method that uses the original agricultural products as the source of triglycerides

* To whom all correspondence should be sent:
E-mail: buzeadinew@gmail.com

instead of purified oil for direct transesterification, and it works virtually with any lipid-bearing material. It can reduce the long production system associated with pre-extracted oil, and it maximizes ester yield. The objective of this study was to investigate the in situ transesterification allowing producing directly biodiesel from *trichilia emetica* seed and evaluate the properties of biodiesel by ASTM D6751.

Experimental Materials

The major feedstock used in this work was *Trichilia emetica* seeds, locally available in Ethiopia. It was purchased at the local market in Tepi, South-west of Ethiopia and cleaned with tap water to remove impurities (Fig. 1 & 2).



Fig. 1. *Trichilia* seed before removing the husk (Directly collected from local market)



Fig. 2. *Trichilia* seed after removed the external cover, cleaned with water & dried

By the stoichiometric equation of the process, 1 mol of *Trichilia emetica* seeds is required to react with 3 moles of butanol to produce 3 moles of the biodiesel and 1 mole of glycerol. 100g *Trichilia emetica* seeds were used for the in-situ transesterification process. Reaction temperature for the process must be below the boiling point of alcohol used. The butanol used, manufactured by Aldrich Chemicals Co. Ltd, England has a boiling

point of 117°C; therefore, a reaction temperature of 80°C was selected. Different researchers have reported different reaction times for in-situ transesterification process as well as the entire biodiesel production process. The reported reaction time ranges from less than 30 minutes to more than 2 hours. Reaction time of 100 minutes was therefore selected. KOH used was manufactured by Aldrich Chemicals Co. Ltd, England.

Experimental Procedures

Potassium Butoxide Production

1000.0g of butanol was measured and poured into a plastic container a funnel and the lid of the butanol container was tightly replaced. 4.0g of KOH was carefully added to the plastic container via a second funnel. The bung and the screw on the cap were replaced tightly. The container was shake a few (about ten) times by swirling round thoroughly for about 2 minutes until the KOH completely dissolved in the butanol, forming potassium butoxide (Fig. 3).

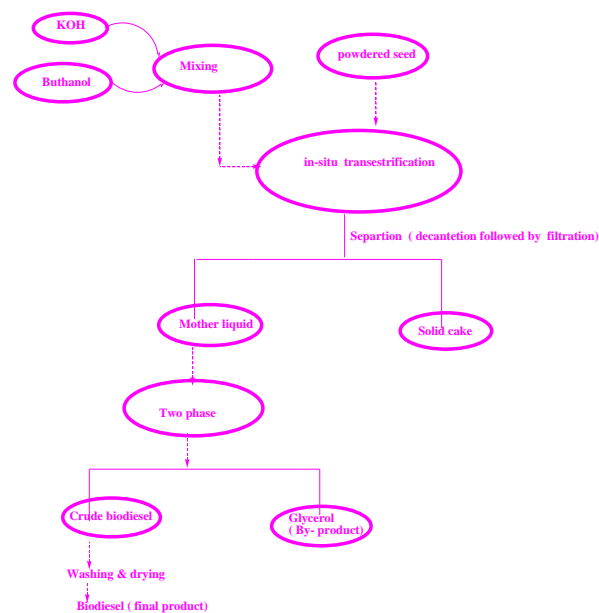


Fig. 3. Flow chart of biodiesel production and purification processes.

In-situ transesterification reaction

100.0g of *Trichilia emetica* seeds powder was measured out in a beaker, pre-heated to the required temperature (80°C) and poured into the blender. With the blender still switched off, the prepared potassium butoxide from the plastic container was carefully poured into the *Trichilia emetica* seeds. The mixture was left to blend for the 100minutes at moderate speed before the blender was switched off. Detail information of in-situ transesterification reaction was presented in Fig. 3.

Settling

The mixture was poured from the blender into a 250ml separator funnel for settling and the lid was screwed on tightly. The reaction mixture was allowed to stand overnight while phase separation occurred by gravity settling into biodiesel on the top and glycerol at the bottom of the bottle (Fig.4). The next day, the *Trichilia emetica* seeds biodiesel/ester at the top was carefully decanted into a volumetric flask leaving the glycerol at the base.

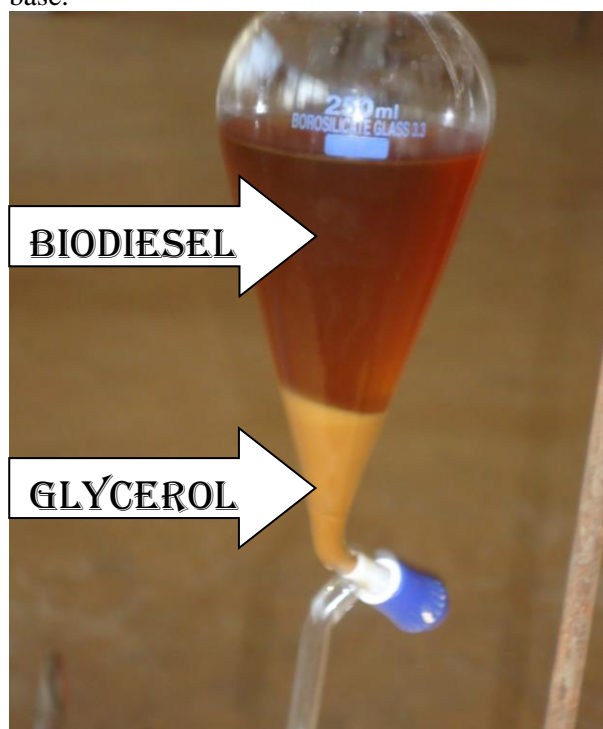


Fig. 4. Phase separation stage (biodiesel from glycerol)

Washing and purification

When biodiesel was first made it was quite caustic with a pH of between 8.0 and 9.0. Washing with water neutralized the product. Traces of butanol along with the catalyst were washed with hot water (45°C) and 0.1% phosphoric acid solution. Since biodiesel has a lower specific gravity than water, the water was sinking to the bottom and the biodiesel was remaining over the water.

After about 40 min the butanol has boiled off to remove the unreacted alcohol then dried with anhydrous MgSO₄ to get rid of any water (Fig. 5).

Biodiesel yield

The biodiesel yield (% wt) after the post-treatment stage, relative to the amount of *Trichilia emetica* seeds poured into the reactor, was calculated from the butyl ester and weights of seeds.

$$\text{Biodieselyield} = \frac{\text{Massofbutylester}}{\text{Massofseedspowder}} \times 100$$

Biodiesel quality analysis

The pure biodiesel obtained through the above procedure gave the ester yield, measured on weight basis. The experiment was replicated three times and average experimental parameters recorded. ASTM D6751 standard fuel characterization was subsequently carried out on the *Trichilia emetica* seeds biodiesel. The physico-chemical properties of biodiesel such as kinematic viscosity (ASTM D445); flash point (ASTM D93); cloud point (ASTM D2500); Conradson carbon residual (ASTM D189); copper strip corrosion ((ASTM D130); total acidity (ASTM D974) and ash content (ASTM D482) was determined by ASTM D6751 standard method [10].

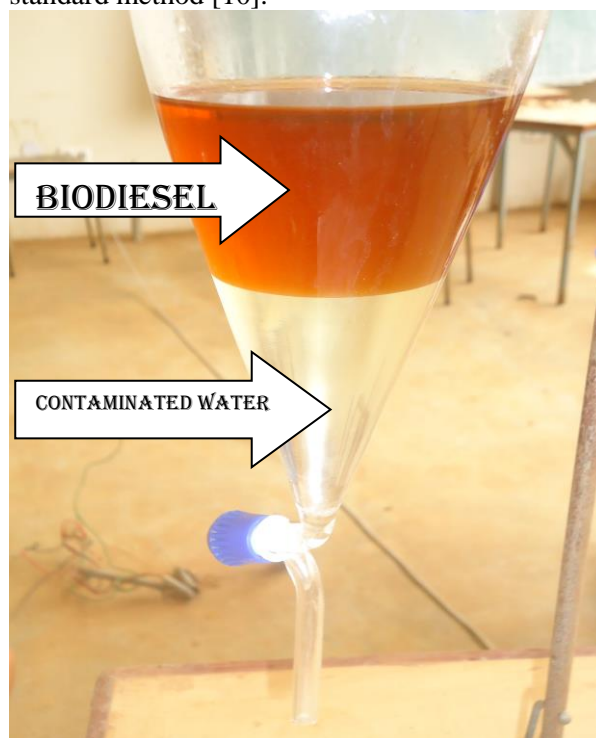


Fig. 5. Purification of biodiesel by hot distilled water (slightly acidic) to remove excess alcohol, soap, catalyst

RESULTS AND DISCUSSIONS

For the alkali-catalysed in-situ transesterification experiment conducted using the stated reaction parameters, the experiment was triplicate and average experimental results evaluated. The physico-chemical parameter of the biodiesel was characterized by Ethiopian petroleum supply enterprise laboratory, Addis Ababa, Ethiopia and the result was presented in **Table 1**. The butyl ester of *Trichilia emetica* seeds biodiesel prepared using 100g *Trichilia emetica* seeds powder, 1000.0g butanol, 4.0% KOH at 80°C and 100 minutes reaction time yielded 84.0g *Trichilia emetica* seeds

biodiesel which is a satisfactory result and the seed is promising in the production of biodiesel in large industrial scale.

Table 1. Physico-chemical parameter of biodiesel

No	Property	Test method ,ASTM	Test ASTM 6751 limit	Biodiesel
1	Flash point (PMCC), °C	D 93	Min. 93	49
2	Cloud point, °C	D 2500	report	18
3	Kinematic viscosity, mm ² /s	D 455	Min. 1.9 Max. 6	5.44
4	Conradson carbon residue	D 189	Max.0.05	0.33
5	Total acidity, mgKOH/g	D 974	Max.0.5	6.28
6	Ash content	D 482	Max.0.02	0.062
7	Copper strip corrosion	D 130	Max.No.3	1a

Kinematic viscosity

Viscosity, the measurement of the internal flow resistance of a liquid, constitutes an intrinsic property of vegetable oils. It is of remarkable influence in the mechanism of atomization of the fuel spray. In-situ transesterification is the most common way to lower this high viscosity. From the result presented in Table 1, the viscosity of *Trichilia emetica* seeds biodiesel (5.44 mm²/s) fall within the range prescribed by ASTM D6751 standard (1.9 – 6.0) mm²/s for biodiesel [11]. This implies that the *Trichilia emetica* seeds biodiesel satisfies the fluidity requirement of an alternative biodiesel.

Copper strip corrosion

This parameter characterizes the tendency of a fuel to cause corrosion to copper, zinc and bronze parts of the engine and the storage tank. This corrosion resulting from biodiesel might be induced by some sulfur compounds and by acids, so this parameter is correlated with acid number. Some experts consider that this parameter does not provide a useful description of the quality of the fuel, as the results are unlikely to give ratings higher than class 1. In this study, the copper strip corrosion was 1a which lies in the biodiesel quality requirement criteria set by ASTM D6751 (Max.No.3). This reveals that, the biodiesel is not producing any rust on the machine engine.

Cloud Point

The cloud point is “the temperature at which a cloud of wax crystals first appears in a liquid when it is cooled down under conditions prescribed in this test method.” The cloud point is a critical factor in cold weather performance for all diesel fuels. Because of climate diversity in different places, the American and European standard, haven’t set any limitations for flow properties. The saturated fatty acid compounds have significantly higher melting points than unsaturated fatty acid compounds [12]. In this study the cloud point of the biodiesel was

180C which is higher than that obtained for the conventional petroleum diesel.

Ash content

The Ash content or mineral content is a measure of the amount of metal contained in the fuel. From the result the ash content of biodiesel is 0.062% slightly greater than the standards. Biodiesel burnt with very low smoke. This implies that biodiesel emissions from exhaust of vehicles will help reduce the pollution introduced to the atmosphere.

Carbon residue

The parameter serves as a measure for the tendency of a fuel sample to produce deposits on injector tips and inside the combustion chamber when used as automotive fuel. It is considered as one of the most important biodiesel quality criteria, as it is linked with many other parameters. So for biodiesel, carbon residue correlates with the respective amounts of glycerides, free fatty acids, soaps and remaining catalyst or contaminants [12]. The carbon residue of the biodiesel 0.33% was higher compared to 0.050max documented. This could be due to the contaminant which might have entered the sample during the heating in the production of biodiesel and the presence of small amount of glycerol left in the final product.

Acid value

Acid value or neutralization number is a measure of free fatty acids contained in a fresh fuel sample and of free fatty acids and acids from degradation in aged samples. The acid value of the present study was 6.28mgKOH/g which is higher than with the ASTM D6751 standards. The acidic compounds that could possibly be found in biodiesel are: 1) residual mineral acids from the production process, 2) residual free fatty acid from the hydrolysis process or the post- hydrolysis process of the esters and 3) oxidation byproducts in the form of other organic acids. Therefore, the

trichilia emetica seeds need acid pretreatment before using for the production of biodiesel.

Flash point

In general, the flash point value specified by the quality standards is relatively high, for safety reasons regarding storage and transport and also to ensure that the alcohol is removed from the finished product. Low flash points may indicate alcohol residue in biodiesel. The flash point for the biodiesel obtained in this study was 490C which is lower than the minimum requirement set by ASTM D6751. This is due the presence of residual alcohol left in the biodiesel during drying processes.

Conclusion

This study has shown that most of the physico-chemical properties evaluated for the biodiesel conform to the ASTM D 6751 standard values. It could be concluded from this study that the biodiesel produced from trichilia emetica seed using in-situ transesterification is a potential replacement for fossil diesel and effective usage of biodiesel will help to reduce the cost of protecting the atmosphere from the hazards in using fossil diesel and hence will boost the economy of the country.

REFERENCES

1. K. Noiroj, P. Intrapong, A. Luengnaruemitchai, *Renew Energy*, 1145 (2009).
2. M. Balat, Potential alternatives to edible oils for biodiesel production- A review of current work. *Energy Conversion Management*, 1479 (2011).
3. M. Canakci, A. Erdil, E. Arcaklioglu, *Applied Energy*, 594 (2006).
4. M. Balat, H. Balat, *Applied Energy*, 1815 (2010).
5. G. Pahl, *Biodiesel: growing a new energy economy*. Vermont (USA): Chelsea Green Publishing Company, 2008.
6. F. Ma, *Bioresource Technol.* **70**, 1 (1999).
7. M.J. Haas, *J. Am. Oil Chem. Soc.* **81**, 83 (2004).
8. K.G. Georgogianni, *Energy Fuel.* **22**, 2120 (2008).
9. A. Demirbas, *Biodiesel: a realistic fuel alternative for diesel engines*. London: Springer, 2008.
10. ASTM Standard D 6751, Standard specification for biodiesel fuel blend stock (B100) for middle distillatefuels. West Conshohocken, PA: ASTM International (2007).
11. G. Knothe, K.S. Steidly, Kinematic viscosity of biodiesel fuel component and related compounds: Influence of compound structure and comparison to petro diesel fuel components. *Fuel*. Elsevier, 1059 (2005).
12. M. Mittelbach, P. Tritthart, *J. Am. Oil Chem. Soc.* **65**, 1185 (1988).

ПОЛУЧАВАНЕ НА БИОДИЗЕЛ ОТ СЕМЕНА НА *TRICHILIA EMETICA* ЧРЕЗ *IN-SITU* ТРАНСЕСТЕРИФИКАЦИЯ

Б. Адиню

Катедра по химия, Университет Мизан-Тепи, Тепи, Етиопия

Постъпила на 8 април, 2013 г.; коригирана на 9 август, 2013 г.

(Резюме)

Основната цел на тази изследователска работа бе производството на биодизел от семена на *trichilia emetica* чрез in-situ трансестерификация. Процесът е изследван при реакционна температура 80 °C и време за реакция 100min. Физико-химичните параметри на биодизела са били проверени чрез ASTM D 6751 стандарти. В това проучване, корозията на медна пластина, кинематичния вискозитет, точката на помътняване, пепелно съдържание имат стойности 1a, 5.44 mm²/s, 180C и 0.062% съответно. Тези стойности отговарят на критериите за качество на биодизел, определени чрез ASTM D6751. Въпреки това, точката на възпламеняване и киселинните стойности на биодизел не отговарят на критериите за качество, определени от ASTM D6751, което се дължи на присъствието на нереагирал (остатъчен) алкохол и остатъчни минерални киселини от производствения процес, съответно. С други думи, 60% от физико-химичните свойства на биодизела отговарят на критериите за качество, определени от ASTM D6751 и е необходимо предварително третиране на семената, за да се повишава качеството на биодизела.

Polymetallic complexes part CIV synthesis, characterization and potential antibacterial study of dimeric & tetrameric complexes of Co(II), Ni(II) Cu(II), Zn(II), Cd(II) and Hg(II) with azodye ligands

B. B. Mahapatra^{1*}, S. N. Dehury², S. N. Chaulia³

^{1,2} Department of Chemistry, G.M. Autonomous College, Sambalpur – 768004, Odisha, (India)

³ Department of Chemistry, Govt. College, Koraput, Odisha.(India)

Received April 15, 2013; Revised July 3, 2013

Six complexes of Co(II), Ni(II), Cu(II), Zn(II), Cd(II) and Hg(II) with one tetradentate azodye ligand and six complexes of above metal ions with one octadentate azodye ligand have been synthesized. All the twelve complexes have been characterised by analytical, conductance, magnetic susceptibility, IR, electronic spectra, E.S.R., NMR, thermogravimetric analysis and XRD powder pattern spectra. In addition to this molecular modelling study of the ligands and complexes has been made. The Co(II) and Ni(II) complexes are found to be octahedral, Cu(II) complexes are distorted octahedral and a tetrahedral stereochemistry has been assigned to Zn(II), Cd(II) and Hg(II) complexes. The antibacterial study of the ligands and six complexes is made against gram-positive bacteria *Staphylococcus aureus* and gram-negative bacteria *Escherichia coli*.

Keywords: Polymetallic complexes, Azodye complexes.

INTRODUCTION

The study of polymetallic complexes containing Polydentate(tetra-, hexa- and octadentate) azodye ligands is of recent interest. Besides chemotherapeutic properties[1], azodyes also possess the property of an indicator and hence are used in chemical laboratories. They also find application in dyeing food stuffs and as preservative for food grains[2]. In continuation of our previous work on the study of with the Pharmacological activities of the azodyes and their complexes[3], we report here the preparation of one (bis-bidentate) Fig. 1 and one (bis-tetradentate) Fig. 2 azodye ligands and their twelve dimeric and tetrameric metal complexes.

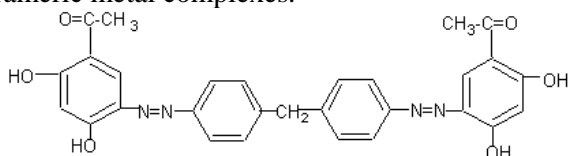


Fig. 1. LH₂ (4,4'-bis(2'-hydroxynaphtholato)diphenyl-ether)

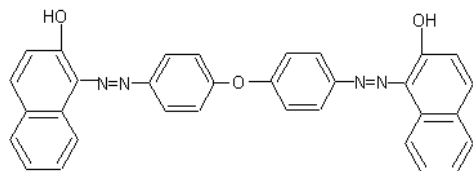


Fig. 2. LH₄ (4,4'-bis(2',4'-dihydroxyacylphenylazo)diphenylmethane)

EXPERIMENTAL

Elemental analysis (C, H, N) were carried out on elemental analyser Perkin Elmer 2400 while metals were determined by EDTA after decomposing the complexes with conc. Nitric acid. All the chemicals were of AR or SRL grade. The chlorine contents were estimated by standard methods. Conductance measurements of the complexes were made using Toshniwal CL 01-06 Conductivity Bridge. The magnetic susceptibility measurements were made at RT by Gouy method using [HgCo(SCN)₄] as calibrant. IR spectra (KBr) were recorded using IFS 660 spectrophotometer, electronic spectra (in DMF) using Hilger-Watt Uv-vis peck spectrophotometer, ESR of the Copper complexes were recorded on an EU- spectrometer, NMR on a Jeol GSX 400 with CDCl₃ and DMSO as solvent and TMS as internal standard and X-ray diffraction (Powder Pattern) of the complex was recorded on a Phillips PW 1130 diffractometer(Cu K α raditions, $\lambda = 154060 \text{ \AA}$) and the generation setting of 30 MA and 40KV, the scan axis is Gonio and Start position (2θ) 10.0011. Thermal data was recorded on MRETTLER STARE SW 9.01 and Molecular modelling of the ligands and complexes was done with the help of Arguslab 4.0 software.

The antibacterial activity of two ligands and six complexes has been studied as per cup-plate method [4]. The solutions of the compounds were prepared in dimethylsulfoxide (DMSO) at 500 μgml^{-1} . The bacterial strains are inoculated into 100

* To whom all correspondence should be sent:
E-mail: mahapatra.bipin@yahoo.com*

ml of the sterile nutrient broth and incubated at 37 ± 1 °C for 24 hours. The density of the bacterial suspension was standardized by Mc Farland method. Well of uniform diameter (6 mm) were made on agar plates after inoculating them separately with the test organisms aseptically. The standard drug and the test compounds were introduced with the help of micropipette and the plates were placed in the refrigerator at 8-10 °C for proper diffusion of drug into the media. After two hours of cold incubation, the petri-plates were transferred to incubator and maintained at 37 ± 2 °C for 18-24 hours. Then the petriplates were observed for zone of inhibition by using vernier scale. The results are reported by comparing the zone of inhibition shown by the test compounds with the standard drug Tetracycline. The results are the mean value of zone of inhibition of three sets measured in millimeter.

Preparation of the Ligands

The azodyes were prepared by the coupling reaction of the diazonium chlorides obtained from 4,4/-diaminodiphenylether (0.01 mol 2.0 gm) and 4,4/-diaminodiphenyl methane (0.01 mol, 1.98 gm) with alkaline solution of β - naphthol (0.02 mol , 3.36 gm) and 2,4-dihydroxyacetophenone (0.02 mol, 3.96 g.) respectively at 0 to 5 °C.

Preparation of the complexes

The metal chlorides in ethanol were mixed separately with ethanolic solution of the ligands with LH₂ and L/H₄ in 2:1 and 4:1 molar ratio respectively. The resulting solutions were heated to 50-60 °C for about 1 hour on a heating mantle. The solution was then cooled down to room temperature and the pH was raised to ~ 7 by adding concentrated ammonia drop by drop with stirring. The solid complexes thus formed were then washed with ethanol followed by ether and dried in vacuum (Fig 3 and Fig 4).

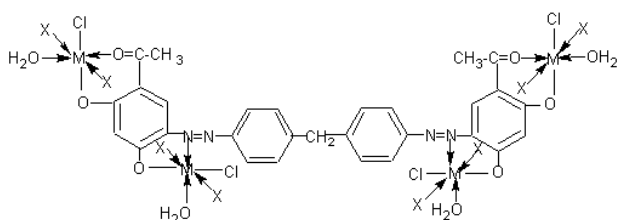


Fig. 3. Proposed Geometry of Co(II), Ni(II), Cu(II), Zn(II), Cd(II) and Hg(II) complexes with LH₂. . (Where $x = \text{H}_2\text{O}$ for CO^{II}, Ni^{II}, Cu^{II}, $X=0$ for Zn^{II}, Cd^{II}, Hg^{II})

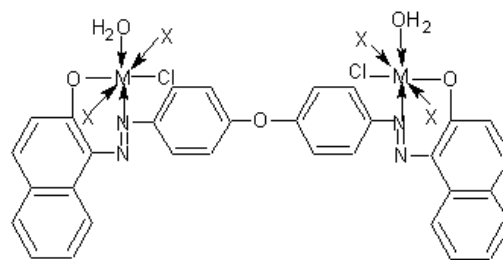


Fig.4. Proposed Geometry of Co(II), Ni(II), Cu(II), Zn(II), Cd(II) and Hg(II) complexes with L/H₄. (Where $x = \text{H}_2\text{O}$ for CO^{II}, Ni^{II}, Cu^{II}, $X=0$ for Zn^{II}, Cd^{II}, Hg^{II})

RESULTS AND DISCUSSION

The elemental analysis data agree well with the following compositions of the metal complexes reported (Table 1), have the compositions [M₂LCl₂(H₂O)₆], [M¹₂LCl₂(H₂O)₂], [M₄L/Cl₄(H₂O)₁₂] and [M¹₄L/Cl₄(H₂O)₄] where M = Co(II), Ni(II), Cu(II); M¹ = Zn(II), Cd(II), Hg(II), LH₂ = C₃₂H₂₂O₃N₄ and L/H₄=C₂₉H₂₄O₆N₄. All the complexes were amorphous in nature, have high melting points and were insoluble in common organic solvents but soluble in dimethylformamide and dimethylsulfoxide. The non-electrolytic nature of the complexes were indicated by the low conductance values (3.5 – 4.8 Ω⁻¹ cm² mol⁻¹) in DMF [5].

IR spectra

In the IR spectra(Table 1)of the ligands, show broad bands were observed at 3445 cm⁻¹ (LH₂) and at 3445 cm⁻¹ (L'H₄) which may be assigned to the stretching vibrations of naphtholic and phenolic -OH group. The broadness of these bands may be the O-H...N and O-H...O intramolecular Hydrogen bonding between naphtholic/phenolic Hydrogen atom with azo N and Carbonyl O atom. The bands at 1490 cm⁻¹ ((LH₂) and 1470 (L'H₄) can be attributed to phenolic C - O vibration and in the metal chelates these bands appear at ~ 1465 - 1471 cm⁻¹ indicating the bonding of phenolic/naphtholic oxygen atoms of the ligands to the metal ions[6]. The sharp bands of the ligands at 1621 cm⁻¹ (L'H₂) and at 1606 cm⁻¹ (L'H₄) can be attributed to ν (N=N) vibration and in the metal chelates these bands are shown at 1614 cm⁻¹ with the former ligand and at ~1594 - 1599 cm⁻¹ with the latter ligand which indicates the coordination of one of the azo nitrogen atoms ions [7]. In the ligand (L'H₄) a sharp band appears at 1635 cm⁻¹ which can be attributed to ν (>C=O) vibration and in the metal chelates it appears at ~1588 cm⁻¹ indicating the bonding of the carbonyl oxygen atom to the metal ions. In the metal complexes, broad bands appear at 3172-3434 cm⁻¹ followed by sharp peaks at 825 -

Table 1. Analytical data of the Ligands and the Complexes

Compound	M.P.	Colour	Found/(Calcd.), %				
			C	Cl	H	N	M
LH ₂	90	Deep red	77.1/(77.4)		3.63/(3.94)	10.01/(10.03)	
L'H ₄	75	Reddish brown	66.01/(66.41)		4.14/(4.65)	10.65/(10.68)	
[Co ₂ LCl ₂ (H ₂ O) ₆]	>240	Red	50.24/(50.64)	8.2/(8.3)	3.35/(3.75)	6.4/(6.5)	13.5/(13.8)
[Co ₄ L'Cl ₄ (H ₂ O) ₁₂]	>240	Brick red	31.1/(31.3)	12.4/(12.7)	3.92/(3.96)	4.7/(5.0)	20.8/(21.1)
[Ni ₂ LCl ₂ (H ₂ O) ₆]	>240	Coffee	50.64/(50.68)	8.1/(8.3)	3.73/(3.75)	6.3/(6.5)	13.5/(13.7)
[Ni ₄ L'Cl ₄ (H ₂ O) ₁₂]	>240	Bright red	31.38/(31.12)	12.6/(12.7)	3.93/(3.96)	4.9/(5.0)	20.8/(21.1)
[Cu ₂ LCl ₂ (H ₂ O) ₆]	>240	Light green	50.09/(50.11)	8.1/(8.3)	3.69/(3.71)	6.3/(6.4)	14.5/(14.7)
[Cu ₄ L'Cl ₄ (H ₂ O) ₁₂]	>240	Brown	30.55/(30.85)	12.3/(12.5)	3.6/(3.7)	4.7/(4.9)	21.1/(21.4)
[Zn ₂ LCl ₂ (H ₂ O) ₂]	>240	Darck brown	54.21/(53.93)	6.8/(7.01)	2.93/(3.02)	5.4/(5.53)	25.6/(25.83)
[Zn ₄ L'Cl ₄ (H ₂ O) ₄]	>240	Light red	34.89/(35.09)	8.7/(8.9)	2.53/(2.82)	5.4/(5.6)	26.1/(26.2)
[Cd ₂ LCl ₂ (H ₂ O) ₂]	>240	Coffee	48.64/(48.65)	7.7/(7.9)	2.55/(2.70)	6.1/(6.3)	(25.3)
[Cd ₄ L'Cl ₄ (H ₂ O) ₄]	>240	Brown	28.88/(29.50)	11.7/(11.9)	2.11/(2.37)	4.7/(4.9)	37.5/(37.6)
[Hg ₂ LCl ₂ (H ₂ O) ₂]	>240	Red	40.64/(40.69)	6.5/(6.6)	2.01/(2.25)	5.1/(5.2)	37.5/(37.6)
[Hg ₄ L'Cl ₄ (H ₂ O) ₄]	>240	Red	22.67 (22.71)	9.0/(9.2)	1.67/(1.82)	3.5/(3.6)	52.1/(52.2)

844 cm⁻¹ and 731 – 749 cm⁻¹ assignable OH stretching, rocking and wagging vibrations respectively indicating the presence of coordinated water molecules in the complexes [8]. The conclusive evidence of bonding of the ligands to the metal ions is proved by the appearance of bands at ~ 503 – 518 cm⁻¹ (M-O) and at ~454 - 457 cm⁻¹ (M-N) [9].

Electronic spectra and Magnetic measurements

In the electronic spectra (Table 2) of Co(II) complexes, four bands appear at 8150(8182) cm⁻¹, 16350(16550) cm⁻¹ and 19765(19950) cm⁻¹ and 31550(32460) cm⁻¹. The first three band assigned to 4T_{1g}(F) → 4T_{2g}(F)(v₁), 4T_{1g}(F) → 4A_{2g}(F)(v₂), 4T_{1g}(F) → 4T_{1g}(P)(v₃) respectively and 4th band is CT band. The ligand field parameters like

Dq = 820 (836.8) cm⁻¹, B = 777.6 (796.9) cm⁻¹, β₃₅ = 0.743(0.757) cm⁻¹ v₂/v₁ = 2.006(2.02) and σ = 25(21.95) suggest the octahedral configuration for the complexes [10]. In the electronic spectra of Ni(II) complexes four bands appear at 10120 (10135) cm⁻¹, 16920(17150) cm⁻¹, 24820(24995) cm⁻¹ and 31340(32160) cm⁻¹. The first three bands can be assigned to 3A_{2g}(F) → 3T_{2g}(F)(v₁), 3A_{2g}(F) → 3T_{1g}(F)(v₂), 3A_{2g}(F) → 3T_{1g}(P)(v₃) transitions respectively and the fourth band is assigned to a CT band. The ligand field parameters like Dq = 1012 (1013.5) cm⁻¹, B = 758.6 (782.6) cm⁻¹, β₃₅ = 0.728 (0.751) cm⁻¹, v₂/v₁ = 1.67 (1.69) and σ = 37.3(31.1) suggest an octahedral geometry for the complexes.

Table 2. IR spectral Data of the ligands and the complexes, v/cm⁻¹

Compound	v/cm ⁻¹				
	(C-O)	(-N=N-)	(C=O)	(M-O)	(M-N)
LH ₂	1490	1621	-	-	-
L'H ₄	1470	1606	1635	-	-
[Co ₂ LCl ₂ (H ₂ O) ₆]	1489	1613	-	518	457
[Co ₄ L'Cl ₄ (H ₂ O) ₁₂]	1465	1544	1586	503	455
[Ni ₂ LCl ₂ (H ₂ O) ₆]	1471	1614	-	517	457
[Ni ₄ L'Cl ₄ (H ₂ O) ₁₂]	1467	1595	1588	505	454
[Cu ₂ LCl ₂ (H ₂ O) ₂]	1468	1614	-	515	455
[Cu ₄ L'Cl ₄ (H ₂ O) ₁₂]	1465	1598	1585	510	454
[Zn ₂ LCl ₂ (H ₂ O) ₂]	1470	1613	-	510	456
[Zn ₄ L'Cl ₄ (H ₂ O) ₄]	1467	1599	1586	505	455
[Cd ₂ LCl ₂ (H ₂ O) ₂]	1468	1613	-	512	457
[Cd ₄ L'Cl ₄ (H ₂ O) ₄]	1467	1595	1585	510	455
[Hg ₂ LCl ₂ (H ₂ O) ₂]	1470	1614	-	515	455
[Hg ₄ L'Cl ₄ (H ₂ O) ₄]	1465	1594	1587	510	454

Table 3. Magnetic and Electronic absorption data of the compounds

Compound	μ_{eff}/μ	ν/cm^{-1}	Band assignment	Geometry
[Co ₂ LCl ₂ (H ₂ O) ₆]	5.01	8150	⁴ T _{1g} (F) → ⁴ T _{2g} (F)	octahedral
		16350	⁴ T _{1g} (F) → ⁴ A _{2g} (F)	
		19765	⁴ T _{1g} (F) → ⁴ T _{1g} (P)	
		31550	INCT ^a	
[Co ₄ L/Cl ₄ (H ₂ O) ₁₂]	5.0	16550	⁴ T _{1g} (F) → ⁴ T _{2g} (F)	octahedral
		19950	⁴ T _{1g} (F) → ⁴ A _{2g} (F)	
		32460	⁴ T _{1g} (F) → ⁴ T _{1g} (P)	
			INCT ^a	
[Ni ₂ LCl ₂ (H ₂ O) ₆]	3.0	10120	³ A _{2g} (F) → ³ T _{2g} (F)	octahedral
		16920	³ A _{2g} (F) → ³ T _{1g} (F)	
		24820	³ A _{2g} (F) → ³ T _{1g} (P)	
		31340	INCT ^a	
[Ni ₄ L/Cl ₄ (H ₂ O) ₁₂]	3.1	1013	³ A _{2g} (F) → ³ T _{2g} (F)	octahedral
		17150	³ A _{2g} (F) → ³ T _{1g} (F)	
		24995	³ A _{2g} (F) → ³ T _{1g} (P)	
[Cu ₂ LCl ₂ (H ₂ O) ₂]	1.8	13350	² E _g → ² T _{2g}	Distorted octahedral
[Cu ₄ L/Cl ₄ (H ₂ O) ₁₂]	1.7	1335	² E _g → ² T _{2g}	Distorted octahedral

1012 (1013.5) cm^{-1} , $B=758.6$ (782.6) cm^{-1} , $\beta_{35}=0.728$ (0.751) cm^{-1} , $\nu_2/\nu_1 = 1.67$ (1.69) and $\sigma=37.3$ (31.1) suggest an octahedral geometry for the complexes [11]. The electronic spectra of Cu(II) complexes exhibit one broad band at $\sim 13350 - 14520 \text{ cm}^{-1}$ with maxima at $\sim 13760 \text{ cm}^{-1}$ assignable to $2E_g \rightarrow 2T_{2g}$ transition supporting a distorted octahedral configuration for the complexes [12]. The effective magnetic moments of Co(II), Ni(II) and Cu(II) complexes were recorded at room temperature and corrected for diamagnetic contribution using pascal's constant. These are around 5.1, 3.1 and 1.8 B.M. respectively which indicating that they have octahedral configuration around the metal ions [13].

ESR spectra

The ESR spectra of the complexes [Cu₂LCl₂(H₂O)₆] and [Cu₄L/Cl₄(H₂O)₁₂] have been recorded at X-band at room temperature. The g values of the complexes are found to be 2.0074 and 2.10655 respectively by applying kneubuhl's method [14]. This type of spectrum might be due to

dynamic or pseudo rotational type of Jahn – Teller distortion. The spin orbit coupling constant λ can be determined from the equation $g_{av}=2(1 - \lambda / 10Dq)$. The values of λ for the complexes are found to be -25.456 cm^{-1} and -365.999 cm^{-1} . The lowering of λ values of the complexes from the free ion value (-830 cm^{-1}) indicates overlapping metal-ligand orbitals.

¹H-NMR spectra

The ¹H NMR spectra of the free ligands LH₂ and L/H₄ were recorded in CDCl₃ of DMSO-d₆ respectively and showed the following signals at δ (ppm): 7.004-8.862 (20H,m,naphthyl), 15.943 (2H,s,naphtholic OH). The spectra of L/H₄ in DMSO showed the following peaks: 6.250-8.883 (12H, m, phenyl), 12.609 (4H,s, phenolic OH), 2.502-2.664 (2H,m,-CH₂-), 2.347 (6H,s,O=C-CH₃). The ¹H NMR spectrum of the Zinc complex was recorded in the solvent DMSO. The complex multiplet is observed at δ 6.839 – 8.676 ppm which corresponds to 20 naphthyl protons [15]. The sharp peak obtained at δ 15.943 ppm (-OH) in the ligand

is found to be absent in the complex indicating deprotonation of the naphtholic proton thereby confirming the bonding of naphtholic oxygen atom to the Zinc ion (Table - 4).

Table 4. ¹H NMR Spectroscopic data, δ/ppm

Compound	δ/ppm			
	Ar-H	-CH ₂ -	OH	CH ₃
LH ₂ ^a	7.004- 8.682	-	15.943	-
L'H ₂ ^b	6.250- 8.333	2.502- 2.664	12.609	3.374
[Zn ₂ LCI ₂ (H ₂ O)] ^b	6.839- 8.676	-	-	-

^a=CDCl₃ ^b=DMSO-d₆

Thermal analysis and kinetic calculation

The thermal decomposition behavior of the complex [Cu₄LCI₄(H₂O)₁₂] was studied (Table-5) by using TG and DTA techniques in an atmosphere of nitrogen at a heating rate of 10 oC per minute. The experimental data shows that the decomposition occurs in multiple stages. The thermo gram of the complex shows a mass loss within 120 oC which indicates removal of lattice held H₂O molecules, supported by an exothermic peak at 110 oC[18]. Thereafter the compound, loses 11.36% of mass (Calcd, 11.013%) which corresponds to loss of seven coordinated H₂O molecules, supported by an exothermic peak at 290 oC. Thereafter, a gradual mass loss of 29.28%

Table 5. Thermal data of the Cu(II) complex with the ligand L/H₄

Decomposition temp(°C)	Mass loss(obs)	Mass loss(calcd)	Assignment
310	11.36%	11.01%	7 Coord.H ₂ O
550	29.28%	29.15%	5 Coord.H ₂ O, parts of ligand
930	47.70%	47.80%	4 chlorine atoms, rest of ligand

(Calcd 29.15%) is observed due to removal of rest of coordinated H₂O molecules and parts of the ligand. Then the compound shows loss of 47.70% (Calcd 47.80%) due to removal of four chlorine atoms and rest of the ligand moiety with the rise of temperature with the formation of CuO at 930 oC supported by an exothermic peak in the DTA curve. The kinetic parameters such as order of reaction, activation energy for the thermal decomposition of [Cu₄LCI₄(H₂O)₁₂] have been determined by Freeman-caroll method [19]. In this method, the equation used is $-dw/dt = Rt = Z/RH e^{-E/RT} W^n$ where RH= rate of heating, w= weight fraction of reacting material, E=activation energy, n=order of

reaction, and z=frequency. This equation in the difference form will be $\Delta \log RT = n \Delta \log w - (E/2.303R) \Delta (1/T)$, when $\Delta (1/T)$ is kept constant, a plot at $\Delta \log RT$ verses $\Delta \log W$ gave a linear relationship whose slope and intercept provides the value of n and E respectively. The order of the decomposition reaction and the activation energy are found to be 1.40 and 5.91J mole⁻¹ respectively. The calculated value of the activation energy is found to be low due to the autocatalytic effect the metal ion on the thermal decomposition of the complex [20,21]. The correlation coefficient (r) of the thermal decomposition is 0.96 which fits well with the experimental finding.

Powder X-ray diffraction analysis

The XRD study (powder pattern) of the complex [Ni₄L/ C14 (H₂O)₁₂] has been studied the help of X-ray diffractometer. The prominent peaks of the X-ray diffraction pattern have been indexed out analysed by using computer programme LSUCRPC[16].The lattice parameters (a,b,c, α, β, γ), volume of the unit cell and the miller indices (h,k,l) have been mentioned in Table-6. The indexing is confirmed by comparing between observed and calculated (2θ) values. It is observed that, the peaks of the XRD powder pattern have been successfully indexed as figure of merit (M) is found to be 8.5 as suggested by De Wolff [17]. The density of the complex was determined by the floatation method in a saturated solution of KBr, NaCl and benzene separately. The number of formula units per unit cell (n) is calculated from the relation $n = dNV/M$ where d= density of the compound, N= Avogadronumber, V= volme of the unit cell, M = Formula weight of the complex. The value of 'n' is found to be 2.0 that agree well with the triclinic crystal structure of the complex. The crystallite size of the same complex was calculated from the diffraction line width using the Debye scherrer relation $D=k\lambda/\beta\cos\theta$ where D=particle size, k=dimensionless shape factor, λ=X-ray wavelength, β=line broadening at half the maximum intensity, θ=diffraction angle. This equation relates the size of the particles in a solid in the broadening of a peak in a diffraction pattern. The particle size of the same complex was found to be 0.64 nm.

Molecular modelling

Molecular modelling of the Ligand LH₂, L/H₄ and metal complexes of Co(II), Zn(II) with LH₂, Ni(II) complex with L/H₄ have been carried out using molecular mechanics and Hartree-Fock (HF) Quantum methods. The standard 6-31 G basis set

was used in conjunction with the H-F method. All calculations are made using Gaussian 98 programme package [22, 23, 24, 25].

The metal complexes were built and optimization of their geometry was done at mm/H-F/6-31G level of theory Fig.5, Fig.6, Fig.7, Fig.8, and Fig.9.

Table 6. XRD Data of the Ni(II) Complex

Compound	Bond	Bond Length(Å)	Bond Angle(°)
Ligand-LH ₂	C(5)-O(7)	1.429	C(5)-C(6)-C(3)-120
	C(2)-N(8)	1.434	C(6)-C(5)-O(7)-120
	C(23)-O(28)	1.407	C(1)-C(2)-N(8)-120
	C(5)-C(6)	1.379	C(2)-N(8)-N(9)-106.7
	N(8)-N(9)	1.270	C(23)-O(38)-H(40)-104.51
[Co ₂ LCl ₂ (H ₂ O) ₆]	O(36)-Co(40)	1.964	O(38)-Co(40)-O(43)-90
	N(9)-Co(40)	1.972	O(38)-Co(40)-Cl(42)-90
	Cl(42)-Co(40)	2.359	O(38)-Co(40)-N(8)-90
			C(18)-N(8)-Co(40)-106.7
[Zn ₂ LCl ₂ (H ₂ O) ₂]	O(38)-Zn(40)	1.883	O(38)-Zn(40)-O(41)-109.47
	N(9)-Zn(40)	1.903	O(38)-Zn(40)-N(8)-109.47
	Zn(40)-Cl(42)	2.273	O(38)-Zn(40)-Cl(42)-109.47
			Zn(40)-O(41)-H(47)-104.51
Ligand-L/H ₄	C(35)-O(11)	1.325	C(5)-C(7)-H(94)-109
	C(26)-O(47)	1.407	C(5)-C(7)-C(35)-109.47
	C(5)-C(7)	1.48	C(43)-C(44)-O(11)-120
	C(5)-C(4)	1.379	
NiL/Cl ₄ (H ₂ O) ₁₂	C(9)-N(25)	1.434	O(12)-Ni(13)-O(15)-90
	O(12)-Ni(13)	1.894	O(11)-Ni(13)-O(14)-90
	O(11)-N(13)	1.871	N(9)-Ni(17)-O(10)-90
	N(8)-Ni(17)	1.885	O(10)-Ni(17)-Cl(18)-90
	Ni(17)-Cl(18)	2.264	N(8)-N(9)-Ni(17)-106.7

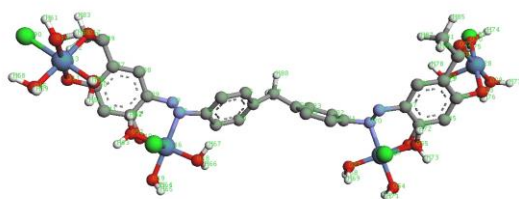


Fig. 5. Optimised Geometry of Ligand (LH₂)

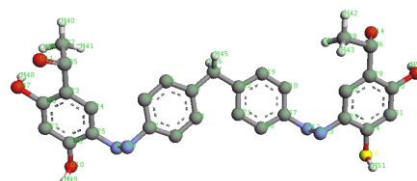


Fig. 6 Optimised Geometry of Ligand(L/H₄)

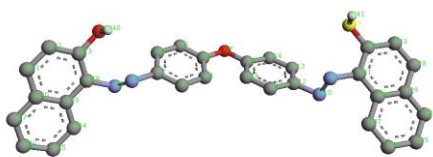


Fig. 7. Optimised Geometry of Co(II) Complex with (LH₂)

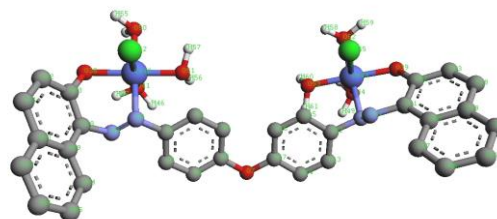


Fig. 8. Optimised Geometry of Zn(II) Complex with (LH₂)

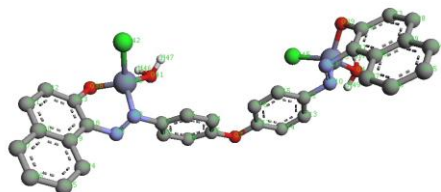


Fig. 9. Optimised Geometry of Ni(II) Complex with L/H₄

Findings of these computed works are in good agreement with the experimental results. The selected band lengths, band the angles of the ligands and complexes are give in Table 7.

Table 7. Selected bond length and bond angle of the ligands and the complexes

Compound	Concentration/ μgml^{-1}	Zone of Inhibition (mm)	
		<i>E.coli</i>	<i>S aureus</i>
LH ₂	500	14	12
L'H ₄	500	10	8
Co ₂ LCl ₂ (H ₂ O) ₆	500	15	13
[Ni ₂ LCl ₂ (H ₂ O) ₆]	500	18	14
Zn ₂ LCl ₂ (H ₂ O) ₂	500	10	6
Cu ₄ LCl ₄ (H ₂ O) ₁₂	500	14	12
Ni ₄ LCl ₄ (H ₂ O) ₁₂	500	12	10
Tetracycline	1000	45	30

In the metal complexes, the metal may be coordinated to either N1 or N2 of the azo group. When it is coordinated to N1, it forms a six-member ring and when it is coordinated to N2 it forms a five-member ring. In case of the Co(II) and Zn(II) complexes with LH₂, the total energy is found to be 184.744 KcalMole⁻¹ and 111.929 KcalMole⁻¹ respectively when they form five member ring, But energy of the complexes has been reduced to 129.413 KcalMole⁻¹ and 103.27 KcalMole⁻¹ which shows that the metal atoms are bonded to N1 of the azo group. In case of Ni(II) complex with L/H₄ the bond energy of the six member ring(378.48 KcalMole⁻¹) is found to be more than the five member ring (321.373 KcalMole⁻¹) which indicates the bonding of Ni atom with the N2 of the azo group.

Antibacterial study

The ligands and metal complexes have been screened for antibacterial activities and the results have been shown in Table-8. The results show that the complexes possess remarkable biological activities against different bacteria. The Co(II) and Ni(II) complexes with LH₂ show more antibacterial activities than and the co(II) and Ni(II) complexes show greater activities than the ligand L/H₄. The increase in biological activity of the metal complexes than the ligands may be due to complexation and it can be explained on the basis of chelation theory [26].

The Zn(II), Cd(II) and Hg(II) complexes have tetrahedral geometry based upon analytical conductance and IR spectral data. The azodye (LH₂) behaves as bis-bidentate (tetradentate) and the azodye L/H₄ behaves as bis-tetradentate (octadentate) ligand forming dimeric and tetrameric complexes respectively

CONCLUSION

Based on physicochemical and spectral data, octahedral geometry for Co(II) and Ni(II) complexes, a distorted octahedral geometry for Cu(II) complexes and a tetrahedral geometry for Zn(II), Cd(II) and Hg(II) complexes are proposed. It is found that the ligand(LH₂) behaves as dibasic ON-NO bis-bidentate and the ligand (LH₄) behaves as tetrabasic OON-NOOO bis-tetradentate, coordinating through the phenolic/naphtholic oxygen, azo nitrogen and carbonyl oxygen atoms. Thermogravimetry study indicates the complex is thermally stable, the XRD study suggested the triclinic crystal system for the nickel complex. All calculations based on molecular mechanics on the optimized geometries fit well with the experimental findings. The ligands and the complexes are pharmacologically active and the complexes possess enhanced antibacterial activities compared to the free ligands.

Acknowledgement: The authors are thankful to The Head, SAIF, I.I.T. Madras, India for providing spectral analysis, MMIT Bhubaneswar, Odisha for kind help of XRD, Thermogravimetric analysis and Dr. J. Panda, Department of Pharmaceutical Chem., Roland Institute of Pharmacy, Berhampur, Odisha, India for providing antibacterial data.

REFERENCES:

1. L.S. Goodman and A. Gilman, The Pharmacological Basis of Therapeutics, 4th Edn, Mc Millan, New York, USA, 1970.
2. R. M. Isa, A. K. Ghoneim, H. A. Dessouki and M. M. Mustafa, *J. Indian Chem. Soc.* **61**, 286 (1984).
3. B. B. Mahapatra and S. K. Panda, *Biokemistri (Nigeria)* **22**, 71 (2011), B. B. Mahapatra and S. K. Panda, *J. Indian Chem. Soc.* **87**, 1447 (2010) and *J. Indian Chem. Soc.* **87**, 1199 (2010), B. B. Mahapatra, A. K. Sadangi and S. K. Panda, *J.T.R. Chem.* **16(2)**, 59 (2009), B. B. Mahapatra and A. K. Sadangi, *J. Indian Chem. Soc.* **86**, 59 (2009).
4. R. S. Brandt and E. R. Miller, *J. Bacteriol* **38(5)**, 525 (1939).
5. J. V. Quagliano, G. Fujita, D. J. Philips, J. Walmsley, S. Y. Tyree, *J. Am. Chem. Soc.* **83**, 770 (1961).
6. L. K. Mishra and B. K. Keshari, *Indian J. Chem, Sect. A* **28**, 883 (1981).
7. R.B. King, *Inorg. Chem.* **5**, 300 (1966).
8. K. Nakamoto, *Infrared Spectra of Inorganic and Co-ordination Compounds*, 3rd Edn, Wiley Interscience, New York, USA, 1970.

9. J. R. Ferraro, Low Frequency Vibration of Inorganic and coordination compounds, Plenum Press, New York, USA, 1971.
10. A. B. P. Lever, Electronic spectroscopy, Elsevier, Amsterdam 1968, R. G. Devota, G. Ponticelli and C. Preti, *J. Inorg. Nucl. Chem.* **37**, 1633 (1957) R. C. Carlin, *Transition Met. Chem.* **1**, 3 (1968).
11. A. B. P. Lever, *Coord. Chem. Rev.* **3** 119, (1968), C. R. Hare and C. J. Ballhausen, *J. Chem. Phys.* **40**, 788 (1964), L. J. Sacconi, *J. Inorg. Nucl. Chem.* **73**, 1 (1968).
12. S. Yamada, *Coord. Chem. Rev.* **1**, 445 (1966), C.K. Jorgensen, *Acta. Chem. Scand.* **10**, 887 (1966).
13. F. A. Cotton and P.G. Wilkinson, *Advanced Inorganic Chemistry*, 3rd Edn, Wiley Eastern, New Delhi, India, 1985.
14. D.H. Williams, I. Fleming, *Spectroscopic methods in organic chemistry*, 4th Edⁿ, Tata Mc Graw Hill, India, 1994.
15. F.K. Kneubuhl, *J. Chem. Phys.* **33**, 1074 (1960), D.Kivelson and R.Nieman, *J. Chem. Phys.* **34**, 149 (1961).
16. J.N. Visser, A fully automated programme for finding the unit cell from power data, *J apply crystal* **2**, 89 (1969).
17. P.M. de Wolff, a simplified citation for reliability of a powder pattern indexing, *J apply Crysta.* **1**, 108 (1968).
18. A-A-A Abu-Hussen, *J. Coord. Chem.* **59**, 157 (2006).
19. E.S. Freeman, B. Carrol, *J. Phys. Chem.* **62**, 394 (1958).
20. A.M. El-Award, *J. Therm. Anal. Calorim.* **61**, 197 (2000).
21. A. Impura, Y. inoue, I. Yasumori, *Bull. Chem. Soc. Jpn.* **56**, 2203 (1983).
22. M.A. Thomson and M.C. Zerner, *J. Am. Chem. Soc.* **113**, 8210 (1991).
23. A.K. Rappe and W.A. Goddard, *J.P.C.* **95**, 3358 (1991).
24. A. K. Rappe, K. S. Colwel and J. Cassewit, *J. Inorganic Chem.* **3**, 3348 (1993).
25. J. Cassewit, K. S. Colwel and A. K. Rappe, *J. A. C. S.* **114**, 10046 (1992).
26. K. Mahanan and S. N. Devi, *Russian Journal of Coord. Chem.* **32**, 600 (2006).

ПОЛИМЕРНИ КОМПЛЕКСИ ЧАСТ CIV СИНТЕЗА, ОХАРАКТЕРИЗИРАНЕ И АНТИБАКТЕРИАЛНО ИЗСЛЕДВАНЕ НА ДИМЕРНИ И ТЕТРАМЕРНИ КОМПЛЕКСИ НА Co(II), Ni(II), Cu(II), Zn(II), Cd(II) И Hg(II) С АЗОБАГРИЛНИ ЛИГАНДИ

Б. Б. Махапатра^{1*}, С. Х. Дехури², С. Н. Чаулиа³

^{1,2} Катедра по химия, Г. М. Автономен колеж, Самбалпур – 768004, Одиша, Индия

³ Катедра по химия, Държавен колеж, Коранут, Одиша, Индия

Постъпила на 15 април, 2013 г.; коригирана на 3 юли, 2013 г.

(Резюме)

Бяха синтезирани шест комплекси на Co (II), Ni (II), Si (II), Zn (II), Cd (II) и Hg (II) с един тетраденатен азобагрилен лиганд и шест комплекси на същите метални йони с един октаденатен азобагрилен лиганд. Всичките дванадесет комплекси са охарактеризирани аналитично, чрез проводимост, магнитна чувствителност, ИЧ, електронен спектри, ЕСР, ЯМР, термогравиметричен анализ и прахова ренгенова дифракция В допълнение към това беше направено изследване на лигандите и комплексите чрез молекулно моделиране. За Co (II) и Ni (II) комплекси се установи, че са осмостенни, Cu (II) комплекси са изкривени осмостенни и четиристенна стереохимия бе присвоена на Zn (II), Cd (II) и Hg (II) комплекси. Антибактериалното проучването на лигандите и шест комплекси беше направено срещу грам-положителни бактерии *Staphylococcus aureus* и грам-отрицателни бактерии *Escherichia coli*.

A convenient synthesis of benzimidazoles using sulfonated ordered nanoporous carbon as efficient solid catalyst

H. Alinezhad*, M. Zare

Department of organic chemistry, Faculty of Chemistry, Mazandaran University, Babolsar, Iran

Received April 8, 2013; accepted November 24, 2013

Sulfonated ordered nanoporous carbon (CMK-5-SO₃H) efficiently catalyzes the synthesis of 2-substituted benzimidazoles using cyclocondensation of various aldehydes and *o*-phenylenediamines. This catalyst can be recovered and reused without significant loss of activity.

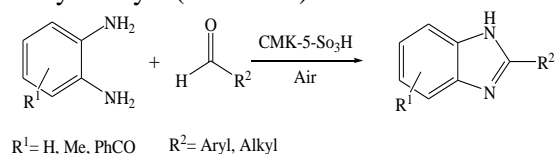
Keywords: sulfonated ordered nanoporous carbon, heterogeneous catalyst, benzimidazole, aldehyde, 1,2-phenylenediamine.

INTRODUCTION

High profile biological activities of benzimidazole derivatives such as anti-fungal, anti-tubercular and anti-cancer have attracted attention for their synthesis [1, 2]. They have been used as ligands, catalysts and synthetic intermediates [3]. Number of methods have been developed for the synthesis of 2-substituted benzimidazole derivatives involving the condensation of 1,2-phenylenediamines with aldehydes [4], carboxylic acids [5], orthoesters [6], nitriles [7] and amidates [8]. Recently, several improved protocols for the synthesis of benzimidazoles have been reported by modification of condensation reaction of aldehydes with *o*-phenylenediamines using various oxidants and catalysts including H₂O₂-CAN [9], K₃Fe(CN)₆ [10], Mn(OAc)₃ in AcOH [11], NaHSO₃ [12], K₂S₂O₈-CuSO₄ [13], SiO₂-Mn(acac)₃ [14], nanoCuO [15], tetrabutylammonium fluoride [16], *P*-TsOH [17], MoO₃/CeO₂-ZrO₂ [18], WO_x/ZrO₂ [4], nanoporousaluminosilicate [19], Yb(OPf)₃ [20], I₂ [21], FeCl₃ [22], In(OTf)₃ [23], Yb(OTf)₃ [24], Co(OH)₂/CoO(II) [25], MnZrO₂ [26] SBA-Pr-SO₃H [27], KF/Al₂O₃ [28] and scolecite [29] etc. Some of these methods suffer from various limitations, which include long reaction times, difficult work-up procedures and the use of corrosive and not recyclable catalysts. Therefore, development of new protocols continues to attract the attention of researchers. On the other hand, increasing awareness of the environmental costs of traditional acid-catalyzed chemical reactions has created an opportunity for solid acids as a catalyst in organic transformations due to their operational simplicity, selectivity and reusability [30]. Carbonaceous

sulfonic acids have attracted considerable interest as a solid catalyst in synthetic organic chemistry [31, 32]. Recently, Wang et al. prepared a novel sulfonic functionalized ordered nanoporous carbon (CMK-5-SO₃H) by covalent attachment of sulfonic acid-containing aryl radical on the surface of nanoporous carbon. CMK-5-SO₃H showed stable and highly efficient catalytic performance and it could be reused for several times without loss of activity [33]. However, to the best of our knowledge, there is no report available on the synthesis of benzimidazoles using CMK-5-SO₃H catalysts in the literature.

Here in, we report a simple, convenient, and efficient method for the syntheses of 2-substituted benzimidazoles by cyclocondensation of various aldehydes with 1,2-phenylenediamines in the presence of CMK-5-SO₃H as a reusable and eco-friendly catalyst (Scheme 1).



Scheme 1

EXPERIMENTAL

Materials were purchased from Fluka and Merck companies. CMK-5-SO₃H was prepared according to the reported procedure [33]. The amount of acid in CMK-5-SO₃H was determined by thermogravimetric analysis (TGA) and ion-exchange pH analysis. The structure of products was characterized by spectral data (¹H NMR, ¹³C NMR) and physical properties and comparison with authentic samples.

* To whom all correspondence should be sent:
E-mail: heshmat@umz.ac.ir

Procedure for the preparation of benzimidazole

o-Phenylenediamine (1.0 mmol) and aldehyde (1.0 mmol) with 2 mol% of CMK-5-SO₃H (0.023 g) (mol of Ph-SO₃H on the CMK-5) in 10 mL 1,4-dioxane were stirred at 100°C for an appropriate time. The progress of the reaction was monitored by TLC (n-Hexane:Ethylacetat 9:1). After completion of the reaction, catalyst was recovered by simple filtration. Water was added to the mixture and product filtered off. The residue was washed with ethyl acetate and the product was obtained. If necessary the product was further purified by column chromatography on silica gel.

Supplementary Data

Experimental procedure and characterization data for CMK-5-SO₃H is available in Supporting Information.

Some Product Characterization Data

5-Benzoyl-2-phenyl-1H-benzimidazole (Table 2, entry 3): IR (KBr): 3340, 3198, 1663, 1620, 1500 cm⁻¹, ¹H NMR spectrum (DMSO-d₆, 400 MHz), δ, ppm: 7.53- 7.78 (10H, m), 7.97 (s, 1H), 8.20- 8.23 (m, 2H), δ 13.33 (br, s, 1H); ¹³C NMR spectrum (100MHz, CDCl₃), δ, ppm: 124.64, 124.67, 124.71, 124.84, 127.20, 128.50, 128.52, 128.90, 129.57, 129.93, 129.98, 130.99, 131.46, 132.56, 135.56, 196.07. CHN Calcd.C, 80.52; H, 4.73; N, 5.36. found: C, 80.50; H, 4.80; N, 5.36.

2-(4-Nitrophenyl)-1H-benzimidazole (Table 2, entry 6): IR (KBr): 3350, 3100, 1612, 1280 cm⁻¹, ¹H NMR spectrum (DMSO-d₆, 400 MHz), δ, ppm: 7.25-7.80 (m, 8H), 12.38 (br, 1H); ¹³C NMR spectrum (100MHz, CDCl₃), δ, ppm: 115.94, 124.52, 136.23, 140.88, 141.89, 149.20. CHN Calcd.C, 65.27; H, 3.79; N, 17.56. Found: C, 65.26; H, 3.80; N, 17.52

4-(1H-Benzimidazole-2-yl)-phenol (Table 2, entry 9): IR (KBr): 3459, 2859, 1620, 1495 cm⁻¹; ¹H NMR spectrum (DMSO-d₆, 400 MHz), δ, ppm: 7.22-8.12 (8H, m), 12.30 (br, 1H); ¹³C NMR spectrum (100MHz, CDCl₃), δ, ppm: 115.11, 120.65, 125.11, 130.20, 138.05, 141.75. CHN Calcd.C, 74.27; H, 4.79; N, 13.33. Found: C, 74.29; H, 4.80; N, 13.30.

5-Benzoyl-2-naphthyl-1H-benzimidazole (Table 2, Entry 12): IR (KBr): 3150, 2934, 1662, 1624, 1560 cm⁻¹, ¹H NMR spectrum (DMSO-d₆, 400 MHz), δ, ppm: 7.57- 7.80 (9H, m), 8.07- 8.13 (m, 4H), 8.32- 8.35 (m, 1H), 8.80 (s, 1H), δ13.50 (br, s, 1H); ¹³C NMR spectrum (100MHz, CDCl₃), δ, ppm: 124.36, 124.76, 124.80, 124.84, 124.88, 126.94, 127.41, 127.53, 127.94, 128.30, 128.90, 129.07, 129.21, 129.96, 131.55, 132.59, 133.20,

134.19, 138.56, 154.53, 156.95. CHN Calcd.C, 82.74; H, 4.59; N, 5.36. found: C, 82.80; H, 4.60; N, 4.50.

2-Pentyl-1H-benzimidazole (Table 2, entry 17): IR (KBr) 3324, 2898, 1640, 3250 cm⁻¹. ¹H NMR spectrum (DMSO-d₆, 400 MHz), δ, ppm: 0.83-0.88 (m, 3H), 1.23-1.24 (m, 4H), 1.75-1.89 (m, 2H) 2.90 (t, J = 7.4 Hz, 2H), 6.41 (br, 1H), 7.18-7.36 (m, 2H), 7.50-7.50 (m, 2H), ¹³C NMR spectrum (100MHz, CDCl₃), δ, ppm: 13.91, 21.68, 27.31, 28.50, 30.66, 110.55, 118.10, 120.87, 134.37, 143.35, 155.10. CHN Calcd.C, 76.56; H, 8.57; N, 14.88. found: C, 76.53; H, 8.58; N, 14.89.

RESULTS AND DISCUSSION

TGA and ion-exchange pH analysis determined the amount of acid in CMK-5-SO₃H. Typically a loading of ca. 0.84 mmol/g was obtained.

In this work, we showed the effect of solvent and catalyst for the preparation of 2-phenyl-1H-benzimidazole. Benzaldehyde (1 mmol) was treated with *o*-phenylenediamine (1 mmol) in the presence of CMK-5-SO₃H (0.023 g: 2 mol%) in various solvents (Table 1). As it is clear from this Table, the highest yield of 2-phenyl-1H-benzimidazole was obtained in 1,4-dioxane (Table 1, entry 1).

Table 1. Preparation of 2-phenyl-1H-benzimidazole in different solvents

Entry	Solvent	Time (h)	Yield(%) ^a
1	1,4-Dioxane	3	96
2	Acetonitrile	5	60
3	Toluene	5	40
4	Water	5	50
5	Ethanol	5	40
6	Dichloromethane	7	25

^a Yields refer to isolated products.

To evaluate the quantity of the catalyst, the model reaction was performed in the presence of different mol% of CMK-5-SO₃H in dioxane at reflux condition (Table 2). It was observed that this reaction carried out well in the presence of 2 mol% catalyst (Table 2 entry2). Using higher amounts of catalyst did not considerable effect on the yield and reaction time (Table 2, entry3 and 4).

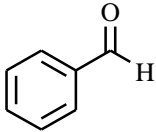
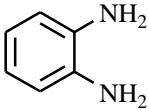
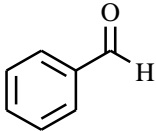
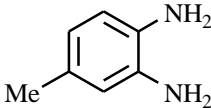
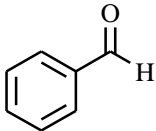
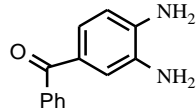
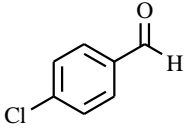
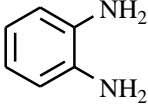
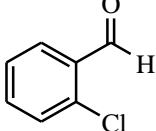
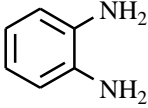
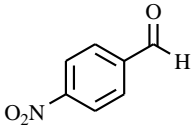
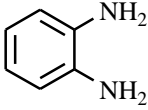
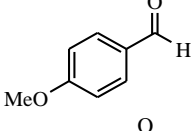
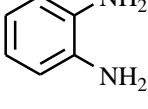
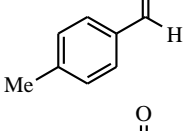
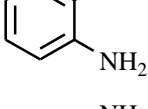
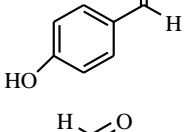
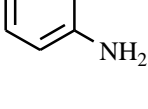
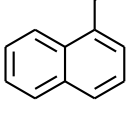
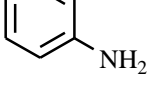
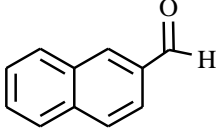
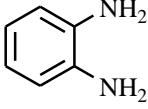
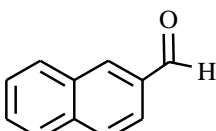
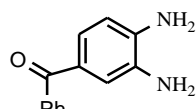
In order to evaluate the scope and generality of this process, various aromatic and aliphatic aldehydes were reacted with several *o*-phenylenediamines under the optimized reaction conditions (Table 3).

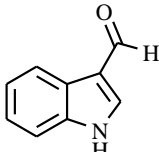
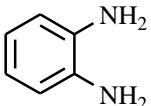
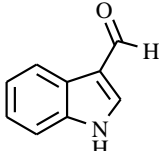
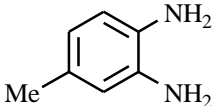
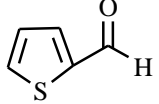
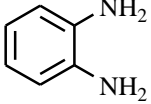
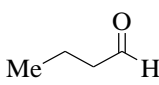
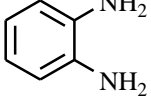
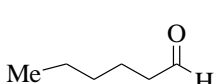
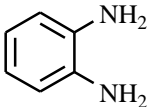
Table 2. Screening of catalyst amount on model reaction

Entry	Catalyst amount (mol %)	Time (h)	Yield(%) ^a
1	1	6	92
2	2	3	96
3	3	3	90
4	5	4	92

^a Yields refer to isolated products.

Table 3. Synthesis of 2-substituted benzimidazoles using a CMK-5-SO₃H catalyst ^a

Entry	Aldehyde	Diamine	Time (h)	Yield ^b	m.p./Lit.
1			3	96	290-293 [4]
2			2.5	98	240-242 [19]
3			7	95	216-219 [-]
4			2	93	290-292 [4]
5			2	92	231-235 [4]
6			2	95	300-302 [4]
7			5	95	223-225 [4]
8			4	93	270-272 [4]
9			3.5	96	218-220 [4]
10			3	90	267-269 [16]
11			3	91	212-215 [19]
12			7	92	239-240 [-]

13			7	95	202-204 [13]
14			5	97	210-213 [34]
15			6	90	230-233 [21]
16			5	72	160-162 [19]
17			5	80	164-165 [23]

^aYields refer to isolated products.

Reactions of benzaldehyde (1 mmol) with various 1,2-diamines (1 mmol) in the presence of CMK-5-SO₃H (2 mol%) in 1,4-dioxane at reflux condition, afforded 2-phenyl-1*H*-benzimidazoles in excellent yields (Table 3, entries 1-3). Similarly benzaldehydes with possessing both electron-donating and electron-withdrawing groups reacted with *o*-phenylenediamine under optimal reaction conditions, to give excellent yield of the desired imidazoles (Table 3, entries 4-9).

In the optimal reaction conditions 1-naphthaldehyde and 2-naphthaldehyde as sterically hindered aldehydes reacted with 1,2-phenylenediamines to afford excellent yield of the corresponding benzimidazoles (Table 3, entries 10 - 12).

This method is also suitable for the preparation of benzimidazoles from a heteroaromatic aldehyde such as 2-thiophenecarbaldehyde and indole-3-carbaldehyde (Table 3, entries 13-15). Aliphatic aldehydes such as butanal and hexanal reacted with *o*-phenylenediamine and produced the corresponding benzimidazoles (Table 3, entries 16-17).

The recyclability of the catalyst was also studied (Table 4). At the end of the reaction of benzaldehyde with *o*-phenylenediamine, the catalyst was filtered off, washed with dichloromethane, dried, and reused as such for subsequent experiments under same reaction conditions. The results in table 4 clearly established

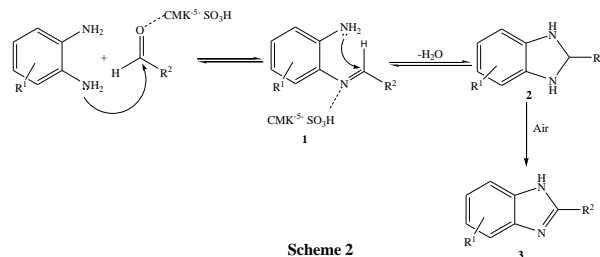
the recyclability and reusability of the catalyst without significant loss of activity.

Table 4. Results of recyclability of the catalyst

Entry	Cycle	Time	Yield (%)
1	1	3	96
2	2	3	95
3	3	3.5	90
4	4	3.5	89

To confirm the role of air as an oxidant in these reactions, the optimal reaction was carried out under N₂ atmosphere. It is noteworthy that only a trace of 2-phenyl-1*H*-benzimidazole was obtained in the absence of air. Hence, the role of air as an oxidant is important in these transformations.

Mechanistically, it is believed that, the electrophilic character of the carbonyl group is enhanced by CMK-5-SO₃H which facilitate the generation of imine. The resulting imine further reacts with another amine group of 1,2-phenylenediamine resulting in the formation of dihydroimidazole which subsequently undergoes oxidative dehydrogenation in air under the reaction conditions to give the 2-substituted benzimidazole as shown in Scheme 2.



CONCLUSIONS

In summary, we have developed an efficient approach and simple work up for the preparation of 2-substituted benzimidazoles by condensation of acid sensitive, sterically hindered, and substituted aromatic and aliphatic aldehydes with various 1,2-phenylenediamines in the presence of CMK-5-SO₃H as a highly active, stable, reusable and eco-Friendly catalyst.

Acknowledgment: This work was supported by Research Grant from University of Mazandaran, Iran.

REFERENCES

1. M. B. Maradolla, S. K. Allam, A. Mandha and G. V. P. Chandramouli, *Arkivoc* (xv), 42 (2008).
2. R. Vinodkumar, S. D. Vaidya, B. V. S. Kumar, U. N. Bhise, S. B. Bhirud and U. C. Mashelkar, *Arkivoc* (xiv), 37 (2008).
3. (a) T. Isobe, K. Fukuda, Y. Araki and T. Ishikawa, *Chem Commun.*, 243 (2001). (b) M. Jung and E. Huang, *Org. Lett.*, **2**, 2659 (2000). (c) I. Y. Oren, I. Yalcin, E. A. Sener and N. Ucarturk, *Eur J. Med. Chem.*, **39**, 291 (2004).
4. R. V. Shingalapur and K. M. Hosamani, *Catal. Lett.*, **137**, 63 (2010).
5. Y. H. So and J. P. Heeschen, *J. Org. Chem.* **62**, 3552 (1997).
6. G. P. Sagitullina, A. K. Garkushenko, E. G. Atavin and R. S. Sagitullin, *Mendeleev Commun.*, **19**, 155 (2009).
7. D. W. Hein, R. J. Alheim and J. Leavitt, *J Am Chem Soc.* **79**, 427 (1957).
8. M. Terashima and M. Ishii, *Synthesis*, 484 (1982).
9. K. Bahrami, M. M. Khodaei and F. Naali, *J. Org. Chem.*, **73**, 6835 (2008).
10. I. Hutchinson, M. F. G. Stevens and A. D. Westwel, *Tetrahedron Lett.*, **41**, 425 (2000).
11. X. J. Mu, J. P. Zou, R. S. Zeng and J C. Wu, *Tetrahedron Lett.*, **46**, 4345 (2005).
12. X. Han, H. Ma and Y. Wang, *Russ J Org Chem.*, **44**, 863(2008).
13. A. Kumar, R. A. Maurya and D. Saxena, *Mol. Divers.*, **14**, 331(2010).
14. R. K. Sodhi and S. Paul, *Catal. Lett.*, **141**, 608 (2011).
15. P. Saha, T. Ramana, N. Purkait, M. A. Ali, R. Paul and T. Punniyamurthy, *J. Org. Chem.*, **74**, 8719 (2009).
16. R. S. Joshi, P. G. Mandhane, S. K. Dabhade and C. H. Gill, *J. Chinese Chem. Soc.*, **57**, 1227 (2010).
17. H. Xiangming, M. Huiqiang and W. Yulu *Arkivoc* (xiii), 150 (2007).
18. S. B. Rathod, M. K. Lande and B. R. Arbad, *Bull. Korean Chem. Soc.*, **31**, 2835 (2010).
19. M. A. Chari, D. Shobha, E. R. Kenawy, S. S. Al-Deyab, B. V. Reddy and A. Vinu, *Tetrahedron, Lett.* **51**, 5195 (2010).
20. G. Shen and C. Cai, *J. Fluorine. Chem.*, **128**, 232 (2007).
21. G. Pranjali and K. Dilip, *Tetrahedron Lett.*, **47**, 79 (2006).
22. C. Ke, T. U. Yong Qiang and Z. Fu Min, *Sci. China. Chem.*, **53**, 130 (2010).
23. R. Trivedi, S. K. De and R. A. Gibbs, *J. Mol. Catal. A: Chem.*, **245**, 8 (2006).
24. M. Curini, F. Epifano, F. Montanari, O. Rosati and S. Taccone, *Synlett*, 1832 (2004).
25. M. A. Chari, D. Shobha and T. Sasaki, *Tetrahedron Lett.*, **52**, 5575 (2011).
26. M. Rekha, A. Hamza, B. R. Venugopal and N. Nagaraju, *Chin. J. Catal.*, 439 (2012).
27. G. Mohammadi Ziarani, A. Badiei, M. Shakiba Nahad and S. Ghadim Alizadeh, *J. N. S.*, **2** 213 (2012).
28. S. Bahadori Khalili and A. R. Sardarian, *Monatsh. Chem.*, **143**, 841, (2012).
29. L. S. Gadekar, B. R. Arbad and M. K. Lande, *Chinese Chem. Lett.*, **21**, 1053 (2010).
30. B. Karimia and D. Zareyee, *Tetrahedron let.*, **46**, 4661 (2005).
31. M. Okamura, A. Takagaki, M. Toda, J. N. Kondo, K. Domen, T. Tatsumi, M. Hara and S. Hayashi, *Chem. Mater.*, **18**, 3039 (2006).
32. D. Zareyee, M. S. Ghandali and M. A. Khalilzadeh, *Catal. Lett.*, 1521 (2011).
33. X. Wang, R. Liu, M. M. Waje, Z. Chen, Y. Yan, K. N. Bozhilov and p. Feng, *Chem. Mater.*, **19**, 2395 (2007).
34. J. S. Biradar and B. Sharanbasappa, *Synth Commun.* **41**, 885 (2011).

Удобна синтеза на бензимидазоли със сулфониран подреден нанопорьозен въглерод като ефикасен твърд катализатор

Х. Алинежад*, М. Заре

Department of organic chemistry, Faculty of Chemistry, Mazandaran University, Babolsar, Iran

Постъпила на 8 април, 2013 г.; коригирана на 24 ноември, 2013 г.

(Резюме)

Сулфониран подреден нанопорьозен въглерод (СМК-5-SO₃H) ефикасно катализира синтеза на 2-заместени бензимидазоли чрез циклокондензация на различни алдехиди и *o*-фенилендиамини. Катализаторът може да се отдели и употреби повторно без значителна загуба на активност.

Removal of phenol from contaminated water by activated carbon, produced from waste coal material

B. G. Tsyntsarski¹, B. N. Petrova¹, T. K. Budinova^{1*}, N. V. Petrov¹, D. K. Teodosiev²

¹ Institute of Organic Chemistry, Bulgarian Academy of Sciences, Sofia

² Space Research and Technology Institute, Bulgarian Academy of Sciences, Sofia

Received April 15, 2013; accepted July 17, 2013

The adsorption behavior towards phenol of different modifications of activation carbon, prepared from mixtures of coal tar pitch and furfural, was investigated. The structure and surface properties were characterized using N₂ adsorption, IR spectroscopy and surface oxygen groups. The activated carbon, obtained by pyrolysis in the presence of water vapor, has higher adsorption ability (150 mg g⁻¹) than the other investigated samples - the oxidized carbon sample (126 mg g⁻¹) and the carbon sample thermally treated (117 mg g⁻¹) up to 1300°C. The adsorption capacity towards phenol of carbon after thermal treatment is similar to the oxidized carbon, in spite of reduced surface area and pore volume of the former. This is probably due to the formation of water molecular clusters. The effect of the micropore structure was discussed, which reveals that the adsorption towards phenol of activated carbon from mixture of furfural and coal tar pitch correlates with its surface area and micropore volume.

Keywords: activated carbon, coal tar-pitch, furfural, adsorption, phenol

pollutants, 16 December 2008).

1. INTRODUCTION

In the last years a lot of countries, especially these from Central and Eastern Europe (CER), continue their efforts to resolve water management problems in the very unique conditions of a transition from the centrally planned to market economies. These processes were accompanied with expansion of heavy industries often using coal as the main source of energy. The pollution effects were intensified by the underpricing and overuse of energy, water and other raw material inputs. Limited steps have been implemented to improve control and safety equipment as well as operating procedures but not much more. As a result, water pollution is one of the most important problems for CER countries, inherited from the past.

In order to ensure consistent protection of surface waters, the European Parliament and the Council of the European Union has announced a number of Directives on the Environmental Quality Standards in the field of water policy. The European Environmental Agency has included different aromatic pollutants in the List of Priority Pollutants to be monitored in industrial effluents (Directive 2008/105/EC Environmental quality standards for priority substances and certain other

Both the environment and human beings are exposed to the hazards of different pollutants (organic, metal ions, etc.) from waste and potable water.

Chemical pollution of surface waters is a serious threat for the aquatic environment, with undesired effects, such as acute and chronic toxicity for aquatic organisms, accumulation in ecosystems and loss of habitats and biodiversity, as well as a threat to human health.

The aromatic organic compounds are frequently present as polluting agents in continental waters, especially phenolic substances, used in production of pesticides, insecticides, surfactants, etc. As a pure substance, phenol is used as a disinfectant, as appetizing agent, as an extracting solvent, for producing phenolic resins, etc. Phenols are also the main organic constituents present in condensate streams in coal gasification and liquefaction processes. Other sources of waste stream waters containing phenols are pharmaceutical, plastic, wood products and pulp and paper industries. Phenol-containing waste waters may not be launched into open water without treatment because of the toxicity of phenol [1]. Well known characteristics of the phenolic chemicals are their resistance towards biodegradation. Phenol compounds rated as No 11 in the list of 126 chemicals issued as priority pollutants by the Environmental Protection Agency of USA. There

* To whom all correspondence should be sent:
E-mail: goriva@orgchm.bas.bg

are many methods such as chlorination [1], catalytic and photocatalytic oxidation [2,3], ozonation [4], nanofiltration [5], adsorption [6]. Thus, chlorination of phenol containing water leads to formation of chlorophenolic substances, which are well known as poisonous and carcinogenic; ozonation and catalytic oxidation are related with use of high doses of the active substance; phenol removal by adsorption is suitable purification process, but the high price of commercial activated carbon decrease the economical efficiency of removal of phenol by adsorption.

Therefore seeking novel effective adsorption materials is still of recent interest. In this sense in the last years a special emphasis on the preparation of activated carbons from different waste materials was made, because of the growing interest in low-cost activated carbons, especially for applications concerning treatment of drinking and waste waters. Activated carbons can be produced from a large variety of precursors. Usually used precursors include bituminous coal, wood, peat, petroleum pitch, polymer and biomass [7-12].

It is well known that coal tar pitches are excellent raw materials in the carbon manufacturing industry, because of their high carbon content, low price and ability to produce carbon with different structure and properties. Chemical composition and physical properties of pitches, which in turn influence their transformation to carbons, are of great importance for controlling the properties of the final product. On the other hand, recent interest in the substances of biomass origin has renewed the attention in furan compounds. Earlier studies have shown that furfural resin is a suitable oxygen-containing raw material for the production of carbon adsorbents with insignificant ash and sulphur content – it should be noted that such activated carbons are characterized with a large number of oxygen-containing groups on the surface. Indeed, carbon adsorbents with different structure and properties have been prepared from mixtures of furfural and biomass-derived tars, while optimizing the operating conditions (including the composition of the mixtures, activation reagents, pre-treatment of the precursors, etc.) [13]. There are many sources for the production of furfural because most agricultural wastes contain sufficient quantities of pentosans to justify industrial exploitation by well-established and relatively simple techniques [14].

In this paper, the application for the phenol removal of new synthesized carbon adsorbents, obtained from coal by-product (coal tar pitch) and

furfural (waste material from pyrolysis of biomass), was studied.

2. EXPERIMENTAL

2.1. Materials and methods

2.1.1. Synthesis procedure for preparation of activated carbon from coal tar pitch and furfural

A mixture of coal tar pitch and furfural (45:55 wt. %) was treated with concentrated H_2SO_4 (drops of H_2SO_4 were added under continuous stirring) at 120 °C until solidification. The obtained solid product was heated at 600 °C in a covered silica crucible with a heating rate of

10 °C min^{-1} under nitrogen atmosphere. The carbonized solid was further submitted to steam activation at 800 °C for 1 h (carbon A).

2.1.2. Oxidation treatment with HNO_3

The synthesized material was oxidized in order to incorporate of oxygen functionalities. For this purpose, the sample Carbon A was oxidized with HNO_3 . The oxidation treatment with HNO_3 was performed according to the following procedure: about 10 g of the sample was treated with 100 mL 10% HNO_3 and boiled for 1 h. After that the sample was washed with distilled water and dried at 105°C and kept in dessicator until use. The oxidized carbon was labeled as carbon B.

2.1.3. Thermal treatment

The activate carbon B was heated at 1300°C at nitrogen atmosphere for 1 h in order to eliminate the oxygen containing groups. This carbon was labeled as carbon D.

2.2. Adsorbent characterization

2.2.1. Pore structure analysis

Nanotexture of the synthesized carbon materials was characterized by N_2 adsorption at -196°C, carried out in an automatic volumetric apparatus (ASAP 2020 from Micromeritics). Before the experiments, the samples were outgassed under vacuum at 120°C for overnight. The isotherms were used to calculate specific surface area S_{BET} , total pore volume V_T , micropore volume W_o [15].

2.2.2. Chemical structure and composition

The samples were further characterized by elemental analysis and Boehm's titration to determine the amount of oxygen incorporated after oxidation treatment and the nature of the formed surface functionalities [16]. Details of the experimental procedure for Boehm's titration have been described elsewhere [17].

The carbon samples were analyzed using FTIR spectroscopy using Bruker IFS 113V. The samples were mixed with potassium bromide and the mixture was pressed into pellets to be used in the analysis.

2.2.3. pH determination

The pH of the carbons was measured according to the following procedure: 4.0 g of carbon was weighed into a 250 mL beaker, and 100 mL of water was added. The beaker was covered with a watch glass, and the mixture was boiled for 5 min. The suspension was set aside, and the supernatant liquid was poured off at 60 °C. The decanted portion was cooled down to ambient temperature and its pH was measured to the nearest 0.1 pH unit.

2.3. Adsorption measurements

Phenol substance was obtained from Merck (99% purity). The phenolic solutions were prepared in unbuffered distilled water in the concentration range of 100-250 mg L⁻¹. About 100 mg of activated carbons were mixed with 50 mL of phenolic solution of the desired concentration, and the suspensions were shaken for 2 h. The samples were filtered and the equilibrium concentrations of the phenolic compounds remaining in solution were

determined spectrophotometrically (at wavelength 269 cm⁻¹) by Pfaro 300 UV spectrometer. Each determination is performed in triplicate.

3. RESULTS AND DISCUSSION

3.1. Characterization of carbon adsorbent from coal tar pitch and furfural.

The elemental analysis of coal tar pitch shows that the amount of oxygen containing structures is not high, whereas the high C/H ratio indicates the presence of considerable amount of aromatic species in the pitch (Table 1). After carbonization and activation of the mixture, a carbonaceous solid is obtained with a final yield of 58 wt%. Analysis of the chemical composition of carbon A shows that, along with the prevailing content of aromatic structures in the pitch, the resulting material has relatively large oxygen content. This confirms the fact that inserting oxygen in the carbon precursor (i.e. furfural) leads to the formation of oxygen containing structures on the surface of the final product.

Table 1. Chemical composition and pH value of the coal tar pitch and the synthesized activated carbons (wt.%)

Sample	Ash	Volatiles (daf)	C	H	N	S	O	C/H
Coal tar pitch	-	-	90.90	4.95	0.90	0.50	2.75	1.53
Carbon A	0.8	1.9	90.81	0.82	0.75	0.51	7.11	9.23
Carbon B	1.5	7.7	86.77	1.02	1.30	0.56	10.35	7.09
Carbon D	0.1	-	98	0.6	0.6	0.4	0.4	13.61

3.2. Chemical character of the surface by Boehm's titration of surface groups

The surface functionalities were further characterized by the Boehm's titration (Table 2). Data shows that the surface chemistry of carbon A

is comprised of carbonyl and phenolic functionalities, which render a basic character to the adsorbent. Despite the large amount of oxygen, the synthesized carbon also displays strong alkaline character, as inferred from the pH value.

Table 2. Data corresponding to Boehm's titration for the quantification and identification of the oxygen surface groups on the activated carbons [meq g⁻¹].

Sample	Carboxylic	Lactonic	Phenolic	Carbonyl	Basic groups	pH
Carbon A	BDL	BDL	0.210	1.356	0.778	8.1
Carbon B	0.109	0.239	0.456	1.767	0.330	3.7
Carbon D	BDL	BDL*	BDL	BDL	0.440**	9.7

*BDL – below detection limits

**basic centers

After oxidation with nitric acid, as expected, there is a slight enhancement in the overall oxygen content, accompanied by a fall of the pH value,

confirming the different nature of the surface functionalities, appearing upon oxidation. In contrast, even if the groups of the parent carbon are

well preserved, oxidation with nitric acid leads to the formation of acidic groups (carboxyl and lactonic structures), which are responsible for the decrease in the pH of the carbon (ca. 4 pH units fall). Along with the incorporation of acidic surface groups, a twofold decrease in the content of basic groups was also observed after oxidation of carbon A. This could be attributed to the incorporation of the surface groups appearing at the edges of the basal planes in the graphene layers, thereby reducing the capacity of these sites to accept H⁺ ions (acting as Lewis base). Thermally treated activated carbon (Carbon B) possess basic centers and basic character of the surface (pH 9.7).

3.3. Pore structure

In a previous work [14], we have observed that the furfural content has a strong effect on the porosity of the resulting carbons. Lower proportions of furfural give rise to activated carbons with a narrow microporosity, which with rising furfural content is gradually opened in favor of large micropores and mesopores. That's why Carbon A was prepared with a moderate proportion of furfural in the precursor mixture (45 wt.%), and as a result it is characterized by a moderate BET surface area and with an well developed microporosity (Table 3 and Figure 1).

The nitrogen adsorption/desorption isotherms of the carbon samples are shown in Fig.1. It can be seen that the adsorption isotherms are of type I, indicating a microporous material.

These porous features should be ideally adapted for the removal of aromatics from aqueous phase. Oxidation brought about a slight decrease in the porous features of the carbon (likely due to the boiling step during oxidation), although the fall in the micropore volume accounts for only 16 %. Thermal treatment at 1300 °C leads to decrease in the surface area and micropore volume. Summarizing, we have prepared three carbon materials with various surface chemistry (oxygen-enriched materials) and different basicity, which are investigated towards adsorption of phenol and to investigate the influence of oxygen containing

groups on the adsorption of phenol from water solution.

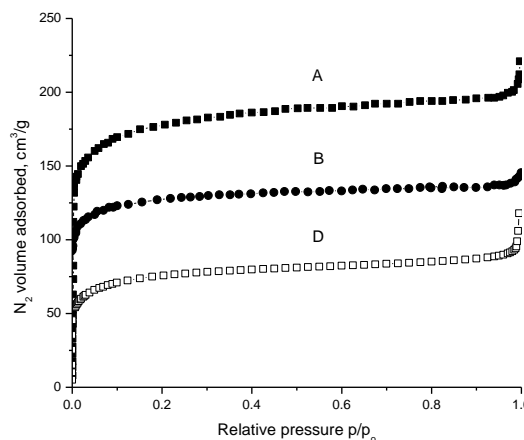


Fig. 1. N₂ adsorption isotherms at -196 °C of the studied carbons (A – Carbon A; B – Carbon B; Carbon D)

3.4. Adsorption isotherm of phenol

Fig. 2 shows the influence of the time of treatment on the adsorption capacity of the carbons. The initial adsorption rate is rapid and a plateau is reached after 15 min for carbon A and 20 min for Carbon B. Moreover, the amounts adsorbed with time show smooth continuous curves in both cases, with a well-defined saturation plateau. This behavior is attributed to the decrease in the number of available adsorption sites on the carbon surface as the adsorption proceeds and only part of the molecules of adsorbate retain. Comparatively, the uptake is slightly faster in the most hydrophobic sample (carbon A). The faster uptake on the hydrophobic carbon A, compared to carbon B, suggests that besides the enhanced water adsorption of the carbon after oxidation, kinetic restrictions for the accessibility of the aromatic compound to the adsorption sites arise, probably due to the fact that the water also competing for these sites

Table 3. Surface characteristics of the samples

Sample	S _{BET}	V _{tot} [*]	V _{micro} ^{**}	V _{meso} ^{**}
Carbon A	678	0.316	0.216	0.030
Carbon B	487	0.217	0.113	0.010
Carbon D	287	0.151	0.080	0.028

* evaluated at p/p₀~0.99

** evaluated from DFT applied to N₂ adsorption data

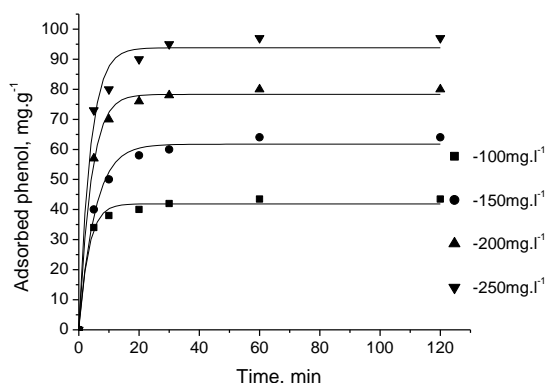


Fig. 2. Effect of contact time on adsorption of phenol on Carbon A.

Equilibrium studies on adsorption provide information about the capacity of the sorbent or the amount required to remove a unit of mass of pollutant. The most widely used isotherm equation for modeling the adsorption equilibrium is the Langmuir equation, which is valid for monolayer

Thermally treated activated carbon (Carbon D) has adsorption properties similar to this of oxidized activated carbon (Carbon B), nevertheless that the micropore volume and specific surface area porosity of the first sample are lower (Table 4). This indicates that the oxygen-containing groups of Carbon B hinder the phenol adsorption.

Figure 4 shows the equilibrium adsorption isotherms of phenol on all three activated carbons. They belong to type L of Giles classification, indicating that adsorption proceeds by the formation of a monolayer in the range of concentrations used [19].

sorption on to a surface with a finite number of identical sites, and is given by the equation [18]:

$$Q_{eq} = Q_o b C_{eq} / (1 + b C_{eq}) \quad (1)$$

where C_{eq} is the equilibrium pollutant concentration remaining in solution after adsorption (mg L^{-1}), Q_{eq} is the amount of pollutant bound to the adsorbent (mg g^{-1}), Q_o is the maximal amount of the pollutant per unit weight of adsorbent (mg g^{-1}), and b is a constant related to the affinity of binding sites (L mg^{-1}).

The adsorption capacity of phenol on activated carbon A is higher than its oxidized form (Carbon B) and than the thermally treated sample (Carbon D). Moreover, the Langmuir linear fitting of experimental data is very good (Fig. 3). The parameters of fitting the experimental adsorption equilibrium data are given in Table 4. The data calculated from the Langmuir equation reveal a pronounced increase of the maximal adsorption capacity (Q_o) for the activated carbon A.

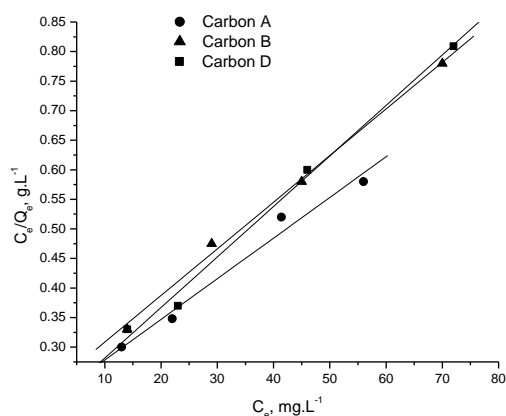


Fig. 3. Langmuir plot for adsorption of phenol. Conditions: Phenol concentration, 100-250 mg. L^{-1} , time of treatment 1 h, carbon concentration, 100 $\text{mg}/50 \text{ mL}$.

Table 4. Results obtained from Langmuir equation applied to the adsorption isotherms of phenol compound on the studied activated carbons.

Sample	$Q_o, \text{mg g}^{-1}$	$b, \text{g L}^{-1}$	R^2
Carbon A	150	0.00670	0.99074
Carbon B	126	0.03436	0.99813
Carbon D	117	0.00855	0.99717

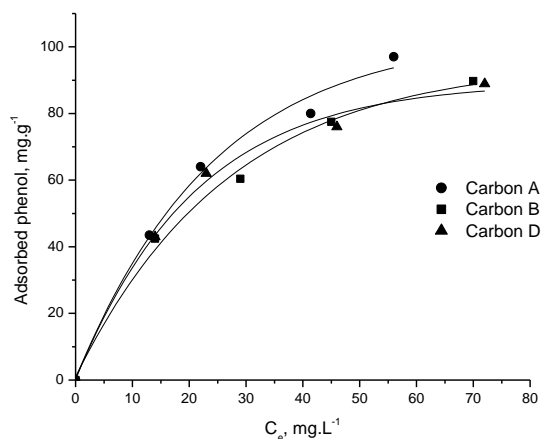


Fig. 4. Equilibrium adsorption isotherms of phenol studied activated carbons, expressed in terms of the amount adsorbed per gram of adsorbent [mg. g⁻¹] and per equilibrium concentrations [mg. L⁻¹]

3.5. Effect of pore structure

Carbon A (with higher BET surface area and micropore volume) shows higher adsorption ability in comparison with carbon B and carbon D. Obviously in this case the maximal phenol adsorption capacity (Q_0) of the activated carbons increases with the surface area and micropore volume. The adsorption capacity depends generally on the accessibility of the organic molecules to inner surface of carbon adsorbent. It is well known that, to some extent, the adsorption of phenol is mainly due to micropore filling especially in the case of microporous carbons. In phenol solutions, water molecules are preferentially adsorbed by the oxygen groups and then the remainder of the surface and/or micropore volume is available to the phenol molecules – this was proven by our investigations on the adsorption of phenol on thermally treated activated carbon (carbon D), which have similar adsorption ability with the oxidized activated carbon (carbon B). The maximal adsorption capacity towards phenol of activated carbon from mixture of furfural and coal tar pitch correlates with its surface area and micropore volume.

3.6. Effect of surface chemistry

Chemical nature of the surface of the activated carbon is the most important factor - apart from the porous structure - that determines its adsorption properties. Table 2 shows the distributions of different oxygen groups on the carbon surface. Carbon B possesses acidic oxygen groups and twice lower content of basic groups, compared to

the initial activated carbon A. The data for Boehm titration were confirmed by the results for IR spectra (Fig. 5), which show, that the bands at 1730 cm^{-1} and 1570 cm^{-1} , assigned according to [20-22] oxygen containing groups - mainly carbonyl and carboxylic - increase in intensity after oxidation, and decrease significantly after thermal treatment.

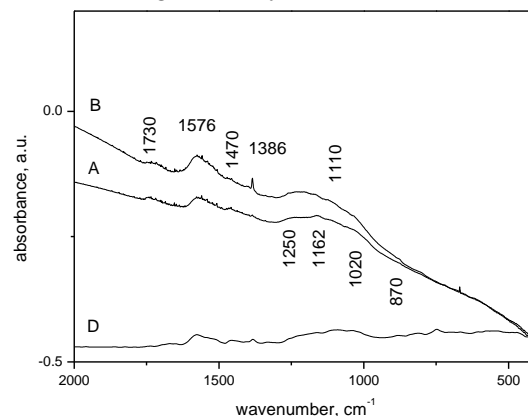


Fig.5. IR spectra of the samples

Predominant impact of oxidation and reduction of activated carbon surface on phenol adsorption was pointed out by some authors. An experimental and theoretical study of the adsorption of aromatics possessing electron-withdrawing and electron-donating functional groups by chemical modified activated carbons was discussed in [23-25].

According to their results, the carboxyl and hydroxyl groups inhibit the adsorption of phenol and increase the affinity of carbon towards adsorption of water molecules, and therefore, the solvent molecules could effectively block some micropores. This effect is explained by phenol adsorption that is governed by π - π dispersion interaction between the basal plane of carbon and the aromatic ring of the adsorbate. Oxygen atoms bound to the graphite edges can localize electrons and, thereby, remove them from π -electron system of the basal plane - consequently, the π - π interaction is weakened. Contrary to these effects of surface carboxyl and hydroxyl groups, the surface of quinone (or carbonyl) groups promote the adsorption of phenols, involving formation of an electron donor-acceptor complex of aromatic ring of adsorbate with the surface carbonyl groups, as proposed by [26, 27]. The data in Table 2 show that the formation of carboxylic groups and the increase of the content of hydroxyl groups leads to the decrease of the adsorption activity of Carbon B towards phenol. However the higher uptake of phenol on activated carbon A (150 mg g^{-1}) is to be expected in the view of the above mentioned. Thus adsorption of phenol on activated carbon is

enhanced on hydrophobic carbon A, in comparison with its oxidation modification carbon B (126 mg g⁻¹).

It has been noted that during thermal treatment (after which it is converted to Carbon D) of Carbon A losses approximately half of its specific surface area. Carbon D shows adsorption ability towards phenol very close to carbon B - this is indication that when a porous carbon comes into contact, water will first adsorb on the hydrophilic polar oxygen groups, including those located at the micropore entrances, because water molecules can form H-bonding with surface oxygen molecules and water molecules are more competitive than phenol towards adsorptive sites.

The adsorbed water molecules will be further associated with each other to form water clusters, which remarkably stabilized in micropores, causing partial blockage of the micropores, reducing the accessible surface area, and impeding or even preventing phenol adsorption. As demonstrated by the data shown in Table 2 thermal treatment can substantially remove oxygen-containing groups, thus lessening the possibility of the formation of water clusters, and enhancing the accessibility of the pores for phenol molecules, as well as improving interaction. That's why activated Carbon D shows adsorption ability close to Carbon B, independently that Carbon B posses more developed texture and higher micropore volume.

3.7. Effect of pH

In this study the influence of pH on phenol adsorption was investigated and interpreted. It was established that the amount adsorbed decreases at high pH values as well as at low pH values. The pK_a value for phenol is 9.89, so the adsorbed species above this pH are mostly anionic. The repulsion interactions between the surface layer and the anionic phenolates leads to reduced adsorption. The low pH value was obtained by using an acidic solution. Obviously additional protons were introduced in the solution in this way, and these protons are competing for the carbonyl sites, and thus 'blocking' them - therefore the adsorption was reduced at low pH. The influence of the pH on the adsorption of phenol on both activated carbons can be seen in Fig. 6.

At acidic pH the amount of phenol adsorbed, Q₀, remains constant or increases slightly with increasing pH, and at a certain value of pH, the value of Q₀ begins to decrease, which continues while pH increases. The decrease in phenol adsorption from pH = 6.3 to pH = 3.07 is due to the

increased H⁺ adsorption on carbonyl sites, which suppresses phenol adsorption on these sites.

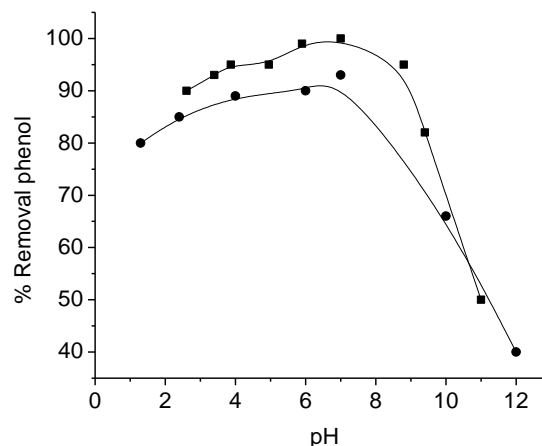


Fig. 6. Effect of pH on the retention of phenol (■ - Carbon A; ● - Carbon B).

On the other hand, the decrease in the phenol amount adsorbed from more alkaline solution is attributed to the greater solubility of dissociated phenol at pH > pK_a as well as to the increased repulsion forces between the dissociated form of the adsorbate and the carbon surface.

CONCLUSIONS

The results reported in this work show that mixtures of coal waste (coal tar pitch) and furfural (material contained in biomass wastes) is appropriate raw materials for the synthesis of nanoporous carbons with negligible ash content and well-developed porosity. The synthetic activated carbon shows higher adsorption activity towards phenol, comparable and higher in comparison with other activated carbons reported in the literature.

The adsorption capacity of the activated carbon and its oxidized modification towards phenol depends on the porous parameters and surface chemistry, the latter governing the retention mechanism - this is confirmed by the investigation of phenol adsorption of thermally treated activated carbon. Thermally treated sample, independently of its lower surface area and micropore volume, has adsorption capacity similar to the oxidized sample. Non-specific interactions are dominant for phenol adsorption on carbon A, whereas for the oxidized adsorbent electrostatic interactions (repulsive and/or attractive) may appear during adsorption process, depending on the pH of the solution.

ACKNOWLEDGEMENT: The authors thank for the financial support – grant DNS 7 FP 01/29 - 15.12.2011.

REFERENCES

- G. Busca, S. Berardinelli, C. Resini, L. Arrighi, Technologies for the removal of phenol from fluid streams: A short review of recent developments. *J. Haz. Mat.* **160**, 265 (2008).
- S. Sinkkonen, T. Rantion, J. Paasivita, S. Peltonen, A. Vattulainen, R. Lammi, Chlorinated phenolic compound in coniferous needles. Effect of metal and paper industry and incineration. *Chemosphere* **35**, 11175 (1997).
- C. Cooper, R. Burch, An investigation of catalytic ozonation for the oxidation of halocarbons in drinking water preparation. *Water Res.* **33**, 3695-3700 (1999).
- F. Larachif, I. Ihuta, K. Belkacemi, Catalytic wet air oxidation with a deactivating catalyst analysis of fixed and sparked three-phase reactors. *Catal.Today.* **649**, 309 (2001).
- V.V. Goncharuk, F. Vakulenko, A.N. Sova, S. Oleinik, Removal of organic contaminants from natural waters by combination of ozonation and UV-irradiation. *Khimia I Tekhnologia Vody* **26**, 34 (2004).
- J.M. Arzuada, M.J. Lopez-Munoz, J. Aguadom, Temperature, pH and concentration effects on retention and transport of organic pollutants across thin-film composite nanofiltration membranes. *Desalination* **221**, 253 (2008).
- Md. Ahmaruzzaman, Adsorption of phenolic compounds on low-cost adsorbents. A review. *Adv.Colloid Interface Sci.***143**, 2008, 48 (2008).
- T.J. Bandoz, Activated carbon surface in environmental remediation, in: T.J.Bandoz (Editor) Interface Science and Technology Series, Elsevier: New York, 2006.
- D. Savova, E. Apak, E. Ekinci, F. Yardim, N. Petrov, T. Budinova, M. Razvigorova, V. Minkova, Biomass conversion to carbon adsorbents and gas. *Biomass Bioenergy* **21**, 133 (2001).
- N. Petrov, T. Budinova, M. Razvigorova, J.B. Parra, P. Galiatsatou, Conversion of olive wastes to volatiles and carbon adsorbents. *Biomass Bioenergy* **32**, 1303 (2008).
- L.F. Velasco, B. Tsyntsarski, B. Petrova, T. Budinova, N. Petrov, J.B. Parra, C.O. Ania Carbon foams as catalyst supports for phenol degradation. *J. Haz. Mat.* **184**, 843 (2010).
- P.J.M. Carrott, M.M.L. Ribeiro-Carrott, R.P. Lima, Preparation of activated carbon “membranes” by physical and chemical activation of cork. *Carbon* **37**, 515 (1999).
- B. Petrova, B. Tsyntsarski, T. Budinova, N. Petrov, C.O. Ania, J.B. Parra, M. Mladenov, P. Tzvetkov, Synthesis of nanoporous carbons from mixtures of coal tar pitch and furfural and their application as electrode materials. *Fuel Proc. Technol.* **91**, 1710 (2010).
- J.I. Kroschwitz (editor), Concise encyclopedia of polymer science engineering; Wiley: New York, 1990, pp 424-425.
- Y.S. Ho, G. McKay, Sorption of dye from aqueous solution by peat. *Chem. Eng. J.* **70**, 115 (1988).
- F. Rouquerol, J. Rouquerol, K. Sing, In: Adsorption by powders and porous solids. Principles, methodology and applications, Academic Press: London.1999.
- H.P. Boehm, Chemical Identification of Surface Groups. In: Eley, D.D., Pines, H., Weisz, P.B.(eds.), Advances in catalysis and Related Subjects, vol.16. Academic Press: New York, 1996, pp.179-274.
- I. Langmuir, The constitution and fundamental properties of solids and liquids, Part I Solids. *J. Am. Chem. Soc.* **38**, 2221 (1916).
- C.H. Giles, T.H. MacEwan, S.N. Nakhwa, D. Smith, D. Studies in adsorption. Part XI. A system of classification of solutions adsorption isotherms, and its use in diagnosis of adsorption mechanisms and in measurement of specific surface areas of solids. *J. Chem. Soc.* 3973 (1960).
- G. Soctrates, Infrared Characteristic Group Frequencies, Wiley, NewYork, 1994.
- S. Biniak, G. Szymanski, J. Siedlewski, A. Swatkowski, The characterization of activated carbons with oxygen and nitrogen surface groups, *Carbon* **35**, 1799 (1997).
- J. Zawadzki, B. Azambre, O. Heintz, A. Krzton, J. Weber, IR study of the adsorption and decomposition of methanol on carbon surfaces and carbon-supported catalysts, *Carbon* **38**, 509 (2000).
- E. Fernandez, D. Hugi-Cleary, M.V. Lopez-Ramon, F. Stoecki, Adsorption of phenol from dilute and concentrated aqueous solutions by activated carbons. *Langmuir* **19**, 9719 (2003).
- D.M. Nevskaja, A. Santianes, V. Munoz, A. Guerrero-Ruiz, Interaction of aqueous solutions of phenol with commercial activated carbons: an adsorption and kinetic study. *Carbon* **37**, 1065 (1999).
- L.R. Radovic, I.F. Silva, J.I. Ume, J.A. Menendez, C.A. Leon, A.W. Scaroni, An experimental and theoretical study of the adsorption of aromatics possessing electron-withdrawing and electron-donating functional groups by chemically modified activated carbons. *Carbon* **35**, 1339 (1999).
- B.D. Epstein, E. Dalle-Molle, J.S. Mattson, Electrochemical investigations of surface functional groups on isotropic pyrolytic carbon. *Carbon* **9**, 609 (1971).
- J.S. Mattson, H.B. Mark Jr., M.D. Malbin, W.J. Weber Jr., Crittenden, J. C. Surface chemistry of

ИЗВЛИЧАНЕ НА ФЕНОЛ ОТ ЗАМЪРСЕНИ ВОДИ ЧРЕЗ АКТИВЕН ВЪГЛЕН, ПОЛУЧЕН ОТ ОТПАДНИ ПРОДУКТИ ОТ ПРЕРАБОТКАТА ВЪГЛИЩА

Б. Г. Цинцарски ¹, Б. Н. Петрова ¹, Т. К. Будинова ^{1*}, Н. В. Петров ¹, Д. К. Теодосиев²

¹ *Институт по органична химия, Българска академия на науките, ул. „Акад. Г. Бончев”, бл. 9, София 1113*

² *Институт по космически изследвания и технологии, Българска академия на науките, ул. „Акад. Г. Бончев”, бл. 1, София 1113*

Постъпила на 15 април, 2013 г.; коригирана на 17 юли, 2013 г.

(Резюме)

Беше изследвана адсорбцията на фенол върху различни модификации от активен въглен, получен от смес от каменовъглен пек и фурфурол. Текстурата, порьозната структура и химическият характер на повърхността бяха изследвани посредством адсорбция на азот, ИЧ спектроскопия и кислородни функционални групи. Активният въглен, получен чрез пиролиз в присъствие на водна пара, има по-висока адсорбционна способност (150 mg g^{-1}) спрямо другите изследвани активни въглени – окислен въглен (126 mg g^{-1}) и въглен, термически обработен (117 mg g^{-1}) до $1300 \text{ }^\circ\text{C}$. Адсорбционният капацитет спрямо фенол на термически обработения активния въглен е много близък до капацитета на окисления въглен, независимо от по-ниската стойност на специфична повърхност и обема на порите. Това вероятно се дължи на образуването на водни асоциати. Резултатите показват, че адсорбцията на фенол върху активен въглен, получен от смес на фурфурол и каменовъглен пек, корелира със специфичната повърхност и обема на порите.

Chemical profiles of the essential oil of wild and *in vitro* regenerated *Zataria multiflora* Boiss. (Lamiaceae)

M. Ghasemi, M. H. Mirjalili*, J. Hadian

Department of Agriculture, Medicinal Plants and Drugs Research Institute, Shahid Beheshti University, G. C., Evin, Tehran, Iran

Received June 24, 2013; Accepted August 5, 2013

Zataria multiflora Boiss. is an aromatic shrub belonging to the family Lamiaceae and its aerial parts are used in traditional medicine, pharmaceutical and food industries. In the present study, the content and chemical composition of the essential oils from regenerated plants grown '*in vitro*' were assessed by gas chromatography-flame ionization detector (GC-FID) and gas chromatography-mass spectrometry (GC-MS) and compared with those of wild plants. In total, 29 and 16 compounds were identified and quantified in wild and *in vitro* regenerated plants, representing 99.6% and 99.4% of the total oil, respectively. The major identified components in the oil from wild and *in vitro* regenerated plants were carvacrol (35.0% and 49.2%), thymol (9.6% and 11.8%), *p*-cymene (11.7% and 5.8%), carvacrol methyl ether (7.5% and 11.3%) and γ -terpinene (4.7% and 9.4%). The oils were dominated by oxygenated monoterpenes followed by monoterpene hydrocarbons. Our results indicate that *in vitro* propagated plants produce oil more rich in oxygenated sesquiterpenes than wild plant. Quantitative and qualitative variations were observed both in wild and in micropropagated plants in relation environmental factors. Thus, micropropagation provides plants suitable for the industrial exploitation of this species.

Key words: *Zataria multiflora* Boiss., Lamiaceae, essential oil, *in vitro* culture, thymol

INTRODUCTION

The family of Lamiaceae is one of the largest and most distinctive families of flowering plants, with *ca.* 258 genera and 6970 species worldwide. Lamiaceae with 46 genera and *ca.* 420 species and subspecies have a great diversity and distribution in the flora Iran [1-3]. Altogether 124 species and subspecies (30%) of this family are endemic to Iran [4]. Lamiaceae plants are well known for the essential oils and many biologically active oils have been isolated from various members of this family [5-7]. Some are one of the major sources of culinary, food flavoring, vegetable, and medicinal plants all over the world. A wide range of compounds such as terpenoids, phenolic compounds, and flavonoids have been reported from the members of the family [8-10].

Zataria multiflora Boiss. as a suffruticose perennial shrub with 40-80 cm height is a member of this family and is known by the common Persian name of "Avishan Shirazi". The plant grows wild on the rocky and gravelly slopes from south to central parts of Iran in the Saharo-Sindian and Irano-Turanian regions and also in Pakistan and Afghanistan. *Z. multiflora* has thyme-like fragrance

and its generic name is derived from the arabic word "za'tar", meaning thyme [11]. *Z. multiflora* is extensively used in traditional medicine as a condiment, antiseptic, analgesic (pain-relieving) and carminative (anti-flatulence and intestine-soothing). Biological activities of the plant have been also attributed to essential oil containing mainly phenolic compounds, thymol and carvacrol [12-15].

In recent years the monograph of *Z. multiflora* has been introduced and presented in Iranian herbal pharmacopoeia [16]. According to this monograph, main chemical constituent of the plant has been described as carvacrol (61.0 %) and thymol (25.0 %) and also its herbal drug should contain at least 0.6 % oil. The huge amounts of herbal drugs of this species are harvested from the wild every year and are sold in the inner markets or exported. In recent years several pharmaceutical and cosmetic products have been introduced to the market by pharmaceutical companies [16].

Owing to over-exploitation of wild plants for commercial purposes and a low propagation rate in nature, *Z. multiflora* is now almost extinct and is listed as an extremely vulnerable species in Iran [17]. *In vitro* culture offers a viable approach to propagate this species since it can also be used as a complimentary strategy for conservation and utilization of genetic resources. Further, *in vitro*

* To whom all correspondence should be sent:
E-mail: m-mirjalili@sbu.ac.ir

plant regeneration through axillary bud culture is large number of consistently uniform and true-to-type plants within a short span of time, but also offer an alternative to field agriculture to manufacture economically important secondary metabolites such as flavors, dyes, and pharmaceuticals within controlled laboratory environments [18,19]. Recently developed *in vitro* propagation techniques offer high-rate multiplication alternatives for plants of horticultural, economical and medicinal importance [20], as well as medium- to long-term conservation of valuable germplasm by means of slow growth storage and cryopreservation [21]. Although the essential oil of *Z. multiflora* has been studied previously [22-24], but to the best of our knowledge, there is no data reporting aroma composition of the essential oil obtained from *in vitro* regenerated plants. Further, we speculate that *in vitro* plantlet culture may offer a means to procure essential oil compounds *in vitro* at the commercial level. In the present work, the chemical composition of the *in vitro* regenerated *Z. multiflora* oil isolated by hydrodistillation was studied and compared with those of wild plants for the first time. These results can be considered for further strategies like *in vitro* shoot cultures for enhanced production of valuable phenolic terpenoids as thymol and carvacrol on a large scale.

EXPRIMENTAL

Plant material

The aerial parts of *Z. multiflora* were collected at vegetative stage from Jiroft (28° 41' N, 57° 42' E at an altitude of 710 m), Kerman Province, Iran. A Voucher specimen has been deposited at the Herbarium of Medicinal Plants and Drugs Research Institute (MPH), Shahid Beheshti University, Tehran, Iran.

In vitro regeneration

In vitro shoot proliferation of *Z. multiflora* were performed by culturing of internodal segments (3 cm) of wild growing stock plant on Murashige and Skoog (MS) medium [25] fortified with 1.5 mg/L BAP plus 1.0 mg/L IBA. Rooting of proliferated shoots was also performed on B5 medium [26] supplemented with 1.5 mg/L IBA. The cultures were incubated at 25 ± 2°C under a 16-h photoperiod, with light provided by cool daylight fluorescent lamps (40 μmol⁻¹ m⁻² s⁻¹), and were proliferated by monthly subcultures to fresh medium of the same type.

Essential oil isolation

not only an easy and economic way of obtaining a

The essential oil of air-dried samples (30 g) was isolated by hydrodistillation for 3 h, using a Clevenger-type apparatus, recommended by the British Pharmacopeia [27]. The essential oil was dried over anhydrous sodium sulfate (Na₂SO₄) and kept at 4°C in dark vial until analyzed and tested.

GC-FID analysis

GC analysis was performed using a Thermoquest gas chromatograph with a flame ionization detector (FID). The analysis was carried out on fused silica capillary DB-5 column (30 m × 0.25 mm i.d.; film thickness 0.25 μm). The injector and detector temperatures were kept at 250 °C and 300 °C, respectively. Nitrogen was used as the carrier gas at a flow rate of 1.1 ml/min; oven temperature program was 60–250 °C at the rate of 4 °C /min and finally held isothermally for 10 min; split ratio was 1:50.

GC-MS analysis

GC-MS analysis was carried out by use of Thermoquest-Finnigan gas chromatograph equipped with fused silica capillary DB-5 column (60 m × 0.25 mm i.d.; film thickness 0.25μm) coupled with a TRACE mass (Manchester, UK). Helium was used as carrier gas with ionization voltage of 70 eV. Ion source and interface temperatures were 200 °C and 250 °C, respectively. Mass range was from 35 to 456 amu. Oven temperature program was the same given above for the GC.

Identification and quantification of the oil components

The constituents of essential oils were identified by calculation of their retention indices under temperature-programmed conditions for *n*-alkanes (C₆–C₂₄) and the oil on a DB-5 column under the same chromatographic conditions. Identification of individual compounds was made by comparison of their mass spectra with those of the internal reference mass spectra library (Adams and Wiley 7.0) or with authentic compounds and confirmed by comparison of their retention indices with authentic compounds or with those of reported in the literature [28]. For quantification purposes, relative area percentages obtained by FID were used without the use of correction factors.

RESULTS AND DISCUSSION

The hydrodistillation of the air-dried aerial parts of wild and *in vitro* regenerated *Z. multiflora* gave yellow pale oils in 2.6 and 0.9 (w/w%, based on dry weight) yield, respectively. The chemical

composition of the oil samples was mainly investigated using both GC-FID and GC-MS techniques. Qualitative and quantitative analytical results are listed in Table in the order of their

elution on the DB-5 column. GC-FID chromatograms of the essential oils from wild and *in vitro* regenerated plants with identified major compounds are shown in the Figure 1.

Table. Essential oil composition of wild and in vitro regenerated plants of *Zataria multiflora*

No.	RI ^a	Compounds	%		Identification methods
			Wild plant	In vitro regenerated plant	
1	929	α -Thujene	1.2	0.4	RI, MS ^b
2	939	α -Pinene	5.0	0.6	RI, MS, CoI ^c
3	954	Camphene	0.4	-	RI, MS
4	983	β -Pinene	1.9	0.2	RI, MS, CoI
5	988	Myrcene	2.0	1.2	RI, MS, CoI
6	1008	α -Phellandrene	0.3	0.1	RI, MS
7	1020	α -Terpinene	1.8	1.5	RI, MS
8	1028	p-Cymene	11.7	5.8	RI, MS
9	1032	Limonene	0.9	-	RI, MS, CoI
10	1035	1,8-Cineol	1.6	-	RI, MS, CoI
11	1060	γ -Terpinene	4.7	9.4	RI, MS
12	1069	cis-Sabinene hydrate	0.6	1.0	RI, MS
13	1091	Terpinolene	0.3	-	RI, MS
14	1097	Linalool	2.6	-	RI, MS, CoI
15	1101	trans-Sabinene hydrate	0.3	-	RI, MS
16	1182	Terpinen-4-ol	1.6	0.2	RI, MS
17	1196	α -Terpineol	1.5	-	RI, MS
18	1202	cis-Dihydro carvone	0.2	-	RI, MS
19	1233	Thymol methyl ether	1.1	-	RI, MS
20	1244	Carvacrol methyl ether	7.5	11.3	RI, MS
21	1288	Thymol	9.6	11.8	RI, MS, CoI
22	1305	Carvacrol	35.0	49.2	RI, MS, CoI
23	1352	Thymol acetate	0.5	-	RI, MS
24	1371	Carvacrol acetate	2.8	0.5	RI, MS
25	1435	(E)-Caryophyllene	2.3	4.8	RI, MS
26	1454	Aromadendrene	0.4	-	RI, MS
27	1508	Viridiflorene	0.2	1.4	RI, MS
28	1593	Spathulenol	0.4	-	RI, MS
29	1600	Caryophyllene oxide	1.2	-	RI, MS
		Monoterpene hydrocarbons	31.1	20.2	
		Oxygenated monoterpenes	64.0	73.0	
		Sesquiterpene hydrocarbons	2.9	6.2	
		Oxygenated Sesquiterpenes	1.6	-	
		Total identified	99.6	99.4	

^aRetention indices relative to C6–C24 n-alkanes on a DB-5 column; ^bmass spectrometry; ^cco-injection with authentic compounds

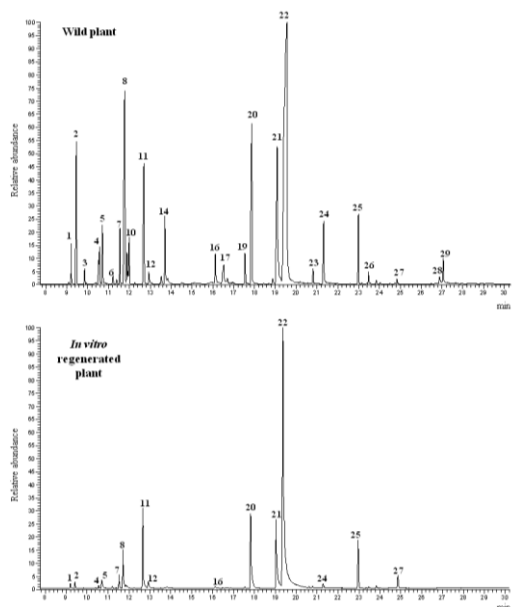


Fig. 1. Gas chromatography–flame ionization detector (GC–FID) chromatograms of the essential oil from wild and *in vitro* regenerated *Zataria multiflora* Boiss.

In total, 29 and 16 compounds were identified and quantified in wild and *in vitro* regenerated plants, representing 99.6% and 99.4% of the total oil, respectively. The major identified components in the oil from wild and *in vitro* regenerated plants were carvacrol (35.0% and 49.2%), thymol (9.6% and 11.8%), *p*-cymene (11.7% and 5.8%), carvacrol methyl ether (7.5% and 11.3%) and γ -terpinene (4.7% and 9.4%).

Chemical structure of the major identified components is shown in the figure 2.

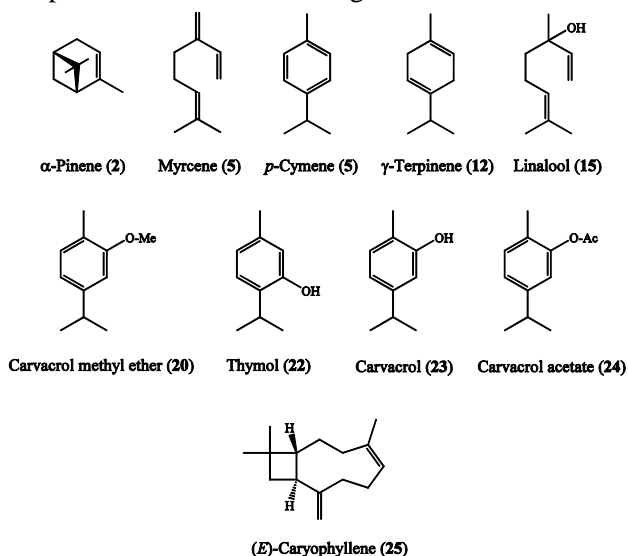


Fig. 2. Chemical structure of the major identified compounds in the essential oil of wild and *in vitro* regenerated *Zataria multiflora* Boiss.

The classification of the identified compounds, based on functional groups is summarized at the

end of Table. The oils were dominated by oxygenated monoterpenes (64.0 and 73.0% in the oils from wild and *in vitro* plants, respectively) followed by monoterpene hydrocarbons (20.2 and 31.1% in the oils from *in vitro* and wild plants, respectively). It was found that the chemical profile of the essential oil from *in vitro* regenerated plant is qualitatively different than wild plant oil. The essential oils of wild and *in vitro* regenerated plants comprised 13 and 9 monoterpene hydrocarbons, 11 and 5 oxygenated monoterpenes, 3 and 2 sesquiterpene hydrocarbons, respectively (Table). Monoterpene hydrocarbons camphene, limonene, terpinolene and *trans*-sabinene hydrate were absent in the essential oil profile of *in vitro* regenerated plants. 1,8 Cineol, linalool, α -terpineol, *cis*-dihydro carvone, thymol methyl ether and thymol acetate as oxygenated monoterpenes were not detected in the essential oil obtained from regenerated plants grown '*in vitro*'. Oxygenated sesquiterpenes spathulenol and caryophyllene oxide were only detected in the essential oil of wild plant. Our results showed that both wild and clonally propagated plants contained high levels of monoterpene hydrocarbons *p*-cymene and γ -terpinene (Table). However, the relative concentration of *p*-cymene was higher and γ -terpinene was lower in the wild plant; as well, α -pinene was also higher. A major difference between the oils from *in vitro* and *in vivo* *Z. multiflora* plants was observed in the content of oxygenated monoterpenes; in the oil from micropropagated plants the amount of the oxygenated monoterpenes carvacrol, thymol and carvacrol methyl ether was higher than that found in the oil from *in vivo* plants. Similarity in the chemical composition of essential oils from *in vitro* and *in vivo* plants has been reported by some other authors [29–31]. For example, Kuźma et al. (2009) [29] have reported that a chemical profile of the essential oil from *Salvia sclarea in vitro* plants was similar to that of the control mother plants, with linalool as the main compound. It has been also reported that a chemical profile of the essential oil from *in vitro* grown *Origanum vulgare* L. ssp. *hirtum* was comparable to that *in vivo* plants [31]. On the other hand, comparative studies on the essential oils from *in vitro* and *in vivo* plants of *Salvia przewalskii* showed numerous differences between the two oil profiles [32]. It has been reported that microshoots, which are the normal sites for secondary metabolism in nature, readily manifest commercially desired secondary metabolites *in vitro* [19,33]. For example, in the Lamiaceae family, essential oil synthesis occurs primarily in

the leaf epidermal cells and storage primarily in glandular leaf trichomes [34]. Examination of the leaf surfaces of foliage from tissue culture plantlets also reveals the occurrence of these leaf trichomes and they also readily produce volatile essential oils [33]. Our results revealed that *Z. multiflora* plantlets grown *in vitro* are quantitatively potent in the production of the major essential oil components as well as the wild plant. It can be concluded that *in vitro* regeneration of *Z. multiflora* would be of great interest for the cloning of valuable genotypes, for example, the plants that contain high level of phenolic terpenoids as carvacrol and thymol. The rapid cloning may represent a way to exploit the natural variability of this species. This technique would also be useful to mass produce this plant, relieving wild populations from the pressure produced by intensive collection. Further, these results strongly suggest that using *in vitro* plantlets as a means to produce secondary metabolites is possible for future commercial applications.

Acknowledgements: The authors gratefully acknowledge the Shahid Beheshti University Research Council for financial support of this project.

REFERENCES

1. C. Hedge, in 'Advances in Labiatae Science'. Eds. R. M. Harley, T. Reynolds, Royal Botanical Gardens, Kew, London, 1992, p. 7.
2. Z. Jamzad, M. Ingrouille, M. S. J. Simmonds, *Taxon*, **52**, 93 (2003).
3. W. S. Judd, C. S. Campbell, E. A. Kellogg, P. F. Stevens, in 'Plant Systematics' A Phylogenetic Approach, Sinauer Association, Inc., Sunderland, USA, 1999, p. 383.
4. K. H. Rechinger, in 'Flora Iranica', Ed. K. H. Rechinger, Akademische Druck-u. Verlagsanstalt, Graz, Austria, 1982, Vol. 150, p. 483.
5. E. Shadia, E.-A. Abd, E. A. Omer, A. S. Sabra, *Res. J. Agric. Biol. Sci.*, **3**, 740 (2007).
6. Sartoratto, A. L. M. Machado, C. Delarmelina, G. M. Figueira, M. C. T. Duarte, V. L. G. Rehder, *Braz. J. Microbiol.*, **35**, 275 (2004).
7. C. Goren, G. Topcu, G. Bilsel, M. Bilsel, Z. Aydogmus, J. M. Pezzuto, *Z. Naturforsch. C*, **57**, 797 (2002).
8. P. Richardson, in 'Advances in Labiatae Science', Eds. R. M. Harley, T. Reynolds, Royal Botanical Gardens, Kew, London, 1992, p. 291.
9. Y. Lu, L. Yeap Foo, *Phytochemistry*, **59**, 117 (2002).
10. G. Zegorka, K. Glowniak, *J. Pharm. Biomed. Anal.*, **26**, 179 (2001).
11. A. Ghahreman, F. Attar, *Biodiversity of Plant Species in Iran*, Tehran University Publications: Tehran, 1999, p. 515.
12. A. Zargari, *Medicinal Plants*. Tehran University Publications: Tehran, 1970, **4**, p. 42.
13. N. Abbasgholizadeh, G. H. Ettehad, R. Arab, A. Nemati, M. Barak, A. Pirzadeh, M. Zarei, *Res. J. Biol. Sci.*, **3**, 345 (2008).
14. H. Gandomi, A. Misaghi, A. A. Basti, S. Bokaei, A. Khosravi, A. Abbasifar, A. J. Javan, *Food Chem. Toxic.*, **47**, 2397 (2009).
15. M. K. Gharib Naseri, H. Mazlomi, M. Goshairesh, G. Vakilzadeh. A. Heidari, *Iranian J. Pharm. Res.*, **5**, 131 (2006).
16. N. Ghassemi Dehkordi, S. E. Sajjadi, A. Ghannadi, Y. Amanzadeh, M. Azadbakht, G. R. Asghari, G. R. Amin, A. Hajiakhoondi, A. M. Taleb, *Iranian Herbal Pharmacopeia*. Ministry of Health, Treatment, and Medical Education: Tehran, 2009, p. 795.
17. A. Jalili, Z. Jamzad, *Red Data Book of Iran, A Preliminary Survey of Endemic, Rare & Endangered Plant Species in Iran*. Research Institute of Forest and Rangelands Publication, Tehran, Iran, 1999, p. 340.
18. E. Pitzcak, M. Wielanek, H. Wysokiska, *Plant Sci.*, **168**, 431 (2005).
19. M. Vanisree, C. Y. Lee, S. F. Lo, S. M. Nalawade, C. Y. Lin, H. S. Tsay, *Bot. Bull. Acad. Sin.*, **45**, 1 (2004).
20. P. K. Pati, S. P. Rath, M. Sharma, A. Sood, P. S. Ahuja., *Biotech. Adv.*, **24**, 94 (2006).
21. A. Previati, C. Benelli, F. Da Re, A. Ozudogru, M. Lambradi, *Propag. Orn. Plants*, **8**, 93 (2008).
22. S. S. Saei-Dehkordi, H. Tajik, M. Moradi, F. Khalighi-Sigaroodi, *Food Chem. Toxicol.* **48**, 1562 (2010).
23. K. Zomorodian, M. J. Saharkhiz, A. Bandegi, G. Shekarkhar, A. Bandegani, K. Pakshir, A. Bazargani, *Pharmacogn. Mag.*, **7**, 53 (2011).
24. J. Hadian, S. Nejad Ebrahimi, M. H. Mirjalili, A. Azizi, H. Ranjbar, W. Friedt, *Chem. Biodiversity*, **8**, 176 (2011).
25. A. Mohammadi Purfard, G. Kavooosi, *J. Food Safety*, **32**, 326 (2012).
26. T. Murashige, F. Skoog, *Physiol. Plant*, **15**, 473 (1962).
27. O. L. Gamborg, R. A. Milar, K. Ojima, *Exp. Cell Res.*, **50**, 151 (1966).
28. British pharmacopoeia, HMSO: London, UK, 1993.
29. R. P. Adams, *Identification of essential oil components by gas chromatography/mass spectroscopy*. Allured, Carol Stream, IL, 2007.
30. L. Kuźma, D. Kalemba, M. Ryzalski, B. Ryzalska, M. Więckowska-Szakiel, U. Krajewska, H. Wysokińska, *Molecules*, **14**, 1438 (2009).
31. A. V. Chebel, E. R. Koroch, H. R. Juliani, H. R. Juliani, V. S. Trippi, *In Vitro Cell. Dev. Biol.-Plant*, **34**, 249 (1998).
32. I. M. Fortunato, P. Avato, *Plant Cell Tiss. Org. Cult.*, **93**, 139 (2008).
33. E. Skała, D. Kalemba, A. Wajs, M. Różalski, U. Krajewska, B. Różalska, M. Więckowska-Szakiel, H. Wysokińska, *Z. Naturforsch.*, **62c**, 839 (2007).

ХИМИЧЕСКИ ПРОФИЛИ НА ЕТЕРИЧНО МАСЛО НА ДИВОРАСТЯЩИ И ИН-ВИТРО РЕГЕНЕРИРАНИ *Zataria multiflora* BOISS. (LAMIACEAE)

М. Гасеми, М. Х. Мирджалили*, Дж. Хадиан

*Департамент по селско стопанство, Институт за изследване на медицински растения и лекарства,
Университет Шахид Бехеци, Г. С., Евин, Техеран, Иран*

Постъпила на 24 юни, 2013 г.; приета на 5 август, 2013 г.

(Резюме)

Zataria multiflora Boiss. е ароматен храст, принадлежащ на семейство Устноцветни (Lamiaceae), чиито надземни части се използват в традиционната медицина, фармацевтичната и хранително-вкусовата промишленост. В текущото проучване са изследвани съдържанието и химическият състав на етеричните масла, получени от регенерирани растения, отгледани „ин витро” чрез газова хроматография – пламъков йонизационен детектор (GC-FID) и газова хроматография – мас спектрометрия (GC-MS) и сравнени с тези на диворастящи растения. Общо 29 и 16 съединения са идентифицирани и определени количествено съответно в диворастящи и ин витро отгледани растения, представляващи 99, 6% и 99, 4% от общото количество на маслата. Основните определени съединения в маслото от дивите и инвитро регенерираните растения са карвакрол (35,0% и 49,2%), тимол (9,6% и 11,8%), п-цимен (11,7% и 5,8%) метилов етер на карвакрола (7,5% и 11,3%) и γ -терпипен (4,7% и 9,4%). Маслата съдържат основно окислени монотерпени, последвани от монотерпенови въглеводороди. Нашите резултати показват, че ин витро размножените растения произвеждат масла, по-богати на окислени сескитерпени в сравнение с дивите. Качествени и количествени различия се наблюдават както при диворастящите, така и в микроразмножените растения в зависимост от условията на околната среда. Това показва, че микроразмножаването осигурява растения, подходящи за промишленото използване на този вид.

Preparation and characterization of composite hydrocolloid films from sodium alginate and high methoxyl pectin

Sv. M. Dyankova*, A.O. Solak

Institute of Cryobiology and Food Technologies, BG – 1407 Sofia, Bulgaria

Received April 11, 2013; Accepted July 16, 2013

A technology for obtaining of a composite biodegradable film on the basis of sodium alginate and apple high methoxyl (HM) pectin has been developed. Good mechanical characteristics have been established when using the two polysaccharides in proportion 1:1. For them the ultimate tensile strength (TS) was 53,53 MPa, the elongation at ultimate strength (E) was 34,48%, Young's modulus (YM)- 202,84 MPa. The composite film showed very poor solubility at low pH, including in a simulated gastric juice. At pH values above 4,0 the alginate films showed slower and the composite films faster and complete disintegration in the medium. Due to the good mechanical characteristics and selective solubility depending on pH, the composite sodium alginate-HM pectin films are appropriate as material for encapsulating of biologically active substances or microorganisms with low activity or survival, under conditions of low pH.

Key words: composite films, alginate, high methoxyl pectin, mechanical properties, dissolution

INTRODUCTION

A wide range of biopolymers are used as a base for films, coatings and therapeutical systems with application in medicine, pharmacy and food industry. Very often the obtained biopolymer systems represent a monohydrocolloid layer of proteins or polysaccharides. During the last several years, however, the technological investigations have been directed towards the development of composite films, which are obtained by combining of proteins, polysaccharides and/or lipids. They are designed with the aim of using the synergetic effect of the combined properties of the separate components [1].

The salts of alginic acid and the pectins are an example of polysaccharides with good film forming properties. The alginates are hydrophilic polysaccharides, extracted from various species brown seaweed (*Phaeophyceae*). They are of interest because of their unique colloid properties and their capacity to form tridimensional networks in the presence of polyvalent cations (for example Ca^{2+}) in water medium as a result of which a gel or an insoluble polymer are obtained [2,3]. By chemical structure the alginates are unbranched binary copolymers, built mainly of (1-4)-linked β -D-mannuronic acid and α -L-guluronic acid residues. There are three types structural elements in the alginates: β (1-4)-D-mannuronate (M-block), α -(1-

4)-L-guluronate (G-block), and the third structure contains both monomers in almost equal proportions (MG-block)[2,3,4]. From the alginic acid salts the sodium alginate is most frequently applied in practice.

The pectins are plant polysaccharides. Their primary structure is a branched chain, in which the main chain consists of acid derivatives of the hexoses (D-galacturonic acid) and the side chains are built of pentoses(D-xylose and L - arabinose) and hexoses (D – glucose and D - galactose). In the main chain the units D-galacturonic acid are linked by α -(1-4) glycoside link, i.e. it is a polygalacturonic acid to which side chains are attached by β -(1-6) glycoside links. The carboxyl groups of the galacturonic acid are partially esterified with methanol and neutralized with metal and ammonia ions obtaining different pectin substances – pectins, pectates and pectic acids [5,6].

Between the full methylation and the complete demethylation of the polygalacturonic acid there are all intermediate stages of partial esterification which results in a great variety in pectins from different raw materials. It is known that the basic index, exerting the greatest effect on the rheological and physicochemical properties of pectin is the degree of esterification (DE) by which is expressed the percentage of the esterified $-\text{COOH}$ groups from the total number. Depending on the degree of esterification pectins are divided into 2 main categories – high methoxyl (HM) and low methoxyl (LM) pectin, and the low methoxyl

* To whom all correspondence should be sent:
E-mail: svetla.diankova@ikht.bg

pectin is subdivided into 2 groups – conventional and amidated. The degree of esterification of the HM pectins varies from 50 to 90%. The LM pectins (DE under 50%) are usually obtained by demethylation of the extracted pectins through enzyme processes or by treating with acids or ammonia in alcohol medium. HM and LM pectins have a different mechanism of gel forming when dissolved in water [7,8].

The wide use of alginates and pectins in the food industry and medicine is dictated by the lack of toxicity and allergenicity, and the unique colloid properties. Both biopolymers are capable to form gels in the presence of divalent cations [4,9]. The alginate and the pectin form synergic mixed gels which lead to structures completely different from those of the pure biopolymers. They are of particular interest when creating films with new improved characteristics.

The nature of the synergy interaction between pectin and alginate has not been fully clarified. The rheological behavior of the mixed solutions and hydrogels has been studied to a great extent [4, 10, 11], while the investigations in the field of the physicochemical properties of the resulting composite films are less developed.

The objective of the present investigation is the preparation of a composite biodegradable film on the base of sodium alginate and apple high methoxyl pectin, and assessment of the physicochemical and mechanical characteristics of the obtained materials.

EXPERIMENTAL

Materials: Apple high methoxyl pectin (CpCelso), sodium alginate (Sigma Aldrich), glycerol p.a. (Merck), calcium chloride p.a. (Merck).

Biopolymer films preparation: Sodium alginate (2,5%) and high methoxyl pectin (2,5%) were dissolved in distilled water. Film forming compositions were prepared by casting sodium alginate and high methoxyl pectin aqueous solutions at the following proportions: 100–0% (AG), 75–25% (C₁AG-P), 50–50% (C₂AG-P) and 25–75% (C₃AG-P). Glycerol was used as a plasticizer (0.6g/g polymers). Four formulations were mixed under continuous stirring (300rpm) until a homogeneous solution was obtained, then the stirring rate was reduced to 100 rpm while 0.1 M CaCl₂ (1ml/100ml) was added. The prepared film forming solutions (FS) were poured onto Petri dishes (0,325 g FS/cm²) and were dried under vacuum (20 kPa, SPT-200 Vacuum Drier) at 35°C.

Dried samples were immersed for 30 minutes in 10 ml of 0.3 M CaCl₂ solution to allow cross-linking, and were washed with distilled water to remove excess Ca²⁺. Films were dried at 25°C and conditioned at 50 ± 1% RH before testing.

Analysis of the source pectin: The content of methoxy-groups, galacturonic acid and the DE was determined by the method described in the monograph for pectin in USP 23 [12].

Moisture content - by express weight method with infrared dryer (Sartorius Thermo Control YTC 01 L).

Determination of pH - pH-meter 3310 (Jenway).

Rheological tests - rotational viscometer (Reomat 108), at temperature of the investigated mixtures 20 ± 1°C.

Film thickness: The thickness of the films was measured with a digital micrometer to the nearest 0.01±5% at five random locations on the film. Mean thickness values for each sample were calculated and used in mechanical properties determination.

Mechanical properties: Mechanical properties were determined according standard BDS EN ISO 527-2:2002 [13] with apparatus UMT: Macro mechanical and tribology tester (CETR-USA). Investigations were made for: strength at the moment of destruction (*Ultimate Strength, TS*); modulus of the elastic deformations (*Young's modulus, YM*); strength at plastic deformation (*Yield strength*) and elongation at destruction (*Elongation at Ultimate strength, E*). The results are presented as average values of 6 measurements for each sample.

In-vitro dissolution tests: Model systems, simulating the conditions in the digestive tract were used. Discs from the trial series (with area 1,77 cm²) were put in simulated gastric juice (pH 2,0; pepsin) and simulated intestinal juice (phosphate buffer pH 8,0; enzyme complex - pancreatin), prepared according to Charteris et al.[14].

Additionally a test was carried out with simulated intestinal juice in Tris-buffer medium with pH 8,0. The changes in the samples were recorded at every hour as a percentage alteration of the area. The results are presented as the mean of three replicates.

Test for dissolution depending on pH. The effect of pH on the disintegration of the different film variants (alginate and alginate-pectin) was followed up. Discs from each variant (with area 1,77 cm²) were placed in buffer media with pH 2,0, 3,0, 4,0, 5,0, 6,0, 7,0, 8,0 and 9,0. The

changes were recorded at every hour as a percentage alteration of the area. The results are presented as the mean of three replicates.

Statistical analysis. Results were analysed by statistical program Minitab 15. One-Way ANOVA and Tukey Test were used to determine statistically significant differences ($p < 0.05$).

RESULTS AND DISCUSSION

Analysis of the source pectin

The quantitative analyses of samples from the source pectin product showed content of pure pectin - 71,50%. As it is known the offered commercial products besides pure pectin also contain neutral sugars and other ballast substances. The content of the galacturonic acid was $753,0 \pm 14,76$ mg/g, and of the methoxy groups - $68,50 \pm 2,36$ mg/g. From the obtained results was calculated the degree of esterification which for this pectin type is 56,90%. By DE the used pectin was determined as high methoxyl but also with presence of a certain percentage free carboxyl groups.

pH of the film forming solutions varies from 2,88 for the pectin up to 6,16 for the sodium alginate (AG). The different variants film forming solutions show pH values in the acid area: C₁AG-P - 4,25; C₂AG-P - 3,78 and C₃AG-P - 3,54.

Characteristics of the obtained films

Visually the films were homogeneous, uninterrupted, with no brittle areas and without air bubbles (Table 1). They were easily manageable and flexible. The color of the alginate films varies from transparent to lightly opaque. The films with high pectin content were with lightly yellowish nuance. The thickness of the obtained materials depends on the applied technology and on the drying conditions, and is an important parameter for determining of the values of the mechanical characteristics. The most popular method for producing of films with controlled thickness is the pouring of a constant quantity film forming mixture for a given area. We applied one and the same proportion for the different variants - 0,325 g FS/cm² as the obtained films were with thickness from 0,039 up to 0,058 mm.

In this investigation the calcium chloride was used as gel forming and cross-linking agent. The polyvalent cations such as Ca²⁺, play the role of bridges between the anion polymer chains of the alginate and build junction zones which form the hydrogel network. The calcium ions are preferentially linked with the G-blocks of the alginate molecule due to the specific conformation structure of the polyguluronic chains and the presence of well defined places for chelate links [15]. It is considered that the forming of gel for the alginates follows the so called "egg-box" model according to which the ion links are between the calcium ions and two parallel G-chains. Notwithstanding that new data from MNR spectroscopy and x-ray diffraction suppose a presence of a more complex three-dimensional structure, the simple dimeric "egg-box" model is still valid as it is principally correct and gives a good idea of the linking properties of the alginates.

For the pectins with DE around 50%, the jellying capacity depends on a majority of factors – concentration of the pectin, the dissolved sugars, pH value of the solution and the quantity of the present calcium or other polyvalent cation. Gel forming of pectin solution was observed at high calcium ions concentration, which is an indication for a certain interaction between the ions and the HM pectin [16]. This process is not specific in contrast to the "egg-box" mechanism for the alginates and the LM pectins and according to Fang et al. [4], is usually polyelectrolyte interaction. The solutions of the two polymers were mixed very well in all studied proportions. The adding of calcium ions in low concentration (1,0 mM) leads to an increase of the viscosity of the mixture at places without local gel forming. For composition C₂AG-P, where the pectin and the sodium alginate are in equal proportions, the obtained result for viscosity was 386 mPa.s (at speed gradient 27,2 s⁻¹) at the beginning and increased up to 1300 mPa.s after adding of Ca²⁺. In such a way an easier manipulation after water evaporation was achieved. The real cross-linking of the resulting film took place after immersion in 0,3M solution of calcium ions.

Film forming solution C₂AG-P was with pH-value 3,78 – higher than pKa of the pectin which

Table 1. Characteristics of films

Composition	Appearance	Thickness (mm)	Residual moisture (%)
AG	transparent, flexible	0,054	11,52
C ₁ AG-P	lightly opaque, flexible	0,050	12,82
C ₂ AG-P	lightly yellowish, flexible	0,048	14,10
C ₃ AG-P	lightly yellowish, flexible	0,043	14,20

implies the presence of uncharged and charged carboxyl groups. After adding of calcium ions electrostatic as well as unspecific hydrophobic interactions with the pectin and specific with the alginate by the “egg box” mechanism were realized.

The residual moisture in the end products depends on a number of factors like the type of the used polymer, the concentration of the plasticizer, the conditions of cross-linking and drying. The films with greater alginate content are with lower residual moisture (Table 1). Up to a given concentration the water contained in the film plays the role of a plasticizer and increases the film elasticity. Residual moisture under 10% deteriorates the mechanical properties of the films and above 20% it can cause substantial changes in the protective properties, it can increase the permeability of the gases (or of the aromatic components) and to induce a danger of bacterial contamination.

Mechanical properties

Important parameters of mechanical properties are: tensile strength, elongation and elastic deformations modulus. The ultimate tensile strength (TS) is an assessment of the mechanical resistance, owing to the cohesion forces between the polymer chains. The elongation at ultimate strength (E) is the maximum change in the length of the tested material before breaking, expressed in percentage towards the initial length of the not deformed sample. The elasticity modulus (Young’s modulus, YM) is expressed as a ratio of linear stress to the linear strain ($Y = \text{stress}/\text{strain}$). The slope of stress-strain curve resulting from these tests present the dependence between the elongation and the applied strength (Fig. 1 and 2). The summarized results from the tests for mechanical properties of AG and C₂AG-P are given in Table 2. The alginate films (AG) showed the following values: TS - 18,30 MPa; E - 78,14 %. These results differ from some data mentioned in literature [17,18,19], as the lower TS values and the higher E values can be explained with the differences in the alginate concentration,

the applied plasticizer and the cross-linking method. For the composite film C₂AG-P the TS value is 53,53 MPa, and E is 34,48%. Usually the increase of TS leads to a decrease of the percentage for E [18, 20]. The obtained values for Young’s modulus increase from 16,61 MPa for AG up to 202,84 MPa for C₂AG-P. The increased TS and YM values and the decreased E values for the composite films can be explained by the higher cross-linking density when combining two anion polysaccharides, which leads to the forming of a more dense network and compact structure of the film after solvent evaporation.

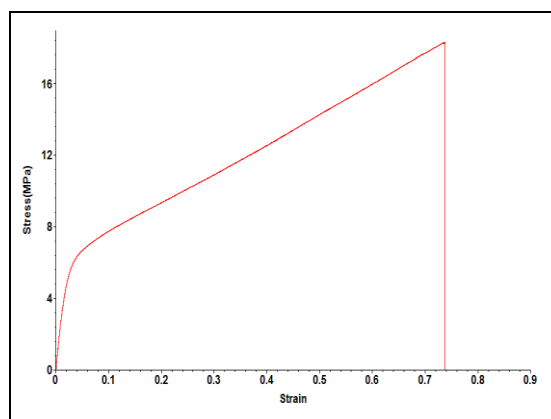


Fig. 1. The “stress-strain” curve for AG films

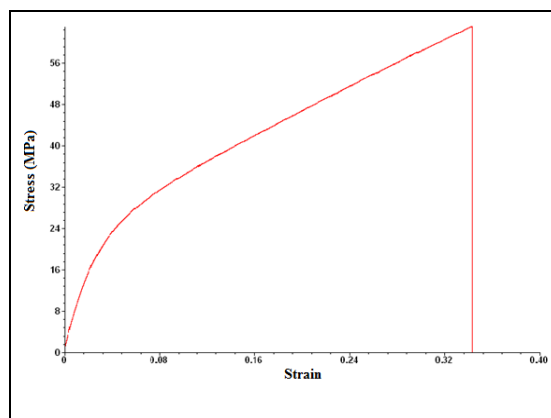


Fig.2. The “stress-strain” curve for C₂AG-P films

Table 2. Mechanical characteristics of AG and C₂AG-P

Mechanical characteristics	Composition					
	AG			C ₂ AG-P		
	Mean	SD	SE	Mean	SD	SE
Yield strength (MPa)	7,37	±0,54	±0,221	18.93	±3.84	±1.57
Ultimate tensile strength (MPa)	18,30	±0,68	±0,276	53.53	±4.25	±1.74
Young’s modulus (MPa)	16,61	±0,78	±0,319	202.84	±21.08	±8.60
Elongation at Ultimate strength (%)	78,14	±6,12	±2,50	34.48	±4.32	±1.76
Toughness (J/mm ³)	7,503	±0,797	±0,325	9.229	±3.143	±1.283
Energy at Yield point (J/mm ³)	0,296	±0,041	±0,017	0.324	±0.119	±0.048

In-vitro dissolution tests

On Figures 3, 4 and 5 are presented the results for the solubility of the films in simulated gastric and intestinal juice, prepared with different buffer media. These tests give a possibility to follow up the disintegration profile when taken with food. In a simulated gastric juice the pure alginate films kept their form and wholeness during the period of investigation, and for the composite film C₂AG-P a minimum disintegration was observed (10%). Much higher level of disintegration was observed when placing the samples in simulated intestinal juice, prepared with phosphate buffer (Fig. 3 and 4).

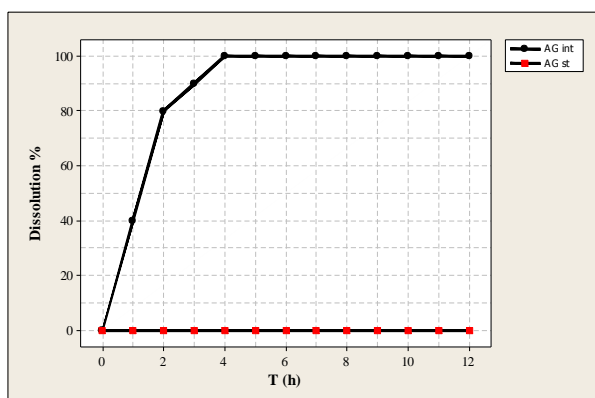


Fig. 3. Dissolution of alginate films in simulated gastric (AG st) and intestinal (AG int) juice

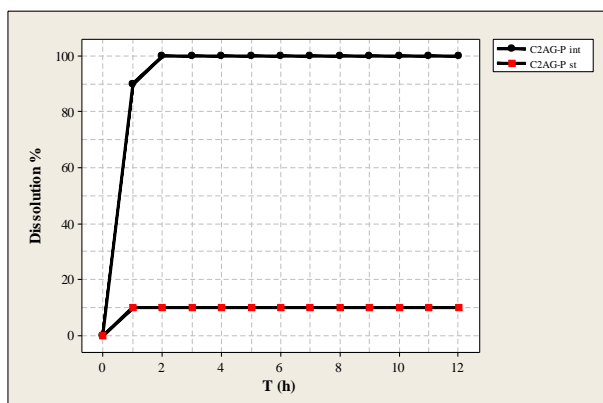


Fig. 4. Dissolution of composite films in simulated gastric (C₂AG-P st) and intestinal (C₂AG-P int) juice

For AG the changes begin yet at the first hour (40%) and reach up to 100% at the fourth hour. For the composite films an even faster disintegration was observed which reached 100% at the second hour. The experiment with simulated intestinal juice prepared with Tris buffer showed different results (Fig. 5). In this case the alginate and composite films were with a lower disintegration level: AG reached 70% disintegration at the fifth hour, and C₂AG-P – up to 80% at the fourth hour.

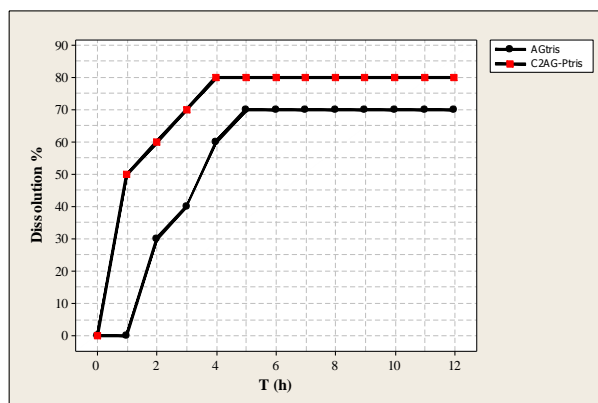


Fig. 5. Dissolution of alginate film (AG tris) and composite film (C₂AG-P tris) in simulated intestinal juice with Tris- buffer

The investigated polysaccharide films kept almost completely their wholeness at the low pH of the simulated gastric juice. When pH of the medium is under pKa of the respective uronic acids, the penetration of the water molecules, the swelling and the dissolving of the film were hampered. In the case of artificial intestinal juice the solubility was much higher, which is related not so much to the activity of the enzyme complex but to the pH of the medium. The buffer salts have an effect as well. The faster dissolving in the phosphate buffer is owing to the extraction of the calcium from alginate-Ca²⁺/pectin-Ca²⁺ complexes. When using a Tris-buffer the disintegration of both film types was slower and till the end of the period full dissolving was not reached.

These observations were also confirmed by the carried out tests for disintegration depending on the pH of the medium (Fig. 6 and 7).

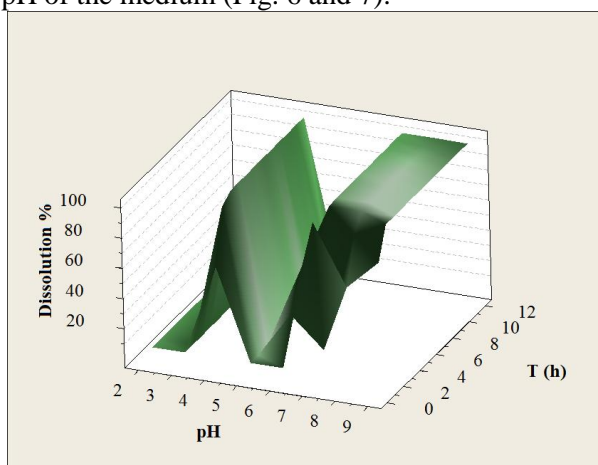


Fig.6. Dissolution of alginate film (AG) for different pH

The AG samples, placed in solutions with pH 2,0, 3,0 and 5,0 preserved their wholeness till the 12th hour. In a solution with pH 6,0 the disintegration of the film reached 60% at the 8th hour. At pH 4,0, 7,0, 8,0 and 9,0, the alginate film

was completely dissolved for a period from 1 to 3 hours. The results for C₂AG-P showed a different disintegration level compared to the pure alginate films. Complete dissolving of the samples was observed for solutions with pH 4,0, 5,0, 6,0, 7,0, 8,0 and 9,0. For the films placed in solutions with pH 2,0 and pH 3,0 at the end of the period the disintegration reached up to 20% and 75%, respectively.

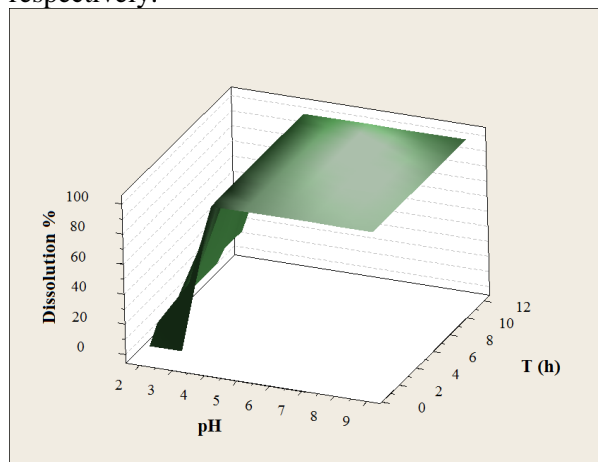


Fig.7. Dissolution of composite film (C₂AG-P) for different pH.

CONCLUSION:

By combining of sodium alginate and high methoxyl pectin were obtained well formed, homogeneous and semi-transparent films. The adding of pectin to the alginate film forming solution in proportion 1:1 improves considerably the film mechanical properties. The alginate and alginate-pectin films show no or very slow dissolution at low pH, including in simulated gastric juice. A difference is observed in the behavior of the two film types at pH values above 4,0, as the composite films show faster and full disintegration in the medium.

Due to the good mechanical characteristics and the selective solubility depending on pH, the composite alginate-pectin films are appropriate as material for encapsulation of biologically active substances or microorganisms, with low level of activity or survival, under low pH conditions.

REFERENCES

1. M. Altenhofen da Silva, A. C. Krause Bierhalz, T. Guenter Kieckbush, *Carbohydr. Polym.* **77**, 736 (2009).
2. K. I. Draget, S. T. Moe, G. Skjak-Braek, O. Smidsrod, in: *Food Polysaccharides and their applications*, 2nd ed., A. M Stephen, G. O. Phillips, P. A Williams (eds.) CRC Press, Taylor and Francis Group, Boca Raton, Fl USA, 2006, p.290.
3. P. A. Williams, *Struct. Chem.*, **20** (2), 299 (2009).
4. Y. Fang, S. Al-Assaf, G. O. Phillips, K. Nishinari, T. Funami, P. A. Williams, *Carbohydr. Polym.*, **72** (2), 334 (2008).
5. S. Dumitriu, *Polysaccharides: Structural Diversity and Functional Versatility*, 2nd ed, New York, CRC Press, 2004.
6. P. A. Williams, *Handbook of Hydrocolloids*, Cambridge Woodhead Publishing, 2000.
7. J. Gigli, C. Garnier, L. Piazza, *Food Hydrocolloid*, **23** (5), 1406 (2009).
8. B. Thakur, R. Singh, A. Handa, *Crit. Rev. Food Sci.*, **37** (1), 47(1997).
9. I. Braccini, S. Perez, *Biomacromolecules*, **2**, 1089 (2001).
10. D. Oakenfull, A. Scott, E. Chai, in: *Gums and stabilizers for the food industry 5*, G. O. Phillips, D. J. Wedlock, P. A. Williams (eds.), IRL. Press, Oxfords, 1990, p. 243.
11. M. A. Rao, H. J. Cooley, *Food Hydrocolloid*, **9**, 229 (1995).
12. The United States Pharmacopeia, 23-rd ed., National Formulary 18, Rockville, United States Pharmacopeial Convention, 1995.
13. BDS EN ISO 527-2:2002.
14. W. P. Charteris, P. M. Kelly, L. Morelli, J. K. Collins, *J. Appl. Microbiol.*, **84** (5), 759 (1998).
15. I. Braccini, R. P. Grasso, S. Perez, *Carbohydr. Res.* **317** (1-4), 119 (1999).
16. Y. Yang, G. Zhang, Y. Hong, G. Zhengbiao, F. Fang, *Food Hydrocolloid*, in press.
17. N. Parris, D. Coffin, R. F. Joubran, H. Pessen, *J. Agr. Food Chem.*, **43** (6), 1432 (1995).
18. G. I. Olivas, G. V. Barbosa-Cánovas, *Food Sci. Technol.- LEB*, **41** (2), 359 (2008).
19. S. Benavides, R. Villalobos-Carvajal, J. E. Reyes, *J. Food Eng.*, **110** (2), 232 (2012).
20. J. W. Rhim, *Lebensm. Wiss.Technol.*, **37** (3), 323 (2004).

ПРИГОТВЯНЕ И ОХАРАКТЕРИЗИРАНЕ НА КОМПОЗИТНИ ХИДРОКОЛОИДНИ ФИЛМИ ОТ НАТРИЕВ АЛГИНАТ И МЕТОКСИЛИРАН ПЕКТИН

Св. М. Дянкова*, А. О. Солак;

Институт по криобиология и хранителни технологии, София 1407, България;

Постъпила на 11 април, 2013 г.; приета на 16 юли, 2013 г.

(Резюме)

Разработена е технология за получаване на композитен биоразградим филм на основата на натриев алгинат и ябълков високометоксилиран (НМ) пектин. Установени са добри механични характеристики при използване на двата полизахарида в съотношение 1:1. За тях крайната якост на опън (TS) е 53.53 МПа, удължението при крайната якост (E) е 34.48%, модулът на Янг (YM) – 202.84 МПа. Композитният филм показва много слаба разтворимост при ниско рН, включително в симулиран стомашен сок. При стойности на рН над 4.0 алгинатните филми показват по-бавно, а композитните филми – по-бързо и пълно разпадане в средата. Благодарение на добрите механични характеристики и селективната разтворимост в зависимост от рН, композитните филми алгинат – НМ-пектин са подходящи като материал за капсуловане на биологично активни вещества или микроорганизми с ниска активност или оцеляващи при условия на ниско рН.

Attenuation effect through methylene group: Part II [1]

R. Sanjeev¹, V. Jagannadham^{2,*}, R. Veda Vratah³

¹ Departments of Chemistry Mizan-Tepi University, Tepi Campus, Tepi, Ethiopia

² Departments of Chemistry Osmania University, Hyderabad, 500 007, India

³ Departments of Chemistry L N Gupta Evening College, Hyderabad-500 002, India

Received March 21, 2013; accepted July 5, 2013

A simple, new and lucid protocol is presented in this article for the evaluation of the Hammett reaction constant (ρ) of the deprotonation process of arenium ions $\text{XC}_6\text{H}_7^+ \rightleftharpoons \text{XC}_6\text{H}_6 + \text{H}^+$ based on the attenuation effect of methylene group on the dissociation equilibria of anilinium ions, benzyl ammonium ions and 2-phenylethyl ammonium ions.

Key words: Hammett reaction constant (ρ), attenuation effect, arenium ions.

INTRODUCTION

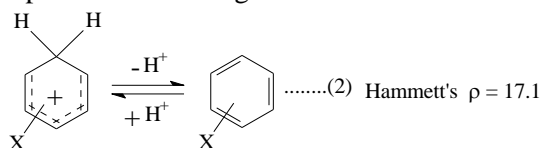
Benzoic acid dissociation equilibria and the chemical reactivity of *meta*- and *para*-substituted benzene derivatives were well explained by Hammett equation² in terms of two parameters the Hammett substituent constant (σ) and the Hammett reaction constant (ρ). Thus the Hammett equation for benzoic acid dissociation equilibria is:

$$\log K_X = \log K_H + \rho\sigma \quad (1)$$

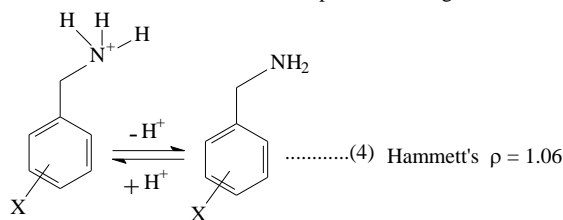
K_X and K_H are acid dissociation constants of substituted and un-substituted benzoic acids respectively. The Hammett reaction constant (ρ) is a measure of the magnitude of the effect of structure on the benzoic acid dissociation equilibria.

DISCUSSION

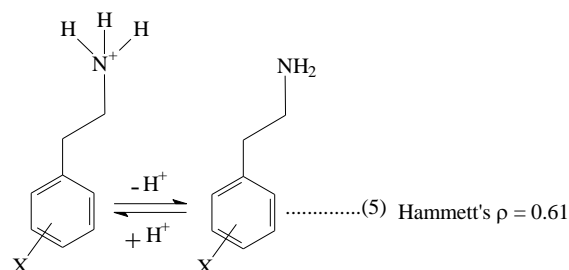
First let us see the dissociation equilibria of arenium ions and different aryl ammonium ions with increasing length of carbon chain between ionizable proton and the ring carbon atom.



number of atoms between ionizable proton and ring carbon atom = 0



number of atoms between ionizable proton and ring carbon atom = 2



number of atoms between ionizable proton and ring carbon atom = 3

To the best of the authors knowledge, as the $\text{p}K_a$ values were not available of the arenium ion dissociations in literature, the Hammett reaction constant (ρ) for the equilibrium 2 i.e. for the dissociation of arenium ions was evaluated from the relative stabilities³ as a function of Hammett σ values. The Hammett reaction constant (ρ) for the equilibria 3 and 4 were evaluated from the respective plots of $\text{p}K_a$ values of the dissociation equilibria of anilinium and benzyl ammonium ions versus Hammett σ values. The $\text{p}K_a$ values of dissociation equilibria of anilinium ions and benzyl ammonium ions are from references 4 and 5 respectively. The Hammett reaction constant (ρ) for the equilibrium 5 was evaluated from the $\text{p}K_a$ values of only two 2-phenylethyl ammonium ions⁶, one is un-substituted and the other is 4-OH substituted.

The substituent effects from the benzene moiety could be spread effectively to the reaction center through resonance. The spreading is more predominant if the conjugated π -electron system is present between the reaction center and the substituent and due to its polarization. This will diminish more rapidly upon introducing methylene groups between the ionizable proton and the ring carbon atom. The sp^3 hybridized $-\text{CH}_2-$ group acts as a σ -electron insulator.

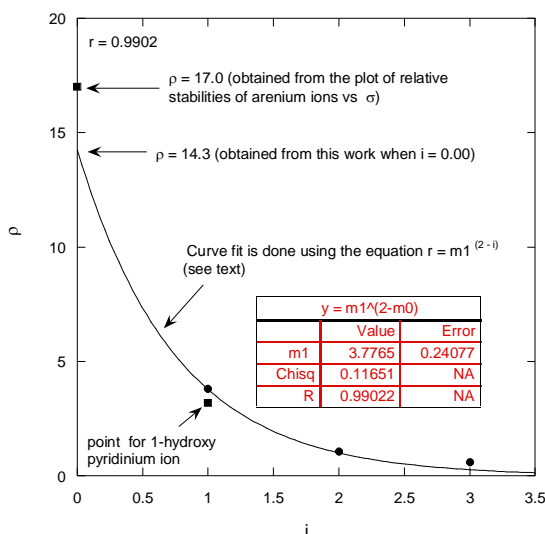
* To whom all correspondence should be sent:
E-mail: jagannadham1950@yahoo.com

This is observed in the above equilibriums 2-5. As such the Hammett reaction constant (ρ) decreases as the number of methylene groups are increased. This is well explained by Andrew Williams⁷ by an empirical equation (eqn. 6):

$$\rho = m_1^{(2-i)} \quad (6)$$

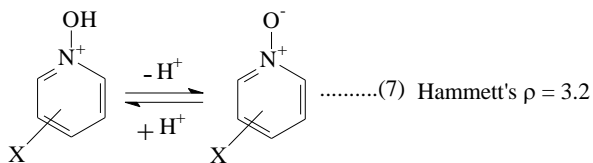
Where ' m_1 ' is a constant and ' i ' is the number of atoms between the ionizable proton and the ring carbon atom. This could be seen as a beautiful exponential decay curve (figure 1):

Figure 1: Plot of Hammett ρ versus i (the number of atoms between the ionizable proton and the ring carbon)



From equation 6 it is clear that if $i = 0$, i.e. if there are no atoms between the ionizable proton and the ring carbon atom, the example would be arenium ion itself. Then the Hammett ρ value would be $m_1^{(2-i)} = m_1^{(2-0)}$. Here, from the curve fit of the data, m_1 was found to be 3.78 (see box in the figure). Thus the Hammett ρ value would be $(3.78)^2 = 14.3$. The value obtained from the Hammett plot of arenium ion stabilities versus Hammett σ was found to be 17.0. The value from the present work is less by a factor of 1.19 than the calculated value from arenium ion stabilities. Yet the trend is unmistakable.

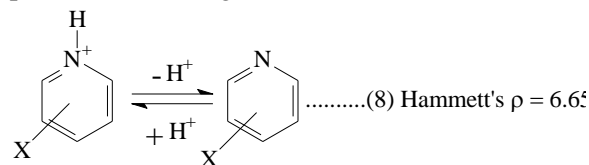
Another notable observation is that about the Hammett ρ value for the dissociation equilibriums of 1-hydroxy pyridinium ions (equilibrium 7). 1-hydroxy pyridinium ion is nothing but the protonated pyridine-N-oxide.



number of atoms between the ionizable proton and the ring atom is zero

Hammett ρ value of 3.2 of this dissociation equilibrium is obtained from the plot of pK_a versus Hammett σ values. The pK_a values are from reference 8. The Hammett ρ value, though it did not fall on the line of fit of the plot of ρ versus i but it is very close to the line of fit (figure 1). This clearly shows that whether the benzene ring atom is carbon or nitrogen and whether it is a nitrogen acid or oxygen acid, if the number of atoms between the ionizable proton and the ring atom are same for two types of acid dissociation equilibriums, the Hammett ρ values would be more or less the same. Here it is the comparison between the dissociation equilibriums of 1-hydroxy pyridinium ions and anilinium ions for which there is only one atom between ionizable proton and the ring atom. In the case of 1-hydroxy pyridinium ion it is 'oxygen' and in the case of anilinium ion it is 'nitrogen'. Therefore it is not the nature of a particular atom that plays the role but it is the only number that matters in creating the σ -electron insulation. But the atom should have an sp^3 hybridization.

The following equilibrium (equation 8) is the dissociation of pyridinium ions. The value of ' i ' is zero. That is there are no atoms between ionizable proton and the ring atom.



number of atoms between the ionizable proton and the ring atom is zero

Hence it should reflect the property of the dissociation of arenium ions with respect to Hammett ρ . But to our surprise the Hammett ρ value obtained from the plot of pK_a versus Hammett σ value was found to be only 6.65 which is far less than the value of 14.3 obtained from this work or 17.1 from the arenium ion stabilities. The pK_a values of pyridinium ion dissociation equilibriums are from references 8 and 9. This discrepancy could not be explained at present.

REFERENCES:

1. For Part I, see V. Jagannadham. *Bulgarian Chem. Commns.*, vol. 41, page 50, (2009)
2. L. P. Hammett, *Physical Organic Chemistry*, McGraw-Hill, New York, 1940, pp. 184-189.
3. M. Kilpatrick and Fred E. Luborsky, *J. Am. Chem.*

- Soc., vol. 75, pp. 577, (1953)
4. Brown, H.C. et al., in Braude, E.A. and F.C. Nachod *Determination of Organic Structures by Physical Methods*, Academic Press, New York, 1955.
 5. L. F. Blackwell, A. Fischer, I. J. Miller, R. D. Topsom and J. Vaughan, *J. Chem. Soc.*, pp. 3588, (1964)
 6. M. M. Tuckerman, J. R. Mayer, and F. C. Nachod, *J. Am. Chem. Soc.* Vol. **81**, pp. 92, (1959)
 7. A. Williams, *Free Energy Relationships in Organic and Bioorganic Chemistry*, Royal Society of Chemistry, Cambridge, 2003, p. 75
 8. H. H. Jaffe and G. O. Doak, *J. Am. Chem. Soc.* **77**, pp. 4441, (1955)
 9. K. Clarke and K. Rothwell, *J. Chem. Soc.*, 1885, 1960

ЕФЕКТ НА ОСЛАБВАНЕ НА МЕТИЛЕНОВИ ГРУПИ: ЧАСТ II

Р. Санджеев¹, В. Джаганнадхам^{2,*}, Р. Веда Вратх³

¹Университет Мизан-Тепи, Университетски район Тепи, Тепи, Етиопия

²Университет Османия, Хайдерабад, 500 007, Индия

³Вечерен колеж Л. Н. Гупта, Хайдерабад 500 002, Индия

Постъпила на 21 март 2013 г.; приета на 5 юли, 2013 г.

(Резюме)

В тази статия се представя нов прост и ясен протокол за изчисляване на реакционната константа на Хамет (ρ) за процеса на депротониране на арениеви йони, базиран на слабване на метиленови групи според дисоциационните равновесия на анилинови йони, бензил-амониеви йони и 2-фенилетил амониеви йони.

The influence of temperature on the corrosion behaviour of high nitrogen austenitic stainless steel in chloride media

B. R. Tzaneva

Department of Chemistry, Technical University, Bulgaria

Received May 17, 2013; accepted July 25, 2013

The electrochemical behaviour of high nitrogen SS in comparison of conventional grade 304 SS was examined in aqueous 3.5% chloride solution at 20-80 °C using open circuit potential vs. time, potentiodynamic and galvanostatic tests. The raising of the temperature was found to have no important influence on the corrosion potential, but destabilise the passive film formation on both steels. At the critical value of anodic polarisation the passive films were damaged and pitting corrosion occurs at lower potential with the increasing of temperature. The high nitrogen steel demonstrates faster formation of passive films, but pitting potential of this steel is more sensitive to temperature changes in comparison with those of chromium-nickel one. The temperature has slight influence on repassivation process, which is generally steel composition dependent. At all experimental conditions the nitrogen steel has greater difficulty to repassivate.

Keywords: corrosion resistance; pitting; stainless steel; temperature; sodium chloride; anodic polarisation.

INTRODUCTION

The establishment of the behaviour of new steel grades in different corrosive conditions is critical for determination of the areas of their practical application. Typically stainless steels are used in environments where they are resistant to general corrosion, but may be affected by local forms of corrosion such as pitting. For example, the stainless steels have found widespread marine and industrial applications, wherein the presence of aggressive chloride ions is frequently combined with a change of the operating temperature. That is why the characterisation of corrosion resistance of a new steel grade is usually performed in chloride media and aims to assess the impact of the factors that can affect the rate of penetration of chloride ions in the passive layer to provoke development of pitting, as well as those factors affecting the contents and the pH of the solution inside growing pits. Such parameters are the temperature and the degree of the anodic polarisation.

The spontaneous or applied anodic polarisation of the steel in concrete corrosive environment provides the possibility of occurrence and development of pitting. To maintain a stable passive state of stainless steel, the potential should not exceed certain critical value called pitting initiation potential. Its value depends on a number of internal and external factors, among which is the

temperature of the system [1-3]. Generally the raising of temperature accelerates the rate of kinetic limitation reactions as well as the diffusion processes in the electrolyte. Furthermore the temperature directly affects the content of oxygen dissolved in the corrosion environment, and hence the rate of formation and stability of the protective layer of stainless steels. It is well known that the rate of transport and chemisorption processes in the passive layer is accelerated at elevated temperature [4]. The result is thinning of the passive layer in some electrochemically active sites which causes local rupture. On the other hand, the high temperature increases desorption of chloride ions and accelerates diffusion processes between the solutions inside and outside the pit. These processes impede respectively the reaching a critical surface chloride concentration needed for breakdown of the passive film and make difficult maintaining of favourable conditions for the stable pit growth. Consequently, interpretations of the influence of temperature on the corrosion resistance of the steels are complex and often occasional [3, 5]. This necessitates the effect of temperature on the corrosion behaviour to be defined only experimentally.

This paper presents research on the influence of the temperature on the corrosion behaviour of high nitrogen austenitic chromium steel Cr23Ni12, developed at Institute of Metal Science - BAS in 3.5% NaCl. As a reference steel the conventional SS 304 (Cr18Ni9) was used.

* To whom all correspondence should be sent:
E-mail: borianatz@tu-sofia.bg

EXPERIMENTAL PART

Two types of austenitic stainless steels have been investigated in this work: high nitrogen chromium steel Cr23N1.2 (22.35% Cr, 1.23% N, 1.10% Mn, 0.04% C, 0.36% Si, balance Fe) and conventional steel Cr18Ni9 (17.49% Cr, 9.37% Ni, 1.29% Mn, 0.05% C, 0.52% Si, balance Fe). The experimental specimens were disk shaped with a working area of 0.5 cm². The preliminary treatment of the specimens included subsequently grinding by abrasive papers to a 600 grit finishing, rinsing with water and drying. Just before the start of the experiment the specimens were polished to an 800 grit finish, followed by rinsing with distilled water and degreasing with an alcohol-ether mixture. The 3.5 wt. % NaCl test solution was prepared using analytical grade reagent and distilled water. The electrochemical tests were performed under open air conditions at temperatures 20, 40, 60 and 80 °C.

Three electrochemical techniques were used in the corrosion measurements. The *open circuit potential (OCP)*-time dependence was measured in the test solutions for an hour at room temperature. Just after OCP record the specimen surface was anodically charged under constant current density 60 µA cm⁻² and the potential change with time was recorded (*galvanostatic tests*). The *cyclic potentiodynamic polarisation* measurements were

performed with potential scan rate 1mV s⁻¹. The specimen was kept for 5 min at initial potential 0.7 V vs. SCE and followed by anodic polarisation (in positive direction). After passing through the passive state and when the current density exceeded 10⁻⁴ A cm⁻², the polarisation in reverse direction was carried out down to the point where the curve intersected the anodic one.

The electrochemical measurements were carried out in a conventional three-electrode cell with a platinum counter electrode and a saturated calomel electrode (SCE) as a reference electrode. The measurements were performed using PAR 263 potentiostat-galvanostat and Power Suite corrosion measurement and analysis software.

RESULTS

Open circuit potential

Figure 1 shows the change of free potential of Cr23N1.2 and Cr18Ni9 steels as function of time at temperatures 20, 40, 60 and 80 °C in 3.5% NaCl solution. The ennoblement of potential is indication about the formation of passive film and self-protection from corrosion. Although both steels tend to become passive, dependences OCP-time show significant differences in its shapes.

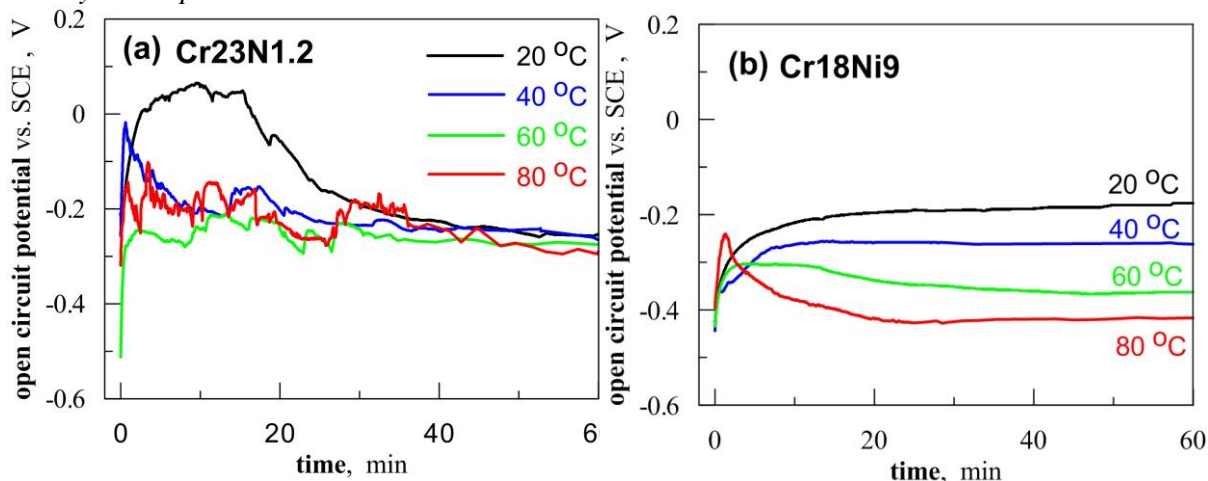


Fig. 1. Open circuit potential of Cr23N1.2 (a) and Cr18Ni9 (b) in 3.5% NaCl; 20÷80°C.

Table 1. Rate of passive film formation, mV s⁻¹.

steel	method	temperature, °C			
		20	40	60	80
Cr23N1.2	open circuit potential	1.8	8.0	7.0	4.5
	galvanostatic polarisation	42.1	12.8	11.2	10.3
Cr18Ni9	open circuit potential	1.2	3.8	3.4	2.7
	galvanostatic polarisation	8.5	6.4	3.8	3.0

For chromium-nitrogen steel a sharp initial increase about 400 mV of the potential is typical. This behaviour presents rapid spontaneous passivation even at high temperatures. The slope of the dependence OCP-time in first seconds of the contact of the metal surface with the corrosive solution may be used as a criterion for rate of passive film formation. Thus determined values of the slope in mV per second for two stainless steels are presented in Table 1. The slopes of Cr18Ni9 steel are about two times smaller than Cr23Ni1.2 steel ones. The higher slope is found at 40°C for both steels. The further temperature raising leads to delay of the passivation.

For nitrogen steel the initial stage of a passive film formation is followed by a prolonged period of potential fluctuations and after some time the potential reaches to stationary value (Fig. 1-a). These fluctuations are associated with local damages of the surface layer. With increasing temperature, the intensity of the oscillation becomes larger and the establishment of the steady values of the potential takes increasingly long time (more than 1 hour at 80°C). The observed behaviour indicates that the high temperature

destabilize the passive film. Nevertheless, the influence of temperature on stationary values of OCP can be considered negligible, since after 40 minutes they are very close.

In the OCP-time dependences obtained for chromium-nickel steel (Fig. 1-b), the oscillations are not observed, which displays a greater stability and electrochemical homogeneity of its passive layer. However, the increased temperature leads to a shift of the stationary potential of nickel steel in a negative direction and his establishment to values typical for an active state (about -0.4 V vs. SCE).

Potentiodynamic polarisation dependences

According to the cyclic potentiodynamic dependences presented in Fig. 2, examined steels are in passive state in 3,5% NaCl. At anodic polarisation above critical potential value (pitting initiation potential E_{pit}), the passivity is breached by pitting corrosion, which can be seen from the hysteresis loop. The increase of current density at decreasing anodic polarisation shows the presence of active points (pits) on the steel surface.

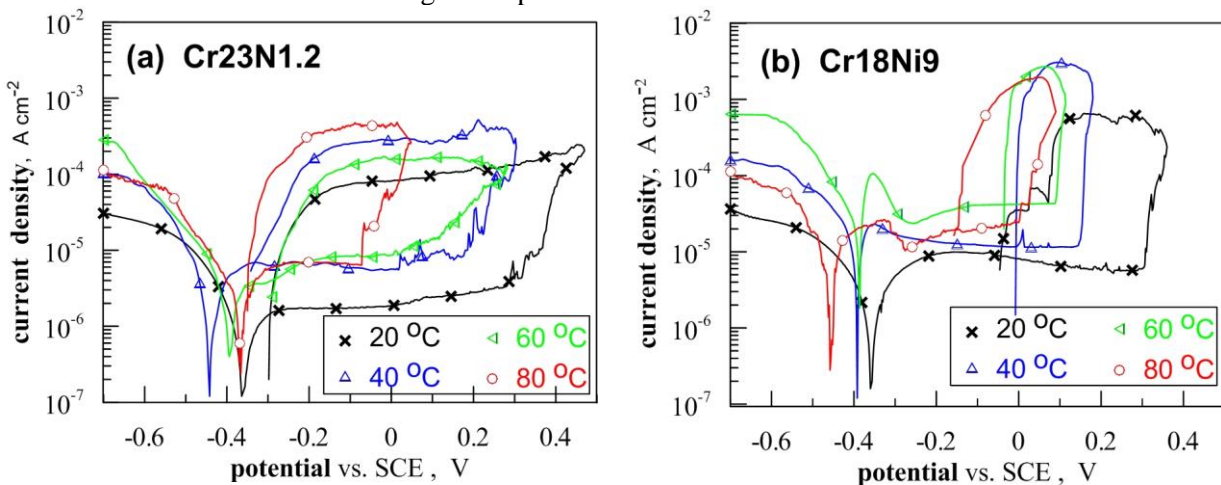


Fig. 2. Cyclic polarisation curves of steels Cr23Ni1.2 (a) and Cr18Ni9 (b) in 3.5% NaCl; 20÷80 °C.

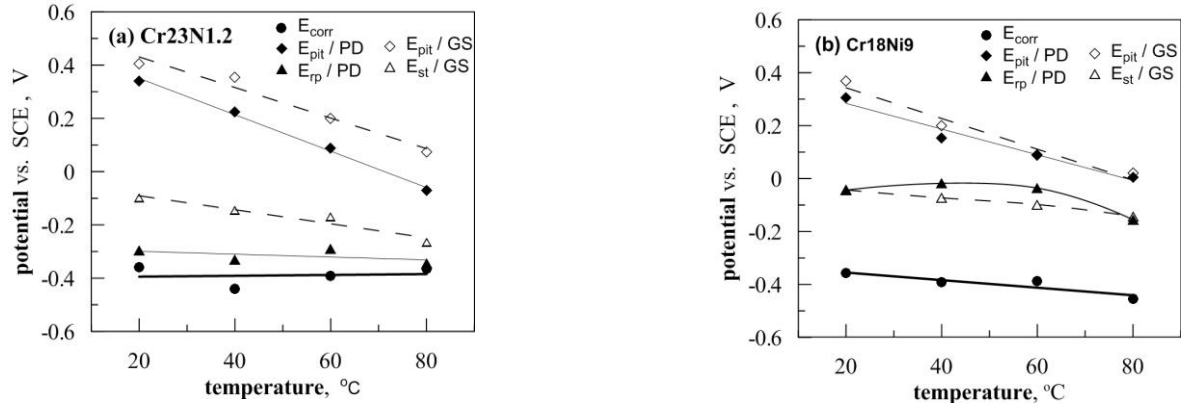


Fig. 3. Influence of temperature on the characteristic potentials obtained by potentiodynamic (black symbols and solid lines) and galvanostatic (blank symbols and dotted lines) tests for Cr23Ni1.2 (a) and Cr18Ni9 (b) stainless steels in 3.5% NaCl.

The characteristic electrochemical parameters vs. temperature determined from the potentiodynamic curves of the two steels are presented in Figs. 3 and 4. They show that the increasing of solution temperature from 20 to 80 °C has no significant effect on corrosion potential E_{corr} , but influences considerably the corrosion current density i_{corr} . The corrosion rate increases more than four times for Cr23Ni1.2 steel and about 10 times for steel Cr18Ni9 (Fig. 4).

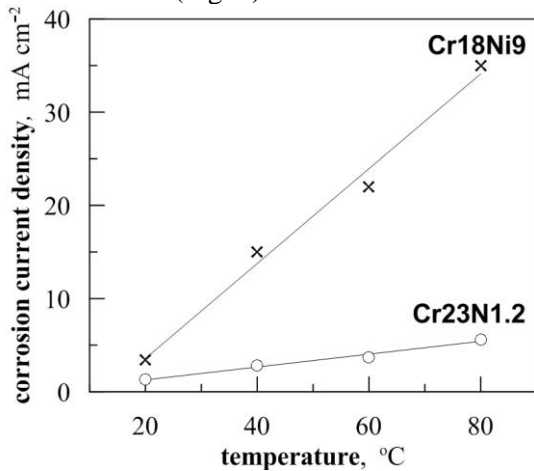
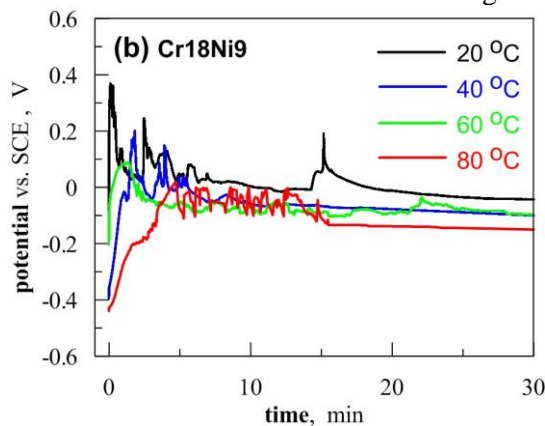


Fig. 4. Influence of temperature on corrosion current density of steels Cr23Ni1.2 and Cr18Ni9 in 3.5% NaCl.

All parameters, which characterise the stability of the passive state, become worse with the temperature increasing. For instance the passive current density i_{pass} increases the pitting initiation E_{pit} and repassivation E_{rp} potentials decrease. Hence the increased temperature deteriorates the protective properties of the passive film. Furthermore, this negative effect of the temperature is stronger for the nitrogen steel than for the conventional steel. In the temperature range 20-80°C, pitting potential E_{pit} decreases by more than 0.4 V for chromium-nitrogen steel and less (about 0.25 V) for chromium-nickel.

When turning the scan in cathodic direction, the current for steel Cr23Ni1.2 remains at high levels in



a large range of potentials and abruptly decreases near to the corrosion potential. Figure 3 shows that the repassivation potential is slightly dependent on the temperature (black triangle and solid lines). Therefore, at temperatures above 60 °C nitrogen steel has increased susceptibility to pit formation and lower repassivation ability than nickel steel.

Galvanostatic results

Figure 5 shows typical galvanostatic polarisation curves for Cr23Ni1.2 and Cr18Ni9 steels in 3.5% NaCl in the temperature range 20-80 °C, obtained at the current density 60 $\mu\text{A cm}^{-2}$. The density of the anodic polarisation current is experimentally chosen as the lowest value sufficient for a stable development of pits in the investigated temperature range.

The dependences potential-time demonstrates that initially the potential increases linearly with the time (Fig. 5). This part of the curve corresponds to the galvanostatic growth of passive layer. The raising of the temperature reduces the slope of the initial linear region (dE/dt), which is an indication of delay in the rate of passive film formation (Table 1). The deviation of the curve from linearity is a result of destabilisation of the passive layer and the local breakdown in it. The maximum reached potential value corresponds to the pitting potential E_{pit} . After reaching this value, the potential decreases due to the metal dissolution in certain active surface areas. The initiation and repassivation of each pit is displayed on chronopotentiometric dependences as potential fluctuation respectively in negative and in positive direction. After some time, the potential is established on its stationary value E_{st} , which corresponds to the potential of the stable pits growth [6]. Several authors identify this potential E_{st} as the potential of repassivation determined

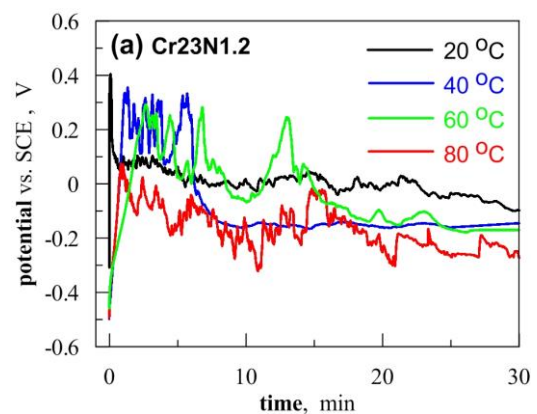


Fig. 5. Chronopotentiometric curves at applied anodic current 60 $\mu\text{A cm}^{-2}$ of steels Cr23Ni1.2 (a) and Cr18Ni9 (b) in 3.5% NaCl, 20-80 °C.

potentiodynamically E_{tp} [7]. Despite the completely different nature of these two potentials, as E_{st} values tend to reach those of the E_{tp} , the stationary potential can be used as a characteristic value for the minimum potential below which pitting does not develop. The increasing of the temperature leads to prolongation of the time required to reach a steady state.

On Fig. 3 the values of pitting potential (E_{pit}) and stationary potential (E_{st}) obtained from galvanostatic potential-time dependences are presented by dotted lines and blank symbols. When raising the temperature from 20 to 80 °C, the pitting potential E_{pit} decreases for both steel approximately with 0.35 V. Figure 3 shows a good correlation between the results obtained by galvanostatic and potentiodynamic methods for the conventional steel. Contrariwise the obtained galvanostatically E_{pit} values for Cr23N1.2 are more positive with 100-200 mV than the corresponding potentiodynamic values. These results can be explained by the longer induction time required for the appearance of pits on nitrogen steel. Due to delay in pits formation, the potential has time to reach more positive values at the abruptly imposed anodic polarisation.

DISCUSSION

The results from OCP measurements and from potentiodynamic method, give information for general corrosion assessment, whereas the galvanostatic polarisation and the cycling potentiodynamic methods allow evaluation of the susceptibility of the steels to pitting corrosion at the experimental conditions.

The three electrochemical methods experimentally proved the expected relatively similar corrosion behaviour of the both steels in 3.5% NaCl solutions. In range of the temperature 20-80 °C similar values of the corrosion potential and the width of the passive zone were registered. Both steels are affected from pitting corrosion at close values of the anodic polarisation. Nevertheless, some important differences, related to the corrosion current density as well as the rate of formation and repassivation of the passive layers on two steels were found out.

The protective layer on the chromium-nitrogen steel forms faster, which is demonstrated by the precipitous slope of the initial linear growing of potential without and with applied anodic polarisation (Table 1, Figs.1 and 4). However the rapid spontaneous anodic polarisation leads to quick attainment of the free potential at which the dissolution of some anodic nonmetallic inclusions

begins and the adsorption of the aggressive ions is stimulated [8-11]. So the fluctuations on the dependencies OCP-time are observed only for Cr23N1.2 steel and they are related to activation and repassivation of the local areas on the surface, most probably dissolution of the nonmetallic inclusions, nascence and repassivation of metastable pits or crevice growth. Though the maximum reached values of OCP are found to be below the critical potential values E_{pit} established by the two others electrochemical methods. Consequently, despite the well-expressed maximum on the OCP-time curve, without external anodic polarisation, the pits would not be developed. The superposition of the stationary values of the open circuit potentials on the respective potentiodynamic dependencies allow to see that the free potentials of both steels are located in the passive region, but for the nitrogen steel they are between E_{pit} and E_{tp} (Fig. 2). Hence, if on the steel Cr23N1.2 surface temporary favourable conditions for pits formation are created, the pit development can be prolonged also at potentials under E_{pit} .

The sharp potential increase in anodic direction under galvanostatic polarisation of the nitrogen steel shows not only rapid formation of the passive layer, but also lower conductivity of the passive films.

The lower values of the corrosion and the passive currents, the fast passivation of steel Cr23N1.2 surface as well as the longer induction time for pits initiation can be explained with the bigger chromium content [12] and the nitrogen incorporation in the passive film and formation of more compact structure [13-15]. Nitrogen enrichment of the passive layer or the accumulation of N on the metal/oxide interface is proved in many investigations, which explain the difficulty in anodic dissolution of the bare metal [13, 15-18]. Furthermore Kumagai *et al.* [16] have established lowering of the thickness of the passive layers at high nitrogen content in the chromium steels. The smaller thickness of the passive layer on the studied nitrogen steel is the probable reason for their easier breakdown in strongly aggressive environments as 3.5% NaCl at 80 °C in comparison with the Cr18Ni9 steel.

CONCLUSION

The temperature rising from 20 to 80 °C in 3.5% NaCl solution increases the corrosion rate of Cr22N1.2 stainless steel slighter that of Cr18Ni9 steel. The high nitrogen steel is characterised with faster formation of the protective passive film. The high temperature deteriorates the protective

properties of the passive film which results in increase of the passive current density and their destruction at smaller anodic polarisation. This negative effect of temperature is stronger for nitrogen steel in comparison with to conventional steel. The temperature has slight influence on repassivation process, which is generally steel composition dependent. At all experimental conditions the nitrogen steel has great difficulty to repassivate.

REFERENCES

1. U. Steinsmo, T. Rogne, J. Drugli, *Corros.*, **53**, 955 (1997).
2. P. Ernst, R. C. Newman, *Corros. Sci.*, **44**, 943 (2002).
3. B. R. Tzaneva, L. B. Fachikov, R. G. Raicheff, *Corros. Eng. Sci. Technol.*, **41**, 62 (2006).
4. I. L. Rozenfeld, *Koroziia i zashtita metalov*, Metalurgia, Moskva, 1969.
5. W. M. Carroll, T. G. Walsh, *Corros. Sci.*, **29**, 1205 (1989).
6. I. L. Rozenfeld, I. S. Danilov, *Zaschita Metallov*, **6**, 14 (1970).
7. S. Frangini, N. De Cristofaro, *Corros. Sci.*, **45**, 2769 (2003).
8. G. Wranglen, *Corros. Sci.*, **14**, 331 (1974).
9. G.S. Eklund, *J. Electroch. Soc.*, **121**, 467 (1974).
10. M. B. Ives, G. Ruijin, S. C. Srivastava, (Proc. 10th Int. Cong. On 'Metallic corrosion', Madras, India, 1987) Ed. by Oxford and IBM Publishing Co, PVT, 1887, Vol. IV, p. 3235
11. M. A. Baker, J. E. Castle, *Corros. Sci.*, **34**, 667 (1993).
12. L. L. Shreir, R. A. Jarman, G. T. Burstein, *Corrosion*, Oxford, Jordan Hill, 2000.
13. H. Y. Ha, H. Jang, H. S. Kwon, S. Kim, *Corros. Sci.*, **51**, 48 (2009).
14. U. K. Mudali, B. Reynders, M. Stratmann, *Corros. Sci.*, **41**, 179 (1999).
15. Y. Fu, X. Wu, E.-H. Han, W. Ke, K. Yang, Z. Jiang, *Electrochim. Acta*, **54**, 4005 (2009).
16. M. Kumagai, S. -T. Myung, S. Kuwata, R. Asaishi, Y. Katada, H. Yashiro, *Electrochim. Acta*, **54**, 1127 (2009).
17. R.D. Willenbruch, C.R. Clayton, M. Oversluizen, D. Kim, Y. Lu, *Corros. Sci.*, **31**, 179 (1990).
18. A. S. Vanini, J.-P. Audouard, P. Marcus, *Corros. Sci.*, **36**, 1825 (1994).

ВЛИЯНИЕ НА ТЕМПЕРАТУРАТА ВЪРХУ КОРОЗИОННОТО ПОВЕДЕНИЕ НА АУСТЕНИТНА НЕРЪЖДАЕМА СТОМАНА С ВИСОКО СЪДЪРЖАНИЕ НА АЗОТ В ХЛОРИДНИ СРЕДИ

Б. Р. Цанева,

Департамент по химия, Технически университет, бул. „Климент Охридски” 8, София 1000, България.

Постъпила на 17 май, 2013 г.; приета на 25 юли, 2013 г.

(Резюме)

Сравнено е електрохимичното поведение на стомана SS с високо съдържание на азот с това на стомана с конвенционалното качество 304 SS в 3.5% воден разтвор на хлориди при 20–80 °C, използвайки потенциала на отворена верига по отношение на времето, потенциодинамични и потенциостатични тестове. По отношение на температурата беше установено, че няма значително влияние върху корозионния потенциал, но дестабилизира образуването на пасивен филм и върху двете стомани. При критични стойности на анодната поляризация пасивните филми се повреждат и точкова корозия се наблюдава при по-нисък потенциал с повишаване на температурата. Високоазотната стомана показва по-бързо образуване на пасивни филми, но питинг потенциалът на тази стомана е по-чувствителен на температурни промени в сравнение с този на хром-никеловата. Температурата има слабо влияние върху процес на репасивиране, което зависи основно от състава на стоманата. При всички експериментални условия азотната стомана по-трудно се репасивира.

Poly-(4-vinylpyridinium nitrate) and silica sulfuric acid (SiO₂-OSO₃H): an efficient and metal-free oxidizing media for the oxidation of 1,4-dihydropyridine and urazole derivatives

A. Ghorbani-Choghamarani, M. Hajjami, M. Norouzi, A. Amiri

Department of Chemistry, Faculty of Science, Ilam University, Iran

Received May 27, 2013; accepted August 28, 2013

An efficient and metal-free oxidative aromatization of alkyl or aryl-substituted derivatives of 1,4-dihydropyridines and urazoles has been studied using poly-(4-vinylpyridinium nitrate) in the presence of silica sulfuric acid (SiO₂-OSO₃H). The reaction was carried out in dichloromethane at room temperature and the products were isolated in good to excellent yields.

Keywords: 1,4-Dihydropyridines, Oxidation, Urazole, Poly-(4-vinylpyridinium nitrate), Triazolinedione

INTRODUCTION

Nitrogen-heterocyclic compounds (NHCs) are produced by chemical industry for a variety of applications, including pharmaceuticals, cosmetics, pesticides, disinfectants, agrochemicals, dyestuffs, antifreeze, corrosion inhibitor, coal-tar wastes and creosote wood preservation [1].

In particular, pyridine and urazol derivatives are used as reagents in manufacture and industry [2,3].

Urazole derivatives (1,2,4-triazolidine-3,5-diones) are very interesting five-membered heterocyclic compounds, which at position 4 can provide a wide variety of aliphatic as well as aromatic constituents. Although a variety of oxidants such as iodobenzenediacetate, N₂O₄, periodic acid, *tert*-butyl hypochlorite or potassium dichromate, have been used for the oxidations of urazoles to triazolinediones, there are harsh conditions involved precluded oxidation of urazoles in the presence of other sensitive groups [4-8], because these compounds are very sensitive to the oxidizing agents and reaction conditions [9, 10]. In addition, most of the reported reagents produce by-products which are difficult to be removed from, the sensitive triazolinedione.

Also 1,4-dihydropyridines (1,4-DHPs) belong to a class of nitrogen containing heterocycles having a six-membered ring. Much attention has been devoted to explore their pharmacological activities [11]. The Oxidation (aromatization) of 1,4-dihydropyridines into the corresponding pyridines is generally the key step in their numerous biological reactions [12-14]. Therefore, oxidation

of 1,4-DHPs have attracted continuing interests of organic and medicinal chemists and a plethora of protocols have been developed [15-20]. Numerous reagents or reagent systems have been recommended for this purpose, such as isoxazolones [21], Fe(ClO₄)₃/HOAc [22], lead (IV) tetraacetate [23], FeCl₃/KMnO₄ [24], triazolinediones [25]. This transformation has attracted a great deal of attentions for the discovery of mild and general.

However, some of these procedures, which have been used for the oxidation of 1,4-dihydropyridines and urazoles have some disadvantages such as long reaction times, low yields of products, the requirement for severe conditions and the use of strong or toxic oxidants.

The use of heterogeneous reagents in different areas of the organic synthesis has now reached significant levels, not only for the possibility to perform environmentally benign synthesis, but also for the good yields frequently, accompanied by selectivity that can be achieved.

Recently, we have reported several new synthetic methods for environmentally reactions using catalytic and metal-free media for *in situ* generation of bromonium ion (Br⁺) and nitronium ion (NO₂⁺) [26-28]. During these studies, it was found that nitronium ion (NO₂⁺) is an excellent oxidant for the oxidation of organic compounds [29-32].

EXPERIMENTAL

Chemicals were purchased from the chemical companies Fluka, Merck and Aldrich. The oxidation products were characterized by comparison of their spectral (IR, ¹H and ¹³C NMR) and physical data with authentic samples.

* To whom all correspondence should be sent:
E-mail: arashghch58@yahoo.com; a.ghorbani@mail.ilam.ac.ir

Oxidation of 4-cyclohexylurazole using poly-(4-vinylpyridinium nitrate) of and silica sulfuric acid and silica sulfuric acid

In a 25 ml round bottom flask, to a solution of **2a** (0.183 g, 1.0 mmol) in CH₂Cl₂ (10 mL), silica sulfuric acid (0.1 g), wet-SiO₂ (0.2 g) and poly-(4-vinylpyridinium nitrate) (0.270 g) was added. The resulting reaction mixture was stirred magnetically at room temperature for 90 min (monitored by TLC). After completion of reaction, the solvent was filtered. Anhydrous Na₂SO₄ (1.5 g) was added to the filtrate. The residue was washed with CH₂Cl₂ (20 ml). Finally, CH₂Cl₂ was evaporated and 4-cyclohexyl-4H-1,2,4-triazole-3,5-dione was obtained in 98% yield.

Oxidation dimethyl 4-(phenyl)-2,6-dimethyl-1,4-dihydropyridine-3,5-dicarboxylate

In a typical procedure, to a mixture **4a** (0.329 g, 1.0 mmol) in CH₂Cl₂ (10 mL), silica sulfuric acid (0.2 g) and poly-(4-vinylpyridinium nitrate) (0.608 g) was added. The resulting reaction mixture was stirred magnetically at room temperature for 100 min (monitored by TLC). After completion of reaction, the solvent was filtered. Anhydrous Na₂SO₄ (1.5 g) was added to the filtrate. The residue was washed with CH₂Cl₂ (20 ml). Finally, CH₂Cl₂ was evaporated and pale yellow solid, diethyl 2,6-dimethyl-1-4-phenylpyridine-3,5-dicarboxylate was obtained in 94% yield.

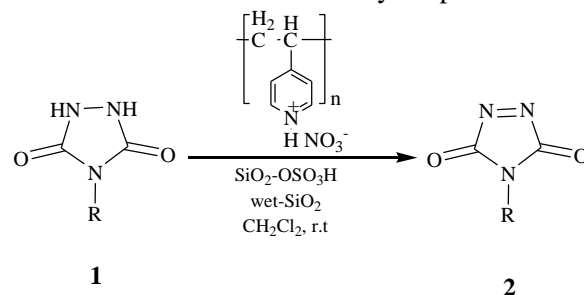
RESULTS AND DISCUSSION

Consequently, we were interested to apply poly-(4-vinylpyridinium nitrate) in the presence of silica sulfuric acid (SiO₂-OSO₃H) as a new source of nitronium ion (NO₂⁺) for the oxidation of urazole and 1,4-dihydropyridines. A white powder of poly-(4-vinylpyridinium nitrate) reagent is obtained by the reaction of poly-(4-vinylpyridine) with nitric acid. This reagent is ideal for 'green chemistry',

because is not toxic and doesn't make environmental pollution.

Initially, oxidation of different types of 4-substituted urazole **1** with poly (4-vinylpyridinium nitrate), silica sulfuric acid and wet SiO₂ in dichloromethane at room temperature have been examined. This reaction gave the corresponding 4-substituted-1,2,4-triazolidine-3,5-diones **2** with excellent yields. General form of this approach has been demonstrated by the oxidation of a wide variety of 4- alkyl or aryl -1,2,4-triazolidine-3,5-diones shown in Table 1 and Scheme 1.

As mentioned above, the oxidation reactions are heterogeneous because urazoles are insoluble in dichloromethane. Therefore, the oxidation reaction has been performed at the surface of wet SiO₂ and appropriate amount of poly-(4-vinylpyridinium nitrate) in the presence of silica sulfuric acid (SiO₂-OSO₃H). Then, the oxidation products migrate to the liquid phase (CH₂Cl₂) immediately. Pure product can be extracted by simple filtration and dichloromethane was removed by evaporation.



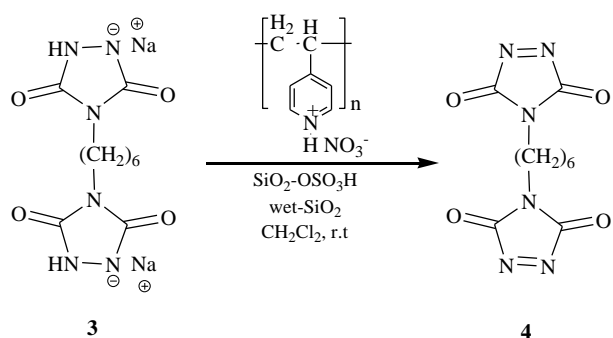
Scheme 1

Also the oxidation reaction has been performed for bis-triazolinedione **3** under mild and completely heterogeneous conditions at room temperature with excellent yield (91%), (Scheme 2). The reaction was readily promoted by stirring starting materials in CH₂Cl₂ at room temperature for 6 hours, and the bis-triazolinedione **4** was isolated by simple filtration and evaporation of the solvent.

Table 1. Oxidation of 4-substituted urazole 1a-k to 4-substituted-1,2,4-triazolidine-3,5-diones 2a-k with poly(4-vinylpyridinium nitrate), silica sulfuric acid and wet SiO₂ (50 %, w/w)^a

Entry	1	R	2	Time (min)	Yield (%) ^b
1	a	C ₆ H ₅	a	90	98
2	b	C ₆ H ₁₁	b	90	98
3	c	(CH ₃) ₃ C	d	104	91
4	d	CH ₃ (CH ₂) ₃	e	100	98
5	e	4-NH ₂ C ₆ H ₄	f	5h	-
6	f	3,4-(Cl) ₂ C ₆ H ₃	g	120	90
7	g	CH ₃ CH ₂	h	90	47
8	h	4-NO ₂ C ₆ H ₄	i	118	98
9	i	4-ClC ₆ H ₄	j	98	87
10	j	CH ₃ CH ₂ CH ₂	k	75	90
11	k	1-naphthyl	l	3h	91

^a Molar ratio of the reagents: urazole / poly-(4-vinylpyridinium nitrate) / silica sulfuric acid / wet SiO₂ for entries 1-12 (1 mmol / 2 mmol / 0.1 g / 0.2 g); ^b Isolated yield.

**Scheme 2**

In order to investigate and develop the scope and limitation of this oxidizing media we decided to examine the oxidation of 1,4-dihydropyridines by described procedure (Scheme 3, Table 2).

Several 1,4-dihydropyridines are oxidized to corresponding pyridines by poly-(4-vinylpyridinium nitrate) in the presence of silica sulfuric acid (SiO₂-OSO₃H). Oxidation reactions were performed under mild and completely heterogeneous conditions at room temperature. After reaction completion, product is extracted by simple filtration and dichloromethane was removed by evaporation.

Table 2. Oxidation of 1,4-dihydropyridines 4a–p to pyridines 5a–p using poly(4-vinylpyridinium nitrate) in the presence of silica sulfuric acid (SiO₂-OSO₃H)^a

Entry	4	R ₁	R ₂	5	Time (min)	Yield (%) ^b	mp(°C)
1	a	C ₆ H ₅	OC ₂ H ₅	a	100	94	83
2	b	CH ₃	OC ₂ H ₅	b	30	90	79-80
3	c	4-OMeC ₆ H ₄	OC ₂ H ₅	c	140	90	68-72
4	d	3,4-(OMe) ₂ C ₆ H ₃	OC ₂ H ₅	d	103	93	72-80
5	e	4-FC ₆ H ₄	OC ₂ H ₅	e	195	90	98-101
6	f	4-ClC ₆ H ₄	OC ₂ H ₅	f	7:35 h	95	68-82
7	g	4-BrC ₆ H ₄	OC ₂ H ₅	g	8:15 h	90	95-98
8	h	C ₆ H ₅	OCH ₃	h	40	98	137-145
9	i	(CH ₂) ₅ CH ₃	OCH ₃	i	90	79	68
10	j	CH ₃	OCH ₃	j	135	97	108-110
11	k	4-OMeC ₆ H ₄	OCH ₃	k	155	98	110
12	l	3,4-(OMe) ₂ C ₆ H ₃	OCH ₃	l	155	98	140-144
13	m	4-FC ₆ H ₄	OCH ₃	m	5:50 h	94	145-149
14	n	4-ClC ₆ H ₄	OCH ₃	n	8:10 h	95	146-149
15	o	4-BrC ₆ H ₄	OCH ₃	o	9:10 h	87	141-144
16	p	3-NO ₂ C ₆ H ₄	OCH ₃	p	35	95	-

^a Molar ratio of the reagents: 1,4-dihydropyridines/ poly-(4-vinylpyridinium nitrate)/ silica sulfuric acid for entries 1-14 (1 mmol/ 0.608 g/ 0.2 g); and for entries 7,15 and 16 (1 mmol/ 0.676 g/ 0.2 g).^b Isolated yield.

Table 3. Comparison of the different methods used for the oxidation of 4-phenyl-1,2,4-triazolidine-3,5-dione to corresponding triazolinedione with different catalyst

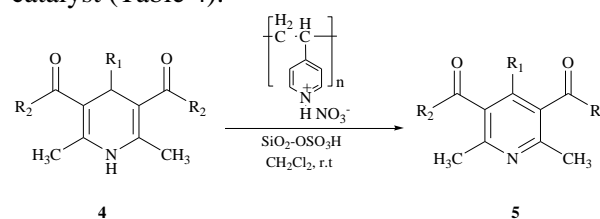
Entry	Catalyst	Time (Min)	Yield (%) ^a	Reference
1	Poly-(4-vinylpyridinium nitrate)	90	98	This work
2	H ₅ IO ₆ , NaNO ₂ and Wet SiO ₂ (50% w/w)	60	80	6
3	K ₂ Cr ₂ O ₇ /AlCl ₃	3	95	8
4	N,N,N',N'-Tetrabromobenzene-1,3-disulfonylamide	120	83	10
5	NaNO ₂ , C ₂ H ₂ O ₄ .2H ₂ O	60	80	33

^aIsolated yield.

As shown in Table 2, both electron donating and electron withdrawing substituents on the precursors are afforded the corresponding pyridines from good to excellent yields.

To show the efficiency of the described system in comparison with previously reported procedures in the literature, we compared our obtained results for the oxidation of 4-phenyl-1,2,4-triazolidine-3,5-dione to corresponding triazolinedione with the best of the well-known data from the literature as shown in (Table 3).

Also, we compared our method for the oxidation of diethyl 1,4-dihydro-2,6-dimethyl-4-phenylpyridine-3,5-dicarboxylate (as a typical example) to corresponding pyridine with different catalyst (Table 4).

**Scheme 3**

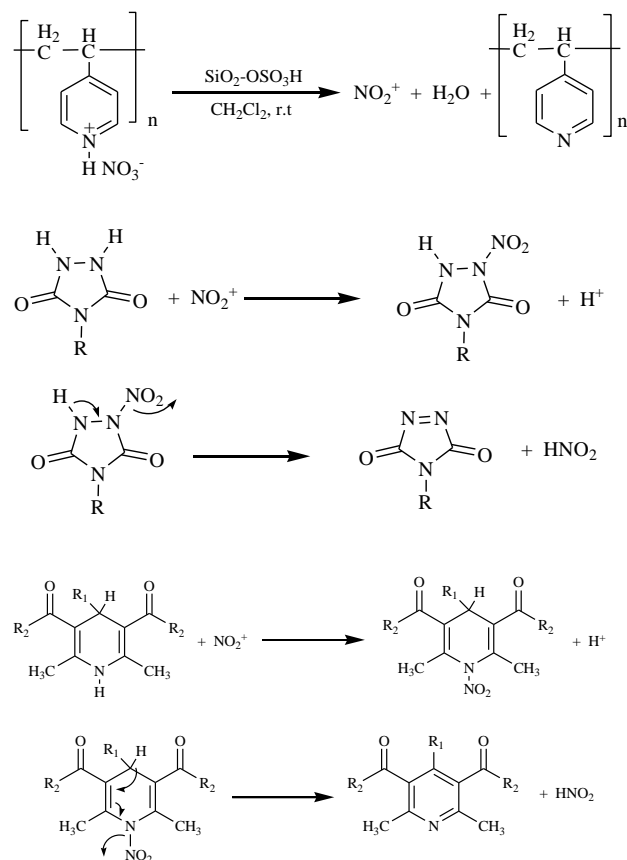
T

phenylpyridine-3,5-dicarboxylate to corresponding pyridine with different catalyst

Entry	Catalyst	Time (Min)	Yield (%) ^a	Reference
1	Poly-(4-vinylpyridinium nitrate)	100	94	This work
2	CO(NH ₂) ₂ / H ₂ O ₂	12h	89	11
3	PhCH ₂ Ph ₃ PHSO ₅ / BiCl ₃	120	89	15
4	N-hydroxyphthalimide, O ₂	4h	99	21(a)
5	RuCl ₃ / O ₂	53h	55	20(a)

^aIsolated yield.

A plausible mechanism for the transformation is shown in Scheme 4.



Scheme 4

In summary, we describe an efficient and mild protocol for the oxidation of urazoles and 1,4-dihydropyridines using poly-(4-vinylpyridinium nitrate) as new oxidizing polymer. Advantages of this method for the oxidation of organic compounds over conventional homogeneous reactions enhanced reaction rates, cleaner products, simple experimental procedures, mild reaction conditions and minimization of chemical wastes as compared to the solution phase counterparts.

ACKNOWLEDGMENT: Financial support to this work by the Ilam University, Ilam, Iran is gratefully acknowledged.

REFERENCES

- X. Xing, X. Zhu, H. Li, Y. Jiang, J. Ni, *Chemosphere*, **86**, 368 (2012).
- T. Jikihara, K. Matsuya, H. Ohta, S. Suzuki, O. Wakabayashi, *Japan. Chemical Abstract*, **95**, 2219 (1981).
- S.E. Mallakpour, *Chem. Edu. J.*, **69**, 238 (1992).
- R.M. Moriarty, I. Prakash, R. Penmasta, *Synth. Commun.*, **17**, 409 (1987).
- M.A. Zolfigol, E. Madrakian, E. Ghaemi, S. Mallakpour, *Synlett*, 1633 (2002).
- M.A. Zolfigol, G. Chehardoli, F. Shirini, S.E. Mallakpour, H. Nasr-Isfahani, *Synth. Commun.*, **31**, 1965 (2001).
- G. Read, N.R. Richardson, *J. Chem. Soc.*, 167 (1996).
- I. Mohammadpoor-Baltork, M.M. Sadeghi, S.E. Mallakpour, A.R. Hajipour, A.H. Adibi, *Synth. Commun.*, **32**, 3445 (2002).
- J.C. Stickler, W.H. Pirkle, *J. Org. Chem.*, **31**, 3444 (1966).
- M.A. Zolfigol, R. Ghorbani-Vaghei, S. Mallakpour, G. Chehardoli, A. Ghorbani-Choghamarani, A.H. Yazdia, *Synthesis*, 1631 (2006).X
- M. Filipan-Litvic, M. Litvic, V. Vinkovic, *Tetrahedron*, **64**, 5649 (2008).
- U. Esiner, J. Kuthan, *Chem. Rev.*, **72**, 1 (1972).
- D.M. Stout, A.I. Meyers, *Chem. Rev.*, **82**, 223 (1982).
- A. Sauains, G. Dubers, *Heterocycles*, **27**, 291 (1988).
- H. Adibia, A.R. Hajipour, *Bioorg. Med. Chem. Lett.*, **17**, 1008 (2007).
- (a) G. Sabitha, G.S.K.K. Reddy, C.S. Reddy, J.S. Yadav, *Tetrahedron Lett.*, **44**, 4129 (2003); (b) M.A. Zolfigol, M. Safaiee, *Synlett*, 827 (2004).
- J.J. Vanden Eynde, R. D'OrazioVan, Y. Haverbeke, *Tetrahedron*, **50**, 2479 (1994); (b) J.S. Yadav, B.V. Subba Reddy, G. Sabitha, G.S.K.K. Reddy, *Synthesis*, 1532 (2000).
- M. Anniyappan, D. Muralidharan, P.T. Perumal, *Tetrahedron*, **58**, 5069 (2002).
- J. Arguello, L.J. Nunez-Vergara, J.C. Sturm, J.A. Squella, *Electrochim. Acta.*, **49**, 4849 (2004).
- (a) S.H. Mashraqui, M.A. Karnik, *Tetrahedron Lett.*, **39**, 4895 (1998); (b) N. Nakamichi, Y. Kawashita, M. Hayashi, *Synthesis*, 1015 (2004).
- (a) B. Han, Q. Liu, Z. Liu, R. Mu, W. Zhang, Z. L. Liu, W. Yu, *Synlett*, 2333 (2005); (b) Z.G. Liu, B. Han, Q. Liu, W. Zhang, L. Yang, Z.L. Liu, W. Yu, *Synlett*, 1579 (2005).

22. M.M. Heravi, F.K. Behbahani, H.A. Oskooie, R.H. Shoar, *Tetrahedron Lett.*, **46**, 2775 (2005).
23. M. Litvic, I. Capanec, M. Filipan, K. Kos, A. Bartolincic, V. Druskovic, M.M. Tibi, V. Vinkovic, *Heterocycles*, **65**, 23 (2005).
24. J.J. Xia, G.W. Wang, *Synthesis*, 2379 (2005).
25. A. Ghorbani-Choghamarani, M. Shahamirian, M. Safaiee, I. Mohammadpoor-Baltork, S. Mallakpour, M. Abdollahi-Alibeik, *Tetrahedron Lett.*, **46**, 5581 (2005).
26. M. Hajjami, A. Ghorbani-Choghamarani, M. Norouzi, *Chin. J. Catal.*, **33**, 1661 (2012).
27. A. Ghorbani-Choghamarani, M. Norouzi, *Bull. Korean Chem. Soc.*, **32**, 1399 (2011).
28. A. Ghorbani-Choghamarani, S. Sardari, *J. Sulfur. Chem.*, **32**, 63 (2011).
29. A. Ghorbani-Choghamarani, S. Sardari, *Chin. J. Catal.* **31**, 1347 (2010).
30. A. Ghorbani-Choghamarani, M. Abbasi, *Chin. J. Catal.*, **22**, 114 (2011).
31. M. Nikoorazm, H. Goudarziafshar, L. Shiri, *Bull. Korean Chem. Soc.*, **30**, 972 (2009).
32. A. Ghorbani-Choghamarani, M.A. Zolfigol, M. Hajjami, S. Rastgoo, *Lett. Org. Chem.*, **7**, 249 (2010).
33. M.A. Zolfigol, S.E. Mallakpour, *Synth. Commun.*, **29**, 4061 (1999).

ПОЛИ-(4-ВИНИЛПИРИДИНИЕВ НИТРАТ) И СИЛИЦИЕВ ДИОКСИД-СЯРНА
КИСЕЛИНА (SiO₂-OSO₃H): ЕФЕКТИВНА И БЕЗМЕТАЛНА СРЕДА ЗА ОКИСЛЕНИЕ НА
1,4-ДИХИДРОПИРИДИН И ПРОИЗВОДНИ НА УРАЗОЛА

А. Горбани - Чогамарани*, М. Хаджами, М. Норузи, Ар. Амири

Департамент по химия, Научен факултет, Иламски университет, ПК 69315516, Илам, Иран

Постъпила на 27 май, 2013 г.; коригирана на 28 август, 2013 г.

(Резюме)

Изследвана е ефективна и безметална окислителна ароматизация на алкил- или арил-заместени производни на 1,4-дихидропиридини и уразоли чрез използване на поли-(4-винилпиридиниев нитрат) в присъствие на силициев диоксид - сярна киселина (SiO₂-OSO₃H). Реакцията протича в дихлорометан при стайна температура и продуктите са изолирани с добри до отлични добиви.

Allergenicity prediction by partial least squares-based discriminant analysis

L. H. Naneva¹, I. D. Dimitrov², I. P. Bangov¹, I. A. Doytchinova^{2*}

¹Konstantin Preslavski Shumen University, Faculty of Natural Sciences, General Chemistry Chair, 115 Universitetska Str., 9712 Shumen, Bulgaria

²Medical University of Sofia, Faculty of Pharmacy, 2 Dunav Str., 1000 Sofia, Bulgaria

Received November 30, 2012; Revised February 5, 2013

Allergenicity of food proteins is a crucial problem associated with the widespread usage of new foods, supplements and herbs, many of them having known or unknown genetically modified origin. Allergenicity is a subtle, non-linearly coded property. Most of the existing methods for allergenicity prediction are based on structural similarity of novel proteins to known allergens. Thus, the identification of a novel, structurally diverse allergen could not be predicted by these methods. In the present study, we propose an alignment-free method for allergenicity prediction, based on the amino acid principal properties as hydrophobicity, size and electronic structure. Proteins are transformed into uniform vectors and analyzed by PLS-based discriminant analysis. The preliminary model derived on the basis of a small set of 120 allergens and 120 non-allergens identified correctly 73% of the proteins included in the external test set of 1,164 allergens and non-allergens. The extended model based on a set of 1,404 proteins (702 allergens and 702 non-allergens) showed 70% accuracy in the cross-validations.

Key words: allergens, non-allergens, α -descriptors, auto- and cross-covariance, discriminant analysis, PLS

INTRODUCTION

Allergy is a growing health problem of modern life. Food allergies affect 10 – 15% of infants and young children [1]. They are caused by different sources: milk, eggs, peanuts, soy, shellfish, fruits, etc. [2-4]. Allergy involves complex reactions to external factors that contribute to the development of diseases characterized by symptoms such as rhinitis, asthma, atopic dermatitis, skin sensitization. In some cases, severe reactions such as acute and fatal anaphylactic shock may occur.

The term "allergy" was introduced in 1906 by the Austrian pediatrician Clemens von Pirquet to denote the modified reaction to smallpox vaccine [5]. Allergy is an altered capacity of the body to react to a foreign substance called allergen. When potential allergens enter the body for the first time, allergen-specific IgE antibodies are produced, which stay around long after the initial allergen is cleared from the body. Most of the antibodies are caught by Fc ϵ receptors, which are IgE-specific receptors that are exposed on the surface of mast cells, basophils and activated eosinophils. These cells are then primed to react the next time the body encounters the allergen. They release stored mediators, which give rise to inflammation and

tissue damage causing a variety of symptoms [6-9].

Although there is no consensus on the structure of the allergen, the United Nations Food and Agriculture Organization (FAO) and World Health Organization (WHO) have developed *Codex alimentarius* guidelines for assessing the potential allergenicity of novel proteins [10-11]. According to these guidelines, protein is a potential allergen, if it has an identity of 6 to 8 contiguous amino acids or greater than 35% similarity within a window of 80 amino acids when compared to known allergens.

Currently, two bioinformatic approaches exist for allergen prediction. The first approach follows the guidelines of FAO and WHO and searches for sequence similarity. There are databases that contain extensive information on known allergens, which are used for sequence similarity search. Such databases are Structural Database of Allergenic Proteins (SDAP) [12], Allermatch [13] and AllerTool [14]. This approach has a good allergen prediction, but generates a large number of false allergens. Moreover, the discovery of new structurally different allergens is limited by the lack of similarity to already known allergens.

The second approach is based on identification of linear motifs for allergenicity. The motif is a sequence of amino acids responsible for a particular activity of the protein. Stadler and Stadler (2003) defined 52 allergenic motifs by comparing

* To whom all correspondence should be sent:
E-mail: doytchinova@gmail.com

allergens to non-allergens [15]. Li and colleagues (2004) identified motifs for allergenicity using clustering of known allergens by hidden Markov model (HMM) [16]. Bjorklund and colleagues (2005) developed a method for identifying allergens by detecting allergenic peptides (allergen-representative peptides, ARP) [17]. AlgPred is a server for predicting allergenic protein that combines four motif search methods: support vector machines (SVM), MEME/MAST program, IgE epitopes and ARP [18].

Both approaches are based on the assumption that allergenicity is a linearly encoded property. To act as an allergen, a protein must contain epitopes for both Th2 cells and B lymphocytes [7]. Epitope is part of the protein that interacts with another protein. The epitopes for Th2 are linear, but the B-cell epitopes are non-linear, conformational patches on the protein surface. Obviously, allergenicity, like immunogenicity and antigenicity, is a property coded linearly as well as nonlinearly. Therefore, the alignment-based approaches are not able to identify such property in an unambiguous manner.

In the present study, we develop and validate an alignment-free method for allergenicity prediction, based on the principal amino acid properties as hydrophobicity, size and electronic properties. Partial least squares-based discriminant analysis is used to develop models for food allergenicity prediction. The models were validated by internal and external test sets of allergens and non-allergens.

DATASETS AND METHODS

Allergens and non-allergens

A dataset of 702 food allergens and 702 non-allergens was collected from the databases CSL (Central Science Laboratory) [19], FARRP (Food Allergen Research and Resource Program) [20] and SDAP (Structural Database of Allergenic Proteins) [21]. The non-allergens were selected from the same species using a BLAST search with 0% identity to allergens at E-value 0.001.

Descriptors of the protein structures

The z -descriptors describe principal properties of amino acids. They are derived by applying principal component analysis on a set of 29 molecular properties of amino acids [22]. The first principal component (1PC), named z_1 , is dominated by the hydrophobicity of amino acids. The second principal component (2PC), named z_2 , relates best to amino acid size. The third principal component

(3PC), named z_3 , explains the electronic properties of amino acids. The scores of these components define the set of z -descriptors for each amino acid. In the present study, the three z -descriptors were used to describe the amino acid sequences of allergens and non-allergens.

The proteins used in the study were of different length. In order to convert them into uniform vectors, the method of auto- and cross-covariance (auto- and cross-covariance, ACC) transformation was used [23]. Auto-covariance (A_{jj}) and cross-covariance (C_{jk}) were calculated by the following formulas:

$$A_{jj}(L) = \sum_i^{n-L} \frac{Z_{j,i} \times Z_{j,i+L}}{n-L}$$

$$C_{jk}(L) = \sum_i^{n-L} \frac{Z_{j,i} \times Z_{k,i+L}}{n-L}$$

The index j refers to the z -descriptors ($j = 1, 2, 3$); the index i indicates the position of amino acid ($i = 1, 2, 3 \dots n$); n is the number of amino acids in protein; l is the lag ($L = 1, 2, \dots, l$). Lag is the length of the frame of contiguous amino acids, for which A_{jj} and C_{jk} are calculated. In the present study, a short lag ($L = 5$) was chosen, as the influence of neighboring amino acids was investigated. Each protein was transformed into a string of 45 elements ($3^2 \times 5$).

Partial least squares-based discriminant analysis (PLS-DA)

The discriminant analysis (DA) is a method for data classification based on a linear combination of explanatory variables [24]. Partial least squares (PLS)-based DA was used in the present study. PLS forms new X variables named principal components (PC) as linear combinations of old variables, and then uses them to predict class membership. The optimum number of PCs was selected by adding components until the predictive ability of the model increases. In the present study, PLS-DA was performed by SIMCA P-8.0 [24].

The projection of the i -th protein on the plane formed by two PSs is called score. Proteins with similar descriptors are projected close to each other and form a cluster. The loading of the i -th descriptor on a PC equals $\cos \alpha$, where α is the angle between the axis of descriptor X_i and the plane formed by two PCs. As more distant is a descriptor from the origin, as higher loading has this descriptor on the corresponding PC.

Receiver Operating Characteristics (ROC) statistics

The predictive ability of the derived final model was assessed by Receiver Operating Characteristic (ROC) statistics [25]. Four outcomes are possible in ROC-statistics: *true positives* (TP, true binders predicted as binders); *true negatives* (TN, true non-binders predicted as non-binders); *false positives* (FP, true non-binders predicted as binders); and *false negatives* (FN, true binders predicted as non-binders). Three classification functions were used in the present study: *sensitivity* (true positives/total positives), *specificity* (true negatives/total negatives) and *accuracy* (true positives and negatives/total). *Sensitivity*, *specificity* and *accuracy* were calculated at different thresholds and the *area under the ROC curve* (*sensitivity*/1-*specificity*) (A_{ROC}) was calculated. A_{ROC} is a quantitative measure of predictive ability and varies from 0.5 for random prediction to 1.0 for perfect prediction.

Variable influence on projection (VIP)

The parameter *VIP* (variable influence on projection) was introduced by Wold in 1993 [26] to describe the importance of each independent variable on the dependent one. It is calculated by the following formula:

$$VIP_{ak} = \sqrt{\left(\sum_{a=1}^A (w_{ak}^2 (SSY_{a-1} - SSY_a)) \frac{K}{SSY_0 - SSY_A} \right)}$$

where w_{ak} is the weight (coefficient) of the variable k on the component a , and SSY_a is the explained variance of Y by the component a . Variables with *VIP*, greater than 1, are the most relevant for explaining Y . *VIP* parameters are calculated by SIMCA-P 8.0.

Model validation

The models derived in the present study were validated by cross-validation and by external test set. The cross-validation (CV) is a procedure for testing the predictive ability of models. The training set is divided into several groups with approximately equal numbers of members in each group. One group is defined as a test set and the rest form a new training set. The training set is used to derive a model, the test set – to test its predictivity. To reduce variability, multiple rounds of cross-validation are performed using different partitions, and the validation results are averaged over the rounds.

The derived models are validated also by external test set containing allergens and non-allergens not included in the training set. The predictive ability of the models was estimated by the parameters *sensitivity*, *specificity*, *accuracy* and A_{ROC} .

RESULTS

Preliminary model for allergenicity prediction

In order to derive a preliminary model for allergenicity prediction, a small set of 120 allergens and 120 non-allergens was compiled randomly from the set of 1,440 proteins used in the study. The structure of proteins was described by the three z -descriptors and each protein was transformed into a string of 45 variables, applying ACC-transformation, as described in "Materials and Methods". The two-class matrix consisting of 240 proteins and 45 variables was subjected to PLS-DA with varying number of principal components from 1 to 5. The models were evaluated using the parameters *sensitivity*, *specificity* and *accuracy* at threshold 0.5. The area under the curve A_{ROC} also was recorded. The results are shown in Figure 1.

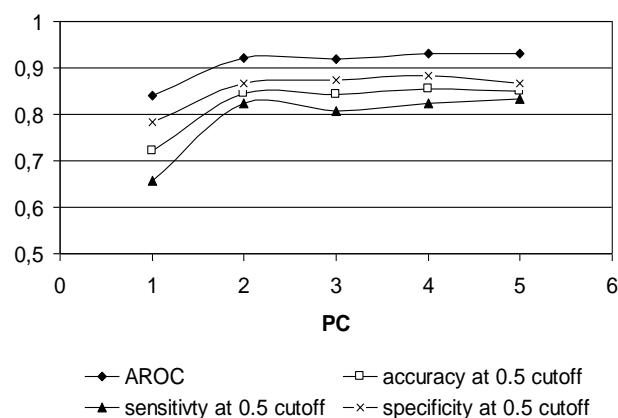


Fig. 1. *Sensitivity*, *specificity* and *accuracy* at threshold 0.5, and A_{ROC} for the preliminary models for allergenicity prediction with different number of PCs.

The results showed that the addition of a second PC significantly increases all parameters of the model. Further addition of PCs initially decreases slightly the parameters, and then increases them slightly. Thus, two PCs was the optimal number of PCs for this model.

The preliminary model for allergenicity prediction is shown in Table 1. The assignment of ACC variables is as follows: the first digit corresponds to the number of z -descriptor for the i -th amino acid in the protein; the second digit corresponds to the number of z -descriptor for the j -th amino acid; the third digit shows the lag. For

Table 1 .VIP values and coefficients of the preliminary model for allergenicity prediction. The constant of the model is 0.998. Variables with VIP > 1.5 and coefficients > |0.100| are given in bold.

<i>variable</i>	<i>VIP</i>	<i>coefficient</i>	<i>variable</i>	<i>VIP</i>	<i>coefficient</i>	<i>variable</i>	<i>VIP</i>	<i>coefficient</i>
ACC334	2.003	-0.178	ACC215	1.121	-0.078	ACC221	0.693	0.003
ACC333	1.656	-0.162	ACC121	1.101	-0.078	ACC122	0.685	-0.036
ACC324	1.586	0.132	ACC332	1.061	-0.097	ACC211	0.575	-0.047
ACC223	1.578	0.052	ACC325	1.011	0.001	ACC125	0.573	-0.055
ACC222	1.413	0.084	ACC234	0.950	-0.096	ACC212	0.526	-0.024
ACC224	1.413	0.065	ACC114	0.928	-0.071	ACC231	0.520	0.032
ACC225	1.344	0.099	ACC322	0.924	-0.031	ACC115	0.510	0.029
ACC314	1.315	-0.142	ACC112	0.896	0.030	ACC133	0.503	-0.051
ACC131	1.252	0.050	ACC132	0.867	0.092	ACC124	0.447	-0.045
ACC335	1.248	-0.083	ACC315	0.793	-0.073	ACC232	0.418	-0.020
ACC111	1.210	0.083	ACC134	0.792	-0.085	ACC214	0.393	0.043
ACC313	1.200	-0.115	ACC323	0.779	-0.081	ACC123	0.381	0.002
ACC331	1.185	-0.125	ACC312	0.770	-0.009	ACC213	0.284	-0.017
ACC311	1.128	0.116	ACC235	0.725	-0.014	ACC135	0.201	-0.021
ACC233	1.123	0.103	ACC113	0.699	0.064	ACC321	0.153	0.007

example, ACC324 assigns the sum of ACC values calculated as $z_3 \cdot z_2$ for each pair amino acids with lag 4 (first and fourth, second and fifth, third and sixth, etc.). The variables in the model are ordered according to their VIP values. Variables with VIP > 1 are essential to the model. Nineteen variables (42%) in the model have a VIP > 1. To differentiate between the most important, the threshold for VIP was increased to 1.500. Only four variables have VIP > 1.500 and coefficient > |0.100|. These are ACC334, ACC333 and ACC324. ACC324 has positive coefficient, ACC334 and ACC333 have negative ones. This means that proteins having negative ACC334 and ACC333, and positive ACC324 are likely to act as allergens. Figure 2A shows the scores of the proteins from the initial set, and Figure 2B gives the loadings of ACC variables. The model distinguishes relatively well allergens (top right, Figure 2A) from non-allergens (bottom left), despite the lack of a clear boundary between the two clusters. The variable ACC324 is situated most distantly from the origin in the upper right quadrant close to the allergenicity variable (assigned as DA1), while variables ACC334 and ACC333 variables are situated most distantly from the origin in the lower left quadrant close to the non-allergenicity variable (assigned as DA2). The

model was tested for *sensitivity*, *specificity* and *accuracy* at threshold 0.5. It detects 83% of allergens, 87% of non-allergens and 85% correctly identified proteins from the initial set. The A_{ROC} value is 0.922, indicating for the excellent predictivity of the model.

The initial model for allergenicity prediction was cross-validated in 6 groups. The initial set of 120 allergens and 120 non-allergens was divided into 6 subsets of 20 allergens and 20 non-allergens. Five subsets were united in a training set; the sixth subset was a test. The training set was used to derive the model; the test set was used to validate it. The procedure was repeated six times, so any protein acts five times as a trainer and one time – as a tester. The average values for the test subsets from the cross-validation are: 77% *sensitivity*, 79% *specificity* and 78% *accuracy* at threshold 0.5, and $A_{ROC} = 0.856$. The cross-validation showed that the preliminary model has a good predictive ability, independent of the training set composition.

Further, the preliminary model was used to predict the allergenicity of external test set of 582 allergens and 582 non-allergens. It recognized 68% of the allergens and 77% of the non-allergens with 73% total *accuracy* at threshold 0.5. The A_{ROC} value was 0.785.

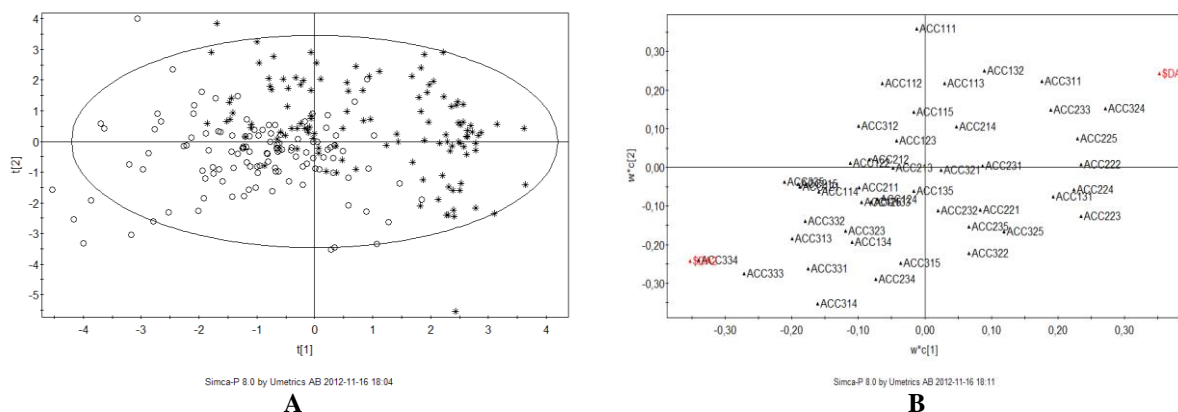


Fig. 2. Scores (A, allergens are given as stars, non-allergens – as blank circles) and loadings (B) according to the preliminary model for allergenicity prediction.

Extended model for allergenicity prediction

Encouraged by the good predictivity of the preliminary model, we derived an extended model for allergenicity prediction based on 702 food allergens and 702 non-allergens. The structure of proteins was described by the three z -descriptors and ACC-transformed into strings of 45 variables. The two-class matrix consisting of 1,404 proteins and 45 variables was subjected to PLS-DA with varying number of principal components from 1 to 5. The models were evaluated using the parameters *sensitivity*, *specificity* and *accuracy* at threshold 0.5. The area under the curve A_{ROC} also was recorded. The results are shown in Figure 3. The highest values of the parameters are obtained by three PCs.

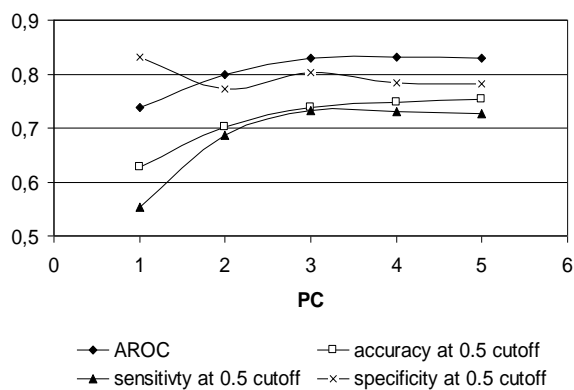


Fig. 3. Sensitivity, specificity and accuracy at threshold 0.5, and A_{ROC} for the extended models for allergenicity prediction with different number of PCs

The model with 3 PCs and the VIP-values of the variables are shown in Table 2. Three variables have $VIP > 1.300$ and coefficient $> |0.100|$. These are ACC333, ACC214 and ACC334. One of them has a positive coefficient (ACC214); the other two are negative (ACC333 and ACC334). The significance of variables and ACC333 ACC334, found in the preliminary model is confirmed here. Figure 4 shows the scores and the loading according to the extended model projected on the plane of the first two PCs. There is one outlier (non-allergen with GI: 315113274) (not shown). The model detects 73% of allergens, 80% of non-allergens and 77% correctly identified proteins from the whole set. The A_{ROC} value is 0.830.

The extended model for allergenicity prediction was cross-validated in 7 groups. The whole set of 702 allergens and 702 non-allergens was divided into 7 subsets of 100 or 101 allergens and 100 or 101 non-allergens. Six subsets were united in a training set; the seventh subset was a test. The training set was used to derive the model; the test set was used to validate it. The procedure was repeated seven times, so any protein acts six times as a trainer and one time – as a tester. The average values for the test subsets from the cross-validation are: 60% *sensitivity*, 79% *specificity* and 70% *accuracy* at threshold 0.5, and $A_{ROC} = 0.746$. The cross-validation showed that the extended model has a lower predictive ability than the preliminary one, but still independent of the training set composition.

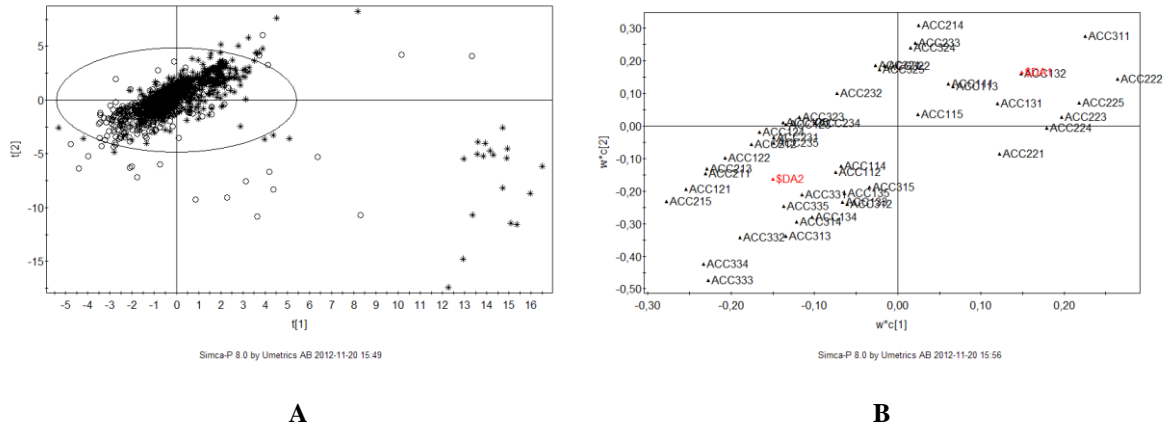


Fig. 4 . Scores (A, allergens are given as stars, non-allergens – as blank circles) and loadings (B) according to the extended model for allergenicity prediction.

Table 2. VIP values and coefficients of the extended model for allergenicity prediction. The constant of the model is 1.000. Variables with VIP > 1.300 and coefficients > |0.100| are given in bold.

<i>variable</i>	<i>VIP</i>	<i>coefficient</i>	<i>variable</i>	<i>VIP</i>	<i>coefficient</i>	<i>variable</i>	<i>VIP</i>	<i>coefficient</i>
ACC333	1.505	-0.158	ACC211	1.044	-0.058	ACC232	0.901	-0.013
ACC214	1.499	0.129	ACC224	1.032	0.030	ACC231	0.895	-0.058
ACC334	1.387	-0.124	ACC311	1.015	0.107	ACC323	0.895	-0.038
ACC335	1.236	-0.030	ACC235	1.008	-0.074	ACC325	0.885	0.020
ACC222	1.227	0.092	ACC233	1.000	0.059	ACC113	0.877	0.083
ACC332	1.215	-0.085	ACC324	0.983	0.048	ACC315	0.871	-0.081
ACC215	1.190	-0.093	ACC124	0.979	-0.007	ACC123	0.833	-0.002
ACC313	1.149	-0.125	ACC314	0.964	-0.103	ACC133	0.790	-0.071
ACC121	1.105	-0.077	ACC221	0.963	-0.001	ACC331	0.758	-0.051
ACC225	1.101	0.066	ACC134	0.958	-0.102	ACC115	0.697	0.049
ACC234	1.078	-0.062	ACC212	0.934	-0.020	ACC135	0.697	-0.067
ACC122	1.077	-0.028	ACC111	0.930	0.086	ACC132	0.681	0.074
ACC312	1.054	-0.104	ACC125	0.929	0.007	ACC112	0.656	-0.021
ACC213	1.050	-0.054	ACC321	0.924	0.026	ACC131	0.590	0.022
ACC223	1.049	0.042	ACC322	0.918	0.022	ACC114	0.471	-0.027

DISCUSSION

Allergenicity of food proteins is a crucial problem associated with the widespread usage of new foods, supplements and herbs, many of them having known or unknown genetically modified origin. Allergenicity is a subtle, non-linearly coded property. Most of the existing methods for allergenicity prediction are based on structural similarity of novel proteins to known allergens. Thus, the identification of a novel, structurally

diverse allergen could not be predicted by these methods.

In the present study, we propose an alignment-free method for allergenicity prediction, based on the amino acid principal properties as hydrophobicity, size and electronic structure. Proteins are transformed into uniform vectors and analyzed by PLS-DA. Initially, a preliminary model was derived based on a small set of 120 allergens and 120 non-allergens. The model was tested by cross-validation and external test set and recognized correctly 73% of the proteins from the

external test set. Then, the dataset was extended to 1,404 proteins (702 allergens and 702 non-allergens) and a new model was derived. The cross-validation study showed that the extended model is able to identify correctly 70% of the tested proteins.

The food allergens involved in the present study have diverse structure, composition and origin, which imply great variance in the set. By increasing the number of proteins in the training set increases the number of PCs needed to explain this variance. In the small initial set used to derive the preliminary model, two PCs were sufficient to obtain a model with good predictive ability. In the extended set of proteins used in the extended model, it was necessary to include a third PC. The model with 3 PCs had the highest predictive ability.

Both models point the importance of the variables ACC333 and ACC334. These variables account for the electronic structure of amino acids located in close proximity but not next to each other. This once again shows that the allergenicity is a hidden, complex property, depending on many factors, some of which are encoded in the primary structure of proteins.

Acknowledgements: This study is supported by the National Research Fund of the Ministry of Education and Science, Bulgaria, Grant 02-1/2009 and Grant FFNNIPO/12-00985.

REFERENCES

1. W. Cookson, *Nat. Rev. Immunol.*, **4**, 978 (2004).
2. H.A. Sampson, *J. Allergy Clin. Immunol.*, **103**, 717 (1999).
3. H.A. Sampson, *J. Allergy Clin. Immunol.*, **103**, 981 (1999).
4. H.A. Sampson, *J. Allergy Clin. Immunol.*, **115**, 139 (2005).
5. S.C. Bukantz, *J. Allergy Clin. Immunol.*, **109**, 724 (2002).
6. P.J. Cooper, *Parasite Immunol.*, **26**, 455 (2004).
7. C.A. Janeway, P. Travers, M. Walport, J. D. Capra, *Immunobiology: the immune system in health and disease*, Current Biology Publications, London, 1999.
8. C. Rusznak, R. J. Davies, *BMJ*, **316**, 686 (1998).
9. R.D.J. Huby, R.J. Dearman, I. Kimber, *Toxicological Sci.*, **55**, 235 (2000).
10. FAO/WHO Agriculture and Consumer Protection, Report of a Joint FAO/WHO Expert Consultation on Allergenicity of Foods Derived from Biotechnology, Rome, Italy, 2001.
11. FAO/WHO Codex Alimentarius Commission. Joint FAO/WHO Food Standards Programme, Rome, Italy, 2003.
12. O. Ivanciuc, C. H. Schein, W. Braun, *Nucleic Acids Res.*, **31**, 359 (2003).
13. M.W.E.J. Fiers, G.A. Kleter, H. Nijland, A.A.C.M. Peijnenburg, J.P. Nap, R.C.H.J. van Ham, *BMC Bioinformatics*, **5**, 133 (2004).
14. Z. H. Zhang, J.L. Koh, G.L. Zhang, K.H. Choo, M.T. Tammi, J.C. Tong, *Bioinformatics*, **23**, 504 (2007).
15. M.B. Stadler, B.M. Stadler, *FASEB J.*, **17**, 1141 (2003).
16. K.B. Li, P. Isaac, P. Krishnan, *Bioinformatics*, **20**, 2572 (2004).
17. A.K. Björklund, D Soeria-Atmadja, A Zorzet, U Hammerling, MG Gustafsson, *Bioinformatics*, **21**, 39 (2005).
18. S. Saha, G. P. S. Raghava, *Nucleic Acids Res.*, **34**, W202 (2006).
19. <http://allergen.csl.gov.uk>
20. <http://www.allergenonline.org>
21. http://fermi.utmb.edu/SDAP/sdap_man.html
22. S. Hellberg, M. Sjöström, B. Skagerberg, S. Wold, *J. Med. Chem.*, **30**, 1126 (1987).
23. S. Wold, J. Jonsson, M. Sjöström, M. Sandberg, S. Rännar, *Anal. Chim. Acta*, **277**, 239 (1993).
24. SIMCA-P 8.0. Umetrics UK Ltd., Wokingham Road, RG42 1PL, Bracknell, UK.
25. A.P. Bradley, *Pattern Recogn.*, **30**, 1145 (1997).
26. L. Eriksson, E. Johansson, N. Kettaneh-Wold, S. Wold, in: *Multi- and Megavariate Data Analysis. Principles and Applications*. Umetrics Academy, Umea, 2001, p.21.

ОЦЕНКА НА АЛЕРГЕННОСТ ЧРЕЗ ДИСКРИМИНАНТЕН АНАЛИЗ ПО МЕТОДА НА ПАРЦИАЛНИТЕ НАЙ-МАЛКИ КВАДРАТИ

Л. Х. Нанева¹, И. Д. Димитров², И. П. Бангов¹, И. А. Дойчинова^{2*}

¹Шуменски университет „Епископ Константин Преславски“, Факултет по природни науки, ул. „Университетска“ 115, Шумен 9712, България

²Медицински университет – София, Фармацевтичен факултет, ул. „Дунав“ 2, София 1000, България

Постъпила на 30 ноември 2012 г.; коригирана на 5 февруари 2013 г.

(Резюме)

Алергенността на хранителните протеини е важен проблем, свързан с широкото използване на нови храни, хранителни добавки и билки, много от които съдържат известни или неизвестни генетично модифицирани протеини. Алергенността е скрито, нелинейно кодирано свойство. Повечето от съществуващите методи за оценка на алергенност се основават на наслагване на секвенции и търсене на структурни прилики с известни алергени. Следователно, идентифицирането на нови, структурно различни алергени не може да бъде осъществено чрез тези методи. В настоящото изследване ние предлагаме нов метод за оценка на алергенност, който не се базира на наслагване на секвенции, а на сравняване на основни свойства на аминокиселините като хидрофобност, размер и електронната структура. Протеините се трансформират във вектори с еднаква дължина и се анализират чрез дискриминантен анализ по метода на парциалните най-малки квадрати. Предварителният модел, получен въз основа на обучаваща група от 120 алергена и 120 неалергена, идентифицира правилно 73% от протеините, включени във външна тестова група от 1164 алергени и неалергени. Разширеният модел, получен въз основа на обучаваща група от 1404 протеина (702 алергена и 702 неалергена) показва 70% точност при кръстосаното валидиране в 7 групи.

Methanesulfonic acid catalyzed one-pot synthesis of pyrano[2,3-c] pyrazole derivatives in water

M. M. Heravi *¹, N. Javanmardi¹, H. A. Oskooie¹, B. Baghernejad²

¹Department of Chemistry, School of Science, Alzahra University, Tehran, Iran

²Department of Chemistry, School of Sciences, Payame Noor University(PNU), 19395-3697, i.r. of Iran

Received May 12, 2013; Revised September 3, 2013

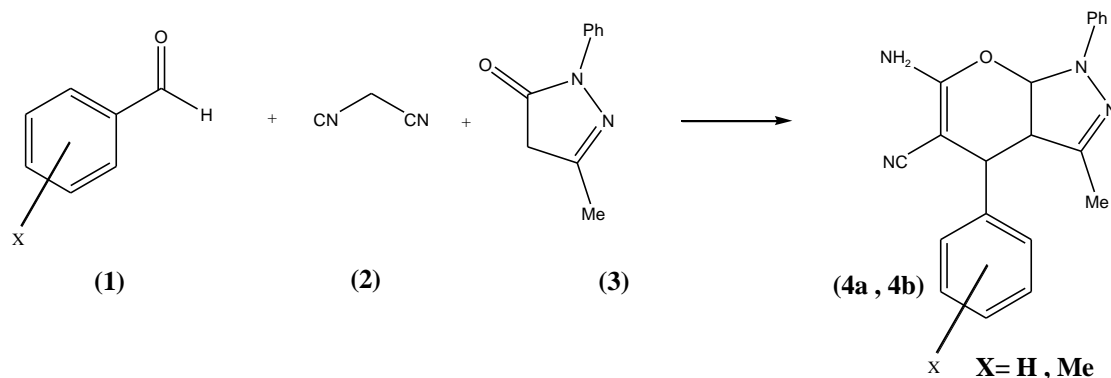
A simple and efficient synthesis of 1,4-Dihydropyrano[2,3-c] pyrazoles was achieved via a one-pot three-component reaction of an aromatic aldehyde, malonitrile and 3-methyl-1-phenyl-2-pyrazolin-5-one using methanesulfonic acid as a catalyst in good yields.

Key words: methanesulfonic acid, 1,4-Dihydropyrano[2,3-c] pyrazole, one-pot synthesis.

INTRODUCTION

It is well known that 4H-pyran and its derivatives are very useful compounds. Substituted pyrano [2,3-c] pyrazoles have been synthesized in a search for new physiologically active compounds, drugs, pesticides, and other compounds of practical significance [1,2]. 2-Amino-3-cyano-4H-pyrans possesses photochemical activity [3]. Poly functionalized 4H-pyrans are a common structural unit in a number of natural products [4]. The 4H-pyran ring can be transformed to pyridine systems, which relate to pharmacologically important calcium antagonists of the DHP type [5, 6]. There are a lot of procedures to synthesis of these compounds but most of them are toxic. The need to reduce the amount of toxic waste and by-products arising from chemical processes requires increasing emphasis on the use of less toxic and environmentally compatible materials in the design of new synthetic methods. One of the most

promising approaches is using water as reaction media. Recently, a great attention has been focused on the use of water as green solvent in various organic transformations. Water is a desirable solvent for chemical reactions because it is safe, non-toxic, environmentally friendly, readily available, and cheap compared to organic solvents [7-9]. Since the pioneering studies on Diels–Alder reactions by Breslow [10,11], there has been increasing recognition that organic reactions can proceed well in aqueous media and offer advantages over those occurring in organic solvents, such as rate enhancement and insolubility of the final products that facilitates their isolation. Herein, we would like to report one-pot synthesis of 1,4-dihydropyrano [2,3-c] pyrazole derivatives by three-component reaction of an aromatic aldehyde, malonitrile and 3-methyl-1-phenyl-2-pyrazolin-5-one using methanesulfonic acid as a catalyst in aqueous media (Scheme 1).



Scheme 1. Preparation route of the compounds (4a, 4b)

* To whom all correspondence should be sent:
E-mail: mmh1331@yahoo.com

EXPERIMENTAL

Material and Equipment

All products are known compounds and were characterized by m.p., IR, ¹H-NMR and GC/MS. All melting points are uncorrected and taken with an Electrothermal melting point apparatus (Electrothermal Eng. Ltd, Essex, UK). The ¹H-NMR spectrums of the synthesized compounds were measured in DMSO-d₆ solution and TMS as the internal standard using a Bruker AQS AVANCE-300 MHz instrument. IR spectra were recorded from KBr disk on the FT-IR Bruker Tensor 27. GC/MS spectra were recorded on an Agilent Technologies 6890 network GC system and an Agilent 5973 network Mass selective detector. Thin layer chromatography (TLC) on commercial aluminum-backed plates of silica gel, 60 F254 was used to monitor the progress of reactions. All products were characterized by spectra and physical data.

General procedure for the synthesis of 1,4-dihydropyrano[2,3-*c*] pyrazole

A mixture of the aromatic aldehydes (**1**) (1 mmol), malononitrile (**2**) (1 mmol), 3-methyl-1-phenyl-2-pyrazolin-5-one (**3**) (1 mmol), and MSA (0.1 mL) in H₂O (10 mL) was refluxed for 45-55 min, and then cooled to room temperature. The crystalline powder formed was collected by filtration, washed with water, and re-crystallized from ethanol to give pure product (**4a**, **4b**) (Scheme 1).

4a: ¹H-NMR (DMSO-d₆, δ/ppm): 1.93 (s, 3H, CH₃), 4.68 (s, 1H), 4.75 (s, 2H, NH₂), 7.16-7.32 (m, 10H, Ph); IR (KBr, cm⁻¹): 3472, 3320, 2195, 1660, 1590, 1264, 1125, 1027, 753. MS (%), *m/z*: 330 (100) [M]⁺, 331 (24) [M+H]⁺.

4b: ¹H-NMR (DMSO-d₆, δ/ppm): 1.78 (s, 3H, CH₃), 2.28 (s, 3H, CH₃), 4.62 (s, 1H), 6.96 (s, 2H, NH₂), 7.02-7.78 (m, 9 H, Ph); IR (KBr, cm⁻¹): 3414, 3314, 2178, 1658, 1594, 1398, 1258, 1128, 1026, 754. MS (%), *m/z*: 344 (100) [M]⁺, 345 (23) [M+H]⁺.

4c: ¹H-NMR (DMSO-d₆, δ/ppm): 1.78 (3H, s, CH₃), 4.91 (s, 1H), 7.02 (s, 2H, NH₂), 7.32-7.98 (m, 9 H, Ph); IR (KBr, cm⁻¹): 3431, 3348, 2189, 1665, 1595, 1517, 1394, 1352, 1126, 1054, 831, 753.

4f: ¹H-NMR (DMSO-d₆, δ/ppm): 1.81 (3H, s, CH₃), 4.83 (s, 1H), 7.08 (s, 2H, NH₂), 7.22-7.88 (m, 9 H, Ph); IR (KBr, cm⁻¹): 3459, 3325, 2202, 1661, 1594, 1518, 1491, 1444, 1391, 1262, 1127, 1089, 1066, 1015, 831, 804, 751, 686.

4g: ¹H-NMR (DMSO-d₆, δ/ppm): 1.77 (3H, s, CH₃), 3.78 (3H, s, CH₃O), 4.77 (s, 1H), 7.02 (s, 2H, NH₂), 7.12-7.68 (m, 9 H, Ph); IR (KBr, cm⁻¹): 3391, 3322, 2192, 1660, 1596, 1514, 1456, 1394, 1250, 1173, 1128, 1073, 1027, 813, 759, 692.

RESULTS AND DISCUSSION

Methanesulfonic acid (MSA) is an alkylsulfonic acid, which has numerous applications, for example, as an esterification or alkylation catalyst, as a polymer solvent, in the electroplating and electrochemistry industry, etc. MSA also is an effective reagent for the conversion of alcohols into corresponding amides [12], Fries-rearrangement [13], Beckmann rearrangement [14], hydration of nitriles into amides [15], monoesterification of diols [16], N-nitrosation of secondary amines [17], and aromatization of 1,4-dihydropyridines [18]. MSA is a strong acid (pK_a= -1.9), which is almost completely ionized at 0.1 M in an aqueous solution and has a low tendency to oxidize organic compounds. It is, however, far less corrosive and toxic than other mineral acids. Under normal conditions, aqueous solutions evolve no dangerous volatiles, making it safe to handle. Finally, it is readily biodegradable within 28 days, only forming CO₂ and sulfate, making them an environmentally benign material [19]. Furthermore, it has the advantage, as will be shown that it can be separated readily from the reaction mixture and reused. As part of our program aimed at developing new selective and environmentally friendly methodologies for the preparation of fine chemicals,²⁰ then we decided to use this catalyst for the synthesis of 1,4-dihydropyrano[2,3-*c*]pyrazoles. In a typical procedure, benzaldehyde (1 mmol), malonitrile (1 mmol) with 3-methyl-1-phenyl-2-pyrazolin-5-one (1 mmol) in the presence of a catalytic amount of MSA in water at reflux temperature afforded the desired 1,4-dihydropyrano[2,3-*c*]pyrazole (**4a**) in 87% yield (Entry **1**, Table 1). The reaction then was applied to a variety of aromatic aldehydes in good yields. (As shown in Table 1) All aromatic aldehydes containing electron- withdrawing groups 3 (such as nitro group, halide) or electron-donating groups (such as hydroxyl group, alkoxy group) were

Table 1. Synthesis of 1,4-dihydropyrano[2,3-c]pyrazole derivatives catalyzed by MSA.

Entry	X	Time (min)	Product	m.p. (°C)		Yield(%) ^a
				Observed	Reported	
1	H	55	4a	172	170-171 ^[21]	87
2	4-Me	50	4b	177	177-178 ^[21]	80
3	4-OH	45	4c	213	210-212 ^[21]	90
4	3-NO ₂	45	4d	191	190-191 ^[21]	95
5	4-NO ₂	45	4e	195	195-196 ^[21]	95
6	4-Cl	50	4f	175	175-176 ^[21]	94
7	4-OMe	45	4g	173	171-172 ^[21]	90

^a Isolated yields**Table 2.** Synthesis of 3a with MSA in the presence of different solvent

Entry	Solvent	Temperature	Time(min)	Yield(%) ^a
1	Water	reflux	55	87
2	Ethanol	reflux	70	80
3	dichloromethane	reflux	120	65
4	chloroform	reflux	120	66
5	Solvent-free	reflux	100	60

^a Yield of isolated products

employed and reacted well to give the corresponding product (**4**) in good to excellent yields under these reaction conditions, so we conclude that no obvious effect of electron and nature of substituents on the aromatic ring were observed. We also found that the reaction did not proceed in the case in which aliphatic aldehyde was used. The reason we think this is the activity of aliphatic aldehydes is less than that of aromatic aldehyde. We performed the effect of various solvents on the synthesis of 4a. This reaction was carried out in various solvents such as water, chloroform, Ethanol, dichloromethane and solvent-free condition. As shown in Table 2, the best results in terms of yield and time obtained in water.

CONCLUSION

In conclusion, we have described a highly efficient procedure for the preparation of pyrano[2,3-c] pyrazole derivatives by a three component condensation using MSA as a catalyst. All the proposed reactions allowed the preparation of products in good yield without further purification. The reaction products were prepared in moderate to 5 average yields, even with different substituted aldehydes. No harmful organic solvents are used. Moreover, the procedure offers several advantages including high yields, operational simplicity, cleaner reaction, minimal environmental impact, and low cost, which make it a useful and attractive process for the synthesis of these compounds.

REFERENCES

- (a) R. Varala, R. Enugala, *Chem. Pharm. Bull.*, **55**, 1254 (2007); (b) J. Ebrahimi, A. Mohanndi, V. Pakjoo, E. Bahramzadeh, A. Habibi, *J. Chem. Sci.*, **124**, 1013 (2012); (c) J. M. Khurana, A. Chaudhary, *Green Chem. Lett. Rev.*, **5**, 633 (2012); E.C. Witte, P. Neubert, A Roesoh, *Ger. Offen.* DE 3427985, *Chem. Abstr.*, **104**, 224915f (1986).
- (a) T. Hyama, H. Saimoto, *Jpn. KoKai Tokkyo Koho, JP.* 62181276, *Chem.* (1987) (b) J.L. Wang, D. Liu, Z.J. Zhang, S. Shan, X. Han, S.M. Srinivasula, C.M.Croce, E. S. Alnemri, Z. Huang, *Proc. Natl. Acad. Sci.*, **97**, 7124 (2000).
- D. Armetso, W.M. Horspool, N. Martin, A. Ramos, C. Seoane, *J. Org. Chem.*, **54**, 3069 (1989).
- L.N. Martin, M. Quinteiro, C. Seoane, J.L. Soto, *Liebigs. Ann. Chem.*, **1**, 101 (1990).
- N. Martin, G. Martin, A.C. Secoane, J.L. Marco, A. Albert, F.H. Cano, *Liebigs. Ann. Chem.*, **7**, 801 (1993).
- J.L. Maco, N. Martin, A.M. Grau, C. Seoane, A. Albert, F. H. Cano, *Tetrahedron*, **50**, 3509 (1994).
- C.J. Li, T.H. Chan, *Organic Reactions in Aqueous Media*; Wiley: New York. (1997).
- P.A. Grieco, *Organic Synthesis in Water*, Ed.; Thomson Science, Glasgow: Scotland. (1998).
- C. J. Li, *Chem. Rev.*, **105**, 3095 (2005).
- R. Breslow, *Acc. Chem. Res.*, **24**, 159 (1991).
- R. Breslow, *Acc. Chem. Res.*, **37**, 471 (2004).
- H. Sharghi, K. Niknam, *Iran. J. Chem. & Chem. Eng.*, **18**, 36 (1999).
- H. Sharghi, B. Kaboudin, *J. Chem. Res. (S)*, 629 (1998).
- H. Sharghi, M. Hosseini Sarvari, *J. Chem. Res. (S)*, 446 (2001).

15. H. Sharghi, M. Hosseini Sarvari, *Synth. Commun.*, **33**, 205 (2003).
16. H. Sharghi, M. Hosseini Sarvari, *Tetrahedron.*, **59**, 3627 (2003).
17. K. Niknam, M.A. Zolfigol, *Synth. Commun.*, **36**, 2311 (2006).
18. K. Niknam, M.A. Zolfigol, S.M. Razavian, I. Mohammadpoor-Baltork, *J. Heterocycl. Chem.*, **43**, 199 (2006).
19. M.D. Gernon, M. Wu, T. Buszta, P. Janney, *Green Chem.*, **3**, 127 (1999).
20. (a) F.F. Bamoharram, M.M. Heravi, M. Roshani, A. Gharib, M. Jahangir, *Applied Catal.*, **302**, 42 (2006).
(b) M.M. Heravi, R. Hekmatshoar, L. Pedram, *J. Mol. Catal. A: Chem.*, **89**, 231 (2005).
21. J.F. Zhou, S. J. Tu, Y. Gao, M. Ji, *J. Org. Chem.*, **21**, 742 (2001).

МЕТАНСУЛФОНОВА КИСЕЛИНА КАТАЛИЗИРАЩА ЕДНОСТАДИЙНА СИНТЕЗА НА ПИРАНО [2,3-С] ПИРАЗОЛНИ ПРОИЗВОДНИ ВЪВ ВОДА

М. М. Херави^{*1}, Н. Джаванмарди¹, Х. А. Оскойе^a, Б. Багернаджад²

¹ Департамент по химия, Научен факултет, Университет Алзахра, Техеран, Иран

² Департамент по химия, Научен факултет, Университет Паям Нуур, 19395-3697, Иран

Постъпила на 12 май 2013 г.; коригирана на 3 септември 2013 г.

(Резюме)

Прост и ефективен начин при добър добив за синтез на 1,4-дихидропирано[2,3-с] пиразоли е постигнат чрез едностадийна, трикомпонентна реакция на ароматен алдехид, малонитрил, и 3-метил-1-фенил-2-пиразолин-5-он при използване на метансулфонова киселина като катализатор

Determination of selected elements in freshwater sponge tissue, natural water and sediments by inductively coupled plasma optical emission spectrometry

S. Rončević, L. P. Svedružić

Laboratory of Analytical Chemistry, Department of Chemistry, Faculty of Science, University of Zagreb, Horvatovac 102A, HR-10000 Zagreb, Croatia

Received June 12, 2013; Revised August 28, 2013

Metal content in the samples of freshwater sponge *Eunapius subterraneus* which is an endemic species of karstic underground in Central Croatia was determined by inductively coupled plasma atomic emission spectrometry (ICP–OES). Additionally, metal content was determined in the samples of water and sediment collected at the same sampling sites. Analytical procedure of sample preparation included acid digestion in open vessel. The accuracy of the applied methods tested by measurement of certified reference samples of water and sediment comprised 5–10% of declared metal concentrations. It was established that metal content (Al, Ba, Ca, Cd, Cu, Fe, Mg, Mn, Ni, Pb, Sr, and Zn) measured in sponge tissue, water and sediment samples is related to sampling site. Influence of anthropogenic pollution through sewage deposition was observed in slightly higher content of Al, Cu, and Zn in water, and also Cu, Pb and Zn in sediment sample. Analysis of two morphologically different sponge samples showed different abundance of Cu, Zn, Pb and Cd.

Key words: ICP-OES, freshwater sponge, metal content.

INTRODUCTION

Determination of metal content in aquatic ecosystem is recognized as extremely important in wide range of different studies which include chemical characterization of species, routine monitoring of environmental pollution, and studies on the ecological and physiological role of toxic and essential metals. Atomic spectrometry methods based on absorption or emission of electromagnetic radiation combined with optical or mass spectrometers are firmly established in elemental analysis of environmental samples and biological tissues [1-3]. For the monitoring purposes of heavy metal pollution in marine ecosystem several species of marine sponges were selected as a potential bioindicator organism [4,5]. More profound insight on the environmental status was achieved by determination of metal content in marine sponges using multielement analytical techniques as inductively coupled plasma atomic emission (ICP–OES) or mass spectrometry (ICP–MS) [6].

Sponges are sessile organisms which have a property of filtering a large volume of water and accumulate metals and other contaminants from the environment. Recent investigations in this field describe the influence of some toxic metals and other pollutants on sponge cell aggregation [7-9].

The uptake of metals is usually influenced with type of metal species and concentration present in either water or sediment, genus of the sponge, and habitat as well [10,11].

Although sponges are wide-spread in marine environment, only a minor number of organisms inhabit groundwater. All freshwater sponges are classified in the Demosponigae, family Spongillidae. Published studies of metabolites of freshwater sponges, namely lipid compounds, included analytical methods as NMR, HPLC, CE, IR and UV [12,13]. The data on element distribution in freshwater sponges are rarely represented in the literature. One of recent examples is the study of element composition of Baikal sponge tissue by ICP–MS which showed the degree of trace elements accumulation [14].

In this work, an inductively coupled plasma atomic emission spectrometry (ICP–OES) is used for the determination of selected metal content in sponge tissue, natural water and sediment samples which were collected from karstic region in Central Croatia. The centre of the region is the city of Ogulin with geographic coordinates: latitude 45° 15' 58N and longitude 15° 13' 43E. The Dinaric karstic area of Croatia Republic is well known as the richest reserve of the subterranean water fauna with high number of endemic species with sponges as a specific example. The only specialised subterranean freshwater sponge known to date is

* To whom all correspondence should be sent:
E-mail: roncevic@chem.pmf.hr

the *Eunapius Subterraneus* Sket & Velikonja, 1984, which includes two morphotypes that inhabit exclusively the karstic subterranean waters of Ogulin region [15,16]. Poor natural purification ability of karstic water streams indicates that monitoring of possible pollution in such ecosystems is of crucial interest. From the first description of endemic sponge species in 1984, there was no systematically collected data on the sponge status. The recent investigations were conducted in order to analyze key morphological features, to record the distribution patterns and to examine the current state of habitat quality and population-threatening changes in the environment [17]. In order to record the present status and to provide the base for the further comparison of possible changes in the ecosystem, the content of the selected metals was determined in sponge tissue, as well as in water and sediment samples collected from habitat.

EXPERIMENTAL

Instrumentation

A *Prodigy High Dispersion ICP* inductively coupled plasma optical emission spectrometer (Teledyne Leeman Labs, Hudson, NH, USA) was used for the metal content determination in all samples. The specifications of spectrometer are

given in Table 1 and operating parameters of instrument are given in Table 2.

Emission lines of elements measured in this work (Al, Ba, Ca, Cd, Cu, Fe, Mg, Mn, Ni, Pb, Sr, and Zn) were selected after collecting spectral images on L-PAD detector. Several intense and weak analytical lines of each element were measured simultaneously without blooming or saturation of detector. The best ones, *i.e.* lines without spectral and background interferences which showed maximal signal-to noise ratio were chosen for analysis. Emission lines of selected metals along with method detection limits are given in Table 3. The detection limits were calculated in accordance to IUPAC recommendation, *i.e.* as the concentration equivalent to three times standard deviation (3σ) of the signal of the method blank solution.

RESULTS AND DISCUSSION

Methanesulfonic acid (MSA) is an alkylsulfonic acid, which has numerous applications, for example, as an esterification or alkylation catalyst, as a polymer solvent, in the electroplating and electrochemistry industry, etc. MSA also is an effective reagent for the conversion of alcohols into corresponding amides [12], Fries-rearrangement [13], Beckmann rearrangement [14], hydration of

Table 1. Specification of the spectrometer and ICP source

Spectrometer	<i>Prodigy</i> high-dispersion echelle spectrometer with dual-viewing optics (radial and axial) , Teledyne Leeman Labs, Hudson, NH, USA
Focal length	800 mm
Grating	Echelle grating 52.13 gr/mm, format of 110 mm x 110 mm UV grade
Dual Pass Prism	fused silica prism
Wavelength range	165 nm – 800 nm
Resolution	< 0.00075 at 200 nm (standard 40 μ m x 100 μ m entrance slit)
Detector	Large Format Programmable Array Detector L-PAD (28 x 28 mm, 1026 x 1026 pixels)
Rf generator	Free-running
Frequency	40.68 MHz
Power output	600 to 2000 W
Nebulizer	Pneumatic (glass concentric - <i>SeaSpray</i>)
Spray chamber	Glass cyclonic
Plasma torch	Fassel type, three concentric quartz tubes, dual-view torch
Pump	12-roler computer-controlled four channels peristaltic pump

Table 2. Operating conditions

Incident power	1.1 kW
Outer argon flow rate	18 L min ⁻¹
Auxiliary gas	0.8 L min ⁻¹
Carrier gas flow rate	0.9 L min ⁻¹
Liquid uptake rate	1.5 mL min ⁻¹
Nebulizer pressure	36 psi
Integration time	10 s

Table 3. Line selection and detection limits

Analytes, wavelengths, λ , nm	Detection limits in pure solvent, c_L , $\mu\text{g L}^{-1}$
Al I 308.215	3.05
Ba II 493.409	0.13
Ca II 396.847	5.88
Cd I 214.441	0.61
Cu I 324.754	0.64
Cr II 267.716	2.88
Fe II 259.940	2.02
Mg II 279.553	3.95
Mn II 257.610	0.41
Ni II 231.604	2.21
Pb II 220.353	6.10
Sr II 407.771	0.06
Zn I 213.856	1.13

Reagents and Test Solutions

High-purity deionised water (Milli-Q Element system, Millipore, USA) was used for preparation of all the sample and standard solutions. Sample dissolution procedures were performed using analytical grade chemicals: nitric acid (65 %) hydrochloric acid (36 %), and hydrogen peroxide (30%) from Kemika, Croatia. Single element standard solutions of Al, Ba, Ca, Cd, Cu, Fe, Mg, Mn, Ni, Pb, Sr, and Zn (Plasma Pure, Leeman Labs, Hudson, NH, USA) and multielement standard ICP-Mehrelement-Standardloesung IV (Merck, Darmstadt, Germany) were used for the preparation of calibration standard solutions and control of plasma positioning. All calibration standards were prepared by appropriate dilution of standard stock solutions (1 g L^{-1}) to obtain the concentration range from 1 to 100 mg L^{-1} .

Strategy

Study area. The study area is located in Central Croatia: Medvedica, Zala, Gojak and Tounjcica. The karstic system of underground caves in Ogulin region of Croatia is known as habitat of several endemic species. Subterranean sponge had inhabited the Medvedica cave system in the past, precisely in 1984 and 1986. No sponge species was found during last sampling in the Medvedica cave. In earlier period some attempts of pedological investigations were made, but afterwards no sustained research of this site has been conducted [18].

Sampling

Water samples: Water samples were collected by scuba diving in winter season when water level was at lowest. Samples of natural water were taken from four caves: Medvedica, Zala, Gojak and Tounjcica and preserved according to ISO 5667- Water quality sampling [19].

Sediment samples: The samples of sediment were collected from the cave Medvedica. All samples were stored immediately in a cool box then transferred to a refrigerator, where they were stored at $4 \text{ }^\circ\text{C}$. Before the digestion, samples were ground in a Retsch BB51 (Haan, Germany) grinding mill and sieved to particle size $< 100 \mu\text{m}$. Powdered samples were dried in drying oven at 105°C [20].

Freshwater sponge samples: Samples of sponges were accessible for collection only in two caves: Gojak and Tounjcica. Samples of sponge from the cave Tounjcica were egg-shaped, they had irregularly wrinkled surface with a size of approximately 3 cm. Other samples from the cave Gojak were cone-shaped with smooth surface and sized approximately 2 cm. Each of sponge samples was washed several times in distilled water in order to remove the majority of viewable sediments and small pieces of impurities. Additional cleaning was performed by washing with high-purity deionised water in ultrasonic bath for 20 minutes. Sponges were dried in drying oven at $105 \text{ }^\circ\text{C}$. Dried residues were grinded in agate mortar.

Digestion procedures

Sediment samples: After drying of powdered sediments, a weighted amount of 100 mg was transferred into Kjeldahl flasks. The analytical digestion procedure included repeated addition of 5 mL aliquots of HCl / HNO₃ mixture [21]. The remaining acidic solutions were transferred into a 50 mL volumetric flask and filled up to mark with high-purity deionised water. In order to control the accuracy of the preparation procedure, the solution of reference stream sediment sample NCS DC 73309 (*China National Analysis Center for Iron and Steel*) was prepared in the same way.

Freshwater sponge samples: The limited amount of endemic sponge tissue samples was the prevailing condition for the selection of digestion procedure. Despite the fact that digestion of biological samples in a closed system such as microwave oven has a notable advantage because the volatilization losses can be minimized [22], the open vessel digestion was the method of choice. An amount of 20 mg of the powdered sample of sponge tissue was weighted and transferred into Kjeldahl flasks. The analytical digestion procedure in open vessel included subsequent addition of mineral acids [23]. A volume of 2 mL of conc. HNO₃ was added into flask and heated until approximately 0.5 mL of starting solution was remained. After cooling, 1 mL of conc. HCl was added and the flask was heated again. Procedure was repeated in several

steps until the clear solution without any precipitate was remained. A volume of 1 mL of hydrogen peroxide was then added into flask and solution was heated until complete peroxide was boiled. The remaining acidic sample solutions were transferred into a 50 mL volumetric flask and filled up to mark with ultra-pure deionised water. A method blank was prepared by following the same procedure.

Water samples: Natural water samples were filtered through PTFE filters with 45 µm pore size to remove the bulk of sediments and suspended materials. In order to achieve the better sensitivity of trace metal determination in water samples, an amount of 500 mL of collected water was preconcentrated by evaporation till dryness. Solid residues were dissolved in the same manner as sponge residues by HNO₃ and HCl addition. The final acidic solutions were transferred into 50 mL volumetric flasks and filled up to the mark with high-purity deionised water. For the control of possible acids impurity effects, the procedure was also repeated using high-purity deionised water to obtain the blank sample. In order to control the accuracy of the analytical procedure, the reference sample of water SLRS-4 River Water Reference Material for Trace Metals (*National Research Council of Canada*) was treated on the same way. All samples were prepared and analysed as replicates.

RESULTS AND DISCUSSION

Determination of Ba, Cd, Cu, Mn, Ni, Pb, Sr and Zn in the presence of Al, Ca, Fe, Mg as matrix constituents in sediments

Certified reference materials stream sediment sample NCS DC 73309

Analytical procedure of sediment digestion was checked by use of certified reference material of stream sediment (NCS DC 73309) and the obtained results are shown in Table 4.

Table 4. Analysis of certified reference stream sediment sample NCS DC 73309

Element	w ^a , mg g ⁻¹ found	RSD, %	w ^b , mg g ⁻¹ certified
Al	48.298 ± 6.661	12.0	54.885 ± 0.875
Ba	0.276 ± 0.030	9.42	0.260 ± 0.017
Cu	0.086 ± 0.005	5.81	0.079 ± 0.003
Fe	2.769 ± 0.224	7.04	(3.070)
Mn	2.348 ± 0.059	2.17	2.490 ± 0.084
Pb	0.571 ± 0.064	9.80	0.636 ± 0.022
Sr	0.030 ± 0.001	3.33	0.029 ± 0.001

^a w = x ± Δx (n = 6)

^b w = mean ± ass.unc.

Statistical comparison of obtained data was performed by two-paired *t*-test at significance level of P = 0.05. Calculated *t*-value of 1.003 is lower than critical value of 2.47, which means that two sets of values were not significantly different. The recovery of metal content for the most of declared elements lay within 10% of certified values. By knowing that the accuracy of ICP-OES method is usually 10% depending on applied analytical procedure, the obtained results imply quite acceptable preparation and measurement conditions. Slightly negative bias was established for Al (88%) and Pb (89.8%), which might be partly denoted to incomplete digestion. The other reason of lower concentration could be explained by mode of emission measurements in plasma which is adjusted for simultaneous multi-element collection of signal, usually called compromise conditions.

Sediment sample from the Medvedica cave

It was already mentioned that subterranean sponge had inhabited the Medvedica cave system in the past, but no sponge species was found during the last sampling in the Medvedica cave. In earlier period some attempts of pedological investigations were made, but meanwhile, habitat was changed under great pressure of groundwater and water pollution. The sediment samples which were collected at this site was analysed by ICP-OES method and the measured metal content is given in Table 5.

Table 5. Metal content in sediment samples from the Medvedica cave

Element	w ^a , mg g ⁻¹	RSD, %
Al	76.8 ± 10.1	11.4
Ba	0.24 ± 0.02	8.33
Ca	51.9 ± 4.7	7.90
Cd	0.0112 ± 0.0009	7.14
Cu	0.160 ± 0.009	5.00
Fe	47.8 ± 2.6	4.81
Mg	14.8 ± 0.3	2.03
Mn	11.2 ± 0.2	1.78
Ni	0.090 ± 0.010	10.0
Pb	0.070 ± 0.007	8.57
Sr	0.140 ± 0.003	2.14
Zn	0.530 ± 0.060	10.0

^a w = x ± Δx (n = 6)

Since additional sediment sampling was disabled, the metal concentrations showed in Table 5 could be compared to the recorded data of same site which were formerly obtained by spectrophotometric measurements of Cu, Fe, Mn, Pb and Zn [18]. Measured concentration of Mn is slightly higher than content of 8.5 mg g⁻¹ published

before. Two-fold higher concentrations of Zn compare to previous 0.25 mg g⁻¹ was established in our measurements. Almost five-fold higher iron content in sediment compare to published 10.5 mg g⁻¹ of Fe was noticed here. As opposed to formerly published data for Cu and Pb of 0.020 mg g⁻¹ and 0.005 mg g⁻¹, ten-fold higher concentrations of those metals are observed in present sediment sample. Generally, the obtained results did not exceed the maximum permissible concentrations of heavy metals which were prescribed by domestic regulations of quality of soils. However, the intention of rising heavy metals concentration was noted here. One of the probable reasons for such change in chemical composition of sediment at same sampling site is that during last decades an additional load of sewage water flew through the underground cave system.

Determination of Al, Ba, Ca, Fe, Mg, Mn, Na and Sr in water samples

Determination of Al, Ba, Ca, Fe, Mg, Mn, Na and Sr in certified standard water SLRS-4.

Analytical preparation of water samples included preconcentration step and for this reason the accuracy was checked using certified reference sample of water (SLRS-4). The obtained results showed in Table 6 impute the factor of 10 to measured values because of the 10-fold sample preconcentration.

Table 6. Analysis of certified reference water sample SLRS-4

Element	γ^a , mg L ⁻¹ found	RSD, %	γ^b , mg L ⁻¹ certified
Al	0.060 ± 0.005	6.67	0.054 ± 0.004
Ba	0.013 ± 0.001	7.69	0.012 ± 0.001
Ca	6.70 ± 0.40	5.22	6.20 ± 0.19
Fe	0.095 ± 0.005	4.21	0.103 ± 0.005
Mg	1.55 ± 0.09	5.16	1.60 ± 0.10
Mn	0.0033 ± 0.0001	3.03	0.0031 ± 0.0007
Na	2.57 ± 0.06	1.94	2.40 ± 0.19
Sr	0.026 ± 0.001	3.85	0.026 ± 0.003

^a $\gamma = x \pm \Delta x$ (n = 6) ^b $\gamma = \text{mean} \pm \text{ass.unc.}$

Statistical comparison of two sets of data was performed by two-paired *t*-test at significance level of P = 0.05. Calculated *t*-value of 1.198 is lower than critical value of 2.364, which means that two sets of values were not significantly different. Compared to general ICP method accuracy of 10% it is obvious that recovery of selected metal content was satisfactory for all measured elements.

Determination of Al, Ba, Ca, Fe, Mg, Mn, Na and Sr in natural water samples, collected from four sampling sites

Samples of natural water collected from four sampling sites were analysed by ICP-OES. The measured content of metals in water samples collected from underground cave system is represented by Figures 1 and 2.

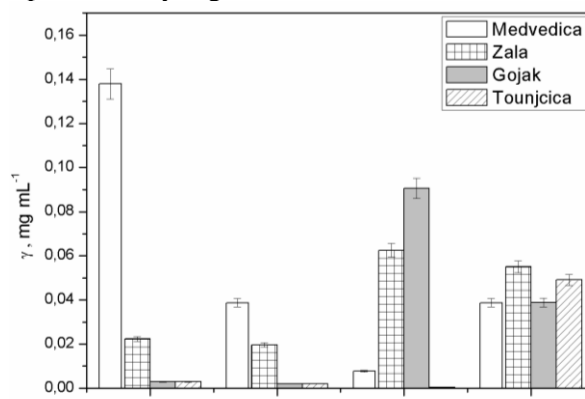


Fig. 1. Major metal constituents of water samples.

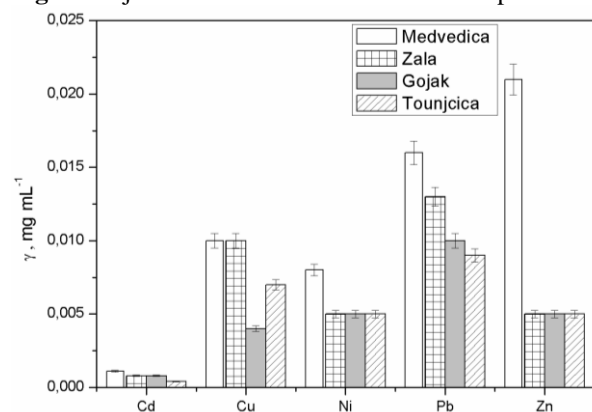


Fig. 2. Trace metal constituents of water samples.

The concentration values included preconcentration factor of 10 and precision measure expressed as relative standard deviation of three replicates. Good precision of measurement (RSD < 2.0%) was obtained on all selected lines. Metal concentrations are showed in separate figures due to different scaling of major and minor constituents. The measured content of Ba and Cr did not exceed the detection limits in all analyzed samples. The measured content of principal constituents in natural water showed slightly variations between 15–20 mg L⁻¹ of Ca and 3–5 mg L⁻¹ of Mg. The groundwaters in karstic area are moderately hard (140–215 mg L⁻¹ of CaCO₃) with low content of non-carbonate ions. In typical karst water the ratio of Ca/Mg content usually ranges from 2.5 to 5 [24]. This ratio is confirmed in all samples measured in our work. However, the lower content of Ca and Mg than in typical moderately hard water was established here which classify examined samples in a class of soft water. From the measured content of other metals showed in Figures 1 and 2, a

significantly higher Al and Zn concentrations and slightly higher Fe, Cu, Ni, and Pb concentrations were measured in water from Medvedica cave than in other three caves. The lead content measured in samples from Medvedica, Zala and Gojak was slightly higher than maximum permissible concentration of 0.01 mg mL^{-1} which is prescribed by the domestic regulations of natural water quality. The observed results imply that continuous pollution through sewage and waste dumping occurs and it is especially pronounced at the site Medvedica [17]. Moreover, the fact that from the recent investigations of distribution of the sponge *Eunapius subterraneus* which showed that they are not found in the Medvedica cave where was inhabited in the past could be explained by obtained results of metal concentrations.

3.3. Determination of Al, Ca, Fe, Mg Ba, Cd, Cu, Mn, Ni, Pb, Sr and Zn in freshwater sponge samples

Two morphotypes of sponge *Eunapius Subterraneus* were analyzed in this work, i.e. the egg-shaped sponges with irregularly wrinkled surface from the Tounjcica cave and the cone-shaped with smooth surface from the Gojak cave. Sponge tissue analysis included complete individual organisms because they were rather small; their base was about 1 cm^2 with up to 3 cm in height. Consequently, digestion procedure which started from dried tissue included weighted amounts of 20 mg of analytical sample. Although the sample mass was restricted, the advantage of ICP-OES method to show excellent linearity in trace and major constituent presence was confirmed. Precision from three replicates of signal measurement was satisfactory for all elements determined and gave the $\text{RSD} < 1.5\%$. Since no reference sample for sponge analysis is available, the control of analytical procedure was based on analysis of the same reference sample of stream sediment used in sediment sample analysis. The main reason for selection of this material is the fact that besides spongin the sponge skeleton is built out of silica spicules and carbonates. It means that after removal of organic substances during sample preparation, this reference material could fit as the most likely to inorganic residue. For this purpose, a smaller amount of 10–20 mg of NCS DC 73309 was digested to check the accuracy at low sample size. The obtained results matched all of measured recoveries from greater scale of 1 g of starting reference material which is presented in Table 4.

Metal concentrations in sponge samples are shown in Figures 3 and 4.

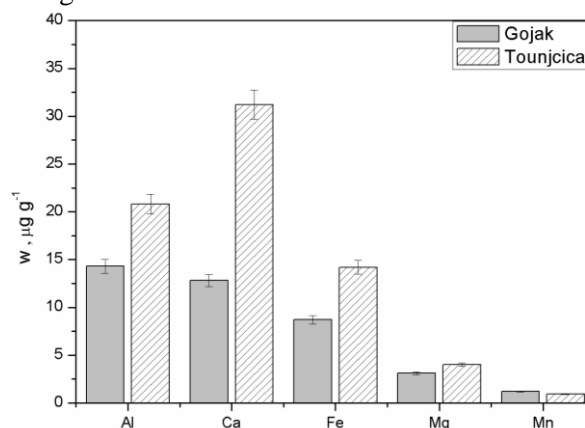


Fig. 3. Major metal constituents of sponge samples.

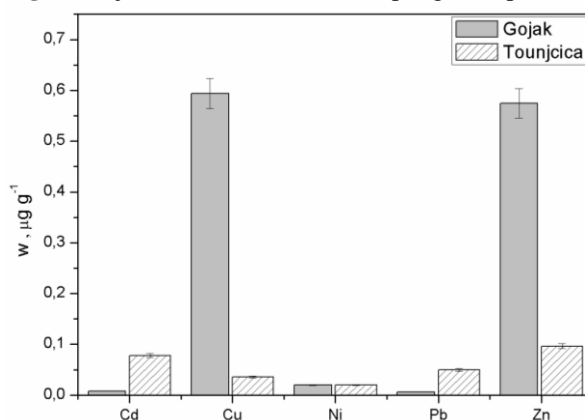


Fig. 4. Trace metal constituents of sponge samples.

The results are expressed as weight ratio, i.e. microgram of element mass per gram of dried sample mass and they include the precision of measured replicates. Ba and Sr were not detected. The concentrations of Ba and Sr in the real samples are below the detection limits. The obtained results mutually show some notable differences regarding to sponge morphotype. Among the major constituents, the different weight ratio is evident for Al, Ca and Fe content (Fig 3). The slightly different content of Cd and Pb is also noted in two kinds of sponge samples (Fig 4). The remarkable higher concentration of Cu and Zn in cone-shaped sponges from Gojak cave compared to egg-shaped sponges from Tounjcica cave was established by measurements. By general comparison of element concentrations present in sponge samples with the metal content measured in water from the same sampling sites, the greater element concentrations in sponge samples was established. Chemical composition of sponge is mostly affected by the water environment, but sponges of different classes and habitats have different capacities of metal accumulation.

The majority of published data concerning the determination of metal content deal with marine sponge organisms. Usually, investigations are conducted in order to examine the influence of heavy metal pollution on estuarine systems [4,5,11]. A higher level of Cd, Cu, and Zn content than samples from surrounding marine area was noted. The accumulation of bivalent metals by sponges at different stages of growth was studied on examples of marine sponges, too [7-9]. It was found that bioaccumulation of some toxic metals, *i.e.* Cu, Pb and V, can alter the behaviour and the physiological response, such as change in shape and growth rate. It was shown that moderate concentrations of Cu and Cd can have positive effects on sponge by enhancing cell aggregation, but long term exposition may alter cell functions. The mechanism of Cd accumulation in sponge tissue is favoured at low pH and low salinity of marine system. Generally, most of the studies confirmed the potential of marine sponges as biomarker organisms in the monitoring of marine pollution.

Unfortunately, there are only a minor number of published data on metal content in freshwater sponge species. Considering the class of Demospongiae, family of Spongillidae, the investigations are primarily focused on isolation of lipid compounds and on phosphatic metabolite variation with changes of habitat [12,13]. The representative work in metal content analysis of endemic family Lubomirskiidae of freshwater sponges is undoubtedly the paper of Paradina et al. [14]. This investigation presents the ICP-MS analysis of nineteen elements in Lake Baikal sponges where authors observed lower metal content than in family of Spongillidae. The accumulation of biologically active elements such Mn, Cu and Co, but also the considerable Cd quantities were established in their work.

Each sponge species has its own spectrum of accumulation of elements which disables mutual comparison of metal content accumulated by different classes of sponge. Metal content in endemic species of *Eunapius Subterraneus* studied in our work emphasise this statement. The relationship between established Cu and Zn content of two morphotypes of sponge and the same elements content in water should not only be attributed to accumulation from water environment, but also to characteristics of sole specie. In addition, a possible pollution impact could hardly be driven based on those first results of metal distribution patterns in sponge and water from

underground habitats. Therefore, the obtained results could serve as the base for the future investigations in aspect of environmental monitoring or study of biological response of the endemic *Eunapius subterraneus* species on changes of chemical parameters in water and sediments.

CONCLUSION

Inductively coupled plasma atomic emission spectrometry (ICP-OES) was used in determination of metal content in samples of freshwater sponge *Eunapius subterraneus* which is the endemic organism of Central Croatian karstic caves. Analysis of two morphologically different sponge samples collected at two different locations, shows mutual variation in content of trace metals (Cu, Zn, Pb and Cd). Although, the causal connections between trace metal accumulation and morphotypes appearance was not targeted in this stage, the obtained data, especially for Cu and Zn, shows that indicators of different metal accumulation are inherent to studied subspecies. The metal content in water collected from habitats and also from the neighbouring sites, where sponges had been spread in the past, was also determined. Greater concentrations of Al, Cu, and Zn in waters exposed to anthropogenic pollution were measured. Also, the greater concentrations of Cu, Pb and Zn in sediment sample from Medvedica cave in comparison with previous investigations were established here. The obtained results coincide with the fact that sponges do not inhabit this cave system as it was in the past. Present study comprises the determination of metal distribution patterns in freshwater sponge tissue for the first time. Consequently, the collected data provides the base for the further projects in active conservation of threatened *Eunapius subterraneus* species especially when very high risk of extinction is already known.

Acknowledgments: We would like to acknowledge our colleagues from Croatian Biospeleology Society, Mrs. Jana Bedek and Mrs. Helena Bilandzija for kindly providing the samples of sponges, water and sediment. This work was funded by the Ministry of Science, Education and Sports of Croatia (Projects No. 0119641).

REFERENCES

1. O.T. Butler, J. M. Cook, C. F. Harrington, S. J. Hill, J. Rieuwert, D.L. Miles, *J. Anal. Atom. Spectrom.*, **22**, 187 (2007).

2. S.E.J. Buykx, R.F.M.J. Cleven, A.A. Hoegge-Wehmann, M.A.G.T. van den Hoop, *Fresen. J. Anal. Chem.*, **363**, 599 (1999).
3. M. Grotti, M.L. Abelmoschi, F. Soggia, R. Frache, *Anal. Bioanal. Chem.*, **375**, 242 (2003).
4. J.V. Rao, P. Kavitha, N.C. Reddy, T.G. Rao, *Chemosphere*, **65**, 634 (2006).
5. J. Selvin, S.S. Priya, G.S. Kiran, T. Thangavelu, N.S. Bai, *Microbiol. Res.*, **164**, 352 (2009).
6. J.V. Rao, K. Srikanth, R. Pallela, T.G. Rao, *Environ. Monit. Assess.*, **156**, 451 (2009).
7. R.B. Philp, *Comp. Biochem. Phys. C*, **124**, 41 (1999).
8. E. Cebrian, M.J. Uriz, *Aquat. Toxicol.*, **81**, 137 (2007).
9. E. Cebrian, M.J. Uriz, *J. Exp. Mar. Biol. Ecol.*, **346**, 60 (2007).
10. R.B. Philp, F. Y. Leung, C. Bradley, *Arch. Environ. Con. Tox.*, **44**, 218 (2003).
11. A. Negri, K. Burns, S. Boyle, D. Brinkman, N. Webster, *Environ. Pollut.*, **143**, 456 (2006).
12. V. M. Dembitsky, T. Rezanka, M. Srebник, *Chem. Phys. Lipids*, 123, 117 (2003).
13. T.A. Early, T. Glonek, *Comp. Biochem. Phys. B*, **123**, 329 (1999).
14. L. P. Paradina, N.N. Kulikova, A.N. Suturin, Y.V. Saibatalova, *Geostand. Geoanal. Res.*, **28**, 225 (2004).
15. B. Sket, M. Velikonja, *Preliminary report of findings of freshwater sponges (Porifera, Spongillidae) in caves in Yugoslavia*, The Ninth Yugoslavian Congress of Speleology, Karlovac, Croatia, 1984, pp. 553–557.
16. B. Sket, M. Velikonja, *Stygologia*, **2**, 254 (1986).
17. H. Bilandžija, J. Bedek, B. Jalžić, S. Gottstein, *Nat. Croat.*, **16**, 1 (2007).
18. B. Vrbeč, *Speleolog*, 34-35, 35 (1986-87).
19. ISO 5667-3: 2012 Water quality – Sampling-preservation and handling of water samples (International Organization for Standardization, 2012).
20. ISO 10381-2:2002, Soil quality - Sampling - Part 2: Guidance on sampling techniques (International Organization for Standardization, 2002).
21. ISO 11466:1995 Soil Quality, Extraction of Trace Elements Soluble in Aqua Regia (International Organization for Standardization, 1995).
22. M. Lalchev, I. Ionov, N. Daskalova, *J. Anal. At. Spectrosc.*, **12**, 21 (1997).
23. M. Thompson, J.N. Walsh, *A Handbook of Inductively Coupled Plasma Spectrometry*, Blackie, Glasgow, 1983.
24. N. Stambuk-Giljanovic, *Environ. Monit. Assess.*, **104**, 235 (2005).

ОПРЕДЕЛЯНЕ НА ИЗБРАНИ ЕЛЕМЕНТИ В ТЪКАН ОТ СЛАДКОВОДНИ ГЪБИ, ПРИРОДНИ ВОДИ И УТАЙКИ ЧРЕЗ ОПТИЧНА ЕМИСИОННА СПЕКТРОМЕТРИЯ С ИНДУКТИВНО СВЪРЗАНА ПЛАЗМА.

С. Рончевич, Л. П. Сведружич

Лаборатория по аналитична химия, Департамент по химия, Факултет по науки, Загребски Университет, Хорватовак 102А, HR – 10000 – Загреб, Хърватия

Постъпила на 12 юни 2013 г.; коригирана на 28 август 2013 г.

(Резюме)

Металното съдържание на проби от сладководни гъби *Eunapius Subterraneus*, които са ендемичен щам от карстовите подземни растения в Централна Хърватия, е определяно чрез атомно-емисионна спектрометрия с индуктивно свързана плазма (ICP – OES). В допълнение, съдържанието на метали е определяно във водни проби и утайки, събирани от някои пунктове за пробонабиране. Аналитичната процедура за обработка на пробата включва киселинна обработка в отворен съд. Точността на приложените методи, тествани чрез измерване на сертифицирани референтни проби на вода и утайка, е от порядъка на 5 – 10 % отклонение от декларираното съдържание на метали. Доказано е, че съдържанието на метали (Al, Ba, Ca, Cd, Cu, Fe, Mg, Mn, Ni, Pb, Sr и Zn), измерено в гъбните тъкани, водата и утаечните проби, съответства на това от пункта за пробонабиране. Забелязва се влияние на антропогенното замърсяване от канални отпадъци в лекото завишаване на съдържанието на Al, Cu и Zn във водата, а също и на Cu, Pb и Zn в пробите от утайка. Анализите на две морфологично различни гъбични проби показват разлика в съдържанието на Cu, Zn, Pb и Cd.

Effect of sulfate containing admixture on C₃A hydration

Z. Glavcheva¹, G. Lalev², Chr.Boiadjieva³, I. Glavchev^{3*}

¹*Institute for Organic Chemistry, Bulgarian Academy of Science, Acad. G. Bonchev Street, Building 9, 1113 Sofia, Bulgaria;*

²*School of Chemistry, Cardiff University, Cardiff, CF10 3AT, UK;*

³*University of Chemical Technology and Metallurgy, Sofia, Bulgaria*

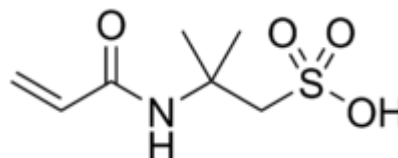
Received June 19, 2013; Revised October 24, 2013

The aim of this study is to investigate the possibility for application of sulfate containing water soluble polymer in hydration process of C₃A (Tricalcium aluminate). XRD was employed to investigate hydrated C₃A and it was confirmed that some part of the macromolecules of applied admixture were included in hydrated inorganic crystals.

Key words: XRD, sulfate containing polymer, C₃A.

INTRODUCTION

The cement admixtures with sulfate group (-SO₃H) are one of the biggest groups of superplasticizers for cement. Many producers of cement admixtures use materials from this group. The application of sulfonated polystyrene (SPS) for superplasticizer of cement was studied in [1] and it was confirmed by XRD, that some part of the SPS macromolecules was included in inorganic crystals of hydrated C₃A (Tricalcium aluminate). It is well known, that C₃A was part of cement and reacted with gypsum. It was also reported in the literature, that the admixtures were adsorbed and consumed to form an organo-mineral phase [2]. Nawa Toyharu investigated different copolymers and the obtained results demonstrated that the polymers with longer graft chains showed better dispersing stability with small amount of adsorption [3]. Kazuo Yamada et al. studied polycarboxylate-type superplasticizer by sulfate ion concentration in aqueous phase [4]. The maxima in XRD data of this additive were given in many articles [5]. It is well known that the inclusion of some atoms in the unit cell of the materials leads to shift of their maxima and change of the values of 2 θ [6]. In this way, with XRD was possible to confirm the inclusion of parts of the macromolecules of the applied admixture in the unit cells of inorganic crystals. The application of polymers of 2-Acrylamido-2-methylpropane sulfonic acid:



(CAS Number 15214-89-8) (PAAMPSA) for superplasticizer of cements was described in the literature [7,8]. With this investigation we like to have better understanding for the interaction of hydrated C₃A with this compound. This material was with known structure and chemical composition for the difference of cement, which composition depended from applied raw materials. To analyze key morphological features, to record the distribution patterns and to examine the current state of habitat quality and population-threatening changes in the environment [17]. In order to record the present status and to provide the base for the further comparison of possible changes in the ecosystem, the content of the selected metals was determined in sponge tissue, as well as in water and sediment samples collected from habitat.

EXPERIMENTAL

The laboratory made sample of C₃A was prepared according method described in [9] from raw materials: CaCO₃ and Al(OH)₃, GR for analysis (Merck). After analyses were made, samples: reference - C₃A: distilled water = 1:1 and mixtures with 0.3 and 0.5% PAAMPSA like 2% water solutions, mixed with applied distilled water. 20% TiO₂ technical grade (Cristal Global) was added in the investigated samples. XRD were made by apparatus TuR – M 62 (CuK α , λ = 1.54056 nm),

* To whom all correspondence should be sent:
E-mail: ivg@uktm.edu

speed 1⁰/min. The hydration of all samples lasted 24 h. The free water was separated by filtration and the dry materials were obtained in oven at 60⁰C, grinded in agate mortar and kept in sealed ampoules. The values of all maxima: the position of the maxima - 2 Θ , grad, the shift of maxima in a presence of PAAMPSA - $\Delta\Theta$, grad, the intensity I,% and the values of the width at half maxima $\Delta h_{1/2}$ were calculated from the XRD patterns.

RESULTS AND DISCUSSION

Water soluble polymer with sulfate group – poly acrylamidopropionic sulfonic acid (PAAMPSA) was used in this investigation. The application of PAAMSA like superplasticizer was studied by several methods, described in BSS EN 934-2 by cement, produced from Holcim Bulgaria, but the obtained results take place in other our manuscript. This polymer has no free sulfuric acid, applied for production of SPS and thus it is not necessary to eliminate H₂SO₄ with BaCl₂ like in the study of this admixture. For better accuracy of XRD measurements, it was used 20% additive TiO₂ which has well known XRD pattern.

The results from XRD investigations are given in tables 1,2,3 and 4. The results in table 2 are similar with those given in the literature [10]. In fact, there are small differences in the values of some maxima, but this may be due to the differences in the investigated materials. The results from the XRD investigation of hydrated C₃A with 20% TiO₂ and 0.5% PAAMPSA are given in in table 3.

It was evident that in the presence of PAAMPSA there are some differences in the values of maxima of hydrated C₃A with and without admixture. The reason for these differences could be a result from including of some part of the macromolecules of applied admixture in the obtained crystals. In the Introduction is given information for this process. There are only few works in support this hypothesis. Biagini et al [11] reported the decreased fluidity of cement paste with sulfurated polystyrene-based admixture by molecular weight 50000 and explained this with adhesion of the long single polymer chain to different cement grains and formation of coagulation due to the generation of bridge effect. This effect was described also by Kim [12]. The values of maxima for TiO₂ in the table 3 have no differences, because the crystals have the same structure before and after hydration. It is evident, that only the data in table 3 for crystals of hydrated C₃A are changed in the presence of investigated admixture PAAMPSA. From the obtained XRD patterns are calculated and the values of $\Delta h_{1/2}$ of some maxima. The results are given in table 4 which are consistent with the hypothesis for the inclusion of parts of macromolecules of PAAMPSA in inorganic crystal of hydrated C₃A.

It is evident that with increasing of the quantity of the admixture from 0.3 to 0.5% in the investigated samples leads to increasing of the values of $\Delta h_{1/2}$ of some maxima which confirms that some parts of macromolecules of applied admixture are included in the crystal of hydrated C₃A.

Table 1. XRD results of hydrated C₃A

2 Θ , grad	17.30	20.00	26.80	28.20	31.70	31.70
I,%	100	48.15	50.62	38.27	83.96	23.46
2 Θ , grad	34.70	36.30	39.50	44.70	52.90	55.00
I,%	14.81	25.93	97.53	91.34	34.57	50.62

Table 2. XRD results of applied TiO₂

2 Θ , grad	27.70	36.20	39.40	41.40	44.10	55.58	56.70
I,%	100	39.17	6.67	17.50	6.67	43.33	11.25

Table 3. XRD results of hydrated C₃A with 20% TiO₂ and 0,5% PAAMPSA

2 Θ , Grad	17.40	20.05	26.90	27.70	28.30	31.90	32.20	34.90	36.20
$\Delta\Theta$, Grad	+0.1	+0.1	+0.5	-	+0.1	+0.2	-1.5	+1.6	-
I,%	100	34.29	42.86	100	40	65.71	11.43	8.57	29.12
2 Θ , Grad	39.30	41.40	44.80	52.5	54.50	55.58	56.70		
$\Delta\Theta$, Grad	-0.2	+0.05	+0.1	-0.4	-0.5	-	-		
I,%	96.30	8.95	77.78	25.93	81.48	23.13	8.05		

Table 4. Results for $\Delta h_{1/2}$ of some maxima in XRD patterns of hydrated C₃A with 20% TiO₂, 0,3% and 0.5 % PAAMPSA

2 Θ , Grad	17.30	28.20	34.70	39.50	44.70	52.90	55.00
$\Delta h_{1/2}$, C ₃ A mm.	0.6	1	0.9	0.8	0.9	0.8	0.8
$\Delta h_{1/2}$, mm. with 20%TiO ₂ , 0,3% PAAMPSA	0.7	1.2	1	1	1	1	1
$\Delta h_{1/2}$, mm with 20%TiO ₂ , 0,5% PAAMPSA	0.8	1.8	1.1	1.2	1.3	1.2	1.3

CONCLUSION

The study demonstrates that water solution of PAAMPSA, made in lab. of Chemical faculty of Sofia state university "St. Kliment Ohridsky" like admixture can be used as a superplasticizer having a profound effect on the hydration process and suggests that some parts of its macromolecules are included in the inorganic crystals of hydrated C₃A.

Acknowledgments: The authors thanks to prof. Georgi Georgiev from Chemical faculty of Sofia State University "Kliment Ohridski for sample of water solution of applied admixture PAAMPSA" syntesed in his laboratory.

REFERENCES

1. Z. Glavcheva, G. Lalev, I. Glavchev, *Oxidation communications*, in print.
2. R. J. Flatt, *Materials and Structures*, 37, 289 (2004).
3. T. Nawa, *Journal of Advanced Concrete Technology*, 4, 225 (2006).
4. K. Yamada, Sh. Ogawa, Sh. e Hanehara, *Cement and Concrete Research*, 31, Issue 3, 375 (2001).
5. R. Vijayalakshmi and V. Rajendran, *Archives of Applied Science Research*, 4 (2) 1183 (2012).
6. S. Umanskii, A. Skakov, A. N. Ivanov, L. N. Rastortcev, *Kristallografia, rengenografija i elektronnaia mikroskopia*, Moskva, Metallurgia, 1982, pp. 382 (in Russian)
7. US Patent 6,569,970
8. EP 0368226 A2
9. D. Delchev, V. Valkov, *Rakovodstvo za laboratorni uprajnenia v tehnologiata na svarzvashtite veshchestva*, University of Chemical S.
10. S. Venkatachalam, H. Hayashi, T. Ebina. H. Nanjo, *Preparation and Characterization of Nanostructured TiO₂ Thin Films by Hydrothermal and Anodization Methods Electrical and Electronic Engineering » "Optoelectronics - Advanced Materials and Devices"*, book edited by Sergei L. Pyshkin and John M. Ballato, ISBN 978-953-51-0922-8, Published: January 16, 2013 under CC BY 3.0 license
11. Biagini, S., Ferrari, G., Maniscalco, V., Casolaro, M., Tanzi, M. C. & Rusconi, L. *Cemento*, 79, 345 (1982).
12. Kim, B.-G. PhD Thesis of Université de Sherbrooke, Sherbrooke, 2000.

ВЛИЯНИЕ НА СУЛФАТСЪДЪРЖАЩА ДОБАВКА ВЪРХУ ХИДРАТАЦИЯТА НА СЗА

З. Главчева¹, Г. Лалев², Хр. Бояджиева³, И. Главчев³

¹ Институт по органична химия, БАН, ул. „Акад. Г. Бончев“, бл. 9, 1113 София;

² Училище по химия, Университет Кардиф, CF 10 3AT, UK;

³ ХТМУ, София, България

Постъпила на 19 юни 2013 г.; коригирана на 24 октомври 2013 г.

(Резюме)

Целта на тази статия е да се изследва възможността за приложение на сулфатсъдържащ водоразтворим полимер в процеса на хидратация на СЗА (Трикалциев алуминат). Използван е XRD за изследване на СЗА и е направено заключение, че някои части от макромолекулите на използваната смес се включват в хидратирани неорганични кристали.

Comparative analyses of chemical composition of royal jelly and drone brood

R. Balkanska^{1*}, I. Karadjova², M. Ignatova¹

¹*Institute of Animal Science, 2232 Kostinbrod, Bulgaria*

²*Faculty of Chemistry and Pharmacy, University of Sofia, 1 James Bourchier Blvd., Sofia 1164, Bulgaria*

Received June 21, 2013; Revised November 26, 2013

Royal jelly (RJ) is commonly consumed for its nutritional properties and it has been widely used in commercial medical products, health foods and cosmetics in many countries. Because of the high price of this product, sometimes RJ can be adulterated by adding other less expensive products, like drone brood (DB). Proper identification of both important products RJ and DB requires complete analysis and determination of major compounds in order to find precise descriptors for their accurate characterization. To investigate the effect of adulteration with DB, the chemical composition on mixtures of RJ and DB were analyzed. Seven RJ sample and seven DB samples were analyzed for water content, protein, fructose, glucose, sucrose, total sugars, pH, total acidity and electrical conductivity. In addition, these parameters were applied to mixtures of RJ and DB samples. All samples were collected from the experimental apiaries of Institute of Animal Science (IAS) and stored at -20 °C before analysis.

Key words: Royal jelly, Drone brood, Bee brood, Chemical composition, Cluster analysis.

INTRODUCTION

Royal jelly (RJ) is a secretion from the hypopharyngeal and mandibular glands of worker bees (*Apis mellifera* L.) and it is the exclusive food of the queen honeybee larva. This secretion is a yellowish, creamy and acidic material with a slightly pungent odor and taste [1]. RJ is a very valuable bee product due to its antioxidant, antibacterial, antifungal and therapeutical properties which are related to the content of different bioactive compounds [2–5]. The composition of RJ is quite complex. It comprises water (60–70%), proteins (9–18%), carbohydrates (7–18%), lipids (3–8%), minerals (0.8–3%), vitamins and amino acids [6, 7]. RJ is a valued bee product which is used and sold pure or mixed with other bee products such as honey, propolis, etc.

Drone brood (DB), comprising a mixture of drone larvae, is close to RJ in some physicochemical characteristics and composition but at different rates. Bee brood has nutritional value and it is increasingly used as a health food supplement. This nontraditional product can also offer a readily accessible and cheap source of biologically active substances, but its biological activity is much lower than that of RJ. From chemical point of view, DB contains water (65–80%), proteins (10–20%), carbohydrates (10–15%), fatty acids and lipids (4–8%), minerals K, Na, Ca, Mg (1–1.5%), amino

acids and hormones (testosterone and estradiol) [8–11]. Various methods have been identified for adulteration of RJ most frequently by mixing it with DB. Garcia-Amoedo and Almeida-Muradian [12] have analyzed the physicochemical profile of the RJ adulterated in different proportions by the following adulterants: natural yogurt, pure water, starch corn slurry, a mixture of sweet condensed milk with propolis and unripe banana. Proper identification of both important products RJ and DB requires complete analysis and determination of major compounds in order to find precise descriptors for their accurate characterization. In the present paper various RJ and DB samples have been analyzed and characterized for major component content. To the best of our knowledge the composition of RJ adulterated with DB has not been fully studied until now. Statistical analysis of results obtained allows precise identification of both products. Such information and data are essential not only from scientific point of view, but it is also important for practical purposes in order easily and efficiently to assess the authenticity of this both commercial product.

EXPERIMENTAL

Samples. Seven RJ samples, seven DB samples and mixtures of them were analyzed. All samples were collected from experimental apiaries of Institute of Animal Science during the period May – August 2011 and were stored at -20°C until

* To whom all correspondence should be sent:
E-mail: r.balkanska@gmail.com

analysis.

Preparation of the adulterated RJ samples. 12-14-day-old DB larvae were taken from the DB cells and were immediately smashed. Mixtures of DB larvae were filtrated and added to the RJ samples in a proportion of 1:1, 1:2 and 2:1 (w/w). The samples were shaken to obtain homogeneous solutions. The adulterations with DB were prepared in the laboratory and the samples were kept in the freezer at -20 °C until the moment of the analysis.

Methods. In brief, the analysis was performed as follows: sugars (fructose, glucose, sucrose) by HPLC as proposed by Sesta [13]; proteins by Folin-Ciocalteu reagent; water content by refractometer; pH values – potentiometrically; total acidity by titration with 0.1 N NaOH according to ON 2576693-84 Fresh and lyophilized royal jelly [14]; electrical conductivity by conductometer (1% water solution of sample) [15].

Statistical Analysis. Data were statistically processed by Student's t-test for the differences

between RJ and DB samples. Means and standards deviations of means were determined with descriptive statistical methods. Differences between means at the 1% ($p < 0.001$) level were considered significant.

Cluster analysis is applied as the method for finding different classes and groups within the obtained data. The cluster analysis is a group of multivariate techniques whose primary purpose is to assemble objects based on the characteristics they possess. The obtained results were processed with MS Office 2007 and STATISTICA 7.0.

RESULTS AND DISCUSSION

Results for major compound content in RJ and DB samples are summarized in Table 1 and 2. Additionally, in order to assess possible changes in composition of adulterated RJ, mixtures of RJ and DB (RJ+DB) have been analyzed and the results are shown in Table 3.

Table 1. Main components and physicochemical characteristics of RJ samples (n=7)

Parameters	Mean \pm SD**	Range
Water content, %	63.39 \pm 1.75	61.00–65.20
Proteins, %	16.73 \pm 1.29	14.65–18.33
Fructose, %	4.88 \pm 0.37	4.24–5.35
Glucose, %	3.46 \pm 0.58	2.70–4.15
Sucrose, %	1.53 \pm 0.55	0.59–2.05
Total sugars, %	9.86 \pm 0.93	8.47–10.80
pH	3.95 \pm 0.09	3.80–4.02
Total acidity, ml 0.1 N NaOH/g	4.07 \pm 0.30	3.68–4.42
Electrical conductivity, μ S/cm	205.14 \pm 8.73	194.00–219.00

* $p < 0.001$; **SD – Standard deviation

Table 2. Main components and physicochemical characteristics of DB samples (n=7)

Parameters	Mean \pm SD**	Range
Water content, %	70.97 \pm 0.72	70.30–72.30
Proteins, %	9.35 \pm 0.63	8.12–10.00
Fructose, %	0.11 \pm 0.11	0.00–0.34
Glucose, %	6.74 \pm 0.65	5.92–7.88
Sucrose, %	0.05 \pm 0.07	0.00–0.18
Total sugars, %	6.92 \pm 0.70	6.22–8.22
pH	6.49 \pm 0.14	6.23–6.63
Total acidity, ml 0.1 N NaOH/g	0.88 \pm 0.15	0.74–1.10
Electrical conductivity, μ S/cm	161.43 \pm 10.67	144.00–178.00

* $p < 0.001$; **SD – Standard deviation

Table 3. Main components and physicochemical characteristics of RJ samples adulterated with DB (n=7)

Parameters	RJ+DB 1:1	RJ+DB 2:1	RJ+DB 1:2
	Mean \pm SD**	Mean \pm SD**	Mean \pm SD**
Water content, %	67.24 \pm 0.59	65.68 \pm 0.79	68.13 \pm 0.40
Proteins, %	14.90 \pm 1.17	15.66 \pm 1.12	13.20 \pm 0.23
Fructose, %	3.17 \pm 0.14	4.24 \pm 0.29	2.30 \pm 0.13
Glucose, %	6.30 \pm 0.48	4.82 \pm 0.20	5.64 \pm 0.23
Sucrose, %	1.23 \pm 0.19	1.02 \pm 0.07	0.85 \pm 0.12
Total sugars, %	10.70 \pm 0.65	10.07 \pm 0.42	8.79 \pm 0.32
pH	4.25 \pm 0.10	4.45 \pm 0.08	5.08 \pm 0.15
Total acidity, ml 0.1 N NaOH/g	2.72 \pm 0.14	3.43 \pm 0.11	2.23 \pm 0.14
Electrical conductivity, μ S/cm	171.14 \pm 7.17	188.76 \pm 3.33	177.83 \pm 4.23

**SD – Standard deviation

The comparison of results from chemical analysis of RJ and DB samples are better visualized in Figure 1.

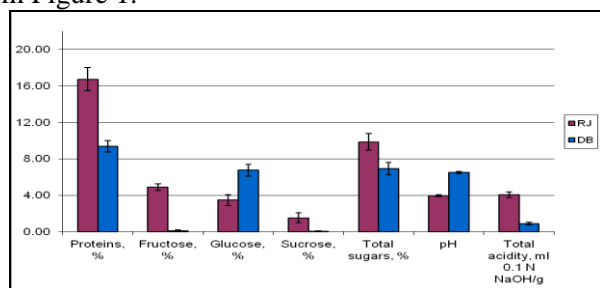


Fig. 1. Average values of proteins, sugars, pH and total acidity of RJ and DB samples (n=7)

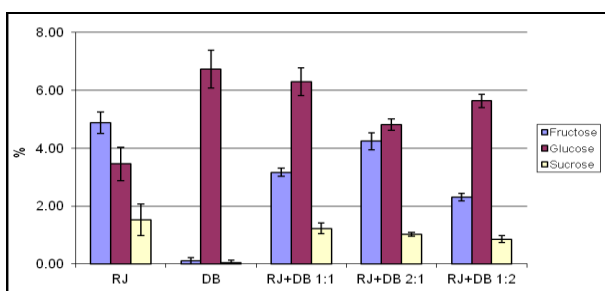


Fig. 2. Average values of sugar profile of RJ, DB samples and their mixtures (n=7)

The results for the average protein content showed relatively narrow range of variation and demonstrated that RJ samples contained almost twice higher protein amount than DB samples. It might be suggested that protein concentration could be a good descriptor for RJ identification. However as can be seen for RJ+DB mixtures protein amount is very close to this of pure RJ (the amount of protein in RJ+DB 1:1 samples is 14.90% and this value is similar to minimal value for pure RJ (14.65%) (see Table 1) which mean that DB proteins quantity should not be the only one descriptor for RJ identification.

Sugars represent second major fraction of compounds in RJ and DB – as a rule the monosaccharides fructose and glucose are the most abundant, while small amounts of disaccharides (mainly maltose and sucrose) are also present; other trisaccharides (erlose), could be found in very small quantities in RJ [13, 16]. As can be seen from results in Table 1 and Table 2 significant differences were observed between average values for total sugar content in RJ and DB samples. Although statistically significant ($p < 0.001$) these variances are not very useful for products identification as far as absolute values found are relatively small. Much better descriptor for differentiation between RJ and DB is sugar profile see Figure 2. The most abundant sugar in both products is glucose which is almost twice higher in

DB in comparison with RJ. The fructose levels in RJ samples are much higher (average value 4.88%) in comparison with these in DB (average value 0.11%), this compound could be used as very good descriptor. Sucrose content in RJ samples is relatively higher than this in DB however values are considerably low and not enough informative. Results obtained for DB in this study are close to the results of Burmistrova [11]. They reported that the proportions of the major sugars in DB are glucose (3.16–5.00%), fructose (0.03–0.50%) and sucrose (0.03–0.50%). Higher content of glucose is specific for DB and this parameter is appropriate for identification purposes.

Relatively significant difference was observed between pH values of RJ and DB – for pure products RJ is acidic with average pH 3.95 (value closed to this reported by Isidorov et al. [17]) while DB is almost neutral average pH 6.49 (value close to this reported by Budnikova [10] for DB, between 5.67 and 6.67 in different larvae stages). However due to high buffer capacity of RJ, mixed samples (see Table 3) showed pH very close to this of pure RJ which mean that pH could not be used for precise RJ identification.

Electrical conductivity depends on the chemical composition of the product, mainly from mineral elements, organic acids, amino acids and proteins content. This parameter should be used for identification purposes.

As might be expected taking into account pH values the pure RJ samples showed higher total acidity (average value 4.07 ml 0.1 N NaOH/g), compared to the samples of DB (average value 0.88 ml 0.1 N NaOH per g sample). Samples of RJ adulterated with DB showed total acidity proportional to the RJ content in the mixture. This parameter could be used for identification purposes.

As shown in Table 2, water content in DB samples is significantly higher in comparison to RJ samples. The average amount of water decreased in order: DB (70.97%) > RJ+DB 1:2 (68.13%) > RJ+DB 1:1 (67.24%) > RJ+DB 2:1 (65.68%) > RJ (63.39%) (Table 1–3). Although good parameter for identification purposes water content strongly depend on storage conditions and it is difficult to control experimental conditions during measurement. From this point of view water amount could not be accepted as enough reliable parameter for identification purposes.

Compared to our results, Budnikova [10] established higher values for protein and sugar levels in drone brood. They can vary depending on the age of the larvae during time of collection. Our

research matches the data reported in the literature [6]. Sugars, water content and proteins are the most common criteria used to characterize RJ composition.

It is worth mention that there was an effect observed on the organoleptic properties of the RJ samples mixed with DB. Pure RJ is an acidic product with a slightly pungent taste. DB has a stronger flavour than RJ. All adulterated samples (RJ+DB) had strong and untypical flavour.

Result of cluster analysis. All the results have gone through a statistical analysis by cluster analysis. It indicates the linkage between the clustered objects with respect to their similarity (distance measure) and takes into account majority of parameters defined for RJ identification. On Figure 3 the dendrogram for linkage of RJ, DB and their mixtures are presented.

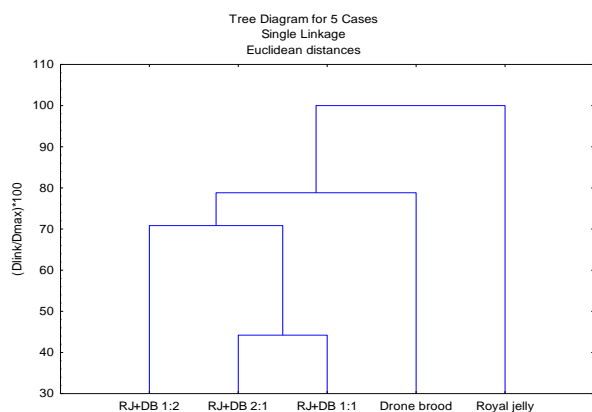


Fig. 3. Dendrogram from cluster analysis of RJ, DB and adulterated samples for all parameters (n=7)

The method of single linkage was chosen as a measure of similarity to classify the RJ, DB and adulterated samples. It could be concluded that Euclidean Distance (the nearest distance method) gives the best result. Two clusters are formed as follows: DB; RJ+DB 1:2, RJ+DB 2:1, RJ+DB 1:1 and RJ as an outlier. It could be concluded from the cluster analysis results that parameters chosen are good descriptors for pure RJ identification as far as relatively good separation between all samples studied and pure RJ is achieved. As can be seen from dendrogram (Figure 4) parameters such as protein and fructose content, total acidity and electrical conductivity could be used for identification purposes.

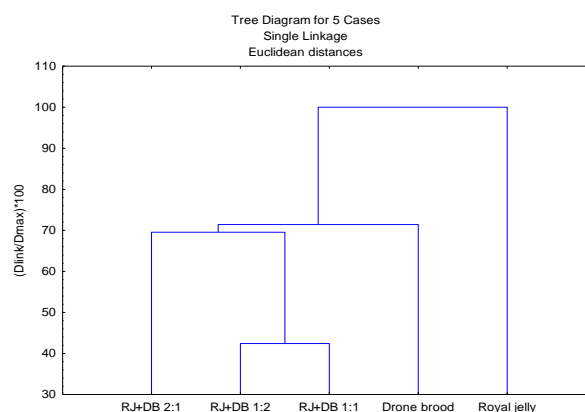


Fig. 4. Dendrogram from cluster analysis of RJ, DB and adulterated samples for parameters protein, fructose, total acidity and electrical conductivity (n=7)

CONCLUSION

The differences in water content, dry mater, proteins, sugars, pH, total acidity, electrical conductivity between RJ and DB samples are significant ($p < 0.001$). The cluster analysis turned out to be useful for finding similarity (or dissimilarity) between pure RJ and mixtures with other products. Parameters such as protein and fructose content, total acidity and electrical conductivity are good descriptors for the evaluation of RJ authenticity. Therefore, the addition of DB in RJ would change in a certain direction the composition on RJ. In Bulgaria, there is no regulation for RJ and for DB separately nor for their combination. These results have to be supplemented with additional measurements in order to confirm and to complete these findings.

REFERENCES

1. M. Genc, A. Aslan, *Journal of Chromatography A*, **839**, 265 (1999).
2. S. Fujiwara, J. Imai, M. Fujiwara, T. Yaeshima, T. Kawashima, K. Kobayashi, *Journal of Biological Chemistry*, **265**, 11333 (1990).
3. M.S. Abd-Alla, A. Mishref, I.M. Ghazi, *Annals of Agricultural Science*, **40**, 597 (1995).
4. K. Attalla, A. Owayss, K. Mohanny, *Annals of Agricultural Science Moshtohor*, **45**, 895 (2007).
5. M. Viuda-Martos, Y. Ruiz-Navajas, J. Fernández-L'opez, J.A. Pérez-Álvarez, *Journal of Food Science*, **73**, 117 (2008).
6. A.G. Sabatini, G. Marcazzan, M.F. Caboni, S. Bogdanov, L.B. Almeida-Muradian, *Journal of ApiProduct and ApiMedical Science*, **1**, 1 (2009).
7. T. Nagai, R. Inoue, *Food Chemistry*, **84**, 181 (2004).

8. M. FINKE, *Ecology of Food and Nutrition*, **44**, 257 (2005).
9. S. Narumi, *Honeybee Science*, **25**, 119 (2004).
10. N. Budnikova, *Pcelovodstvo*, **6** (2009).
11. L. Burmistrova, PhD Thesis, Ryazan Medical University, Russia, 1999.
12. L.H. Garcia-Amoedo, L.B. Almeida-Muradian, *Quimica Nova*, **30**, 257 (2007).
13. G. Sesta, *Apidologie*, **37**, 84 (2006).
14. ON 2576693-84 Fresh and lyophilized royal jelly.
15. S. Bogdanov, P. Martin, C. Lüllmann, *Apidologie*, extra issue, 14 (1997).
16. G. Daniele, H. Casabianca, *Food Chemistry*, **134**, 1025 (2012).
17. V.A. Isidorov, S. Bakier, I. Grzech, *Journal of Chromatography B*, **885–886**, 109 (2012).

СРАВНИТЕЛНИ АНАЛИЗИ НА ХИМИЧНИЯ СЪСТАВ НА ПЧЕЛНО МЛЕЧИЦЕ И ПИЛО ОТ ТЪРТЕИ

Р. Балканска¹, И. Караджова², М. Игнатова¹

¹ *Институт по животновъдство, 2232 – Костинброд, България;*

² *Факултет по химия и фармация, СУ, бул. „ Джеймс Баучер ”, София 1164, България*

Постъпила на 21 юни 2013 г.; коригирана на 26 ноември 2013 г.

(Резюме)

Пчелното млечице (RJ) обикновено се консумира заради хранителните си свойства и е широко използвано в комерсиалните медицински продукти. Понякога RJ може да бъде смесено с други, по-евтини продукти, подобни на пило от търтеи (DB). Правилната идентификация на двата важни продукта RJ и DB изисква пълен анализ и определяне на основните съединения, за да се намерят точни описания за тяхното охарактеризиране.

За да се изследва ефектът от смесването с DB, е анализиран химичният състав на смеси от RJ и DB. Седем проби от RJ и DB са анализирани за водно съдържание, протеини, фруктоза, глюкоза, захароза, тотални захари, рН, обща киселинност и електропроводимост. В допълнение, тези параметри са изследвани и за смесени от RJ и DB проби. Всички проби са събирани от експерименталните пчеларници на института по животновъдство и са съхранявани при -20°C преди анализите.

Recovery of precious (Au, Ag, Pd, Pt) and other Metals by e-scrap processing

S. B. Dimitrijević¹, Ml. B. Mirić², Vl. K. Trujić¹, B. N. Madić¹, St. P. Dimitrijević³

¹ Mining and Metallurgy Institute Bor, Zelene bulevar 35, Bor, Serbia

² Directorate of Measures and Precious Metals, Mike Alasa 14, Beograd, Department of the control subjects in precious metals, Generala Boze Jankovica 32, Niš, Serbia

³ Innovation center of the Faculty of Technology and Metallurgy, University of Belgrade, Karnegijeva 4, Belgrade, Serbia

Received July 2, 2013; Revised October 10, 2013

The professional paper is a brief report of an investigation results to be adopted into production. In fact it is a resume of a study on the idea of e-scrap processing and metal production in Mining and Metallurgy Institute Bor, Serbia, based on its expert team investigations of the relevant literature and practice evidences and own research results. The investigations results are presented shortly in the First part of the paper where the chosen technological solution is described including the basic parameters for economic analysis. The second part of the paper is a resume of the economic analysis that approves benefits of the e-scrap processing and profitability of the metals production. Conclusion signifies the investigations and the study importance for realization of a project expected to generate important ecological and economical benefits.

Key words: e-scrap processing; Au; Ag; Pd; metal production; investigation; technology; economy.

INTRODUCTION

E-scrap processing of based metal production in Mining and Metallurgy Institute Bor, Serbia is a project based on serious considerations of the actual trends in related technology and economy fields. As an (Research and Development) R&D institution, we have adequate experience, staff and equipment for the processing and profitability production.

As the e-scrap is one of the growing global ecological problems and its processing is in the focus of the researchers and others interested in the problem solution all over the world. Growing electronic industry production in the last decades caused the e-scrap quantity increase. E-scrap contains number of different metals such as copper, zinc, iron, precious metals, cadmium, lead, mercury and other materials such as plastics, glass and organic materials [1, 2]. Some of the metals are well marketable according to its prices trends [3] and the metal production based on e-scrap processing appears to be profitable.

According to the actual reports e-scrap quantity has been gradually rising at the annually rate of 3-5% which means 10-50 billion tones every year [4]. Global recycling rate of e-scrap is variable: while it is 86% in Japan, 50-60% in EU and 12-13% only in Serbia [5]. To raise the e-scrap recycling rate in

Serbia it is necessary to organize it better from the initial phase of gathering and sorting to the final processing and supporting activities. It is also important to organize it in accordance with the European Union legislation. Aiming that, Serbian Government has adopted the Law on Waste Management and the Law on Packaging and Waste Packaging [6]. Required framework for the e-scrap management in Serbia including its gathering and processing has been established.

In the aim to keep step with the actual trends and the situation in the field, Mining and Metallurgy Institute Bor, with its reach R&D experiences, qualified staff and equipments capacities (Figure 1), has undertook approximate investigations and framed the project of e-scrap processing and metal production as a part of its medium-term development plan. The project is planned to be realized and is expected to be important from both economical and ecological aspects.

E-SCRAP PROCESSING AND METAL PRODUCTION TECHNOLOGY

Pilot Plant Equipment.

All tests were performed in pilot plant presented on Figure 1.

Description of the Accepted Technology

Printed Circuit Board – PCB as the basic row for the special metal production was analyzed first. Chemical composition of PCB is shown in Table 1.

* To whom all correspondence should be sent:
E-mail: mladenmiriczulu@gmail.com

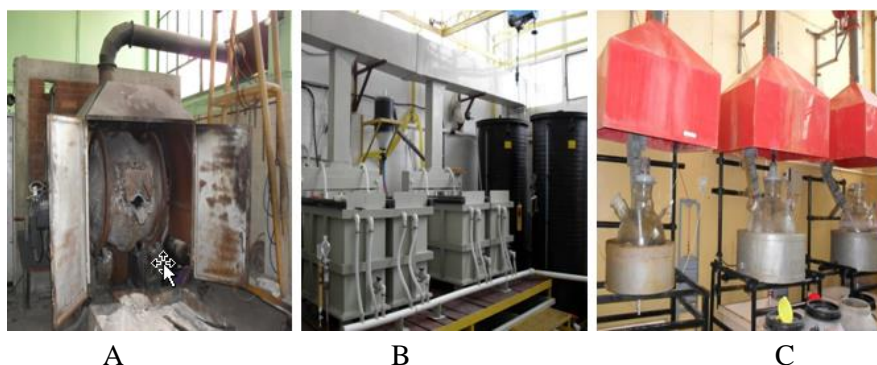


Fig. 1. Pilot plant equipment: a) Electrolytic arc furnace; b) Plant for electrolytic refining of copper;c) Glass reactor for dissolving

Table 1. Chemical composition of PCB

Element	%	Element	%	Element	%
Ag	0.014	Cr	0.001	Mg	0.0141
Cu	22.601	Ba	0.008	Cd	6.79x10 ⁻⁶
Sn	3.713	Si	0.015	As	0.0019
Pb	1.342	Mo	0.0002	Ag	0.0158
Ni	0.242	Zr	0.002	Ti	0.0073
Au	0.0068	Sr	0.0003	Se	0.00034
Mn	0.003	Co	0.0014	Fe	0.91
Sb	0.019	Al	0.0082	Zn	1.86
Cr	0.001	Mg	0.0141	Ca	0.11
Ba	0.008	Cd	6.79x10 ⁻⁶	Insoluble residue	69.104

Our investigations of seven types of PCB have led to the following conclusion: the average metal part of the PCB content is 28.6% including the copper dominating 22.6%. Precious metals content was considered as the most important for their share in the market value of the metal production was estimated to be 65-80%.

Technological process of the computer e-scrap recycling starts with the following phases:

- Used computer equipment transportation
- Computer equipment acceptance
- Computer equipment storage

The process continues with the phase of disassembling of the components that includes:

- Probity and functionality check
- Disassembly
- Separation
- Temporary storage of components, recyclable and non recyclable
- Some components transportation for further processing and/or refuse

The PCB processing is the most complex phase of the technological process for its complex composition meaning variety of materials. The processing phase includes the processes of

pyrometallurgy, electrolysis and refinement shortly described below.

Pyrometallurgy

In the preparation phase it is necessary to remove the capacitors containing very harmful and toxic materials. After grinding to the required grain size and separation of plastic, first follows magnetic separation and then separation of aluminum parts. Lead and tin in solder are very harmful for the further processing, especially in the electrolytic refining of copper. These metals must be removed by low-temperature heating process (320–350°C). Melting and casting of copper anode containing collected precious metals was performed in the Electric arc furnace-Birlac (Figure 1a) by conventional techniques for copper.

Electrolytic refining

Electrolytic refining of anodes, obtained by melting e-scrap was performed in two cathode periods in new pilot plant for electrolytic refining of anode with non-standard chemical composition (Figure 1b) in the aim to obtain copper cathodes of the commercial quality (99.99% Cu). The anode sludge is subject to further hydrometallurgical processes in order to obtain precious metals of commercial quality.

Refinement

The anode slime obtained by electrolytic refinement of the copper anodes with high content of precious metals was processed in the Laboratory for refinement of precious metals in the special 100 dm³ glass reactors (Figure 1c). The first phase of the refinement is the process of decopperisation of anode slime by leaching with diluted sulfuric acid in the presence of oxygen as the oxidant. After the process of decopperisation, the anode slime contains max. 2% of copper. Anode slime without copper is a raw material for the next stages of processes in the aim to obtaining gold, silver and palladium.

Two illustrations of the described processing technology are presented on the following figures. On Figure 2 is shown technology block scheme proposed by Park and Fray [7] and on Figure 3 adopted technology in Mining and Metallurgy Institute Bor.

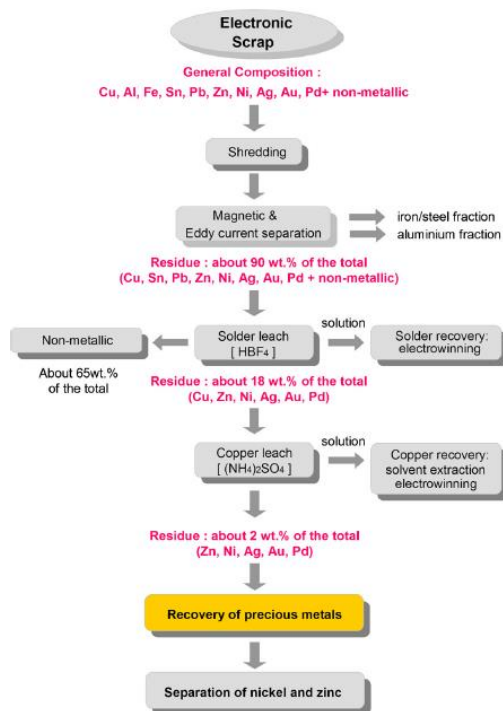


Fig. 2. E-scrap processing and metal production technology block scheme [7]

TECHNOLOGICAL PARAMETERS RELEVANT FOR ECONOMIC ANALYSIS

Pyrometallurgy

Expected electronic waste quantity or PCBs to be processed is 16 t per year.

After the separation of metal and non metal part of the PCBs the metal part containing, 1.8 t of copper is subject of the pyrometallurgical process.

During the pyrometallurgical treatment certain metals losses are inevitable (Zn and Pb mainly). These metals evaporate with the melting gases or, eventually, through the slag. The melting losses of the metals are about 2.5%. After the melting phase 11.5 t of copper anodes (11.8×0.975) contains 11.2 t of copper and 0.3t of precious metals with impurities.

Metal recovery by the hydrometallurgical treatment of metal parts is: for copper ≈ 99%, for gold ≈ 98%, for silver ≈ 93% and for palladium ≈ 98%. This means that electrolysis will have at disposal: 11.0/12 = 0.92 t of anodes per month, while the average weight of anodes will be 958/28 = 32.86 kg. (28 anodes is the electrolysis capacity, which annually is 336 anodes) [8].

Electrolysis

After melting and casting the electrolysis is provided with 11 tons of anodes, with 95% Cu-10.45 t.

The content of precious metals in the anodes is: max 0.1% - 0.011 t, respectively: Au: 3.183 kg, Ag: 7.7616 kg. Impurities (Pb, Sn, Zn, Fe): 4% - 0.44 t.

The process of electrolysis will result in the loss of certain metals, roughly 9%. The metal recovery in the electrolytic process will be: for Cu: 95%, for Ag: 97% and for Au: 98%.

After the electrolytic refining the following masses are obtained:

- 9.9275 t - 9.9 t of copper cathodes (as the final product)
- 550 kg of anode slime containing 275 kg of Cu, 7.529 kg of Ag and 3.12 kg of Au.
- 270 kg impurities (Pb, Sn, Zn, and Fe) distributed in the anode slime and partly in the electrolyte.

After the electrolytic refinement of the anodes the obtained slime (550 kg) is to be set copper free to the copper content in the sludge of 2% for the further precious metals refining [9].

Refinement

Copper free anode sludge of 275.00 kg contains the following amount of precious metals:

- 3130.00 g Au
- 8215.00 g Ag
- 900.00 g Pd

With the following adopted recovery of precious metals (based on laboratory experiments): 99% for gold, 98% for silver and 96% for palladium the final products quantities per year are:

- 3100.00 g Au
- 8050.00 g Ag
- 860.00 g Pd [8, 9].

ECONOMIC ANALYSIS AND THE PROJECT EVALUATION

Market Analysis

In Serbia there is still no significant competition in the field of e-waste processing and metal production based on it. Only a few organizations has potential to be e-scrap recyclers. Finished products of this type have specific markets. Since the products are stock market subjects there are reputable and reliable buyers of these products. Established business links provide the right to believe that the main buyers of precious metals to be companies such as: Heraeus GMBH or Metalor Group Switzerland. The export mediator would be exporting company Jugotehna, Belgrade, Serbia.

The final calculation of the revenue was based on the planned selling prices of RBB – RTB Bor Company for Cu, Au and Ag [10] although the World Bank forecasts are a bit different [11]. For palladium value calculation the minimum current world market price is used [12, 13]. Thus the projected prices for the calculation of revenues are as follows: Cu - 4 600 €/t; Au - 24 000 €/kg; Ag - 360 €/kg and Pd - 12 000 €/kg. As far as the supply market is concerned the printed circuit boards, as the main raw material for this type of production, shall be procured through the existing collection centers in Serbia and the region. Procurement of normative materials will be performed mainly on the domestic market. The existing 10 kV substation would supply the production facility with electricity, water, fuel, oil and lubricants will be procured through appropriate services in accordance with the processing and production dynamics.

BASIC PARAMETERS

Production capacity, structure and value

- Copper: 10.260 t/year x 4600 €/t = 47196 €

- Gold : 3.100 kg/year x 24000 €/kg = 74400 €

- Silver: 8.050 kg/year x 360 €/kg = 2898 €

- Palladium: 0.860 kg/year x 12000 €/kg = 10750 €

Investments

Equipment 50200 €, Working capital 18290 € and Others 10642 €.

Funding

Own funds 31.49% or 24920 €; Bank loan for new equipment: 68.51% or 54212€

Capital costs

Depreciation 10%, Maintenance 5% and Insurance 0,5% of the equipment value, Interest 15%

Material and energy costs

Pyrometallurgy 4044 €, Electrolysis 7080 € and Refinement 3568 €.

Labor costs

Pyrometallurgy 5520 €, Electrolysis 14670 € and Refinement 9112 €.

Other expenses

Processing: Cu 700 €/t, Au 150 €/kg, Ag 10 €/kg, Pd 150 €/kg,

Environmental costs: 1000 €/year, Export supporting services 8% of Au and Ag income, Chemical analysis 1200 €/year, other expenses 2000 €/year.

Financial Projections and the Project Evaluation

All financial projections (Tables 2, 3, 4) for the six year period, including one year of investment and five years of production, indicate the project feasibility.

Table 2. Income Statement

	1	2	3	4	5	6	Total €
Incomes		135244	135244	135244	135244	135244	676220
1.Selling Cu		47196	47196	47196	47196	47196	235980
2.Selling Au		74400	74400	74400	74400	74400	372000
3.Selling Ag		2898	2898	2898	2898	2898	14490
4.Selling Pd		10750	10750	10750	10750	10750	53750
Costs		81507	80301	78914	77319	75484	393525
1.operational costs		73375	73375	73375	73375	73375	366875
2.Funding costs		8132	6926	5539	3944	2109	26650
Gross profit		53737	54943	56330	57925	59760	282695
Taxes		5374	5494	5633	5793	5976	28270
Net profit		48363	49449	50697	52133	53784	254426
Cumulative		48363	97812	148510	200642	254426	

Table 3. Financial cash Flow

	1	2	3	4	5	6	Total €
Total inflows	79132	135244	135244	135244	135244	160344	780452
Total outflows	79132	89901	90022	90160	90320	90503	530038
Net cash flow		45343	45222	45084	44924	69841	250414
Cumulative		45343	90565	135649	180573	250414	
Discounted with 15%		39429	34195	29643	25686	34723	163675

Table .- Economic Cash Flow

	1	2	3	4	5	6	Total €
Total inflows		135244	135244	135244	135244	160344	701320
Total outflows	79132	73729	73849	73988	74148	74331	449177
Net cash flow	-79132	61515	61395	61256	61096	86013	252143
Cumulative	-79132	-17617	43778	105034	166130	252143	
Discounted with 15%	-79132	53492	46423	40277	34932	42764	138755
Discounted with 74.2 % (IRR)	-79132	35314	20233	11589	6635	5362	0

- Income Statement indicates profit throughout the years of the production period
- Financial Cash Flow indicates permanent liquidity and continual positive net cash flows
- Economical Cash Flow indicates positive indicators of the project profitability:
 - ✓ Internal rate of return IRR = 74.20%,
 - ✓ Net present value (discounted at 15%) NPV_{15%} = 138 755 €
 - ✓ Pay back period PBP = 2 years

Final evaluation of the investment in the project of e-scrap processing and metal production is completely positive. Based on the projected technology and basic parameters the project feasibility is out of question. Even with the more pessimistic basic parameters profitability of the project would be enviable and with significant ecological benefits.

CONCLUSION

The paper presents results of e-scrap processing and metal production project. The project is expected to be realised in the Mining and Metallurgy Institute Bor special production department within the medium term development plan.

The research results were the basis for the adopted technological solution described as one of the possible processing variants. Basing on the adopted processing technology and the production

capacity the initial parameters for economic analysis were determined.

Economic analysis including short market analysis, the basic parameters and the financial projections (Income Statement, Financial Cash Flow and Economic Cash Flow) resulted with positive appraisal indicators. The analysis basic indicators, internal rate of return, net present value and payback period, approve the feasibility and profitability of the metal production based on e-scrap processing.

Beside the feasibility and the profitability the metal production based on e-scrap processing in Mining and Metallurgy Institute Bor is fully justified also from the environmental aspect. The project is expected to generate great economic and also ecological benefits not only for the investor but also for the Serbia and the Balkan region.

Acknowledgement: This work has resulted from the Project funded by the Ministry of Education, Science and Technological Development of the Republic of Serbia, No. 34024 "Development of Technologies for Recycling of Precious, Rare and Associated Metals from Solid Waste in Serbia to High Purity Products" for which the authors on this occasion would like to thank.

REFERENCES

1. Ž. Kamberović, M. Korać, M. Ranitidović, *Metalurgija-Journal of Metallurgy*, **17** (3), 139, (2011)
2. Ž. Kamberović, M. Korać, D. Ivšić, V. Nikolić, M. Ranitidović, *Metalurgija-Journal of Metallurgy*, **15**(4), 231, (2009)
3. S. Dimitrijević, A. Ivanović, D. Simonović, Ž. Kamberović, M. Korać.: Electrodeposition of copper and precious metals from waste sulfuric acid solution, 15th International Research TMT 2011, Prague, Czech Republic, , pp. 689-692, (2011)
4. <http://www.recyclingtoday.com/un-electronics-report.aspx> accessed in June 2010
5. <http://www.abiresearch.com/research/1004501>, accessed in June 2010
- 6.[6] Official Gazette, Republic of Serbia, 36/09, Law on Waste Management and Low on Packaging and Packaging Waste (2009)
7. Y.J. Park, D. J. Fray, *Hazardous Materials*, **164**, 1152, (2009)
8. V. Marjanović, A. Ivanović, B. Rajković, V. Cvetković-Stamenković, Scrap of Electronics, 41st International October Conference on Mining and Metallurgy, Proceedings (2009)
9. A. Ivanović, V. Stamenković, V. Marjanović: The industrial, economic, and environmental dimensions of recycling, 41st IOC on Mining and Metallurgy, Proceedings (2009)
10. www.rtb.co.rs
11. <http://go.worldbank.org/4R17TIA330>, accessed in June 2010.
12. <http://palladiumprice.org/palladium-price-per-kilo.html>, accessed in June 2010
13. www.metalprices.com, www.lme.com, www.kitconet.com , accessed in June 2010

ДОБИВАНЕ НА ЦЕННИ (Au, Ag, Pd, Pt) И ДРУГИ МЕТАЛИ ЧРЕЗ E-SCRAP ПРОЦЕС

С. Б. Димитриевић¹, Мл. Б. Мирич², Вл.К. Тружич¹, Б. Н Мадич¹, С. П, Димитриевић

¹ Минен и металургичен институт Бор, Зелени булевард № 35, Бор, Србија;

² Дирекција за измервања и ценни метали, Мике Аласа № 14, Белград, Департамент за контрол на содржание в ценни метали, Генерал Бозе Јанковица 32, Ниш, Србија

³ Център за иновации на Факултет по технологии и металургия, Белградски университет, Карнеджијева 4, Белград, Србија

Постъпила на 2 јули 2013 г.; коригирана на 10 октомври 2013 г.

(Резюме)

Настоящата професионална статия е кратък отчет на резултати от изследване, което да бъде внедрено в производствената практика. В действителност то е резюме на изследване върху идеята за e-scrap обработване и добив на метали в Минния и металургичен институт Бор, Србија, основана на резултати от проучване на съответната литература, данни от практиката и резултати от собствени изследвания. Резултатите са представени накратко в първата част на работата, където е описано избраното технологично решение, включително основните параметри на икономическия анализ. Втората част на статията е обобщение на икономическия анализ, който показва ползите на e-scrap обработването и рентабилността на процеса за добив на метали. Заклученията показват важноста на изследването за реализация на проект, от който се очакват важни екологични и икономически ползи.

Thermodynamic analysis of processes with the participation of zeolites

T. Marsagishvili*, M. Machavariani, G. Tatishvili, E. Ckhakaia

Iv. Javakhishvili Tbilisi State University, R. Agladze Institute of Inorganic Chemistry and Electrochemistry, 11, Mindeli str., 0186 Tbilisi, Georgia

Received August 19, 2012; Accepted October 1, 2012.

The quantum calculation of the free energy of polyatomic dipole-active polarizable particles revealed two mechanisms of free energy change during interaction with a polar medium (solvation and fluctuation mechanisms).

For charged particles the main contribution to complete free energy change is given by the solvation mechanism. Correspondingly, for simple charged particles in homogeneous isotropic polar medium without spatial dispersion this brings to Born free energy of solvation. For uncharged particles with equilibrium dipole moment, solvation mechanism also contributes to the change in system's free energy, and this contribution for spherical particles is in direct proportion to the quadratic dipole moment of the particle and in inverse proportion to its volume. In the frame of the solvation mechanism, effects of nonisotropy and nonlocality of medium (like zeolites), effects of spatial dispersion may be taken into account.

The fluctuation mechanism of free energy change of the system has usually a minor contribution to the complete change of system's free energy, but it should be considered for systems where contribution of solvation mechanism is not great and also for systems, where vibration frequencies of the impurity particle change greatly upon placing it in a polar medium.

The obtained results will promote the investigations of adsorption processes on the zeolite surface, the study of kinetics of charge transfer and particle transfer process in channels of composite materials.

Key words: thermodynamic analysis, polar medium, free energies, spatial dispersion, frequency dispersion, zeolites.

INTRODUCTION

Natural and synthetic zeolites have wide application in gas separation installations, gas generators, purification plants, for creation of ionisators, super-condensers, and accumulators. Their wide application is connected with the specific structure of zeolites, the form of their nanopores providing unique sorption properties. The surface of zeolites is very active, so they are fine catalysts for many processes. Size, form and properties of the surface of nano-sized materials may be adapted and optimized for a particular application. Placing different ions in the pores of natural and synthetic zeolites we obtain modified materials, which have unique properties. For determination of the realization possibility of processes with participation of zeolites, first of all, thermodynamic analysis of the corresponding system has to be conducted.

1. FREE ENERGIES OF POLYATOMIC POLARIZABLE DIPOLE-ACTIVE PARTICLES IN POLAR MEDIUM

Complete change of system's free energy includes the following components:

- a) Work connected with cavity formation in the medium, where the impurity particle is placed;
- b) Free energy connected with the translational and rotational motion of the impurity as a whole;
- c) Electrostatic part connected with the interaction of the impurity particle with the medium (zeolite and liquid in canals).

Below we shall calculate the latter component, which in the majority of cases, makes the greatest contribution to the free energy change.

2. HAMILTONIAN OF THE SYSTEM

Existence of electrostatic interaction between impurity and medium causes polarization of the medium. In turn, polarized medium influences the impurity particle and polarizes it. The Hamiltonian of the system may be represented

* To whom all correspondence should be sent:

as:

$$H = H_m + H_p - \int \langle \vec{P}(\vec{r}) \rangle_0 \vec{E}(\vec{r}, Q_0) d\vec{r} - \int \delta \vec{P}(\vec{r}) \vec{E}(\vec{r}, Q_0) d\vec{r}, \quad (1)$$

where H_m^s - is Hamiltonian of the system; H_p - is Hamiltonian of the particle; $\langle P(\vec{r}) \rangle_0$ - is the average value of medium polarization induced by the electric field of the particle, with field intensity $E(\vec{r}, Q^0)$ [1], (Q^0 - is the set of intramolecular coordinates of the impurity). Going from the Hamiltonian of the nonpolarized medium H_m^s to the Hamiltonian of the polarized medium H_m , in dielectric approximation we have:

$$H = H_m + H_p - \frac{1}{2} \int \langle \vec{P}(\vec{r}) \rangle_0 \vec{E}(\vec{r}, Q_0) d\vec{r} - \int \delta \vec{P}(\vec{r}) \vec{E}(\vec{r}, Q_0) d\vec{r}, \quad (2)$$

According to the fluctuation - dissipative theorem:

$$\langle P_i(\vec{r}, t) \rangle_0 = - \int d\vec{r}' \int dt' G_{P_i P_k}^R(\vec{r}, \vec{r}'; t - t') E_k(\vec{r}', t'), \quad (3)$$

where G_{PP}^R is the retarded Green function of operators of medium polarization [1].

For the intensity of the electric field of impurity particles in dipole approximation the expression may be used:

$$\varepsilon_\alpha(\vec{r}) = - \int d\vec{r}' G_{E_\alpha E_\beta}(\vec{r}, \vec{r}') \sum_{i=1}^N \mu_\beta^i(\vec{R}_i) \delta(\vec{r} - \vec{R}_i) + G_{E_\alpha \rho}(\vec{r}, R) \rho(\vec{R}). \quad (4)$$

Here G_{EE} and G_{E_ρ} are Green functions of the operators of electric field intensity and the scalar potential of the condensed medium; they may be expressed by the Green functions $G_{\varphi\varphi}$, which may be simply defined from the solution of the electrostatic task (see [1, 2]). μ^i is the dipole moment of i-th bond of the particle, R_i is the radius-vector of the i-th dipole of the particle, ρ , R is the charge of the particle and the radius-vector of the charge localization point.

For a polarizable particle the value of μ^i differs from the corresponding vacuum value μ_0^i , it could be determined through:

$$\mu_\alpha^i = \mu_0^i + \sum_{j=1}^N \alpha_{\alpha\beta}^i \{ G_{E_\beta E_\gamma} \mu_\gamma^i + G_{E_\alpha \rho} \rho \} \quad (5)$$

where $\alpha_{\alpha\beta}^i$ is the polarizability tensor of the i-th bond of the particle. It is obvious that if all components of the polarizability tensor and the vacuum values of the dipole moment of the bond are known, then all 3N values of μ may be found from system (5). As Green functions, the corresponding solutions of electrostatic tasks of model functions may be used, which allows taking into account the effects of spatial dispersion of the medium. Further, substituting the found values μ_α^i into correlation (4) we define the electric field intensity of the system $\varepsilon(\vec{r}, R_i)$ and from (3) we find the polarization of medium $\langle P(\vec{r}) \rangle_0$.

Substituting (3) into (2) we rewrite the Hamiltonian of the system in the following form:

$$H = H_m + H_p + \frac{1}{2} \int \vec{E}(\vec{r}, Q) G_{PP}^R(\vec{r}, \vec{r}') \vec{E}(\vec{r}, Q) d\vec{r} d\vec{r}' - \int \delta \vec{P}(\vec{r}) \vec{E}(\vec{r}, Q) d\vec{r}. \quad (6)$$

In this formula we expand the electric field intensity into a series by Q^0 up to linear terms,

$$H = \delta \Omega_0 + H_p + H_m - \int d\vec{r} \delta \vec{P}(\vec{r}) \vec{E}(\vec{r}, Q). \quad (7)$$

Here H_p is the Hamiltonian of the polarized solvated particle,

$$H^p = H^{p0} + \sum_n d_n Q_n^0 + \sum_{mn'} h_{mn'} Q_n^0 Q_{n'}^0, \quad (8)$$

where

$$h_{mn'} = \frac{1}{2} \frac{\partial E^0}{\partial Q_n^0} G_{PP}^R \frac{\partial E^0}{\partial Q_{m'}^0}, \quad (9)$$

$$d_n = \frac{1}{2} (E^0 G_{PP}^R \frac{\partial E^0}{\partial Q_n^0} + \frac{\partial E^0}{\partial Q_n^0} G_{PP}^R E^0)_{Q_n^0 = Q_{n0}^0}$$

In (7) $\delta \Omega_0$ is the free energy of the solvated particle, which has the following form:

$$\delta \Omega_0 = \frac{1}{2} \int dt dt' \int d\vec{r} d\vec{r}' E_\alpha(\vec{r}, Q_0) G_{P_\alpha P_\beta}^R(\vec{r}, \vec{r}', t - t') E_\beta(\vec{r}', Q_0) \quad (10)$$

By transformation of coordinates (shift and turn) H_p may be reduced to quadratic form with frequencies ω_s and coordinates Q_s .

$$H_p = \frac{1}{2} \sum_s \omega_s \left[(Q_s - Q_{s0})^2 - \frac{\partial^2}{\partial Q_s^2} \right] + J, \quad (11)$$

where Q_{s0} is the equilibrium value of coordinate Q_s , J – the minimal energy of the particle.

It is obvious that the influence of a solvated polarized particle on the medium leads to additional polarization of the medium. Therefore, it is necessary to use the characteristics of the polar particle in (7) - (11) and introduce $E(Q_0)$ instead of $E(Q)$.

In formula (7) we expand into series the electric field intensity E by $Q - Q_0$ up to a linear term. Consequently:

$$H = \delta\Omega_0 + H_m + H_p + H_{int}^{(1)} + H_{int}^{(2)}, \quad (12)$$

where

$$H_{int}^{(1)} = -\int \delta\vec{P}\vec{E}(\vec{r}, Q_0) d\vec{r}, \quad (13)$$

is the interaction of the medium polarization fluctuations with the static field of the impurity, and

$$H_{int}^{(2)} = -\sum_s \int d\vec{r} \delta\vec{P}(\vec{r}) \delta Q_s \vec{V}_s(\vec{r});$$

$$\vec{V}_s(\vec{r}) = \frac{\partial \vec{E}(\vec{r}, Q)}{\partial Q_s} \Big|_{Q_s=Q_{s0}}, \quad (14)$$

is the interaction of the medium polarization fluctuations with intramolecular vibrations of the impurity.

$$\delta\Omega_1 = -\frac{1}{2} \int d\vec{r} \langle \vec{P}(\vec{r}) \rangle \vec{E}_0(\vec{r}, Q_0) - \frac{1}{2} \int_0^\beta d\tau \int_0^\beta d\tau' \int d\vec{r} d\vec{r}' \vec{E}_{0\alpha}(\vec{r}, Q_0) \vec{E}_{0\beta}(\vec{r}', Q_0) G_{\delta P_\alpha \delta P_\beta}(\vec{r}, \vec{r}'; \tau, \tau') \quad (18)$$

Where $\beta = 1/kT$, k is the Boltzmann constant, T - temperature, $G_{\delta P_\alpha \delta P_\beta}$ - temperature Green functions of medium polarization fluctuation operators [1],

$$G_{\delta P_\alpha \delta P_\beta}(\vec{r}, \vec{r}'; \tau - \tau') = -\langle T_\tau \delta P_\alpha(\vec{r}, \tau) \delta P_\beta(\vec{r}', \tau') \rangle \quad (19)$$

$$\delta\Omega_1 = \frac{1}{2} \int d\vec{r} d\vec{r}' \vec{E}_{0\alpha}(\vec{r}, Q_0) \left[G_{P_\alpha P_\beta}^{R_0}(\vec{r}, \vec{r}'; \omega = 0) - G_{\delta P_\alpha \delta P_\beta}(\vec{r}, \vec{r}'; \omega = 0) \right] \vec{E}_{0\beta}(\vec{r}) \quad (20)$$

Green functions G_{PP}^0 and $G_{\delta P \delta P}$ are phonon Green functions of the medium, when $\omega = 0$ they are equal, so

$$\delta\Omega_1 = 0 \quad (21)$$

By integrating formula (10) over τ and τ' we

The electrostatic part of the free energy change connected with introduction of polyatomic dipole-active impurities in the polar medium may be written in the following form [3]:

$$\delta\Omega = \delta\Omega_0 + \delta\Omega_1 + \delta\Omega_2 + \delta\Omega_3, \quad (15)$$

where $\delta\Omega_1$ and $\delta\Omega_2$ are the changes of the system free energy connected with $H_{int}^{(1)}$ and $H_{int}^{(2)}$ interactions, correspondingly, $\delta\Omega_3$ is the change of the vibrational free energy of the impurity particle.

3. CALCULATION OF THE FREE ENERGIES OF SOLUTION $\Delta\Omega_0$ AND $\Delta\Omega_1$

The change of free energy $\delta\Omega_1$ may be expressed through the matrix

$$\delta\Omega_1 = -kT \ln \langle S^{(1)} \rangle. \quad (16)$$

Here, averaging is carried out over the states of polar medium and $S^{(1)}$ matrix has the form:

$$S^{(1)} = T_\tau \exp \left\{ \int_0^\beta d\tau \int d\vec{r} \delta\vec{P}(\vec{r}, \tau) \vec{E}_0(\vec{r}) \right\} \quad (17)$$

After $S^{(1)}$ matrix expansion into series and calculation of quantum-statistical averages of δP operators, we obtain [4]:

Substituting $\langle P \rangle$ in the formula (18) to the value from formula (3) and integrating over τ, τ', t, t' , we obtain:

obtain the following expression $\delta\Omega_0$:

$$\delta\Omega_0 = \frac{1}{2} \int d\vec{r} d\vec{r}' \vec{E}_\alpha^0(\vec{r}) G_{P_\alpha P_\beta}^R(\vec{r}, \vec{r}'; \omega = 0) \vec{E}_\beta^0(\vec{r}'). \quad (22)$$

For a homogeneous local isotropic medium, for which

$$G_{P_{\alpha}P_{\beta}}(\vec{r}, \vec{r}'; \omega = 0) = -\frac{1}{4\pi} \left(1 - \frac{1}{\varepsilon}\right) \delta_{\alpha\beta} \delta(\vec{r} - \vec{r}'). \quad (23)$$

the free energy of the solution $\delta\Omega_0$ takes the form:

$$\delta\Omega_0 = -\frac{C}{8\pi} \left(1 - \frac{1}{\varepsilon}\right) \int d\vec{r} (\vec{E}^0(\vec{r}))^2 \quad (24)$$

Here ε is the static value of dielectric permeability. For spherically symmetric particles with z charge the formula (24) brings about the Born solvation energy:

$$Q = e^2/2r\varepsilon \quad (25)$$

If the particle is not charged but has an equilibrium dipole moment, then for spherically symmetric particles we obtain:

$$\delta\Omega_0 = -\left(1 - \frac{1}{\varepsilon}\right) \frac{\mu^2}{3r_0^3}, \quad (26)$$

where r_0 – radius of particle.

4. EFFECTS OF MEDIUM SPATIAL DISPERSION.

Taking into account the spatial dispersion of the medium let us rewrite (22) in the following form:

$$\delta\Omega_0 = -\frac{1}{2} \int \rho(\vec{r}) G_{\varphi\varphi}(\vec{r}, \vec{r}') \rho(\vec{r}') d\vec{r} d\vec{r}' \quad (27)$$

where $G_{\varphi\varphi}$ is the Green function (GF) of the medium scalar potential operators, ρ is the charge density of the impurity which creates an electric field with intensity E_0 .

Effects of spatial dispersion of the medium may be considered, when calculating the free energy change of the system, if some model functions are used as Green functions of operators of polarization fluctuation or charge density or a medium scalar potential. For determination of GF $G_{\varphi\varphi}(\vec{r}, \vec{r}')$ the results of solving electrostatic tasks may be used: accurate within electron charge GF $G_{\varphi\varphi}(\vec{r}, \vec{r}')$ coincides with the magnitude of the electrostatic potential in point \vec{r} of the system, if in point \vec{r}' a unit charge is placed. Considering the above mentioned, it should be expected that allowance behavior of GF $G_{\varphi\varphi}(\vec{r}, \vec{r}')$ will be of type:

$$G_{\varphi\varphi}(\vec{r}, \vec{r}') = C(\vec{r}) \frac{1}{|\vec{r} - \vec{r}'|}, \quad (28)$$

In this case, the behavior of GF $G_{\varphi\varphi}$ and $G_{\rho\varphi}$

will be of type:

$$G_{\varphi\rho}(\vec{r}, \vec{r}') = G_{\rho\varphi}(\vec{r}, \vec{r}') = -f(\vec{r})\delta(\vec{r} - \vec{r}') \quad (29)$$

The Fourier component of $f(\vec{r})$ function may be connected with the longitudinal component of the dielectric permeability $\varepsilon^l(k)$. After standard conversions we get:

$$f(\vec{r}) = \frac{1}{(2\pi)^{3/2}} \int e^{i\vec{k}\vec{r}} f(\vec{k}) \quad (30)$$

and

$$f(\vec{k}) = \frac{1}{4\pi} \left(1 - \frac{1}{\varepsilon^l(k)}\right) \quad (31)$$

Hereby, for Fourier components we have the following correlation:

$$G_{\varphi\varphi}(\vec{k}, \vec{k}') = -\frac{1}{4\pi} \left(1 - \frac{1}{\varepsilon^l(k)}\right) \delta_{\vec{k}\vec{k}'}. \quad (32)$$

In case of a local homogeneous medium, from the previous formula we get:

$$G_{\varphi\varphi}(\vec{k}, \vec{k}') = -\frac{1}{4\pi} \left(1 - \frac{1}{\varepsilon^l(k)}\right) \delta_{\vec{k}\vec{k}'} = -\frac{C_0}{4\pi} \delta_{\vec{k}, \vec{k}'} \quad (33)$$

In the \vec{r} space the latter formula has the form:

$$G_{\varphi\varphi}(\vec{r}, \vec{r}') = -\frac{1}{4\pi} C_0 \delta(\vec{r} - \vec{r}') \quad (34)$$

If the impurity particle is spherically symmetric, has z charge and radius r_0 , then for the change of free energy $\delta\Omega_1$ we get:

$$\delta\Omega_1 = -\frac{C_0 z^2}{2r_0} = -\frac{z^2}{2r_0} \left(1 - \frac{1}{\varepsilon}\right) \quad (35)$$

For consideration of space dispersion effects, instead of δ -function in formula (34) the function may be used:

$$G_{\varphi\varphi}^{(\lambda)}(\vec{r}, \vec{r}') = -\frac{C_0}{4\pi} \Delta_{\lambda}(|\vec{r} - \vec{r}'|) \quad (36)$$

In the capacity of $\Delta_{\lambda}(|\vec{r} - \vec{r}'|)$ function the exponentially damped function normalized on unity must be selected:

$$\Delta_{\lambda}(|\vec{r} - \vec{r}'|) = \frac{1}{8\pi\lambda^3} e^{-\frac{|\vec{r} - \vec{r}'|}{\lambda}} \quad (37)$$

If for charge density of impurity particle ρ^{ex} classic approximation is used and assuming that the point of charge localization coincides with the origin of coordinates, then

$$\rho^{\text{ex}}(\vec{r}) = z\delta(\vec{r}) \quad (38)$$

In this case for $\delta\Omega_1$ we have:

$$\delta\Omega_1 = -\frac{C_0 z^2}{16\pi\lambda} = -\frac{z^2}{16\pi\lambda} \left(1 - \frac{1}{\varepsilon}\right) \quad (39)$$

Analogously, the change of free energies of the system, where space dispersion effects of the medium are described by more complicated functions, may be calculated. For example, if Δ_λ describes oscillations with attenuation:

$$\Delta_\lambda(|\vec{r} - \vec{r}'|) = \frac{v(v^2 - 3\bar{\lambda}^2)}{8\pi} e^{-v|\vec{r} - \vec{r}'|} \cos(\bar{\lambda}|\vec{r} - \vec{r}'|) \quad (40)$$

Then for the free energy change $\delta\Omega_1$ we obtain:

$$\delta\Omega_1 = -\frac{C_0 z^2}{16\pi} \frac{v(v^2 - 3\bar{\lambda}^2)(v^2 - \bar{\lambda}^2)}{(v^2 + \bar{\lambda}^2)^2} \quad (41)$$

Here the parameter $1/\lambda$ will be approximately equal to the diameter of the solvent molecule. If for charge density ρ^{ex} quantum approximation is used, then

$$\delta\Omega_1 = -\frac{e^2 C_0 \alpha^6}{(8\pi)^4 \lambda^3} \int d\vec{r} d\vec{r}' d\vec{r}'' \exp\left(-\frac{|\vec{r} - \vec{r}'|}{\lambda} - \alpha(\vec{r} + \vec{r}'')\right) \frac{1}{|\vec{r}' - \vec{r}''|} \quad (45)$$

Omitting cumbersome calculations, we give the result in the form:

$$\delta\Omega_1 = \frac{e^2 C_0 \lambda^2}{8\pi(\alpha/2)^4} (32\alpha^7 - 4\alpha^9 \lambda^2 + \frac{4\alpha^6}{\lambda} - \frac{55\alpha^5}{\lambda^2} - \frac{21\alpha^4}{\lambda^3} + \frac{38\alpha^3}{\lambda^4} + \frac{26\alpha^2}{\lambda^5} - \frac{20\alpha}{\lambda^6} - \frac{12}{\lambda^7}). \quad (46)$$

For description of space dispersion effects of the medium, the function may be used:

$$\Delta_\lambda(|\vec{r} - \vec{r}'|) = \frac{1}{\pi^{3/2} \lambda^3} \exp\left(-\frac{|\vec{r} - \vec{r}'|^2}{\lambda^2}\right) \quad (47)$$

If we take (43) as wave function $\Psi(\vec{r})$, then for $\delta\Omega_1$ we obtain:

$$\delta\Omega_1 = -\frac{e^2 C_0 \alpha^3}{4} \int_0^\infty dr r e^{-\alpha r} \Phi\left(\frac{r}{\lambda}\right) \quad (48)$$

where $\Phi\left(\frac{r}{\lambda}\right)$ - is the error integral:

$$\Phi\left(\frac{r}{\lambda}\right) = \frac{2}{\sqrt{\pi}} \int_0^{r/\lambda} e^{-t^2} dt \quad (49)$$

During numerical calculations by formula (49) it is convenient to use an approximate expression for the error integral:

$$\delta\Omega_1 = -\frac{9e^2 C_0 \alpha}{56} + \frac{e^2 C_0 \alpha^3}{14\sqrt{2}\pi} \int_0^\infty d\vec{r} \left\{ r \left(1 + \frac{\alpha r}{2}\right)^2 [b_1 t + b_2 t^2 + b_3 t^3 + b_4 t^4 + b_5 t^5] e^{-\left(\alpha r + \frac{r^2}{\lambda^2}\right)} \right\} \quad (53)$$

If space dispersion effects of medium are described by function (47), and for charge density the function is used:

$$\rho^{\text{ex}}(\vec{r}) = e|\Psi(\vec{r})|^2 \quad (42)$$

where $\Psi(\vec{r})$ is wave function.

In the capacity of wave function we take the normalized function:

$$\Psi(\vec{r}) = \frac{\alpha^{3/2}}{(8\pi)^{1/2}} e^{-\frac{\alpha r}{2}} \quad (43)$$

GF of operators of medium scalar potential we take in the form (36). Free energy change $\delta\Omega_1$ has the form:

$$\delta\Omega_1 = -\frac{e^2 C_0}{32\pi^2} \int d\vec{r} d\vec{r}' d\vec{r}'' \Delta_\lambda(|\vec{r} - \vec{r}'|) \frac{|\Psi(\vec{r})|^2 |\Psi(\vec{r}'')|^2}{|\vec{r} - \vec{r}''|} \quad (44)$$

Using here the form of the function $\Delta_\lambda(|\vec{r} - \vec{r}'|)$ (37) and the wave function $\Psi(\vec{r})$ in the form (43), we get:

$$\Phi\left(\frac{r}{\lambda}\right) = 1 - \sqrt{\frac{2}{\pi}} e^{-(r/\lambda)^2} [b_1 t + b_2 t^2 + b_3 t^3 + b_4 t^4 + b_5 t^5] \quad (50)$$

$$\text{where } t = \frac{1}{1 + P\sqrt{2} \frac{r}{\lambda}},$$

$$P = 0,2316; b_1 = 0,3194; b_2 = -0,3566; b_3 = 1,7815; b_4 = -1,8213; b_5 = 1,3303. \quad (51)$$

In quantum case for charge density of the particle also the following function may be used:

$$\rho(\vec{r}) = \frac{e\alpha^3}{56\pi} \left(1 + \frac{\alpha r}{2}\right)^2 e^{-\alpha r} \quad (52)$$

If expression (47) is used for Δ_λ function, then for $\delta\Omega_1$ we have:

$$\rho(\vec{r}) = \frac{4e\beta^3}{4\sqrt{2}\pi} e^{-2\beta^2 r^2} \quad (54)$$

then the free energy change will be equal to:

$$\delta\Omega_1 = -\frac{2e^2C_0\beta}{\sqrt{2\pi}} + \frac{8e^2C_0\beta^3}{\pi} \int_0^\infty drre^{-\left(2\beta^2 + \frac{1}{\lambda^2}\right)r^2} [b_1t + b_2t^2 + b_3t^3 + b_4t^4 + b_5t^5] \quad (55)$$

In the capacity of Δ_λ function describing space dispersion effects of the medium the step function may be selected:

$$\Delta_\lambda(|\vec{r} - \vec{r}'|) = \frac{3}{4\pi\lambda^3} \theta(|\vec{r} - \vec{r}'|) \theta(\lambda - |\vec{r} - \vec{r}'|) \quad (56)$$

$$\delta\Omega_1 = \frac{81e^2C_0}{14\lambda^3\alpha^2} - \frac{3e^2C_0}{4\lambda} - \frac{3e^2C_0}{56\lambda} e^{-\alpha\lambda} \left[4\lambda^2\alpha^2 + 7\lambda\alpha + 40 + \frac{106}{\lambda\alpha} + \frac{106}{\lambda^2\alpha^2} \right] \quad (57)$$

For a model in which charge density is described by a function of the type (43), we have:

$$\delta A\Omega_1 = 3\frac{e^2C_0}{\lambda} \left[\frac{1}{(\alpha\lambda)^2} - \frac{1}{4} \right] + \frac{e^2C_0\alpha}{4} \left[2 - \frac{3}{\alpha\lambda} - \left(1 + \frac{1}{\alpha\lambda} \right) \right] e^{-\alpha\lambda} \quad (58)$$

If charge density has the form (54), then

$$\delta\Omega_1 = -\frac{3e^2C_0}{4\lambda} \left[1 - \frac{1}{(2\lambda\beta)^2} \right] - \frac{4e^2C_0}{\sqrt{2\pi}} e^{-2\beta^2\lambda^2} \left\{ \frac{\beta}{2} + \frac{3 - 4\lambda^2\beta^2 - 32\lambda^4\beta^4}{32\lambda^3\beta^2} (b_1t + b_2t^2 + b_3t^3 + b_4t^4 + b_5t^5) + \frac{12\lambda^2\beta^2 - 1}{4\lambda^2\beta} P(b_1t^2 + 2b_2t^3 + 3b_3t^4 + 4b_4t^5 + 5b_5t^6) - \frac{P^2}{4\lambda} (2b_1t^3 + 6b_2t^4 + 12b_3t^5 + 20b_4t^6 + 30b_5t^7) \right\} \quad (59)$$

Thus, for the free energy change of the system, when a polyatomic polarizable nondipole charged particle is introduced into a condensed medium, the calculations may be carried out with different precision, considering various effects: in case of quantum or classic behavior of the degrees of freedom of the impurity, effects of spatial dispersion of the medium, which may be described by a set of different model functions; interactions of intramolecular vibrations of the impurity with polarization fluctuations of the medium.

For obtaining the equilibrium dipole moment of an impurity particle in classic approximation for the charge density of a particle placed in a local homogeneous isotropic medium, we have the following expression:

$$\delta\Omega_1^d = -\int d\vec{r}d\vec{r}' (\vec{E}(\vec{r})\vec{E}(\vec{r}')) \delta(\vec{r} - \vec{r}') \frac{C_0}{4\pi} \quad (60)$$

After corresponding integration we obtain:

$$\delta\Omega_1^d = -\left[8\pi C_0 / (3r_0^3) \right] (\partial d / \partial Q)^2 \quad (61)$$

where r_0 is the particle radius.

Naturally, a total change of free energy for a charged dipole particle will be equal to the sum of changes for charged impurity (35) and dipole impurity (61):

$$\delta\Omega_1 + \delta\Omega_1^d = -\frac{8\pi C_0}{3r_0^3} \left(\frac{\partial d}{\partial Q} \right)^2 - \frac{z^2 C_0}{8\pi r_0} \quad (62)$$

In regard to obtaining the space dispersion of the medium for dipole particles, representation of the free energy change of the system in one of the following forms is more convenient:

$$\delta\Omega_1 = \int d\vec{r}d\vec{r}' \nabla_{\vec{r}\alpha} \nabla_{\vec{r}'\beta} G_{\varphi\varphi}(\vec{r}, \vec{r}') P_\alpha^{\text{ex}}(\vec{r}) P_\beta^{\text{ex}}(\vec{r}') = \int G_{E_\alpha E_\beta}(\vec{r}, \vec{r}') P_\alpha^{\text{ex}}(\vec{r}) P_\beta^{\text{ex}}(\vec{r}') d\vec{r}d\vec{r}' \quad (63)$$

For particle polarization ρ^{ex} point approximation may be used:

$$\vec{\rho}^{\text{ex}}(\vec{r}) = \vec{d}\delta(\vec{r}) \quad (64)$$

For GF, $G_{\varphi\varphi}$ and G_{EE} different model functions may be used.

Most acceptable way for calculation of $\delta\Omega_1$ for the charge density of charged dipole particle in quantum approximation is to use correctly selected wave functions Ψ_d and to carry out integration by formula (44) for various types of Δ_λ functions.

5. CALCULATION OF THE FLUCTUATION PART OF FREE ENERGY CHANGE

Let us write the change of free energy in the following form:

$$\delta\Omega_2 = -kT \ln \langle S^{(2)} \rangle \quad (65)$$

where

$$S^{(2)} = T_\tau \exp \left\{ \int_0^\beta d\tau \int d\vec{r} \delta \vec{P}(\vec{r}, \tau) \vec{V}_s(\vec{r}) Q_s(\tau) \right\} \quad (66)$$

Let us formally represent the matrix as:

$$S^{(2)}(\lambda) = T_\tau \exp \left\{ \lambda \int_0^\beta d\tau \int d\vec{r} \delta \bar{P}(\vec{r}) \bar{V}_s(\vec{r}) Q_s(\tau) \right\}. \quad (67)$$

$$W_{ss'}(\lambda, \omega_n) = \int d\vec{r} d\vec{r}' \lambda V_{\alpha s}(\vec{r}) G_{\delta P_\alpha \delta P_\beta}(\vec{r}, \vec{r}'; \omega_n) \lambda V_{\beta s'}(\vec{r}'), \quad (72)$$

and the corresponding free energy $\delta\Omega_2(\lambda)$, similarly to correlation (16), like this [1]:

$$\frac{\partial \delta\Omega_2(\lambda)}{\partial \lambda} = kT \frac{\partial \langle S^{(2)}(\lambda) \rangle_0}{\langle S^{(2)}(\lambda) \rangle_0}, \quad (68)$$

Integrating this correlation accordingly by λ from 0 up to 1 and taking into account the condition $\delta\Omega_{12} = \Omega(\lambda = 1) - \Omega(\lambda = 0)$, we express $\delta\Omega_2$ through Green function

$$\delta\Omega_2 = - \int_0^1 \frac{\partial \lambda}{\lambda} \int d\tau \int d\vec{r} \lambda V_{s\alpha}(\vec{r}) \{ G_{\delta P_\alpha Q_s}(\vec{r}, \lambda, \tau = 0) \}, \quad (69)$$

where $G_{\delta P Q}$ is the Green function of operators δP and Q with effective interaction $\lambda V_s(\vec{r})$.

Expanding the Green function into Fourier series by τ and integrating by τ we have:

$$\delta\Omega_2 = -kT \int_0^1 \frac{\partial \lambda}{\lambda} \int d\vec{r} \lambda V_{s\alpha}(\vec{r}) \sum_{n=-\infty}^{\infty} G_{\delta P_\alpha Q_s}(\vec{r}, \lambda, \omega_n), \quad (70)$$

Taking into account the results [1-5] it follows that:

$$\delta\Omega_2 = -kT \int_0^1 \frac{\partial \lambda}{\lambda} \sum_n W_{ss'}(\lambda, \omega_n) G_{Q_s Q_s'}(\lambda, \omega_n), \quad (71)$$

where W is renormalized interaction of intramolecular vibrations with each other through the polar medium. This quantity may be calculated quantum-chemically or may be simulated by a suitable function with consideration of above mentioned formulas.

$$\delta\Omega_2 = \frac{kT}{2} \ln \left(1 - \frac{W(0)}{\omega_s} \right) + kT \ln \prod_{n=1}^{\infty} \left[1 - \sum_{i=1}^m \frac{u_i \omega_s}{(\omega_n^2 + \omega_s^2)(\omega_i - \omega_n)} \right], \quad (76)$$

here ω_s is the frequency of intramolecular vibrations of the impurity. Expression in brackets

$$1 - \sum_{i=1}^m \frac{u_i \omega_s}{(\omega_n^2 + \omega_s^2)(\omega_i - \omega_n)} = \frac{\left[\left(\frac{\omega_s}{2\pi kT} \right)^2 + n^2 \right] \prod_{i=1}^m \left(\frac{\omega_i}{2\pi kT} - n \right) - \sum_{i=1}^m \frac{u_i \omega_s}{(2\pi kT)^2} \prod_{i=1}^m \left(\frac{\omega_i}{2\pi kT} - n \right)}{\left[\left(\frac{\omega_s}{2\pi kT} \right)^2 + n^2 \right] \prod_{i=1}^m \left(\frac{u_i}{2\pi kT} - n \right)}. \quad (77)$$

If condition [6] is fulfilled,

$$a_1 + \dots + a_1 = b_1 + \dots + b_1 \quad (78)$$

Then, as it is known from the theory of Γ -functions

Green functions of normal coordinate operators of intramolecular vibrations of the solvated impurity satisfy the system of linear algebraic nonhomogeneous equations:

$$G_{Q_s Q_s'}(\lambda) = G_{Q_s Q_s'}^0 + G_{Q_s Q_s'}^0(\lambda) W_{ss'}(\lambda) G_{Q_s Q_s'}(\lambda). \quad (73)$$

Here $G_{Q_s Q_s}^0$ are the Green functions of the oscillator.

So solving (73) for any finite number of intramolecular degrees of freedom N , the components $G_{Q_s Q_s'}(\lambda, \omega_n)$ may be determined and accordingly integrated by λ and summed by n in (71) for calculation of $\delta\Omega_2$.

For a simple model, when the system has one dipole-active degree of freedom, we get:

$$\delta\Omega_2 = \frac{kT}{2} \sum_n \text{Sp} \ln |G_{QQ}^0 G_{QQ}^{-1}| = \frac{kT}{2} \sum_n \text{Sp} \ln |1 - G_{QQ}^0 W| \quad (74)$$

In order to show the possibilities of the calculations in accordance with (74), we use a polar approximation (which includes Debye and resonance function) for the Green function of medium polarization fluctuation operators. In this case,

$$W(\omega_n) = \sum_{i=1}^m \frac{u_i}{|\omega_i - \omega_n|}, \quad (75)$$

where u_i are experimental constants, and m - the number of poles of the Green function.

Substituting (89) into (88), we get:

in this correlation may be presented in the form of a ratio of two polynomials,

$$\prod_{n=1}^{\infty} \frac{(n - a_1) \dots (n - a_1)}{(n - b_1) \dots (n - b_1)} = \prod_{i=1}^1 \frac{\Gamma(1 - b_i)}{\Gamma(1 - a_i)} \quad (79)$$

In our case condition (78) is fulfilled, so

$$\delta\Omega_2 = kT \ln \frac{kT}{\omega_s} + kT \ln \left(2 \operatorname{sh} \frac{\omega_s}{2kT} \right) + \frac{kT}{2} \ln \left(1 - \frac{W(0)}{\omega_s} \right) + kT \ln \prod_{j=1}^{m+2} \Gamma \left(1 - \frac{\overline{\omega}_{j_j}}{2\pi kT} \right) - kT \ln \prod_{i=1}^m \Gamma \left(1 - \frac{\omega_i}{2\pi kT} \right) \quad (80)$$

where $\overline{\omega}_j$ is the root of (74). $W(\omega=0)/\omega_2$ should be always less than unit. If the ratio is close to unit, then such molecules dissociate.

CONCLUSIONS

A method of calculation of the free energy change of polyatomic polarizable dipole-active particles during their dissolution in heterogeneous polar medium is presented. Two mechanisms of interaction of these particles with the polar medium are considered: solvation and fluctuation mechanism, including ion-dipole and dipole-dipole interactions. The obtained analytic expressions allow realization of quantitative calculations for dissolved particles with any finite number of degrees of freedom of intra-molecular vibrations, under consideration of the spatial and frequency dispersion of the medium.

Thereby, at the expense of the “fluctuation” mechanism of interaction of the intramolecular vibrations of a particle with the medium polarization fluctuations, dissociation of the molecule is possible, although solvation of this molecule by the medium does not allow the molecule to dissociate to ions. This mechanism is

also important for chemical adsorption – the adsorbed molecule may desorb because of the “fluctuation” mechanism. Moreover, the adsorbed molecule may dissociate to ions owing to this mechanism.

ACKNOWLEDGEMENT: This work was supported by the BS-ERA.net program, FP7, project HYSULFCEL.

REFERENCES

- 1.A.A. Abrikosov, L. Gorkov E. Dzyaloshonski, “Methods of Quantum Field Theory in Statistical Physics”, Dover Publications Inc., New York, 1975.
- 2.R.R. Dogonadze, T.A. Marsagishvili, *Surface Sci.* **101**,439 (1980).
- 3.T.A. Marsagishvili, M.N. Machavariani, *Phys. Stat. Sol. (b)* **154**, 97 (1989).
- 4.R.R. Dogonadze, T.A. Marsagishvili, in: The Chemical Physics of Solvation, Part A, R. Dogonadze (editor), Elsevier Publ. Co., Amsterdam 1985, p. 39.
- 5.R.R. Dogonadze, T.A. Marsagishvili, M.N. Machavariani, *Bull. Acad. Sci. Georgian SSR*, **127**, 65 (1987).
- 6.H. Bateman, A. Erdelyi, “Higher Transcendental Functions”, McGraw-Hill Publ. Co., New York/Toronto/London, 1955.

ТЕРМОДИНАМИЧЕН АНАЛИЗ НА ПРОЦЕСИ С УЧАСТИЕ НА ЗЕОЛИТИ

Т. Марсагишвили*, М. Мачавариани, Г. Татишвили, Е. Цхакария

Държавен университет “Ив. Явахишвили”, Тбилиси, Институт по неорганична химия и електрохимия “Р. Агладзе”, 0186 Тбилиси, Грузия

Постъпила на 19 август, 2012 г.; приета на 1 октомври, 2012 г.

Квантово-химичните пресмятания разкриват два механизма на изменение на вободната енергия на дипол-активни поляризуеми частици при взаимодействие с полярна среда (солватация и флукуационен механизъм).

При заредени частици главният принос за пълното изменение на свободната енергия се дава от солватационния механизъм. Съответно, при прости заредени частици в хомогенна изотропна среда без пространствена дисперсия това води до свободна енергия на солватация по Борн. За незаредени частици с равновесен диполен момент солватационният механизъм също води до промяна на свободната енергия на системата, а за сферични частици тя е право пропорционална на квадрата на диполния омент на частицата и обратно пропорционална на обема ѝ. В рамките на солватационния механизъм ефектите на анизотропия и не-локализирането на средата (напр. при зеолити) трябва да се държи сметка за пространствената дисперсия.

Флукуационният механизъм на изменението на свободната енергия в системата обикновено има малък принос за общото изменение. Той трябва да се отчита в системи със слабо влияние на солватационния механизъм или при които вибрационните честоти на онечистванията се променят значително при постаянето им в полярна среда.

Получените резултати ще насърчат изследванията върху адсорбционните процеси на повърхността на зеолити, кинетиката на пренос на заряда и преносните процеси в порите на композитни материали.

Investigation of *Trichophyton verrucosum* proteins by sodium dodecyl sulfate polyacrylamide gel electrophoresis (SDS-PAGE)

Z. Abedian¹, A.R. Khosravi², A.R. Mesbah³, F. Abedian^{4*}

¹Cellular and Molecular Biology Research Center, Babol University of medical Sciences, Babol, Iran

²Department of Microbiology, Faculty of Veterinary Medicine, Tehran University, Tehran, Iran

³Department of Biochemistry, Faculty of medicine, Tarbiat modarres University, Tehran, Iran

⁴Department of Immunology Department, Mazandaran university of medical sciences, Sari, Iran

Received: January 2, 2014; revised: February 9, 2014

Trichophyton verrucosum is one of the most common dermatophyte that parasitizes keratinized tissues in human and animal. This study compares the proteins of 5 varieties of *Trichophyton verrucosum*, which obtained from human and animals. At first, they were cultured on the specific media separately and incubated at 37 °C for one month. For preparation of protein extracts, the colonies of fungi were transferred to Sabouraud's liquid medium and the amount of proteins was determined by Bradford method after growth of fungi. SDS-PAGE with 13% polyacrylamide separating gel and a discontinuous buffer system was carried out for protein analysis. Coomassie blue G250 was used for gel staining and different bands were appeared. Gel was scanned with a Helena densitometer for protein patterns. Fourteen protein bands with different molecular weights between 12730-92250 Dalton were detected from the supernatant of samples. In addition to these 14 bands two other bands (38020 and 34670 Da) were observed in the pellet of samples. In spite of different morphology of colonies there were no differences between either supernatant to each other or pellet of five *T. verrucosum* isolates.

Key words: Dermatophyte, *Trichophyton verrucosum*, Protein extraction

INTRODUCTION

Superficial mycoses in human and domestic animals caused by dermatophytes are found worldwide. The diseases have zoonotic importance because persons can be infected by contact with animals. In dairy beef production and also in public health, dermatophytoses may be of economic importance due to costs of treatment, decreased skin value and weight [1 - 3].

Trichophyton verrucosum is a zoophilic dermatophyte and is an agent of ringworm disease in human and domestic animals like camel, cow and cattle [4]. Direct contact with this fungus causes of infection of nail, skin and hair in human. The infection is usually with high inflammation such as in tinea mannum bullosa. *T. verrucosum* also makes economical lose in domestic animals [5]. It is transmitted to human through direct contact with contaminated cattle or its products in infected patients with inflammatory lesion in head, face etc. [6].

Since the proteins of fungi are used for immunization of animals thus it has generated considerable interest for determination of protein pattern and effective prophylactic programs against

dermatophytosis due to *T. verrucosum* infections in animals [7 - 10].

EXPERIMENTAL

Clinical isolates of *T. verrucosum* were obtained from veterinary faculty of Tehran University. They were identified according to conventional morphological criteria.

Extract preparation

Isolates were cultured on Sabouraud's dextrose agar and blood agar and incubated at 30 °C and 37 °C. They were transferred to 500 ml of Sabouraud's broth and incubated for 40 days at 30 °C. Mycelia were harvested by filtration and washed with PBS twice. The extraction fluid comprised borax, boric acid, EDTA and 500 ml distilled water. Freeze-thawing method and grinder instrument were used for grinding of colonies. The extracts were separated from the debris by centrifugation at 4000g, followed by 2000g for 45 min at 4 °C. Then supernatant and pellet were isolated. Protein assay was done by using Bradford method and then the extracts were concentrated by freeze drying [11 - 12].

* To whom all correspondence should be sent:

E-mail:

Electrophoretic Technique

Electrophoretic separation of proteins was carried out in resolving gel 13% and with discontinuous buffer system. Reference standards in the molecular weight range 12300-78000 da were included on each gel to facilitate comparison of the bands. Gel was stained in coomassie blue G250. Protein patterns were scanned with Helena densitometer and 590 nm filter [13 - 15]

RESULTS

The morphology of colonies were different completely but there were similarities in all protein patterns obtained from either supernatant, or pellet of isolates separately. Although the colony forms of isolates were different but no differences were seen between them (Fig 1).

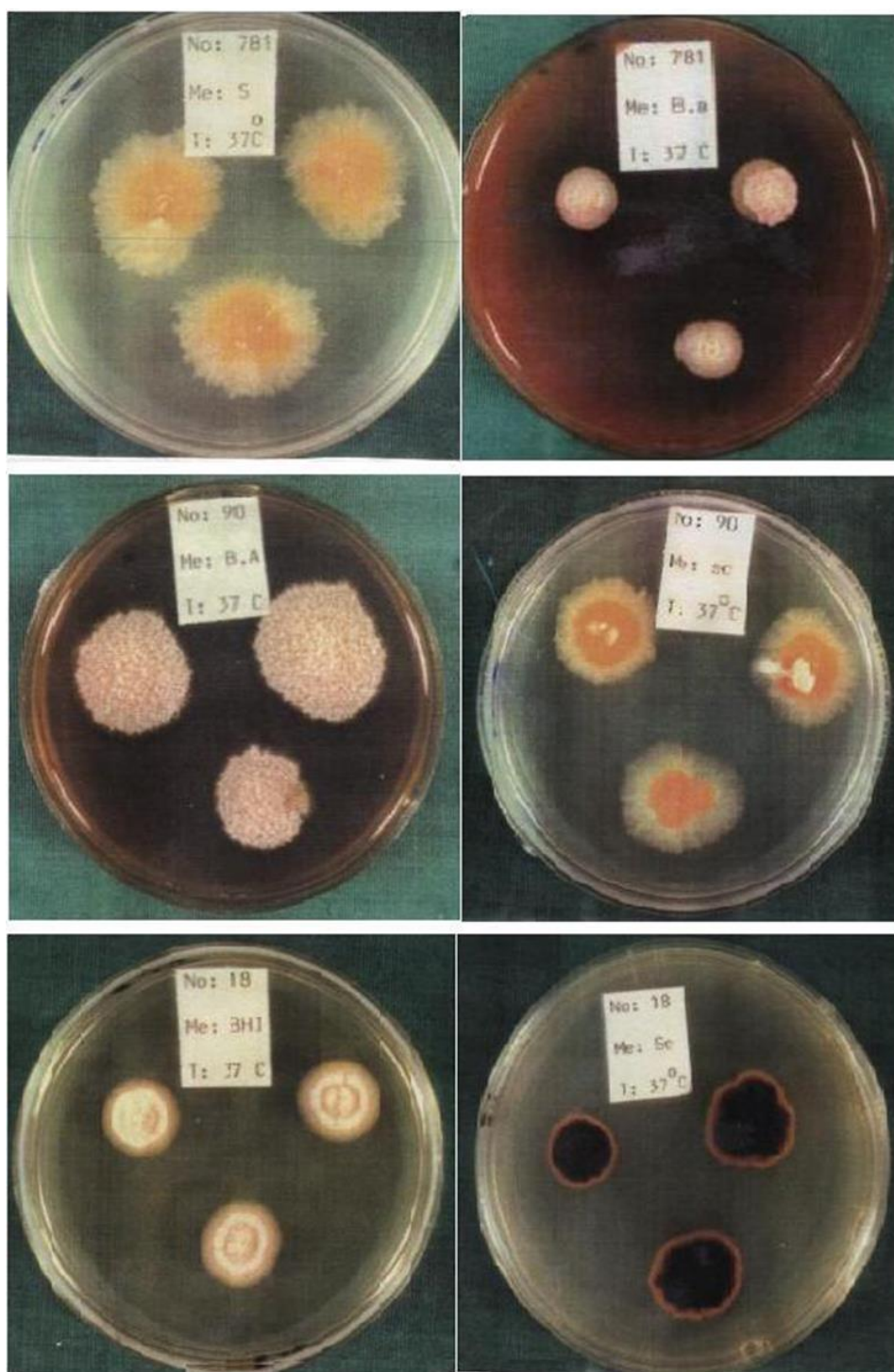


Fig. 1. The colonies of *Trichophyton verrucosum* at different media after 4 weeks

There were differences between protein patterns of supernatant and pellet in two bands. 14 protein bands with different molecular weights were observed in supernatant. In pellet of samples, 16 protein bands were detected which were the same as supernatant bands (Fig 2) and the molecular weight of two remainders were 38020 and 34670 Da (Table 1). The gel was scanned and the density of proteins were determined (Fig 3), protein standard curve was shown in Fig 4.

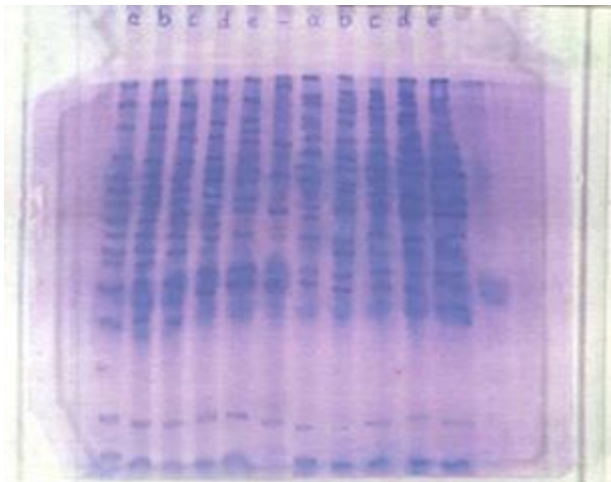


Fig. 2. Left to right a, b, c, d, e respectively: Supernatant of samples, standard, Pellet of samples

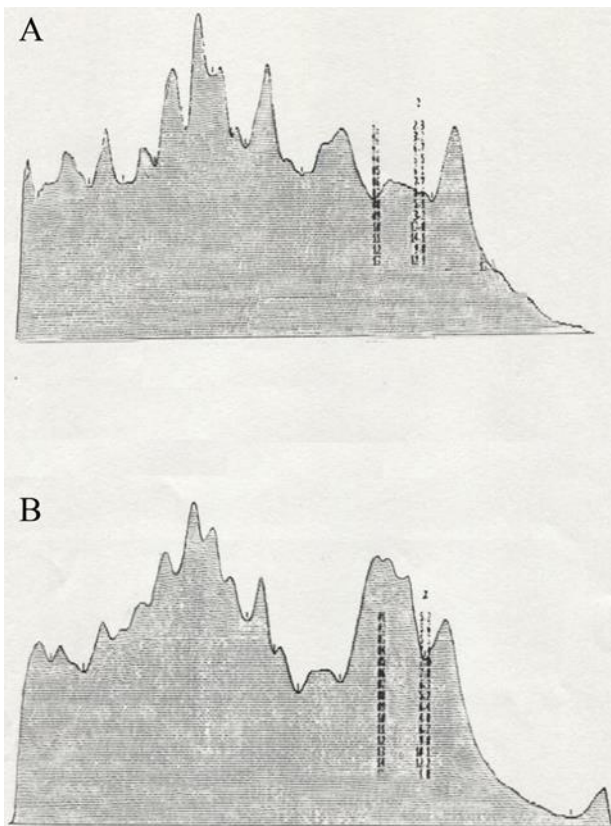


Fig. 3. Scanning of **A:** supernatant SDS-PAGE; **B:** pellet SDS-PAGE

Table 1. The molecular weights of proteins in supernatant and pellet

Mol Weights	Sample No									
	1		2		3		4		5	
	S	P	S	P	S	P	S	P	S	P
92250	+	+	+	+	+	+	+	+	+	+
81280	+	+	+	+	+	+	+	+	+	+
74990	+	+	+	+	+	+	+	+	+	+
72440	+	+	+	+	+	+	+	+	+	+
70790	+	+	+	+	+	+	+	+	+	+
63100	+	+	+	+	+	+	+	+	+	+
60000	+	+	+	+	+	+	+	+	+	+
56890	+	+	+	+	+	+	+	+	+	+
51880	+	+	+	+	+	+	+	+	+	+
48420	+	+	+	+	+	+	+	+	+	+
44150	+	+	+	+	+	+	+	+	+	+
41680	+	+	+	+	+	+	+	+	+	+
38020	-	+	-	+	-	+	-	+	-	+
34670	-	+	-	+	-	+	-	+	-	+
29150	+	+	+	+	+	+	+	+	+	+
12730	+	+	+	+	+	+	+	+	+	+

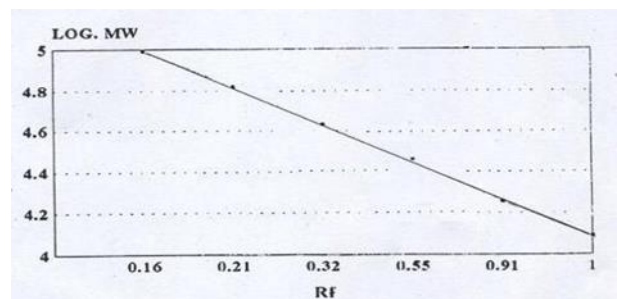


Fig. 4. Standard curve

DISCUSSION

Trichophyton verrucosum is an important zoophilic dermatophyte that causes acute dermatophytosis in human and animals [16].

This investigation was based on differences of morphology and virulence of isolates that were probably related to their proteins, but SDS-PAGE of samples showed that there were similarities in protein patterns of *T. verrucosum* isolates. On the basis of Tucker and Noble detection there was great similarity in all protein patterns of clinical isolates and no consistent differences were seen. Moreover, no differences were observed between the typical and dysgenic form of *Microsporum canis* [12]. The presence of bands 63100, 70700 and 92250 da in *T. verrucosum* and absence of them in *Microsporum canis* can probably distinguish it from other dermatophytes and specific proteins of *T. verrucosum* can be determined. On the basis of G. Grzywnowicz et al reports, *T. verrucosum* secretes enzymes into the growth medium and this strong enzymatic activity of the extracellular type of proteases is largely responsible for the relatively quick and extensive pathogenic changes. The other characterization of proteolytic enzymes of *T. gallinae* and *T. verrucosum* showed that their

properties were in many respects similar to the enzymatic activities of other dermatophytes. Therefore it would appear that like other dermatophytes a complex of several proteolytic enzymes exist [17]. Therefore the traces of protein patterns obtained were not as clear as those commonly obtained for bacteria and this may be due to the powerful proteases possessed by these fungi which were not entirely suppressed by the anti proteolytic cocktail and low temperatures employed [12].

It is concluded that different morphology and pathogenesis of *T. verrucosum* isolates may be related to enzymatic activity. Also existence of pigment may cause extensive pathogenic changes, for example *Vangiella dermatidis* and *Cryptococcus neoformance*. *Cryptococcus neoformance* without melanin shows slight pathogenesis in mouse [18]. Anyhow this is the first study about differentiation of *T. verrucosum* proteins in Iran and is introduced as protein pattern of this fungus.

REFERENCES

- 1.D.H.Howard, Fungi Pathogenic for Humans and Animals ,New York: M. Dekker; (1985).
- 2.K.J. Kwon-Chung, J.E. Bennet, Medical Mycology. Pennsylvania: Lea & Febiger; 105, 1992.
- 3.M.G. Jones, W.C. Noble, *J. Gen. Microbiol.*; **128**(5),1101 (1982).
- 4.E. Oborilova, A. Rybnikar, *Mycoses*, **48**(3) 187 (2005).
- 5.F.J .Cabanes, *Revista Iberoamericana de Micología*. 104 (2000).
- 6.R.Chermette, L.Ferrero, J.Guillot, *Mycopathologia*, **166**, 385 (2008).
- 7.H.E. Jones, J.H. Reinhardt, M.G.Rinaldi, *Arch. Dermatol.*; **109**(6), 840 (1974).
- 8.A.Rybnikar, J. Chumela, V.Vrzal , *Vet. Med. (Praha)* ;**34**(2):97 (1989).
- 9.A. Rybnikar, J. Chumela, V.Vrzal, V.Krupka, *Mycoses*, **34**(9-10), 433 (1991).
- 10.A. Rybnikar, V. Vrzal, J.Chumela, *Vet. Med. (Praha)* **36**(10),593 (1991).
- 11.G.Apodaca, J.H.McKerrow, *Infect .Immun.* **57**(10), 3072 (1989).
- 12.W.D. Tucker, W.C. Noble, *J. Med. Vet. Mycol.*, **28**(2),117 (1990).
- 13.T.G.Cooper, Electrophoresis. Tools of Biochemistry: Wiley; 194, 1977.
- 14.S.F.Grappel, C.T. Bishop, F. Blank,. *Bacteriol. Rev.*; **38**(2), 222 (1974).
- 15.B.D. Hames, D. Rickwood, A Practical Approach: Oxford University, 22 (1998).
- 16.H.C. Korting, H.Zienicke, *Mycoses*, **33**(2), 86 (1990).
- 17.G.Grzywnowicz, J.Lobarzewski, K.Wawrzkiwicz, T.Wolski, *J. Med. Vet. Mycol.*, **27**(5), 319 (1989).
- 18.G.m. Gow NARaG,.Cell walls and Cell membranes. The growing fungus. UK: Chapman &Hall; 41, 1995.

ИЗСЛЕДВАНЕ НА ПРОТЕИНИ ОТ *TRICHOPHYTON VERRUCOSUM* ЧРЕЗ ЕЛЕКТРОФОРЕЗА В НАТРИЕВ ДОДЕЦИЛ СУЛФАТ - ПОЛИАКРИЛАМИДЕН ГЕЛ (SDS-PAGE)

З. Абедиан¹, А.Р. Кхосрави², А.Р. Месбах³, Ф. Абедиан^{4*}

¹ Изследователски център по клетъчна и молекулярна биология, Медицински университет Бабол, Бабол, Иран

² Катедра по микробиология, Факултет по ветеринарна медицина, Техерански университет, Техеран, Иран

³ Катедра по биохимия, Медицински факултет, Университет Тарбиат модарес, Техеран, Иран

⁴ Катедра по имунология, Университет по медицински науки Мазадаран, Сари, Иран

Получена на 2 януари, 2014 г.; коригирана на 9 февруари, 2014 г.

Trichophyton verrucosum е един от най-честите дерматофити, който паразитира в кератинизирани тъкани на хора и животни. Това проучване сравнява протеините на пет разновидности на *Trichophyton verrucosum*, които са получени от хора и животни. Най-напред, те се култивират на специфични среди по-отделно и се инкубират при 37 °C в продължение на един месец. За получаване на протеинови екстракти, колонииите от гъбички се прехвърлят в течна среда Sabouraud и количеството на протеини се определя по метода на Bradford след растежа на гъбичките. Проведена бе SDS – PAGE електрофореза с разделящ 13% полиакриламиден гел и периодична буферна система за анализ за протеин . Кумазиново синьо G250 се използва за оцветяване на гела и се появяват различни ивици . Гелът се сканира с денситометър Helena за протеинови модели. Четиринадесет протеинови ивици с различни молекулни тегла между 12730-92250 Dalton бяха открити в супернатантата на пробите. В допълнение към тези 14 ивици се наблюдават две ивици (38 020 и 34 670 Da) в утайката на пробите. Въпреки различната морфология на колонииите, не са установени разлики между двете супернатанти както една от друга, така и за пелети от петте *T. verrucosum* изолати.

BULGARIAN CHEMICAL COMMUNICATIONS

Instructions about Preparation of Manuscripts

General remarks: Manuscripts are submitted in English by e-mail or by mail (in duplicate). The text must be typed double-spaced, on A4 format paper using Times New Roman font size 12, normal character spacing. The manuscript should not exceed 15 pages (about 3500 words), including photographs, tables, drawings, formulae, etc. Authors are requested to use margins of 3 cm on all sides. For mail submission hard copies, made by a clearly legible duplication process, are requested. Manuscripts should be subdivided into labelled sections, e.g. **Introduction, Experimental, Results and Discussion**, etc.

The title page comprises headline, author's names and affiliations, abstract and key words.

Attention is drawn to the following:

a) **The title** of the manuscript should reflect concisely the purpose and findings of the work. Abbreviations, symbols, chemical formulas, references and footnotes should be avoided. If indispensable, abbreviations and formulas should be given in parentheses immediately after the respective full form.

b) **The author's** first and middle name initials, and family name in full should be given, followed by the address (or addresses) of the contributing laboratory (laboratories). **The affiliation** of the author(s) should be listed in detail (no abbreviations!). The author to whom correspondence and/or inquiries should be sent should be indicated by asterisk (*).

The abstract should be self-explanatory and intelligible without any references to the text and containing not more than 250 words. It should be followed by key words (not more than six).

References should be numbered sequentially in the order, in which they are cited in the text. The numbers in the text should be enclosed in brackets [2], [5, 6], [9–12], etc., set on the text line. References, typed with double spacing, are to be listed in numerical order on a separate sheet. All references are to be given in Latin letters. The names of the authors are given without inversion. Titles of journals must be abbreviated according to Chemical Abstracts and given in italics, the volume is typed in bold, the initial page is given and the year in parentheses. Attention is drawn to the following conventions:

a) The names of all authors of a certain publications should be given. The use of “*et al.*” in

the list of references is not acceptable.

b) Only the initials of the first and middle names should be given.

In the manuscripts, the reference to author(s) of cited works should be made without giving initials, e.g. “Bush and Smith [7] pioneered...”. If the reference carries the names of three or more authors it should be quoted as “Bush *et al.* [7]”, if Bush is the first author, or as “Bush and co-workers [7]”, if Bush is the senior author.

Footnotes should be reduced to a minimum. Each footnote should be typed double-spaced at the bottom of the page, on which its subject is first mentioned.

Tables are numbered with Arabic numerals on the left-hand top. Each table should be referred to in the text. Column headings should be as short as possible but they must define units unambiguously. The units are to be separated from the preceding symbols by a comma or brackets.

Note: The following format should be used when figures, equations, etc. are referred to the text (followed by the respective numbers): Fig., Eqns., Table, Scheme.

Schemes and figures. Each manuscript (hard copy) should contain or be accompanied by the respective illustrative material as well as by the respective figure captions in a separate file (sheet). As far as presentation of units is concerned, SI units are to be used. However, some non-SI units are also acceptable, such as °C, ml, l, etc.

The author(s) name(s), the title of the manuscript, the number of drawings, photographs, diagrams, etc., should be written in black pencil on the back of the illustrative material (hard copies) in accordance with the list enclosed. Avoid using more than 6 (12 for reviews, respectively) figures in the manuscript. Since most of the illustrative materials are to be presented as 8-cm wide pictures, attention should be paid that all axis titles, numerals, legend(s) and texts are legible.

The authors are asked to submit **the final text** (after the manuscript has been accepted for publication) in electronic form either by e-mail or mail on a 3.5” diskette (CD) using a PC Word-processor. The main text, list of references, tables and figure captions should be saved in separate files (as *.rtf or *.doc) with clearly identifiable file names. It is essential that the name and version of

the word-processing program and the format of the text files is clearly indicated. It is recommended that the pictures are presented in *.tif, *.jpg, *.cdr or *.bmp format, the equations are written using "Equation Editor" and chemical reaction schemes are written using ISIS Draw or ChemDraw programme.

The authors are required to submit the final text with a list of three individuals and their e-mail addresses that can be considered by the Editors as potential reviewers. Please, note that the reviewers should be outside the authors' own institution or organization. The Editorial Board of the journal is not obliged to accept these proposals.

EXAMPLES FOR PRESENTATION OF REFERENCES

REFERENCES

1. D. S. Newsome, *Catal. Rev.–Sci. Eng.*, **21**, 275 (1980).
2. C.-H. Lin, C.-Y. Hsu, *J. Chem. Soc. Chem. Commun.*, 1479 (1992).
3. R. G. Parr, W. Yang, *Density Functional Theory of Atoms and Molecules*, Oxford Univ. Press, New York, 1989.
4. V. Ponec, G. C. Bond, *Catalysis by Metals and Alloys* (Stud. Surf. Sci. Catal., vol. 95), Elsevier, Amsterdam, 1995.
5. G. Kadinov, S. Todorova, A. Palazov, in: *New Frontiers in Catalysis* (Proc. 10th Int. Congr. Catal., Budapest, 1992), L. Guzzi, F. Solymosi, P. Tetenyi (eds.), Akademiai Kiado, Budapest, 1993, Part C, p. 2817.
6. G. L. C. Maire, F. Garin, in: *Catalysis. Science and Technology*, J. R. Anderson, M. Boudart (eds), vol. 6, Springer-Verlag, Berlin, 1984, p. 161.
7. D. Pocknell, *GB Patent 2 207 355* (1949).
8. G. Angelov, PhD Thesis, UCTM, Sofia, 2001.
9. JCPDS International Center for Diffraction Data, Power Diffraction File, Swarthmore, PA, 1991.
10. *CA* **127**, 184 762q (1998).
11. P. Hou, H. Wise, *J. Catal.*, in press.
12. M. Sinev, private communication.
13. <http://www.chemweb.com/alchem/articles/1051611477211.html>.

CONTENTS

A. Gharib, N. Noroozi Pesyan, M. Jahangir, M. Roshani, J. (Hans) W. Scheeren, L. Bakhtiari, S. Mohadeszadeh, Sh. Lagzian, S. Ahmadi, Heteropolyacids accelerated multi-component synthesis of <i>N</i> -phenylquinazolin-4-amines by using silica-supported Preyssler nanoparticles in green solvent	215
A. Gharib, B. R. Hashemipour Khorasani, M. Jahangir, M. Roshani, L. Bakhtiari, S. Mohadeszadeh, S. Ahmadi, Preyssler heteropolyacid supported on nano-SiO ₂ , H ₁₄ [NaP ₅ W ₃₀ O ₁₁₀]/SiO ₂ : a green and reusable catalyst in the synthesis of polysubstituted quinolines.....	223
V. N. Atanasov, S. S. Stoykova, Y. A. Goranova, A. N. Nedzhib, L. P. Tancheva, Ju. M. Ivanova, I. N. Pantcheva, Preliminary study on <i>in vivo</i> toxicity of monensin, salinomycin and their metal complexes	233
D. Kumar, A. Kumar, D. Dass, Syntheses, structural and biological studies of Mn(II), Cu(II), Zn(II), Fe(III) and MoO ₂ (VI) complexes of a tridentate OOS donor thiazolidin-4-one	238
A. Ahmadi, Synthesis, characterization and biological evaluation of some novel Benzimidazole derivatives	245
Sh. Feng, T. Sun, B. Lu, Q. Cai, Synthesis of dimethyl carbonate from urea and methanol catalyzed by iron-chloride ionic liquid	253
B. A. Fil, C. Özmetin, M. Korkmaz, Characterization and electrokinetic properties of montmorillonite	258
D. Shahabi, M. A. Amrollahi, A. Mobinikhaledi, Synthesis of some novel and water-soluble 2,4,6-substituted 3,5-dihydroxymethylpyridines	264
V. D. Mitic, V. P. Stankov-Jovanovic, M. D. Ilic, P. J. Vasiljevic, A. Lj. Zabar, G. S. Stojanovic, The antioxidant, hemolytic and cholinesterase inhibition properties of <i>Galium verum</i> L. and <i>Tragopogon pratensis</i> subsp. <i>pratensis</i>	269
N. Djordjevic, D. Djordjevic, M. Miljkovic, S. Urosevic, Activated carbon from cotton waste as an adsorbent in the purification process of azo-dyes	277
D. Stoychev, E. Dobрева, N. Razkazov, M. Stoycheva, N. Koteva, Electroless deposition of composite Co-P-diamond layers and their polishing properties	283
B. Ivanov, B. Dimitrova, D. Dobrudzhaliev, Optimal design and planning of biodiesel supply chain considering crop rotation model. Part 1. Mathematical model formulation of the problem	294
B. Ivanov, B. Dimitrova, D. Dobrudzhaliev, Optimal design and planning of biodiesel supply chain considering crop rotation model. Part 2. Location of biodiesel production plants on the Bulgarian scale	306
H. A. Attia, A. L. Aboul-Hassan, M. A. M. Abdeen, A. El-Din Abdin, MHD flow of a dusty fluid between two infinite parallel plates with temperature dependent physical properties under exponentially decaying pressure gradient	320
B. Adinew, Physico-chemical properties of <i>Trichilia emetica</i> seeds oil and its comparison with some selected oilseed oils	330
B. Adinew, Biodiesel production from <i>Trichilia emetica</i> seeds using <i>in-situ</i> transesterification	334
B. B. Mahapatra, S. N. Dehury, S. N. Chaulia, Polymetallic complexes part CIV synthesis, characterization and potential antibacterial study of dimeric & tetrameric complexes of Co(II), Ni(II) Cu(II), Zn(II), Cd(II) and Hg(II) with azodye ligands	339
H. Alinezhad, M. Zare, A convenient synthesis of benzimidazoles using sulfonated ordered nanoporous carbon as efficient solid catalyst	347
B. G. Tsyntsarski, B. N. Petrova, T. K. Budinova, N. V. Petrov, D. K. Teodosiev, Removal of phenol from contaminated water by activated carbon, produced from waste coal material	353
M. Ghasemi, M. H. Mirjalili, J. Hadian, Chemical profiles of the essential oil of wild and <i>in vitro</i> regenerated <i>Zataria multiflora</i> Boiss. (Lamiaceae)	362
Sv. M. Dyankova, A.O. Solak, Preparation and characterization of composite hydrocolloid films from sodium alginate and high methoxyl pectin	368
R. Sanjeev, V. Jagannadham, R. Veda Vraath, Attenuation effect through methylene group: Part II	375
B. R. Tzaneva, The influence of temperature on the corrosion behaviour of high nitrogen austenitic stainless steel in chloride media	378
A. Ghorbani-Choghamarani, M. Hajjami, M. Norouzi, A. Amiri, Poly-(4-vinylpyridinium nitrate) and silica sulfuric acid (SiO ₂ -OSO ₃ H): an efficient and metal-free oxidizing media for the oxidation of 1,4-dihydropyridine and urazole derivatives	384
L. H. Naneva, I. D. Dimitrov, I. P. Bangov, I. A. Doychinova, Allergenicity prediction by partial least squares-based discriminant analysis	389
Z. Glavcheva, G. Lalev, Chr.Boiadjieva, I. Glavchev, Effect of sulfate containing admixture on C3A hydration ..	409
R. Balkanska, I. Karadjova, M. Ignatova, Comparative analyses of chemical composition of royal jelly and drone brood	412
S. B. Dimitrijević, Ml. B. Mirić, Vl. K. Trujić, B. N. Madić, St. P. Dimitrijević, Recovery of precious (Au, Ag, Pd, Pt) and other Metals by e-scrap processing	417
T. Marsagishvili, M.Machavariani, G.Tatishvili, E.Ckhakaia, Thermodynamic analysis of processes with the participation of zeolites	423
	437

Z. Abedian, A.R. Khosravi, A.R. Mesbah, F. Abedian, Investigation of Trichophyton verrucosum proteins by sodium dodecyl sulfate polyacrylamide gel electrophoresis (SDS-PAGE)	431
INSTRUCTIONS TO THE AUTHORS.....	435

СЪДЪРЖАНИЕ

A. Гариб, Н. Н. Песян, М. Джахангир, М. Рошани, Й. (Ханс) В. Схеерен, Л. Бахтиари, С. Мохадезаде, Ш. Лагзян, С. Ахмади, Ускорена много-компонентна синтеза на N-фенилхиназолин-4-амини използвайки Preyssler'ови наночастици върху носител от силициев диоксид и хетерополикиселини в "зелен" разтворител	222
A. Гариб, Б.Р.Х. Хоразани, М. Джахангир, М. Рошани, Л. Бахтиари, С. Мохадезаде, С. Ahmadi, Preyssler'ови хетерополикиселини $H_{14}[NaP_5W_{30}O_{110}]$, нанесени върху наночастици от силициев диоксид: зелен и рециклируем катализатор за синтезата на поли-заместени хинолини.....	232
B. H. Атанасов, С. С. Стойкова, Я. А. Горанова, А. Н. Неджиб, Л. П. Танчева, Ю. М. Иванова, И. Н. Панчева, <i>In vivo</i> токсичност на монензин, салиномицин и техни метални комплекси (предварително изследване).....	237
Д. Кумар, А. Кумар, Д. Дас, Синтези, сруктурни и биологични изследвания на комплекси на Mn(II), Cu(II), Zn(II), Fe (III) и MoO ₂ (VI) с донор от тридентат-4-он	244
A. Ахмади, Синтеза, характеристики и биологична оценка на някои нови производни на бензимидазола ...	252
Ш. Фенг, Т. Сун, Б. Лу, К. Цай, Синтеза на диметил-карбонат от карбамид и метанол, катализирана от йонна течност и железен трихлорид)	257
Б. А. Фил, Дж. Йозметин, М. Коркмаз, Охарактеризиране и електрокинетични свойства на монтморилонит.....	263
Д. Шахаби, М. А. Амралахи, А. Мобинихаледи, Синтеза на някои нови водо-разтворими 2,4,6-заместени 3,5-дихидрометил-пиридили	268
B. Д. Митич, В. П. Станков-Йованович, М. Д. Илич, П. Й. Васильевич, А. Л. Забар, Г. С. Стоянович, Антиоксидантни и хемолитични свойства и инхибиране на холинестераза чрез <i>Galium verum</i> L. и <i>Tragorogon pratensis</i> subsp. <i>pratensis</i>	276
H. Джорджевич, Д. Джорджевич, М. Милькович, С. Урошевич, Активен въглен от памучни отпадъци като адсорбент при пречистването от азо-багрила	282
Д. Стойчев, Е. Добрева, Н. Разказов, М. Стойчева, Н. Котева, Безелектролизно отлагане на композитни слоеве от кобалт, фосфор и диаманти и техните полиращи свойства	293
Б. Иванов, Б. Димитрова, Д. Добруджалиев, Оптимално проектиране и планиране на ресурсно осигурителната верига за производство и доставки на биодизел с отчитане на сеитбообращението. Част 1. Формулировка на математичния модел	305
Б. Иванов, Б. Димитрова, Д. Добруджалиев, Оптимално проектиране и планиране на ресурсно осигурителната верига за производство и доставки на биодизел с отчитане на сеитбообращението. Част 2. Определяне на местоположението на биорафинериите за територията на България	319
X. A. Атия, А. Л. Абул-Хасан, М. А. М. Абдин, А. Ел-Дин Абдин, Магнитохидродинамично течение на запрашен флуид между две безкрайни успоредни плоскости с температурно зависими физични свойства при експоненциално затихващ градиент на налягането	329
Б. Адиню, Физико-химични свойства на маслодайни семена от <i>Trichilia emetica</i> и сравняване с някои избрани растителни масла	333
Б. Адиню, Получаване на биодизел от семена на <i>Trichilia emetica</i> чрез <i>in-situ</i> трансестерификация	338
Б. Б. Маханатра, С. Х. Дехури, С. Н. Чаулиа, Полимерни комплекси част CIV синтеза, охарактеризиране и антибактериално изследване на димерни и тетрамерни комплекси на Co(II), Ni(II), Cu(II), Zn(II), Cd(II) и Hg(II) с азобагрилни лиганди	346
X. Алинежад, М. Заре, Удобна синтеза на бензимидазоли със сулфониран подреден нанопорьозен въглерод като ефикасен твърд катализатор	352
Б. Г. Цинцарски, Б. Н. Петрова, Т. К. Будинова, Н. В. Петров, Д. К. Теодосиев, Извличане на фенол от замърсени води чрез активен въглен, получен от отпадни продукти от преработката на въглища	361
М. Гасеми, М. Х. Мирджалили, Дж. Хадиан, Химически профили на етерично маслона диворастващи и <i>in-vitro</i> регенерирани <i>Zataria multiflora</i> BOISS. (LAMIACEAE)	367
Св. М. Дянкова, А. О. Солак, Приготвяне и охарактеризиране на композитни филми от натриев алгинат и метоксилиран пектин.....	374
P. Санджеев, В. Джаганнадхам, P. Веда Вратх, Ефект на ослабване на метиленови групи: Част II.....	377

Б. Р. Цанева, Влияние на температурата върху корозионното поведение на аустенитна неръждаема стомана с високо съдържание на азот в хлоридни среди.....	383
А. Горбани-Чогамарани, М. Хаджами, М. Нороузи, Ар. Амири, Поли-(4-винилпиридиниев нитрат) и силициев диоксид-сярна киселина (SiO ₂ -OSO ₃ H): ефективна и безметална среда за окисление на 1,4-дихидропиридин и производни на уразола	388
Л. Х. Нанева, И. Д. Димитров, И. П. Бангов, И. А. Дойчинова, Оценка на алергенност чрез дискриминантен анализ по метода на парциалните най-малки квадрати	396
З. Главчева, Г. Лалев, Хр. Бояджиева, И. Главчев, Влияние на сулфатсъдържаща добавка върху хидратацията на СЗА	411
Р. Балканска, И. Караджова, М. Игнатова, Сравнителни анализи на химичния състав на пчелно млечиче и пило от търтеи	416
С. Б. Димитриевич, Мл. Б. Мирич, Вл.К. Тружич, Б. Н Мадич, С. П. Димитриевич,, Добиване на ценни (Au, Ag, Pd, Pt) и други метали чрез e-scrap процес	422
Т. Марсагишвили, М. Мачавариани, Г. Татишвили, Е. Цхакария, Термодинамичен анализ на процеси с участие на зеолити	430
З. Абедиан, А.Р. Кхосрави, А.Р. Месбах, Ф. Абедиан Изследване на протеини от <i>Trichophyton verrucosum</i> чрез електрофореза в натриев додецил сулфат -полиакриламиден гел (SDS-PAGE)	434
ИНСТРУКЦИЯ ЗА АВТОРИТЕ	435